Contents

OVERVIEW OF MUON COOLING*

Daniel M. Kaplan,† Physics Dept., Illinois Institute of Technology, Chicago, IL 60616, USA

Abstract

Muon cooling techniques are surveyed, along with a concise overview of relevant recent R&D.

INTRODUCTION

Muon cooling enables muon colliders and neutrino factories, and enhances low-energy muon experiments. At high energies, use of muons rather than electrons substantially suppresses radiative processes ($\propto m_{\rm lepton}^{-4}$), allowing acceleration and collision in rings — greatly reducing lepton-collider footprint and cost — as well as more-monochromatic collisions and feasibility at much higher energies (10 TeV or more) [1]. While muon decay (mean lifetime = 2.2 μs) complicates beam handling, it enables stored-muon-beam neutrino factories, the most capable technique for precision measurements of neutrino oscillation [2].

Figure 1 schematically compares these two types of high-energy muon facility, for both of which the performance and cost depend on how well a muon beam can be cooled. They are seen to have much in common:

- In both designs, a high-intensity (MW-scale), medium-energy "proton driver" illuminates a high-power capable target in a heavily shielded enclosure, copiously producing charged pions, which decay into intense broadband muon beams.
- Bunching and "phase rotation" (reducing the energy spread by accelerating slower muon bunches and decelerating faster ones) prepare the muon beams to be cooled. The "initial cooling" stage completes the facility "front end" [3], which is similar if not identical in the two cases.
- After cooling, the beams are accelerated to the desired energy and injected into storage rings, where they circulate for $O(10^3)$ turns.

Rubbia has emphasized the importance of muon colliders for Higgs-boson studies [4]. To test for physics beyond the standard model (SM) requires sub-percent measurements of Higgs branching ratios as well as a precision scan of the resonance lineshape, possible only with s-channel production at a 125 GeV muon collider. Studies of the Higgs self-coupling are also needed, requiring a $\gtrsim$ TeV muon collider.[1] Hints are emerging for possible new physics in the $\gtrsim 2$ TeV region [5]. Above $\approx$ 1–2 TeV, the muon collider is arguably the most capable and cost-effective lepton collider [6].

A natural muon collider staging plan thus emerges [6, 7]:

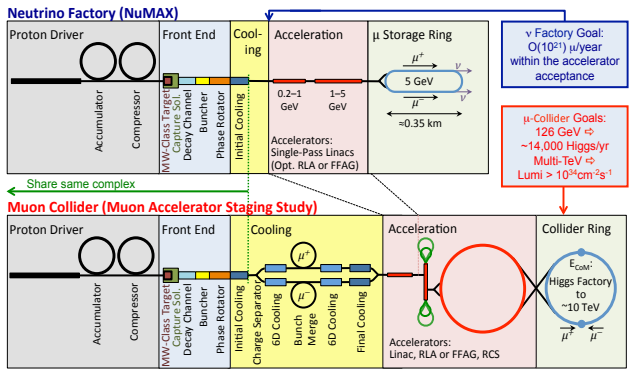

Figure 1: Neutrino factory (top) / muon collider (bottom) comparison. The "front end" (muon production, collection, bunching, phase rotation, and initial cooling) can be very similar for both. It is followed in a neutrino factory by acceleration of the muons to multi-GeV energy and injection into a storage ring, with long straight sections in which muon decay forms intense neutrino beams aimed at near and far detectors. For a muon collider, it is followed by 6-dimensional cooling, bunch coalescence, acceleration (e.g., to 62.5 GeV for a precision "Higgs Factory"), and injection into a collider ring, where μ^+ and μ^- bunches circulate for $\sim 10^3$ turns.

1. Start by building a neutrino factory,[2] which can do competitive physics with no cooling, and ultimately requires only "initial" cooling by a factor of ~ 10 in six-dimensional (6D) emittance.
2. Then upgrade the facility to a 125 GeV "Higgs Factory" muon collider, requiring $O(10^6)$ or more emittance reduction.
3. Then upgrade to a $\gtrsim$ TeV collider.

At low energies, cooling can give smaller and more intense stopping-muon beams [8, 9]. A subject of ongoing R&D at the Paul Scherrer Institute, it may enable enhanced studies of muonium spectroscopy, searches for muon–electron conversion and muonium–antimuonium oscillations, and a test of antimuon gravity [10], among other measurements [11].

BRIEF HISTORY

Muon colliders have been discussed since the 1960s [12, 13]. The key idea enabling high luminosity — ionization cooling — came later [14, 15], and its theory was not fully understood until the 1990s [16].

In the mid-1990s the ("grass roots") Muon Collider Collaboration formed, producing a report on muon colliders

* Work supported by DOE via the Muon Accelerator Program.

† kaplan@iit.edu

[1] As time passes and nothing below 1 TeV besides the Higgs is seen at LHC, comparable measurements with electrons seem increasingly unlikely.

[2] The nuSTORM short-baseline muon strorage-ring facility, aimed at precision cross-section measurements and sterile-neutrino searches, requires no cooling and no new technology and has been proposed as an even earlier step [18].

ISBN 978-3-95450-174-8

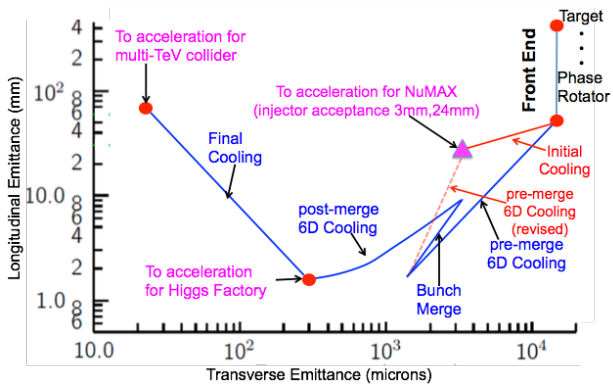

Figure 2: Cooling "trajectory" in longitudinal and transverse emittance, with red points showing MAP emittance goals.

for the 1996 Snowmass meeting [19]. The following year the neutrino factory concept was born [20], leading to a collaboration expansion and change of name (to the Neutrino Factory and Muon Collider Collaboration, NFMCC) [21], and stimulating a series of neutrino factory feasibility studies [22–25], workshops [26], and the development of the Muon Ionization Cooling Experiment [27], among others [28, 29]. In 2006 a directed effort to develop a site-specific muon collider proposal, the Muon Collider Task Force (MCTF) [30], was initiated at Fermilab. This led the DOE to request a concerted effort, the Muon Accelerator Program (MAP) [31], which began in 2011. Sadly, MAP is now a casualty of the P5 process [32] and is in the midst of a funding rampdown.

EMITTANCE GOALS

It is useful to enumerate briefly the emittance targets that have been identified for various physics goals. These are best understood in terms of "cooling trajectories" on the longitudinal vs. transverse normalized-emittance plane (Fig. 2) [33].

1. As mentioned, an initial neutrino factory configuration without cooling, producing $O(10^{20})$ neutrinos/yr, can be cost-effectively upgraded to $O(10^{21})$ neutrinos/yr (in the so-called NuMAX configuration) by adding an order of magnitude of 6D cooling [6]. This works together with a dual-use linac that accelerates protons from 3.0 to 6.75 GeV as part of the proton driver and then accelerates cooled muons from 1.25 to 5 GeV, requiring muon input transverse and longitudinal emittances of $\approx 3\pi$ mm·rad for full acceptance.

2. A Higgs Factory muon collider requires exquisite energy spread to support a precision Higgs-lineshape energy scan ($\Gamma^{SM}_{\rm Higgs} = 4$ MeV). The MAP goal is transverse/longitudinal emittances of $\approx 0.3/1.5\pi$ mm·rad, achieved in a series of "6D" cooling channels, enabling 5×10^{31} cm^{-2} s^{-1} luminosity and 5 MeV energy spread.

3. Above 1 TeV collision energy the MAP goal is transverse/longitudinal emittances of $\approx 0.025/70\pi$ mm·rad, enabling $\gtrsim 10^{34}$ cm^{-2} s^{-1} luminosity. Following the 6D cooling channels, these parameters are achieved by means of "final cooling," incorporating significant transverse→longitudinal emittance exchange.

PRINCIPLES OF MUON COOLING

The short lifetime of the muon vitiates all beam-cooling methods currently in use.[3] However, a method almost uniquely applicable to the muon — ionization cooling [15] — seems equal to the challenge. In this, muons are made to pass through an energy absorber of low atomic number (Z) in a suitable magnetic focusing field; the normalized transverse emittance $\epsilon_{\perp,n}$ then obeys [16]

$$\frac{d\epsilon_{\perp,n}}{ds} \approx -\frac{1}{\beta^2}\left\langle\frac{dE_\mu}{ds}\right\rangle\frac{\epsilon_{\perp,n}}{E_\mu} + \frac{1}{\beta^3}\frac{\beta_\perp(0.014\,\text{GeV})^2}{2\,E_\mu m_\mu X_0}, \quad (1)$$

where βc, $\langle dE_\mu/ds\rangle$, $\beta_\perp$, m_μ, and X_0 are the muon velocity, average energy loss per unit length, betatron function at the absorber, muon mass, and absorber material radiation length. (This is the expression appropriate to the cylindrically symmetric case of solenoidal focusing, for which $\beta_x = \beta_y \equiv \beta_\perp$ and cooling occurs equally in the x-x' and y-y' phase planes.) The first term in Eq. 1 is the cooling term, and the second describes heating due to multiple scattering.[4] The heating term is minimized via small $\beta_\perp$ and large X_0 (low-Z absorber material). For a given cooling-channel design, an equilibrium emittance is reached when the heating and cooling terms balance, after which a revised design with lower $\beta_\perp$ is required if cooling is to continue.

Somewhat counterintuitively, the optimal momentum for cooling is found to be ≈ 200 MeV/c [16], near the *minimum* of the ionization energy-loss ("dE/dx") curve in matter [17]. This is a compromise between the heating effects of the "straggling tail" at higher momentum and the negative slope of the dE/dx curve below the ionization minimum (creating problematic, *positive* feedback for energy-loss fluctuations).

The physics of Eq. 1 is well established, yet engineering details — or poorly modeled tails of distributions — could profoundly affect ionization cooling-channel cost and performance. This motivates an effort to build and test a realistic section of cooling channel: the international Muon Ionization Cooling Experiment (MICE) [34], discussed in detail elsewhere [35].

STAGES OF MUON COOLING

Bunching and Phase Rotation

Before the muon beam is cooled one wants to reduce its $\sim 100\%$ initial energy spread. First an energy–time correlation is developed within an RF-free drift region, then the beam is bunched, then the faster bunches decelerated and

[3] I.e., electron and stochastic, laser cooling being in any case inapplicable to an object without internal degrees of freedom, and synchrotron radiation being negligible by virtue of the muon's large mass.

[4] There is a direct analogy to synchrotron-radiation cooling, in which energy loss likewise provides cooling, while the heating is caused by quantum fluctuations.

ISBN 978-3-95450-174-8

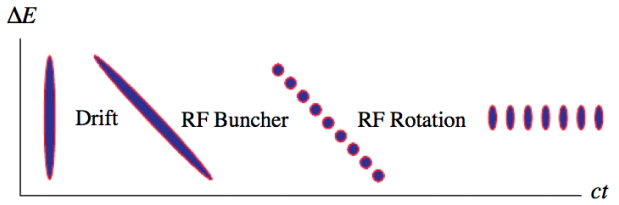

Figure 3: Cartoon of bunching and phase-rotation process.

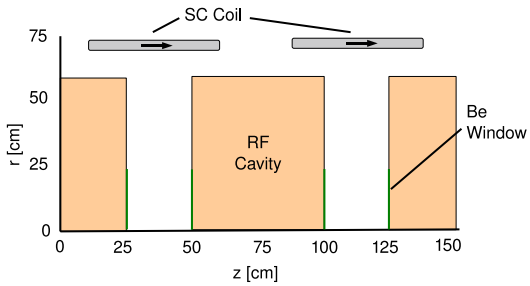

Figure 4: Lattice cell used for bunching and phase rotation (accelerating gradient doubled via thin Be cavity windows).

the slower ones accelerated ("phase-rotation") (Fig. 3) [3]. The lattice of Fig. 4 is used, with a series of RF cavities of decreasing frequency ranging from ≈ 500 down to 325 MHz.

Initial Cooling

Successful, purely transverse ionization-cooling lattices were developed by the year 2000 [36], when Neutrino Factory Feasibility Study II (FS2) was carried out [24]. The FS2 design employed two magnetic-field harmonics, allowing small $\beta_\perp$ to be achieved by working between the resulting "π" and "$\pi/2$" resonances. A simplified, more cost-effective design (Fig. 5) was adopted by the International Design Study for the Neutrino Factory (IDS-NF) [37]. In contrast to the bunching and phase rotation lattice of Fig. 4, in these cooling lattices, alternating solenoid-field directions prevent the buildup of a net canonical angular momentum due to energy loss and re-acceleration within a solenoidal field. (Since solenoids focus in both transverse directions, these lattices are generically referred to as "FOFO," in contrast to FODO alternating-gradient quadrupole lattices.)

The neutrino factory and muon collider designs can be better unified by employing a six-dimensional (rather than

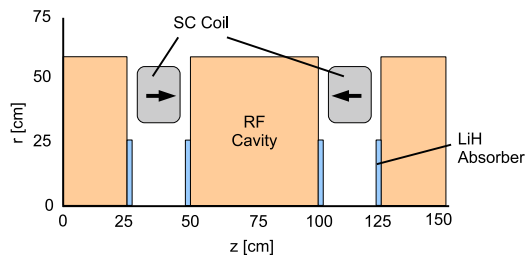

Figure 5: IDS-NF transverse cooling lattice cell, with alternating solenoids to create low-β regions between RF cavities and thin, Be-coated LiH absorbers as cavity windows.

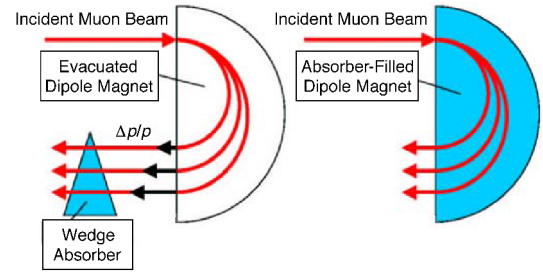

Figure 6: Two emittance exchange approaches: small beam with nonzero momentum spread is converted into more monoenergetic beam with transverse position spread. The reverse occurs in "Final Cooling." (Figure: Muons, Inc.)

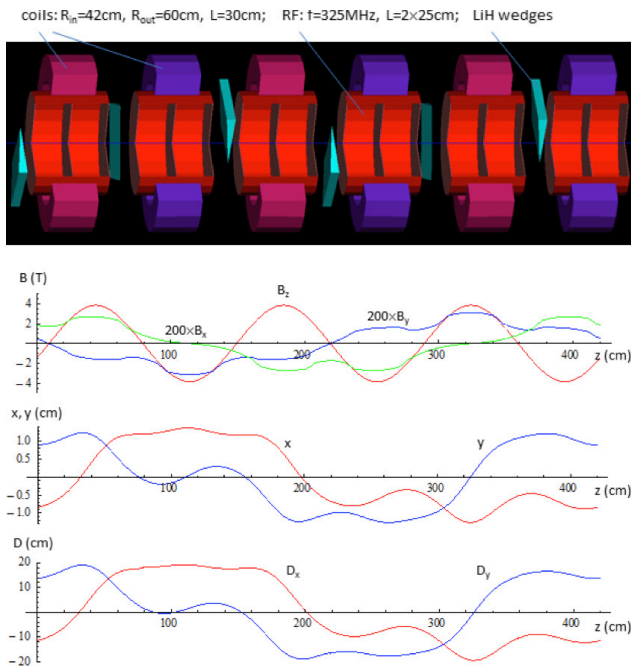

Figure 7: (top) HFOFO Snake lattice scheme, combining tilted solenoids with LiH-wedge and gaseous-hydrogen absorbers and RF cavities; (bottom) B_z, beam positions, and dispersion vs. distance along beam axis [38].

transverse) initial cooling lattice, which (as mentioned) also permits cost savings by allowing a dual-use (proton–muon) linac. The purely transverse ionization-cooling effect can be shared among the transverse and longitudinal phase planes in a lattice in which dispersion causes momentum-dependent path-length through an absorbing medium ("emittance exchange"), e.g., as depicted in Fig. 6. Since, at the large transverse emittance of the initial beam, charge separation would be challenging, a 6D cooling lattice that works simultaneously for both muon charge signs is desirable. This design challenge is met by the "HFOFO Snake" (Fig. 7) [3, 38], in which small tilts of the solenoids relative to the beam axis, in orientations that rotate about the beam axis by 120° per step, create a small, rotating-dipole field component. This

ISBN 978-3-95450-174-8

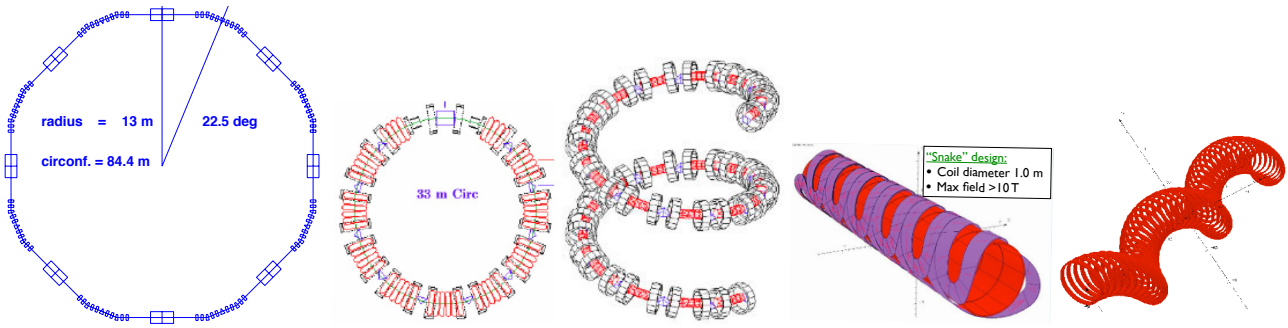

Figure 8: Examples of 6D cooling apparatus that have been shown to work in simulation: (left to right) quadrupole–dipole ring, "RFOFO" solenoid-focused ring, "RFOFO Guggenheim" helix, helical cooling channel (two versions).

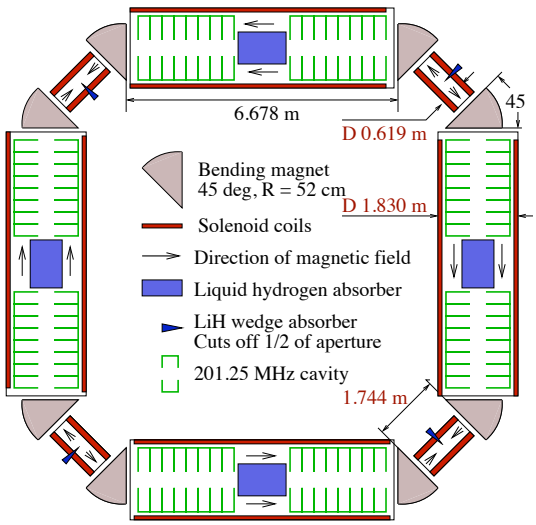

Figure 9: First successful 6D cooling design: Balbekov's "tetra" ring cooler [43].

creates periodic orbits and dispersion that are isomorphic, with a half-period offset, for the two charges.

Six-Dimensional Cooling

A high-luminosity Higgs Factory ($\mathcal{L} \gtrsim 10^{32}\,\mathrm{cm}^{-2}\,\mathrm{s}^{-1}$) or TeV muon collider ($\mathcal{L} \gtrsim 10^{34}\,\mathrm{cm}^{-2}\,\mathrm{s}^{-1}$) requires a cooling scheme that reduces both transverse and longitudinal emittances by an overall factor of 10^6 or more in 6D emittance. Various approaches to this goal [1, 39, 40] were developed by the NFMCC, MCTF, and two small R&D firms with SBIR/STTR funding: Muons, Inc. [41] and Particle-Beam Lasers (PBL) [42]. Under the MAP program [31], this work has been continued by many of the same people. Three approaches were shown to work in simulation (Fig. 8): rings, helices, and snakes (a fourth, the "Rectilinear FOFO," is discussed below). Like transverse-cooling lattices, most 6D-cooler designs employ superconducting-solenoid focusing and benefit from the ability of such solenoids to accommodate a large beam, generate low β, and focus simultaneously in both x and y, enabling compact lattices that minimize muon decay in flight.

The earliest successful example of a 6D cooling channel was the 4-sided solenoid-focused ring of Balbekov [36, 43], but it was so tightly packed as to lack space for beam injection and extraction (Fig. 9). This first "in principle" success led to the development of the approaches depicted in Fig. 8: rings with space allocated for the above functions [44, 45], and helices [46, 47], which can embody the symmetries of rings, but are open at the ends for beam ingress and egress.

Helical channels, through which each bunch passes only once, reduce beam loading on absorbers and RF cavities. They can also provide faster cooling via "tapering": increasing the focusing strength along the channel, thereby decreasing the equilibrium emittance as the beam is cooled. The Helical Cooling Channel (HCC), based on a Hamiltonian theory [46], uses a combination of "Siberian snake"-like helical dipole and solenoid fields; it also employs a continuous, high-pressure, gaseous-hydrogen absorber so as to minimize both the deleterious effects of windows and (via pressurized RF cavities, discussed below) the length of the channel. Following the HCC's invention, its (required) solenoid, helical dipole, and (desired, for increased acceptance) helical quadrupole field components were shown to arise naturally from a simple sequence of offset current rings (Fig. 8, far right) [48], which follow the winding path of the beam envelope around the helix [49]. Simulations of a series of HCCs have demonstrated cooling to 0.6/0.9 mm·rad emittances, close to the MAP Higgs Factory goal [49]. The helical geometry requires two sets of 6D cooling channels for a muon collider, one for each muon charge sign. The "HFOFO Snake" channel (Fig. 7) [38], the "least circular" of these approaches, as mentioned can simultaneously cool muons of both signs and would thus be followed by a charge separator in order to feed the 6D channels.

While helical designs have been shown to perform well, their engineering could be challenging. For example, "Guggenheim" channels could fill a large volume (Fig. 10) and require magnetic shielding between turns. This led to a search for alternatives. Surprisingly, a rectilinear geometry promising the same cooling performance was found [50], and its performance borne out by detailed simulation studies [51]. Figure 11 shows the geometry and a representative performance plot [52]; a 10^5 6D cooling factor is achieved,

ISBN 978-3-95450-174-8

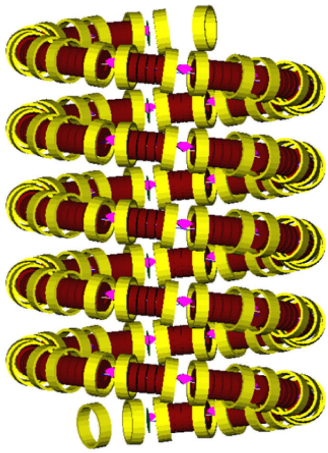

Figure 10: To-scale rendering of five periods of Guggenheim 6D cooler; vertical extent is about 20 m.

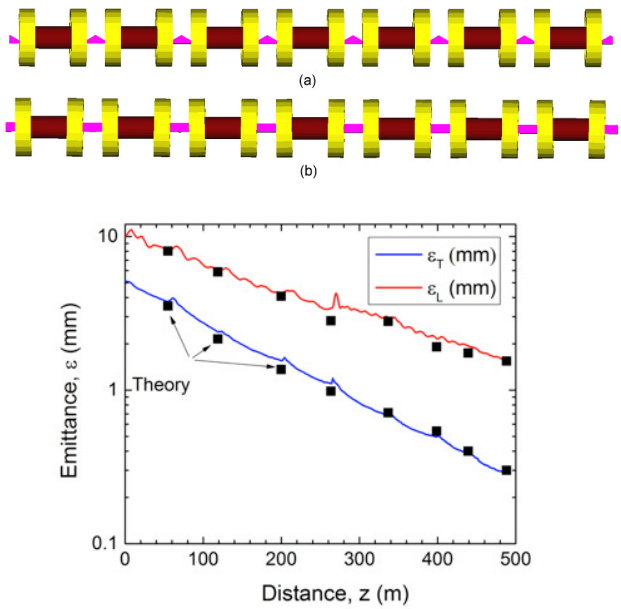

Figure 11: "Rectilinear FOFO" lattice scheme and example of its cooling performance [52].

with final emittances 0.28/1.5 mm·rad, exceeding the MAP Higgs Factory goal.

Final Cooling

After 6D cooling, at the lowest point of the Fig. 2 curve (labeled "To acceleration for Higgs Factory"), the transverse emittance is about an order of magnitude too large, and the muon bunches shorter than necessary, for a high-luminosity TeV collider; the 6D emittance is an order of magnitude larger than desired. In principle this gap can be closed with "final cooling" (Fig. 12) in extremely high-field (30–40 T), narrow-bore solenoids enclosing LH_2 absorbers, in which transverse cooling can be carried out as the muon momentum is allowed to fall towards the Bragg peak of the dE/dx curve [17], while the longitudinal emittance grows due to

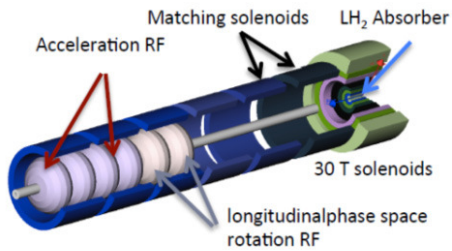

Figure 12: High-field-solenoid "final cooling" lattice cell.

dE/dx positive feedback. Such solenoids should be feasible using high-temperature superconductor (e.g., Bi-2223 tape) operated at LHe temperature. Despite promising initial results obtained [53] by a PBL-BNL magnet R&D effort, given magnetic force and quench issues, further R&D will be required in order to realize a complete magnet system. (Very high-field dipoles are also desired in muon collider rings in order to increase the average luminosity via smaller ring circumference, giving more collisions per muon lifetime.)

Such a channel has been shown in simulation to approach the MAP final-emittance goals, falling short by a factor ≈ 2 in transverse emittance if 30 T solenoids are used [54]. This emittance gap might be closed with the use of higher field. Alternative final-cooling ideas are also under study [55, 56]. These include reverse emittance exchange in wedge absorbers and transverse ionization cooling in quadrupole-focused channels [56], which can achieve $\beta^* < 1$ cm.

"Advanced" Cooling Ideas

While the scheme of Fig. 12, and others that have been studied within MAP, can move from the "Higgs Factory" emittance point towards larger longitudinal and smaller transverse emittances, they have not been shown to provide the higher luminosity along with small energy spread at the Higgs called for by Rubbia [4]. One scheme that could potentially satisfy Rubbia's requirements is Derbenev's "Phase-resonant Ionization Cooling" (PIC), which has been shown to work in principle but still requires a detailed aberration correction scheme to be worked out [57]. PIC is based on the "inverse" of slow extraction: a resonance is used to drive the beam towards small displacement and large angle, with ionization-cooling absorbers providing beam angular stabilization (Fig. 13). Other schemes for reaching smaller emittances have also been proposed [58–60]. Rubbia's goal provides an excellent challenge for next-generation studies.

FRICTIONAL COOLING

The schemes described above all work at momenta well above the dE/dx Bragg peak, and most operate at $\gamma\beta \approx 2$, near the ionization *minimum*. An entirely different approach seeks to exploit the much higher ionization energy-loss rate near the Bragg peak ($\gamma\beta \approx 0.01$) [17] but must cope with significant challenges (e.g., sufficiently rapid acceleration, making windows thin enough to overcome multiple scattering, and avoiding high-voltage breakdown in gas, or elec-

ISBN 978-3-95450-174-8

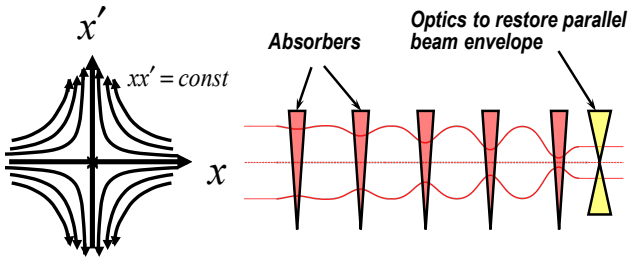

Figure 13: (Left) PIC-induced hyperbolic beam motion in horizontal plane; (right) PIC lattice concept.

tron multiplication in thin foils). This "frictional cooling" regime has been studied experimentally [61] and R&D continues [11,62]. A potential conceptual advance, the "particle refrigerator" [63], seeks to increase frictional cooling channel energy acceptance by two to three orders of magnitude, could lead to very compact high-flux muon sources, and may also be applicable to decelerating and cooling other particle species besides muons [64]. In contrast to the schemes discussed previously, by taking advantage of the *positive* slope of the dE/dx curve just below the Bragg peak, frictional cooling can cool directly in 6D, without emittance exchange.

R&D ISSUES

High-Field Solenoids

Since muon ionization cooling depends on strongly focusing muons as they traverse material, high-field magnets are a requirement for low emittance to be achieved. The 6D cooling channels studied by MAP achieve their goals using solenoids wound with NbTi or Nb_3Sn conductor. To go beyond those goals will require high-temperature (HTS) magnets (as already discussed in the "final cooling" context). The PBL-BNL progress on such magnets [53] (achieving 15 T — a world record for an all-HTS magnet) is thus quite encouraging and bodes well both for final cooling and for extension of existing 6D cooling-lattice designs to yet lower emittances. The continued development of such magnets is anticipated for other purposes [65] and will be closely watched by muon-cooling proponents.

RF Technology

A "cost driver" for muon accelerator facilities is RF acceleration. Most ionization cooling channel designs require operation of RF cavities in multi-tesla fields, precluding the use of superconducting cavities. To accommodate the large initial beam sizes, the lowest cavity frequencies are typically in the ballpark of 200–325 MHz; however, much of the R&D is done on "1/4-scale" (805 MHz) prototypes. (These are not only easier to fabricate, test, and modify, but are also similar to those that would be used in later stages of the cooling system, where the beam is smaller.) Cavity electrical efficiency is maximized by "pillbox" geometry, with apertures closed by thin conductive windows (Fig. 14) — a technique suitable

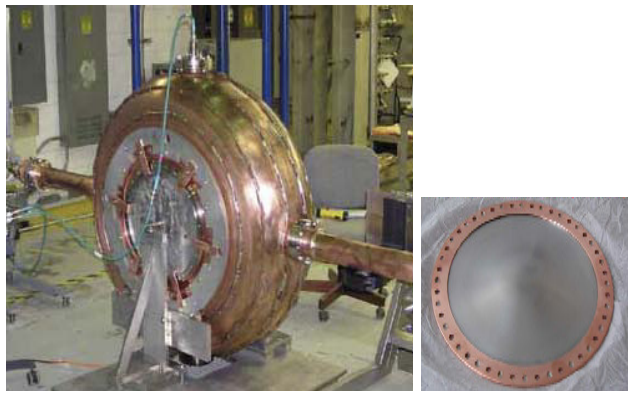

Figure 14: (left) MICE prototype 201 MHz cavity; (right) photo of curved beryllium window for 805 MHz cavity.

only for muons. For a given input power or maximum surface electric field, closed-aperture cavities have twice the on-axis accelerating gradient of standard, open-cell cavities. They incur the possible penalty of focused surface-emitted electrons from one window being accelerated across the gap and damaging the window opposite.

While the maximum magnetic field on the RF-cavity windows in the MICE cooling lattice is about 2 T, in later cooling stages, where lower equilibrium emittance requires stronger focusing, the field is many times stronger. Early data obtained by the NFMCC on an 805 MHz copper cavity operated in a solenoidal magnetic field [66] indicated that beyond a limiting accelerating gradient, damaging sparks occurred, degrading the cavity conditioning. The observed loss in accelerating gradient ranged up to a factor ≈ 3 at 4 T. However, more recent cavities display a far less egregious behavior [67], and the early results now appear to have been related to coupler arrangement and other design details that have since been improved. Thus cavity operation in multi-tesla magnetic field seems no longer a potential showstopper [68]. This is one of the major pieces of recent progress in muon cooling R&D.

Cavities pressurized with hydrogen gas were initially proposed as a means of raising operating gradients via the Paschen effect [69]. They were subsequently found to mitigate magnetic-field-induced gradient degradation as well (Fig. 15) [70]. As mentioned, used aggressively, they enable the continuous, "combined-function," HCC cooling channels in which the ionization energy loss and re-acceleration take place simultaneously throughout the length of the channel [46, 69]. A less ambitious application has also been suggested: using them in a "conventional" ionization-cooling channel (e.g., those of Figs. 7 and 11) with just enough hydrogen pressure to overcome any magnetic-field-induced degradation [71]. In pressurized cavities a potential pitfall is cavity loading due to acceleration of ionization electrons [72]; theory and experimental studies show that this can be overcome via a small (0.01%) admixture of electronegative gas [67, 72, 73].

ISBN 978-3-95450-174-8

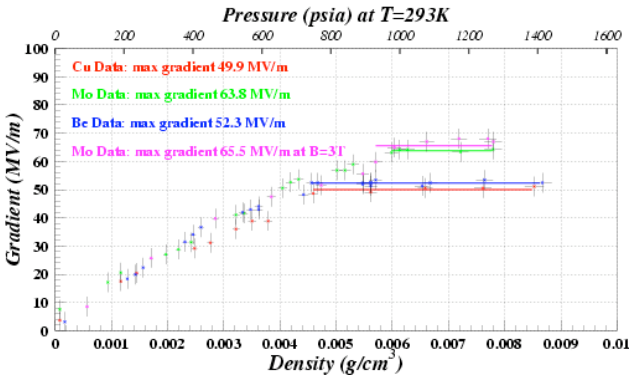

Figure 15: Observed dependence of maximum safe surface electric field in GH_2-pressurized 805 MHz cavity vs. hydrogen density and pressure for various electrode materials. Molybdenum electrodes were tested without (green points) and with (magenta) a 3 T axial field, with no observed degradation in maximum safe electric field [70].

System Tests

As mentioned, the MICE experiment is assembling a cooling cell and testing it in a muon beam, which will go a long way towards establishing the feasibility of the ionization cooling technique. Beyond MICE, it will be desirable, or even essential, to demonstrate the performance of the chosen 6D cooling lattice, as well as PIC or whichever advanced technique is chosen to go beyond the MAP emittance specs.

CONCLUSIONS

Muon cooling looks feasible, both for neutrino factories and muon colliders. Promising designs for these facilities have been conceived. The neutrino factory has been shown to be the best future facility for the precision study of neutrino oscillation and the search for non-standard neutrino physics. Muon colliders remain compelling and have been proposed by Rubbia as especially well suited for the precision study of the Higgs, provided the luminosity can be increased over that of the MAP Higgs Factory design. The latter would thus benefit from new cooling ideas that go beyond "conventional" ionization cooling; appealing solutions have been proposed and are the subject of ongoing work. A premature end of this U.S. R&D program has however been dictated by the P5 committee. In light of interest in Europe [74], it is hoped that muon-cooling research will nevertheless continue to be pursued.

ACKNOWLEDGMENTS

The author thanks his colleagues of MAP, the NFMCC, the MICE Collaboration, Muons, Inc., and the MCTF for many stimulating and enlightening conversations and interactions over many years. This paper is dedicated to the memories of the late Andy Sessler, Dave Cline, and Mike Zisman, who all passed away in 2015.

REFERENCES

[1] R. Palmer, "Muon Colliders," Rev. Accel. Sci. Tech. **7** (2015) 137.

[2] S. Geer, "Neutrino beams from muon storage rings: Characteristics and physics potential," Phys. Rev. D **57**, 6989 (1998); *ibid.* **59**, 039903E (1999);
C. T. Rogers *et al.*, "Muon front end for the neutrino factory," Phys. Rev. ST Accel. Beams **16**, 040104 (2013);
S. Choubey *et al.* (IDS-NF Collaboration), "International Design Study for the Neutrino Factory, Interim Design Report," arXiv:1112.2853 [hep-ex] (Mar. 2011);
A. Bandyopadhyay *et al.*, "Physics at a future Neutrino Factory and super-beam facility," Rep. Prog. Phys. **72**, 106201 (2009), arXiv:0802.4023 [physics.acc-ph];
M. Lindner, "The physics potential of future long baseline neutrino oscillation experiments," in *Neutrino Mass*, ed. G. Altarelli, K. Winter, Springer Tracts in Modern Physics **190**, 209 (2003);
M. Apollonio *et al.*, "Oscillation Physics with a Neutrino Factory," CERN-TH-2002-208 (Oct. 2002);
C. Albright *et al.*, "Physics at a Neutrino Factory," FERMILAB-FN-692 (May 2000), hep-ex/0008064.

[3] D. Neuffer, "Progress of Front End and HFOFO Snake," this workshop.

[4] C. Rubbia, "A complete demonstrator of a muon cooled Higgs factory," arXiv:1308.6612 (2013), and presentation to Muon Accelerator Program Spring 2015 Meeting, Fermilab, May 18–23, 2015, `https://indico.fnal.gov/conferenceDisplay.py?confId=9752` and `http://tinyurl.com/oe9yesf` (2015).

[5] K. Lane, "Is the Standard Model about to crater?," CERN Courier, Nov., 2015, p. 21, `http://cerncourier.com/cws/article/cern/62874`.

[6] J.-P. Delahaye *et al.*, "A Staged Muon Accelerator Facility for Neutrino and Collider Physics," Proc. IPAC2014 Conference, Dresden, Germany, paper WEZA02 (2014).

[7] "Enabling Intensity and Energy Frontier Science with a Muon Accelerator Facility in the U.S.: A White Paper Submitted to the 2013 U.S. Community Summer Study of the Division of Particles and Fields of the American Physical Society," ed. J.-P. Delahaye *et al.*, arXiv:1308.0494 (2013).

[8] See e.g. D. Taqqu, "Ultraslow Muonium for a Muon beam of ultra high quality," Phys. Procedia **17** (2011) 216.

[9] Mu2e home page: `http://mu2e.fnal.gov/`;
C. M. Ankenbrandt *et al.*, "Intense Stopping Muon Beams," presented at PAC09 (*op. cit.*), paper MO6RFP080;
K. Yonehara *et al.*, "MANX, A 6-D Muon Beam Cooling Experiment for RAL," *ibid.*, paper WE6PFP090;
S. A. Kahn *et al.*, "Integrating the MANX 6-D Muon Cooling Experiment into the MICE Spectrometers," *ibid.*, paper WE6PFP095.

[10] D. M. Kaplan *et al.*, "Measuring Antimatter Gravity with Muonium," Proc. New Frontiers in Physics 2014, EPJ Web Conf. **95** (2015) 05008.

[11] A. Knecht, this workshop.

[12] F. F. Tikhonin, "On the Effects with Muon Colliding Beams," JINR Report P2-4120 (Dubna, 1968);
G. I. Budker, "Accelerators and Colliding Beams," in Proc.

ISBN 978-3-95450-174-8

7th Int. Conf. (Yerevan, 1969); extract available in AIP Conf. Proc. **352**, 4 (1996).

[13] D. V. Neuffer, R. B. Palmer, "A high-energy high-luminosity μ^+-μ^- collider," Proc. 1994 Eur. Particle Accelerator Conf. (EPAC94), p. 52;
R. Palmer *et al.*, Nucl. Phys. Proc. Suppl. **51A** (1996) 61;
C. M. Ankenbrandt *et al.*, "Status of Muon Collider Research and Development and Future Plans," Phys. Rev. ST Accel. Beams **2**, 081001 (1999);
D. Ayres *et al.*, "Expression of Interest in R&D towards a Neutrino Factory Based on a Storage Ring and a Muon Collider," arXiv:physics/9911009.

[14] Y. M. Ado, V. I. Balbekov, "Use of ionization friction in the storage of heavy particles," At. Energ. **31**(1) 40 (1971), English translation in Atomic Energy (Springer) **31**(1) 731, http://www.springerlink.com/content/v766810126338571/.

[15] G. I. Budker, A. N. Skrinsky, Sov. J. Part. Nucl. **21**, 277 (1978);
A. N. Skrinsky, V. V. Parkhomchuk, Sov. J. Part. Nucl. **12**, 223 (1981);
D. Neuffer, "Principles and Applications of Muon Cooling," Part. Accel. **14** (1983) 75;
D. Neuffer, AIP Conf. Proc. **156**, p. 201 (1987).

[16] D. Neuffer, "$\mu^+\mu^-$ Colliders," Yellow Report CERN-99-12 (1999);
R. C. Fernow, J. C. Gallardo, Phys. Rev. E **52**, 1039 (1995).

[17] See e.g. "Passage of Particles Through Matter," in K. A. Olive *et al.* [Particle Data Group], Chin. Phys. C **38**, 090001 (2014).

[18] P. Kyberd *et al.*, "nuSTORM: Neutrinos from STORed Muons," arXiv:1206.0294 (2012).

[19] J. C. Gallardo *et al.*, "Muon Muon Collider: Feasibility Study," prepared for. 1996 DPF/DPB Summer Study on New Directions in High-Energy Physics (Snowmass96), BNL-52503, available from http://www.cap.bnl.gov/mumu/pubs/snowmass96.html

[20] S. Geer, in **Workshop on Physics at the First Muon Collider and Front-End of a Muon Collider**, S. Geer, R. Raja, eds., AIP Conf. Proc. **435** (American Institute of Physics, New York, 1998), p. 384.

[21] Neutrino Factory and Muon Collider Collaboration home page: http://cap.bnl.gov/mumu.

[22] B. Autin, A. Blondel, J. Ellis, "Prospective study of muon storage rings at CERN," Tech. Rep. CERN 99-02, CERN, Geneva, Switzerland, April 1999.

[23] D. Finley, N. Holtkamp (eds.), "Feasibility Study on a Neutrino Source Based on a Muon Storage Ring," SLAC-REPRINT-2000-054, FERMILAB-PUB-00/108-E (2000).

[24] S. Ozaki, R. Palmer, M. Zisman, J. Gallardo (Eds.), "Feasibility Study-II of a Muon-Based Neutrino Source," BNL-52623 (2001), available from http://www.cap.bnl.gov/mumu/studyii/FS2-report.html.

[25] Y. Kuno et al., "A feasibility study of a neutrino factory in Japan," HTTP://WWW-PRISM.KEK.JP/NUFACTJ/, May 2001.

[26] See NuFact 2015 website, https://indico.fnal.gov/conferenceDisplay.py?ovw=True&confId=8903, and links therefrom.

[27] G. Gregoire *et al.*, "An International Muon Ionization Cooling Experiment (MICE)," Proposal to Rutherford Appleton Laboratory, http://mice.iit.edu/micenotes/public/pdf/MICE0021/MICE0021.pdf;

[28] MERIT home page: http://proj-hiptarget.web.cern.ch/proj-hiptarget/.

[29] S. Machida *et al.*, Nat. Phys., March 2012 **8** 3 243;
T. R. Edgecock *et al.*, "EMMA – the World's First Non-scaling FFAG," Proc. 11th Eur. Particle Accelerator Conf. (EPAC 08), Magazzini del Cotone, Genoa, Italy, 23–27 June 2008, p. 3380.

[30] Muon Collider Task Force (MCTF) home page: https://mctf.fnal.gov/.

[31] Muon Accelerator Program home page: http://map.fnal.gov.

[32] Particle Physics Project Prioritization Panel, "Building for Discovery: Strategic Plan for U.S. Particle Physics in the Global Context," http://science.energy.gov/~/media/hep/hepap/pdf/May%202014/FINAL_P5_Report_053014.pdf

[33] Such plots have been in use for years within the muon collider R&D program; see, e.g., P. Snopok, "Muon Cooling," ICFA Beam Dyn. Newslett. **65**, 45 (2014).

[34] MICE website: http://mice.iit.edu.

[35] C. Rogers, "Status, Recent Results and Prospect of the International Muon Ionization Cooling Experiment (MICE)," this workshop.

[36] M. M. Alsharo'a *et al.*, "Recent progress in neutrino factory and muon collider research within the Muon Collaboration," Phys. Rev. ST Accel. Beams **6**, 081001 (2003).

[37] The ISS Accelerator Working Group, "Accelerator design concept for future neutrino facilities," JINST **4**, P07001 (2009);
S. Choubey *et al.* (IDS-NF Collaboration), "International Design Study for the Neutrino Factory, Interim Design Report," arXiv:1112.2853 [hep-ex] (Mar. 2011).

[38] Y. Alexahin, "Helical FOFO Snake for Initial 6D Cooling of Muons," ICFA Beam Dyn. Newslett. **65**, 49 (2014).

[39] R. B. Palmer *et al.*, "A Complete Scheme of Ionization Cooling for a Muon Collider," Proc. 2007 Particle Accelerator Conf. (PAC07), p. 3193 (2007), arXiv:0711.4275 [physics.acc-ph].

[40] R. P. Johnson, Ya. Derbenev, "Low Emittance Muon Colliders," in Proc. PAC07 (*op. cit.*), p. 706.

[41] Muons, Inc. home page: http://www.muonsinc.com.

[42] A now-defunct SBIR-funded R&D company led by D. Cline.

[43] V. Balbekov *et al.*, "Muon Ring Cooler for the MUCOOL Experiment," Proc. 2001 Particle Accelerator Conf. (PAC01), p. 3867.

[44] R. B. Palmer *et al.*, "Ionization cooling ring for muons," Phys. Rev. ST Accel. Beams **8**, 061003 (2005).

[45] X. Ding *et al.*, "6D 'Garren' snake cooler and ring cooler for $\mu^\pm$ cooling of a muon collider," Nucl. Instrum. Meth. A **768** (2014) 9;
D. Cline *et al.*, "Comparison of 6D Ring Cooler Schemes and Dipole Cooler for $\mu^+\mu^-$ Collider Development," Proc. PAC07 (*op. cit.*), p. 3038;

ISBN 978-3-95450-174-8

H. Kirk *et al.*, "Muon Storage Rings for 6D Phase-Space Cooling," Proc. 2003 Particle Accelerator Conf. (PAC03), p. 2008.

[46] Ya. Derbenev, R. P. Johnson, "Six-dimensional muon beam cooling using a homogeneous absorber: Concepts, beam dynamics, cooling decrements, and equilibrium emittances in a helical dipole channel," Phys. Rev. ST Accel. Beams **8**, 041002 (2005).

[47] P. Snopok, G. Hanson, A. Klier, "Recent progress on the 6D cooling simulations in the Guggenheim channel," Int. J. Mod. Phys. A **24**, 987 (2009).

[48] S. A. Kahn *et al.*, "Magnet System for Helical Muon Cooling Channels," Proc. PAC07 (*op. cit.*), p. 443;
V. Kashikhin *et al.*, "Magnets for the Manx 6-D Muon Cooling Demonstration Experiment.," *ibid.*, p. 461.

[49] K. Yonehara, "Study of Helical Cooling Channel for Intense Muon Source," this workshop.

[50] V. Balbekov, "R_FOFO snake channel for 6D muon cooling," http://map-docdb.fnal.gov/cgi-bin/ShowDocument?docid=4365.

[51] D. Stratakis, R. Palmer, "Rectilinear six-dimensional ionization cooling channel for a muon collider: A theoretical and numerical study," Phys. Rev. ST Accel. Beams **18**, 031003 (2015).

[52] D. Stratakis, "Rectilinear Channel for Muon Cooling Towards Micron Scale Emittances," this workshop.

[53] R. Gupta *et al.*, "High Field HTS Solenoid for a Muon Collider–Demonstrations, Challenges, and Strategies," IEEE Trans. Appl. Supercond. **24** (2014) 4301705.

[54] H. K. Sayed, R. Palmer, D. Neuffer, "High Field - Low Energy Muon Ionization Cooling Channel," Phys. Rev. ST Accel. Beams **18**, 091001 (2015).

[55] D. Neuffer, "Final Cooling for a High Energy High Luminosity Collider," this workshop;
D. Neuffer *et al.*, "Final Cooling for a High Energy High-Luminosity High-Energy Lepton Collider," Proc. PAC2015, paper TUBD2.

[56] J. G. Acosta, "Final Muon Ionization Cooling Channel using Quadrupole Doublets for Strong Focusing," this workshop.

[57] V. Morozov, "Progress on Parametric-resonance Ionization Cooling," this workshop;
A. Afanasev *et al.*, "Epicyclic Helical Channels for Parametric Resonance Ionization Cooling," presented at PAC09 (*op. cit.*), paper FR5RFP012.

[58] Y. Fukui *et al.*, "Progress in Designing a Muon Cooling Ring with Lithium Lenses," Proc. 2003 Particle Accelerator Conf. (PAC03), p. 1787.

[59] A. Zholents, M. Zolotorev, W. Wan, "Optical stochastic cooling of muons," Phys. Rev. ST Accel. Beams **4**, 031001 (2001).

[60] See e.g. V. Litvinenko, "Recent Progress in the Coherent Electron Cooling Experiment," this workshop.

[61] M. Mühlbauer *et al.*, Hyperfine Interact. **119**, 305 (1999).

[62] D. Greenwald, Y. Bao, A. Caldwell, "Frictional Cooling Scheme for Use in a Muon Collider ," Proc. NuFact09, AIP Conf. Proc. **1222** (2010) 293;
D. J. Summers *et al.*, "6D muon ionization cooling with an inverse cyclotron," Proc. Int. Workshop on Beam Cooling and Related Topics (COOL05), AIP Conf. Proc. **821**, 432 (2006).

[63] T. J. Roberts, D. M. Kaplan, "Particle Refrigerator," presented PAC09 (*op. cit.*), paper WE6PFP096.

[64] For example, 40% survival of antiprotons with deceleration from several MeV down to 40 keV has been demonstrated in simulation studies [63].

[65] See e.g. H. W. Weijers *et al.*, "Tests of HTS insert coils above 30 T," Int. Symp. on Superconductivity, Tsukuba, Japan, 27–29 Oct. 2008, http://www.magnet.fsu.edu/library/presentations/NHMFL_Presentation-4065.pdf;
D. Hazelton, "Continued developments in high magnetic fields enabled by econd-generation high-temperature superconductors," Magnetics Conf,, Chicago, IL, 15–16 Apr. 2009, http://www.superpower-inc.com/system/files/2009_0415_Magnetics_Conf_2G_Coils_DWH.pdf;
D. C. Larbalestier *et al.*, Nat. Mat. **13** (2014) 375, http://www.nature.com/nmat/journal/v13/n4/full/nmat3887.html.

[66] D. Huang *et al.*, "RF Studies at Fermilab MuCool Test Area," presented at PAC09 (*op. cit.*), paper TU5PFP032;
D. Huang, "Vacuum RF Tests," 2009 NFMCC Collaboration Meeting, available from http://www.cap.bnl.gov/mumu/conf/MC-090125/agenda.html.

[67] B. Freemire, " Rf Technologies for Ionization Cooling Channels," this workshop.

[68] M. Palmer, "The Muon Accelerator Program: R&D Towards Future Neutrino Factory and Lepton Collider Capabilities," this workshop.

[69] R. P. Johnson *et al.*, "Gaseous Hydrogen and Muon Accelerators," AIP Conf. Proc. **671**, 328 (2003);
R. Johnson, D. M. Kaplan, "A Gaseous Energy Absorber for Ionization Cooling of Muon Beams, MuCool Note 195, http://nfmcc-docdb.fnal.gov/cgi-bin/RetrieveFile?docid=195&version=1&filename=muc0195.pdf (2001).

[70] P. M. Hanlet *et al.*, "Studies of RF Breakdown of Metals in Dense Gases," Proc. 2005 Part. Accel. Conf. (PAC 05), Knoxville, Tennessee, 16–20 May 2005, p. 3259.

[71] J. C. Gallardo, M. Zisman, "A Possible Hybrid Cooling Channel for a Neutrino Factory," Proc. IPAC'10, paper WEPE074;
J. C. Gallardo, M. Zisman, "Thoughts on Incorporating HPRF in a Linear Cooling Channel," Proc. NuFact09, AIP Conf. Proc. **1222** (2010) 308.

[72] A. Tollestrup, "Handbook for Gas Filled RF Cavity Aficionados," FERMILAB-TM-2430-APC, May 2009, http://www-spires.fnal.gov/spires/find/hep?key=8276862.

[73] M. Chung *et al.*, "Pressurized H2 RF Cavities in Ionizing Beams and Magnetic Fields," Phys. Rev. Lett. **111** (2013) 184802.

[74] "Discussion of the scientific potential of muon beams," CERN, 17 Nov. 2015, https://indico.cern.ch/event/450863/timetable/#20151118.

ISBN 978-3-95450-174-8

EXPERIMENTAL OBSERVATION OF LONGITUDINAL ELECTRON COOLING OF DC AND BUNCHED PROTON BEAM AT 2425 MeV/c AT COSY

V. B. Reva, M. I. Bryzgunov, V. V. Parkhomchuk (BINP SB RAS, Novosibirsk)
V. Kamerdzhiev, T. Katayama, R. Stassen, H. Stockhorst (FZJ, Jülich)

Abstract

The 2 MeV electron cooling system for COSY-Julich started operation in 2013 years. The cooling process was observed in the wide energy range of the electron beam from 100 keV to 908 keV. Vertical, horizontal and longitudinal cooling was tested at bunched and continuous beams. The cooler was operated with electron current up to 0.9 A. This report deals with the description of the experimental observation of longitudinal electron cooling of DC and bunched proton beam at 2425 MeV/c at COSY.

SETUP DESCRIPTION

New generation of the accelerators for study nuclear physics at range of relativistic energy 1-8 Gev/u requires very powerful cooling to obtain high luminosity. In the present time the large experience of using magnetized cooling was collected. The first experiments in BINP and further experiments in the others scientific centers show the usefulness of the idea of magnetized cooling. There are many electron cooler devices that operate now at low and middle energy (CSRm, CSRe, LEIR, ESR, e.t.c). The 2 MeV electron cooling system for COSY-Julich has the highest energy from all coolers that were made with idea of magnetized electron cooling and transport of the electron beam. The COSY cooler is designed on the classic scheme of low energy coolers like coolers CSRm, CSRe, LEIR that were produced in BINP before. It can be used for beam cooling at injection energy and for testing new features of the high energy electron cooler for COSY and HESR.

The schematic design of the setup is shown in Fig. 1. The design of the cooler and its main parameters are described in [1-2]. The electron beam is accelerated by an electrostatic generator that consists of 33 individual sections connected in series. Each section has two high-voltage power supplies with maximum voltage 30 kV and current 1 mA. The electron beam is generated in electron gun immersed into the longitudinal magnetic field. After that the electron beam is accelerated, moves in the transport line to the cooling section where it will interact with protons and deuterons of COSY storage ring. After interaction the electron beam returns to electrostatic generator where it is decelerated and absorbed in the collector.

The optics of 2 MeV cooler for COSY is designed close to the classical low-energy coolers. The motion of the electron beam is magnetized (or close to magnetized conditions) along whole trajectory from a gun to a collector. This decision is stimulated by requirement to operate in the wide energy range from 25 keV to 2 MeV. So, the longitudinal field is higher then transverse component of the magnetic fields. The bend magnets and linear magnets of the cooler are separated by a section with large coils for the location of the BPMs, pumps and a comfort of the setup assembling.

EXPERIMENTS SETUP

The detailed experiments with electron cooling were carried out with the proton energy 2425 MeV that corresponds to the electron energy 908 keV. This working point was investigated carefully in the previous experiments and there was a large collection of the hardware setups for the operation. Moreover the stochastic cooling was accessible at this energy. The experimental setup involves the barrier bucket and RF of 1-st harmonic. The diagnostic of the proton beam was based on IPM (ionization profile monitor), BPM and pickup of the stochastic cooling system. The proton current is measured by DCCT.

The main parameters of COSY regime at this point are listed in Table 1.

Table 1: COSY Regime Parameters

Parametere	Value
Gamma transition	2.26
Alpha	0.196
Proton numbers	10^{8}-10^{9}
Vacuum	10^{-9}-10^{-10} mbar
Qx	3.589
Qy	3.675
Slip-factor	-0.066
Perimeter	183.5 m
Kinetic energy	1.662 GeV
Gamma	2.771
Frequency	1.5239 MHz
Dipole field	1.156 T
Horizontal beta function in cooling section	9 m
Vertical beta function in cooling section	15 m
Dispersion in cooling section, m	0

ISBN 978-3-95450-174-8

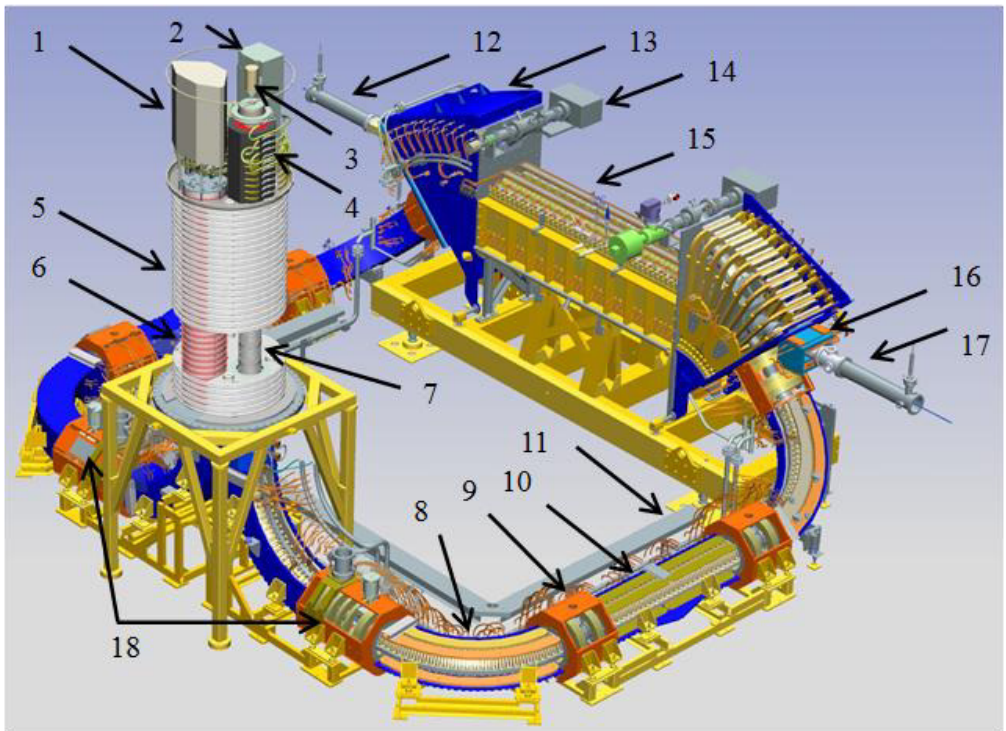

Figure 1: 3D design of 2 MeV COSY cooler. Collector PS is 1, SGF system is 2, ion pump of collector is 3, collector with magnetic system is 4, HV section is 5, cascade transformer is 6, acceleration tube is 7, bend 90 degrees is 8, straight section is 9, line section is 10, cable path is 11, input of the proton beam is 12, toroid 45 is 13, vacuum pump is 14, cooling section is 15, ion dipole is 16, output of the ion beam is 17, the elements with short dipole kicks of the electron beam is 18.

ELECTRON COOL TUNING

The first attempts of the cooling shows the essential role of the coherent Larmor rotation to the cooling process. That is why the e-cool tuning to the given working point contains the following procedures. The vertical and horizontal overlap of the proton and electron beam was adjusted using the BPM. The scan of the electron energy gives the possibility to obtain initial cooling process. The difference in 200-500 V is enough for significant influence on the cooling process because the exact energy value isn't easy to calculate from the experimental value of the proton energy. In final the Larmor rotation is minimize. The magnetic field in the cooling section was changed in order to see the Larmor motion of the e-beam center in the BPM located after cooling section. The short magnetic dipole coils located in the section Fig. 1, 18 enable to provide additional dipole kicks eliminating the initial Larmor motion. As result the Larmor oscillation with radius 10-30 um can be reached in the transport channel. Unfortunately this oscillation depends on the most parameters of the electron beam: energy, position in the cooling section and current. So, the tuning of the optimal parameters of the electron beam was done with several iterations. Each iteration allows reaching the improvement of the cooling process.

As the result the proton beam with the momentum spread $\Delta p/p = \pm 2 \cdot 10^{-3}$ was cooled down during about 200 s. The Schottky spectrum shown in Fig. 2. demonstrates this process. The initial proton momentum spread was widened using white noise beam excitation for the process demonstration. The electron current was 400 mA and the proton number $7 \cdot 10^8$ in this experiment.

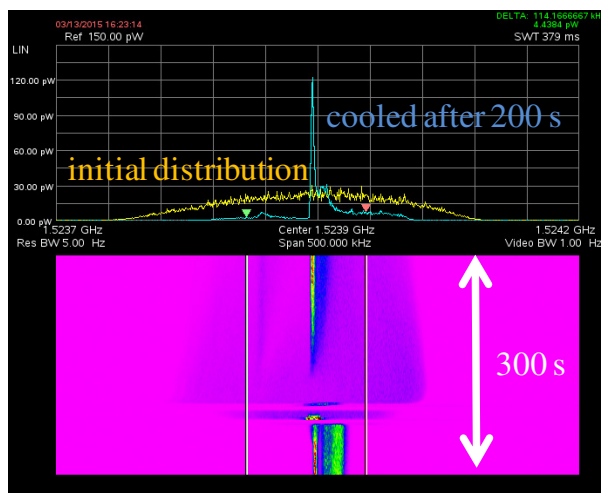

Figure 2: Schottky spectrum (linear scale) of the proton beam during cooling ($\gamma > \gamma_{tr} = 2.26$).

ISBN 978-3-95450-174-8

Figure 2 shows that the distribution function of the proton beam consists from the central high peak and the tail directed to the low energy area. The location of the working point above gamma transition leads to the location of the low energy area in right side of the spectrum. This tail was observed in the most experiments with cooling of the proton beam so this problem was investigated in more detail. Results of our investigations are described below.

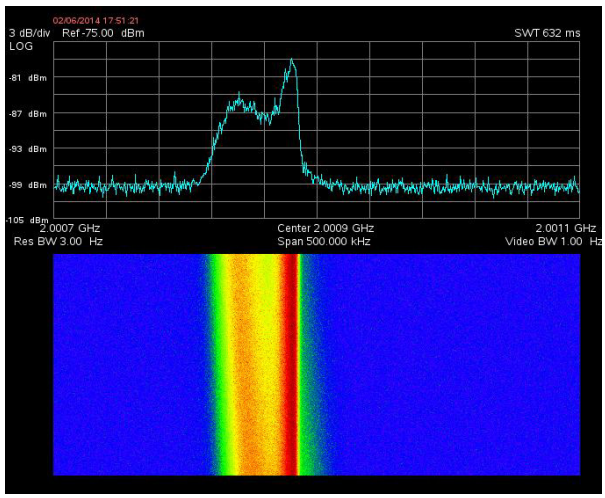

Figure 3: Schottky spectrum (log scale) of the proton beam under cooling process at the case $\gamma<\gamma_{tr}$=4.2. The proton number is Np=5.5·10^8. The electron current is 310 mA.

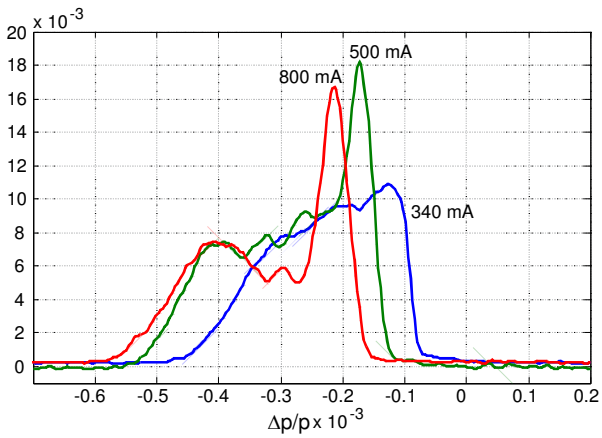

Figure 4: Distribution function of the longitudinal momentum for cooling with different electron current. The time is fixed as 370 s after the injection. The distribution function is normalized to unity (scale is linear). The proton number is Np=3·10^8.

The exact shape of the distribution function depends from both parameters of the proton and electron beam: number of particles and the electron current (see Fig. 4). The shift of the peak to the lowest value of the proton energy can be explained by the space charge. The changing energy in the center of the electron beam can be calculated from the equation

$$\frac{\Delta p}{p}=\frac{eJ}{\gamma\beta^3 c}\frac{1}{m_e c^2}\left(2\ln\left(\frac{b}{a}\right)+1\right).$$

that gives $\Delta p/p$ =8.5·10^{-5} at the parameters Je=500 mA, b=5 cm, a=3 cm. So, the shift of the peak of the distribution function can be described by the space charge, but the tail itself can't be described with simple theory.

The potential sagging inside the electron beam induced by the space charge leads to the maximum momentum distribution

$$\frac{\delta p}{p}=\frac{eJ}{\gamma\beta^3 c}\frac{1}{m_e c^2}.$$

that gives $\delta p/p$ =1.3·10^{-5} at the electron current Je=500 mA that isn't enough from the quantitative point of view. Moreover the effect of the potential sagging leads to an increase of energy of all particles respect to the particle passed through the center of the electron beam. So, the position of the proton beam in alignment with the electron beam should effect the tail on the high energy side. The opposite behavior is observed.

The role of the vacuum can't be significant either. The ionization loss can be estimated as

$$\frac{\delta p}{p}f_0=\frac{4\pi n_a r_e^2 c}{\gamma\beta^3}\frac{m_e}{m_p}L_C$$

where n_a=1.3·10^8 cm^{-3} is the density of the residual gas in COSY, r_e is classical electron radius, $L_C\approx 20$ is Coulomb logarithm, m_e/m_p - ratio between electron and ion mass. The loss rate of the energy is about 2·10^{-8} c^{-1} that isn't enough for describing of the experiments. Moreover the direct experiment with the degradation of the vacuum condition in COSY to a few times doesn't show the visible effect in the picture of the cooling process.

The effect related to the different Larmor radiuses in cross-section of the electron beam may also induce the cooling to the different electron energies. Suppose that the outer electrons oscillate with radius R_L=100 um and the electron in the center has R_L=0 um than the difference of the longitudinal energy between edge and center of the e-beam will be

$$\frac{\Delta p_{\|}}{p}=\frac{1}{2}\left(\frac{eB}{\gamma\beta m_e c^2}\right)^2 R_L^2$$

$\Delta p_{\|}/p$ =1.2·10^{-5} at the magnetic field B=1500 G. So, this effect is negligible too.

COHERENT INSTABILITY HYPOTHESIS

The behaviour of the cooled and noncooled proton beam may be significantly different [3]. The electron cooling decreasing the momentum spread can reveal the problems that were hidden by high momentum spread of the proton beam. As it is known the "Landau damping" suppressed many natural coherent instability like negative mass instability or instability at

ISBN 978-3-95450-174-8

interaction with resonance mode. Decreasing the momentum spread of the proton beam to the range 10^{-4} suppressed the Landau damping. So, because of the interaction with surrounding electrodes the quality of such beams can be limited by coherent instabilities. In this section we evaluate the behaviour of the distribution function due to instability of coherent oscillations. The direct simulation of the set of the particle was taken as model. The macro-particle interacts with surrounding electrodes with impedance

$$Z_q = R \cdot \frac{1 + iQ_{res}\left(\frac{q_{res}}{q} - \frac{q}{q_{res}}\right)}{1 + Q_{res}^2\left(\frac{q_{res}}{q} - \frac{q}{q_{res}}\right)^2}$$

where q_{res} is number of resonance harmonic, Q_{res} is quality factor, $R = Z_0 \cdot Q_{res} \cdot q_{res}$ is taken in such way that Z_q limits to the impedance of the smooth vacuum chamber at $q \to 0$.

The cooling step is taken as approximation of the Parkhomchuk's equation [4]

$$\delta p_{n+1} = \delta p_0 + (\delta p_n - \delta p_0) \cdot$$

$$\cdot \exp\left[-\frac{N_M A_{cool}}{\left((\delta p_n - \delta p_0)^2 + \gamma^2 \theta_{eff}^2\right)^{3/2}}\right]$$

where $A_{cool} = \frac{4 r_e r_p L_{cool}}{\gamma^2 \beta^3 c \pi a_e^2} Ln_C \left(\frac{J_e}{e}\right)$.

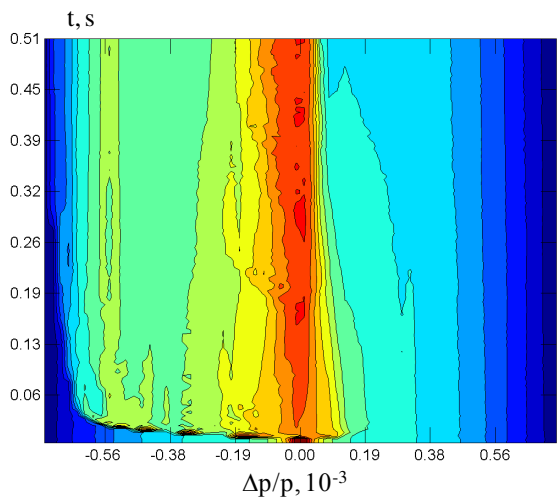

Figure 5: Spectrogram (Ln scale) of the longitudinal distribution function versus time as result of simulation. The colour scale as rainbow denotes the number of the particle in the momentum scale (x -axis) during time process (y-scale).

During each macro-step the coherent field was calculated with Fourier transformation of the density distribution of the particle. The distribution density along azimuthally angle was estimated with 64 space cells. As result the momentum and azimuthal position of the macro-particle was calculated taking into account e-cool force and impedance inducing field. This model may be expanded to the estimation of the external RF field (sin-like or barrier-bucket types). The complexity of the algorithm makes simulations of longer time intervals difficult. Because the instability rate was artificially increased in order to analyze the qualitative factors. The process of the initial cooling also is eliminated from simulation. The result of simulation of another computer code is used as initial parameters of the particles.

The simulation parameters: $Np=1.2 \cdot 10^{10}$ is particle number, $\Pi=180$ m is perimeter of the storage ring, a=0.5 cm is radius of the proton beam, b=5 cm is radius of the vacuum chamber, $\eta=-0.05$ is slip-factor, Je=0.3 A is the electron current, Ee=908 keV is the electron energy, $a_e=0.5$ cm is electron beam radius, $Ln_c=5.0$ and $\theta_{eff}=3 \cdot 10^{-5}$ is Coulomb logarithm and effective angle in the equation for the cooling force, $L_{cool}=250$ cm is length of the cooling section, number of the macro-particle for the simulation is 300 000, the number of the macro-step is 40 000, the number of the revolution turns in one macro-step is $N_M=20$, the harmonic multiplier is 2, the maximum harmonic number is 32, the impedance parameters are $Q_{res}=20$, $q_{res}=19.05$.

Figure 5 shows that the initial cooled beam acquires very fast the tail of the particle. After that the tail is stable and is located on the low energy side. The particle having positive momentum shift continues cooling to the equilibrium energy. The distribution function may have an additional peak located at some distance from the equilibrium energy about $\delta p_0=0$. This behavior is similar to the experimental facts shown in Fig. 2-4.

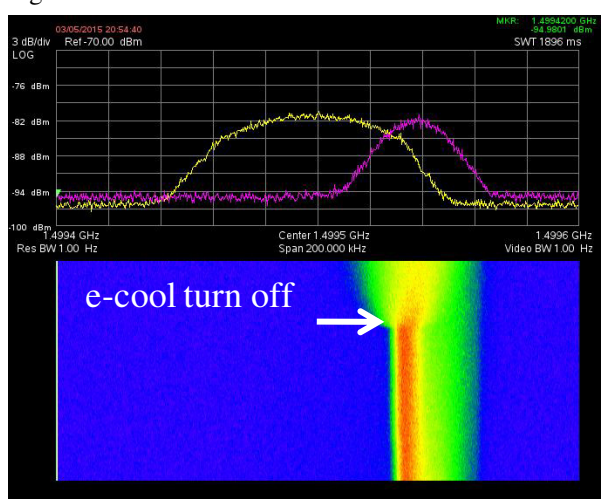

Figure 6: Schottky spectrum (log scale) of the proton beam at time of switching off electron current. The proton number is $Np=8.5 \cdot 10^8$, $\gamma > \gamma_{tr}=2.25$. The electron current is 300 mA.

Besides the qualitative simulation analysis of the coherent process, the additional experimental facts can be explained by some coherent phenomena.

ISBN 978-3-95450-174-8

The tail effect is strongly related to the e-cooling process. Figure 6 shows that turning off of the electron beam makes the tail disappear and to changes the distribution function to a symmetrical shape.

The presence of stochastic cooling and barrier bucket also suppresses the collective behaviour. The stochastic cooling may be considered as broadband feedback system, so this system can suppress the fluctuation of the space charge. The top picture (see Fig. 7) shows the proton beam deeply cooled by e-cool system. One can see very narrow peak and tail. The switching on of the stochastic cooling system makes the distribution function symmetrical and wider. The middle picture (see Fig. 7) shows the distribution function under action of the stochastic cooling. The bottom picture shows transition from one state to the other.

The barrier bucket RF action can be described in the following way. The loss energy particle acquires energy from RF voltage. So, a mixing process in the phase space occurs here. Thus the shape of distribution function becomes symmetric shape (see Fig. 8).

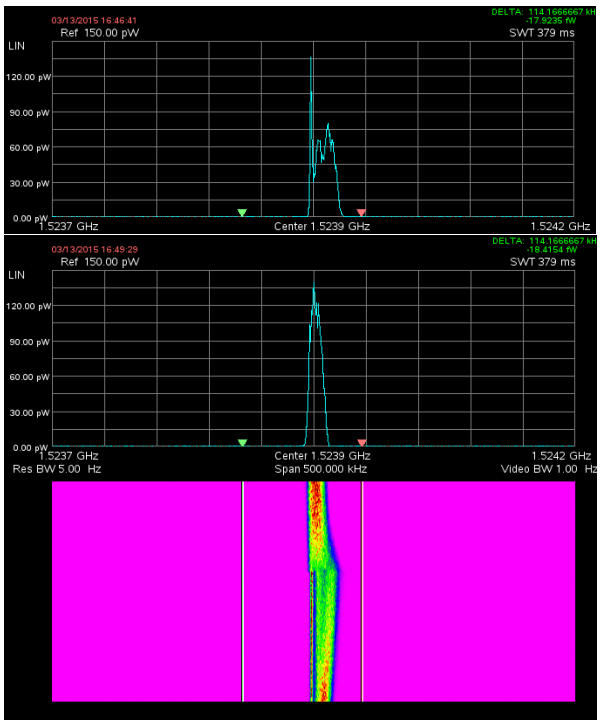

Figure 7: Schottky spectrum of the proton beam under cooling process without (top picture) and with stochastic cooling (middle picture). The proton number is $Np=7\cdot10^8$, $\gamma>\gamma_{tr}=2.25$. The electron current is 400 mA.

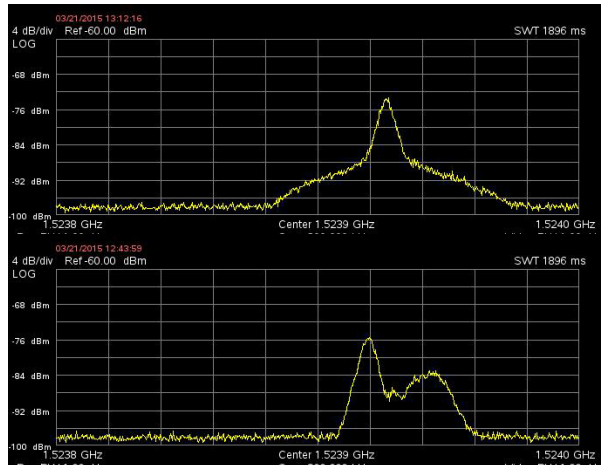

Figure 8: Schottky spectrum (log scale) of the proton beam under cooling process with (top picture) and without RF (bottom picture). The proton number is $Np=3\cdot10^8$, $\gamma>\gamma_{tr}=2.25$. The electron current is 810 mA. Amplitude of barrier bucket RF voltage is 240 V.

SUMMARY

The electron cooling can reveal the problems that were hidden by high momentum spread of the proton beam. The collective effects can describe some features of behaviour of the distribution function during cooling process in COSY. Certainly, the simulation gives only the general description of the cooling process in the presence of the collective instability. Improvement of the situation with coherent instability may be obtained by paying additional attention to impedance budget or use of working point with larger slip-factor.

REFERENCES

[1] N. Alinovsky et al., "The first commission results of the high-voltage magnetized cooler for COSY" ECOOL'11, Alushta, Semptember 2011, THIOA02, p. 37-42; http://www.JACoW.org.

[2] V. B. Reva, N.I. Alinovskiy, T. V. Bedareva et al. Proc. "Commissioning COSY cooler with electron beam at Novosibirsk". COOL-13, Murren, Switzerland, 2013, p.79-83

[3] N.S. Dikansky and D.V. Pestrikov., "The Physics of Intense Beams and Storage Rings" AIP Press (1994).

[4] V.V.Parkhomchuk. "New insights in the theory of electron cooling". Nucl. Instr. Meth. A 441 (2000), p. 9-17.

ISBN 978-3-95450-174-8

STOCHASTIC COOLING OF HEAVY IONS IN THE HESR

R. Stassen, B. Breitkreutz, G. Schug, H. Stockhorst, Forschungszentrum Jülich, Germany

Abstract

Due to the Modularized Start Version (MSV) of the FAIR project with the postponed New Experimental Storage Ring (NESR), the High Energy Storage Ring (HESR) became very attractive for experiments with heavy ions. Although the HESR is optimized for the storage of antiprotons it is also well suited for heavy ion beams with slight changes in the optics. Within the MSV only stochastic cooling and no electron cooling will be available, but even the main 2 - 4 GHz stochastic cooling system will be capable to fulfil the beam requirements for heavy ions. Most critical parts of the active elements are the high power amplifiers. The stochastic cooling amplifiers for the HESR will be based on new GaN devices. Nonlinearities of these devices necessitate a dedicated analysis of the use in stochastic cooling systems.

STOCHASTIC COOLING SYSTEM OF HESR

The stochastic cooling system of the HESR is based on completely new structures especially designed for the HESR [1]. Each beam surrounding slot of these so called slot-ring couplers covers the whole image current without a reduction of the HESR aperture. Each resonant ring structure is heavily loaded with eight 50 Ω electrodes for a broadband operation. The single rings are screwed together to a self-supporting structure in stacks of 16 rings. Four of these stacks will build the spindle for one tank.

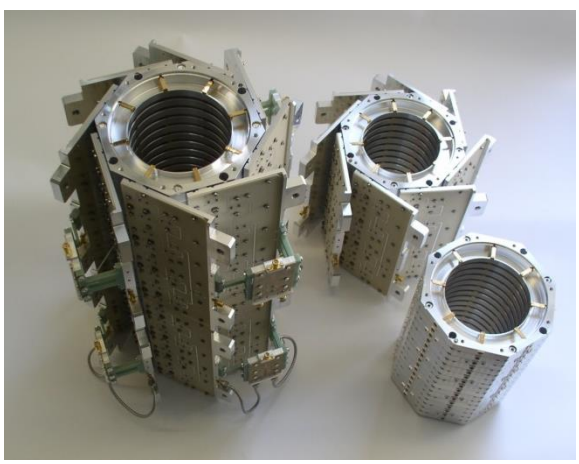

Figure 1: Stacks of slot ring couplers with and without 16:1 combiner-boards and two stacks mounted together including 2:1 combiner with heat-trap.

These structures have the great advantage that they can be simultaneously used in all three cooling planes (horizontal, vertical and longitudinal) just by skilful combining the signals of the electrodes. Another advantage in the case of the HESR is the fact that no movable parts in the vacuum are needed to obtain a good signal to noise ratio. The basic parameters of the main stochastic cooling system are summarized in table 1.

Table 1: Basic Parameters of Main System

Main system	**Based on slot-ring couplers**	
Bandwidth	2 - 4	GHz
Cooling methods	transverse, longitudinal filter cooling, longitudinal ToF cooling	
β-range	0.83-0.99	
Pickup:	**2**	**tanks**
No. of rings /tank	64	
Shunt impedance Z_{pu} / ring	9	Ohm
Total impedance	1152	Ohm
Structure temp.	30	K
Kicker	**3**	**tanks**
	2 tanks for transverse **or** longitudinal cooling, 1 tank longitudinal cooling only	
No. of rings /tank	64	
Shunt impedance Z_k / ring	36	Ohm
Impedance /tank	2304	Ohm
Installed power/tank	640 (longitudinal cooling) 320 (transverse cooling)	W W

Beside extensive test as pickup in the Cooler Synchrotron COSY Jülich [2] one small pickup and one kicker each equipped with 16 rings were installed into the Nuclotron in Dubna. This experimental stochastic cooling setup was initiated as a preparatory work for the NICA collider [3, 4]. During a few runs in 2013 and 2014 the system was commissioned and D^+ and C^{6+} beams were successful longitudinal cooled [5].

Cooling of Heavy Ions using Existing Design

The HESR stochastic cooling system was designed to cool pbars in the whole momentum range of the HESR lasting from 1.5 GeV/c to 15 GeV/c. Two operation modes have been analysed: first, the High-Resolution mode (HR) with 10^{10} pbars and a momentum spread of $\Delta p/p \approx 5\times10^{-5}$ and second, the High-Luminosity mode (HL) with 10^{11} pbars and a momentum spread of $\Delta p/p$

ISBN 978-3-95450-174-8

less than 1×10^{-4}. Due to the MSV with the postponed Recycled Experimental Storage Ring (RESR) a concept of longitudinal beam accumulation with moving barrier buckets and strong longitudinal stochastic filter cooling has been worked out [6,7] and the design of the stochastic cooling slightly changed to achieve the requirements for a pbar accumulation in the HESR of up to 10^{10} particles. A proof-of-principle experiment was done at the GSI in Darmstadt [8].

Extensive simulations carried out in [9] give the following demands concerning Schottky-power and the system gain:

- Accumulation pbars:
  $P \leq 70$ W, $G_a = 130$ dB, $N = 10^{10}$
- Longitudinal cooling @ 3 GeV pbars, (hydrogen-target $N_T = 4\times10^{15}$ /cm²)
  $P \leq 5$ W, $G_a = 110$ dB, $N = 10^{10}$
- Transversal cooling @ 3 GeV pbars
  $P \leq 35$ W, $G_a = 130$ dB, $N = 10^{10}$

Regarding safety margin, cable attenuation and noise peaks the installed power at each tank is sufficient (rule of thumb: factor 5 - 10 between Schottky-power and P_{1db}).

The shielding of the HESR was planned regarding a pbar production rate of 2×10^7 / s. This will limit the numbers of heavy ions in the HESR. The average loss-rate should not exceed 10^6 particles per second. Together with the cycle-length this will limit the number of particles to $N = 10^8$ per cycle. As example fully stripped uranium ions were simulated to define maximum Schottky-power and gain [10]:

- Longitudinal ToF cooling @ 740 MeV/u, $^{238}U^{92+}$ (hydrogen-target $N_T = 4\times10^{15}$ /cm²) $P \leq 13$ W, Ga = 85 dB, $N = 10^8$ (limited due to radiation safety)
- Longitudinal filter cooling @ 2 GeV/u, $^{238}U^{92+}$ (hydrogen-target $N_T = 4\times10^{15}$ /cm²) $P \leq 60$ W, Ga = 108 dB, $N = 10^8$ (limited due to radiation safety)

The power and gain requirements can easily be fulfilled with the designed system without any changes. But all combiner stages limit the useful operation of the stochastic cooling system to a minimum energy. In a first stage 16:1 combiners will add the signals of 16 rings within the vacuum tank. The dependence of the combiner losses from the energy of pbars can be found in Fig. 2 together with a comparison when the smallest group will be changed to 8 rings.

These rigidly combined groups define the lowest possible cooling energy given by the velocity of the species. In the case of the 16:1 combiner the lowest β is 0.83. This corresponds to the injection energy of uranium (740 MeV/u). The lowest energy for pbars will change from 0.7 GeV to 0.38 GeV only by changing the groups to 8 rings each combined within the tank. But this will significantly increase the costs because this measure will double the number of combiner-boards, vacuum feed-troughs and preamplifiers and the additional heat load demands a re-design of pickup-tank and a new power distribution at the kicker.

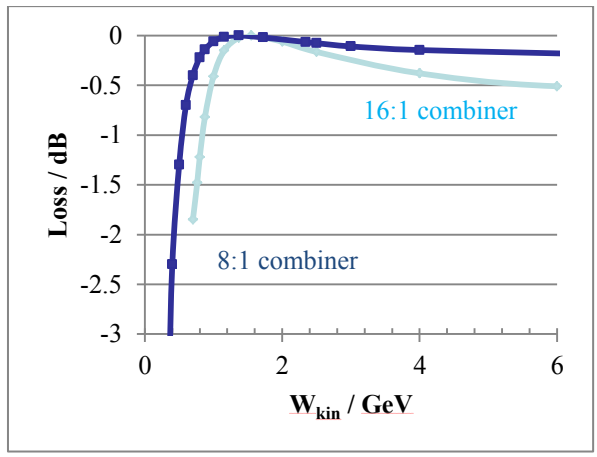

Figure 2: Losses of 16:1 combiner compared to 8:1 combiner.

The signal combination for each cooling plane outside the tanks takes place in 3 layers (Fig. 3). Hereby, switchable delay lines are required to compensate for the energy-dependent beam drift time. The delay lines will be switched in steps of 10 mm of electrical length at the first layer (PV1) and 20 mm at the further layers (PV2, PV4). The Wilkinson couplers, which combine two input signals after the switching stages, are already included. A deviation of 10 mm from the ideal length leads to a phase difference between the Wilkinson inputs that causes at 4 GHz an additional attenuation of nearly 0.8 dB. The last Wilkinson layer adds the power of both adjoining tanks. This allows stochastic cooling of pbars in the whole energy range of the HESR (0.8 - 14 GeV).

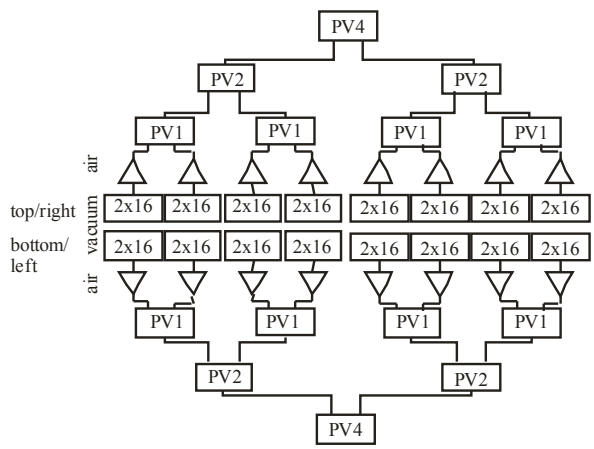

Figure 3: Double tank signal combination; PV1, PV2, PV4 programmable delay lines including Wilkinson couplers for optimum signal combination at different energies.

ISBN 978-3-95450-174-8

To minimize the number of switches, the reference plane is shifted at different energies but this can be easily compensated by adjusting the delay-line between pickup and kicker. Further, each signal-path of the delay-lines contains the same number of switches, and has therefore a similar amplitude-frequency characteristic which is compensated in the last stage of delay-lines. The change to 8:1 combiners inside the tank requires the installation of a fourth stage of programmable delay-lines.

The designed stochastic cooling system is already well prepared to cool bare uranium from injection energy 740 MeV/u to maximum energy 5 GeV/u. Cooling of heavy ions at energies lower than the injection energy is only possible with significant change of the whole system design.

One possible solution for stochastic cooling of heavy ions below the injection energy will be to add a system dedicated to lower energies. The signal to noise ratio is proportional to the square of the charge ($S/N \sim Z^2$). Thus the numbers of rings can be significantly reduced. Units of 16 rings seem feasible. Figure 4 shows the combiner losses of a 16:1 combiner-board optimized for uranium at 10 Tm ($\beta = 0.77$) versus the kinetic energy of uranium. Such a small unit is only effective in a kinetic energy-range of about 0.4 GeV/u to nearly 1 GeV/u.

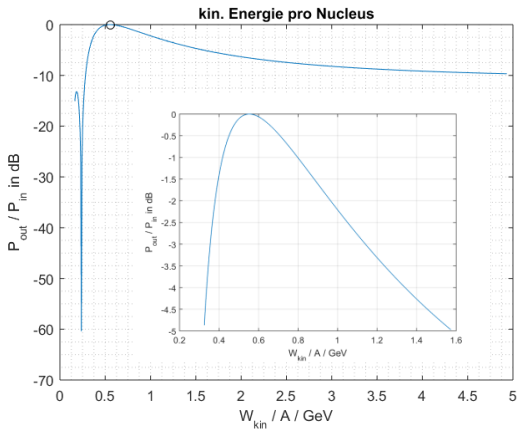

Figure 4: P_{out}/P_{in} of 16:1 combiner optimized for uranium at 10 Tm vs. kinetic energy of uranium.

Stochastic cooling of particles below a velocity of $\beta = 0.69$ is not useful with the designed structure because the decrease of the shunt impedance is too high (see table 2).

Table 2: Change of Shunt Impedance at 2 GHz

β-value	0.99	0.89	0.79	0.69
Z_k / Ω	30	20	11	6

HIGH POWER AMPLIFIERS

One of the most critical parts in the active chain will be the high power amplifiers. Several decades ago GaAs (gallium-arsenide) was the first choice to build high power solid-state amplifiers in the GHz-range. Since some years GaN (gallium-nitride) technology became very attractive not only for expensive military applications [11]. Higher voltages and higher heat-densities allow much higher power with better efficiencies.

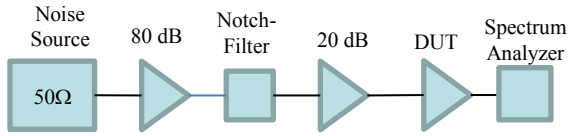

Figure 5: Setup to determine intermodulation products due to non-linearities with the aid of a notch-filter.

Stochastic cooling is mostly dominated by highly amplified noise. Noise-peaks can easily drive amplifiers into saturation. Due to non-linearities intermodulation products (IMD) will always occur even far below the 1 dB compression point (P_{1dB}). Normally, these IMD products are not visible, but with a notch-filter (comb-filter) where the noise is significantly reduced at the notch the IMDs lead to a filling up of the notch-depths. Figure 5 and 6 show a corresponding measurement. Starting with a 50 Ω load as noise-source, two low-noise preamplifiers boost the noise level (blue curve) to -80 dBm. After the notch-filter one can clearly see the noise reduction by the notch (notch-depth: about 35 dB). The insertion loss of the notch-filter can be compensated by an additional medium power amplifier (green curve). After the high-power amplifiers (DUT: device under test) the notch-depths are reduced. The results of one 50 W GaAs amplifier and an 80 W GaN based prototype already optimized for the HESR cooling system are shown.

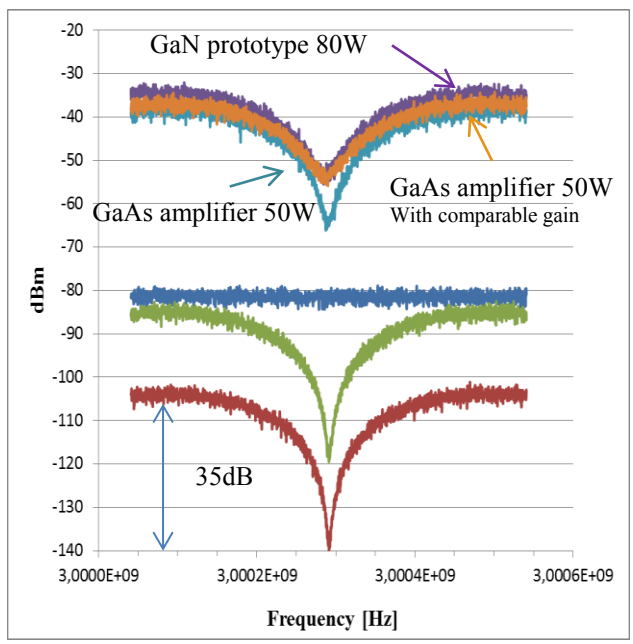

Figure 6: Filling up the notches due to IMDs-products of noise by non-linearities of power-amplifiers.

ISBN 978-3-95450-174-8

In a first view the GaAs amplifier looks better than the GaN prototype. But when the input level was increased to a comparable gain regarding the 1 dB compression point, no great difference could be realized. One has to keep in mind here that the noise level is far away from the 1dB compression point.

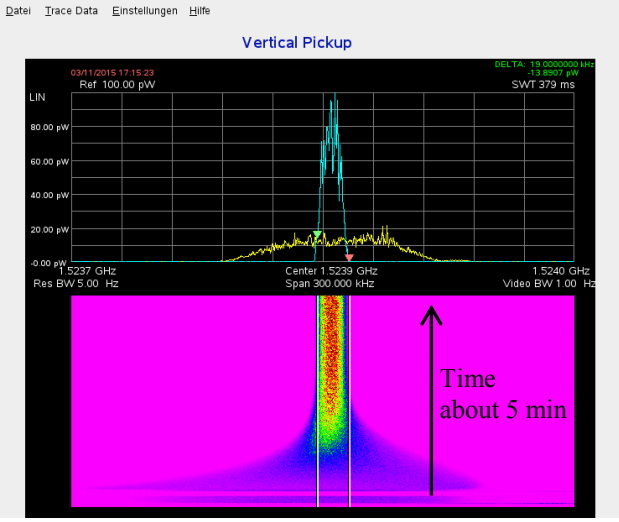

Figure 7: Starting and final beam distribution with a notch-depth of more than 30 dB.

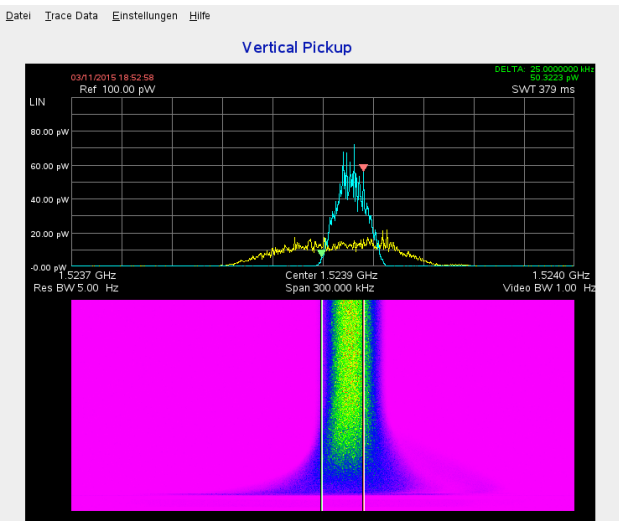

Figure 8: Starting and final beam distribution with a notch-depth of about 15 dB.

High notch-depths are essential for a good stochastic filter cooling. IMD products will create additional noise which acts as an additional heating term to the beam particles. The cooling time and particularly the equilibrium momentum spread will be increased. The existing stochastic cooling system of COSY was used to demonstrate this. The notch-depth of the optical notch-filter can be easily changed. Figure 7 shows the normal longitudinal cooling of 5×10^8 protons at 2.6 GeV/c with the initial momentum distribution (yellow) and the final distribution (blue). The average notch-depth was in the order of 30 dB and better.

The equilibrium momentum spread was reached after about 200 seconds. After changing the notch-depth to about 15 dB the equilibrium value was doubled (Fig. 8).

The same behaviour can be found in the simulations as demonstrated in Figure 9.

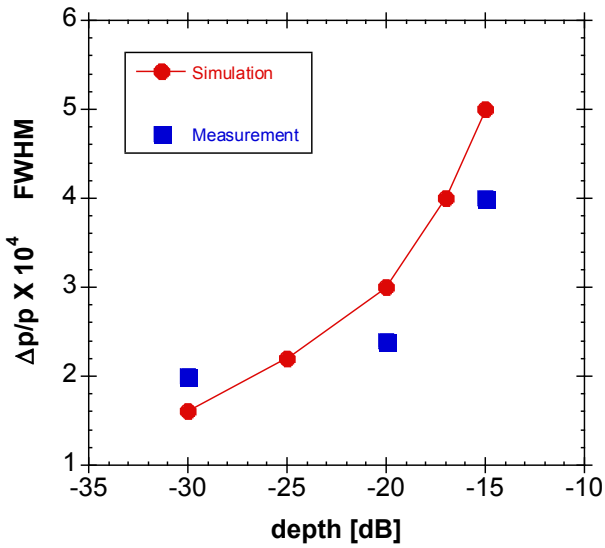

Figure 9: Simulated and measured beam equilibrium as function of different notch-depths.

OUTLOOK

The main stochastic cooling system for the HESR is now in the production phase. To test the performance of the cooling system the first pickup with 64 slot-coupler rings will be installed in COSY during the Christmas shutdown 2015/2016. The first kicker is scheduled to be installed in COSY in the middle of 2016 and commissioning of the whole system is expected at the end of 2016.

REFERENCES

[1] R. Stassen, P. Brittner, R. Greven, H. Singer, H. Stockhorst, L. Thorndahl, "Recent Developments for the HESR Stochastic Cooling System", Proceedings COOL07, Bad Kreuznach, Germany, 2007

[2] R. Stassen, F.J. Etzkorn, R. Maier, D. Prasuhn, H. Stockhorst, L. Thorndahl, "COSY as Ideal Test Facility for HESR RF and Stochastic Cooling Hardware", Proceedings PAC09, Vancouver, Canada, 2009

[3] G. Trubnikov et al., "Project of the Nuclotron-based Ion Collider Facility (NICA) at JINR", Proceedings of EPAC08, Genoa, Italy, 2008

[4] G. Trubnikov, A. Sidorin, N. Shurkhno, "NICA Cooling Program", Cybernetics and Physics Journal, Vol. 3, No. 3, 2014

ISBN 978-3-95450-174-8

[5] N. Shurkhno et al., "Study for Stochastic Cooling at Nuclotron", JINR, Proceedings of COOL13, Murren, Switzerland, 2013
[6] H. Stockhorst, R. Maier, D. Prasuhn, R. Stassen, "Status of Stochastic Cooling Predictions at the HESR", Proceedings of IPAC11, San Sebastian, Spain, 2011
[7] T. Katayama, T. Kikuchi, R. Maier, I. Meshkov, D. Prasuhn, R. Stassen, M. Steck, H. Stockhorst, "Beam Accumulation with Barrier Voltage and Stochastic Cooling", Proceedings of IPAC10, Kyoto, Japan, 2010
[8] M. Steck et al., "Demonstration of Longitudinal Stacking in the ESR with Stochastic Cooling", Proc. of COOL11, Alushta, 2011
[9] H. Stockhorst, T.Katayama, B. Lorentz, R. Maier, D. Prasuhn, R. Stassen, "Stochastic Beam Cooling in the Storage Rings COSY and the Future HESR with Internal Target Operation", ICFA Beam Dynamics Newsletter No. 64, p121 ff, 2014
[10] H. Stockhorst et al., "Heavy Ion Storage and Acceleration in the HESR with Stochastic Cooling and Internal Target", Proceedings STORI14, St. Goar, Germany, 2014
[11] P. Saad et al., "Design of a Highly Efficient 2-4GHz Octave Bandwidth GaN-HEMT Power Amplifier", IEEE Transactions on Microwave Theory and Techniques, Vol. 58, No7, July 2010

ISBN 978-3-95450-174-8

STOCHASTIC COOLING SYSTEM FOR HESR: THEORETICAL AND SIMULATION STUDIES

H. Stockhorst, B. Lorentz, R. Maier, D. Prasuhn and R. Stassen,
Forschungszentrum Juelich GmbH, Germany
T. Katayama, Nihon University, Narashino, Chiba, Japan

Abstract

The High-Energy Storage Ring (HESR) is part of the upcoming International Facility for Antiproton and Ion Research (FAIR) at GSI in Darmstadt. The HESR dedicates to the field of high-energy antiproton physics to explore the research areas of charmonium spectroscopy, hadronic structure, and quark-gluon dynamics with high-quality beams over a broad momentum range from *1.5* to *15 GeV/c*. High momentum resolution beams are mandatory for internal target experiments which are prepared with the well-established filter method in stochastic momentum cooling. This cooling technique will also be applied for antiproton accumulation in the HESR as well as in heavy ion beam cooling experiments with internal targets. Fast beam cooling is achieved with a *(2 – 4) GHz* system. In cases when the momentum spread exceeds the filter cooling acceptance the Time-Of-Flight (TOF) method, which is easily set up when filter cooling is already available, is applied to pre-cool the beam prior to filter cooling. To compare both cooling methods the basics of the theory is presented. Beam experiments at COSY are outlined to verify these aspects of the cooling theory.

INTRODUCTION

The HESR [1] has been originally designed for storage and acceleration of up to 10^{11} antiprotons for internal target experiments with high momentum resolution up to $\approx 1 \cdot 10^{-5}$ in the momentum range *1.5 GeV/c to 15 GeV/c*. Since in the modularized start version [1] the storage rings RESR and NESR are postponed the accumulation of the beam delivered by the CR has to be accomplished in the HESR itself. The well-established stochastic stacking method [2] is however not applicable. Instead a different method using moving barriers and stochastic filter momentum cooling is established [3] to accumulate 10^{10} antiprotons within *1000 s*. Recently, the feasibility of the HESR storage ring for the application of heavy ion beams with the special emphasis on the experimental program of the SPARC collaboration at FAIR has been investigated in detail [4]. The magnetic rigidity range $5Tm \le B\rho \le 50Tm$ allows the storage of $^{132}Sn^{50+}$ and $^{238}U^{92+}$ ions in the kinetic energy range *165 MeV/u* up to ≈ *5 GeV/u*.

Both, transverse and longitudinal cooling is available at the HESR. Transverse cooling is mainly applied to compensate a transverse beam blow up due to the beam-target interaction. The highest demands are made on longitudinal cooling, especially in the high momentum resolution mode. To fulfil this goal the bandwidth of the cooling system will be *(2 – 4) GHz* with the extended option of *(2 - 6) GHz* in a later stage [5]. High sensitive pickup/kicker structures have been developed and tested at COSY [5]. The filter cooling technique [6] is applied for longitudinal cooling in the momentum range above *3.8 GeV/c*. Below *3.8 GeV/c* the Time-Of-Flight momentum (TOF-) cooling technique [7] will be used.

MOMENTUM COOLING METHODS

Stochastic momentum cooling is described with the Fokker-Planck Equation (FPE) [6]

$$\frac{\partial \Psi}{\partial t} = -\frac{\partial}{\partial \delta}\left[F\Psi - D\frac{\partial \Psi}{\partial \delta} \right] \qquad (1)$$

for the time evolution of the momentum distribution $\Psi(\delta,t)$ of ions with relative momentum deviation δ. The explicit expressions for the drift F describing cooling and diffusion D depend on the cooling method.

In the Filter cooling method a pickup in sum mode measures the beam current and the discrimination of particles with different momentum deviations is obtained by inserting a notch filter and a *90* degree phase shifter in the signal path before it drives a kicker in sum mode. Besides pre-amplifiers and power amplifiers a variable delay is available to adjust the signal transit time from pickup to kicker to the time-of-flight of a particle with nominal momentum. The basic system arrangement is illustrated in figure 1.

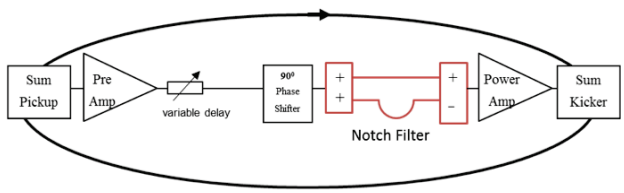

Figure 1: Basic system configuration for filter cooling.

A severe restriction in the practical cooling bandwidth comes from mixing between pickup and kicker. Large mixing from pickup to kicker will reduce the maximum momentum spread that can be cooled for a given upper cooling frequency without particle losses. Figure 2 illustrates a simulation [8] for an antiproton beam at *3.8 GeV/c* in the HESR with 10^{10} particles. The electronic gain is *110 dB*. The relative momentum spread is $5 \cdot 10^{-4}$. It shows the drift term (the energy change per second a particle receives at the kicker due to its on momentum

ISBN 978-3-95450-174-8

deviation at the pickup) in FPE for filter method (red curve) neglecting beam feedback. Particles that are outside the cooling acceptance indicated by the arrow will be heated and will be subsequently lost.

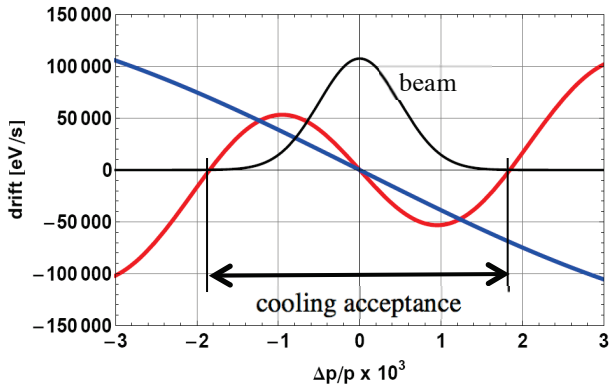

Figure 2: Drift term for filter (red) and TOF (blue) cooling for the same gain of *110 dB*. The cooling acceptance for filter cooling is indicated by an arrow. TOF cooling possesses a much larger cooling acceptance.

The advantage of the filter method is that Schottky particle noise and thermal electronic noise is substantially suppressed in the centre of the particle momentum distribution as is shown in figure 3, red curve.

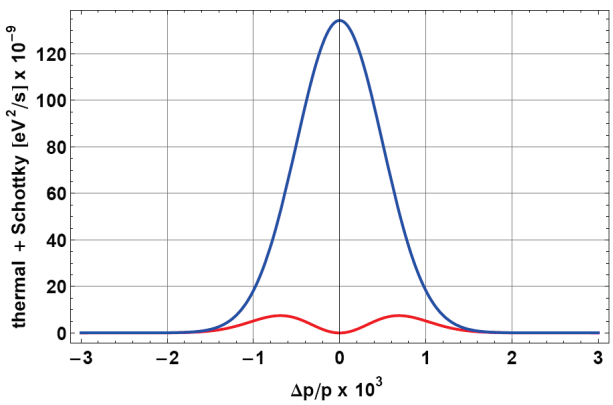

Figure 3: The diffusion term for filter cooling (red) show the suppression of thermal and Schottky noise in the center of the beam distribution. For the same gain the diffusion in TOF cooling (blue) is much larger. There is no suppression.

Strong unwanted mixing from pickup to kicker especially prevents filter cooling of antiprotons below *3.8 GeV/c*. In the low momentum range *1.5 GeV/c* up to *3.8 GeV/c* TOF cooling is therefore envisaged. TOF cooling is also applied in the heavy ion mode of the HESR at injection energy *740 MeV/u* [4]. In this method the filter in the cooling chain is opened as indicated in figure 4 and the signal transit time from pickup to kicker is adjusted with the same delay as applied for filter cooling to the time-of-flight of a particle with nominal momentum. As compared to filter cooling an additional *180* degree phase shifter is necessary to obtain cooling. Mixing from pickup to kicker can now be used to discriminate between particles of different momenta [8]. In figure 2 it is visible that the drift term for TOF cooling (blue curve) at *3.8 GeV/c* with the same electronic gain possesses a significantly larger cooling acceptance as filter cooling. However, the diffusion is much larger as is shown in figure 3. To avoid too much heating a reduced electronic gain has to be chosen in order to achieve cooling. Since thermal and Schottky noise heating is not suppressed in the center of the beam distribution the cooling time and the achievable beam equilibrium momentum value will be larger [8].

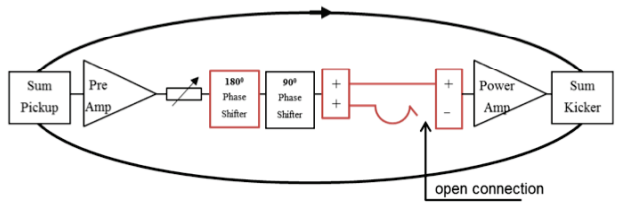

Figure 4: System configuration for TOF cooling.

A detailed analysis [8] shows that the range where the drift term either for filter or TOF cooling depends almost linearly on the relative momentum spread $\delta = \Delta p/p$ can be estimated by the expressions for

Filter cooling: *TOF cooling:*

$$|\delta| < \frac{f_0}{2|\eta + 2r\eta_{PK}| \cdot f_+} \quad \text{and} \quad |\delta| < \frac{f_0}{2|2r\eta_{PK}| \cdot f_+}.$$

The frequency slip factor from pickup to kicker is denoted by η_{PK} and for the whole ring by η. The revolution frequency is f_0. The ratio of the nominal particle travelling time from pickup to kicker to the revolution period is given by r. For filter cooling both slip factors contribute resulting in a smaller cooling acceptance as compared to TOF cooling. Increasing the upper frequency limit f_+ of the cooling system decreases the linear range and the cooling acceptance.

In recent beam experiments at COSY it could be demonstrated that TOF cooling has the larger cooling acceptance as predicted by the cooling model and that it is an appropriate technique to pre-cool the beam prior to filter cooling if the initial momentum spread exceeds the cooling acceptance of filter cooling [9].

BEAM EXPERIMENTS AT COSY

A full description of stochastic cooling has to take into account that the cooling system forms a feedback loop via the beam and has therefore to include the beam transfer function from kicker to pickup. Optimal cooling is only achieved if the system gain and phase of the feedback loop is adjusted appropriately at each harmonic in the cooling bandwidth. For filter cooling it is well-known that cooling is obtained if at each harmonic the open loop gain is adjusted as shown in figure 5 for a proton beam at

ISBN 978-3-95450-174-8

2.4 GeV/c on COSY. The band II *(1.8 – 3) GHz* momentum cooling system is used. The measurement displays the Nyquist diagram (blue curve) of the open loop gain *S* at one harmonic in the cooling bandwidth. The figure also displays the magnitude of the open loop gain (yellow curve) showing the suppression of Schottky and thermal noise in the center of the distribution. The delay is adjusted for cooling. The gain is however below the optimal one where noticeable signal suppression [8] in filter cooling is observed. The cooling loop is stable since the real part of the open loop gain *S* is well below one.

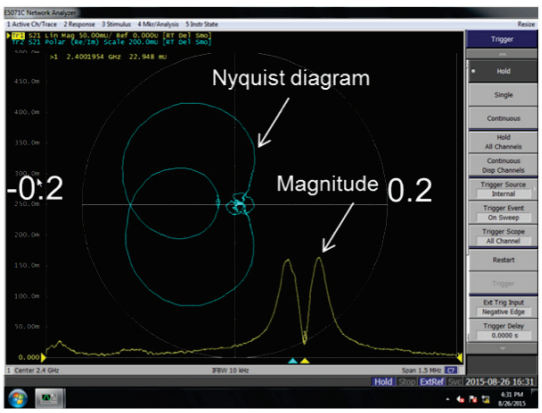

Figure 5: Nyquist diagram of the open loop gain for filter cooling (blue). The magnitude (yellow) of the open loop gain shows the suppression due to the notch filter.

The resulting momentum cooling of 10^9 protons is displayed in figure 6. The filter notch depth is *30 dB*. The initial distribution is shown in blue and the equilibrium distribution is shown in yellow after 300 s cooling.

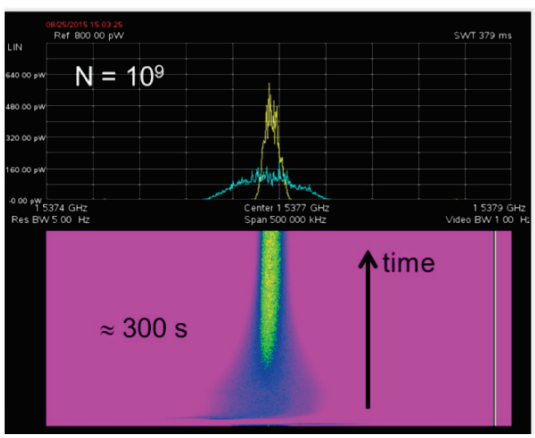

Figure 6: Filter momentum cooling.

TOF cooling has been investigated at *2.6 GeV/c* since at this slightly larger momentum the frequency slip factor is larger and thus more mixing from pickup to kicker is achieved. The open loop gain measurement is depicted in figure 7. As compared to filter cooling Schottky and thermal noise are not suppressed in the center of the distribution as shown by the magnitude of the open loop gain (yellow trace) in figure 7.

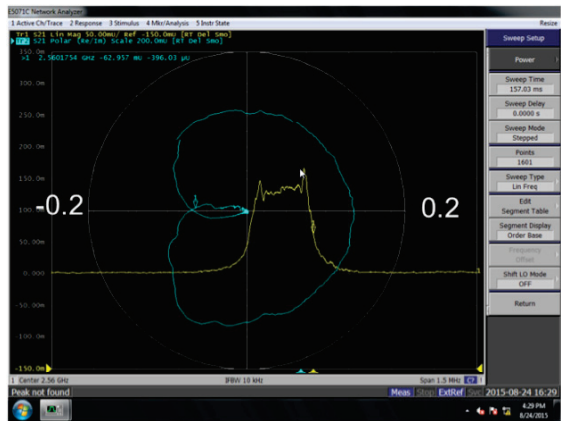

Figure 7: Nyquist diagram of the open loop gain for TOF cooling (blue). The magnitude of the open loop gain is shown in yellow.

The real part of the open loop gain now extends into the right hand plane of the Nyquist plot. The system gain must be reduced in order to stay with the open loop gain well below the critical point (1, 0) in the Nyquist plot. Heating the beam, e.g. with an internal target, leads similarly to a stable cooling loop [8].

The measurement of the open loop gain for TOF cooling at COSY, figure 7, confirms the model prediction for the HERS cooling system presented in figure 8 at harmonic number *5927*. The same beam and system parameters as for figure 2 and 3 have been used. To obtain a stable cooling loop during cooling the electronic gain was reduced from *110 dB* to *98 dB*.

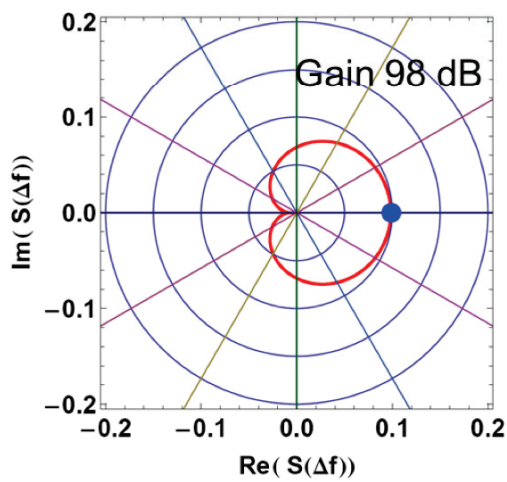

Figure 8: Simulated Nyquist plot of the open loop gain *S* for TOF cooling at *3.8 GeV/c* in the HESR. The gain is reduced from *110 dB* to *98 dB* to obtain stable cooling.

Beam feedback modifies the drift term *F* in the FPE, eq. (1), at each harmonic in the cooling bandwidth of the cooling system by the real part of $1/(1-S)$ and the diffusion term *D* by $1/|1-S|^2$. The impact of the beam feedback on the drift and diffusion terms is shown in figure 9.

ISBN 978-3-95450-174-8

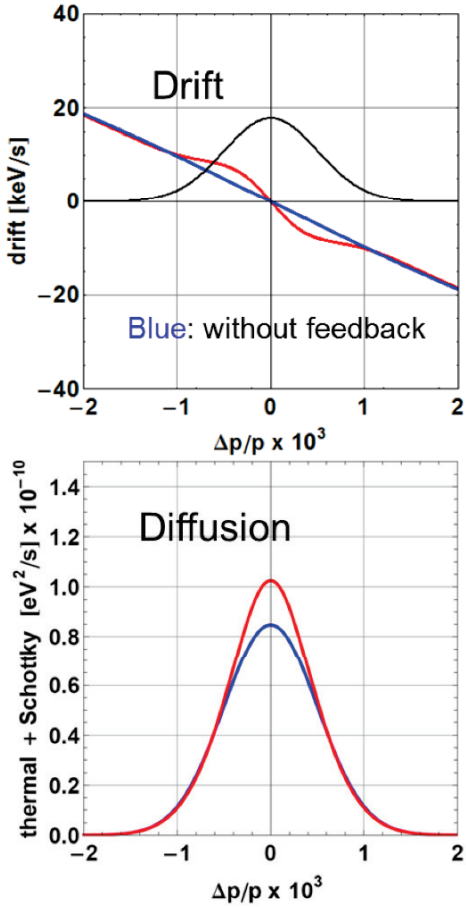

Figure 9: Drift and diffusion term in the FPE for TOF cooling with (red) and without (blue) beam feedback.

Compared to filter cooling no signal suppression is observed in TOF cooling. Instead a signal enhancement is visible which leads to an increase of the drift term in the center of the distribution which vanishes towards the edges of the beam distribution as is depicted in the upper panel of figure 9. Simultaneously, the diffusion is increased in the center of the distribution.

The initially heated beam distribution with a relative momentum spread of $1 \cdot 10^{-3}$ develops during TOF cooling with the reduced electronic gain as presented in figure 10.

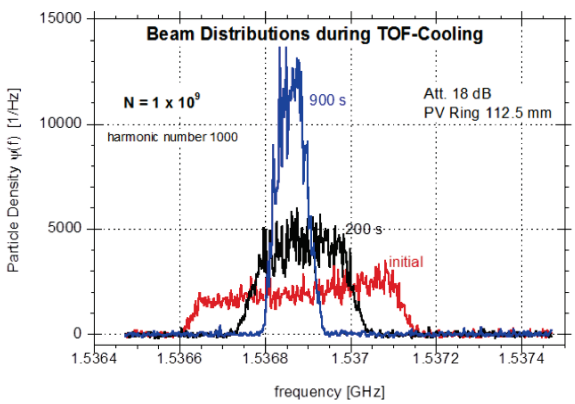

Figure 10: TOF cooling of an initially heated beam.

The experimental result in figure 10 is compared with a simulation shown in figure 11. The predictions reveal in accordance with the results shown in figure 9 that beam feedback has no significant impact on TOF cooling due to the reduced gain and the initially increased momentum spread of the beam distribution.

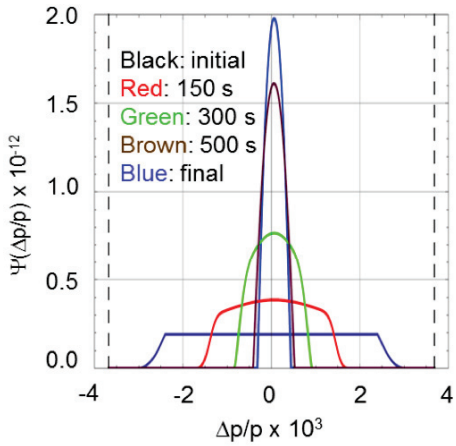

Figure 11: Simulated beam distributions during TOF cooling of an initially heated beam.

In figure 12 the rms-relative momentum spread versus time as predicted by the model is compared with the measurement results. It is visible that the model predicts fairly well the beam equilibrium value. It is also visible that the equilibrium value does not depend on the initial value of the momentum spread.

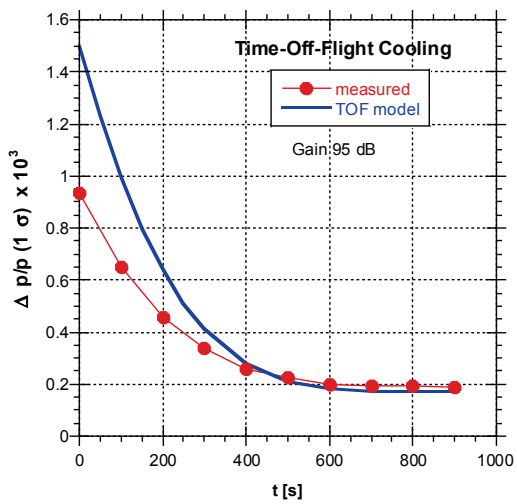

Figure 12: Model prediction of the relative momentum spread versus time during TOF cooling compared with the measurement.

The delay in TOF cooling must be adjusted very carefully in order to avoid a shift of the average momentum of the final momentum distribution. A change of the cooling system delay length by $+7.5\ mm$ results in a shifted final beam frequency distribution as shown in figure 13. This corresponds to a shift of the average final

ISBN 978-3-95450-174-8

momentum to a larger value since the working point of the machine is above transition energy

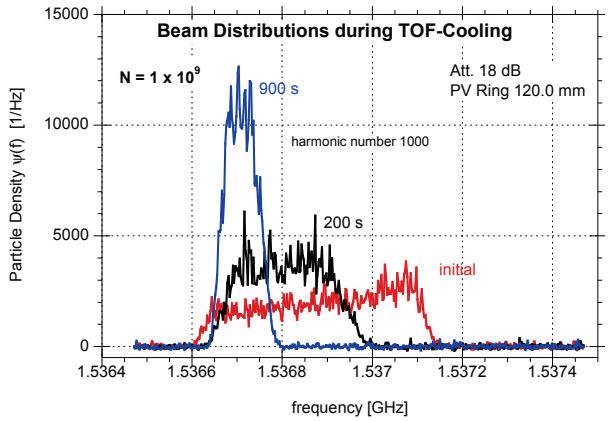

Figure 13: TOF cooling as in figure 10 but with a delay length change of *+7.5 mm*.

A simulation of TOF cooling with a delay length change of *–11 mm* is depicted in figure 14. It is visible that the shortening of the delay length for the machine working point above transition energy leads to a decrease of the average momentum in the final momentum distribution.

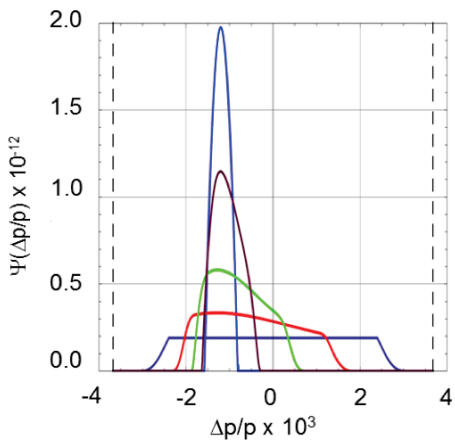

Figure 14: TOF cooling as in figure 11 but with a system delay length reduced by *-11 mm*.

Comparing the final distributions in figure 11 and 14 one notices that a delay length change only alters the final momentum. The final momentum spread does not change.

The experiments as well as the model predictions for TOF cooling demonstrate the possibility to vary the final momentum spread similarly as in filter cooling by changing the notch frequency. The mean energy loss due to an internal target with a moderate target thickness can thus be biased by a delay change prior to cooling likewise as in filter cooling by adjusting the notch frequency appropriately.

SUMMARY

Strong filter momentum cooling in the HESR for antiproton beam accumulation and internal target experiments with antiproton or ion beams is accomplished with a *(2 – 4) GHz* with the future upgrade option to extend the upper frequency limit to *6 GHz*. A detailed comparison of the theory of TOF and filter cooling including beam feedback has been worked out. The theoretical predictions are compared to the experimental cooling studies carried out at COSY. The beam cooling experiments at COSY confirm that the TOF cooling is easily established when filter cooling is already installed. The Palmer cooling method [6], which possesses a larger cooling acceptance as compared to filter cooling, cannot be implemented in the HESR due to cost and space restrictions. The TOF cooling technique thus plays a major role in the HESR for cases where the initial momentum spread exceeds the filter cooling acceptance and pre-cooling is essential prior to filter cooling.

REFERENCES

[1] "FAIR - Facility for Antiproton and Ion Research", Green Paper - The Modularized Start Version, October 2009; http://www.faircenter.de/fileadmin/fair/publications_FAIR/FAIR_GreenPaper_2009.pdf

[2] F. Caspers and D. Möhl, "Stacking with Stochastic Cooling", CERN-AB-2004-028 RF

[3] T. Katayama, M. Steck, H. Stockhorst, I. Meshkov and T. Kikuchii, "Beam Accumulation and Bunching with Cooling", Proc. of COOL 13, 10-14 June 2013, Murren, Switzerland

[4] H. Stockhorst, T. Katayama, A. Lehrach, B. Lorentz, R. Maier, D. Prasuhn and R. Stassen, "Heavy ion storage and acceleration in the HESR with stochastic cooling and internal target", Proc. of STORI 14, September 28 - October 3, 2014, Schloss Rheinfels, St. Goar, Germany, to be published in *Physica Scripta*

[5] R. Stassen, B. Breitkreutz, G. Schug, H. Stockhorst, "Stochastic Cooling of Heavy Ions in the HESR", invited contribution to this conference

[6] D. Möhl, Stochastic Cooling of Particle Beams, Lecture Notes in Physics 866, Springer Verlag, 2013, ISBN 978-3-642-34978-2

[7] W. Kells, "Filterless Fast Momentum Cooling", Proc. of the 11th Int. Conf. on High-Energy Accelerators, Geneva, Switzerland, July 7-11, 1980, p. 777, and ref. therein

[8] H. Stockhorst, T. Katayama and R. Maier, "Beam Cooling at COSY and HESR – Theory and Simulation -, to be published

[9] H. Stockhorst, R. Stassen, D. Prasuhn, R. Maier, T. Katayama and L. Thorndahl, "Compensation of Mean Energy Loss due to an Internal Target by Application of a Barrier Bucket and Stochastic Momentum Cooling at COSY", Proc. of COOL 09, August 31 – September 4, 2009, Lanzhou, China

ISBN 978-3-95450-174-8

STOCHASTIC COOLING DEVELOPMENTS FOR THE COLLECTOR RING AT FAIR

C. Dimopoulou, D. Barker, R. Böhm, R. Hettrich, W. Maier
C. Peschke, A. Stuhl, S. Wunderlich, GSI, Darmstadt, Germany
L. Thorndahl, CERN, Geneva, Switzerland

Abstract

A Status report on the ongoing developments for the demanding stochastic cooling system of the Collector Ring is given. The system operates in the frequency band 1-2 GHz, it has to provide fast 3D cooling of antiproton, rare isotope (RIBs) and stable heavy ion beams. The main challenges are (i) the cooling of antiprotons by means of cryogenic movable pick-up electrodes and (ii) the fast two-stage cooling (pre-cooling by the Palmer method, followed by the notch filter method) of the hot rare isotope beams. Progress in designing, testing and integrating the hardware is discussed.

INTRODUCTION

The CR stochastic cooling system is described in [1, 2]. In summary: Antiproton cooling is limited by the poor ratio Schottky signal/thermal noise, that is why it is foreseen: (i) to keep the slotline pickup electrodes at cryogenic temperatures (20-30 K), (ii) to strive for large sensitivity by moving (plunging) the pickup electrodes as the beam shrinks, (iii) for longitudinal cooling, to implement the notch filter technique, which is the best choice since it advantageously filters out the thermal noise. The chosen ring slip factor $|\eta|$=0.011 guarantees optimum momentum acceptance for the notch filter cooling, but slows down the simultaneous transverse cooling due to the high mixing M between kicker and pickup. A remedy comes from the flexibility of the CR lattice in setting different γ_{tr} values. As $\delta p/p$ shrinks during the 10 s of cooling, $|\eta|$ can be slightly increased by a factor 2-3 (decrease γ_{tr}), by small tuning of the quadrupole strength, so as to control $M(t) \sim (|\eta(t)|\delta p(t)/p)^{-1}$. At the end of cooling the beam is rebunched and extracted, then the quadrupoles must ramp fast back to their initial value ($|\eta|$=0.011) before new beam is injected. The lattice, the quadrupoles and their power supplies must be specified from the beginning for ramping in the range $|\eta| \approx 1 - 3\%$ within shortest time with respect to the cooling/cycle time. This $|\eta|$-ramping procedure will be optimized during commissioning with beam, at present it may be studied with cooling simulations in all 3 planes.

Heavy ion cooling is limited by the undesired mixing. In the beginning, for the hot RIBs, only the Palmer method can be applied with a dedicated pickup (pre-cooling stage). Recently, the option of time of flight (TOF) longitudinal cooling using the Palmer pickup in sum mode has been included. The TOF option can be useful for precooling the tails of hot RIB beams since it suffers less from the interplay with the horizontal betatron motion than the Palmer method. In a second stage, after δp/p has decreased, it is planned to switch to cooling with the slotline pickups and the notch filter until the final beam quality is reached.

The option of TOF longitudinal cooling for antiprotons or RIBs is useful for moderate requirements on the final $\delta p/p$ or on the cooling time (e.g. lower particle number, longer cycles) or, due to its larger momentum acceptance, as pre-cooling before the notch filter takes over.

For primary beams of stable ions coming with better quality after acceleration in the synchrotrons, one-stage cooling by the TOF or notch filter method with the slotline pickups should be sufficient.

Table 1: Required Cooling Performance in the CR. For parameters in red there is no safety margin, for those in blue larger values can be accepted with the HESR downstream.

3 GeV, 10^8 antiprotons, coasting beam		
	δp/p (rms)	$\epsilon_{h,v}$ (rms) π mm mrad
Before cooling	0.35 %	40
After cooling	0.05 %	1.25
Cooling down time	≤9 s	
Cycle time	10 s	

740 MeV/u, 10^8 RIBs, coasting beam		
	δp/p (rms)	$\epsilon_{h,v}$ (rms) π mm mrad
Before cooling	0.2 %	35
After cooling	0.025 %	0.125
Cooling down time	≤1 s	
Cycle time	≤1.5 s	

Table 1 shows the updated cooling requirements for 10^8 antiprotons and RIBs in the CR. In the present FAIR scenario the CR delivers to the HESR [3] pre-cooled antiprotons and stable ions/RIBs for accumulation and in-ring experiments. Taking into account the rebunching of the antiprotons/ions for transfer to the HESR as well as the small momentum acceptance of the HESR and its stochastic cooling systems, up to 30% lower final δp/p would be needed after cooling in the CR. On the other hand, higher emittances can be accepted in the HESR. For the most demanding case of 10^8 antiprotons in a 10 s cycle, the momentum spread budget should be within reach by optimizing the interplay among the longitudinal and transverse cooling in the CR, the rebunching/debunching procedures in the transfer as well as the longitudinal cooling in the HESR. The stable ions are less critical since they are initially not so hot as the RIBs.

ISBN 978-3-95450-174-8

What is more, stable ions/RIBs can be pre-cooled longer in the CR (e.g. 2-5 s) if high beam quality is needed for precision experiments in the HESR.

PICKUP DEVELOPMENTS

Prototype Cryogenic Pickup Tank with Plunging Slotline Electrodes

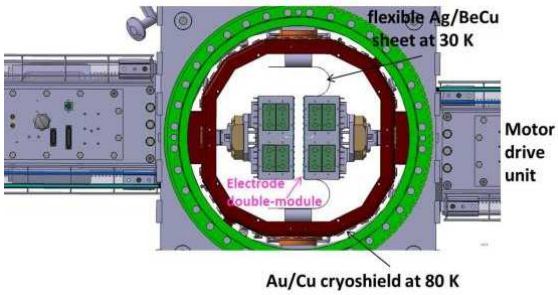

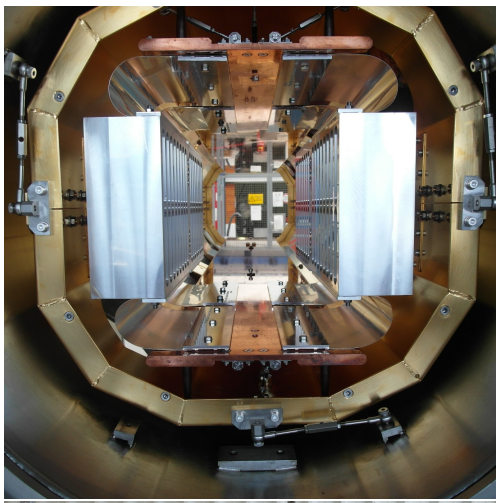

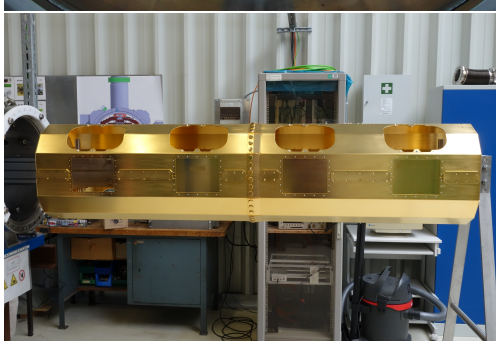

Figure 1: Section of the prototype pickup tank (2 m long, DN500COF flange), where the mechanical and thermal concepts are being tested. Top: The cryoshield, the Ag/BeCu sheets and the motor drive units driving synchronously the slotline electrode modules are shown. Middle: Final assembly in the tank before pumping down and performing the cryogenic test. Bottom: Gold-plated copper cryoshield before mounting in the tank.

Figure 1-top shows the concept in the prototype pickup tank. The movable slotline electrode modules are thermally coupled to flexible silver-plated copper beryllium sheets. These sheets are fixed on Cu bars along the tank (Fig. 1-top, middle) which are cooled by the 2nd stage of cryoheads to about 20-30 K. The intermediate cryoshield inside the pickup tank will be held at 80 K by the 1st stage of the cryoheads. It consists of 4 half-shells, each 1 m long, and bears holes for the motor drives and for assembling, it is made of oxygen-free copper, galvanically gold-plated so as to reach very low thermal emissivity (Fig. 1-bottom). The water-cooled linear motor drive units, tested synchronously in the prototype pickup tank (Fig. 1-top) at room temperature, fulfill the specifications: (i) their max. range of plunging is 70 mm following the shrinking beam size during stochastic cooling and (ii) at the end of the cycle, they move back out to their max. aperture within 200 ms, before a new beam is injected. The motor drive units are fully controlled, statically and dynamically, by real-time software.

The assembly inside the tank (Fig. 1-middle) comprising 2 motor drive units (instead of 8 in the full version) bearing dummy modules (i.e. without slotline electrodes), the flexible Ag/BeCu sheets mounted on the long Cu bars, the cryoshield and the two cryoheads (up, down on the tank) has been completed and first UHV and cryogenic tests have been performed.

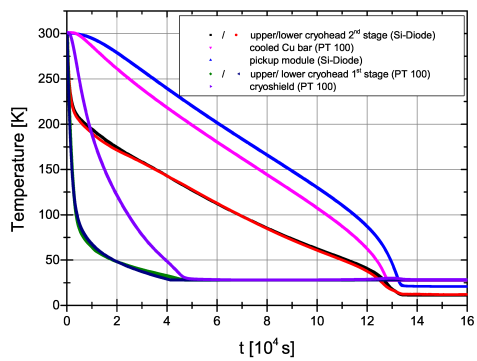

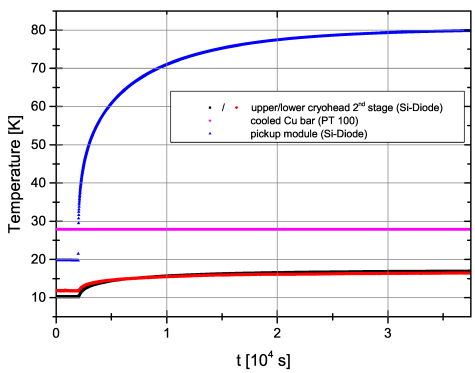

Figure 2: Temperatures of components in the prototype pickup tank versus time. The PT100 temperature sensor does not measure below 28 K, the Si-diode covers the full range. Top: Cooling down. The vacuum pressure dropped from $3 \cdot 10^{-6}$ down to $1 \cdot 10^{-9}$ mbar within $5 \cdot 10^4$ s. Bottom: Heating up the module simulating the heat load of 8 modules.

ISBN 978-3-95450-174-8

As shown in Fig. 2-top the 2nd stage of the cryoheads and the module reached 10-12 K and 20 K, respectively, the Cu bar temperature lied in between (i.e. in the worst case 10 K above the cryoheads 2nd stage). After cooling down, by means of resistive heating elements the module was heated up so as to simulate the expected heat load of 8 modules–in total 18 W–(Fig. 2-bottom). The 2nd stage of the cryoheads increased to 17 K, the Cu bar stayed below 28 K. These first results confirmed that the thermal concept with the 2 cryoheads and the cryoshield is appropriate (i.e. not underspecified) for the full version. Further systematic measurements and quantitative analysis are underway.

A special chamber for testing motor drive units under pre-vacuum conditions, at room temperature, was engineered, built and commissioned. It permits long-term tests in horizontal or vertical orientation in view of improvements for the final pickup tanks. It consists of 1/8 of pickup tank with Cu-cryoshield dummy and an observation window (Fig. 3). One motor drive unit with electrode module can be mounted so as to slide along the Ag/BeCu sheets. In the tests, the Ag/BeCu sheets (the ones shown in Fig. 1-middle) were found unreliable because they break after typically 10^5 cycles (aim is 10 million cycles). An improved concept for these sheets (geometry, manufacturing process) is in preparation. Systematic RF tests of a (moving) slotline electrode module can be carried out in the chamber, too.

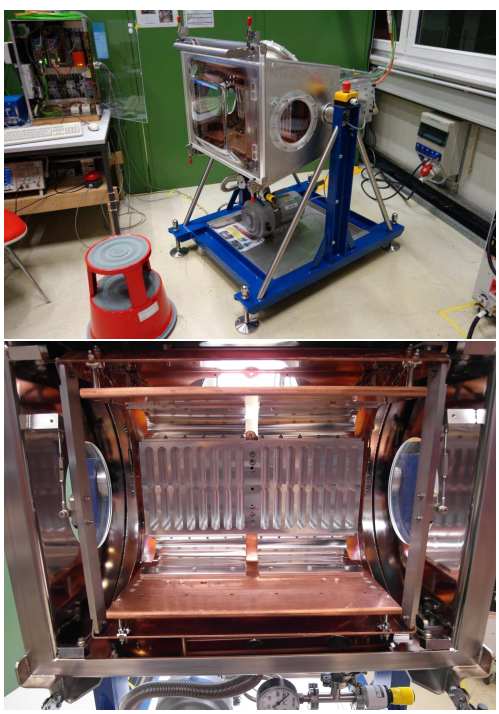

Figure 3: The chamber for lifetime tests of motor drive units and all moving components.

Palmer Pickup with Faltin Electrodes

Plunging of the pickup electrodes is not needed for pre-cooling of RIBs. A pickup with very large horizontal (± 200 mm) and vertical (± 66 mm) apertures with respect to the beam axis is specified, so as not to intercept the injected beams (before the bunch rotation). The former implies that many unwanted rf modes lie inside the cooling band 1–2 GHz, these must be damped by filling the structure with ferrite. The latter limits the sensitivity of the pickup, so that a long structure (1.7 m, 2 m pickup installation length) is needed to reach sufficient impedance, but implies high phase non-linearity in the output signal with respect to the particle pulse. After dedicated electromagnetic simulations with the HFSS code and measurements on prototypes the geometry and rf properties of the proposed Faltin structures including ferrite have been optimized in the band 1–2 GHz [4]. The solution is the best compromise for (i) maximum pickup impedance coupled to the beam, (ii) linear output signal phase with respect to the particle pulse (iii) flat frequency response $S_{21}(f)$, avoiding resonances, (iv) suppression of unwanted rf modes. Thus, the engineering of the electrodes and the pickup tank can start soon.

RF SIGNAL PROCESSING

The RF block diagram of the complete stochastic cooling system [5] and its integration into the building is being refined so as to save electrical length, since the flight time of the quasi-relativistic particles from pickup to kicker is very short. The time delay budgets from pickup to kicker have been checked including realistic electrical lengths of the designed slotline/Faltin electrodes as well as conservative assumptions for the electrical length of the kicker electrodes and all intermediate signal processing components and cables. For the power amplifiers at the kickers the specified max. electrical length of 16 ns for each unit was assumed. There is almost no margin, especially for the Palmer cooling branch of RIBs.

The signal processing chain from the Palmer pickup (at high dispersion) to the kickers (at zero dispersion) uses the 4 Faltin electrodes in difference mode for i) the vertical cooling branch and ii) the combined horizontal and longitudinal cooling branch with the Palmer method. In addition, the option of TOF longitudinal cooling by taking the 4 Faltin electrodes in sum mode is foreseen (Fig. 4). The signal processing chain from the slotline pickups to the kickers includes the transverse (horizontal, vertical) cooling branches as well as the longitudinal cooling using the notch filter or the TOF method (Fig. 4).

Recent activities on the demanding RF components in the band 1–2 GHz are reported in detail in [6]. In short: The complex pickup module controller is currently under development. The beta switch combiners and the variable attenuators have been designed, some updating and final consolidation is needed before ordering the small series. The design of the phase shifters is in good progress. A functioning prototype of the embedded powermeter is now available, after refinement the series can be ordered. In-house development of an optical notch filter and its successful implementation with beam in the ESR have been reported before [7].

ISBN 978-3-95450-174-8

Recently, 2 optical notch filters with thermally stabilized delay lines were built and are ready for the CR (one for antiprotons at v=0.97 c, one for RIBs at v=0.83 c). Their measured RF properties fulfill the specification i.e. notch depth below −30 dB within 1–2 GHz. The water cooled 1–2 GHz power amplifiers at the kickers (250 W units) have been ordered, the preseries device is under development.

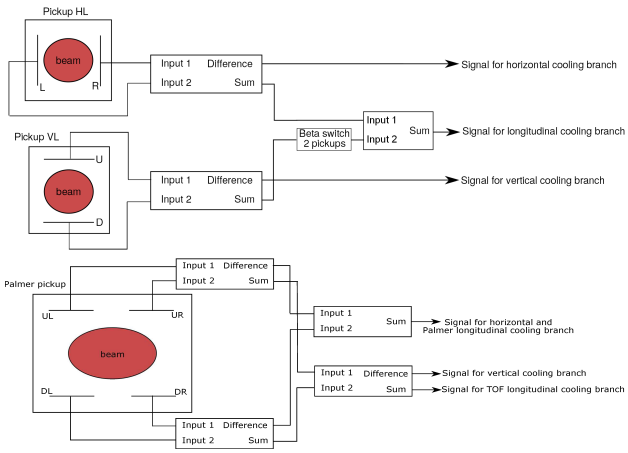

Figure 4: Principle of signal processing for the Palmer and the slotline pickups.

ACKNOWLEDGMENT

This work would not have been possible without our technicians J. Krieg and M. Bräscher. Special thanks goes to L. Lück, to the engineering department, the galavanisation and technology labs, the UHV group as well as to the mechanical workshop at GSI for their continuous support. We also thank F. Nolden, O. Dolinskyy, R. Stassen and H. Stockhorst for fruitful discussions.

REFERENCES

[1] C. Dimopoulou et al., JACoW Proc. COOL'11, Alushta, TUIOB02 (2011); JACoW Proc. IPAC'12, New Orleans, MOPPD005 (2012); JACoW Proc. COOL'13, Mürren, TUAM1HA01 (2013).

[2] C. Dimopoulou, ICFA Beam Dynamics Newsletter No. 64, p.108 (2014).

[3] R. Maier et al., JACoW Proc. PAC'11, New York, THOCN2 (2011); H. Stockhorst et al., ICFA Beam Dynamics Newsletter No. 64, p.122 (2014).

[4] D. Barker et al., presented at COOL'15, Newport News, VA, USA, paper FRWAUD03, *These Proceedings*.

[5] C. Peschke et al., JACoW Proc. COOL'13, Mürren, WEPPO20 (2013).

[6] S. Wunderlich et al., presented at COOL'15, Newport News, VA, USA, paper TUPF07, *These Proceedings*.

[7] W. Maier et al., JACoW Proc. COOL'13, Mürren, WEPPO19 (2013).

ISBN 978-3-95450-174-8

THE GREEN ENERGY TURBINE AS TURBO GENERATOR FOR POWERING THE HV-SOLENOIDS AT A RELATIVISTIC ELECTRON COOLER

A. Hofmann, K. Aulenbacher, M.-W. Bruker, J. Dietrich, T. Weilbach
Helmholtz-Institut Mainz, Germany
V.V. Parkhomchuk, V.B. Reva, BINP SB RAS, Russia

Abstract

One of the challenges in the development of a relativistic electron cooler is the powering of components, e.g. the HV-solenoids, which sit on different high potentials within a high voltage vessel and therefore need a floating power supply.

In this report we present the turbo generator "Green Energy Turbine" (GET), an assembly of a turbine and a generator, as a possible candidate for powering e.g. the HV-solenoids and give an overview over the future road map.

INTRODUCTION

In many experiments in hadron physics it is essential to keep the emittance constant, counteracting the emittance blow up e.g. due to scattering experiments. One way to prevent the emittance from increasing is the electron cooling technique [1], which will be used for example at the High Energy Storage Ring (HESR) at GSI/FAIR to permit high energy antiproton experiments [2]. The HESR has a circumference of 575 m and can operate in two modes, the "High Luminosity" (HL) and "High Resolution" (HR) mode. Some experimental demands are summarised in Table 1 [3].

Table 1: Experimental Demands of the HESR

	HL	HR
Momentum range	$1.5 - 15\ \frac{\mathrm{GeV}}{\mathrm{c}}$	$1.5 - 9\ \frac{\mathrm{GeV}}{\mathrm{c}}$
Peak luminositiy	$2 \cdot 10^{32}\ \frac{1}{\mathrm{cm^2 s}}$	$2 \cdot 10^{31}\ \frac{1}{\mathrm{cm^2 s}}$
Momentum resolution	$\frac{\Delta p}{p} = 10^{-4}$	$\frac{\Delta p}{p} = 10^{-5}$

To meet these requirements for the high resolution mode, magnetised electron cooling with a 4.5 MeV, 1 A electron beam is necessary. An intention for the HESR is an upgrade to the Electron Nucleon Collider (ENC). The ENC will allow experiments with polarised electrons and protons [4], which also need magnetised electron cooling. In that case, an 8 MeV, 3 A electron beam is needed. In order to solve critical technical issues, the Helmholtz-Institut Mainz (HIM) promotes collaborations with other Institutes such as Forschungszentrum Juelich (FZJ), Budker Institute of Nuclear Research Novosibirsk (BINP SB RAS), Russia and Lehrstuhl fuer Technische Thermodynamik und Transportprozesse (LTTT), University Bayreuth. One of the challenges is the powering of HV-solenoids, which are located on different electrical potentials inside a high voltage vessel, which is why they need a floating power supply.

Within a design study, BINP SB RAS has proposed two possibilities to build a power supply in a modular way. The first proposal is to use two cascade transformers per module. One cascade transformer powers 22 small HV-solenoids, the second one should generate the acceleration/deceleration voltage for the electron beam. The cascade transformers themselves are fed by a turbo generator, which is powered by a gas under high pressure that could be generated outside of the high voltage vessel. The second possibility is to use two large HV-solenoids per module, which are composed of four small coils. In this proposal, the HV-solenoids are powered directly by a turbo generator [5]. Both concepts have in common that they need a suitable turbo generator which delivers a power of 5 kW. A research for proper turbo generators has identified the Green Energy Turbine (GET) from the company DEPRAG as a potential candidate [6]. At HIM, two GET were bought and tested.

GREEN ENERGY TURBINE

The GET (Figure 1) is an assembly composed essentially of a turbine and a generator. Dry compressed air enters the

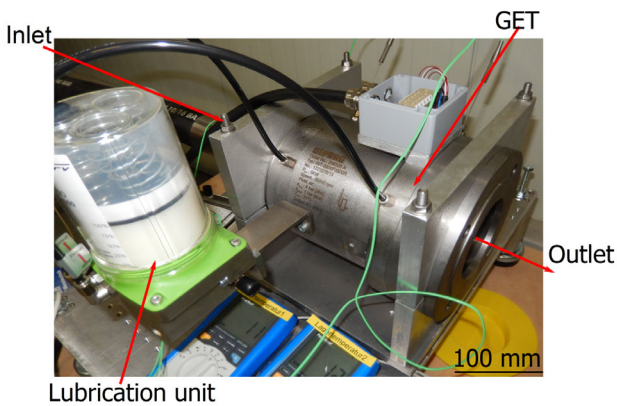

Figure 1: The turbo generator Green Energy Turbine (GET) with lubrication unit.

GET on the inlet side and is expanded through a nozzle. The resulting accelerated air drives a turbine, which in turn drives a generator. After the expansion, the air is diverted around the generator and leaves the GET on the outlet side at normal pressure. The generator is connected in delta configuration, which generates three-phase current. The turbine and the generator are supported by ball bearings, which was believed

ISBN 978-3-95450-174-8

to need a small amount of fresh lubricant after 100 hours in regular operation [7].

Therefore, a lubrication unit which pumps 300 mm^3 lubricant into the bearings is mounted at the GET. The used lubricant is stored in special containers which are cleaned during maintenance, so that the contamination of the driving air is minimal. The GET itself should work the typical time for one production run at the HESR which is of the order of one year without maintenance. Further properties of the GET are listed in Table 2.

Table 2: Properties of the GET

Property	Value
Power	5 kW
Revolution speed	35000 min^{-1}
Pressure (in)	4 bar
Pressure (out)	1 bar
Mass Flow	4 $\frac{m^3}{min}$
Pressure condensation point	−20°C
Voltage phase to phase	263 V
Current	12 A
Norminal frequency	583 Hz

CHARACTERISATION OF THE GET

In order to characterise the GET, different test measurements with the turbo generator were done at HIM. The test set-up is shown in Figure 2. A buffer tank is filled by a compressor, which is outside of the hall and consumes a power of 40 kW to generate compressed air at 4 bar and an airflow of 4 $\frac{m^3}{min}$. In the buffer tank the air is heated to reduce the condensation (from the ambient air) due to the cooling of the air after the expansion, which also cools down the GET housing. The three-phase alternating current generated by the generator is rectified, as load resistors are used. To protect the GET, a fast closing valve is additionally installed, which immediately closes if the limits of the GET (e.g. $n_{critical}$ = 36000 min^{-1}, $I_{critical}$ = 16 A) are exceeded.

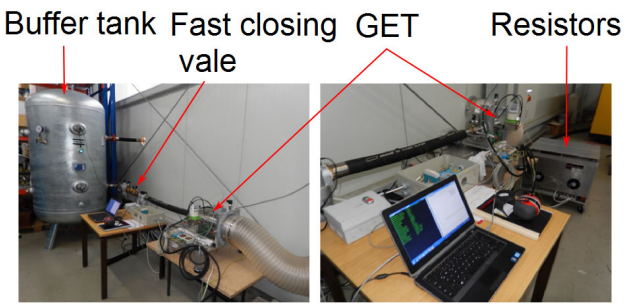

Figure 2: Test set-up at HIM for characterising the GET. Inside the buffer tanks heaters are installed for heating the pressurised air before it enters the turbo generator. The heaters are powered by the GET itself.

Figure 3 shows the measurement of the DC power as function of the revolution speed and the input pressure for different loads.

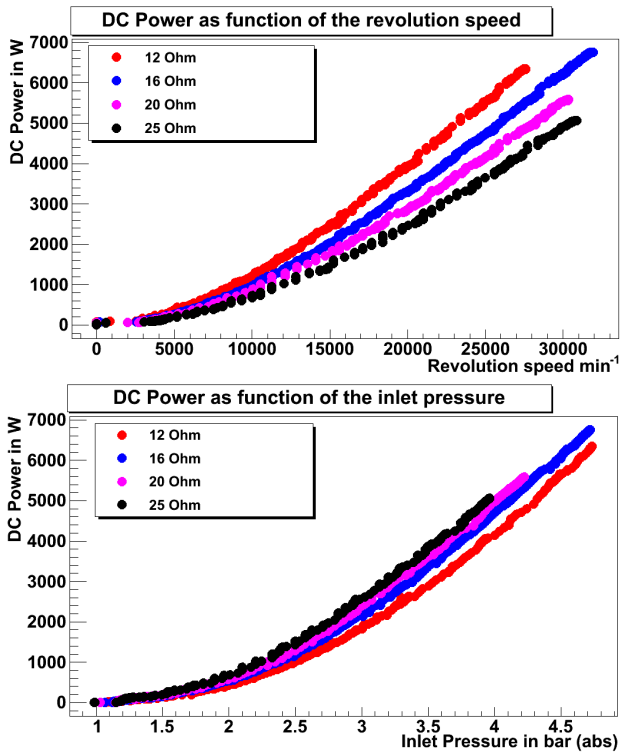

Figure 3: Measurement of the DC power as function of the revolution speed and the inlet pressure for different loads

The measurements show that it is possible to generate the needed power of 5 kW within the limits of the GET. The outlet temperature of the air for a load of 22.9 Ω is presented in Figure 4.

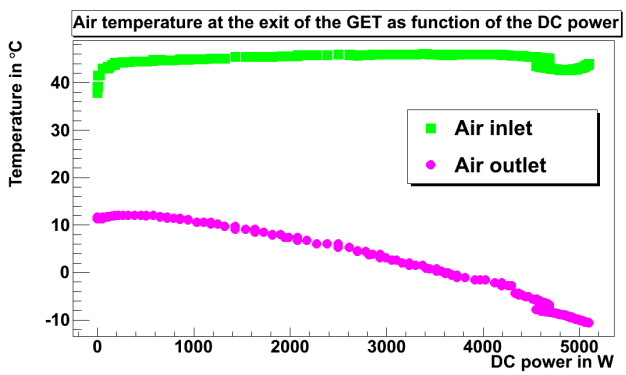

Figure 4: Air outlet temperature as function of the DC power for a load of 22.9 Ω. The measurement time was 2 min; the temperature drop of the air after the expansion is 53°C.

For a number of measurements with a load of 22.9 Ω a drop of the air temperature is in the order of (50 ± 5)°C and also cools down the GET housing.

ISBN 978-3-95450-174-8

Another important point is the reliability of the turbo generator. For this reason, a long-term test over 1025 operation hours with a load of 22.9 Ω including many start and stop cycles was successfully carried out. The ball bearings were only lubricated at the beginning but not during the long-term test. During the test, the temperature change of the bearings and the excitation windings of the generator were recorded as well. The bearing temperature decreases in the order of 10°C due to cooling by the exhaust air, the temperature of the excitation windings increases in the range of 10 to 15°C.

FURTHER ROAD MAP

During its normal operation, the turbo generator will be inside a high pressure tank, which is filled with Sulphur hexafluoride at a pressure of 10 bar. This means that the turbo generator must be pressure-resistant at least until 10 bar. Therefore a modification of the test set-up is in preparation. The GET will be installed within a small pressure tank, which will be filled with dry nitrogen. Subsequently some of the characterisation measurements are repeated, e.g. the long-term test. But before the turbo generator can be installed in a pressure tank, it's necessary to modify the lubrication unit, because it is not pressure-resistant. The current lubrication is replaced by a pressure-resistant box as shown in Figure 5. If the tests with the modified turbo generator are successful, both GET are sent to BINP SB RAS to implement them in a test set-up for powering HV-solenoids, which will be sent and installed at HIM later [5].

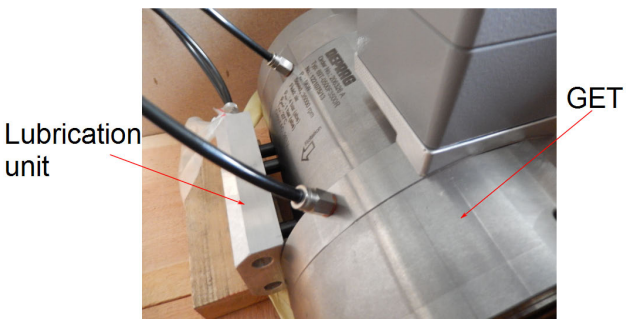

Figure 5: GET with modified pressure-resistant lubrication unit. The lubrication unit must be operated manually

However, an additional disadvantage of the lubrication unit is a potential pollution of the driving gas with lubricant. In case of leakage, the Sulphur hexafluoride in the high voltage vessel might also be affected. To avoid this risk, a lubrication-free turbo generator would be beneficial, which is why a further prototype will be built in which the ball bearings are replaced by gas bearings. Furthermore the new turbo generator will work with pure nitrogen in a closed circuit instead of ambient air in an open circuit. But the price for the lubrication free turbo generator is that special precautions need to be taken. Firstly, the installation position is mandatory and not optional (the inlet side must be on the top) and secondly the gas bearings require a special start procedure to reduce the wear. Before the nitrogen can enter the GET, it must be started smoothly in the "motor mode". That means the generator operates as a motor and causes the gas bearings in a slow rotation movement. If a certain rotation speed is reached, the turbo generator can be used in the usual way. This turbo generator is currently in development and its delivery is expected at the end of the year. It will be later implemented in the HV-solenoid test set-up from BINP SB RAS.

Another open question is the driving gas itself. Because the turbo generator will work in a Sulphur hexafluoride environment, Sulphur hexafluoride would be the ideal driving gas. But the generation of compressed Sulphur hexafluoride to drive a 5 kW turbo generator is another challenge. So far we have not been able to identify a commercial compressor system for Sulphur hexafluoride which would offer attractive operating conditions. A solution could be an Organic Rankine Cycle (ORC) with Sulphur hexafluoride, which is investigated by LTTT in a feasibility study [5]. However, a first analysis has shown, that pressures of the order of 40 bar would be needed. This would require research and development effort for the turbines and the gas distribution system. We therefore favour using dry nitrogen as a medium and to use a conventional compressor stage. A small portion of nitrogen in the Sulphur hexafluoride environment is unproblematic, therefore leakage of the nitrogen into the Sulphur hexafluoride environment can be tolerated up to certain extent.

REFERENCES

[1] J. Bosser, Electron Cooling in CERN Acc. School, CERN 95-06, p, 673 (1995).

[2] PANDA Collaboration, Physics Performance Report for PANDA, Strong Interaction Studies with Antiprotons.

[3] A. Lehrach et al., "Beam Performance and Luminosity Limitations in the High Energy Storage Ring (HESR)" , STORI'08, Lanzhou, China.

[4] A. Lehrach et al., "The polarized electron-nucleon collider project ENC at GSI/FAIR", 19th International Spin Physics Symposium (SPIN2010).

[5] A. Hofmann et al., "Turbo Generators for Powering the HV-Solenoids at the HESR Electron Cooler", IPAC 2014, Dresden, Germany.

[6] www.deprag.com

[7] Manual GET

ISBN 978-3-95450-174-8

ELECTRON LENSES AND COOLING FOR THE FERMILAB INTEGRABLE OPTICS TEST ACCELERATOR*

G. Stancari†, A. Burov, V. Lebedev, S. Nagaitsev, E. Prebys, A. Valishev, Fermilab, Batavia IL, USA

Abstract

Recently, the study of integrable Hamiltonian systems has led to nonlinear accelerator lattices with one or two transverse invariants and wide stable tune spreads. These lattices may drastically improve the performance of high-intensity machines, providing Landau damping to protect the beam from instabilities, while preserving dynamic aperture. The Integrable Optics Test Accelerator (IOTA) is being built at Fermilab to study these concepts with 150-MeV pencil electron beams (single-particle dynamics) and 2.5-MeV protons (dynamics with self fields). One way to obtain a nonlinear integrable lattice is by using the fields generated by a magnetically confined electron beam (electron lens) overlapping with the circulating beam. The required parameters are similar to the ones of existing devices. In addition, the electron lens will be used in cooling mode to control the brightness of the proton beam and to measure transverse profiles through recombination. More generally, it is of great interest to investigate whether nonlinear integrable optics allows electron coolers to exceed limitations set by both coherent or incoherent instabilities excited by space charge.

INTRODUCTION

In many areas of particle physics, such as the study of neutrinos and of rare processes, high-power accelerators and high-brightness beams are needed. The performance of these accelerators is limited by several factors, including tolerable losses and beam halo, space-charge effects, and instabilities. Nonlinear integrable optics, self-consistent or compensated dynamics with self fields, and beam cooling beyond the present state of the art are being actively pursued because of their potential impact.

In particular, the Integrable Optics Test Accelerator (IOTA, Fig. 1) is a research storage ring with a circumference of 40 m being built at Fermilab [1, 2]. Its main purposes are the practical implementation of nonlinear integrable lattices in a real machine, the study of space-charge compensation in rings, and a demonstration of optical stochastic cooling. IOTA is designed to circulate pencil beams of electrons at 150 MeV for the study of single-particle linear and nonlinear dynamics. For experiments on dynamics with self fields, protons at 2.5 MeV (momentum 69 MeV/c) will be used.

In accelerator physics, nonlinear integrable optics involves a small number of special nonlinear focusing elements added to the lattice of a conventional machine in order to generate large tune spreads while preserving dynamic aperture [3], thus providing improved stability to perturbations and mitigation of collective instabilities through Landau damping.

One way to generate a nonlinear integrable lattice is with specially segmented multipole magnets [3]. There are also two concepts based on electron lenses [4]: (a) axially symmetric thin kicks with a specific amplitude dependence [5–7]; and (b) axially symmetric kicks in a thick lens at constant amplitude function [8, 9]. These concepts use the electromagnetic field generated by the electron beam distribution to provide the desired nonlinear transverse kicks to the circulating beam.

In IOTA, the electron lens can also be used as an electron cooler for protons. In this paper, we present a preliminary exploration of the research opportunities enabled by the cooler option: beam dynamics with self fields can be studied in a wider brightness range; spontaneous recombination provides fast proton diagnostics; and, lastly, perhaps the most interesting question is whether the combination of electron cooling and nonlinear integrable optics leads to higher brightnesses than presently achievable.

NONLINEAR INTEGRABLE OPTICS WITH ELECTRON LENSES

Electron lenses are pulsed, magnetically confined, low-energy electron beams whose electromagnetic fields are used for active manipulation of circulating beams [10, 11]. One of the main features of an electron lens is the possibility to control the current-density profile of the electron beam (flat, Gaussian, hollow, etc.) by shaping the cathode and the extraction electrodes. Electron lenses have a wide range of applications [12–22]. In particular, they can be used as nonlinear lenses with tunable kicks and controllable shape as a function of betatron amplitude.

The goal of the nonlinear integrable optics experiments, including the ones with electron lenses, is to achieve a large tune spread, of the order of 0.25 or more, while preserv-

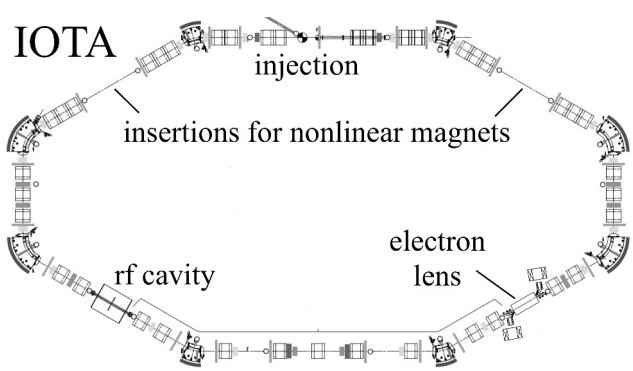

Figure 1: Layout of the IOTA ring.

* Fermilab is operated by Fermi Research Alliance, LLC under Contract No. DE-AC02-07CH11359 with the United States Department of Energy. Report number: FERMILAB-CONF-15-446-AD-APC.

† Email: ⟨stancari@fnal.gov⟩.

ISBN 978-3-95450-174-8

ing the dynamic aperture and lifetime of the circulating beam. Experimentally, this will be observed by recording the lifetime and turn-by-turn position of a low-intensity, low-emittance 150-MeV circulating electron bunch, injected and kicked to different betatron amplitudes, for different settings of the nonlinear elements (magnets or electron lenses).

The cathode-anode voltage V determines the velocity $v_e = \beta_e c$ of the electrons in the device, which is assumed to have length L and to be located in a region of the ring with lattice amplitude function $\beta_{\rm lat}$. When acting on a circulating beam with magnetic rigidity $(B\rho)$ and velocity $v_z = \beta_z c$, the linear focusing strength k_e for circulating particles with small betatron amplitudes is proportional to the electron current density on axis j_0:

$$k_e = 2\pi \frac{j_0 L(1 \pm \beta_e\beta_z)}{(B\rho)\beta_e\beta_z c^2}\left(\frac{1}{4\pi\epsilon_0}\right). \quad (1)$$

The '+' sign applies when the beams are counter-propagating and the electric and magnetic forces act in the same direction. For small strengths and away from the half-integer resonance, these kicks translate into the tune shift

$$\Delta\nu = \frac{\beta_{\rm lat} j_0 L(1 \pm \beta_e\beta_z)}{2(B\rho)\beta_e\beta_z c^2}\left(\frac{1}{4\pi\epsilon_0}\right). \quad (2)$$

for particles circulating near the axis.

There are two concepts of electron lenses for nonlinear integrable optics.

Thin Radial Kick of McMillan Type

The integrability of axially symmetric thin-lens kicks was studied in 1 dimension by McMillan [5, 6]. It was then extended to 2 dimensions [7] and experimentally tested with colliding beams [23]. Let $j(r)$ be a specific radial dependence of the current density of the electron-lens beam, with j_0 its value on axis and a its effective radius: $j(r) = j_0 a^4/(r^2 + a^2)^2$. The total current is $I_e = j_0\pi a^2$. The circulating beam experiences nonlinear transverse kicks: $\theta(r) = k_e a^2 r/(r^2 + a^2)$. For such a radial dependence of the kick, if the element is thin ($L \ll \beta_{\rm lat}$) and if the betatron phase advance in the rest of the ring is near an odd multiple of $\pi/2$, there are 2 independent invariants of motion in the 4-dimensional transverse phase space. Neglecting longitudinal effects, all particle trajectories are regular and bounded. The achievable nonlinear tune spread $\Delta\nu$ (i.e., the tune difference between small and large amplitude particles) is of the order of $\beta_{\rm lat} k_e/4\pi$ (Eq. 2). A more general expression applies when taking into account machine coupling and the electron-lens solenoid. For the thin McMillan lens, it is critical to achieve and preserve the desired current-density profile.

Axially Symmetric Kick in Constant Beta Function

The concept of axially symmetric thick-lens kicks relies on a section of the ring with constant and equal amplitude functions. This can be achieved with a solenoid with axial field $B_z = 2(B\rho)/\beta_{\rm lat}$ to provide focusing for the circulating beam and lattice functions $\beta_{\rm lat} \equiv \beta_x = \beta_y$. The same solenoid magnetically confines the low-energy beam in the electron lens. In this case, any axially symmetric electron-lens current distribution $j(r)$ generates 2 conserved quantities (the Hamiltonian and the longitudinal component of the angular momentum), as long as the betatron phase advance in the rest of the ring is an integer multiple of π. At large electron beam currents in the electron lens, the focusing of the electron beam itself dominates over the solenoid focusing and can be chosen to be the source of the constant amplitude functions. Because the machine operates near the integer or half integer resonances, the achievable tune spread in this case is of the order of $L/(2\pi\beta_{\rm lat})$. This scenario favors thick lenses and it is insensitive to the current-density distribution in the electron lens.

Several operating scenarios for the IOTA electron lenses are possible within the currently available parameter space [4]. The feasibility and robustness of these designs against deviations from the ideal cases are being studied with analytical calculations and numerical tracking simulations.

Typical electron-lens parameter ranges for IOTA are shown in Table 1.

Table 1: Typical Electron-Lens Parameters for IOTA

Parameter	Value
Cathode-anode voltage, V	0.1–10 kV
Beam current, I_e	5 mA – 5 A
Current density on axis, j_0	0.1–12 A/cm^2
Main solenoid length, L	0.7 m
Main solenoid field, B_z	0.1–0.8 T
Gun/collector solenoid fields, B_g	0.1–0.4 T
Max. cathode radius, $(a_g)_{\rm max}$	15 mm
Amplitude function, $\beta_{\rm lat}$	0.5–10 m
Circulating beam size (rms), σ_e	0.1–0.5 mm (e^-)
	1–5 mm (p)

ELECTRON COOLING IN IOTA

We investigate the benefits of an electron cooler in the ring and the possible difficulties of running an electron lens in cooling configuration.

Electron cooling in IOTA would extend the range of available brightnesses for space-charge experiments with protons. It would also provide a flow of neutral hydrogen atoms through spontaneous recombination for beam diagnostics downstream of the electron lens. Of greater scientific interest is the question of whether nonlinear integrable optics allows cooled beams to exceed the limitations of space-charge tune spreads and instabilities. Here we discuss these three aspects in more detail.

Electron Cooling of Protons

Proton parameters are shown in Table 2. The parameters are chosen to balance the dominant heating and cooling

ISBN 978-3-95450-174-8

Table 2: Proton Parameters for Cooling in IOTA

Parameter	Value
Kinetic energy, T_p	2.5 MeV
Normalized velocity, β_p	0.073
Number of particles, N_p	5×10^9
Beam current, I_p	0.44 mA
Normalized rms emittance, ϵ_{pn}	$0.3 \rightarrow 0.03$ μm
Rms beam size at cooler, y_p	4→1.3 mm
Momentum spread, σ_p/p	5×10^{-4}
Space-charge tune shift, $\Delta\nu_{sc}$	$-0.028 \rightarrow -0.28$
Transv. temperature (avg.), $\langle kT_{p\perp}\rangle$	5→0.5 eV
Long. temperature, $kT_{p\parallel}$	0.6 eV

mechanisms, while achieving significant space-charge tune shifts. To match the proton velocity, the accelerating voltage in the electron lens has to be $V = 1.36$ kV.

At these energies, proton lifetime is dominated by residual-gas scattering and by intrabeam scattering, due to emittance growth in the absence of cooling. (Charge neutralization is discussed below.) At the residual gas pressure of 10^{-10} mbar, the lifetime contributions of emittance growth due to multiple Coulomb scattering and of losses from single Coulomb scattering are 40 s and 40 min, respectively.

Intrabeam scattering has a stronger effect. Whereas the transverse emittance growth time is 120 s, the longitudinal growth time can be as small as 2.5 s, indicating a possible heat transfer from the longitudinal to the transverse degrees of freedom, which must be mitigated by keeping the effective longitudinal temperature of the electrons (which is dominated by the space-charge depression and therefore by the density n_e) low enough. At the same time, one needs to ensure that the heating term of the magnetized cooling force is negligible. One can achieve cooling rates of about 20 ms and reduce the transverse emittance by about a factor 10, with a corresponding increase in brightness.

Diagnostics through Recombination

IOTA is a research machine and diagnostics is critical to study beam evolution over the time scales of instability growth. The baseline solution for profile measurement consists of ionization monitors, with or without gas injection. In IOTA, with $N_p = 5 \times 10^9$ circulating protons, for a residual gas pressure of 10^{-10} mbar, one can expect 9 ionizations per turn, or a ionization rate of 4.9 MHz.

Spontaneous recombination $p + e^- \rightarrow H^0 + h\nu$ has proven to be a useful diagnostics for optimizing the cooler settings and to determine the profile of the circulating beam.

Neutral hydrogen is formed in a distribution of excited Rydberg states, which have to survive Lorentz stripping through the electron lens toroid and through the next ring dipole to be detected. For IOTA parameters and magnetic fields, atomic states up to $n = 12$ can survive. The corresponding recombination coefficient is $\alpha_r = 9.6\times10^{-19}$ m^3/s for $\sqrt{kT_e} = 0.1$ eV (and scales as $1/\sqrt{kT_e}$).

The total recombination rate R is also proportional to the fraction of the ring occupied by the cooler, $L/C = (0.7\text{ m})/(40\text{ m})$ and to the electron density, n_e:

$$R = N_p \alpha_r n_e (L/C)(1/\gamma^2) \quad (3)$$

For $N_p = 5\times10^9$ and $n_e = 5.8\times10^{14}$ m^{-3}, one obtains a rate $R = 48$ kHz, which is small enough not to significantly affect beam lifetime, but large enough for relatively fast diagnostics complementary to the ionization profile monitors.

Electron Cooling and Nonlinear Integrable Optics

A new research direction is suggested by these studies: in the cases where electron cooling is limited by instabilities or by space-charge tune spread, does nonlinear integrable optics combined with cooling enable higher brightnesses? It seems feasible to investigate this question experimentally in IOTA.

The more straightforward scenario includes electron cooling parameters such as the ones described above. Integrability and tune spreads are provided separately by the nonlinear magnets. Space-charge tune spreads of 0.25 or more, and comparable nonlinear tune spreads, are attainable.

An appealing but more challenging solution would be to combine in the same device, the electron lens, both cooling and nonlinearity (a lens of the McMillan type, for instance). If successful, such a solution would have a direct impact on existing electron coolers in machines that are flexible enough to incorporate the linear part of the nonlinear integrable optics scheme (the T-insert described in Ref. [3]). Preliminary studies indicate that it is challenging to incorporate both the constraints of cooling and the high currents needed to achieve sizable tune spreads, unless one can suppress the space-charge depression. This option is still under study.

As a general comment, we add that instabilities are often driven by impedance. In a research machine dedicated to high-brightness beams, it is useful to be able to vary the electromagnetic response of the beam environment. For this reason, positive feedback with a transverse damper system is being proposed to explore the stability of cooled and uncooled beams with self fields in linear and nonlinear lattices.

CONCLUSIONS

In the Fermilab Integrable Optics Test Accelerator, nonlinear lenses based on magnetically confined electron beams will be used for experimental tests of integrable transfer maps.

With circulating protons, electron lenses can also be used as electron coolers. Cooling times of less than a second can be achieved, allowing one to access a wider range of equilibrium brightnesses for the planned experiments of beam dynamics with self fields.

A recombination detector downstream of the electron lens will complement ionization monitors for measurements of transverse parameters and instabilities.

An electron cooler in the nonlinear integrable lattice also enables new research on the nature of brightness limits for

ISBN 978-3-95450-174-8

high-intensity cooled beams. Having the electron lens act both as nonlinear element and as cooler seems challenging. However, one can rely on the IOTA nonlinear magnets for stable tune spread generation. In addition, the damper system will enable research on beam stability with controlled excitations.

ACKNOWLEDGMENTS

The authors would like to acknowledge the contributions of D. Broemmelsiek, K. Carlson, D. Crawford, W. Johnson, M. McGee, L. Nobrega, H. Piekarz, A. Romanov, J. Ruan, V. Shiltsev, J. Thangaraj, R. Thurman-Keup, T. Zolkin (Fermilab), S. Antipov (University of Chicago and Fermilab) in developing theoretical concepts and technical solutions for the Fermilab Integrable Optics Test Accelerator.

REFERENCES

[1] S. Nagaitsev et al., in *Proceedings of the 2012 International Particle Accelerator Conference* (IPAC12), New Orleans, LA, USA, May 2012, edited by J. Corbett, C. Eyberger, K. Morris, C. Petit-Jean-Genaz, T. Satogata, and V. R. W. Schaa (IPAC'12 / IEEE, 2012), p. 16; FERMILAB-CONF-12-247-AD (2012).

[2] A. Valishev et al., in *Proceedings of the 2012 International Particle Accelerator Conference* (IPAC12), New Orleans, LA, USA, May 2012, edited by J. Corbett, C. Eyberger, K. Morris, C. Petit-Jean-Genaz, T. Satogata, and V. R. W. Schaa (IPAC'12 / IEEE, 2012), p. 1371; FERMILAB-CONF-12-209-AD-APC (2012).

[3] V. Danilov and S. Nagaitsev, Phys. Rev. ST Accel. Beams **13**, 084002 (2010).

[4] G. Stancari et al., in *Proceedings of the 2015 International Particle Accelerator Conference* (IPAC15), Richmond, VA, USA, May 2015, edited by S. Henderson, E. Ayers, T. Satogata, V. R. W. Schaa (JACoW, 2015), p. 46; FERMILAB-CONF-15-136-AD-APC (2015).

[5] E. M. McMillan, University of California Report UCRL-17795 (1967).

[6] E. M. McMillan, in *Topics in Modern Physics*, edited by W. E. Brittin and H. Odabasi (Colorado Associated University Press, Boulder, Colorado, 1971), p. 219.

[7] V. Danilov and E. A. Perevedentsev, in *Proceedings of the 1997 Particle Accelerator Conference* (PAC97), Vancouver, Canada, May 1997, edited by M. K. Craddock and M. Reiser (IEEE, 1998), p. 1759.

[8] S. Nagaitsev and A. Valishev (private communication, 2013).

[9] G. Stancari, in *Proceedings of the 16th Advanced Accelerator Concepts Workshop* (AAC 2014), San Jose, CA, USA, July 2014, edited by M. Hogan (AIP Conf. Proc., submitted), FERMILAB-CONF-14-314-APC, arXiv:1409.3615 [physics.acc-ph] (2014).

[10] V. Shiltsev et al., Phys. Rev. ST Accel. Beams **11**, 103501 (2008).

[11] V. Shiltsev, in *Handbook of Accelerator Physics and Engineering*, edited by A. W. Chao, K. H. Mess, M. Tigner, and F. Zimmermann (2nd ed., World Scientific, 2013), p. 641.

[12] V. Shiltsev et al., Phys. Rev. ST Accel. Beams **2**, 071001 (1999); New J. Phys. **10**, 043042 (2008).

[13] V. Shiltsev et al., Phys. Rev. Lett. **99**, 244801 (2007).

[14] X. Zhang et al. Phys. Rev. ST Accel. Beams **11**, 051002 (2008).

[15] G. Stancari and A. Valishev, in *Proceedings of the ICFA Mini-Workshop on Beam-Beam Effects in Hadron Colliders* (BB2013), CERN, Geneva, Switzerland, March 2013, edited by W. Herr and G. Papotti, CERN-2014-004 (CERN, Geneva, 2014), p. 121; FERMILAB-CONF-13-046-APC (2013).

[16] G. Stancari et al., Phys. Rev. Lett. **107**, 084802 (2011).

[17] G. Stancari, in *Proceedings of the Meeting of the Division of Particles and Fields of the American Physical Society*, Providence, RI, USA, August 2011, edited by T. Speer (SLAC eConf C110809); preprint arXiv:1110.0144 [physics.acc-ph] (2011); FERMILAB-CONF-11-506-AD-APC (2011).

[18] W. Fischer et al., in *Proceedings of the 2013 International Particle Accelerator Conference* (IPAC13), Shanghai, China, May 2013, edited by Z. Dai, C. Petit-Jean-Genaz, V. R. W. Schaa, and C. Zhang (JACoW, 2013), p. 1526.

[19] W. Fischer et al., in *Proceedings of the 2014 International Particle Accelerator Conference* (IPAC14), Dresden, Germany, June 2014, edited by C. Petit-Jean-Genaz, G. Arduini, P. Michel, and V. R. W. Schaa (JACoW, 2014), p. 913.

[20] G. Stancari et al., Conceptual design of hollow electron lenses for beam halo control in the Large Hadron Collider, CERN-ACC-2014-0248, FERMILAB-TM-2572-APC, arXiv:1405.2033 [physics.acc-ph] (2014).

[21] A. Valishev and G. Stancari, Electron lens as beam-beam wire compensator in HL-LHC, FERMILAB-TM-2571-APC, arXiv:1312.1660 [physics.acc-ph] (2013).

[22] A. Valishev, S. D. Fartoukh, and D. Shatilov, in *Proceedings of the 2015 International Particle Accelerator Conference* (IPAC15), Richmond, VA, USA, May 2015, edited by S. Henderson, E. Ayers, T. Satogata, V. R. W. Schaa (JACoW, 2015), p. 2199.

[23] D. Shwartz et al., in *Proceedings of the ICFA Mini-Workshop on Beam-Beam Effects in Hadron Colliders* (BB2013), CERN, Geneva, Switzerland, March 2013, edited by W. Herr and G. Papotti, CERN-2014-004 (CERN, Geneva, 2014), p. 43.

ISBN 978-3-95450-174-8

A COOLING STORAGE RING FOR AN ELECTRON-ION COLLIDER

J. Gerity#, P. McIntyre, Texas A&M University, College Station, TX

Abstract

Electron cooling offers performance advantages to the design of an electron-ion collider. A first design of a 6 GeV/u storage ring for the cooling of ions in MEIC is presented, along with some remarks on the particulars of electron cooling in this ring.

INTRODUCTION

Previously, we have proposed the design of a fixed-energy storage ring [1] for electron cooling as an improvement to the MEIC baseline [2], which plans for DC electron cooling at 0.1 GeV/u and 2 GeV/u in the Booster, and bunched beam cooling using an energy recovery linac (ERL) at 7.9 GeV/u and at collision energy, 100 GeV/u. Most of this cooling is aimed at suppression of IBS and maintenance of emittance during the beam lifecycle. To supplement this approach, our design aims to reduce emittance with DC cooling at the fixed energy of 6 GeV/u. The primary design criteria for the ring are: 1) accumulation of ions by momentum stacking, 2) electron cooling and stacking times commensurate with the existing MEIC structure, so as not to bottleneck the acceleration process, 3) minimization of additional cost to accommodate the ring, compared with the benefits offered.

CURRENT DESIGN

Regarding criterion (1), lab-frame longitudinal cooling force $F_\parallel$ scales with $1/\gamma$, lab-frame cooling rate τ^{-1} scales with $1/\gamma^2$ [3]. This motivates DC cooling at lower energies, and a lower limit is established by space charge dominance. An operating point near the top energy of the MEIC booster (~7-8 GeV/u) is a good compromise between these opposing constraints, as well as the operational flow of the machine. With this energy and electron current of hundreds of mA, the characteristic cooling time (due to Spitzer) for protons in MEIC is

$$\tau_{\text{lab}} = \frac{3}{8\sqrt{2\pi}n_e Z^2 r_e r_i c\Lambda}\left[\frac{T_e}{m_e c^2} + \frac{T_i}{m_i c^2}\right] \leq 5 \text{ min},$$

meeting the needs of criterion (2) assuming a physics time of ~1 hr in the collision ring and ~10 cycles of the Booster. With a dedicated cooling ring, once a beam has been transferred to the collision ring for final acceleration and collision operation, preparation and storage of a new beam can begin immediately, bringing down the time needed between dumping old beam and resumption of physics operations. The integration of the arcs (Figure 2) in the same cryostat as the ion collision ring (in currently unallocated space) goes a long way to meeting criterion (3), as no addition provisions need be taken for the cryogenic systems. The magnet strengths given in Table 1 do not represent large demands on top of the existing cryogenic design.

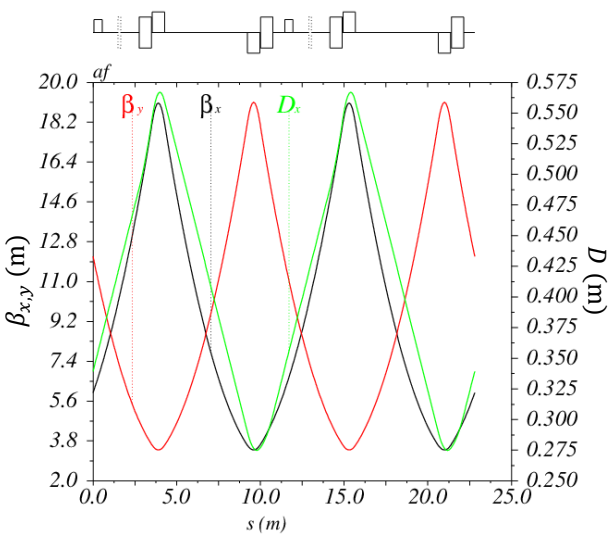

Figure 1: Arc cell optics, shown over the length of one collision ring period.

Figure 2: Schematic layout of placeholder cooling ring integrated above the collider ring in the same cryostat.

Table 1: Cooling Ring Parameters

Arc dipole	0.245 T
Focusing gradient	9.363 T/m
Defocusing gradient	9.424 T/m
Cooling solenoid field	>1.0 T
Electron energy	3-4 MeV
Electron beam current	>250 mA

In the electron cooling section (see Figure 3), the dispersion is matched to zero to maximize the effectiveness of electron cooling. If the dispersion is non-zero, there will be some ions whose velocity is less than that of the electron beam on many turns, resulting in heating and eventual loss of these particles. Note that although the betatron function is shown in the figure, the cooling solenoids occupying the drift spaces will couple the transverse motions and provide

jgerity@tamu.edu

ISBN 978-3-95450-174-8

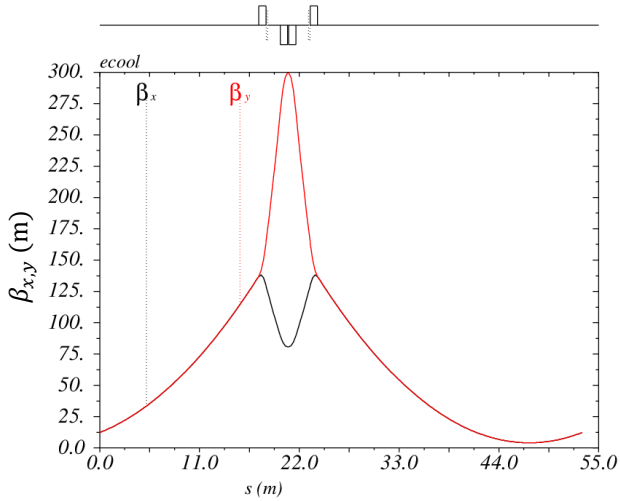

Figure 3: Electron cooling period optics.

focusing. The Courant-Snyder formalism (and thus the betatron amplitude function) are therefore not valid in this region, but an analogous description of the true motion is possible [4]. Quadrupoles between the solenoids will be used for additional control of the beam, and it may be necessary to operate with a skew component for compensation of the transverse coupling introduced by the solenoids.

Injection is performed in the opposing straight, with an insertion (Figure 4) that has a large constant dispersion, to allow side-by-side injection (at an appropriate offset velocity) of new beam which will then be merged with the circulating beam and cooled, making room for more injected beam, and so on. The design of the injection insertion is based on the conceptual design [5] of a beta-beam facility, which has similar requirements for stacking.

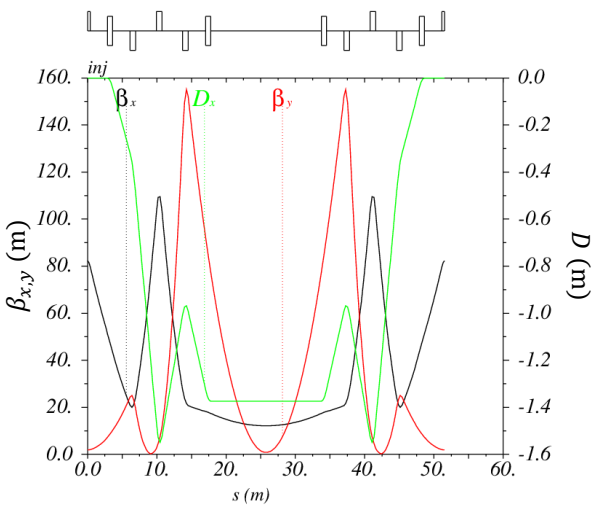

Figure 4: Fixed-dispersion injection insert optics.

ELECTRON COOLING

Our approach to the design of the electron cooling ring is inspired in large part by the success of DC cooling of antiprotons at the Fermilab Recycler. Storage ring cooling of a similar form would augment the MEIC baseline's provisions for bunched beam electron cooling, enabling greater performance without straying prohibitively far from 'traditional' electron cooling. In the Recycler, a magnetic field of ≤600 G was used in the cooling region. [6] Stronger magnetization results in confinement of the charged particles to a smaller gyroradius, and this improves cooling, as the electrons will traverse many periods during a single collision, so that the contribution from their transverse motion is cancelled.

With higher electron density, collisions will occur more frequently, such that the cooling rate scales with the density. The effect of space charge in the cooling section is an $\vec{E} \times \vec{B}$ 'drift' term, creating a radially-varying azimuthal velocity in the electron beam. For steady-state operation this can be approximated as:

$$\frac{\Delta E(r)}{E_0} \approx \frac{I_e r_e}{ec} \frac{\gamma + 1}{\beta_0^3 \gamma^2} \left(\frac{r}{r_0}\right)^2.$$

This drift term places a limit on the useful perveance that can be used for magnetized cooling. To overcome this limit requires neutralization of the space charge, which was successfully implemented at Fermilab and LEAR in a series of experiments focused on trapping residual gas ions. [7,8] We propose to extend the 'conventional' approach to cooling used in the Recycler by utilizing both strong magnetization and neutralization of space charge by the same ion trapping techniques used in those experiments.

In MEIC, the longitudinal temperature of the ion beam at the top of the booster is likely to be much higher than the 'natural' distribution of the electrons. To some extent, cooling scales with $\Delta v_{\parallel}$, but eventually the difference in velocity distributions results in a slower cooling rate because of the rarity of favourable Coulomb collisions. Therefore, we wish to investigate a variable energy scheme relying on sweeping the mean electron energy through a range of values, creating an inertial force term that 'drags' the extremes of the ion beam velocity distribution to a central value, and reduces the cooling time. This cooling strategy has been investigated experimentally at LEAR and TSR [9,10], and may prove to be extremely advantageous for the cooling ring envisioned here.

CONCLUSION

With this first design of a 6 GeV/u in place, we will proceed toward simulations of the cooling process in this ring, beginning with transport of electrons born in a strong field into the cooling region, and working towards additional quantitative metrics for measuring the benefits of this ring to the MEIC layout. We also plan to investigate the dynamics of the magnetized and neutralized cooling with simulation in the code WARP. In particular, we intend to first focus on simulation of electrons born immersed in a strong magnetic field, transported in a non-immersed section, and matched to a strongly magnetized cooling section using the method proposed by Derbenev [11]. From there, the combination of neutralization and magnetization can be studied, and finally a full study of

ISBN 978-3-95450-174-8

cooling of ions under these conditions may be undertaken to characterize the improved luminosity and other metrics relevant to MEIC.

Additionally, some cooling hardware from the Fermilab Recycler is available for repurposed use, including parts of the Pelletron. We would like to acquire this hardware and assemble a testbed for the key technologies involved in the cooling process we propose, allowing for feedback between simulation and experimental processes. Once complete, this testbed could be transported to the site of MEIC construction and integrated as a piece of production hardware.

ACKNOWLEDGMENT

For their helpful comments and stimulating conversation, we would like to thank Saeed Assadi, David Bruhwiler, Yaroslava Derbenev, Igor Meshkov, Vasiliy Morozov, Sergei Nagaitsev, Ilya Pogorelov, Lionel Prost, and Kiersten Ruisard.

REFERENCES

[1] P. M. McIntyre et al., “Fixed-energy Cooling and Stacking for an Electron Ion Collider,” in IPAC 2015, Richmond, VA, 2015.
[2] S. Abeyratne et al., “MEIC Design Summary,” 2015.
[3] H. Poth, “Electron cooling: Theory, experiment, application,” Physics Reports, vol. 196, no. 3, pp. 135-297, 1990/11/01, 1990.
[4] V. A. Lebedev, and S. A. Bogacz, “Betatron motion with coupling of horizontal and vertical degrees of freedom,” JINST, vol. 5, pp. P10010, 2010.
[5] M. Benedikt et al., “Conceptual design report for a Beta-Beam facility,” Eur.Phys.J., vol. A47, pp. 24, 2011.
[6] A. Shemyakin, and L. R. Prost, “The Recycler Electron Cooler,” 2013.
[7] J. Bosser et al., "Neutralisation of the LEAR electron-cooling beam: experimental results." pp. 2943-2945 vol.5.
[8] W.P. Kells et al., ‘The electron beam for the Fermilab Electron Cooling Experiment: initial operation and studies’, Fermilab TM-918 (1979).
[9] J. Bosser et al., “Variable energy electron cooling at LEAR,” Conf.Proc., vol. C920324, pp. 845-847, 1992.
[10] H. Fadil et al., “Electron cooling of longitudinally hot ion beams,” Nuclear Instruments and Methods in Physics Research Section A: Accelerators, Spectrometers, Detectors and Associated Equipment, vol. 517, no. 1–3, pp. 1-8, 1/21/, 2004.
[11] Y. S. Derbenev, “Advanced optical concepts for electron cooling,” Nucl.Instrum.Meth., vol. A441, pp. 223-233, 2000.

ISBN 978-3-95450-174-8

QUANTIFICATION OF THE ELECTRON PLASMA IN TITAN'S COOLER PENNING TRAP*

B. Kootte, U. Chowdhury, TRIUMF, Vancouver B.C., V6T 2A3, Canada & University of Manitoba, Winnipeg, MB, R3T 2N2, Canada
J. C. Bale, J. Dilling, A. Finlay, A. T. Gallant, E. Leistenschneider, TRIUMF, Vancouver B.C., V6T 2A3, Canada & University of British Columbia, Vancouver, BC, V6T 1Z4, Canada
B. R. Barquest, J. Even, M. Good, A. A. Kwiatkowski†, D. Lascar, K. G. Leach‡, A. Lennarz, TRIUMF, Vancouver B.C., V6T 2A3, Canada
R. Klawitter, R. Schupp, TRIUMF, Vancouver B.C., V6T 2A3, Canada & University of Heidelberg, 69117 Heidelberg, Germany
D. Short, TRIUMF, Vancouver B.C., V6T 2A3, Canada & Simon Fraser University, Burnaby, BC, V5A 1S6, Canada
G. Gwinner, University of Manitoba, Winnipeg, MB, R3T 2N2, Canada
C. Andreoiu, Simon Fraser University, Burnaby, BC, V5A 1S6, Canada
M. Alanssari, D. Frekers, University of Münster, 48149 Münster, Germany
T. Li, University of Waterloo, Waterloo, ON, N2L 3G1, Canada
A. J. Mayer, University of Calgary, Calgary, AB, T2N 1N4, Canada

Abstract

Modern rare isotope facilities provide beams of short-lived radionuclides primarily for studies in the field of nuclear structure, nuclear astrophysics, and low energy particle physics. At these facilities, many activities such as re-acceleration, improvement of resolving power, and precision experimental measurements require charge breeding of ions. However, the charge breeding process can increase the energy spread of an ion bunch, adversely affecting the experiment. A Cooler Penning Trap (CPET) is being developed to address such an energy spread by means of sympathetic electron cooling of the Highly Charged Ion bunches to $\lesssim 1$ eV/q. Recent work has focused on developing a strategy to effectively detect the trapped electron plasma without obstructing the passage of ions through the beamline. The first offline tests demonstrate the ability to trap and detect more than 10^8 electrons. This was achieved by using a novel wire mesh detector as a diagnostic tool for the electrons.

INTRODUCTION

Nuclear masses serve as critical inputs in models of nucleosynthesis [1] and provide insight into nuclear structure [2], among numerous other applications. Penning trap mass spectrometry presently offers the highest precision and accuracy for mass measurements of radioactive nuclides [3].

Penning traps use a combination of static electric and magnetic fields to confine charged particles in space. A particle with charge, q, precesses in the magnetic field, B, with a cyclotron frequency given by

$$\omega_c = qB/m. \quad (1)$$

Since the cyclotron frequency is inversely proportional to the mass, we can readily determine the mass by measuring this frequency with a Penning trap.

At TRIUMF's Ion Trap for Atomic and Nuclear science (TITAN) [4] the masses of short-lived isotopes are measured with precisions of 1 part in 10^7 and better. TITAN has successfully performed mass measurements at these precisions for the shortest-lived isotopes ever studied in a Penning trap (e.g. ^{11}Li at $t_{1/2} = 8.75$ ms) [5].

At the TITAN facility, beams of singly charged, radioactive ions from the Isotope Separator and ACcelerator (ISAC) [6] are cooled and bunched in TITANs Radio Frequency Quadrupole ion trap before being delivered to TITAN's Measurement Penning Trap (MPET) [7] for precision mass measurement.

Precision in MPET is limited by

$$\frac{\delta m}{m} \propto \frac{m}{qBT_{RF}\sqrt{N}}, \quad (2)$$

where $\frac{\delta m}{m}$ is the mass uncertainty, m is the mass, q is the charge state, B is the magnetic field of the trap, T_{RF} is the period over which the ion is resonantly excited in the trap, and N is the total number of ions individually trapped and measured [8]. Therefore, in order to achieve the best possible precision, a stable and homogeneous magnetic field, a long excitation time, and a large number of ions are needed.

* TRIUMF receives federal funding via a contribution agreement with the National Research Council of Canada (NRC). This work was partially supported by the Natural Sciences and Engineering Research Council of Canada (NSERC) and the Canada Foundation for Innovation (CFI). BK and UC acknowledge support from a University of Manitoba Faculty of Science Studentship. JE gratefully acknowledges the financial support from the German Academic Exchange Service (DAAD Postdoc program)
† Current address: Texas A&M Univ., College Station, TX 77843, USA
‡ Current address: Colorado School of Mines, Golden, CO 80401, USA

ISBN 978-3-95450-174-8

However, the number of relevant ions available is limited by the low intensities of rare isotope beams (down to ~10/s); the excitation time is limited by the half-life of the isotope; and TITAN's magnetic field is fixed at 3.7 T. Therefore, the option exists at TITAN to send the singly charged ions to an Electron Beam Ion Trap (EBIT) [9], where they are trapped and charge-bred before injection into MPET. The charge state of the ions is increased in EBIT using electron impact ionization, and this increases the precision possible within a given experimental duration [10].

However, the possible gains in precision due to the EBIT are counteracted by an increase in the energy spread of the ion bunch that results from its interaction with the electron beam. A large energy spread reduces the precision of a mass measurement. This makes many of the lowest intensity isotope beams produced at ISAC impossible to study. In order to fully utilize the benefits of charge breeding in the EBIT, the energy spread of the ion bunch needs to be minimized, ideally to $\lesssim 1$ eV/q [11]. Therefore, a Cooler PEnning Trap (CPET) is being commissioned to reduce this energy spread by sympathetically cooling these Highly Charged Ions (HCIs) with electrons, thereby enhancing the mass measurement program at TITAN. HCIs are sympathetically cooled as they lose energy, through Coulomb scattering, to a plasma of colder electrons trapped in the same region. In this paper we report on initial measurements of the trapped plasma using a wire mesh detector. This detection method will be able to serve as a long-term diagnostic procedure to monitor the electron plasma in CPET.

THE COOLER PENNING TRAP (CPET)

CPET is a cylindrical Penning trap designed for cooling HCIs. It confines charged particles radially using a 7 T magnetic field, and axially using electrostatic fields generated by two gate electrodes (as well as a series of cylindrical trap electrodes in the future) (see Fig. 1).

A sympathetic cooling configuration is envisioned in which electrons are simultaneously trapped alongside positively charged ions using so called "nested" potentials to create a region in which the hot ions can interact electrostatically with cold electrons. A series of electrodes will be used to trap both the electrons and the ions by using the trap electrodes to create one or more local potential minima for the electrons to reside in within a globally negative trapping potential for the ions. The trap's 7 T superconducting magnet is strong enough for electrons to self-cool by emitting synchrotron radiation with a cooling time constant of 0.07 s [12]. Since the electrons have the ability to quickly self-cool, it is therefore possible to use the same bunch of trapped electrons to cool multiple subsequent ion bunches. This mitigates the system dead-time associated with reloading the trap and cooling a new electron bunch, which would reduce the statistics of an experiment.

CPET will eventually be integrated into the TITAN beamline to reliably cool radioactive ions with electrons on demand.

At the present time, CPET is undergoing tests in order to prepare it for integration into the TITAN beamline for cooling HCIs. Current study is focused on the establishment of a suitable electron plasma for cooling.

Simulations by Ke et al. (see [12]) have established constraints on the cooling plasma. They indicate that ions of 300 eV/q can be cooled to 0.1 eV/q in 0.4 s if $\frac{N_e}{N_i} = 10^4$, N_i being the number of ions and N_e the number of electrons. This gives us an order of magnitude for a reasonable ratio of electrons to ions for a relatively short cooling time of < 0.5 s. Compressing the plasma to greater density could further improve the cooling time.

In the current plasma loading scheme, the hot filament floating at ~1400 V serves as an electron source. Emitted electrons are then accelerated by an anode and sent through optics which are designed to optimize injection into the trap. The trapping region is defined by two gate electrodes ordinarily biased at −2100 V (see Fig. 1). To load the trap with electrons, the injection electrode is lowered to −800 V for 300 ms and then raised back to −2100 V. The electrons then remain trapped between the two electrodes in the trap region biased at −630 V for a chosen period of time until they are ejected from the trap for detection by lowering the ejection electrode to −100 V.

The electrons are not radially centred within the trap by default but rather orbit around the central axis in what is known as the $m = 1$ diochotron mode, a collective motion seen in non-neutral plasmas [13] [14]. The challenge with this radial offset from the axis of the trap is that the radius of the diochotron motion is substantially magnified upon extraction of the electrons from the trap. Due to the rapidly diverging magnetic field lines as electrons move out of the trap, they get farther from the central axis. For this reason, detecting the electrons outside the solenoid magnet is impossible, as they will collide with the components inside the CPET beamline before they can be detected.

ELECTRON DETECTION

To ensure the effective operation of CPET, it is important to be able to establish the presence of electrons in the trap. If the number of electrons in the trap is known, we can then determine the expected rate of cooling the ions. Effectively detecting the electrons will therefore allow us to estimate the capacity of CPET for cooling ions.

Previously, in order to address the diverging electron plasma, we mounted a phosphor screen within the drift tube beyond the ejection gate electrode. The phosphor screen has the advantage of being position-sensitive and able to operate within a magnetic field. Since the detector is still inside the magnetic field, we were able to observe that the radius of the diochotron motion damps over time [15]. The fact that the plasma settles to the centre of the trap is encouraging evidence that it will spatially overlap with the ions, thus enabling sympathetic cooling.

When CPET is integrated into the TITAN beamline it will need to allow the passage of ions under normal operation.

ISBN 978-3-95450-174-8

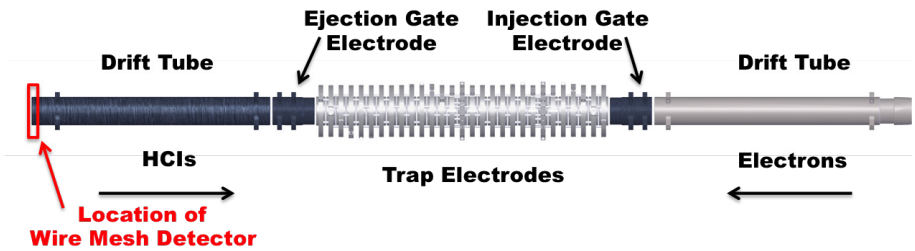

Figure 1: Arrangement of the drift tubes, gate electrodes, and trap electrodes within CPET. Location of the wire mesh detector is shown. Arrows indicate the path of electrons and future HCIs in the trap.

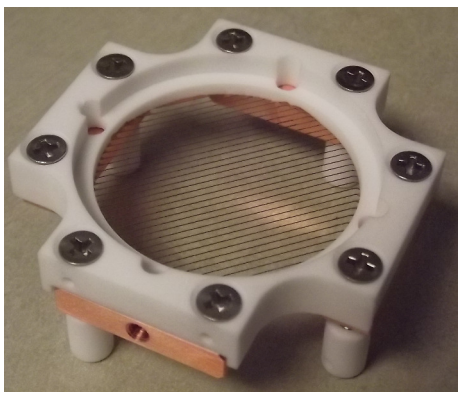

Figure 2: Image of the wire mesh detector.

The phosphor screen blocks the transmission of ions through CPET and space at the mounting location in the drift tube is limited by the size of the magnet's bore. This limits options for detection, and a retractable detector at that location would be impractical due to space constraints. We have therefore designed a wire mesh detector that can either be used as an anode on which to collect electrons, or be biased to drift tube potential to allow regular passage of ions for operation [16]. Detection of electrons is accomplished by grounding the wire mesh and reading out the voltage induced by the electrons collected on the mesh. The mesh sits at the bottom of a potential well made with the electrodes in order to direct the electrons onto the mesh.

The detector is an anode made from a 0.1 mm copper plate with 0.1 mm parallel wires photochemically etched from the material. The circular area of the wire grid has a 34 mm diameter. The wires are spaced with 1 wire per millimeter (see Fig. 2).

The mesh detector is positioned just outside the ejection gate electrode (see Fig. 1). It has been successfully commissioned. This mesh will serve as a long-term diagnostic tool to test the effectiveness of electron trapping.

Measurements with the mesh detector were taken for a range of electron storage times in the trap. The integrated voltage over time on the detector was read out on a oscilloscope which was triggered when the ejection gate electrode was opened. This allowed us to evaluate the total charge deposited on the wire mesh.

An averaged electron signal over 50 trapping/storing/ejection cycles was taken for trapping times of 2, 6, 10, and 14 seconds. We frequently recorded signals for which no electrons were loaded into the trap by using an unbiased Faraday cup as a beamstop. This allowed us to confirm the stability of voltages induced on the wire mesh due to the switching of the trap electrodes and noise from the environment. In this way we ruled out potential systematic uncertainties due to the background on the order of minutes and hours. From one trapping cycle to the next, variations of about 5% in the number of electrons collected on the mesh were seen. These variations were unrelated to the background. No major systematic drifts in the signal over time were observed. Therefore, averaging the measurements was no longer necessary to achieve the required precision; 1 cycle was taken for both the 22 and 30 second trapping times, and 10 cycles for 60 seconds.

Figure 3 summarizes the results of the measurements of the electron number for various trapping times. Approximately 10^8 electrons per ejection were detected on the mesh detector.

We see an initial rise in electron number when the trapping time increases from 2 to 6 seconds. The number of electrons then drops by more than one half over a trapping time of one minute.

One possible reason for the initial increase in the number of detected electrons is the damping of the diochotron motion seen in [15]; as the radial position of the plasma shrinks, more electrons hit the detector. Although 10^8 electrons should be amply sufficient for cooling HCIs in CPET, the gradual decline in electron number over time will necessitate periodic reloading of the trap with electrons.

SUMMARY AND OUTLOOK

CPET is currently being prepared to sympathetically cool HCIs at the TITAN facility. This will require a detector to monitor the trapping of the electron plasma coolant, while still allowing the passage of ions when CPET is incorporated into the TITAN beamline. A novel mesh detector has therefore been implemented to detect electrons in the 7 T magnetic field. We have successfully measured ~10^8 electrons which were trapped for over 30 seconds in CPET. This is a sufficient number to cool many short-lived isotopes to 0.1 eV/q in a reasonable time of < 0.4 s with potential for

ISBN 978-3-95450-174-8

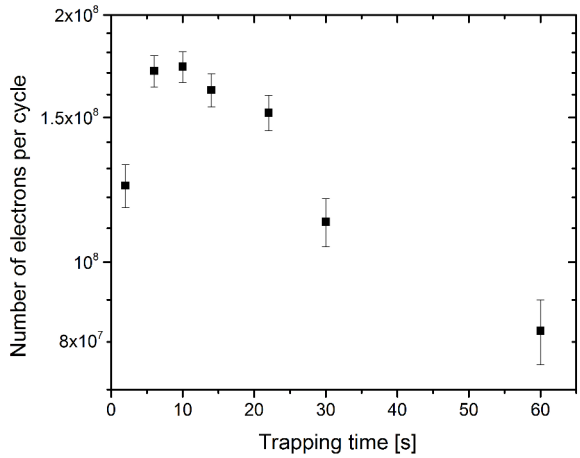

Figure 3: Number of electrons as calculated from the average charge deposited on the wire mesh detector for a range of different trapping durations in CPET. The initial increase in detection number appears to be due to the damping of the diocotron motion.

improvement. To ensure reliable cooling, periodic refilling of the electrons will be required to replace those which are lost over time. Plans are currently in place for CPET to be incorporated into the TITAN beam line with the mesh detector as the standard diagnostic tool for the plasma.

This work demonstrates the mesh detector to be an effective, yet economical solution for many low energy physics applications. Such a selectively transparent, yet robust charged particle detector could be a useful solution in extreme environments like our magnetic field, as well as many other applications.

REFERENCES

[1] E.M. Burbidge, G.R. Burbidge, W.A. Fowler, F. Hoyle, Reviews of Modern Physics **29**, 547 (1957). DOI 10.1103/RevModPhys.29.547

[2] V.V. Simon, T. Brunner, U. Chowdhury, B. Eberhardt, S. Ettenauer, a.T. Gallant, E. Mané, M.C. Simon, P. Delheij, M.R. Pearson, G. Audi, G. Gwinner, D. Lunney, H. Schatz, J. Dilling, Physical Review C - Nuclear Physics **85**(6), 1 (2012). DOI 10.1103/PhysRevC.85.064308

[3] K. Blaum, J. Dilling, W. Nörtershäuser, Physica Scripta **2013**(T152), 014017 (2013)

[4] A. Chaudhuri, C. Andreoiu, M. Brodeur, T. Brunner, U. Chowdhury, S. Ettenauer, A.T. Gallant, A. Grossheim, G. Gwinner, R. Klawitter, A.A. Kwiatkowski, K.G. Leach, A. Lennarz, D. Lunney, T.D. Macdonald, R. Ringle, B.E. Schultz, V.V. Simon, M.C. Simon, J. Dilling, Applied Physics B: Lasers and Optics **114**, 99 (2014). DOI 10.1007/s00340-013-5618-8

[5] M. Smith, M. Brodeur, T. Brunner, S. Ettenauer, A. Lapierre, R. Ringle, V.L. Ryjkov, F. Ames, P. Bricault, G.W.F. Drake, P. Delheij, D. Lunney, F. Sarazin, J. Dilling, Physical Review Letters **101**(20), 202501 (2008). DOI 10.1103/PhysRevLett.101.202501

[6] J. Dilling, R. Krücken, Hyperfine Interactions **225**(1-3), 111 (2014). DOI 10.1007/s10751-013-0886-6

[7] J. Dilling, P. Bricault, M. Smith, H.J. Kluge, Nuclear Instruments and Methods in Physics Research Section B: Beam Interactions with Materials and Atoms **204**, 492 (2003). DOI http://dx.doi.org/10.1016/S0168-583X(02)02118-3. 14th International Conference on Electromagnetic Isotope Separators and Techniques Related to their Applications

[8] G. Bollen, R.B. Moore, G. Savard, H. Stolzenberg, Journal of Applied Physics **68**(9), 4355 (1990). DOI 10.1063/1.346185

[9] A. Lapierre, M. Brodeur, T. Brunner, S. Ettenauer, A. Gallant, V. Simon, M. Good, M. Froese, J. Crespo López-Urrutia, P. Delheij, S. Epp, R. Ringle, S. Schwarz, J. Ullrich, J. Dilling, Nuclear Instruments and Methods in Physics Research Section A: Accelerators, Spectrometers, Detectors and Associated Equipment **624**(1), 54 (2010). DOI 10.1016/j.nima.2010.09.030

[10] A. Kwiatkowski, T. Macdonald, C. Andreoiu, J. Bale, T. Brunner, A. Chaudhuri, U. Chowdhury, S. Ettenauer, A. Gallant, A. Grossheim, A. Lennarz, E. Mané, M. Pearson, B. Schultz, M. Simon, V. Simon, J. Dilling, Nuclear Instruments and Methods in Physics Research Section B: Beam Interactions with Materials and Atoms **317, Part B**, 517 (2013). DOI http://dx.doi.org/10.1016/j.nimb.2013.05.087. {XVIth} International Conference on ElectroMagnetic Isotope Separators and Techniques Related to their Applications, December 2–7, 2012 at Matsue, Japan

[11] V. Simon, P. Delheij, J. Dilling, Z. Ke, W. Shi, G. Gwinner, Hyperfine Interactions **199**(1-3), 151 (2011). DOI 10.1007/s10751-011-0309-5

[12] Z. Ke, W. Shi, G. Gwinner, K. Sharma, S. Toews, J. Dilling, V. Ryjkov, Hyperfine Interactions **173**(1-3), 103 (2006). DOI 10.1007/s10751-007-9548-x

[13] R.H. Levy, Physics of Fluids **8**(7), 1288 (1965). DOI 10.1063/1.1761400

[14] W.D. White, J.H. Malmberg, C.F. Driscoll, Physical Review Letters **49**(25), 1822 (1982). DOI 10.1103/PhysRevLett.49.1822

[15] U. Chowdhury, M. Good, B. Kootte, D. Lascar, B.E. Schultz, J. Dilling, G. Gwinner, AIP Conference Proceedings **1640**, 120 (2015). DOI 10.1063/1.4905408

[16] D. Lascar, A. Kwiatkowski, M. Alanssari, U. Chowdhury, J. Even, A. Finlay, A. Gallant, M. Good, R. Klawitter, B. Kootte, T.Li, K. Leach, A. Lennarz, E. Leistenschneider, A. Mayer, B. Schultz, R. Schupp, D. Short, C. Andreoiu, J. Dilling, G. Gwinner, arXiv:1508.06693, submitted to Nuclear Instrumentation and Methods B Proceedings (2015)

ISBN 978-3-95450-174-8

FINAL MUON IONIZATION COOLING CHANNEL USING QUADRUPOLE DOUBLETS FOR STRONG FOCUSING

J. G. Acosta, L. M. Cremaldi, T. L. Hart, S. J. Oliveros, and D. J. Summers
University of Mississippi - Oxford, University, MS 38677 USA
D. V. Neuffer
Fermilab, Batavia, IL 60510 USA

Abstract

Considerable progress has been made in the design of muon ionization cooling for a collider. A 6D normalized emittance of $\epsilon_{6D} = 0.123\,\mathrm{mm}^3$ has been achieved in simulation, almost a factor of a million in cooling. However, the 6D emittance required by a high luminosity muon collider is $\epsilon_{6D} = 0.044\,\mathrm{mm}^3$. We explore a final cooling channel composed of quadrupole doublets limited to 14 Tesla. Flat beams formed by a skew quadrupole triplet are used. The low β^* regions, as low as 5 mm, produced by the strong focusing quadrupoles are occupied by dense, low Z absorbers that cool the beam. Work is in progress to keep muons with different path lengths in phase with the RF located between cells and to modestly enlarge quadrupole admittance. Calculations and individual cell simulations indicate that the final cooling needed may be possible. Full simulations are in progress. After cooling, emittance exchange in vacuum reduces the transverse emittance to 25 μm and lets the ϵ_L grow to 70 mm as needed by a collider. Septa slice a bunch into 17 parts. RF deflector cavities, as used in CLIC tests, form a 3.7 m long bunch train. Snap bunch coalescence combines the 17 bunches into one in a 21 GeV ring in 55 microseconds.

INTRODUCTION

The muon collider [1] offers several advantages, as compared to hadron colliders [2], to explore rare and massive events at the energy frontier due to the point like behavior of muons. It allows a relatively small collider ring. But, muons have to be cooled quickly and efficiently due to the short muon lifetime. Ionization cooling is the best cooling technique for muons and is being tested at the MICE [3] experiment. The equations describing the transverse and longitudinal cooling are given by [4]:

$$\frac{d\epsilon_\perp}{ds} = -\frac{g_t}{\beta^2}\frac{dE_\mu}{ds}\frac{\epsilon_\perp}{E_\mu} + \frac{1}{\beta^3}\frac{\beta^*_\perp}{2}\frac{(13.6\,\mathrm{MeV})^2}{E_\mu m_\mu c^2 L_R} \quad (1)$$

$$\frac{d\epsilon_L}{ds} = \frac{-g_L}{\beta^2 E_\mu}\frac{dE_\mu}{ds}\epsilon_L + \frac{\gamma^3\beta_L}{\beta c^2 p^2}\pi(r_e m_e c^2)^2 n_e(2-\beta^2) \quad (2)$$

where dE_μ/ds is the energy lost calculated by the Bethe-Bloch equation. $\beta^*_\perp$ and β_L are transverse and longitudinal betatron functions. g_L and g_t are partition numbers that depend on the absorber geometry. $\epsilon_{\perp,eq}$ and $\epsilon_{L,eq}$ are the equilibrium emittances which are calculated as:

$$\epsilon_{\perp,eq} \simeq \frac{\beta^*_\perp (13.6MeV)^2}{2g_t\beta m_\mu c^2 L_R\,(dE/ds)} \quad (3)$$

$$\epsilon_{L,eq} \simeq \frac{\beta_L m_e c^2 \beta\gamma^2(2-\beta^2)}{4g_L m_\mu c^2\left[\ln\left[\frac{2m_e c^2\gamma^2\beta^2}{I(Z)}\right]-\beta^2\right]} \quad (4)$$

The transverse betatron function at the absorber should be small in order to keep the equilibrium emittance low and to reduce the heating due to multiple scattering. Strong focusing is required to cool the beam. Emittance evolution is estimated using the cooling characteristic equation 5, where i = x, y, z [4].

$$\epsilon_i(s) = (\epsilon_{0,i} - \epsilon_{i,equi})\exp(-s\frac{g_i(dP_\mu/ds)}{P_\mu}) + \epsilon_{i,equi} \quad (5)$$

Two muon cooling channels [5, 6] using the transverse cooling principle and emittance exchange have been simulated. Both show a large ϵ_{6D} reduction, but not quite enough for a muon collider as noted in Table 1.

Table 1: Helical and Rectilinear Cooling Channel normalized 6D emittances ϵ_{6D} from simulations and the emittance needed for a muon collider. The channels cool by over five orders of magnitude and need less than a factor of 10 more for a collider. The 21 bunches present after initial phase rotation are also merged into one bunch during cooling.

	ϵ_x mm	ϵ_y mm	ϵ_y mm	ϵ_{6D} mm^3
Initial Emittance [6]	48.6	48.6	17.0	40,200
Helical Cooling [5]	0.523	0.523	1.54	0.421
Rectilinear Cooling [6]	0.28	0.28	1.57	0.123
Muon Collider [7]	0.025	0.025	70	0.044

CHANNEL DESIGN

Channel Cell

According to equation 3, low equilibrium emittance requires low $\beta^*_\perp$. Strong quadrupole focusing [8] can achieve $\beta^*_\perp$ values within the required 0.5 to 2.0 cm range. A half cell is composed of two quadrupole magnets separated by a short drift space to avoid excessive fringe field interference [9] between magnets, as shown in Fig. 1 and 2. The bore diameter and length for the first quadrupole magnet

ISBN 978-3-95450-174-8

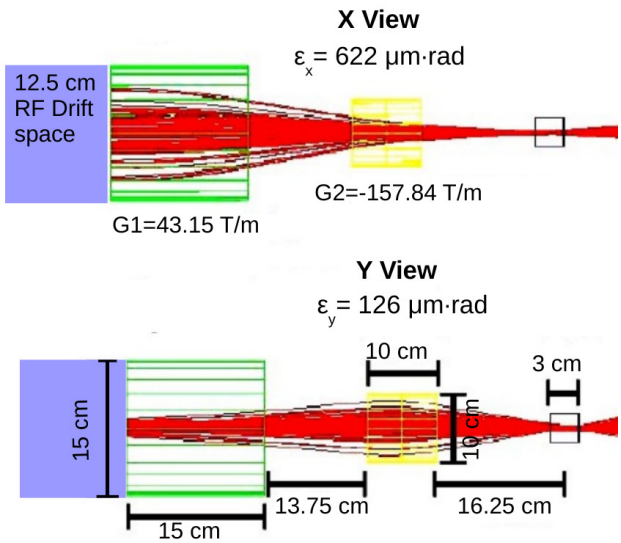

Figure 1: Half cell dimensions. RF occupies 12.5 cm on the left giving a total half cell length of 67.5 cm.

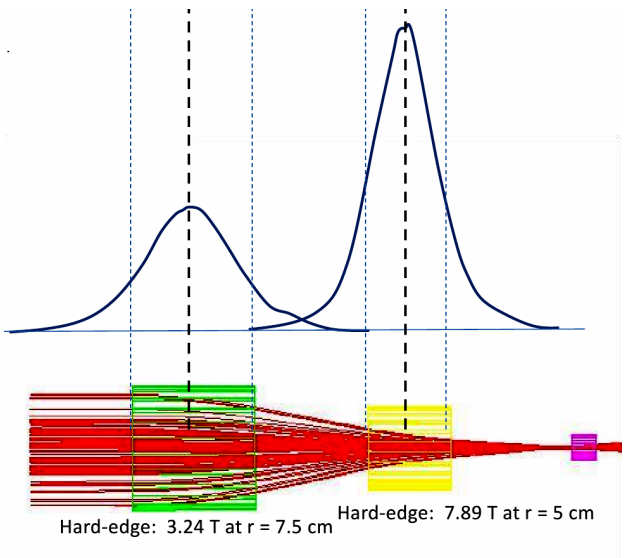

Figure 2: The fringe fields of quadrupoles [9] into each other are small. The bore diameters and lengths for the square green and yellow quadrupoles are 15 and 10 cm, respectively. The gap between quadrupoles is 13.75 cm. Quadrupole fields decrease as the cube of distance.

(Q1) is 15 cm. The bore diameter and length for the second quadrupole (Q2) is 10 cm. This configuration provides strong focusing using magnetic pole tip fields of Q1 = 3.24 T and Q2 = 7.89 T. Quadrupoles with peak fields of more than 12 T have been built with Nb_3Sn [10]. The betatron function evolution for the half cell is shown in Fig. 3.

The chosen quadrupole doublet configuration works with a flat beam near 600 MeV/c to make β_x^* and β_y^* have a 2.0 cm minimum located at the flat, 3 cm long lithium hydride absorber. As noted in Fig. 3, β^* is only small over a limited distance. So the absorber must be dense and short [12].

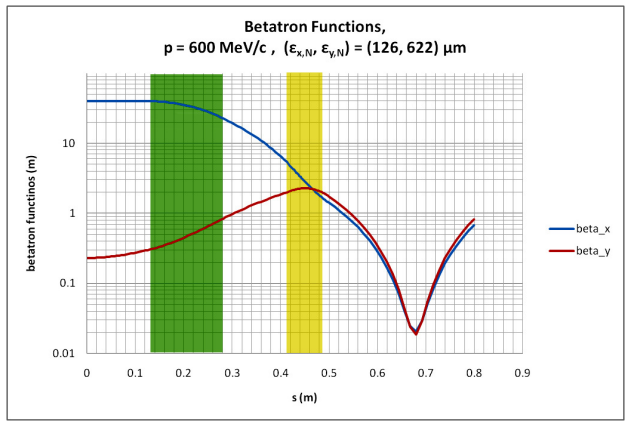

Figure 3: Half cell betatron function vs. distance s. The Courant-Snyder [11] parameters evolution through the cell is calculated using a hard edge matrix approximation and 600 MeV/c muons.

The incoming round beam has to be transformed into a flat beam. Simulations show that a round spinning, muon beam with angular momentum can be transformed into a flat non-spinning beam with a skew quadrupole triplet [13]. Cooling channels [5, 6] can impart angular momentum to a beam, but it may not be smooth enough. Alternatively and at the cost of some heating, wedges might lower x emittance and raise z emittance and then lower z emittance and raise y emittance [14].

The full cell is composed by two half cells and radio frequency cavities to recovery the longitudinal momentum lost in the absorbers. The 650 MHz radio frequency cavities are 0.125 m long, have a phase of 54.7° with respect to rising zero crossing, and a gradient of 26 MV/m. When two consecutive cells are added there are two RF cavities to recover the momentum lost. To evaluate the cell stability the trace from the transport R matrix is taken. The x and y momentum band passes overlap between 598 and 658 MeV/c. Adding another quadrupole at the absorber may be worth exploring.

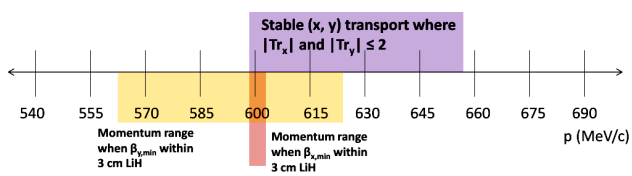

Figure 4: The cell R matrix has $|Tr(R)| < 2$ for stable transport between 598 and 658 MeV/c.

Momentum variations affect the locations for β_x^* and β_y^* as Fig. 4 shows, and can shift the minimums out of the absorbers. This effect is more visible in the x dimension for which the channel has a very narrow acceptable momentum range. To correct the $\beta_\perp^*$ shifts, sextupoles and bending magnets are being tested with a half cell to try to correct the chromaticity [15]. Bending magnets will also be needed

ISBN 978-3-95450-174-8

for emittance exchange when wedge shaped absorbers are added to the simulations.

Sextupole Addition

Introducing a bending magnet before each cell creates dispersion that with the addition of a sextupole before Q2 correct the focus shift for beams with momenta of 570 and 630 MeV/c. Figure 5 shows a bichromatic beam that has two momenta and the correction effect made by a sextupole.

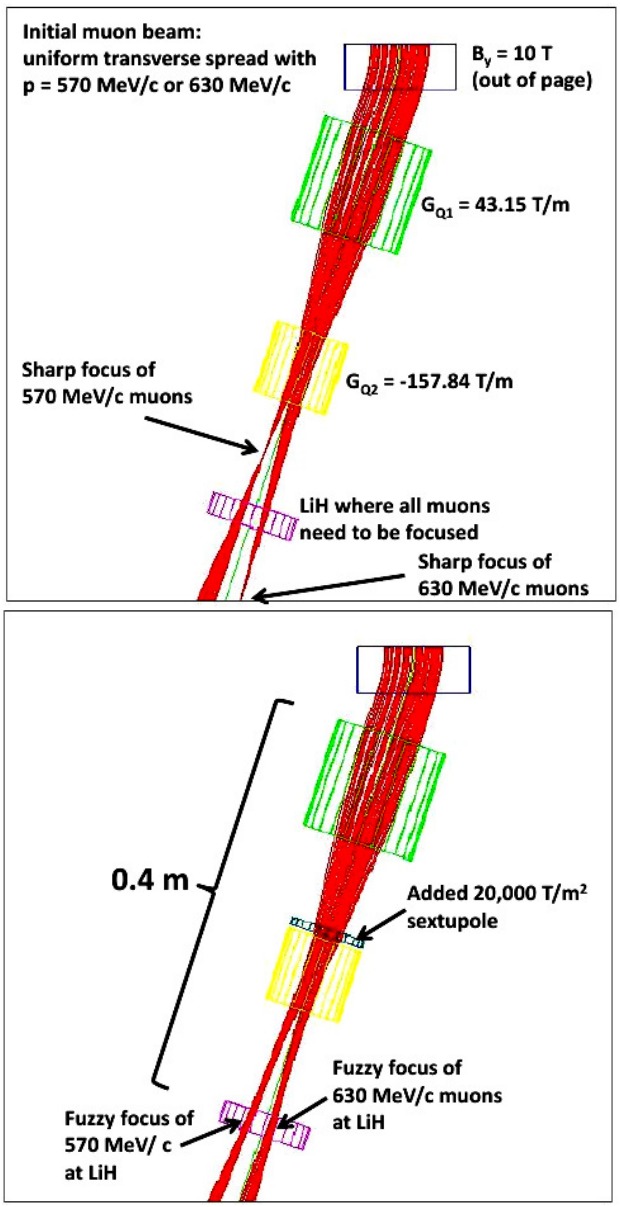

Figure 5: Half Cell with a bending magnet and sextupole to test chromaticity correction.

The sextupole shifts the focus location moving it into the absorber, but the fuzzy foci need to be fixed. This channel chromaticity correction study is in progress and not yet concluded. One possibility is to make space and put a combined function quadrupole/dipole between the RF cavities and to turn each of the two original quadrupoles into combined function quadrupole/sextupole magnets [16] by adding cos (3θ) windings.

Channel Stages

Calculations [17], but not simulations, have been done for more channel stages to complete the 6D cooling.

The low $\beta^*_\perp$ regions are occupied by absorbers made with different low Z materials such as lithium hydride, beryllium, and diamond. Table 2 shows why diamond is being considered. In spite of the equilibrium emittance increment of a factor of two from LiH to Diamond, density increases by a factor of four. Thus, the absorber thickness can be less with the same energy loss. And if β^* is reduced enough, the desired cooling can still occur.

Table 2: Material Properties for 600 MeV/c Muons [18]

Material	**Density** g/cm^3	**L_R** cm	**dE/ds** MeV/cm	**$\epsilon_{\perp,eq}$** (mm · rad)
H_2 gas	8.4×10^{-5}	7.5×10^{5}	3.522×10^{-4}	0.037
LiH	0.82	97	1.665	0.061
Be	1.85	35.3	3.164	0.087
B_4C	2.52	19.9	4.469	0.112
Diamond	3.52	12.1	6.670	0.122

To optimize the channel length, several stages with different material absorbers are required. The expected emittance evolution through the channel is plotted in Fig. 6 for 800 MeV/c muons. ϵ_{6D} is calculated using equation 5 and β^* declines from 2.0 to 0.55 cm. Each channel stage length is optimized in order to keep the total length as short as is possible. Nevertheless, cell lengths are long because a lot of RF was put in to keep β_L and the longitudinal emittance small. Shorter cell lengths may be possible.

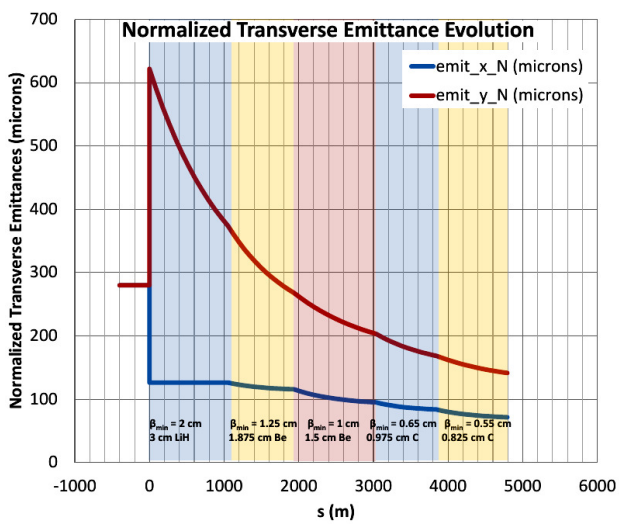

Figure 6: Expected emittance evolution [17].

Emittance exchange wedges might be placed between channel stages to optimize to flatness of the beam. Wedges might lower x emittance and raise z emittance and then lower

ISBN 978-3-95450-174-8

z emittance and raise y emittance [14]. Cooling is faster if the transverse emittance is larger.

FIRST STAGE SIMULATION

The first stage of the channel is simulated using G4beamline [19] and ICOOL [20]. The simulation runs 1000 622 ± 2 MeV/c muons through 210 cells and gets 99% muon transmission with no RF or absorber, just quadrupoles. A beam plot for the last two cells is shown in Fig. 7.

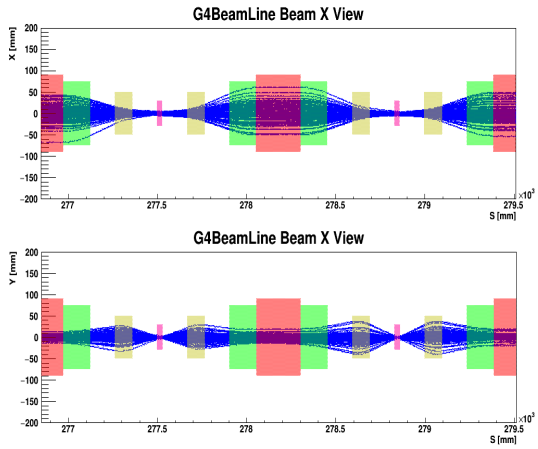

Figure 7: Last two cells for a beam emittance ϵ_x =126 μm rad and ϵ_y = 622 μm rad through 210 cells with p = 622 ± 2 MeV/c. Red is RF. Green and yellow are quadrupoles.

When absorbers and RF are included, but the stochastic process are off, the transmission drops to 50%. Finally, the transmission is 20 % when straggling and delta rays, but not scattering or decays, are activated as Fig. 8 shows.

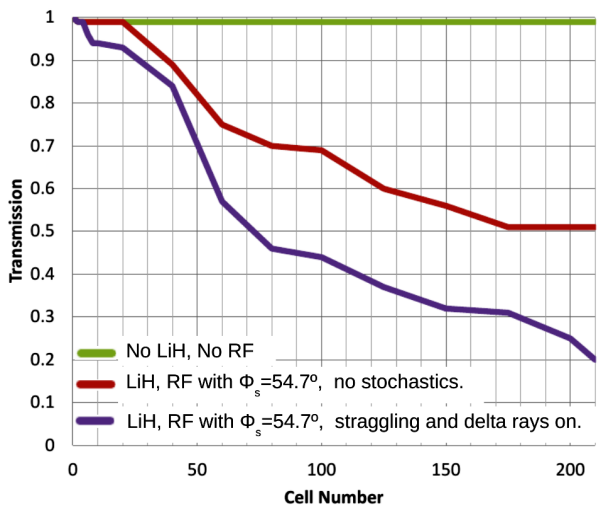

Figure 8: Transmission for a channel with 210 1.35 m cells.

The first channel stage was simulated using ICOOL and G4Beamline with p = 622 ± 2 MeV/c. Initial emittance was $\epsilon_{x,y,z}$ = (0.126, 0.622, 0.0) mm rad. Momentum shifts caused by synchrotron oscillations and perhaps different path lengths as Fig. 9 shows, mandate the addition of sextupoles.

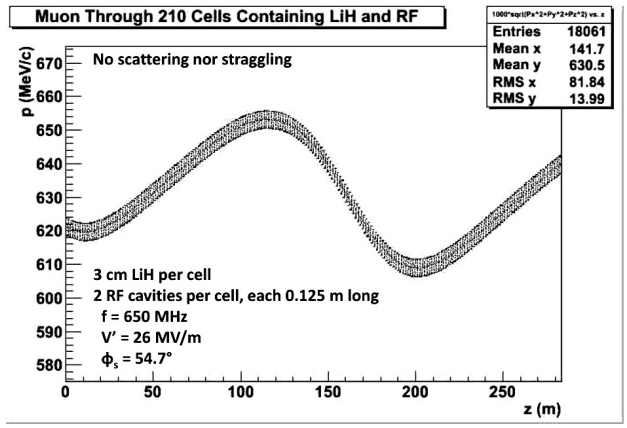

Figure 9: Longitudinal momentum oscillation for one muon through a channel with absorbers and RF.

EMITTANCE EXCHANGE

The transverse cooling is limited by the equilibrium emittance that requires very high magnetic field and dense materials to reduce the transverse emittance even modestly. Therefore, the emittance exchange proposed in [17] is placed at the end of the last cooling stage. It converts the emittance from $\epsilon_{x,y,z}$ = (0.0714, 0.141, 2.418) mm-rad to a narrower, longer $\epsilon_{x,y,z}$ = (0.025, 0.025, 70) mm-rad emittance. Fig. 10 shows a simplified illustration of the process.

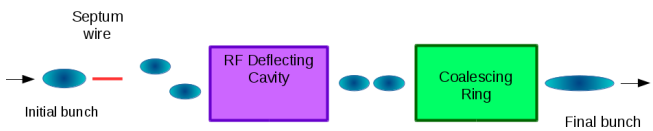

Figure 10: Emittance exchange system schema.

The system includes 16 electrostatic septa that slice the bunch into 17 parts. The Fermilab Fixed Target Switchyard used eight electrostatic septa strings to deliver beam to nine primary slow spill users and one fast spill user [21]. The bunches are interleaved into a 3.7 m long bunch train using CLIC RF deflector cavities [22]. After that snap bunch coalescense [23] combines 17 muon bunches into a single long bunch with RF in a 21 GeV ring [24,25]. The coalescing time during a quarter synchrotron period is 55 μs and the muon decay loss is 13%. The packing fraction approaches 87% [26].

CONCLUSION

The quadrupole doublet channel shows some transmission through the first stage. The transmission needs to be improved by adding magnetic sextupoles for chromatic correction. Admittance needs be moderately improved. If chromatic correction can be made to work, the channel has the potential to reduce the 6D emittance to the level needed for a high luminosity muon collider.

ISBN 978-3-95450-174-8

REFERENCES

[1] J. Gallardo et al., Snowmass 1996, BNL -52503;
D. Neuffer and R. Palmer, Conf.Proc. C940627 (1994) 52;
R. Palmer et al., Nucl. Phys. Proc. Suppl. **51A** (1996) 61;
D. Cline and D. Neuffer, AIP Conf. Proc. **68** (1980) 856;
D. Neuffer, eConf C801002 (1980) 199;
D. Neuffer, IEEE Trans. Nucl. Sci. **28** (1981) 2034;
S. Ozaki et al., BNL-52623 (2001);
D. Adey et al., Phys. Rev. **D80** (2014) 071301;
D. Neuffer, CERN-YELLOW-99 -12;
Andrew M. Sessler, Phys. Today **51N3** (1998) 48;
C. M. Ankenbrandt et al., PRSTAB **2** (1999) 081001;
M. M. Alsharo'a et al., PRSTAB **6** (2003) 081001;
R. Palmer et al., PRSTAB **8** (2005) 061003;
D. J. Summers et al., PAC 2007, arXiv:0707.0302;
D. J. Summers et al., IPAC 2012, arXiv:1207.6730;
G. T. Lyons, Master's Thesis, arXiv:1112.1105;
J. Gallardo and M. Zisman, AIP Conf. Proc. **122** (2010) 308;
Y. Alexahin et al., arXiv:1307.6129;
C. Rubbia, arXiv:1308.6612;
E. Eichten and A. Martin, Phys. Lett. **B728** (2014) 125;
V. Barger et al., Phys. Rev. **D88** (2014) 115003;
N. Chakrabarty et al., Phys. Rev. **D91** (2015) 015008;
M.-H. Wang, Y. Nosochkov, Y. Cai, and M. Palmer, IPAC-2015-TUPTY081.

[2] Michael Benedikt, Daniel Schulte, and Frank Zimmermann, Phys. Rev. ST Accel. Beams **18** (2015) 101002;
J. Tang et al., arXiv:1507.03224;
D. J. Summers et al., AIP Conf. Proc. **1507** (2012) 860;
S. J. Oliveros et al., COOL-2015-TUPF01.

[3] M. Bogomilov et al., JINST **7** (2012) P05009;
D. Adams et al., Eur. Phys. J. **C73** (2013) 2582;
D. Adams et al., arXiv:1510.08306;
L. Cremaldi et al., IEEE Trans. Nucl. Sci. **56** (2009) 1475;
D. A. Sanders, arXiv:0910.1322;
D. Adams et al., *Pion contamination in the MICE muon beam.*

[4] D. Neuffer, arXiv:1312.1266.

[5] C. Yoshikawa et al., IPAC-2014 -TUPME016.

[6] D. Stratakis and R. Palmer, PRSTAB **18** (2015) 031003.

[7] R. B. Palmer et al., PAC 2007, arXiv:0711.4275.

[8] S. Feher and J. Strait, Snowmass -1996-ACC042;
M. Berz et al., AIP Conf. Proc. **721** (2004) 413.

[9] C. Johnstone, M. Berz, D. Errede, and K. Makino, Fig. 5 on page 479, Nucl. Instrum. Meth. **A519** (2004) 472.

[10] F. Borgnolutti et al., IEEE Trans. Appl. Supercond. **24** (2014) 4003005; P. Ferracin et al., IEEE Trans. Appl. Supercond. **24** (2014) 4002306.

[11] E. D. Courant and H. S. Snyder, Annals Phys. **3** (1958) 1.

[12] D. Neuffer, Part. Accel. **14** (1983) 75.

[13] D. J. Summers et al., arXiv:1504.03972.

[14] D. Neuffer, AIP Conf. Proc., **441** (1998) 270;
D. Neuffer et al., COOL-2015-MOPF01;
D. Neuffer et al., to be published in JINST.

[15] P. Raimondi and A. Seryi, Phys. Rev.Lett. **86** (2001) 2779.

[16] V. N. Litvinenko et al., Conf.Proc. C950501 (1996) 796.

[17] D. Summers et al., IPAC 2015, arXiv:1505.01832.

[18] http://pdg.lbl.gov/2014/AtomicNuclearProperties/ ;
K. A. Olive et al., Chin. Phys. **C38** (2014) 090001.

[19] T. J. Roberts *et al.,* Conf. Proc. C0806233 (2008) WEPP120.

[20] R. C. Fernow, eConf C990329 (1999) THP31;
R. C. Fernow, Conf.Proc. C0505161 (2005) 2651.

[21] R. Joshel et al., Conf.Proc. C870316 (1987) 515;
L. W. Oleksiuk et al., IEEE Trans. Nucl. Sci. **20** (1973) 428;
C. H. Rode et al., IEEE Trans. Nucl. Sci. **18** (1971) 984.

[22] M. Aicheler et al., CERN-2012-007, p. 32;
Robert Corsini et al., PRSTAB **7** (2004) 040101.

[23] G. W. Foster, FERMILAB -TM-1902 (1994);
I. Kourbanis et al., Conf. Proc. C930517 (1993) 3799;
S. Stahl and J. MacLachlan, FERMILAB -TM-1650 (1990).

[24] R. P. Johnson, C. Ankenbrandt, C. Bhat, M. Popovic, S. A. Bogacz, and Y. Derbenev, *Muon Bunch Coalescing,* PAC07-THPMN095 (2007).

[25] Alex Bogacz, *Lattices for Bunch Coalescing,* MAP-DOC-4406 (Feb 2006).

[26] Chandra Bhat, private communication, 2015.

ISBN 978-3-95450-174-8

SECONDARY ELECTRON MEASUREMENTS AT THE HIM ELECTRON COOLER TEST SET-UP

M. W. Bruker, A. Hofmann, T. Weilbach, K. Aulenbacher, J. Dietrich
Helmholtz-Institut Mainz, Mainz, Germany

Abstract

The planned advances in electron cooling technology aimed at improving the operation of future hadron storage rings include an increase in electron beam current and acceleration voltage. A test set-up has been built at Helmholtz-Insitut Mainz (HIM) to optimize the recuperation efficiency of such high-current beams in energy recovery operation, requiring a thorough understanding of their interaction with external electric and magnetic fields, such as those found in a Wien velocity filter. Beam diagnostics are carried out using a BPM and current-sensing scraper electrodes. At present, the set-up can be successfully operated at $U = 17\,\mathrm{kV}$, $I = 600\,\mathrm{mA}$, showing a relative secondary electron current of $\approx 2 \times 10^{-4}$. We present the current state of the project and its objectives for the foreseeable future.

INTRODUCTION

Electron coolers are designed for energy recuperation so that the total deposited energy is independent of the acceleration voltage. However, the electrostatic symmetry induced by this approach leads to the problem that secondary electrons reflected from the collector surface can traverse the beam pipe in the wrong direction. Recent progress made by BINP [1] suggests that this effect can be eliminated using a Wien filter, at the same time allowing for measurement of the secondary electron current. Consequently, such a filter has been designed and successfully implemented in our cooler test set-up with the different properties of the components in mind [2].

A schematic view of the set-up is shown in Fig. 1. Using an isolating transformer, it is possible to use the same negative high-voltage power supply for the cathode and the collector, with an additional 6.5 kV, 1.5 A power supply providing the potential difference between cathode and collector to account for the finite perveance. This way, the beam pipe is at ground potential, greatly facilitating beam diagnostics. After the Wien filter, the set-up includes a moveable fluorescent screen, a beam position monitor obtained from BINP [3], and a mutually isolated double aperture to distinguish between secondary and primary current hitting the plates.

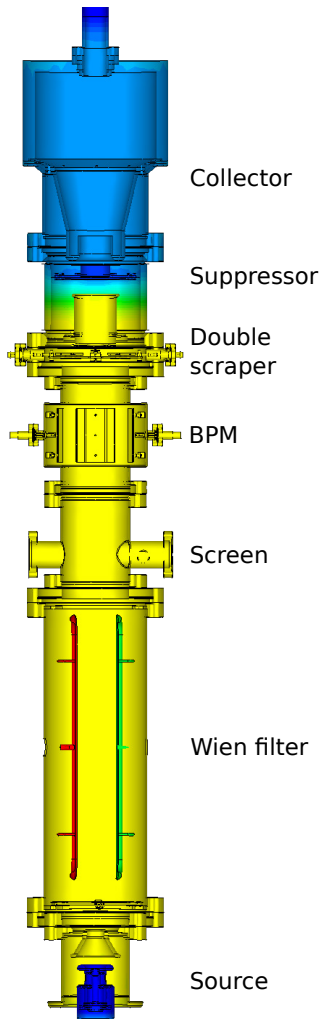

Figure 1: Schematic view of the vacuum chamber. Blue: $U < 0$. Yellow: $U = 0$.

GAS DISCHARGES IN THE ELECTRON SOURCE

When operation of our test set-up started, it quickly turned out that the electron source obtained from TSL [4] could not be operated with the desired parameters ($U = 26\,\mathrm{kV}$, $B_z = 200\,\mathrm{mT}$) because of gas discharges between the electrodes [5]. In an attempt to identify the reason, CST simulations of electric fields and particle trajectories were carried out. The result of a particle simulation with the whole outer surface of the Pierce electrode emitting electrons is shown in Fig. 2. It can be seen that due to the electric field components caused by the varying distance between the outer Pierce electrode and the surrounding pipe, there are two local maximums of electric potential (indicated by arrows) along the symmetry axis of the source (vertical direction in the picture). Given a longitudinal magnetic field sufficiently high to confine the radial movement of electrons to a narrow space, all particles starting at one of the surfaces with a kinetic energy close to zero will oscillate between the potential minimums, greatly increasing the ionization probability of the residual gas. This constitutes a variety of the cylindrical magnetron where the

ISBN 978-3-95450-174-8

threshold voltage for electrical breakdown depends strongly on the magnetic field [6]. It is expected that the problem can be solved by redesigning the Pierce electrode and its mechanical support so that a monotonous behaviour of the electric potential is obtained in the high-field region.

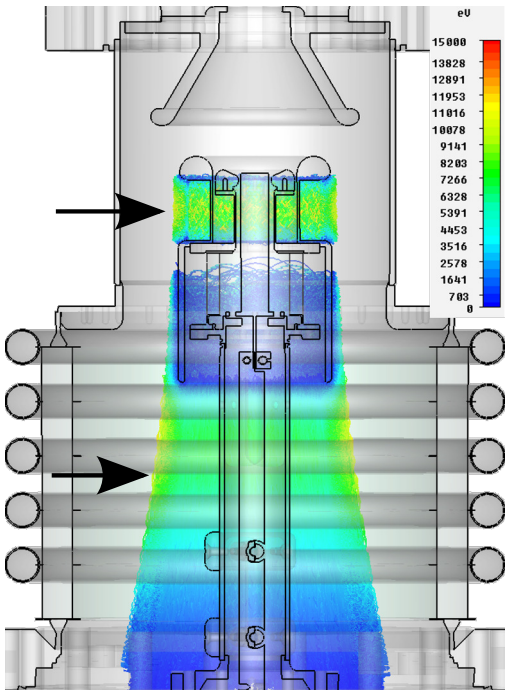

Figure 2: CST simulation of electron trajectories originating from the surface of the Pierce electrode. $t = 400\,\mathrm{ns}$, all crashed trajectories are hidden. $U_{\mathrm{Pierce}} = U_{\mathrm{Cathode}} = -30\,\mathrm{kV}$.

COLLECTION EFFICIENCY MEASUREMENT USING A WIEN FILTER

In order to measure the current of secondary electrons not captured by the aperture plates, a Wien velocity filter is used that breaks the symmetry between the primary and the secondary beam (Fig. 3) [2]. This filter consists of two electrostatic plates that impose a transverse electric field on the beams. On the other hand, a magnetic field perpendicular to both the longitudinal magnetic field and the transverse electric field is created such that the corresponding Lorentz force

$$\vec{F} = q(\vec{E} + \vec{v} \times \vec{B}) = 0 \qquad (1)$$

in the case of the primary beam. However, any secondary particles are deflected because they have a different velocity vector. Given a certain energy distribution of the secondary electrons depending on the collector voltage, the total field strength can be chosen accordingly so all particles are captured by a plate that is insulated from the beam pipe to allow for independent current measurement.

Since the dipole coils have a different geometry than the electrostatic plates and the use of iron for arbitrary field forming is problematic due to the additional longitudinal

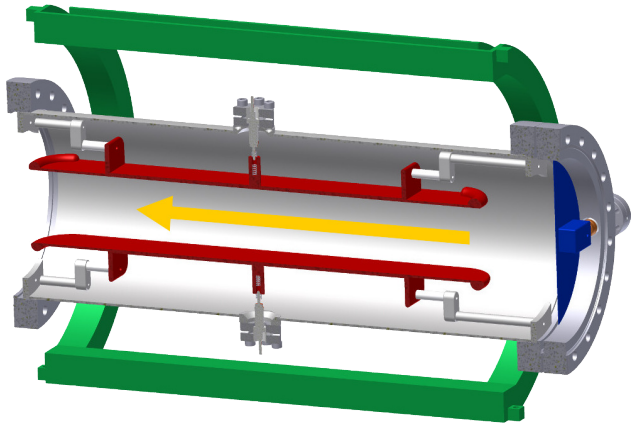

Figure 3: Schematic view of the Wien filter [2]. Red: electrostatic plates. Green: dipole coils. Blue: collecting plate.

field, equation 1 generally does not hold everywhere, which causes an undesired spatial displacement of the primary beam. While the exact value of this displacement (in our case $\approx 3\,\mathrm{mm}$) is not critical because the Wien filter is usually placed directly in front of the collector aperture, it is too large to be able to fit a 20 mm beam through a 25 mm hole, which is why the beam reacts extremely sensitively to the value of the longitudinal field. To solve this problem, a correction coil was introduced to flatten the magnetic field profile in the vicinity of the peak. According to CST tracking simulations, the beam offset should be reduced to less than 1 mm. The geometry of the coils and the field errors are shown in Figs. 4 and 5, respectively.

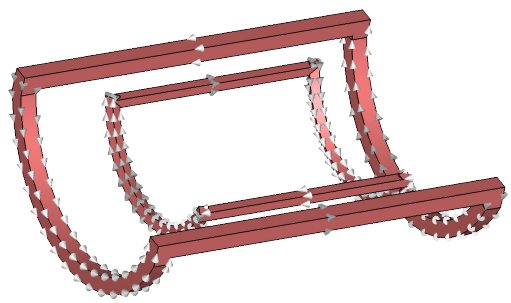

Figure 4: Wien filter dipole coils with added correction coils.

EXPERIMENTAL RESULTS

Without the aforementioned improvements, our set-up can be successfully operated at $U = 17\,\mathrm{kV}$, $B_{z,\mathrm{max}} = 80\,\mathrm{mT}$. Depending on the voltage applied to the Pierce electrode, collector currents in the range of 600 mA can be obtained without any signs of instability. The relative loss current at anode potential is 2×10^{-4} in total, about half of which flows through the beam pipe in a way that is yet experimentally undetermined. According to CST simulations, secondary current flowing into the positive deceleration electrode is the most likely cause. This assumption is strongly supported by

ISBN 978-3-95450-174-8

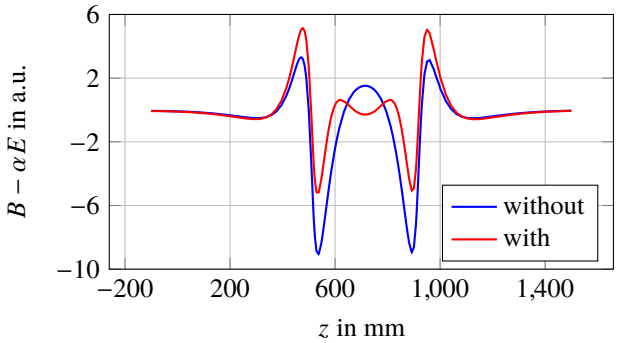

Figure 5: Lorentz force imposed on primary particles by the Wien filter field geometry before and after optimization. Vertical scale depends on operating parameters.

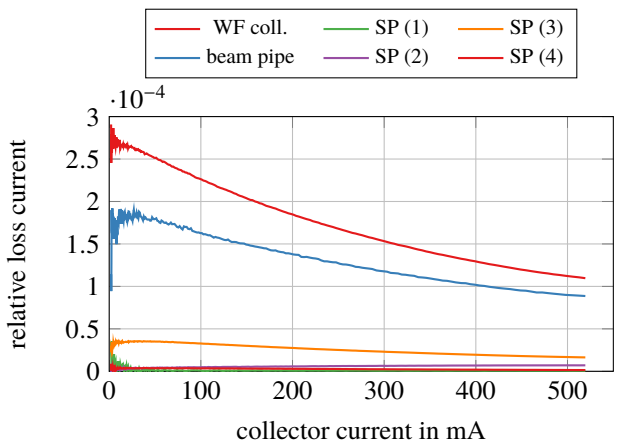

Figure 6: Electron current lost at anode potential. WF: Wien filter collector plate, SP: scraper plates.

the fact that the beam pipe current shows the same primary current dependence as the Wien filter current.

IMPROVED DECELERATION OPTICS

CST simulations have shown that given the original positive electrode in the deceleration system, the original high-voltage insulator, and the BINP collector, the space left for the suppressor electrode is not enough to be able to obtain a reasonably low potential minimum. Therefore, both electrodes have been redesigned, at the same time changing the mechanical support of the positive one in such a way that the current flowing into it can be measured independently. This way, we hope to show that all secondary particles behave in accordance with our simulations. The potential distribution of the new system is shown in Fig. 7.

OUTLOOK

It is likely that the optimization steps described above regarding the Wien filter and the deceleration optics will be completed in November 2015, after which we hope to operate the set-up without any unknown sources of loss current. The complete control of secondary emission by the Wien filter will strongly suppress any undesired electron flow, thereby facilitating diagnostics and high-voltage operation in a real cooler. We believe the relative number of resulting secondaries to be $\ll 10^{-5}$.

The test device can then be used to conduct further studies on suppression of optical background, which is a challenge to be overcome in order to advance development of the Thomson Laser Scanning technique in coolers [7]. Additionally, it is planned to further increase the electron current to look for possible limitations that might present themselves.

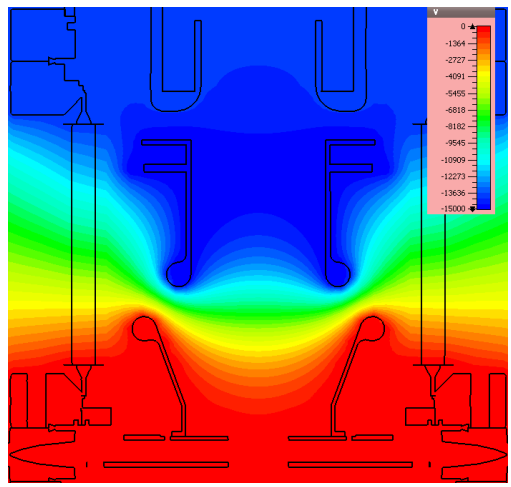

Figure 7: Distribution of electric potential with new deceleration electrodes. Cutplane at $x = 0$.

REFERENCES

[1] M. Bryzgunov et al., “Efficiency Improvement of an Electron Collector Intended for Electron Cooling Systems Using a Wien Filter”, Technical Physics Vol. 58 No. 6, 2013.

[2] S. Friederich, “Kollektoreffizienzmessung an einem linearen Elektronenstrahlfuehrungsaufbau mit Hilfe eines Wien-Filters” (in German), Master’s thesis, University of Mainz, Germany, 2013.

[3] E. A. Bekhtenev et al., “Beam position monitor system for 2 MeV electron cooler for COSY”, Proceedings of RUPAC2012, WEPPD028.

[4] “HESR Electron Cooler Design Study”, The Svedberg Laboratory, Uppsala, 2009.

[5] M. Bruker et al., “Operational experience with the HESR electron cooler test set-up”, Proceedings of COOL2013, WEPPO03.

[6] S. N. Abolmasov, “Physics and engineering of crossed-field discharge devices”, Plasma Sources Sci. Technol. 21 (2012) 035006.

[7] T. Weilbach et al., “Beam profile measurement for high intensity electron beams”, Proceedings of IPAC2013, MOPEA022, p. 118.

ISBN 978-3-95450-174-8

SIGNALS FROM A BEAM PERFORMING BETATRON OSCILLATIONS USING AN ELECTROSTATIC ELECTRODE MODEL WITH RECTANGULAR BOUNDARIES

F. Nolden, GSI, Darmstadt, Germany
J.X. Wu, IMP, Lanzhou, China

Abstract

We investigate the non-linear response of a pick-up structure using electrostatic models with the formalism introduced by Bisognano and Leeman. As an example we show results from the pick-up structure at the CSRe storage ring at the IMP in Lanzhou.

ELECTROSTATIC MODELS OF AN ELECTRODE PLATE

Electrostatic Models of Relativistic Beam Response

Electrostatic models have been applied for a long time to the investigation of the response of both pick-ups and kickers. A classical overview of this subject is due to G. Lambertson [1]. He gives also an equation of the non-relativistic case, but this is meant to show that the electrostatic approximation is good for large Lorentz factors γ.

A more naive approach to the non-relativistic case is to replace the extremely short field disk of ultra-relativistic particles by the correct expressions for a free particle [2, 3]. This leads to analytical expressions of the correction, however the boundary conditions of a real vacuum chamber are not taken into account.

As this paper mainly aims at a study of the response to betatron oscillations, the electrostatic approximation is used throughout.

Parallel Boundaries without Borders

The electrostatic model with parallel boundaries was first introduced by Neuffer [4]. The underlying conformal mapping is explained in some detail in [3]. However we use here a different coordinate system where the y coordinate is zero in the center of the vacuum chamber (see Fig. 1).

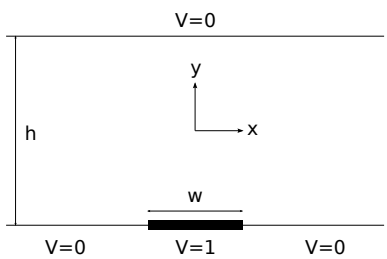

Figure 1: Electrode with parallel boundaries

The model can be calculated as follows. Take

$$z = \frac{\cos(\pi y/h)\sinh(\pi w/2h)}{\cosh(\pi x/h) + \sin(\pi y/h)\cosh(\pi w/2h)} \qquad (1)$$

where w is the width of one electrode and h is the height of the chamber.

$$S(x,y) = \begin{cases} \frac{1}{\pi}\arctan z & \text{if} \quad z > 0 \\ 0.5 & \text{if} \quad z = 0 \\ 1 + \frac{1}{\pi}\arctan z & \text{if} \quad z < 0 \end{cases} \qquad (2)$$

The case distinction is necessary because one has to switch between Riemann sheets of the inverse tangent function in order to get an analytic potential. The third case occurs if the point (x, y) gets vertically close to the electrode.

Rectangular Borders

To model a rectangular chamber requires a slightly more complicated conformal mapping.

A rectangular chamber in the $z = x - y$-plane extends from $-a/2$ to $a/2$ in x and from 0 to b in y (see Fig. 2). A potential V is supposed to exist from x_1 to x_2 along the x-axis.

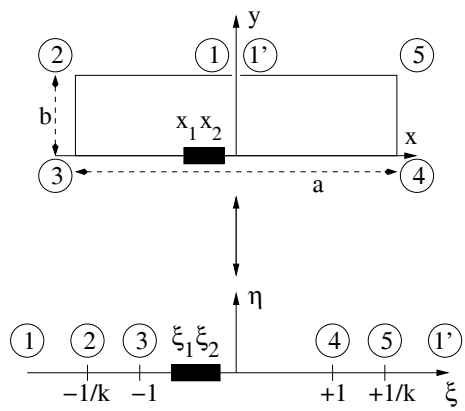

Figure 2: Conformal mapping of inner part of a rectangle to the upper half plane ($k^2 = m$).

The potential is calculated after a conformal mapping of the interiour of the rectangle to the upper complex half-plane.

$$z = x + iy \;\mapsto\; \zeta = \xi + i\eta \qquad (3)$$

Such a mapping can be realized by [5]

$$\zeta = \mathrm{sn}\left(\frac{2K(m)}{a} z|m\right) \qquad (4)$$

where sn is one of the Jacobian elliptic functions (using the notation from [6]) and K is a complete elliptic integral of the first kind. The parameter m depends on the aspect ratio a/b of the rectangle. It solves the equation [5]

$$\frac{a}{b} - \frac{2K(m)}{K(1-m)} = 0 \qquad (5)$$

ISBN 978-3-95450-174-8

which is due to the periods $4K(m)$ and $2iK(1-m)$ of the doubly periodic function $\mathrm{sn}(z|m)$ (see [6]).

The Jacobian elliptic functions of a complex argument are calculated from real arguments using (see [6])

$$\mathrm{sn}(x+iy|m) = \frac{s\,d_1 + i\,c\,d\,s_1\,c_1}{c_1^2 + m\,s^2\,s_1^2} \tag{6}$$

where

$$\begin{aligned} s &= \mathrm{sn}(x|m), \quad & s_1 &= \mathrm{sn}(y|1-m) \\ c &= \mathrm{cn}(x|m), \quad & c_1 &= \mathrm{cn}(y|1-m) \\ d &= \mathrm{dn}(x|m), \quad & d_1 &= \mathrm{dn}(y|1-m) \end{aligned} \tag{7}$$

and where cn and dn are also Jacobian elliptic functions.

In order to calculate the potential at a point (x, y), one maps $z = x + iy \mapsto \zeta$ and gets the physical potential V as the real part of

$$\Phi(\zeta) = \frac{i}{\pi} \log\left[\frac{\zeta - \xi_2}{\zeta - \xi_1}\right] \tag{8}$$

where the edges of the electrode are mapped according to $(x_{12}, 0) \mapsto (\xi_{12}, 0)$.

This gives rise to using an inverse tangent function, because

$$\mathrm{Im}\left[\log(u+iv)\right] = \arctan\frac{v}{u} \tag{9}$$

The Riemann sheets of the inverse tangent are chosen in exactly the same way as in Eq. (2).

NON-LINEAR RESPONSE FORMALISM

In the case of betatron motion, the particle coordinates at the pick-up oscillate:

$$x_n = x_\delta + A_x \sin\alpha_{x,n} \tag{10}$$

$$y_n = A_y \sin\alpha_{y,n} \tag{11}$$

where $x_\delta = D\delta p/p$ is a dispersive offset, and $A_{x,y} = \sqrt{\epsilon_{x,y}\beta_{x,y}}$ are the betatron amplitudes calculated in the usual way from the one-particle emittances $\epsilon_{x,y}$ and the betatron functions $\beta_{x,y}$. The betatron angles

$$\alpha_{y,n} = 2\pi n Q_{xy} + \mu_{x,y} \tag{12}$$

where Q_{xy} is the number of betatron oscillations per turn and $\mu_{x,y}$ is an initial phase.

To deal with the oscillating particle positions, Bisognano and Leeman [7] proposed the following elegant formalism:

Make a wave number decomposition of $S(x, y)$, i.e. introduce the 2D Fourier transform

$$\tilde{S}(k_x, k_y) = \iint_{\mathbb{R}^2} dx\,dy\; S(x,y) e^{-i(k_x x + k_y y)} \tag{13}$$

Transforming backwards yields

$$S(x,y) = \frac{1}{(2\pi)^2} \iint_{\mathbb{R}^2} dk_x\,dk_y\; \tilde{S}(k_x,k_y) e^{+i(k_x x + k_y y)} \tag{14}$$

where the coordinates x, y now appear only in the exponential. With the Bessel function expansion

$$e^{+ik_x x_n} = e^{+ik_x x_\delta} \sum_{l_x=-\infty}^{\infty} J_{l_x}(k_x A_x) e^{+il_x\alpha_x} \tag{15}$$

$$e^{+ik_y y_n} = \sum_{l_y=-\infty}^{\infty} J_{l_y}(k_y A_y) e^{+il_y\alpha_y} \tag{16}$$

one can therefore write, after reversing the order of sums and integrals:

$$S(x_n, y_n) = \sum_{l_x-\infty}^{\infty} \sum_{l_y-\infty}^{\infty} S_{l_x,l_y}(A_x, A_y, x_\delta) e^{+i(l_x\alpha_x + l_y\alpha_y)} \tag{17}$$

with the coefficients

$$\begin{aligned} S_{l_x,l_y}(A_x, A_y, x_\delta) &= \frac{1}{(2\pi)^2} \iint_{\mathbb{R}^2} dx\,dy\; \tilde{S}(k_x,k_y) \\ &\times J_{l_x}(k_x A_x) J_{l_y}(k_y A_y) e^{+ik_x x_\delta} \end{aligned} \tag{18}$$

Using Eq. (10), Eq. (11) it can be shown [3] that the response of a pick-up yields generally a signal at the frequencies

$$\omega(m, l_x, l_y) = \left(m + l_x Q_x + l_y Q_y\right)\omega_{\mathrm{rev}} \tag{19}$$

where ω_{rev} is the particle revolution frequency. Which of these frequencies dominate, depends on the construction of the pick-up and on the betatron amplitudes. Large signals are usually detected only at the central harmonics ($l_x = l_y = 0$) and at the betatron sidebands ($|l_x| = 1$ and $|l_y| = 1$).

Particularly important is the case of small betatron amplitudes $A_{x,y}$. Then one can can use the appromixations $J_0(z) \approx 1$, and $J_1(z) \approx z/2$. One gets

$$S_{0,0} \approx S(x_\delta, y) \tag{20}$$

$$S_{1,0} \approx \frac{A_x}{2i}\frac{\partial S(x_\delta, y)}{\partial x} \tag{21}$$

$$S_{0,1} \approx \frac{A_y}{2i}\frac{\partial S(x_\delta, y)}{\partial y} \tag{22}$$

A more detailed discussion is given in [3, 7].

SIMULATION RESULTS FOR CSRE STOCHASTIC COOLING

Electrode Geometry

Presently a stochastic cooling system is being installed at the CSRe storage ring at the Institute of Modern Physics in Lanzhou, China [8]. Three pick-up and kicker systems have been installed which all share the same transverse geometry [9].

The pick-up (Fig. 3) consists of four equal electrodes with $w = 87$ mm and $h = 62$ mm (using the notation of Fig. 1). The electrodes are arranged symmetrically with respect to the center of the vacuum chamber. The horizontal distance from the center to the center of each electrode is 57.5 mm.

ISBN 978-3-95450-174-8

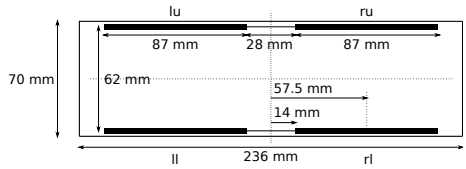

Figure 3: Geometry of CSRe electrodes.

We denote the different electrodes with the symbols *lu* (left upper), *ll* (left lower), *ru* (right upper), and *rl* (right lower). The signals of each single electrodes can be processed in three different modes:

1. The sum mode (symbollically $lu + ll + ru + rl$). This mode can be used for longitudinal cooling (time of flight or notch filter).

2. The horizontal difference mode (symbollically $lu + ll - ru - rl$). This mode can be used for longitudinal cooling (Palmer) and for horizontal betatron cooling.

3. The vertical difference mode (symbollically $lu - ll + ru - rl$). This mode can be used for vertical betatron cooling.

Sum Mode

Figure 4 shows the case if the sum from all four electrodes is taken. We examine this case in some detail.

Each curve in Fig. 4 shows the sensitivity as a function of x for fixed y. The different curves are plotted for different values of the vertical coordinate y. For $x = y = 0$ the value of the sensitivity is $S \approx 0.58$. Towards the middle of the plates $(x, y) = (\pm 57.5\,\text{mm}, 0\,\text{mm})$ it rises on both sides to $S \approx 0.85$ and drops steeply to 0 towards higher values of $|x|$. At $x = 0$ the sensitivity drops rapidly to 0 if the verical position approaches the $V = 0$ position in the gap between the plates. On the other hand it gets close to 1 in the vicinity of the plates.

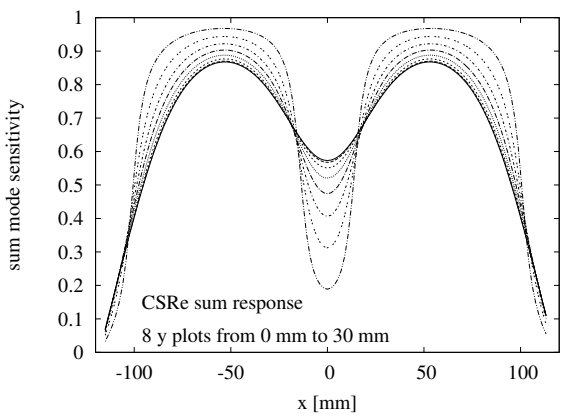

Figure 4: CSRe sum response.

Figure 5 shows the sensitivity $S_{0,0}$ (central revolution frequency harmonics) for a particle with $x_\delta = 0\,\text{mm}$ performing betatron oscillations with various amplitudes A_x and A_y. Each curve is plotted for fixed A_y and 16 curves are plotted for $0\,\text{mm} \leq A_y \leq 30\,\text{mm}$.

As to be expected the sensitivity for zero amplitudes is $S \approx 0.58$. As a function of A_x the sensitivity rises until the betatron amplitude is slightly larger than 57.5 mm. For very small horizontal amplitudes A_x, the sensitivity decreases for large A_y, but for $A_x \approx 35\,\text{mm}$ a point is reached where $S_{0,0}$ becomes roughly independent of A_y.

As a practical consequence of such considerations, it might be too naive to derive the number of particles in a beam from the area in the Schottky spectra, if they are measured at significantly different transverse emittances.

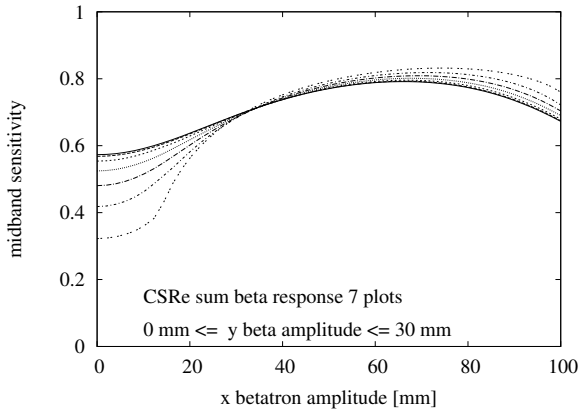

Figure 5: CSRe response to betatron oscillations in sum mode.

Horizontal Difference Mode

Figure 6 shows the response in the horizontal difference mode. The plot is made in the same way as Fig. 4. The horizontal response is more or less linear up to $|x| \approx 40mm$ and the dependence on y becomes predominant only in the vicinity of the plates.

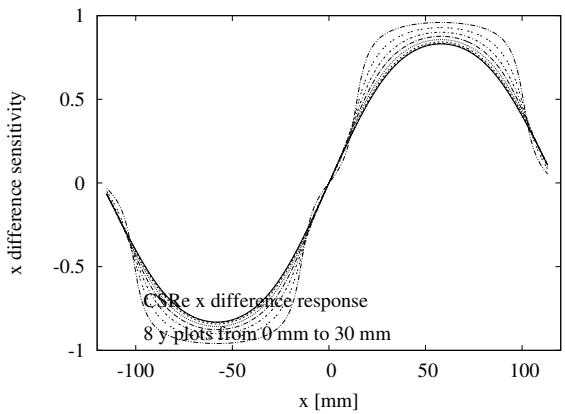

Figure 6: CSRe horizontal difference response.

Figure 7 shows the response $S_{1,0}$ in the same way as Fig. 5. The linearity in A_x is very good for small amplitudes and the dependence on A_y is almost negligible.

ISBN 978-3-95450-174-8

Curves like these can also be used to verify the approximation Eq. (21).

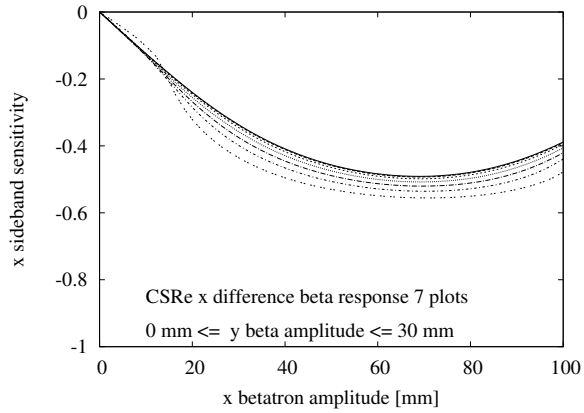

Figure 7: CSRe response to betatron oscillations in horizontal difference mode.

Vertical Difference Mode

Figure 8 shows the response in the vertical difference mode. The plot is made in the same way as Figure 4 At $x = 0$ mm the sensitivity does not exceed $|S| \approx 0.15$. Whereas it is approximately linear in y in the vicinity of the plates (for $|x| \approx 57.5$ mm), there is a maximum at $y \approx 16$ mm, if $x \lessapprox 20$ mm.

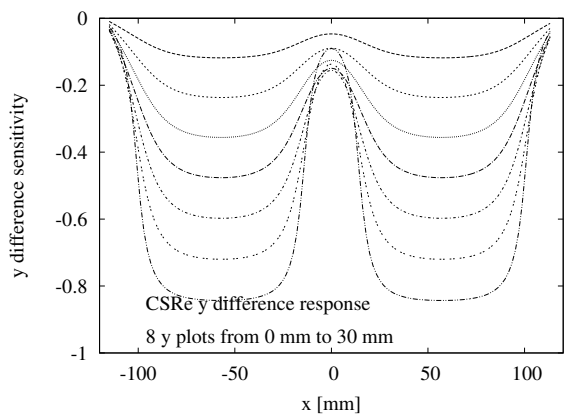

Figure 8: CSRe vertical difference response

Figure 9 shows the response $S_{0,1}$ in the same way as Figure 5.

The nonlinearity for $x \lessapprox 20$ mm mentioned above is also clearly visible in the $S_{0,1}$ response. As a result it might be argued that pick-ups with a horizontal gap in the middle are not ideally suited for vertical betatron cooling.

CONCLUSIONS

It has been shown that the non-linear response formalism yields detailed informations on the response of electrode structures to particles performing betatron oscillations.

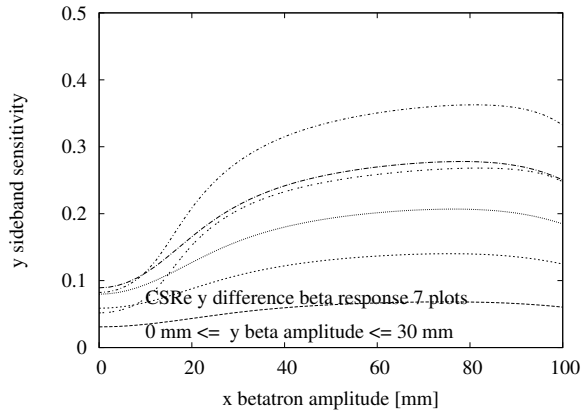

Figure 9: CSRe response to betatron oscillations in vertical difference mode

It is straightforward to implement it on a computer using digital Fourier transform techniques.

It is recommended to use it as a valuable tool for electrode design.

REFERENCES

[1] G. Lambertson, in Physics of High Energy Accelerators, SLAC Summer School 1985, Fermilab Summer School 1984, AIP Conf. Proc. 153, pp. 1413–1442, (1984).

[2] F. Caspers, G. Dôme, Reciprocity between Pick-up and Kicker Structures Including the Far-Field Zone, Proc. EPAC 1994, pp. 1208–1210, (1994).

[3] F. Nolden, Stochastic Cooling and Related RF Components, in CERN Accelerator School on RF Engineering, CERN Yellow Report 2005-003, pp. 400–420, (2005).

[4] D. Neuffer, Fermilab pbar note 201, (1982).

[5] E. Durand, Electrostatique, Tôme II (Problèmes généraux conducteurs), Masson (Paris), (1966).

[6] M. Abramovitz, I. Stegun, Handbook of Mathematical Functions, National Bureau of Standards Applied Mathematics Series 55, (1972).

[7] J. Bisognano, C. Leemann, in Physics of High Energy Accelerators, Fermilab School 1981, AIP Conf. Proc. **87**, (1982).

[8] J.X. Wu et al., Stochastic Cooling Project at the Experimental Storage Ring CSRe at IMP, Proc. of Cool'11, pp. 64–66, (2011).

[9] Y. Zhang et al., An Improved Forward Travelling Wave Structure Design For Stochastic Cooling at Experimental Storage Ring (CSRe) at the Institute of Modern Physics (IMP) in China, Proc. of Cool'11, pp. 132–135, (2011).

ISBN 978-3-95450-174-8

DESIGN OF BEAM DIAGNOSTIC SYSTEM FOR OPTICAL STOCHASTIC COOLING AT IOTA RING*

K. Yonehara†, Fermilab, Batavia, IL 60510, USA

Abstract

Design of beam diagnostic system for Optical Stochastic Cooling (OSC) at IOTA ring is described in the document. Cooling parameter will be measured by the longitudinal interference pattern of synchrotron radiation lights from two undulators. Light optics and detector system are discussed.

INTRODUCTION

Damping rate of the stochastic cooling (τ^{-1}) is proportional to the bandwidth of the electromagnetic wave (W) and the beam bunch length (σ_s), i.e. $\frac{1}{\tau} \propto W\sigma_s$. It indicates that Optical Stochastic Cooling (OSC) has a great potential to cool TeV-scale proton beams, e.g. LHC and FCC because the bandwidth of radiation lights is typically $\sim 10^{14}$ Hz (wavelength of radiation lights is $\lambda \sim \mu m$) which is four or five orders of magnitude higher (shorter) than a microwave that is used in the conventional stochastic device.

Theoretical investigation of the OSC has been done [1]. Here, several critical formulae are picked up for our discussion. Damping force applies to the longitudinal phase space. The force ($\delta p/p$) is tuned by the path length (Δs) that is adjusted by a chicane,

$$\delta p/p = \kappa \sin(k\Delta s), \tag{1}$$

where κ is the undulator strength and k is the wavenumber of a radiation light. The longitudinal kick is partitioned into the horizontal phase space (x) due to dispersion. To evaluate the stochastic process, the force is averaged along the beam path in a whole ring lattice. It is given as

$$F_1(a_x, a_p) = 2J_0(a_p)J_1(a_x)/a_x, \tag{2}$$

$$F_2(a_x, a_p) = 2J_0(a_x)J_1(a_p)/a_p, \tag{3}$$

where J_0 and J_1 are the 0-th and 1-st order Bessel functions, respectively. a_x and a_p are the dimensionless amplitude that represents the phase advance of beams in the kicker undulator in horizontal (x) and longitudinal (s) phase spaces, respectively. In order to realize the positive average damping force, the phase advance between the beam and the kicker light should be $|a_x, a_p| < \mu_{01} \sim 2.405$.

Proof-of-principle experiment will be done at IOTA ring in Fermilab by using an electron beam. Figure 2 is a layout of cooling insert at IOTA ring. No optical amplifier is used in the first test. Table 1 shows the main beam parameter and the beam optics parameter in the cooling insert at IOTA ring. Dipole and quadrupole magnets are a main tuning knob to adjust the beam path length. A sextupole magnet is applied in the beam line to increase the acceptance by correcting the chromaticity. It significantly changes the path length, thus it changes the cooling condition as shown in Fig. 3. Major goal of the designed beam diagnostic system is to measure the beam path length as a function of the sextupole field strength and to observe this correlation.

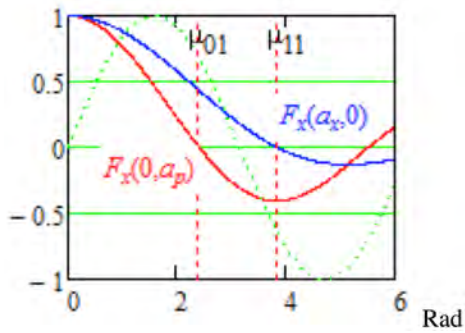

Figure 1: Averaged damping forces.

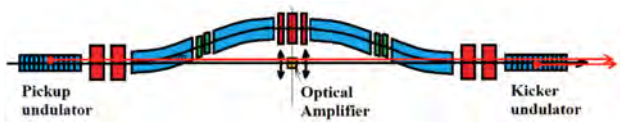

Figure 2: A cooling insert for the OSC in IOTA ring. The blue box is a bending magnet. The red and green boxes are a quadrupole and a sextupole magnets, respectively. The orange line shows a path of a synchrotron radiation light.

Table 1: Beam Parameter

IOTA ring	
Circumference	40 m
Nominal electron beam energy	100 MeV
Bending field of main dipoles	4.8 kG
Revolution	7.5 MHz
Undulators	
Radiation wavelength at zero angle, $\lambda_{\gamma,0}$	2.2 μ m
Undulator parameter	0.8
Undulator period	12.9 cm
Number of periods	6
Total undulator length	0.77 m
Peak magnetic field	664 G
Distance between centers of undulators	3.3 m
Energy loss per undulator per pass	22 meV
Optical system aperture	13 mm
Radiation spot size in the kicker, HWHM	0.35 mm
θ_{max}	4 mrad
$\gamma\theta_{max}$	0.63

* Work supported by Fermilab Research Alliance, LLC under Contract No. DE-AC02-07CH11359

† yonehara@fnal.gov

ISBN 978-3-95450-174-8

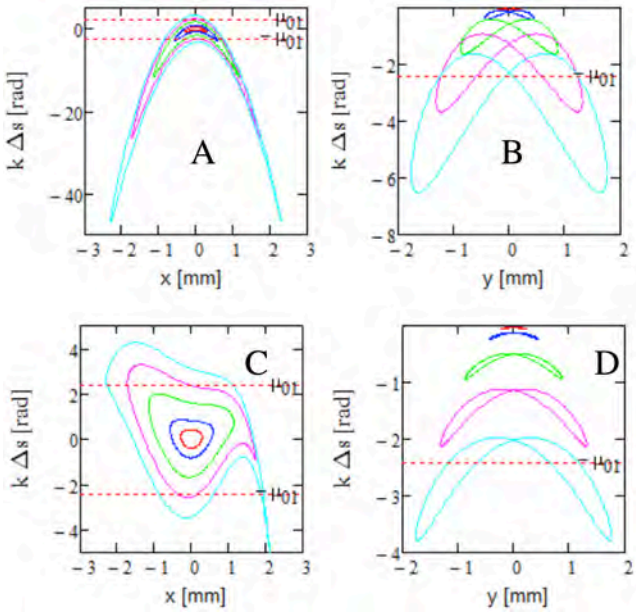

Figure 3: (Left) beam path length as a function of horizontal beam position without (A) and with (C) a sextupole magnet. (Right) beam path length as a function of vertical beam position without (B) and with (D) a sextupole magnet.

Table 2: Cooling Parameters

Cooling parameter	
Radiation band	2.2 - 3.2 μ m
Damping rate (x/s)	6.3/5.2 s^{-1}
RMS bunch length (no OSC)	22 cm
Number of particles per bunch	10^6

DESIGN OPTICS FOR SYNCHROTRON RADIATION IN UNDULATOR

Optical transport for the synchrotron radiation light is discussed. Primary goal of the design of transport optics is maintaining the phase space of object (synchrotron radiation lights) in the pickup undulator to the image in the kicker undulator. Then, two lights are extracted from the beam line to use for the beam diagnostics.

Synchrotron Radiation from Undulator

First, the synchrotron radiation light produced in the undulator is characterized. By taking into account the angular dependent Doppler shift, there is a strong correlation between spectrum and angular distribution of synchrotron light, which is given

$$\lambda_\gamma = \frac{\lambda_p}{2\gamma^2}\left(1+\gamma^2\left(\frac{1}{2}\theta_e^2+\theta^2\right)\right) = \lambda_{\gamma,0}+\frac{\lambda_p}{2}\theta^2, \quad (4)$$

where $\lambda_{\gamma,0}$ is the shortest wavelength at zero radiation angle emitted in the pickup undulator. According to the diffraction limit, the angular distribution of synchrotron light from an undulator is restricted by $\theta \sim 1/\gamma$ [2]. Therefore, the second term in eq. (4) is given

$$\frac{\lambda_p}{2}\theta^2 \equiv \Delta\lambda \sim \frac{\lambda_p}{2\gamma^2}. \quad (5)$$

Figure 4 shows the estimated wavelength as a function of the conical angle from the light source. Because the optical system aperture is 13 mm and the gap between two undulators is 3.3 m the geometric acceptance of the radiation light is ~4 mrad. It limits the longest wavelength of radiation ~3.2 μm.

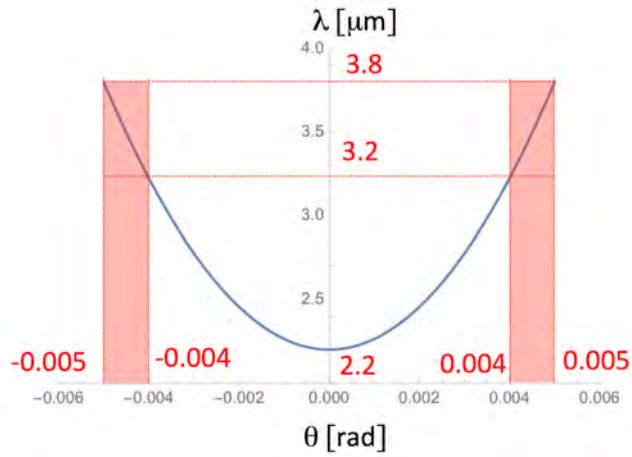

Figure 4: Spectrum of synchrotron light from the pickup undulator. A red area is the boundary of optical aperture.

Transfer Matrix of Synchrotron Radiation

A triplet lens is applied. A transfer matrix of the triplet lens with the paraxial optics model is

$$F_1 = \begin{bmatrix} 1 & 0 \\ \frac{1}{f_1} & 1 \end{bmatrix}, F_2 = \begin{bmatrix} 1 & 0 \\ \frac{1}{f_2} & 1 \end{bmatrix}, T = \begin{bmatrix} 1 & t \\ 0 & 1 \end{bmatrix}, L = \begin{bmatrix} 1 & l \\ 0 & 1 \end{bmatrix}, \quad (6)$$

$$M = L.F_1.T.F_2.T.F_1.L, \quad (7)$$

where f_1 is a focal length of the first and third lenses while f_2 is a focal length of the middle one. t is a gap between F_1 and F_2, and F_2 and F_1. l is a gap between the middle point of the pickup undulator and the first F_1, and the second F_1 to the middle point of the kicker undulator. In order to maintain the phase space of source object in the pickup undulator to the kicker one, the transfer matrix should be the identity matrix, $M = \pm I$. f_1 and f_2 are the function of t,

$$f_1^{-1} = -\frac{1}{t}, \quad f_2^{-1} = \frac{1}{t}. \quad (8)$$

The result shows that the focal length is independent from l.

Ray Trace Simulation

Ray trace simulation has been done by using a custom made code based on LensLab [3]. Geometry and refraction index of lenses are modeled from real lens. Figure 5 shows an example of ray tracing in a triplet lens.

ISBN 978-3-95450-174-8

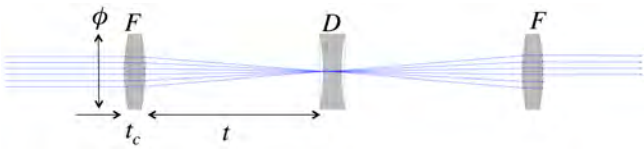

Figure 5: Demonstration of a triplet lens.

Because the focal length is independent from l the displacement of light source (object) from the center of pickup undulator is maintained to the displacement of the image from the center of kicker undulator. Figure 6 verifies this concept.

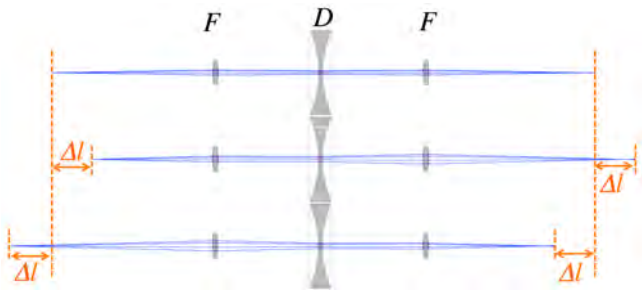

Figure 6: Longitudinal displacement of the object and the image in the triplet lens. Transverse displacement of the object is also maintained in the triplet lens although it does not show in this figure.

Table 3 shows the geometry of lens what we used in the simulation. The values are picked up from a catalog provided by Melles Griot [4]. We assume that the glass material is a standard BK7. It is important to point out that the total amount of glass should be ~6 mm because the time of flight of radiation light must synchronize to the electron beam. The present lens design is close enough to the requirement.

Table 3: Cooling Parameters

Element	Focal length f	Diameter ϕ	Thickness t_c
Unit	mm	mm	mm
F_1	50	12.5	2.8
F_2	-50	42.0	2.0

Figure 7 shows the simulated image spot in the kicker undulator produced by single electron in ray trace simulation. Largest radius (λ = 3.2 μm) is 65 nm in this analysis. On the other hand, the estimated spot size from the diffraction limit is $\sigma_x \sim R(1-\cos\theta) \sim R(1-\cos\gamma^{-1}) \sim 5$ μm in this undulator where R is a bending radius in the undulator. Besides, the beam size is a couple of hundreds of μm. Therefore, the chromaticity is not an issue in this system.

DESIGN OF BEAM DIAGNOSTIC SYSTEM

It is essential to demonstrate the cooling performance by tuning the sextuple magnet. The longitudinal interference pattern will be observed to measure the phase-offset. In case of the single electron, the longitudinal interference pattern is given,

$$1 + \exp(i\delta) = 2\cos^2\left(\frac{\delta}{2}\right), \quad (9)$$

where δ is the phase offset between the electron and synchrotron light in the kicker undulator. The power of two synchrotron lights will be changed as sinusoidal function with respect to the phase offset. This approximation is valid when the synchrotron light is coherent. As the next step, time structure of the beam and beam quality has been involved in ray trace simulation to investigate the coherence of synchrotron lights.

An electron beam is oscillated in horizontal plane in the undulator and emit near-infrared linearly polarized lights. Since an electron loses energy by 22 meV every passing in the undulator the production rate of photons are $\Delta\varepsilon/h\nu \sim 0.04$. Revolution of beams are 7.5 MHz. Therefore, the total number of photons are $0.04\times10^6\times7.5\cdot10^6 \sim 3\cdot10^{11}$ photons/sec. Figure 8 shows the schematic of beam diagnostic system. Synchrotron radiation lights are extracted from the beam line through a viewer. The lights is filtered by a band-pass filter to select the short narrow-band light. They take a part by a splitter. One goes into a photo detector array to measure the spatial distribution and other goes into a fast photo detector to measure the interference light.

There are several Near-IR photon detectors. HgCdTe PEM-detector is the standard semiconductor NIR photon detector. It can be very fast rise time (τ << 1 ns) and the total pulse width is 3~4 ns. This should be applicable for the time domain single photon counter. On the other hand, a superconducting nano-wire bolometer has been developed for the single NIR photon counter. This is also very fast rise time ($\tau \sim 10$ ps) but it has a long recovery time. It can achieve a very fine spatial resolution, order of μm. The superconducting bolometer needs a cryogenics.

REFERENCES

[1] V. Lebedev, *"Optical Stochastic Cooling"*, *ICFA News Letter* **65** (2014) 100.

[2] K.J. Kim, *"Angular Distribution of Undulator Power for an Arbitrary Deflection Parameter K"*, *Nucl. Inst. Meth.* **A246** (1986) 67.

[3] *http://library.wolfram.com/infocenter/MathSource/655/.*

[4] *http://mellesgriot.com/.*

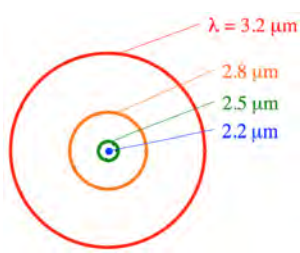

Figure 7: Simulated image spot at the center of kicker undulator from single electron in ray trace simulation.

ISBN 978-3-95450-174-8

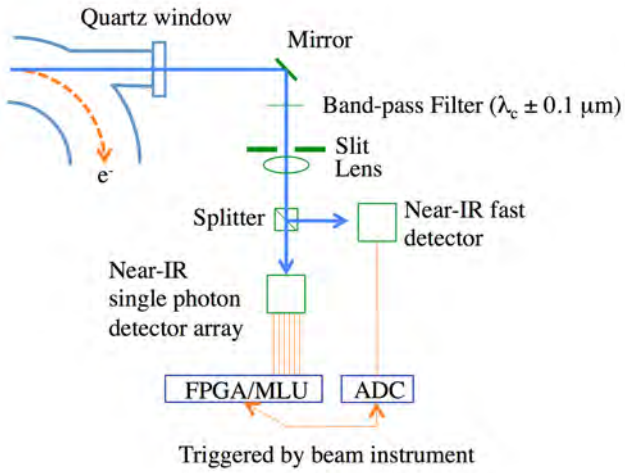

Figure 8: Schematic of beam diagnostic system.

ISBN 978-3-95450-174-8

N-BODY CODE TO DEMONSTRATE ELECTRON COOLING

S. Abeyratne†, B. Erdelyi⋆†
† Department of Physics, Northern Illinois University, DeKalb, IL 60115
⋆ Physics Division, Argonne National Laboratory, Argonne, IL 60439

Abstract

In the Electron Ion Collider (EIC), the collision between the electron beam and the proton, or heavy ion, beam results in emittance growth of the proton beam. Electron cooling, where an electron beam and the proton beam co-propagate, is the desired cooling method to cool or mitigate the emittance growth of the proton beam. The pre-booster, the larger booster, and the collider ring in EIC are the major components that require electron cooling. To study the cooling effect, we previously proposed Particles' High order Adaptive Dynamics (PHAD) code that uses the Fast Multiple Method (FMM) to calculate the Coulomb interactions among charged particles. We further used the Strang splitting technique to improve the code's efficiency and used Picard iteration-based novel integrators to maintain very high accuracy. In this paper we explain how this code is used to treat relativistic particle collisions. We are able calculate the transverse emittances of protons and electrons in the cooling section while still maintaining high accuracy. This presentation will be an update on the progress with the parallelization of the code and the status of production runs.

INTRODUCTION

A set of many objects, which undergoes self-interactions and external forces, can be mathematically modeled as an N-body problem. As the number of objects, N, becomes larger, the force calculation demands remarkably high computing power.

In a charged particle beam, the mathematical formulation of the study of particles' behavior leads to an electromagnetic N-body problem. In order to calculate potential, field and Coulomb interactions among particles, we have to solve 6N differential equations (3N for x, y, z and another 3N for p_x, p_y, p_z). We have developed a code based on a novel FMM algorithm [1, 2] using certain differential algebraic techniques to solve differential equations efficiently while maintaining high accuracy.

ALGORITHM

The time taken for calculating the interaction among particles using the point-to-point or direct method exhibits quadratic growth, i.e. $O(\mathrm{N}^2)$. Even today's high-performance supercomputers cannot provide the necessary computational power to solve this problem in a reasonable amount of time. Therefore, the sheer necessity arises for finding computationally efficient and accurate methods to calculate the Coulomb interactions. From the literature review, one can find several approximate methods to calculate interactions, which are relatively efficient compared to the direct method, namely: 1. Basis function methods; 2. Particle-mesh methods; 3. Hierarchical domain decomposition methods. Due to certain drawbacks in the first and the second method, we choose the third [3]. The third group can be further divided into three sub-groups: tree, cluster and fast multipole methods (FMM). Tree and cluster groups, however, are merely special versions of the FMM. We employ a novel FMM [1] since it has many advantages over the original FMM algorithms. The FMM calculates interaction forces within a prescribed accuracy in linear time and memory usage.

In the 3D (2D) FMM, particles reside in small boxes, or octree (quadtree) nodes. The force calculation in FMM can be interpreted as the force calculation between these boxes. Due to the particle domain decomposition, the FMM enables to identify the near and far regions and calculates the far-field interactions rapidly. The near field interactions are still based on the particle–particle calculation method.

Further, we developed a code named PHAD, which is comprised of three important techniques that guarantee efficiency and accuracy. Firstly, we have shown that FMM calculates the far-field interactions with a variable but a priori guaranteed accuracy that can be adjusted by setting an appropriate FMM order. The fact that, at the optimum conditions, its calculation cost is in the order of N implies that FMM is efficient.

As the second technique, we used a variable order Picard iteration-based integrator [4, 5] to calculate the particle distributions' propagation in time. The adjustable time step size of the integrator for each particle allows investigating close encounters. In addition, the Picard integrator provides a dense output. Hence, the ability to adjust the optimum Picard order and the time step size automatically enable to calculate the near range interactions precisely, and with the appropriate number of iterations govern the efficiency.

Finally, we used a second order accurate operator splitting method, the Strang splitting, to speed up the performance of PHAD. It splits the complicated system into two simpler parts: far-range and near-range with external fields. The FMM is time-wise the most expensive procedure, thus we need to reduce the number of FMM calls. Each particle in the beam undergoes fast varying forces and slow varying forces. The fast varying forces are a result of the close encounters between the particle and its neighbors. The collective interaction due to the far away particles can be expressed as the mean field and the slow varying forces are due to this mean field. We need to select the appropriate time step size such that the slow forces stay approximately unchanged. However, in order to calculate the fast varying forces, this time interval should be split into smaller time steps. Due to this fact, we

ISBN 978-3-95450-174-8

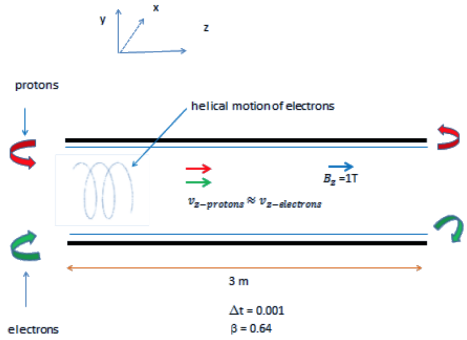

Figure 1: Cooling section in the pre-booster.

can identify two time step sizes for fast and slow varying forces. The smaller time step size depends on the distance between the target and the source particle and their relative speed, and hence we have individualized adaptive time steps. We call FMM only for the larger time steps and it implies that we can reduce the number of FMM calls. As a result, the computational cost can be substantially minimized in PHAD [3, 6].

We validated the accuracy of PHAD by comparing its results with the stand-alone N-body code, and they show an excellent agreement [3, 6].

PERFORMANCE ANALYSIS

In the Medium Energy Ion Collider, protons or ions are generated in the ion source and accelerated by the linac before being injected into the pre-booster. At the assumed injection, the kinetic energy of a proton beam is about 280 MeV and that of a lead ion beam is about 112 MeV per nucleon.

In this paper, our simulation is restricted to a proton beam. In the pre-booster ring, the average velocity of 280 MeV protons in the longitudinal direction is 0.64c ms^{-1}. The pre-booster, which also functions as the accumulator ring, accumulates protons and cools them to raise the beam current. The straight section of the pre-booster accommodates a ~3 m long cooling section and the 'hot' proton beam co-propagates with the 'cold' electron beam in this cooling section (Fig. 1). The electron beam takes 3.6 ns to pass the cooling section. Since the cooling section is immersed in a longitudinal magnetic field of ~1 T the electrons make a spiraling motion around the magnetic field and the estimated period for one revolution is about 35.77 ps. Therefore, in the 3 m long cooling section, the electrons make about 100 revolutions.

To evaluate the cooling motion, we studied the revolutions in increments of time. Even though large time steps can be prized as being computationally efficient, they might mask important physics such as close encounters of particles. To avoid this, we further divide the 35.77 ps period into ~10 small time steps of 3.57 ps each. Hence, the total number of such small time steps that the electron beam undergoes in the cooling section before exiting is ~1000. According to the design Medium-energy Electron Ion Collider (MEIC) parameters [7], the cooling time in pre-booster ring is in the millisecond range. This suggests that the proton beam has to pass the cooling section about 10^6 times before it is cooled.

Table 1: Simulation Parameters

Time step) size(m)	FMM order	Picard order	Picard iterations
0.001	9	16	1

In our proof-of-principle simulation, we used 100 protons and 1000 electrons as the two particle beams. Since they must co-propagate in the cooling section, the initial momenta of the particles in the longitudinal direction, p_z, were chosen such that the average longitudinal velocities of both beams are 0.64c, where c is the speed of light. Therefore, the corresponding relativistic gamma factor in the pre-booster is 1.3. In addition, the transverse momenta, p_x and p_y, were chosen as 1% of the longitudinal momenta. The initial configuration of protons and electrons were randomly generated such that they lie on the x-y plane and they are spatially close mimicking a high-density particle beam.

The proton beam and the electron beam were launched in the cooling section and data was gathered for 150k time steps of size 3.6 ps each. In our simulation, we used a scaling factor for the time and the transferred time step size has units of 1/c, where c is the speed of light. Therefore, the time step size is equivalent to 0.001 m. The simulation parameters are shown in Table 1.

The Figures 2 and 3 show the transverse emittance plots for protons and electrons, respectively. In the longitudinal direction, the average velocity of both protons and electrons stay around 0.64c and it implies that all particles are co-moving in the cooling section. Table 2 shows the average velocities of protons and electrons and their difference. The velocity difference diminishes as time passes (Fig. 4).

In addition, the 'frozen snapshots' of the cross sections of the beam in the x-z plane and y-z plane (Fig. 5) show that all protons and electrons have traveled the same distance, on average, in the longitudinal or z direction.

Even After 150k time steps the particles have traversed a very short distance in the cooling section. According to the estimated values, the ion beam has to pass the cooling section about 10^6 times and it may take longer time. Currently, we have a serial version of the PHAD code and in order to see the long-term effects it is inevitable to have the parallelized version. We are in the process of developing the parallelized version of the PHAD code.

The FMM piece of PHAD includes two parts: data structuring and calculation of Coulomb interactions. The former is implemented in C++ while the latter is in COSY INFINITY [8]. The remaining parts of PHAD are written in COSYScript.

The rms emittance, $\epsilon_{x,y}$, is given by:

$$\epsilon_{x,rms} = \sqrt{< x^2 > < x'^2 > - < xx' >^2} \qquad (1)$$

ISBN 978-3-95450-174-8

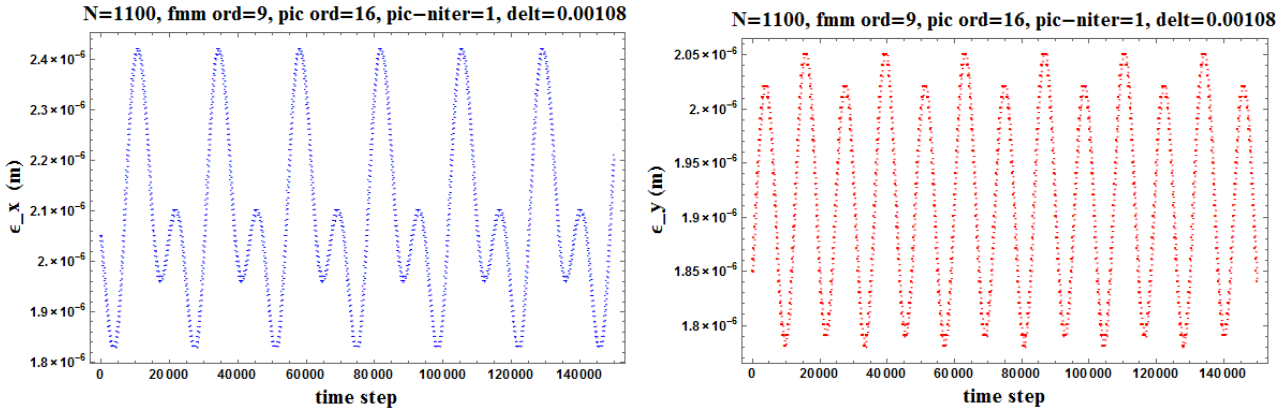

(a) (b)

Figure 2: Transverse emittances of protons.

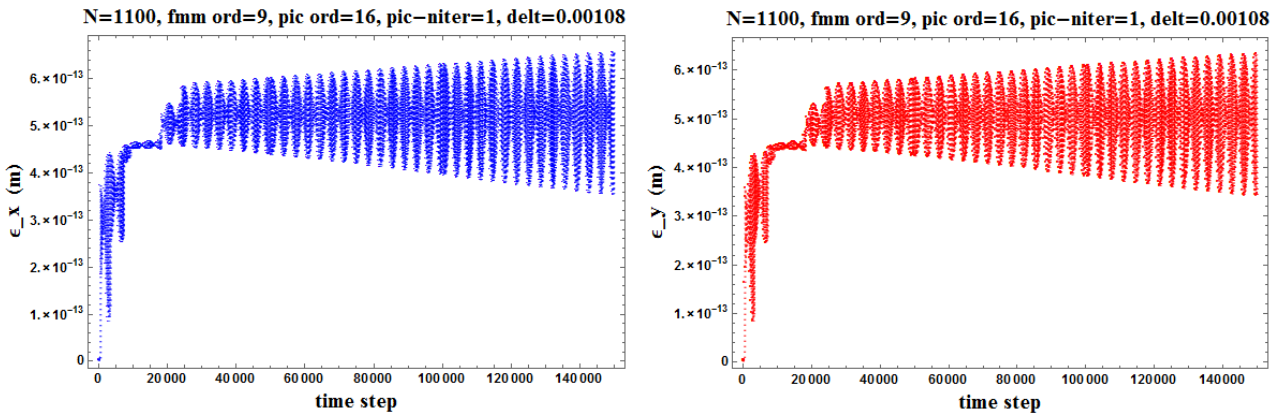

(a) (b)

Figure 3: Transverse emittances of electrons.

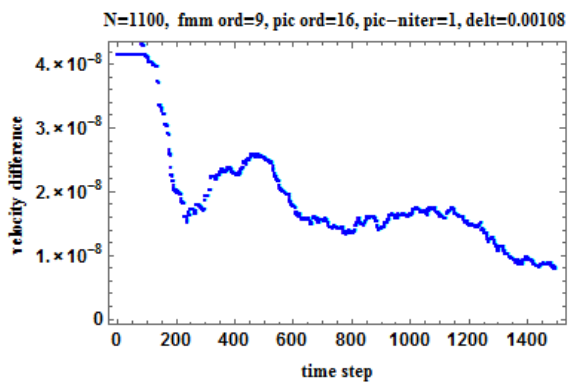

Figure 4: Average velocity difference between protons and electrons in the longitudinal direction.

Table 2: Longitudinal Velocities of Protons and Electrons

Number of time steps	Velocity of protons $\times c$	Velocity of electrons $\times c$	Velocity difference $\times c$
1	0.638 971 004 227	0.638 971 066 378	6.21×10^{-8}
150k	0.638 971 004 521	0.638 971 012 295	7.77×10^{-9}

SUMMARY

Modelling and simulation of the electromagnetic N-body problem can be performed with the aid of suitably developed algorithms and high performance computers. In this paper we discussed a novel code developed to model and simulate the dynamic behaviour of charged particles in a beam efficiently and accurately. Fast multipole method improves the efficiency and accuracy of calculating the Coulomb interaction force. Picard iteration process is used to investigate the close encounters of particles. The number of FMM calls is reduced with Strang splitting method and the efficiency is immensely improved. Effective symplecticity is preserved with high-order Picard runs.

FMM and Strang splitting do introduce certain approximations and splitting errors, respectively. By choosing appropriate FMM orders and time step sizes we can mini-

ISBN 978-3-95450-174-8

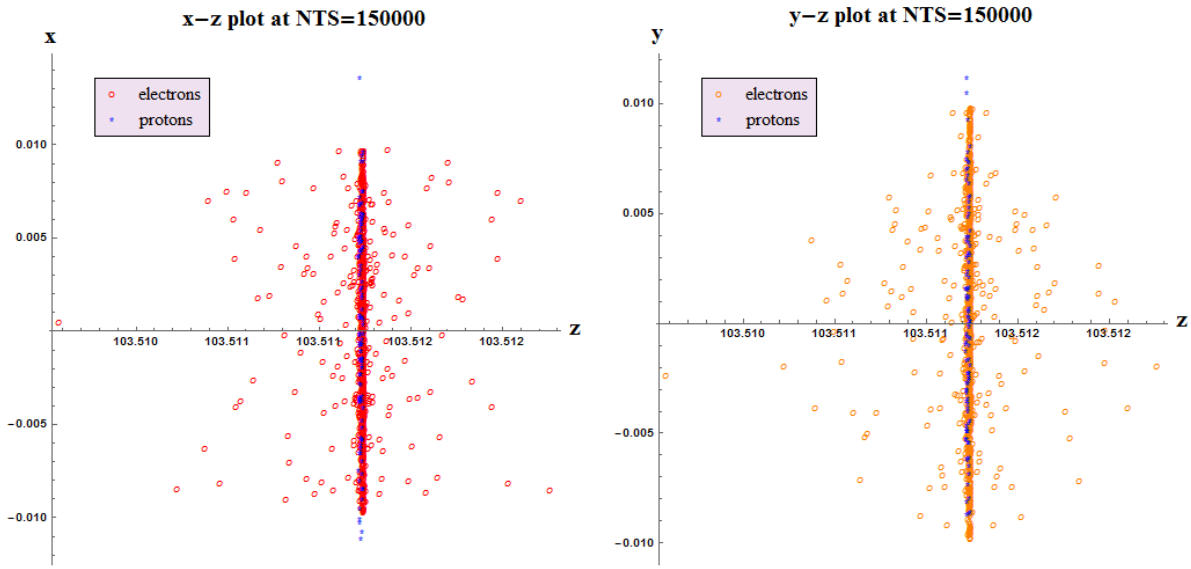

(a) (b)

Figure 5: Particle distribution on x-z and y-z plane at NTS=150k.

mize the influence of such errors on long term properties of the system [3].

This paper presented an update on the current status of the PHAD code. Subsequent work will give the high priority to parallelization of PHAD to expedite the time stepping.

ACKNOWLEDGEMENT

This work was supported by the U.S. Department of Energy, Office of Nuclear Physics, under Contract No. DE-SC0008588.

REFERENCES

[1] S Abeyratne, S Manikonda, and B Erdelyi. A Novel Differential Algebraic Adaptive Fast Multipole Method. In *Proceedings of IPAC'13*, pages 1055–1057, Shanghai, 2013.

[2] S Abeyratne and B Erdelyi. Optimization of the multipole to local translation operator in the adaptive fast multipole method. In *Proceedings of NA-PAC'13*, pages 201–203, Pasadena, 2013.

[3] B Erdelyi, S Abeyratne, and H Schaumburg. A New High-Order Adaptive Dynamics Code with Applications to Electron-Ion Collider. In *Proceedings of EIC14*, Newport News, 2014.

[4] H Schaumburg and B Erdelyi. A Picard Iteration Based Integrator. In *Proceedings of NA-PAC'13*, pages 210–212, Pasadena, 2013.

[5] Ernst Hairer, Gerhard Wanner, and Christian Lubich. *Geometric Numerical Integration*. New York: Springer Berlin Heidelberg, 2006.

[6] B Erdelyi and S Abeyratne. A Novel Code with High-Order Adaptive Dynamics to Solve the N-body Problem. In *Proceedings of HB2014*, East Lansing, 2014.

[7] S Abeyratne, A Accardi, S Ahmed, D Barber, J Bisognano, A Bogacz, A Castilla, P Chevtsov, S Corneliussen, W Deconinck, et al. Science requirements and conceptual design for a polarized medium energy electron-ion collider at jefferson lab. 2012.

[8] Kyoko Makino and Martin Berz. Cosy infinity version 9. *Nuclear Instruments and Methods in Physics Research Section A: Accelerators, Spectrometers, Detectors and Associated Equipment*, 558(1):346–350, 2006.

ISBN 978-3-95450-174-8

TAPER AND TUNER SCHEME OF A MULTI-FREQUENCY CAVITY FOR THE FAST KICKER RESONATOR IN MEIC ELECTRON CIRCULAR COOLER RING*

Y. Huang#,1,2,3, H. Wang[1], R.A. Rimmer[1], S. Wang[1]
[1] Thomas Jefferson National Accelerator Facility, Newport News, VA 23606, USA
[2] Institute of Modern Physics, Chinese Academy of Sciences, Lanzhou 730000, China
[3] University of Chinese Academy of Sciences, Beijing 100049, China

Abstract

An ultra-fast harmonic kicker consisted of normal conducting resonators with high transverse shunt impedance thus less RF power consumption was designed for the proposed Medium energy Electron Ion Collider (MEIC). In the prototype design, four quarter wave resonator (QWR) based deflecting cavities are used to generate ten cosine harmonic waveforms, the electron bunches passing through these cavities will experience an integral effect of all the harmonic fields, thus every 10th bunch in a continues bunch train of 10th harmonic bunch frequency will be kicked while all the other bunches un-kicked. Ten harmonic waves are distributed in the four cavities with the proportion of 5:3:1:1. For the multi-frequency cavities, a great challenge is to tune each harmonic to be exact frequency. In this paper, the taper and tuning scheme for the 5-modes cavity is presented. Five taper points in the inner conductor are chosen to make the five frequencies to be odd harmonics. Five stub tuners on the outer conductor are used to tune every harmonic back to its target frequency from the manufacturing errors.

INTRODUCTION

Electron cooling is essential for the proposed MEIC to attain low emittance and high luminosity [1]. The present MEIC design utilizes a scheme of multi-stage cooling, a DC cooler in the booster and the bunched electron beam cooler in Energy Recovery Linac (ERL) in the ion collider ring. To achieve a high electron beam current in the cooling channel but a relative low current in ERL, a circulator ring is proposed as a backup scheme. The electron bunches will recirculate for 25 turns, thus the current in the ERL can be reduced by a factor of 25. Two ultra-fast kickers are required in this circulator ring, one for kick-in, one for kick-out, all with half pulse width less than 2.1ns (1/476.3MHz) and a high repetition frequency of 19.052MHz (1/25 of 476.3MHz). JLab started an LDRD proposal to develop such a kicker. Our approach is to use RF resonant cavities other than transmission line type devices. Electron bunches passing through these cavities will experience an integral effect of all the harmonic fields, thus every 25th bunch in the bunch train will be kicked while all the other bunches un-kicked. Here we present a simplified design of a prototype with every 10th bunch kicked, using four QWR based cavities to generate 10 harmonic modes. The generation of the flat-top kick voltage with finite harmonic modes, shunt impedance formula, cavity structure optimization, power consumption calculation, and the concept design of stub tuners and loop couplers are already presented in [2]-[3]. In addition, the harmonic voltage combining scheme have been also discussed in [4]. Here we only focused on the taper and tuning scheme design of the 5-harmonics cavity.

*Work supported by Jefferson Science Associates, LLC under U.S.DOE Contract No. DE-AC05-06OR23177
#yulu@jlab.org

CAVITY WITHOUT TAPER

The cavity model used to generate harmonic modes is quarter wave transmission line shorted at one end and a capacitor loaded at the other end, as shown in Figure 1.

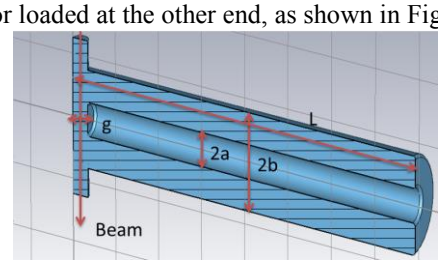

Figure 1: Cavity model without taper

Beam passes through the capacitive gap and is deflected primarily by a transverse electric field. The cavity geometry parameters for the 5-modes cavity are summarized in Tab.1.

Table 1: Cavity Geometry Parameters without Taper

Parameter	Length (mm)
Cavity Length (L)	1578
Inner Radius (a)	55
Outer Radius (b)	157
Gap Distance (g)	70
Beam Pipe Length	500

Here cavity length *L* is optimized to make maximum required tuning range is minimized. The relationship between the *L* and the required tuning range of the un-tapered cavity is shown in Fig.2.

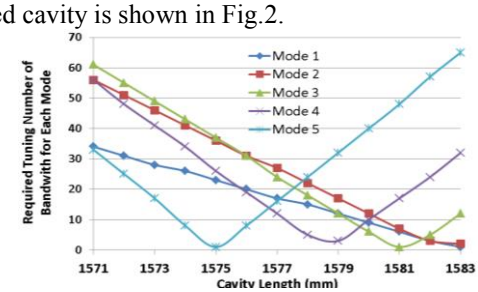

Figure 2: Required tuning range verses cavity lengths.

ISBN 978-3-95450-174-8

Here the curve deflection is due to the tuning range going to other direction from the target frequency. Required tuning range for these 5 modes at the select cavity length listed in Tab.2

Table 2: Required Tuning Range for the Select Cavity Length. Minimum bandwidth is for mode coupling β=1

Design freq. (MHz)	Freq. without taper (MHz)	Q_0 for 300K copper	Min. bandwidth (kHz)	Required tuning in number of bandwidth
47.63	47.790	8613	11	15
142.89	143.304	14921	19	22
238.15	238.611	19276	25	18
333.41	333.541	22826	29	5
428.67	427.874	25896	33	24

Outer radius *b* is chosen as the half wavelength of highest modes (476.3MHz) of all harmonic modes (not the highest modes of this single cavity). Inner radius *a* is optimized to get the highest transverse shunt impedance. Gap distance *g* (also the beam pipe diameter) is chosen as the nominal size of the CEBAF cavity beam pipe. Beam pipe length was chosen to make sure the highest mode frequency would not affect by the beam pipe boundary conditions.

STUB TUNER DESIGN

In order to get all the 5 frequencies tuned, 5 stub tuners insertion to the outer conductor is used. To determine the tuner positions, a stub radius R=40mm, insertion height H=15mm is moved along the cavity outer wall to see the frequency response of each modes, which can be shown in Fig.3. The "cross-talk" by the scheme of all tuner stubs on the same side of outer conductor has been confirmed to be secondary perturbation by the multi-stub simulations.

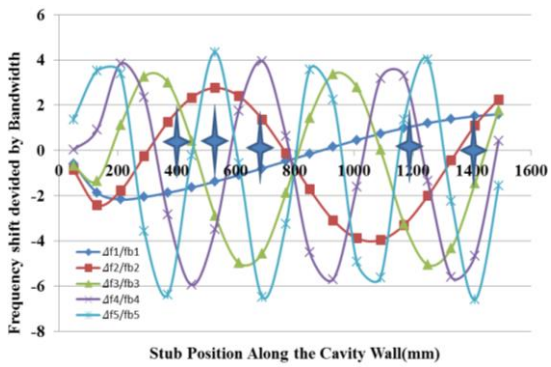

Figure 3: Tuner position simulation for the 5 harmonics modes cavity with a R=40mm H=15mm cylinder perturbation.

Five tuner positions are chosen in order to avoid the zero frequency response point. The position of each tuner is summarized in Tab.3.

Tab.3. Tuner Position along the Cavity Outer Wall

Tuner #1	Tuner #2	Tuner #3	Tuner #4	Tuner #5
400mm	530mm	690 mm	1190mm	1400mm

It is also obvious from Fig.3 that we can't get all 5 modes to be harmonics only with these tuners since the tuning range of the stub tuner is limited. Then tapering of inner conductor is needed. Before the tapering, five stub tuners are inserted 25mm into the cavity vacuum as the baseline, as shown in Fig.4. With such a design, the nonlinearity of the tuner response caused by the curved cavity surface is minimized, and on the other hand, it will achieve a larger tuning range of the stub.

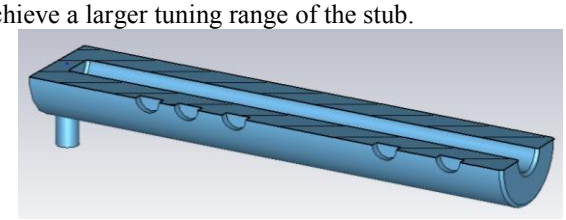

Figure 4: 5 stub tuners inserted H=25mm in the cavity wall as the baseline shape before the taper design.

TAPER DESIGN ITERATION

For the 5-modes cavity, 4 tapering sections are needed. There are many methods to choose these taper points and here we just present one of them. Two end points at *a*1 and *a*5 are chosen to get the least tapering slops along the cylinder; three straight tapering transition points *a*2 to *a*4 corresponding to the 3 middle tuner positions are chosen to make sure the manufactural errors on these points can be easily tuned back by the stub tuners. The positions of each taper section can be shown in Fig.5 and summarized in Tab.4.

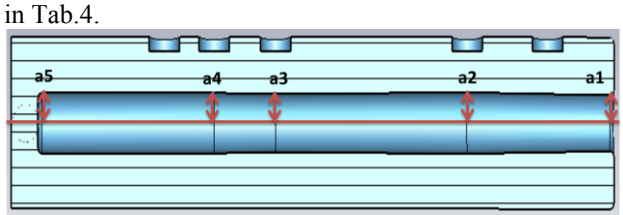

Figure 5: Straight taper sections for the 5-mode cavity

Table 4: Taper Transition Position along the Cavity Inner Conductor Cylinder

Taper #1	Taper #2	Taper #3	Taper #4	Taper #5
1578mm	1190mm	690 mm	530mm	70mm

To calculate the frequency response to each mode at each point, we have got a linear tuning matrix M_{taper}, and solve the equation (1) to get the taper value $a_n=a_0(55\text{mm})+\Delta a_n$:

$$M_{taper}\Delta a_n = \frac{\Delta f_n}{f_{BWn}} \quad (1)$$

Here Δa_n is for the n^{th} mode in *mm*, and

$$\Delta a_n = \begin{pmatrix}\Delta a_1 & \Delta a_2 & \Delta a_3 & \Delta a_4 & \Delta a_5\end{pmatrix}^T \quad (2)$$

Δf_n is the frequency shift of nth mode; Δf_{BWn} is the bandwidth of nth mode, and

$$\frac{\Delta f_n}{\Delta f_{BWn}} = \begin{pmatrix}\frac{\Delta f_1}{\Delta f_{BW1}} & \frac{\Delta f_2}{\Delta f_{BW2}} & \frac{\Delta f_3}{\Delta f_{BW3}} & \frac{\Delta f_4}{\Delta f_{BW4}} & \frac{\Delta f_5}{\Delta f_{BW5}}\end{pmatrix}^T \quad (3)$$

M_{taper} is the taper matrix, and the element m_{ij} is the liner frequency response relative to mode bandwidth (BW) of mode *i* to taper point *j* per mm. Fig.6 shows an example of linear response of these 5 modes to taper point #4 at position 1190mm with the element unit of BW/mm.

ISBN 978-3-95450-174-8

$$M_{taper} = \begin{pmatrix} 8.8634 & 13.266 & 0.2663 & -9.9226 & -13.297 \\ 10.129 & -16.086 & -0.1363 & 15.615 & -10.758 \\ 4.6755 & -4.7684 & -2.8073 & 2.749 & -2.2498 \\ 0.4749 & -1.0485 & 6.4026 & -6.3078 & -2.1708 \\ 0.0679 & 1.2901 & -7.2542 & 6.2967 & -3.6237 \end{pmatrix} \quad (4)$$

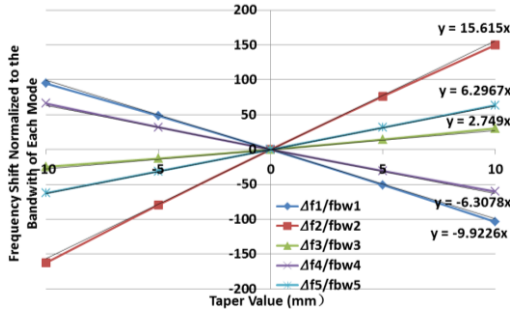

Figure 6: Tuning response of each mode at taper point #4

With this taper matrix, after one or several iterations in CST simulation, we can find the proper taper design values *a*2 to *a*4 getting every design mode within the bandwidth. The frequency and taper design value convergence with simulation iterations are shown in Fig.7 and Fig.8.

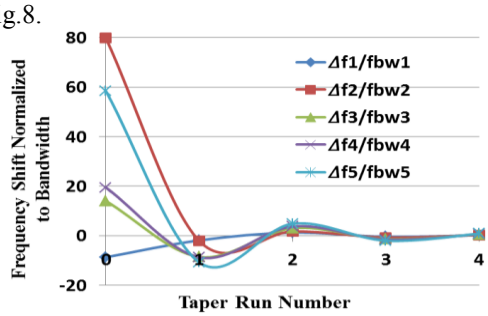

Figure 7: Frequency convergence with taper simulation iteration

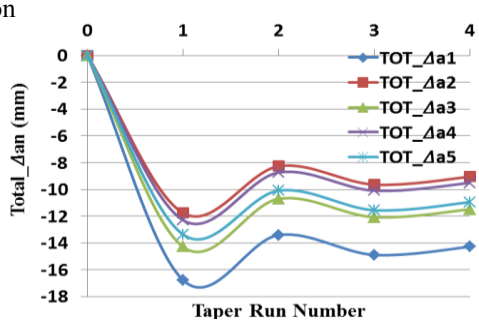

Figure 8: Taper design value convergence with taper simulation iteration

Here the cavity length L is 1578mm, the relative taper result at each point is

$$a_n = (40.728, 45.953, 43.521, 45.495, 44.056)^T \quad (5)$$

From the result, we find the average value of the inner conductor radius is reduced, we then have to change the cavity length *L* to re-taper the inner conductor which uses same matrix in the equation (4). The taper design result at different cavity length L can be shown in Fig. 9. Finally we can adjust the inner radii close to the optimized value of 55 mm to minimize the tapering slopes. When the cavity length L is at 1573 mm, the radius at taper #5 is about 55 mm, which was also optimized gap length for the shunt impedance. The re-tapered design result is

$$a_n = (51.24, 56.135, 53.154, 55.355, 54.983)^T \quad (6)$$

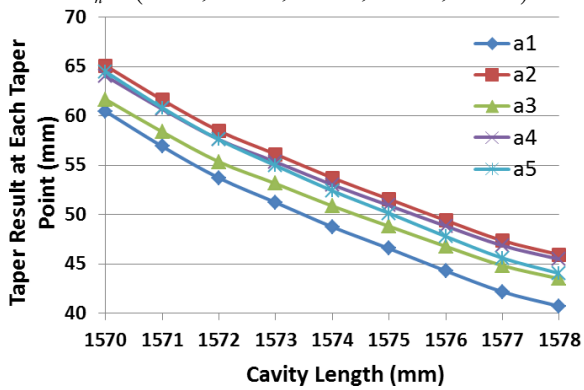

Figure 9: The relationship between inner radius at each taper point and cavity length with 5 stub tuners at each design locations above at R=40mm and H=25mm.

TUNER ITERATION

After the cavity is properly tapered, we can calculate the tuning sensitivity of each mode for each tuner, just as what we have done for the taper design. The tuner equation is

$$M_{tuner}\Delta h_n = \frac{\Delta f_n}{f_{BWn}} \quad (7)$$

Δh_n is the tuning insertion depth value in *mm* of n^{th} tuner,

$$\Delta h_n = (\Delta h_1 \quad \Delta h_2 \quad \Delta h_3 \quad \Delta h_4 \quad \Delta h_5)^T \quad (8)$$

M_{tuner} is the taper sensitivity matrix, and the element n_{ij} is the approximately linear frequency response relative to each bandwidth of i^{th} mode to j^{th} tuner tuning depth per mm. Fig.10 shows an example of linear response of these 5 modes to tuner #3.

$$M_{tuner} = \begin{pmatrix} -0.4203 & -0.3341 & -0.2145 & 0.108 & 0.1949 \\ 0.184 & 0.3762 & 0.1141 & -0.7598 & 0.0506 \\ 0.242 & -0.7703 & -1.0321 & -0.9785 & -0.4635 \\ -1.178 & -0.844 & 0.5083 & 0.1279 & -1.154 \\ -1.179 & 0.6265 & -1.6784 & 0.422 & -1.7042 \end{pmatrix} \quad (9)$$

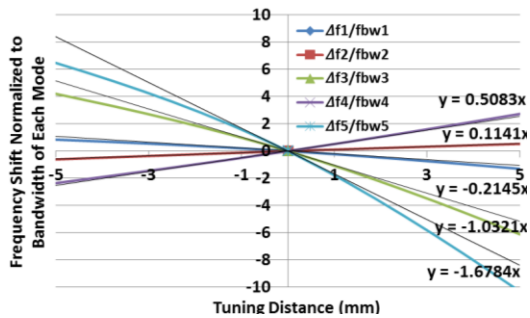

Figure 10: Frequency tuning response of each mode at tuner 3

COUPLER AND PICKUP

When the coupler is inserted, with the coupler loop size in the current design, all mode frequencies are reduced due to the frequency pulling effect. The highest pulling is at the mode 5 in about 500 kHz. A slight change of the cavity length and related taper values within mm range is

ISBN 978-3-95450-174-8

readjusted in order to reduce the required tuning ranges. No adjustment is needed when the pickup port is added since output coupling is very weak.

CONCLUSION

The taper and tuner design scheme of the 5-mode harmonic cavity has been elaborated in this paper. With the present taper design, a very gentle taper slop design is achieved thus the transverse shunt impedance is almost unaffected compared with the non-tapered cavity. With the present tuner design, it has no problem to tune all harmonic modes back within half (12.5mm) tuning range to its target frequencies within the manufactural error of 0.5 mm at two end taper points and even larger at three middle taper points. A half scale prototype cavity is under mechanical design for fabrication, with the input coupler port and output pickup port, low power RF bench measurement will be taken after the prototype cavity is fabricated.

REFERENCES

[1] MEIC Design Summary. January 12, 2015.
[2] Y. Huang et al., "Harmonic Resonant Kicker Design for the MEIC Electron Circular Cooler Ring", IPAC'15 proceedings, Richmond, VA, USA (2015)
[3] Y. Huang et al., "Ultra-fast Harmonic Resonant Kicker Design for the MEIC Electron Circular Cooler Ring", ERL2015 proceedings, Stony Brook, NY, USA (2015)
[4] J. Guo et al., "Harmonic Stripline Kicker for MEIC Bunched Beam Cooler", COOL2015, these Proceedings.

ISBN 978-3-95450-174-8

STATUS, RECENT RESULTS AND PROSPECTS OF THE INTERNATIONAL MUON IONIZATION COOLING EXPERIMENT

C. T. Rogers, Rutherford Appleton Laboratory, Didcot, UK on behalf of the MICE collaboration

Abstract

Muon accelerators have been proposed as a means to produce intense, high energy muon beams for particle physics. Designs call for beam cooling to provide suitable beams. Existing cooling schemes cannot operate on time scales that are competitive with the muon lifetime. Ionisation cooling has been proposed as a means to achieve sufficient cooling, but it has never been demonstrated practically. In the Muon Ionisation Cooling Experiment (MICE), based at the Rutherford Appleton Laboratory (RAL), ionisation cooling will be demonstrated. MICE Step IV is currently in progress and will be completed in 2016. Muons are brought onto an absorber, resulting in a reduction of momentum and hence reduction of normalised transverse emittance. The full Demonstration of Ionisation Cooling will take place in 2017. An extra magnet module and RF cavities will be installed, as in a cell of a cooling channel. This will enable the demonstration of reduction of emittance and subsequent re-acceleration, both critical components for a realistic ionisation cooling channel.

COOLING FOR MUON ACCELERATORS

Muon accelerators have been proposed as a source for high energy neutrino beams, at the Neutrino Factory, as a source of Higgs particles in a Higgs factory and as a multi-TeV lepton collider for searches for higher energy phenomena [1, 2].

Muons are created by firing an intense beam of protons onto a high power target. Pions are produced which are captured in high field solenoids where they decay to muons. The resultant muon beam has large emittance.

In order to provide sufficient muons within the acceptance of the Neutrino Factory acceleration system, it is desirable to cool the muon beam prior to acceleration. In order to reach luminosities appropriate for a Muon Collider it is essential to cool the muon beam.

Muon cooling is performed by ionisation cooling [3–5]. This is the only technique that is competitive with the 2.2 μs muon life time. Particles are passed through an absorber where the momentum of the muons is reduced in transverse and longitudinal directions, then passed through an RF cavity where momentum is restored only in the longitudinal direction, resulting in a reduction in beam emittance.

Multiple scattering produces random momentum kicks that tend to degrade the cooling effect or even heat the beam. Low-Z materials like liquid hydrogen or lithium hydride give less multiple scattering for a given energy loss, so these are considered as absorber materials. A tight focus means that the beam has relatively high transverse momentum, so that the multiple scatters are less significant.

Muon cooling has never been demonstrated before. The Muon Ioniation Cooling Experiment (MICE) collaboration is building a section of a cooling channel in order to demonstrate the technique [6].

THE MICE PROGRAM

The MICE program is planned to operate in several installation steps [7]. Step IV is now fully installed and the equipment is being commissioned. Installation of the final step, known as the Demonstration of Ionisation Cooling, will begin in mid-2016. Schematics of Step IV and the Demonstration of Ionisation Cooling are shown in Fig. 1.

In Step IV the full diagnostics system has been installed together with a single absorber system. In this configuration MICE will study the material physics properties of the MICE absorbers and measure transverse normalised emittance reduction .

In the Demonstration of Ionisation Cooling, a cooling cell will be installed including RF equipment. This will enable the measurement of ionisation cooling with reacceleration.

In order to accommodate the characteristics of muon beams, MICE has a number of features which make it a unique accelerator physics experiment. These features are outlined below.

High resolution particle-by-particle diagnostics

MICE is similar to a small section of a much longer cooling channel, so will produce a cooling effect of only a few percent. In order to measure such a cooling effect with high precision, a high resolution detector system has been designed.

MICE will measure individual particles' position, momentum and time with respect to the RF pulse once RF is installed [8]. This enables the collaboration to make a full correlated measurement of the beam upstream and downstream of the cooling equipment.

MICE can also reject beam impurities such as undecayed pions and electrons from muon decay on a particle-by-particle basis.

The position and momentum of particles are measured using two scintillating fibre trackers upstream and downstream of the cooling region. Three 50 ps time-of-flight counters (TOFs) provide time measurement and velocity measurement. Comparison of velocity and momentum enables measurement of particle mass. Cherenkov threshold counters (Ckov), the KL pre-shower and Electron Muon Ranger (EMR) calorimeter provide additional

ISBN 978-3-95450-174-8

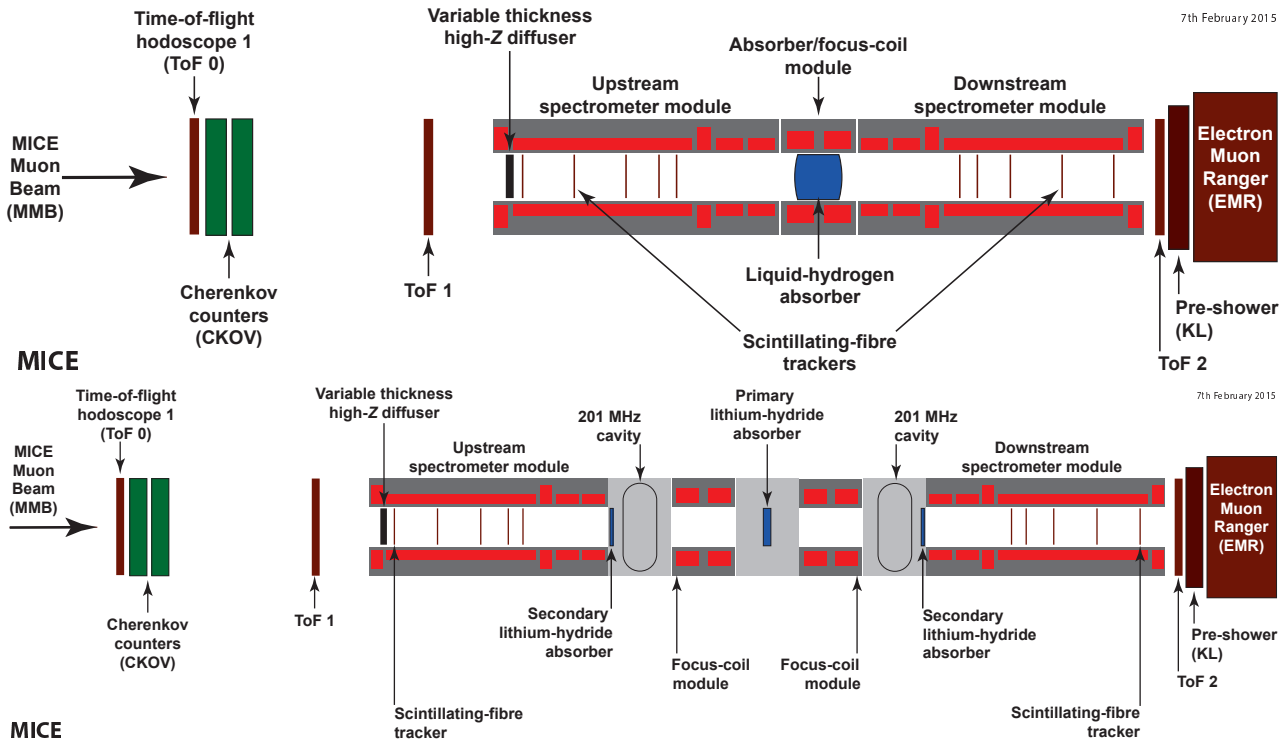

Figure 1: Schematic of the MICE cooling channel at Step IV (top) and for the full demonstration of ionisation cooling (bottom).

particle identification.

High Aperture Superconducting Solenoids

At Step IV MICE has three superconducting solenoid assemblies: two 5-coil Spectrometer Solenoids (SSU and SSD) and one 2-coil Focus Coil module (FC). SSU and SSD provide a uniform 4 T field which is necessary for reconstruction of particle momentum in the tracker. Match coils provide matching to the final focus enabling independent selection of β and β'. FC can operate with the coils having the same polarity (solenoid mode) or opposite polarite (flip mode). In the Demonstration of Ionisation Cooling an additional Focus Coil module will be installed.

The bore aperture of the magnets is more than 200 mm radius and the magnets are closely packed at Step IV, resulting in magnetic coupling between adjacent modules.

Liquid Hydrogen and Lithium Hydride Absorbers

At Step IV, energy loss is provided by either liquid hydrogen or lithium hydride absorbers. Both will be operated separately. During the Demonstration of Ionisation Cooling, only lithium hydride absorbers will be operated.

The liquid hydrogen absorbers present 350 mm thickness of liquid hydrogen on the beam axis. The hydrogen is encapsulated in a pair aluminium windows of 150 micron thickness. An additional pair of windows protect the rest of the experiment in the case of a burst of the main windows. The windows are curved, enabling a thinner construction. This results in less scattering.

The lithium hydride absorber is a 65 mm thickness disk of lithium-6 enriched lithium hydride.

COMMISSIONING STATUS OF THE MICE MAGNETS

The Step IV magnet assemblies have all been tested and trained to design currents during the construction phase of the project. They have been transported to the MICE hall and were installed on the beam line in 2014. A partial return yoke was installed around the MICE magnets in 2015 so that stray fields from the MICE magnets do not impinge on nearby equipment. The magnets have been cooled down and all magnets have been successfully powered.

- SSU has been fully trained to production current. SSU awaits a soak test before it can be considered fully commissioned.

- SSD has been trained to near production currents. During one of the training cycles the low temperature lead to Match Coil 1 of SSD failed, making the coil inoperable at Step IV. MICE has designed a new baseline optics to accommodate the failed coil.

- FC has been cooled and powered with a 114 A current, followed by a 20 hour soak test at 120 A, demonstrating the full range of operational currents with the coils in solenoid mode. Tests in flip mode will follow.

ISBN 978-3-95450-174-8

Once the individual coil assemblies have been shown to power correctly, the entire line will be powered together. Adjacent magnets are coupled. This may result in a requirement for combined training of coils in the presence of the field of neighbouring coils. Additionally, simulations indicate that a quench in one coil will quench the line. A combined quench protection system has been designed and will be tested with all the magnets in combination.

COMMISSIONING STATUS OF THE MICE DIAGNOSTICS

The MICE diagnostics is now commissioned and operational.

Scintillating Fibre Trackers

The MICE scintillating fibre trackers consist of planes of fibres laid across the beam pipe. Three planes are arranged into a station, adjacent planes rotated through 120 degrees, providing a measurement of the position of particles at each station. Five stations make up each tracker. By fitting the expected helical trajectory to the observed space points, MICE determines the momentum of each particle. Combined with the position measurement and time measurement at the TOFs, MICE is able to reconstruct the full phase space of particles in the beam.

The MICE scintillating fibre trackers were installed in the MICE spectrometers prior to their move to the Hall. The cabling was completed during April and a series of calibration runs were performed using a pulser trigger and light provided by a set of LEDs in the magnet bore. Subsequently a muon beam was passed through the trackers and the tracker readout was synchronised with the other detector readouts. The tracker efficiency has been measured using this beam and found to meet specification. Final numbers await a full analysis.

Particle Identification Detectors

The EMR is a totally active scintillator detector at the downstream end of MICE. Muons that pass into the detector are stopped. Particle identification is achieved by examining the characteristics of energy deposition in the detector.

The EMR was commissioned in 2013 and shown to achieve a good rejection of electrons from muon decays. Several features of the energy deposited by electron showers and muons were used to characterise these different particle species. Analysis has shown 99.6% of muons tagged as muons while 95% of electrons are tagged as electrons. The MICE muon beam has on a small electron impurity, and so the EMR should enable good rejection of electrons.

The Ckov, KL and TOF detectors have been installed and operational for many years and continue to function reliably.

Beam Based Alignment

The MICE beam has been used to validate individual detector reconstruction and to provide a global alignment of the diagnostics with each other. The beam based alignment of the diagnostics validates the surveyed alignment.

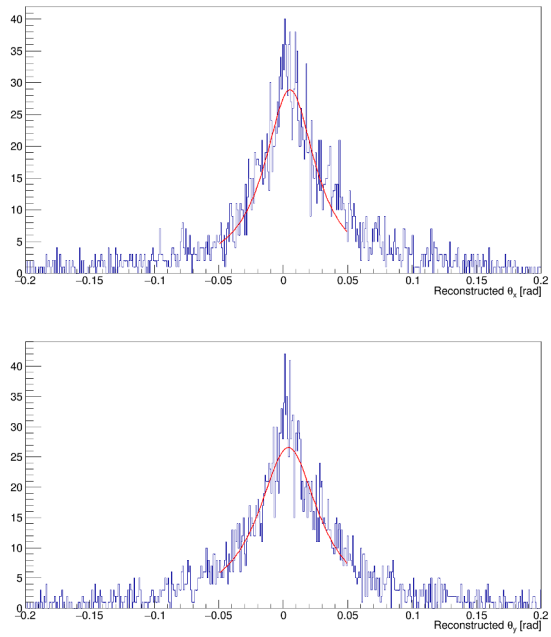

Figure 2: Angular distribution of axis of helices, fitted to tracker station hits in the tracker region.

The tracking detectors have been aligned with respect to one another by means of propagating straight tracks from one detector to the other in the absence of fields in the magnets. By performing the analysis track by track, effects that are dependent on momentum or other phase space variables can be neglected. Analysis indicates alignments in line with expectations from survey and other measurements.

A similar procedure has been used to align the other detectors. For these detectors, the position resolution is insufficient to be competitive with the survey and the measurement merely validates the survey. All of the detector positions have been found to be consistent with the survey except for TOF0, where the analysis of the alignment has not yet been completed.

Reconstruction has been performed in the MICE trackers in order to measure the alignment of the trackers to the solenoids. Space points were projected onto a single $x - y$ plane and a cycloid was fitted, enabling a calculation of the estimated track tilt for each track. By calculating the distribution peak, the tracker tilt was found with respect to the solenoid axis.

The distribution of angles for a set of reconstructed tracks is shown in Fig. 2. The spectrometer solenoids were running in a pre-commissioning state in a reduced field of 1.46 T. A 4 T field will be used when the trackers are fully commissioned. The measurement is expected to have a significant systematic error that has yet to be calculated. Alignments were found to be of order mrad, which is compatible with the survey and field measurements.

ISBN 978-3-95450-174-8

PLANS FOR STEP IV

The beam-based alignment of the cooling channel will continue. Measurement of magnet alignment will be performed by projecting tracks from the upstream tracker to the downstream tracker and comparing with simulation.

The beam will be passed through the cooling channel without an absorber and the optical properties of the beamline will be checked. Absorbers will be placed in the beamline and the transported emittance with and without the absorber will be measured.

DEMONSTRATION OF IONISATION COOLING

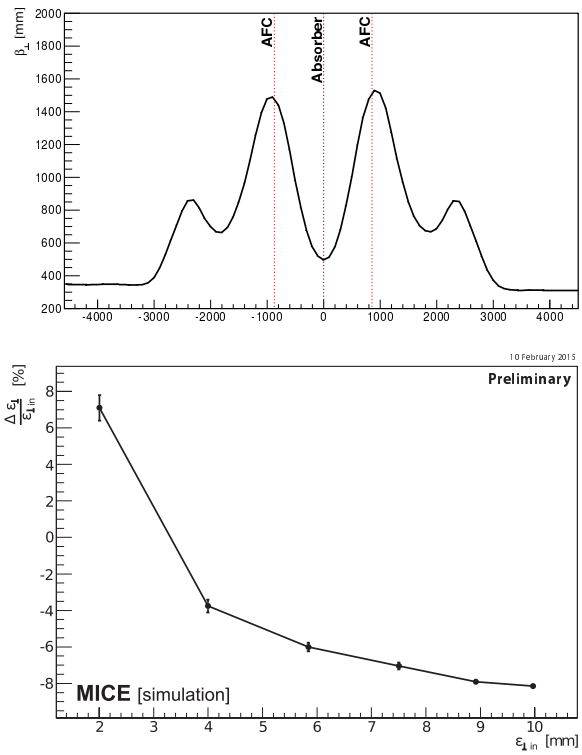

Figure 3: (Top) optical β function and (Bottom) simulated emittance reduction as a function of input emittance in the full demonstration lattice.

A revised lattice for the Demonstration of Ionisation Cooling has been devised in the light of experience from the Step IV construction phase [11]. This step reuses the existing Step IV hardware, with the addition of two 200 MHz RF cavities and an additional Focus Coil module that has already been constructed and operated successfully.

The lattice has a focus at the central point of the two Focus Coil modules, where the primary lithium hydride absorber sits. Additional secondary absorbers sit at the outer edge of the lattice. These secondary absorbers serve to shield the tracking detectors from the RF cavities and to provide additional cooling. The simulated optical function is shown in Fig. 3.

The 430 mm long RF cavities will operate at around 10 MV/m and 201.25 MHz. The gradient is enhanced by beryllium windows on the axis which helps to keep the electric field more axial to the beamline. The energy recovered by the RF cavities will be less than the energy lost by the beam in the absorbers, but should be sufficient to show the principle of energy recovery.

The performance of the lattice is shown in Fig. 3. The equilibrium emittance is expected to be around 3 mm while transverse emittance reduction around 7% is expected for higher emittance beams.

Construction of the Demonstration of Ionisation Cooling will begin in the summer of 2016, following the end of Step IV operations. First beam is expected in 2017.

CONCLUSIONS

Muon accelerators have the potential to make definitive measurements of neutrino oscillations at the Neutrino Factory, and to serve as either a Higgs factory or a discovery machine in a Muon Collider.

Ionisation cooling is the critical enabling technique for muon accelerators. MICE is intended to demonstrate muon ionisation cooling for the first time.

MICE Step IV is in the final stages of commissioning for data taking late in 2015 or early in 2016. The MICE Demonstration of Ionisation Cooling is in the final design stage, with most of the major design components on site at RAL.

REFERENCES

[1] M. Alsharo'a et al. Phys. Rev. ST Accel. Beams 6 (Aug, 2003) 081001.

[2] IDS-NF Collaboration, S. Choubey et al., International Design Study for the Neutrino Factory, Interim Design Report, tech. rep., 2011. arXiv:1112.2853.

[3] V. Parkhomchuck and A. Skrinsky, Cooling Methods for Charged Particle Beams, Rev.Accel.Sci.Tech. 1 no. 1, (2008) 237.

[4] C. Yoshikawa et al., "Status of the Complete Muon Cooling Channel Design and Simulations," IPAC-2014-TUPME016

[5] D. Stratakis and R. Palmer, "Rectilinear six-dimensional ionization cooling channel for a muon collider: A theoretical and numerical study", Phys. Rev. ST Accel. Beams 18 (2015) 031003

[6] MICE Collaboration, G. Gregoire, G. Ryckewaert, L. Chevalier, J. Rey, M. Catanesi, et al., Proposal to the Rutherford Appleton Laboratory: an International Muon Ionization Cooling Experiment (MICE),. http://mice.iit.edu/micenotes/public/pdf/MICE0021/MICE0021.pdf. MICE-NOTE-21

[7] M. Bogomilov et al, "The MICE Muon Beam on ISIS and the beam-line instrumentation of the Muon Ionization Cooling Experiment", JINST 7 (2012) P05009.

[8] D. Adams et al, "Characterisation of the muon beams for the Muon Ionization Cooling Experiment", European Journal of Physics C, Volume 73, Number 10.

ISBN 978-3-95450-174-8

[9] D. Adams et al., "Electron-Muon Ranger: performance in the MICE Muon Beam", arXiv:1510.08306.

[10] D. Adams et al., "Pion contamination in the MICE muon beam", arXiv:1511.00556.

[11] MICE Collaboration, V. Blackmore, C. Hunt, J. Pasternak, C. Rogers, P. Snopok, and H. Witte, MICE Ionization Cooling Demonstration: Technical Note,. http://mice.iit.edu/mnp/MICE0452.pdf. MICE-NOTE-DET-452.

ISBN 978-3-95450-174-8

STATUS OF HELICAL COOLING CHANNELS FOR INTENSE MUON SOURCES*

K. Yonehara†, Fermilab, Batavia, IL 60510, USA

Abstract

Status of the design and simulation study of a homogeneously distributed hydrogen gas-filled helical cooling channel (HCC) is presented. The helical cooling theory has been verified by numerical cooling simulations. Flexibility of cooling decrements and equilibrium emittance in the HCC were demonstrated by tuning the helical cooling lattice. Preliminary analysis of a beam-plasma interaction in a solenoid magnetic field and a gas-filled RF cavity was made. As a result, a beam-induced plasma neutralizes a space charge of the incident beam and a plasma-lens effect appears. It indicates that the beam dynamics and cooling performance in the final cooling segment will be affected by the plasma-lens.

INTRODUCTION

Ionization cooling has a great potential to shrink a muon beam phase space by factor 10^6 within their short lifetime (2.2γ μs) since the collision frequency in a cooling media is extremely high by comparing with a conventional cooling method [1]. However, a large angle scattering takes place by the Coulomb interaction with nuclei in the media, so called a multiple scattering, and grows the muon beam phase space (heating). To minimize the heating, an ionization cooling channel consists of a strong magnetic field to overcome the multiple scattering, and a high-gradient RF cavity in the magnet to immediately compensate the lost-energy via ionization process. Hydrogen is the best cooling material since it has a high energy-loss rate and a long radiation length.

Early days' designs of a cooling channel have a liquid hydrogen flask and a high gradient vacuum RF cavity in a strong magnetic field. However, soon channel designers realize a critical issue that the maximum available RF gradient is strongly limited by the magnetic field strength in the cavity [2]. One plausible model is that dark current densities in the cavity are increased due to focused by magnetic fields. It induces a RF electric breakdown at lower RF gradients in stronger magnetic fields. A possible solution is filling a RF cavity with a dense hydrogen gas [3]. Gas resists the dark current flow and, therefore suppresses RF electric breakdowns even the cavity is operated in a strong magnetic field. In addition, a dense gaseous hydrogen works as an ionization cooling media.

A helical cooling channel (HCC) is designed to maximize the advantage of utilizing the gas-filled RF cavities for a six-dimensional (6D) ionization-cooling channel [4]. Beam trajectory is a spiral by a solenoid and helical magnetic components (Fig. 1). To avoid any pressure gap on the beam path, hydrogen gas is distributed homogeneously in the channel. RF cavities are located along the helical beam path without any spatial gap. A thin RF window is located between adjacent cavities to electrically isolate each other. A solenoid and helical dipole components are applied to generate a continuous dispersion. An emittance-exchange occurs during the cooling process with the dispersion, therefore it induces 6D phase space cooling. A helical field gradient continuously focuses the beam and stabilizes the phase space. Large acceptance of the channel is achieved since there is no betatron resonance in the continuous focusing channel. Thus, the channel length is shorter than other ionization cooling channels.

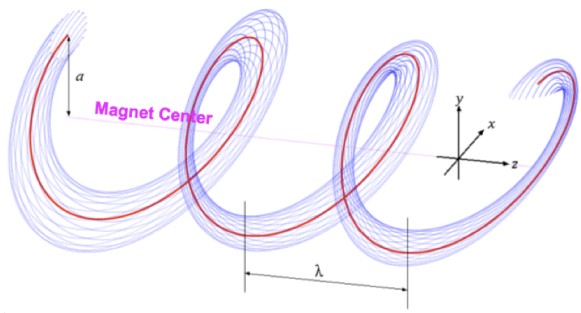

Figure 1: Beam path in a helical lattice. A red line is a reference orbit and a blue line is an orbit of an envelop particle.

Dense hydrogen gas-filled RF cavity is a unique device for beam applications. Particularly, a beam-induced gas-plasma in a dense hydrogen gas opens many interesting subjects. Ionization electrons are quickly thermalized by momentum exchange interaction with molecular hydrogens. The plasma regains kinetic energy from RF fields. The energy is transferred into hydrogen gas via the thermalization. As a result, RF power is transformed into the gas temperature. The rate is proportional to the plasma density in the cavity. It is called plasma loading effect [5]. The effect can be mitigated by doping a small amount of electronegative gas in the cavity. From experiment, 0.2 % Oxygen was sufficient to be ineffective the plasma loading for beam acceleration. Plasma parameters were measured in experiments [6]. These are used in a numerical plasma simulation to evaluate the collective effect in the cavity for intense muon beam applications. As a result, the space charge of beam is neutralized by plasma motions excited by the space charge fields and the tail of the bunched beam is strongly focused by the self-induced axial magnetic field [7, 8]. This phenomenon is similar as the plasma lens that has been developed for the electron-positron collider at SLAC [9]. Since the HCC is a positive energy transition

* Work supported by Fermilab Research Alliance, LLC under Contract No. DE-AC02-07CH11359

† yonehara@fnal.gov

ISBN 978-3-95450-174-8

channel the longitudinal space charge force becomes focusing. Therefore, transverse and longitudinal space-charge forces in the HCC will enhance cooling.

Characteristics of the HCC lattice is presented in the first part of document. Then, we discuss about the preliminary study of a gas-plasma dynamics and a beam-plasma interaction in the rest of document.

DEMONSTRATE COOLING PERFORMANCE IN HCC

First Cooling Simulation Study

HCC cooling simulation has been done in G4Beamline [10] which has been executed in a parallel grid core processor at NERSC [11]. A solid red line in Fig. 2 shows the simulated emittance evolution in the HCC. An initial cooling channel (a gas-filled helical FOFO, HFOFO snake channel [12]) is applied (a red dash line in Fig. 2) to shrink the initial beam phase space from 15 mm and 45 mm to 4 mm and 7 mm in the transverse and longitudinal phase spaces, respectively.

A matching-in channel is located downstream of the HFOFO to adapt the beam into the HCC with energy transition jump because the HFOFO has a negative energy transition [13]. Current best transmission efficiency is 80 %. The HCC shrinks the 6D beam phase space further. RF frequency is shifted from 325 MHz to 650 MHz in the HCC when the longitudinal beam size becomes small enough to be captured in a high frequency RF bucket. It permits to design a smaller-bore helical magnets that can generate stronger magnetic fields. There are four helical lattice configurations in the first simulation study: The first two HCC segments (f = 325 MHz, helical period λ = 1.0, 0.8 m) are designed to have a large acceptance while the last two segments (f = 650 MHz, λ = 0.5, 0.4 m) have strong magnetic fields to reach low equilibrium emittances. Helical magnetic field is presented by using analytical field formulae in this simulation [14].

The first cooling cycle in the HCC starts from segment 2. The beam has 21 bunches in this cycle. The bunched beam is merged into one in a low energy helical bunch merge channel to increase beam luminosity [15]. Since the beam size after merge becomes large the second cooling cycle is resumed which will be started from the HCC segment 1. Final emittance is 0.62 mm and 0.88 mm in the transverse and longitudinal planes, respectively. Total channel length and the transmission efficiency including with the matching in the first cooling cycle are 300 m and 48 %, respectively. The HCC theory predicts the equilibrium emittance accurately, 0.62 mm and 0.87 mm in transverse and longitudinal planes, respectively. The prediction agrees quite well with the simulation result.

Table 1 shows the summary of beam parameters and cooling lattice from the design and simulation study. The second cooling cycle has not been accomplished yet since the beam after the bunch merge channel is not ready. Beam growth by mismatching occurs at beginning of each segment. Some amount of particles (~5 %) are lost by mismatching. This

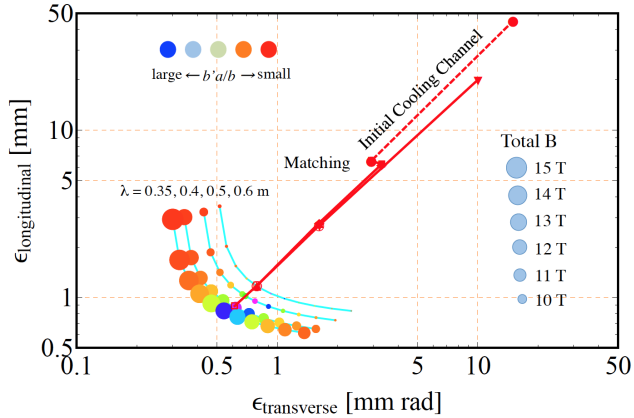

Figure 2: Simulated emittance evolution in the HCC. A light-blue line is the theoretical limit of cooling with various helical periods.

can be eliminated by using more segmented HCCs to make smooth transition.

Table 1: Beam parameters in the HCC. Segment 0 is the initial cooling channel. β_T and β_L are beta functions in transverse and longitudinal planes, respectively. "Tran" is a transmission efficiency at each segment. Segment 4′ is the proposed longitudinal enhance cooling channel.

Seg	L	λ	β_T	β_L	ϵ_t	ϵ_l	Tran
	m	m	cm	m	mm	mm	
0	100	–	60	–	4.2	7.2	0.68
1	(100)	1.0	20	2.1	–	–	–
2	100	0.8	16	2.1	1.5	2.5	0.83
3	120	0.5	9.8	1.5	0.75	1.2	0.82
4	80	0.4	7.9	1.5	0.62	0.89	0.88
4′	–	0.35	7.3	1.3	0.75	0.72	–

Critical Beam Element Parameter for Cooling Simulation

Figure 3 shows a schematic drawing of the segmented HCC per one helical period. Critical beam parameter is determined from the technological boundary. A magnetron is considered as a RF source that has been developed for accelerator applications [16, 17]. Energy efficiency of a magnetron is extremely high. If the magnetron becomes practical the peak RF power ~1 MW will be available. This may be sufficient to excite each high-Q cavity. To this end, the cavity will be operated at 80 K. The peak RF gradient is set to 20 MV/m from the RF power limitation. The estimated RF power deposition in the cavity is less than 0.5 kW/m. A commercial liquid nitrogen chiller is available which has enough cooling power to remove the deposition heat from cavities.

Since the HCC is a positive phase slip factor the RF accelerating phase is set ~160 degrees, which generates reasonable longitudinal focusing and cooling rate. The average energy loss rate is ~6 MeV/m (~10 MeV per unit channel

ISBN 978-3-95450-174-8

length). It determines the hydrogen gas density 13.4 mg/cm^3, which corresponds to the gas pressure 160 atm at room temperature (44 atm at 80 K). The cavity length is 10 and 5 cm for 325 and 650 MHz, respectively. In order to make a room in radial direction between RF cavities and helical magnetic coils, a dielectric loaded gas-filled RF cavity has been considered. Proof of principle test of the dielectric loaded RF cavity was made [18]. The radial size of cavity can be reduced by 20 ~ 50 %. A helical re-entrant cavity has also been considered as the option [19].

A 60-μm-thick Beryllium foil is used for a RF window in the cooling simulation. Since hydrogen gas acts as a coolant the frequency detuning due to thermal expansion of the window is negligible. On the other hand, the RF window shape should be curved to avoid the Lorentz force detuning. However, emittance is grown even in the thin RF window. Besides, a small amount of Oxygen dopant which is applied in the cavity also increases the equilibrium emittance. An effective radiation length is given $X_{0,eff}^{-1} = X_{0,GH_2}^{-1} + X_{0,Be}^{-1} + X_{0,O_2}^{-1}$. Impurity materials change the equilibrium longitudinal emittance by additional energy loss rates. Modified energy loss rate is applied in the HCC theory to evaluate the longitudinal equilibrium emittance. The effective radiation length model agrees with the numerical simulation although larger discrepancy is seen in thicker RF window.

Helical solenoid coil is innovated to generate proper helical magnetic fields. Solenoid and helical dipole components are naturally generated by superimposing between a main and end (fringe) fields. A helical field gradient is tuned by the coil geometry. A straight solenoid is used to correct the solenoid component. In the magnet design study, the HCC with λ = 0.5 m seems to be feasible since the total magnetic field is less than 10 Tesla. However, the last segment, λ = 0.4 m is extremely challenging. The total magnetic field becomes ~11 Tesla on the helical beam path. Besides, the field on the coil is ~17 Tesla that reaches to the maximum available field strength for Nb_3Sn. Table 2 shows the summary of helical lattice parameters. Huge stored magnetic energy is estimated in last two segments which is generated by the correction solenoid.

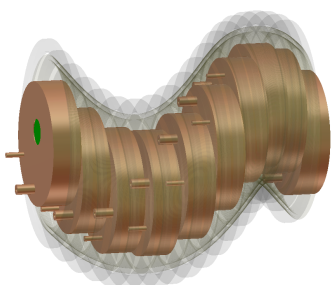

Figure 3: Design concept of the HCC segment. A brown disk is the gas-filled RF cavity which is located on the helical beam path. Each cavity has a power inlet line and a probe. A green surface on the cavity is the RF beam entrance window which is made of a 60-μm-thick Be foil. A gray transparent ring outside the cavity is a helical solenoid coil, which generates proper helical magnetic component. There is a pressure wall between the helical solenoid coils and the RF cavities. Gas sealing and high-pressure feedthrough have been developed in the high-pressure RF experiments.

Table 2: Cooling lattice parameters in the HCC. b, b', and b_z are the helical dipole, field gradient, and solenoid components on a reference orbit, respectively. Segment 4′ corresponds to the proposed longitudinal enhance cooling channel instead of using Segment 4. Peak RF power was estimated for the Al_2O_3 ceramic loaded RF cavity operating at 80 K.

Seg.	b	b'	b_z	peak RF	Stored B
	T	T/m	T	MW/cavity	MJ/m
1	1.24	-0.21	4.2	1.1	4.5
2	1.56	-0.32	5.3	1.1	4.7
3	2.49	-0.83	8.5	0.6	10.7
4	3.11	-1.29	10.6	0.6	10.5
4′	3.09	5.17	11.6	0.6	–

Reconfigure Cooling Path

It is harder to generate a negative helical field gradient for shorter helical period channel to realize the equal cooling decrements [20]. Adding correction coils and using an elliptic helical solenoid coil have been considered [21]. Here, we discuss another approaches that the helical cooling lattice is reconfigured to mitigate the magnetic field constraint. According to the HCC theory, the longitudinal phase space cooling can be enhanced with smaller dispersion factor, which requires lower helical dipole component than the equal cooling decrements. As a result, a short helical period may be feasible, 0.35 m in the longitudinal enhance cooling. Circles in Fig. 2 shows the predicted achievable equilibrium emittance with various helical periods at various dispersion factors. An emittance which is above (below) a red solid line is generated with larger (smaller) dispersion factor than the factor for the equal cooling decrements. It predicts 0.75 mm and 0.72 mm in the transverse and longitudinal emittances with the magnetic field 12 Tesla (see segment 4′ in Tables 1 and 2). Especially, the required helical field gradient is positive for the longitudinal enhance cooling lattice. It significantly mitigates constraint of the helical magnet design and the strength of correction solenoid may be significantly low. This is more plausible solution of the HCC design to achieve lower equilibrium 6D emittance than the original one. We note that the admittance becomes small with a small dispersion factor. Therefore, the dispersion factor should be modulated in the final cooling.

STUDY BEAM-PLASMA INTERACTION

Gas-filled RF cavity is a unique accelerator device. Three different matters, high energy charged particles, a dense neutral gas, and a beam-induced gas-plasma, exist in the cavity (Figure 4). Ionization process is well-known theoretically

ISBN 978-3-95450-174-8

and experimentally. Since gas density is nine-orders of magnitude higher than the density of incident beam no collective effect is concerned in the ionization process. On the other hand, interactions between plasma and dense gas, so called plasma chemistry, is a complicated subject. Hydrogen ions are immediately formed to a hydrogen cluster with molecular hydrogens, i.e. H_n^+ (n = 3,5,7. . .). They have different hydrogen neutralization rates and mobilities. Mobilities of electrons strongly depends on a density of hydrogen due to a quantum effect, i.e. the cross-section of Coulomb scattering becomes large when the de Broglie wavelength of thermal electrons is comparable with an average inter distance among molecular hydrogens. Electron capture rate of O_2 dopant is strongly dependent on the density of H_2 since the process occurs as a three-body reaction. Fortunately, overall reactions of the plasma chemistry and plasma processing in a dense gas can be measured in experiments even we do not know the branching ratio for each reaction [6]. The observed values were tested with numerical simulations [8] in which the electron dynamics is described as simple kinematics of electron conduction in a matter.

However, the third interaction, a beam-plasma interaction, cannot be characterized by experiment since there is no accelerator facility to produce 10^{12} cm^{-3} beam in nuclear kinetic energies and inject it into a gas-filled RF cavity. We investigated the beam-plasma interaction in numerical simulation. Plasma process is modeled from experimental results. Ionization electrons is quickly thermalized, within a few tens pico seconds, by interacting with a neutral gas. The drift velocity of electrons can be presented by a simple formula, $v_d = \mu E$, where μ is the mobility of electrons in a gas and E is a superimposed electric field between the external RF field and the space charge of incident beam. The drift velocity is order of 10^4 m/s that is much slower than the

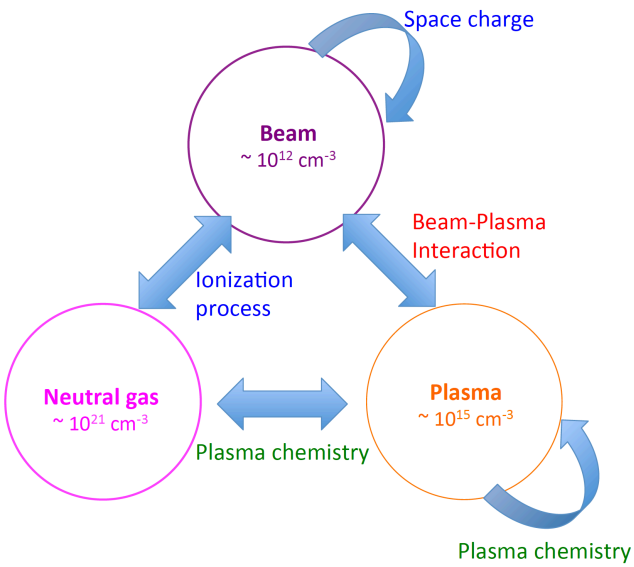

Figure 4: Three states in a gas-filled RF cavity with intense muon beam. Density in each matter is estimated for a muon collider cooling channel.

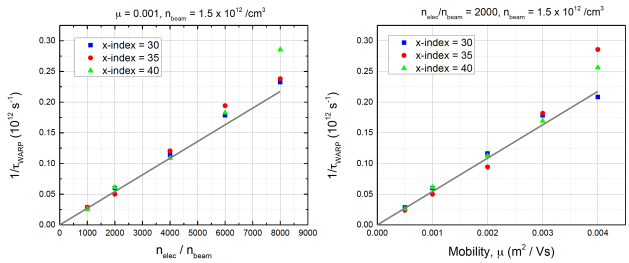

Figure 5: Estimated time constant for the space charge neutralization in the gas-filled RF cavity. Index in plot is the radial distance from the cavity center, i.e. x-index=40 is the cavity center and x-index=30 is the radius of beam.

velocity of an incident beam. However, the density of ionization electrons are three orders of magnitude larger than the incident beam. A density fraction of electrons changes the net electric field strength in the beam volume. If charge of incident muons is negative (positive), electrons are pushed out (in) from the beam volume until net electric fields which is generated by the incident beam and residual positive ions in the beam volume becomes neutral. It is called space charge neutralization.

Time constant of the space charge neutralization is estimated by using a simple formula, $\tau = \epsilon_0/(n_e/n_b)\,\mu E$ and compared to a numerical simulation. Figure 5 shows the estimated time constant of space charge neutralization in analytical and numerical investigations. In this simulation, the plasma was pre-formed before beam injection and plasma and beam densities were uniform. Estimated time constant is ~20 ps which is much shorter than the bunch length, 100 ps. When the space charge is neutralized the self-induced axial magnetic field becomes dominant and the plasma lens appears.

The plasma lens effect has been studied with a preliminary beam-plasma interaction model. The front end particles generates the plasma, it neutralizes the tailed beam, then the beam is focused by the self-induced axial magnetic field. Envelop equation with the plasma lens is given,

$$\frac{d^2 r_b}{dz^2} + \left(\kappa_{sf} + \frac{\alpha K_b}{r_b^2}\right) r_b = \frac{\epsilon_{KV}^2}{r_b^3}, \quad (1)$$

$$\alpha = \frac{[\beta^2(1-f_m) - (1-f_q)]}{1-\beta^2}, \quad (2)$$

$$K_b = \frac{2r_e}{\gamma^3\beta^2}\frac{N}{\sqrt{2\pi}\sigma_z}, \quad (3)$$

where r_b is the radius of beam, κ_{sf} is a focusing strength of a beam lattice, K_b is a strength of electromagnetic force by the beam, α is a form factor of the plasma lens. f_m and f_q in α present the fraction of magnetic and electric charges of neutralization plasma. $\alpha = -1$ corresponds to a pure space charge condition where $f_m = f_q = 0$, while $\alpha = \gamma^2\beta^2$ is in the complete space charge neutralization where $f_m = 0, f_q = 1$. The focusing force is $\gamma^2\beta^2$ larger than the space charge force. Therefore, even the space charge

ISBN 978-3-95450-174-8

is not affected on the beam dynamics the plasma lens can show up and influence on the beam dynamics. Figure 6 shows the result of plasma lens in numerical simulation by using WARP [22].

The plasma focusing force is stronger with smaller phase space beam. There is no theoretical limit on the plasma focusing until the beam size reaches to the quantum thermal noise. The process seems to be the new focusing mechanism to have the extremely cold muon beam. Further study is required.

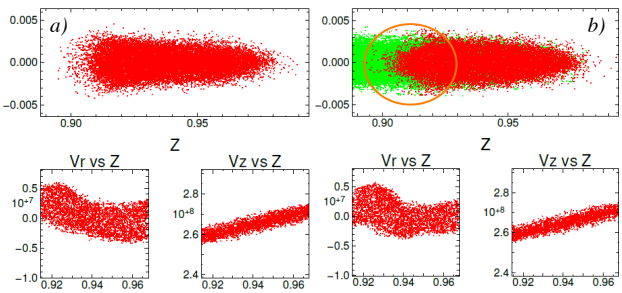

Figure 6: WARP simulation shows the plasma lens effect without gas (*a*) and with gas (*b*). Only a straight solenoidal magnetic field and RF fields are applied, but no dispersion in this simulation. Orange circle shows that the beam is focused by the plasma lens.

ACKNOWLEDGMENT

Author thanks to the helical cooling channel design and simulation group. Author also thanks to MAP and Muons, Inc. for great supporting the design efforts and the machine developments.

REFERENCES

[1] D. Neuffer, *Particle Accelerators* **14** (1983) 75. ; A.N. Skrinsky and V.V. Parkhomchuk, *J. Nucl. Physics* **12** (1981) 3. ; D. Neuffer, *"Introduction to Muon Cooling"*, *Nucl. Inst. and Meth.* **A532** (2004) 26.

[2] A. Moretti et al., *"Effects of high solenoidal magnetic fields on rf accelerating cavities"*, *Phys. Rev. STAB* **8** (2005) 072001.

[3] R.P. Johnson et al., *"High Pressure, High Gradient RF Cavities for Muon Beam Cooling"*, *Proc. of LINAC2004* (2004) 266.; P. Hanlet et al., *"High Pressure RF Cavities in Magnetic Fields"*, *Proc. of EPAC2006* (2006) 1364.

[4] Y.S. Derbenev and R.P. Johnson, *"Six-dimensional muon beam cooling using a homogeneous absorber; Concepts, beam dynamics, cooling decrements, and equilibrium emittances in a helical dipole channel"*, *Phys. Rev. STAB* **8** (2005) 041002.

[5] M. Chung et al., *"Pressurized H_2 rf Cavities in Ionizing Beams and Magnetic Fields"*, *Phys. Rev. Lett.* **111** (2013) 184802.

[6] B. Freemire et al., *"Pressurized RF Cavities in Ionizing Beams"*, Submitted to *Phys. Rev. STAB*.

[7] J. Ellison et al., *"Beam-plasma Effects in Muon Ionization Cooling Lattices"*, *Proc. of IPAC2015* (2015) 2649.

[8] K. Yu et al., *"SPACE code for Beam-plasma Interaction"*, *Proc. of IPAC2015* (2015) 728.; K. Yu et al., *"Simulation of beam-induced plasma in a gas-filled RF cavity"*, Submitted to JINST.

[9] T. Katsouleas et al., *"Plasma physics at the final focus of high-energy colliders"*, *Phys. of Fluids* **B2** (1990) 1384.

[10] G4beamline, *http://public.muonsinc.com/Projects/G4beamline.aspx*

[11] NERSC, *https://www.nersc.gov/*.

[12] Y. Alexahin, *"Helical FOFO Snake for Initial 6D Cooling of Muons"*, *ICFA Beam Dyn. Newslett.* **65** (2014) 49.

[13] C. Yoshikawa et al., *"Design and Simulation of A Matching System into the Helical Cooling Channel"*, *Proc. of IPAC2014* (2014) 1382.

[14] T. Tominaka et al., *"Analytical Field Calculation of Helical Coils"*, *Nucl. Instr. Meth.* **A459** (2001) 398.

[15] A. Sy et al., *"Matching into the Helical Bunch Coalescing Channel for a High Luminosity Muon Collider"*, *Proc. of IPAC2015* (2015) 2315.

[16] G. Kazakevich et al., *"High-power Magnetron Transmitter as an RF Source for Superconducting Linear Accelerators"*, *Nucl. Instr. Meth.* **A760** (2014) 19.

[17] B. Chase et al., *"Precision Vector Control of a Superconducting RF Cavity Driven by an Injection Locked Magnetron"*, *JINST* **arXiv:1502.04118v1** (2014).

[18] L.M. Nash et al., *"High Power Tests of Alumina in High Pressure RF Cavities for Muon Ionization Cooling Channel"*, *Proc. of IPAC2013* (2013) 1508.; B. Freemire et al., *"Low Powered RF Measurements of Dielectric Materials for use in High Pressure Gas Filled RF Cavities"*, *Proc. of IPAC2015* (2015) 3387.

[19] F. Marhauser et al., *"RF Cavity Design Aspects for a Helical Muon Beam Cooling Channel"*, *Proc. of IPAC2014* (2014) 3352.

[20] M. Lopes et al., *"Magnetic Design Constraints of Helical Solenoids"*, *Proc. of IPAC2014* (2014) 2731.

[21] S.T. Krave et al., *"A Concept for a High-Field Helical Solenoid"*, *Proc. of IPAC2015* (2015) 3345.; S. Kahn et al., *"Conceptual Design of the Muon Cooling Channel to Incorporate RF Cavities"*, *Proc. of IPAC2014* (2014) 1325.; M.L. Lopes et al., *"Alternate Methods for Field Corrections in Helical Solenoids"*, *Proc. of IPAC2015* (2015) 3409.

[22] WARP, *http://blast.lbl.gov/BLASTcodes_Warp.html*.

ISBN 978-3-95450-174-8

PROGRESS ON PARAMETRIC-RESONANCE IONIZATION COOLING*

V.S. Morozov#, Ya.S. Derbenev, A. Sy, Jefferson Lab, Newport News, VA 23606, USA
A. Afanasev, George Washington University, Washington, DC 20052, USA
R.P. Johnson, Muons, Inc., Batavia, IL 60510, USA
J.A. Maloney†, Northern Illinois University, DeKalb, IL 60115, USA

Abstract

Proposed next-generation muon collider will require major technical advances to achieve the rapid muon beam cooling requirements. Parametric-resonance Ionization Cooling (PIC) is proposed as the final 6D cooling stage of a high-luminosity muon collider. In PIC, a half-integer parametric resonance causes strong focusing of a muon beam at appropriately placed energy absorbers while ionization cooling limits the beam's angular spread. Combining muon ionization cooling with parametric resonant dynamics in this way should then allow much smaller final transverse muon beam sizes than conventional ionization cooling alone. One of the PIC challenges is compensation of beam aberrations over a sufficiently wide parameter range while maintaining the dynamical stability with correlated behavior of the horizontal and vertical betatron motion and dispersion. We explore use of transverse coupling to reduce the dimensionality of the problem and to shift the dynamics away from non-linear resonances. PIC simulations are presented.

MOTIVATION

Experiments at energy-frontier colliders require high luminosities of order 10^{34} cm^{-2} sec^{-1} or more in order to obtain reasonable rates for events having point-like cross sections. High luminosity colliders require intense beams with small transverse emittances and a small beta function at the collision point. For muon colliders, high beam intensities and small emittances are difficult and expensive to achieve because muons are produced diffusely and must be cooled drastically within their short lifetimes. The muon does not interact by the strong interaction, and its high mass relative to the electron means that it can pass through matter without hadronic or electromagnetic showers. Thus, it is the perfect candidate for ionization cooling. Muons lose energy by passing through a low-Z material and only the longitudinal component is replaced by an RF cavity. This technique allows the angular spread of a beam of muons to be reduced in a very short time close to the limit determined by multiple scattering.

Ionization cooling as it is presently envisioned will not cool the beam sizes sufficiently well to provide adequate luminosity without large muon intensities. For example, a muon-collider s-channel Higgs factory, a logical prerequisite to an energy-frontier muon collider, would be compelling if the luminosity were high enough. The 4 MeV energy resolution needed to directly study the Higgs width is only possible with such a machine. Also, the mass-dependent muon-Higgs coupling gives a factor of over 40,000 cross-section advantage relative to an electron collider. Numerical simulations of muon cooling channels based on technical innovations made and experimentally tested in this millennium have shown 6D emittance reductions of almost 6 orders of magnitude. Parametric-resonance Ionization Cooling (PIC) can achieve an additional two orders of emittance reduction for an additional factor of 10 in luminosity.

In addition, to the extent that the transverse emittances can be reduced further than with conventional ionization cooling, several problems can be alleviated. Lower transverse emittance allows a reduced muon current for a given luminosity, which implies:

- a proton driver with reduced demands to produce enough proton power to create the muons,
- reduced site boundary radiation limits from muons decaying into neutrinos that interact with the earth,
- reduced detector background due to electrons from muon decay,
- reduced proton target heat deposition and radiation levels,
- reduced heating of the ionization cooling energy absorber,
- less beam loading and wake field effects in the accelerating RF cavities,
- reduced space charge effect.

Smaller transverse emittance has virtues beyond reducing the required beam currents, namely:

- smaller higher-frequency RF cavities with higher gradient can be used for acceleration,
- beam transport is easier with smaller-aperture magnetic and vacuum systems,
- stronger collider interaction point (IP) focusing can be used, since that is limited by the maximum achievable beam extension prior to the IP.

PARAMETRIC-RESONANCE IONIZATION COOLING (PIC)

Concept and Analytic Theory

The limit on the minimum achievable emittances in muon ionization cooling comes from the equilibrium between the cooling process and multiple Coulomb scattering in the absorber material. The concept of

* Work supported in part by U.S. DOE STTR Grants DE-SC0005589 and DE-SC0007634. Authored by Jefferson Science Associates, LLC under U.S. DOE Contract No. DE-AC05-06OR23177.
# morozov@jlab.org
† now at TRIUMF, Vancouver, BC, Canada

ISBN 978-3-95450-174-8

Parametric-resonance Ionization Cooling (PIC) [1, 2] is to push this limit by an order of magnitude in each transverse dimension by focusing the muon beam very strongly in both planes at thin absorber plates. This creates a large angular spread of the beam at the absorber locations, which is then cooled to its equilibrium value resulting in greatly reduced transverse emittances. Achieving adequately strong focusing using conventional magnetic optics would require unrealistically strong magnetic fields. Instead, PIC relies on a resonant process to provide the necessary focusing. A half-integer parametric resonance is induced in a cooling channel, causing focusing of the beam with the period of the channel's free oscillations.

The resonant perturbation changes the particles' phase-space trajectories at periodic locations along the channel from their normal elliptical shapes to hyperbolic ones as shown in Figure 1. Thus, at certain periodic focal positions, the beam becomes progressively narrower in x and wider in x' as it passes down the channel. Without damping, the beam dynamics are not stable because the beam envelope grows with every period. Placing energy absorbers at the focal points stabilizes the beam motion by limiting the beam's angular divergence at those points through the usual ionization cooling mechanism. These dynamics then result in a strong reduction of the beam spot size at the absorber locations leading to transverse beam emittances that are an order of magnitude smaller than without the resonance. The longitudinal emittance is maintained constant against energy struggling by emittance exchange occurring due to dispersion or its slope at the locations of wedge or flat absorbers.

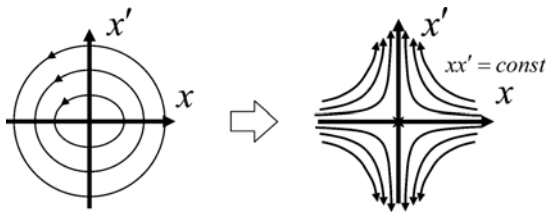

Figure 1: Transformation of a particle's phase-space motion by a half-integer parametric resonance: elliptical phase-space trajectories become hyperbolic. The trajectories are illustrated at the focal points.

The normalized equilibrium transverse emittance achievable in PIC is given by [1, 2]

$$\varepsilon_{n\perp} = \frac{\sqrt{3}}{4\beta}(Z+1)\frac{m_e}{m_\mu}w, \qquad (1)$$

where $\beta = v/c$ is the relativistic factor, Z is the absorber material's atomic number, m_e and m_μ are the electron and muon masses, respectively, and w is the average absorber thickness in the beam direction.

The expected PIC parameters are summarized in Table 1. Note that the absorbers are thicker at the beginning of the channel in order to produce a higher cooling rate of an initially larger-emittance beam. As the beam being cooled is propagated down the channel, the absorber thickness is gradually reduced in order to reach the minimum practical transverse emittance. Since the cooling rate gets lower for thinner absorbers, the minimum practical absorber thickness is determined by the practically acceptable beam loss due to muon decay.

Table 1: Expected PIC Performance

Parameter	Unit	Initial	Final
Muon beam momentum, p	MeV/c	250	250
Number of particles per bunch, N_b	10^{10}	1	1
Be ($Z = 4$) absorber thickness, w	mm	20	2
Normalized transverse emittance (rms), $\varepsilon_x = \varepsilon_y$	μm	230	23
Beam size at absorbers (rms), $\sigma_a = \sigma_x = \sigma_y$	mm	0.7	0.1
Angular spread at absorbers (rms), $\theta_a = \theta_x = \theta_y$	mrad	130	130
Momentum spread (rms), $\Delta p/p$	%	2	2
Bunch length (rms), σ_z	mm	10	10

Correlated-Optics Channel

To attain simultaneous focusing in both planes at regular locations, the horizontal and vertical betatron oscillation periods must be commensurate with each other and with the channel's period, e.g. as illustrated in Figure 2. A magnetic channel possessing such optical properties, called a twin-helix channel, has been successfully developed and simulated [3]. In a twin-helix channel, two equal-strength helical dipole harmonics with equal periods but opposite helicities are superimposed leading to its name. Analogous to how combining two circularly-polarized waves produces a linearly-polarized one, the magnetic field in the midplane of this configuration is transverse to the plane. This means that the periodic orbit is flat and lies in the midplane. The horizontal and vertical motions are stable and uncoupled. A continuous straight quadrupole is added to the system in order to redistribute focusing between the horizontal and vertical dimensions.

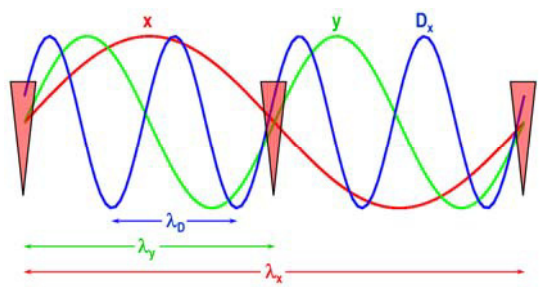

Figure 2: Particle's horizontal x and vertical y betatron trajectories and horizontal dispersion D_x for the case of correlated optics.

ISBN 978-3-95450-174-8

Simulation

A twin-helix channel with wedge absorbers and energy-restoring RF cavities has been implemented [3] in G4beamline [4]. The simulation setup along with muon tracks is illustrated in Figure 3. The RF cavities are placed symmetrically between the absorbers. This allows for ease of compensation of a parasitic parametric resonance caused by the periodic energy modulation in correlated optics [5].

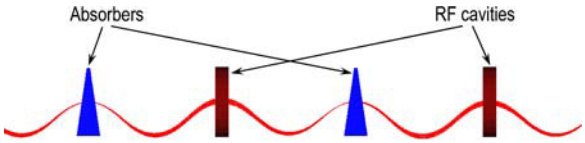

Figure 3: PIC simulation setup in G4beamline.

A parametric resonance is induced in each transverse plane by an additional pair of opposite-helicity but otherwise identical helical quadrupoles. The frequency of each pair is twice the frequency of betatron oscillations in the respective plane. The amplitude and phase of each pair are adjusted to provide appropriate parametric-resonance strength and focal point location, respectively. Figure 4 shows the resulting single-particle horizontal and vertical phase-space trajectories at the focal point without stochastic effects.

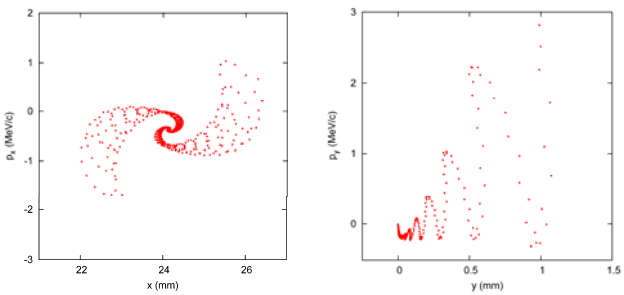

Figure 4: Horizontal (left) and vertical (right) phase-space trajectories of PIC.

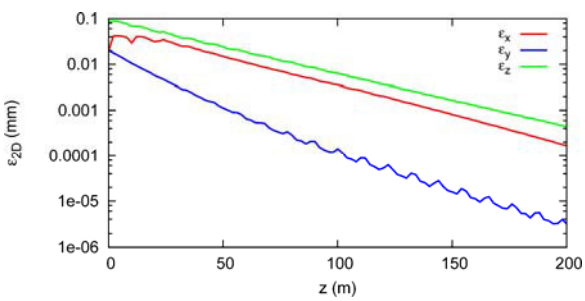

Figure 5: Horizontal ε_x, vertical ε_y, and longitudinal ε_z 2D emittances along the channel without stochastic effects.

Figure 5 shows evolution of the three 2D emittances along the cooling channel obtained in a PIC simulation using this setup. The initial emittance values are intentionally chosen relatively small to stay close to the linear regime to allow comparisons with the first-order simulations in [6]. Since the stochastic effects are off and the dynamics are stable, the emittances cool virtually to zero.

Aberration Impact

To proceed to cooling simulations including stochastic effects, compensation of beam aberrations is required. This was verified by running a first-order simulation with stochastics included [6]. Aberrations from one absorber to another must be compensated to a degree where they are small compared to the beam size at the absorber. Since the equilibrium angular spread in Table 1 is on the order of a hundred milliradians, the angle-dependent aberrations must be precisely compensated over the angular range of a few hundred milliradians. This is a challenging task.

Figure 6 demonstrates one example of aberration compensation. A set of particles with systematically-arranged initial angles is started from a focal point on the reference trajectory and tracked to the next focal point to determine the aberration-induced beam smear at that location. A general optimization procedure is used to minimize the beam smear by introducing various-order continuous multipole fields [3]. Using field harmonics up to octupole allows for compensation of an angular spread of up to ±260 mrad. A more systematic approach to aberration compensation using COSY Infinity has been investigated [6]. However, multipole fields in combination with correlated optics introduce another serious problem, namely, non-linear resonances causing loss of dynamical stability.

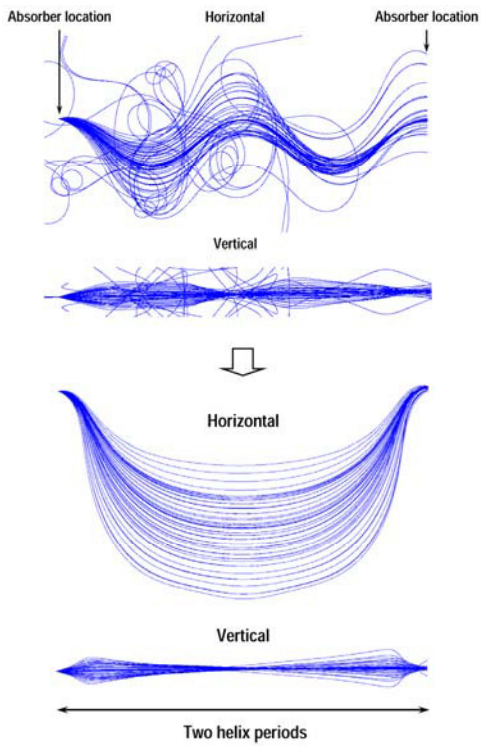

Figure 6: Demonstration of aberration compensation in a twin helix for horizontal and vertical angles of ±260 mrad: 250 MeV/c muon tracks are shown from one focal point to the next before (a) and after (b) aberration compensation using field harmonics up to octupole.

ISBN 978-3-95450-174-8

To illustrate this problem, consider the Hamiltonian term of a continuous harmonically-varying octupole field $H_{oct} = n_{oct}(6x^2y^2 - x^4 - y^4)/4$ where $n_{oct} \sim \cos(2\pi mz/L)$ is the normalized octupole strength, m is an integer, z is the longitudinal coordinate, L is the channel period length, $x \sim \cos(2\pi\nu_x z/L)$ and $y \sim \cos(2\pi\nu_y z/L)$ are the horizontal and vertical transverse betatron coordinates, respectively, and ν_x and ν_y are the horizontal and vertical betatron tunes, respectively. Multiple octupole harmonics are needed in a cooling channel to compensate spherical aberrations. However, as can be clearly seen from the Hamiltonian, with our choice of betatron tunes of $\nu_x = 0.25$ and $\nu_y = 0.5$, any octupole harmonic m causes resonances in both planes. Dispersion further complicates the resonance structure. Selecting different betatron tunes does not help; as long as the betatron periods are integer multiples of the channel period as required by PIC, multipole fields will tend to cause non-linear resonance. This makes it difficult to find a set of multipoles sufficient for aberration compensation that does not cause beam instabilities.

SKEW PIC

Concept

To overcome the non-linear resonance problem, we developed the concept of Skew PIC [7, 8]. We introduce coupling in a cooling channel in such a way that the point-to-point focusing needed for PIC is preserved but the canonical betatron tunes are shifted from their resonant values, i.e. the canonical phase advances in the two planes are shifted from $m\pi$ values. A simple way to think of it is that the beam is azimuthally rotated between consecutive focal points. This moves the dispersion and betatron motion away from non-linear resonances. It also offers a number of other benefits:

- it allows for control of the dispersion size for chromatic compensation;
- it reduces the dimensionality of the aberration compensation problem to just the radial dimension and therefore reduces the number of required compensating multipoles;
- it equates the parametric resonance rates in the two planes, and therefore only one resonance harmonic is needed;
- it equates the two cooling decrements in the two transverse dimensions

Analytic Solution

Skew PIC is based on inducing a linear betatron coupling resonance in a PIC transport line between the horizontal (x) and vertical (y) planes. Previously developed twin-helix magnetic system is supplemented with skew quads that generate coupling between the horizontal and vertical betatron motions. Let us first consider the effect of such coupling using a simplified model. The equations for coupled betatron oscillations are

$$\begin{aligned} x'' + [K^2(s) - n]x + g(s)y &= K(s)\delta, \\ y'' + ny + g(s)x &= 0, \end{aligned} \tag{2}$$

where K is the curvature, n is the normalized straight quadrupole strength, g is the normalized skew quadrupole strength, and δ is the relative momentum offset. We find a solution with one-period linear transfer matrix of the form:

$$\begin{pmatrix} x_f \\ y_f \\ x'_f \\ y'_f \end{pmatrix} = T \begin{pmatrix} x_i \\ y_i \\ x'_i \\ y'_i \end{pmatrix}, \quad T = \begin{pmatrix} M & 0 \\ L & N \end{pmatrix}, \tag{3}$$
$$\det(T) = \det(M)\cdot\det(N) = 1,$$

i.e., where the spatial coordinates are "decoupled" from the angular ones. Such a transformation preserves the point-to-point focusing feature of the correlated optics while not requiring resonant values of the betatron tunes as will be shown later. This solution does not violate the symplecticity requirement. It imposes three independent constraints. The criterion of linear motion stability is $\det(M) = \det(N) = 1$.

For a simplified model of step-like K and g functions illustrated in Figure 7, there exists an analytic solution of Eqs. (2) satisfying Eq. (3) [7]:

$$T = \begin{pmatrix} M & 0 \\ 0 & N \end{pmatrix}, \quad M = N = \begin{pmatrix} \cos(4\theta) & -\sin(4\theta) \\ \sin(4\theta) & \cos(4\theta) \end{pmatrix}, \tag{4}$$
$$\tan\theta = \frac{K^2 - 2n - \sqrt{(K^2 - 2n)^2 + 4g^2}}{2g},$$

The solution in Eq. (4) represents independent rotations in the spatial and angular phase spaces by an angle 4θ. Thus, we developed a system where the canonical variable pairs are (x, y) and (x', y') rather than the usual (x, x') and (y, y'). The eigenvalues of the transfer matrix in Eq. (4) are $\exp(\pm i4\theta)$. Therefore, the canonical betatron tunes are $\pm 2\theta/\pi$. Note that $\theta \to 0$ when $g \to 0$ (uncoupled case).

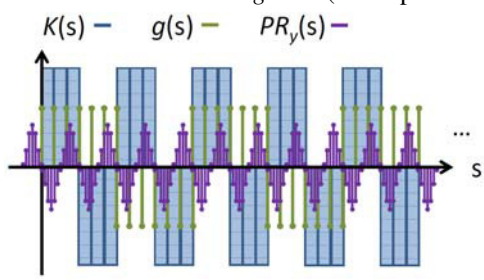

Figure 7: Curvature $K(s)$, skew quadrupole strength $g(s)$, and parametric-resonance harmonic $PR_y(s)$ along the cooling channel's length s.

ISBN 978-3-95450-174-8

Simulation

We verified the solution in Eq. (4) by numerically solving Eq. (2) [7] and by implementing the model shown in Figure 7 in MAD-X [8]. Tracking in MAD-X demonstrated the expected rotational behavior of the (x, y) and (x', y') coordinates as shown in Figure 8. The canonical tune values calculated by PTC in MAD-X also agreed with the analytic solution.

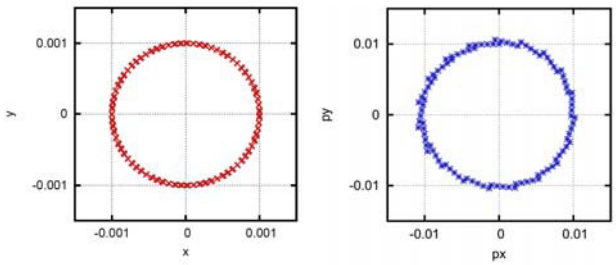

Figure 8: (x, y) and (x', y') phase-space trajectories obtained using PTC tracking in MAD-X.

We then tested the effect of a sextupole in PIC channels with *uncoupled* and *coupled correlated* optics. The radial displacement of a particle along each of the channels is shown in Figure 9. Clearly, there is a sextupole-induced non-linear resonance in the uncoupled case. In the skew channel, optics is still radially correlated; however, the betatron tunes are shifted from rational values and the resonance does not occur.

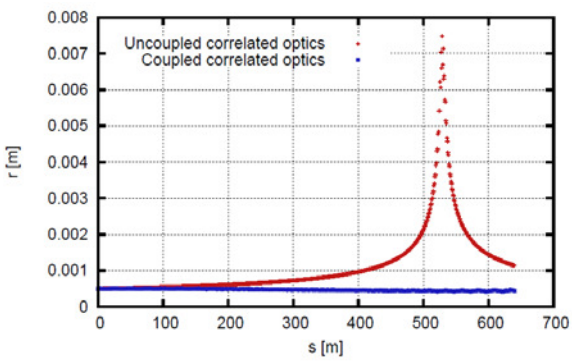

Figure 9: Radial displacement of a particle along PIC channel with uncoupled and coupled correlated optics in the presence of a sextupole harmonic.

We next induced a half-integer parametric resonance using a resonant quadrupole harmonic in the vertical plane as shown in Figure 7. We confirmed that a parametric resonance excited in one plane is equally distributed by the coupling resonance between the two transverse dimensions. Figure 10 shows the x and y coordinates of a particle at consecutive focal points along the channel. The two transverse coordinates are damping at the same rates. It is also quantitatively confirmed by the fact that the two transverse canonical betatron tunes have imaginary components of equal magnitudes.

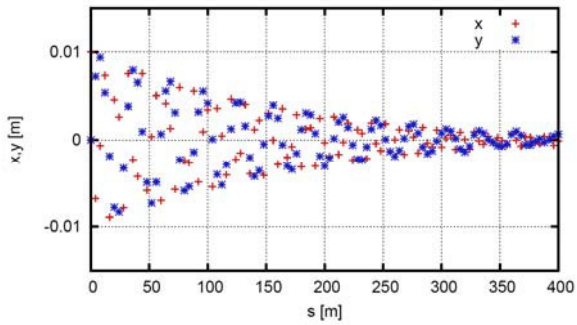

Figure 10: x and y coordinates of a particle at focal points along a skew PIC channel with a half-integer parametric resonance induced in one of the planes.

CONCLUSION

PIC combines muon ionization cooling with parametric resonant dynamics to allow final equilibrium transverse beam emittances that are an order of magnitude smaller than those achievable with conventional ionization cooling alone. Linearized PIC simulations with full stochastic effects are in good agreement with the analytic theory [6]. PIC has also been demonstrated in non-linear G4beamline simulations, however, with stochastic effects ignored [3]. A self-consistent simulation combining both stochastic and non-linear effects requires sufficient linearization of the beam dynamics through aberration compensation. Correction of aberrations in a transversely uncoupled channel has been challenging due to many non-linear resonances associated with correlated optics. We solve the problem by introducing a special type of coupling into the system that preserves the point-to-point focusing feature of correlated optics while shifting the canonical betatron tunes away from resonant values. Some of the expected features of Skew PIC were confirmed by numerical simulations [7, 8].

REFERENCES

[1] Ya.S. Derbenev and R.P. Johnson, in Proc. PAC05, Knoxville, TN (IEEE, Knoxville, Tennessee, 2005), p. 1374.
[2] Ya.S. Derbenev et al., arXiv:1205.3476v1 [physics. acc-ph].
[3] V.S. Morozov et al., AIP Conf. Proc. 1507, 843-848 (2012).
[4] G4beamline, http://g4beamline.muonsinc.com
[5] V.S. Morozov et al., in Proc. PAC'11, New York, NY (IEEE, New York, 2011), MOP036, p. 163.
[6] J.A. Maloney et al., in Proc. IPAC'12, New Orleans, LA, TUPPD011 (2012), p. 1428.
[7] A. Afanasev et al., in Proc. IPAC'15, Richmond, VA, TUPHA013 (2015), p. 1993.
[8] A. Sy et al., in Proc. IPAC'15, Richmond, VA, WEPJE015 (2015), p. 2705.

ISBN 978-3-95450-174-8

PROJECT OF ELECTRON COOLER FOR NICA

I.N. Meshkov[1], E.V. Ahmanova[1], A.G. Kobets[1, 2], O.S. Orlov[1], V.I. Shokin[1], A.A. Sidorin[1], M.P. Kokurkin[3], N.Y. Lysov[3], S.L. Yakovenko[1]
[1] JINR, Dubna, Russia
[2] Institute of Electrophysics and Radiation Technologies NAS of Ukraine, Kharkiv, Ukraine
[3] All-Russian Electrotechnical Institute, Moscow, Russia

Abstract

The problems of development of high energy electron coolers are discussed on the basis of the existing experience. Necessities of electron cooling application to NICA collider are considered and the project parameters of the electron cooler at NICA collider are presented.

Electron cooler of the NICA Collider is under design and development of its elements at JINR. It will provide the formation of an intense ion beam and maintain it in the electron energy range of 0.5–2.5 MeV. To achieve the required energy of the electrons all the elements of the Cooler are placed in the tanks filled with sulfur hexafluoride (SF_6) gas under pressure of 6 atm. For testing the Cooler elements the test bench «Recuperator» is used and upgraded. The results of testing of the prototypes of the Cooler elements and the present stage of the technical design of the Cooler are described in this paper.

INTRODUCTION

The first question to be answered is: "Why do need HV E-Cooler for the NICA collider?" This Collider will have to operate at the energy of heavy ions like $^{197}Au^{79+}$ in the range of 1÷4.5 GeV/u. To reach the project luminosity one needs to form short and high intense ion bunches and maintain their parameters during a long time, of the order of 1 hour at least. In NICA project two energy ranges of the Collider and two its regimes are considered.

A) Space charge (SC) dominated regime:
E_{ion} = 1–3 GeV/u. Electron cooling is mandatory here when acceptance is filled with ions up to the Laslett tune shift $\Delta Q = \Delta Q_{max} = 0.05$. Then beam intensity and Collider luminosity are limited (see details in [1]):

$$L \le L_{max} = (0.01–1)\times 10^{27}\ cm^{-2}\cdot s^{-1}.$$

B) Intrabeam scattering (IBS) dominated regime:
E_{ion} = 3–4.5 GeV/u. With energy increase SC effect becomes small, luminosity can be increased up to

$$L = 1\times 10^{27}\ cm^{-2}\cdot s^{-1}$$

and is maintained constant. However, to keep bunch parameters one has now to suppress IBS. It can be done by application of stochastic and electron cooling. At the energy above 3 GeV/u luminosity is artificially limited by max event rate acceptable for detector MPD. In this energy range electron and stochastic cooling are supposed to be used in the NICA Collider simultaneously providing a long life time of the Collider luminosity.

Nowadays electron coolers are demanded in the energy range up to tens MeV. There are several well advanced projects. In general one can divide then in two groups: high voltage (HV) and high energy (HE) electron coolers. The first ones use conventional DC HV schemes. These coolers can be used, practically, up to 10–15 MeV electron energy. Such projects are under development at COSY (FZJ), NICA (JINR), HESR (FAIR), HIAF (Lanzhou). The second group — HE electron coolers are developed on basis of several different novel approaches, like coherent e-cooling, optical e-cooling, and some others. Most feasible of them looks option of "energy recovering linac" (ERL) [2] that is under development at RHIC BES (BNL) and MEIC (JLab) projects.

THE EXPERIENCE WE HAVE

Presently we have only two examples of HV electron cooler. One is well known electron cooler at Recycler storage ring at Fermilab that was designed and constructed by the team led by S. Nagaitsev [3]. The cooler had electron energy up to 4.3 MeV at working electron current of 0.1–0.5 A (max electron current 1.6 A). The cooler design was based on the Pelletron scheme — a version of electrostatic accelerator. It had unmagnetized electron beam. Presently the machine is dismantled.

The second electron cooler was designed by original scheme and constructed by the team of V. Parkhomchuk at Budker INP [4, 5]. The cooler has maximum design electron energy of 2 MeV at the Electron beam current of 3.0 A. HV generator is made by the cascade transformer scheme, electron beam is magnetized. The "COSY cooler" is under commissioning presently [4], [5].

These two machines characterize the level of technical development in this field today.

THE CONCEPTS OF A HV E-COOLER FOR AN ION COLLIDER

The First Consideration

The NICA electron cooler is the very first experience of design and construction of such cooling system with two cooling electron beams. Therefore some consideration of a general character has been done.

An evident scheme based on two independent cooling electron beams has been proposed in the NICA project (see below). More sophisticated scheme — one (common) electron beam to cool two ion beams was

ISBN 978-3-95450-174-8

proposed for NICA Collider by Budker INP team. The solution is technically good, however the electron beam is a feed back between two ion beams: an instability in one ion beam excites electron beam that brings the instability signal to another ion beam, i.e. we have "the three beams' instability"! Finally the scheme with common electron beam has been rejected.

Two Concepts of the HV Electron Cooler with Two Electron Beams

Two schemes of HV electron cooler for the NICA Collider were proposed. Both schemes had to meet the specifications formulated in the NICA project (Table 1).

Table 1: Main Parameters of the NICA Electron Cooler

DC magnetized electron beam	
Electron energy, MeV	0.5–2.5
Electron beam current, Amp	0.1–1.0
Solenoid magnetic field, T	0.1–0.2
Electron transverse temperature in PRF, eV	1.0–5.0
Electron longitudinal temperature in PRF, meV	5.0
Electron energy spread in Lab. system, $\Delta E/E$	1e-5

The first scheme proposed and being developed by JINR group has three tanks filled with SF_6 gas at the pressure of 6 atm and connected each other with coaxial feeder (Fig. 1). The leftmost and rightmost tanks contain by two accelerating/decelerating tubes for two electron beams of the opposite direction for cooling the ions circulating in the upper Collider ring and the lower one, correspondingly. The tubes are equipped with electron guns and collectors (Fig. 3). The middle tank contains the HV generator and terminal with the power supplies for the electron guns and the collectors.

Advantage of this scheme is a short solenoid system and a reliable scheme of the voltage multiplier applied for HV generation. The disadvantage is probable problems at tuning of the cooler regimes when electron beams are ON.

The second scheme proposed by Budker INP group is based on the design of the "COSY cooler". It is actually two "COSY cooler" with independent solenoid systems and power supplies (Fig. 2). The advantage of such approach is evident: the existing machine that demonstrated its reliability in the first tests. As disadvantages one can specify are the long solenoid system (approximately twice longer than in the NICA scheme) and problematic design for SC solenoids inside the tanks (see the next section): the COSY design is not applicable et al. in this case.

SC Solenoids

The solenoids in both concepts are supposed to be superconducting, because warm solenoids in such device consume a lot of electric power due to the large length. In the project the feasibility of the application of HTSC tape is considered as well. The tape with dimensions of 12×0.5 mm^2 is commercially available presently. Conceptual design of the NICA cooler has shown the possibility of formation of the magnetic field of the sufficient homogeneity using a conic solenoid (Fig. 3).

Such design allows one to save significantly the tape amount. An important issue is the critical magnetic field for the HTSC tape at 77 K (LN_2) that is about 1.0 T. This constraint required to reduce the maximum magnetic field on the HTSC winding of the conic solenoid.

The HV Generator

Several types of the HV generators were considered: Pelletron (van der Graaf), cascade transformer, dynamitron scheme, voltage multiplier ("Cockroft – Walton"), turbine driven generator [6]. Preliminary analysis of all the options (Table 2) forced us to choose the voltage multiplier option. Such HV power supply is developed presently by the group from All-Russian Institute for Electrotechnique (Moscow) in collaboration with JINR.

Table 2: Typical Parameters of HV Generators

Generator type	**Max. voltage, MV**	**Max. current, mA**	**Reliability**
Pelletron	13.0	0.1 (per chain)	Longstanding experience (Nat. Electrostatic Corp., Madison,USA)
Cascade transformer	2.0	1.0 (?)	BINP, commissioning stage
Dynamitron	25.0	?	World experience
Voltage multiplier	5.0	2.0	ARIE, Moscow, RF ("old" experience)
Turbine driven generator	?	?	BINP & Mainz Univ. R & D (very promising)

MODELING OF THE COOLER ELEMENTS

The element of the NICA electron cooler designed by the NICA group are tested at the test bench "Recuperator" (Fig. 4). It was constructed and used in the end of the 1980th — beginning of the 1990th for test of the electron

ISBN 978-3-95450-174-8

collector and electron gun for the electron cooler of LEAR. The test bench is a good training ground for young researchers. The Electron Cooling Group of Dzhelepov Lab. of Nucl. Problems of JINR is developing new schemes of the electron collector and electron gun for the HV electron cooler of the NICA Collider and the methods for testing parameters of these devices.

CONCLUDING REMARKS

HV electron cooler for an ion collider *has to be equipped with* two independent beams of magnetized electrons (preferably), which are generated by an electron gun with a "hollow" electron beam and the sectioned "Pierce electrode". It allows one to avoid/reduce recombination of the ions to be cooled with the cooling electrons and provide electron beam positioning using the beam current modulation and PU electrodes in the beam transfer line.

The electron cooler solenoids are to be superconducting. Application of HTSC winding looks realistic presently and is very promising.

Application of the HV generator of the voltage multiplier type is considered as most practical for the moment.

The three tanks' scheme seems adequate to the parameters of the HV electron cooler for the NICA collider.

REFERENCES

[1] G. Trubnikov, COOL'2015, THXCR02.
[2] A. Skrinsky, ibid., MOWAUD03.
[3] A. Shemyakin et al., FERMILAB-CONF-06-194-AD.
[4] V. Reva, COOL'2015, MOXAUD03.
[5] V. Kamerdzhiev, ibid., MOXAUD01.
[6] V.Parkhomchuk et al., ibid., MOPF2.

ISBN 978-3-95450-174-8

FORMATION OF BUNCHED ELECTRON BEAM AT THE ELECTRON COOLER OF CSRm*

Xiaodong Yang#, Lijun Mao, Xiaoming Ma, Tailai Yan, Jie Li, Meitang Tang
IMP, CAS, Lanzhou, 730000, P. R. China

Abstract

The motivation for formation of bunched electron beam at the electron cooler of CSRm is based on the three requirements. Firstly, the high energy electron cooling, especially, the ion beam with TeV energy, the bunched electron beam for cooling would be easier than the DC operating mode. Secondly, the electric field induced by the intensity modulated electron beam will be used for the suppression of instability developed in the high intensity ion beam after accumulation with the help of electron cooling, Thirdly, the electron beam was required to turn on and off in the different period of the atomic physics experiments. Some initial design and consideration were presented in this paper. And also the current situation and condition of CSRm electron cooler were described here. An off-line testbench will be established in the laboratory, and the test and the optimization will be explored in this experimentation. The validity of this system will be verified in the near future. The procedure of the modulation on the voltage of control electrode in the electron gun of the CSRm cooler was discussed. The scheme of off-line measurement was devised according to the progress.

INTRODUCTION

The electron coolers of HIRFL-CSR have operated for ten years from 2005. The performance and upgrade was reported in the paper [1]. The latest experiments and results can be found in the report [2]. During the routine operation, especially in the case of higher accumulated ion beam intensity, the instability of ion beam was observed [3, 4], some information can be found in the references [5]. It is an essential problem to find the way to suppress the instability in order to obtain the higher accumulated and stored ion beam in HIRFL-CSR.

As the described in reference [6], the conventional way to suppress the instability was adopting the feedback system. From the report [7] the feedback system was helpful to increase the accumulated ion beam intensity, the action on the instability was not clear. Another solution was proposed in the paper [8], in order to avoid the overcooling, additional heating on the electron beam was used to suppress the instability. The results were presented in the reference [9].

A more efficient way [10] to suppress the instability was increasing the energy spread with the help of modulation.

A new method was proposed in this paper, the idea came from the electron beam as 3d kicker for stochastic cooling [11,12]. The intensity of the electron beam was modulated transversely and longitudinally. The distribution of electron became asymmetrical and inhomogenous, as a result, the electron beam becomes the electron bunches. The space charge field between the bunches acts as the kicking on the ion beam. These actions can be used to suppress the instability of ion beam.

The electrostatic field produced by the space charge of electron beam in the cooler by means of modulation on the voltage of control electrode in the electron gun will act as a travelling wave in the cooling section. This action will be attempted to suppress the ion beam instability in the presence of electron cooling device.

Another application of this work can be used to demonstrate the cooling effects of bunched electron beam [13,14].

SOME CONSIDERATIONS

Generally, the bunched electron beam was easily produced by the pulse electron gun. Unfortunately, the electron gun in the CSR coolers was direct current. On the other hand, the limitations come from the normal routine operation and heavy load beamtime in CSR.

From the technical point of view, the cathode of electron gun of the electron cooler was thermic cathode. It was continuously heated during the operation. The configuration of electrodes in the electron gun presents capacitive feature. The charge and discharge rate of the electron gun should be taken into account. Due to lack of the diagnostic instruments in the electron cooler, the measurement of the bunch should be solved offline.

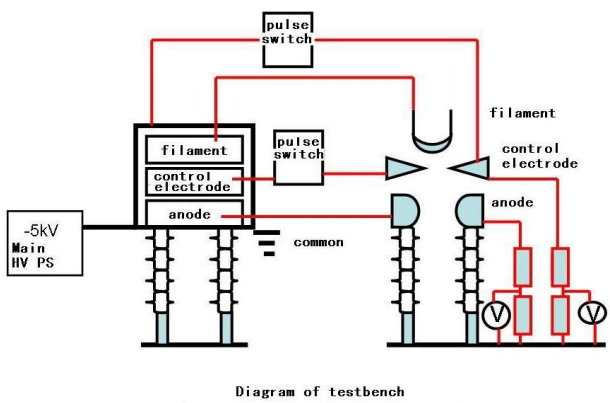

Figure 1: Layout of offline testbench.

A simplified solution was derived in this plan. The DC voltage of control electrode in the gun which was used to extraction of electron from the surface of cathode will be replaced by a new bipolar pulse power supply, in additional, a fast switch among the positive, negative and

*Work supported by The National Natural Science Foundation of China, NSFC(Grant No. 11375245, 11475235, 1122106)
yangxd@impcas.ac.cn

ISBN 978-3-95450-174-8

ground outputs will adopt to charge and discharge for the control electrode as illustrated in the Fig. 1. In this case, the electron pulse beam will formed in the electron cooler.

In the past year, a model of electron gun was designed and fabricated. The waveform of voltage at the control electrode was roughly explored. The scenario of the test bench was carefully considered.

The real waveform of voltage at the control electrode, the response times of gun and power supply will be measured offline in the test bench this year. The feasibility, reliability and stability of this system will be tested and validated.

A new power supply for control electrode will be installed into the electron cooler system, the output of this PS will be connected the computer. The voltage output parameters such as shape of wave, frequency, and the interval of pulses will be controlled by this computer. The cooling force and cooling time, accumulation process, the instability suppression will be investigated in the different bunched electron beam. Demonstration of electron cooling by the bunched electron beam will be performed in the near future.

The electron beam will be turn on and off optionally in the different period according to the requirement of atomic physics experiment situation.

Limitation

The cathode of CSR electron cooler [15,16] was thermal dispenser cathode, it was heated continuously, there are electron cloud existing in the surface of the cathode, once an enough strong electric field was established, the electron will be extracted from the surface of the cathode, forming the electron beam. On the other hand, when the extracting electric field disappeared, namely extracting was suppression, the electron beam was vanished, the electron beam was turn off. When the voltage on the control electrode of the gun was less than a proper value, maybe negative value, the electron beam will be turn off. In this case, if the voltage of the control electrode changes from positive one to negative one, the electron beam will be switched off as demonstrated in the Fig. 2.

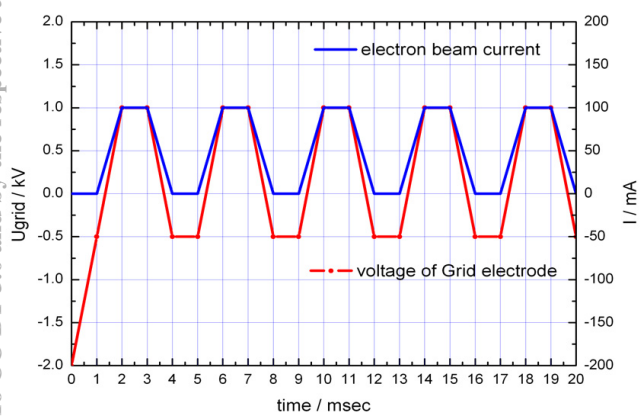

Figure 2: Waveform of electron beam current and the voltage on the control electrode of the gun.

Plan and Procedure

The scheme for the DC operation mode converts into pulse mode in the existing facility, specially the waveform of voltage on the control electrode of the electron gun varying with time was studied carefully. From the point of technical view, one possible solution was adopted directly the pulse HV power supply for the control electrode. The other alterative optional way was described as the following way. Add a pulse switch between the control electrode and the common terminal. A special twigger for switch on and off the electron beam was adopted during atomic experiments as shown in the Fig. 3. The modulation frequency will be an important parameter, it will be set as the time dimension such as the injection interval of ion beam, or the revolution period of the ion beam in the ring, or the expected cooling time.

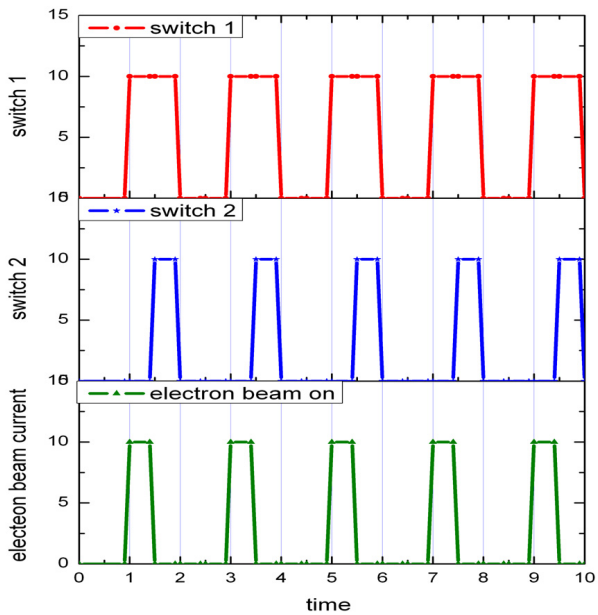

Figure 3: Two switches alternately act on the control electrode as chopper to get the different pulse length and interval.

The parameters of the pulse electron beam such as pulse width, interval of pulses, and the longitudinal and transverse distribution of pulse are the essential one. The offline measurement of these parameters will be performed in the existing electron cooler.

Due to the different electron kinetic energy, the longitudinal velocity of electron beam will be different in the experiments, in the other hand, in order to cool different ion beam, the parameters of the electron pulse should vary according to the essential situation. By the way, the length of the cooling section was fixed, the relation between the kinetic energy of electron beam and the modulation frequency should be explored clearly.

Toroid

The electron pulse propagates through the toroid in the cooler. Because of the electron beam transverse dimension and different path length in the toroid, the linear ve-

ISBN 978-3-95450-174-8

locity, namely the kinetic energy of electron beam are the same before entre the toroid. But the path lengths are different in the toroid, the electron pulse will slightly incline, as a result, the space between the pulses will become smaller. Another point was the precession motion of the whole electron beam due to the transverse electric field and the longitudinal magnetic field, the electron beam was rotated slowly around the beam axis, the whole electron beam has a same angular velocity, this effect will influence on the spatial distribution of the pulse electron beam. The influence of the different modulation frequency on the length of the electron pulse and interval in the case of fixed electron energy and the influence of the same modulation frequency on the length of the electron pulse and interval in the case of fixed electron energy should be taken into account.

Diagnostics

The most important point was that the judgement criterion should be found to realize the situation of the electron beam after modulation, the electron beam becomes the separated pulse, or it becomes fluctuation on the base of the DC flow as shown in the Fig. 4.

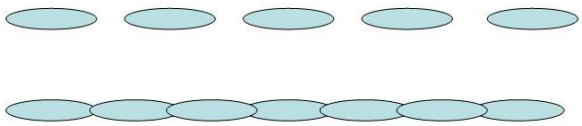

Figure 4: Schematic diagram of the electron beam distribution.

Offline Test

A set of test system was established in the laboratory. A prototype of the electron gun was fabricated. And a new HV power supplies were contrived. The modulation system was conceived. The measurement system of voltage on the control electrode was planned and prepared. The control and trigger system were taken into account. Due to the control electron power supply was placed on the main 35kV HV power supply, and the signals from this part should be insulated and transferred by the optical fibre. The data acquisition system was programmed.

CONCLUSION

Based on the offline experiments results, the proper modulation system of control electrode in the gun will be discovered to satisfy the requirements for produce the pulsed bunch electron beam. The proved modulation system will be migrated to the electron cooler system of CSRm. The real bunched electron beam will be formed in the cooler. The parameters such as length of bunch, interval of the bunches and the distribution of bunch will be measured with the help of diagnostic instruments in the cooler. The action and effect of this system will be tested in the presence of ion beam. The function of this system will be applied in the following aspects:

- suppress the instability of ion beam,
- increase the maximum accumulated ion beam intensity,
- improve the beam stability after accumulation,
- decrease the cooling time,
- verify the results of bunched electron beam cooling ability in the lower energy range.

REFERENCES

[1] Xiaodong Yang, “Eletron Cooling At IMP”,Beam Dynamics Newsletter No. 64, pp.55-65, August 2014.

[2] Youjin Yuan, “Status and Upgrade of HIRFL Accelerator Complex at IMP”, presented at COOL'15, Newport News, VA, USA, paper THXCR04, *these proceedings*.

[3] Parkhomchuk V.V., “Stability Limits of Cooled Beams”, COOL2001.

[4] Xiaodong Yang, Jie Li, Lijun Mao, et al. “Beam Instability Phenomena Observed At HIRFL-CSR In The Presence Of Electron Cooler”, Proceedings of RUPAC2012, Saint-Petersburg, Russia, MOZCH01, pp. 33-37.

[5] Xiaodong Yang, Jie Li, Lijun Mao , et al “Infuence of Electron Energy Detuning on The Lifetime And Stability Of Ion Beam In CSRm”, Proceedings of COOL2013, Murren, Switzerland, WEAM1HA02, pp. 84-88.

[6] V. Kamerdzhiev, J. Dietrich, I. Moho, et al. “Transverse Feedback System For The Cooler Synchrotron COSY-JÜLICH – First Results”, Proceedings DIPAC 2003 – Mainz, Germany, PT19, pp. 214-215.

[7] Yu.Korotaev, I.Meshkov, A.Sidorin, et al. “Intensive Ion Beam In Storage Rings With Electron Cooling”, Proceedings of RuPAC XIX, Dubna 2004, THBI03, pp. 13-17.

[8] V. Kamerdzhieva, J. Dietricha, R. Maier, et al. “Instability Phenomena of Electron-cooled Ion Beams at COSY”, NIMA 532 (2004), pp. 285-290.

[9] .I. Meshkov, Yu. Korotaev, A. Sidorin, et al. “Electron Cooling Of Proton Beam In COSY And S-LSR”, Proceedings of RuPAC 2006, Novosibirsk, Russia, WEBO04, pp. 31-33.

[10] L. Hermansson, D. Reistad, “Electron cooling at CELSIUS”, NIM in PR A 441 (2000), pp. 140-144.

[11] V.V. Parkhomchuk, V.B. Reva, A.V. Ivanov, “Electron Beams As Stochastic 3D Kickers”, Proceedings of COOL 2007, Bad Kreuznach, Germany, THM2I06, pp. 154-158.

[12] V.V. Parkhomchuk, “Novel Ideas In Electron Cooling”, Proceedings of COOL2013, Murren, Switzerland, TUAM2HA01, pp. 55-59.

[13] Alexei Fedotov, “Towards Demonstration Of Electron Cooling With Bunched Electron Beam”, BNL-96824-2012-IR, C-A/AP/#445 Jan. 2012.

[14] A.V. Fedotov, S. Belomestnykh, I. Ben-Zvi, et al. “Bunched Beam Electron Cooler For Low-Energy RHIC Operation”, Proceedings of PAC2013, Pasadena, CA USA, TUOAA1, pp. 363-365.

ISBN 978-3-95450-174-8

[15] A. Bubley, A. Goncharov, A. Ivanov, et al. "The Electron Gun With Variable Beam Profile For Optimization Of Electron Cooling", Proceedings of EPAC 2002, Paris, France, WEPRI049.

[16] M. Bryzgunov, A. Bubley, A. Ivanov, et al. "Electron Gun With Variable Beam Profile For COSY Cooler", Proceedings of COOL'11, Alushta, Ukraine, TUPS06, pp. 99-102.

ISBN 978-3-95450-174-8

DEVELOPMENT OF AN ULTRA FAST RF KICKER FOR AN ERL-BASED ELECTRON COOLER

A. Sy#, A. Kimber, J. Musson, Jefferson Lab, Newport News, VA 23606, USA

Abstract

The staged approach to electron cooling proposed for Jefferson Lab's Medium Energy Electron-Ion Collider (MEIC) utilizes bunched beam electron cooling with a single-pass energy recovery linac (ERL) for cooling in the ion collider ring. Possible luminosity upgrades make use of an ERL and full circulator ring and will require ultra-fast kickers that are beyond current technology. A novel approach to generating the necessary ultra fast (ns-level) RF kicking pulse involves the summation of specific subharmonics of the cooling electron bunch frequency; the resultant kicking pulse is then naturally constrained to have rise and fall times equal to the electron bunch frequency. The uniformity of such a pulse and its effects on the beam dynamics of the cooling electron bunch are discussed.

INTRODUCTION

JLab's proposed MEIC requires bunched beam cooling of ions at collision energy to maintain design emittances for high luminosity. In the baseline design [1], the bunched electron beam is accelerated and decelerated using an energy recovery linac (ERL) to reduce the active beam power at the beam dump. More intense electron cooling provides a path to a luminosity upgrade, with the required higher average electron current provided by a full circulator cooler ring. Figure 1 shows a schematic of the ERL and circulator cooler ring concept. Use of the circulator ring relaxes the current requirement from the injector by allowing each electron bunch to cool multiple ion bunches. The circulator cooler ring concept requires ultra fast transverse beam kickers to deflect electron bunches into and out of the circulator ring. For a cooler ring frequency of 476 MHz, the bunch spacing is 2.1 ns and the kicker must be able to deflect a single bunch without disturbing the preceding or following bunches in the bunch train. Each pass that a single bunch makes in the circulator ring reduces the required current from the injector by the same amount; for n passes in the circulator ring, the injector current is reduced by a factor 1/n. The transverse beam kicker should then operate at a frequency of 476/n MHz, kicking every n-th bunch in the bunch train into or out of the ring. Thus a suitable kicking pulse will have rise and fall times on the order of the bunch spacing, with MHz repetition rates. A kicking pulse of this type is beyond current driver technology. We describe a novel method for generation of such a suitable kicking pulse and discuss the effects of the kicking pulse on the quality of the cooling electron bunches.

#amysy@jlab.org

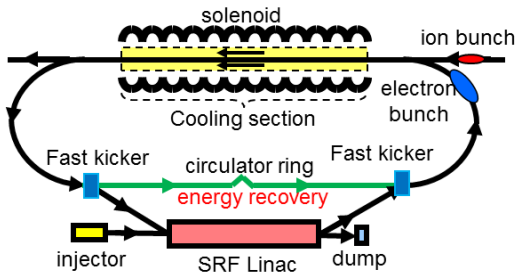

Figure 1: Schematic of an ERL-based electron cooler with full circulator ring.

CONCEPT

The ultra fast RF kicking pulse required for use in the circulator cooling ring concept can be generated by summing subharmonics of the bunch frequency with appropriate phases and amplitudes. A similar concept using the Fourier series representation of a periodic delta function with higher harmonics of the bunch frequency has been explored for the TESLA damping ring [2]. The use of subharmonics of the bunch frequency allows for adjustment of the kicker waveform according to the desired characteristics of the waveform, particularly at intermediate positions between kicking pulses at which circulating bunches should be left undisturbed. The constraints of zero amplitude and zero gradient of the kicking pulse at these undisturbed bunch positions result in the kicking pulse described by

$$f\left(\theta;\vec{a}\right)=\sum_{i=0}^{n-1} a_i \cos i\theta \tag{1}$$

where

n = number of bunches in the bunch train
θ = bunch frequency/n = 476/n MHz
a_i = amplitude coefficients of the subharmonics

$$a_0 = \frac{1}{n} \tag{2}$$

$$a_j = \frac{2(n-j)}{n^2}, j = 1,2,\ldots,n \tag{3}$$

The resultant kicker waveform and the subharmonics required for the case of n=25 bunches in the bunch train is plotted in Figure 2. The peaks of the kicking pulse occur with a frequency of 476/25=19.04 MHz, and both the amplitude and gradient of the kicking pulse are zero for non-kicked bunches in the bunch train. The rise and fall time of the pulse is exactly equal to the bunch spacing.

ISBN 978-3-95450-174-8

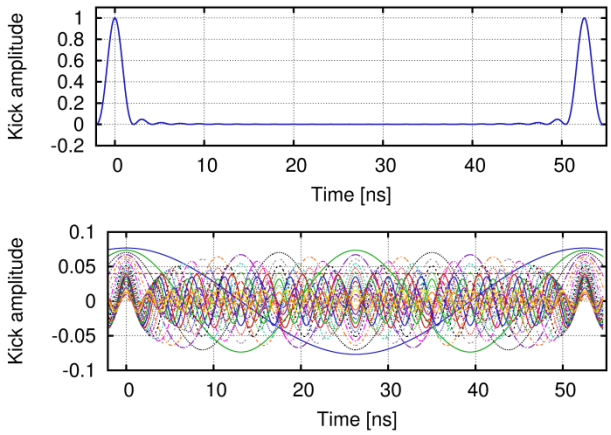

Figure 2: Kicker waveform (top) resulting from summation of 25 subharmonics of the nominal bunch frequency of 476 MHz (bottom).

Kicking Pulse Non-uniformity

The short rise and fall times required of the kicking pulse create a pulse that is not uniform over the length of the cooling electron bunch, and this non-uniformity will have adverse effects on the transverse beam quality of the kicked bunch. The non-uniformity of the kicking pulse is quantified by the percentage of the peak amplitude of the pulse at the center of the bunch seen by the head and tail of the full bunch length. For the waveform described earlier ("zero-gradient pulse") with n=25 bunches, the pulse non-uniformity is 6.4% for an RMS bunch length σ_s=3 cm. Figure 3 shows the non-uniformity of the zero-gradient kicking pulse over the full beam size of +/- 3σ_s.

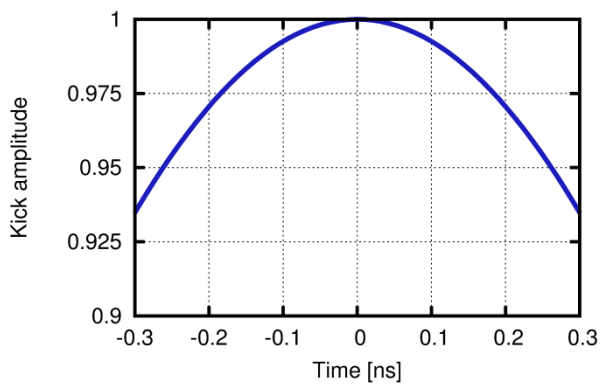

Figure 3: Non-uniformity of zero-gradient kicking pulse over +/- 3σ_s of kicked electron bunch.

The non-uniformity of the kicking pulse can be improved through adjustment of the phases and amplitudes of the subharmonic frequencies comprising the waveform. A waveform with improved non-uniformity of 0.1% ("flat-top pulse") [3] can also be generated and its effects on the transverse beam quality are studied for comparison. The improvement in non-uniformity of the flat-top pulse comes at the expense of nonzero voltage gradients at the nominally undisturbed bunch positions. Figure 4 compares the zero-gradient and flat-top waveforms previously discussed.

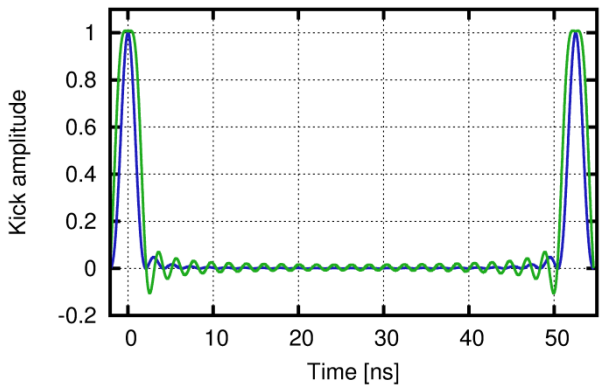

Figure 4: Zero-gradient pulse (blue) and flat-top pulse (green) for nominal bunch frequency of 476 MHz, n=25 bunches.

Residual Voltages

The non-uniformity of the kicking pulse implies a non-uniformity of the waveform in the vicinity of the non-kicked bunches. Though the amplitude and gradient of the voltage waveform are zero at the center of each non-kicked bunch for the zero-gradient pulse, the head and tail of each of these intermediate bunches may also see adverse effects on the transverse beam quality due to these residual voltages. For the flat-top pulse, the voltage gradients are always nonzero for non-kicked bunches and will distort the transverse phase space of the circulating electron bunch. A suitable fast kicker waveform will appropriately balance the phase space distortion from the non-uniformity of the pulse with that from residual voltages seen as the electron bunch circulates in the circulator ring.

SIMULATIONS

The adverse effects on transverse beam quality for both kicked and non-kicked bunches were simulated using elegant [4]. Gaussian electron bunches with P=55 MeV/c, ε_x= ε_y=10 nm, σ_s=3 cm were generated with the proper offset such that the horizontal kick aligned the kicked bunch with the design orbit. The circulator cooler ring was approximated with a one-turn linear transfer matrix. The kicker waveforms were generated with a series of zero-length RF deflectors with the appropriate phases, amplitudes, and frequencies. The peak amplitude of the kicking pulse was chosen to give a 1 mrad deflection. Table 1 lists notable simulation parameters. Each simulated bunch is kicked onto the design orbit, circulates for n turns, and sees the kicking pulse again after the n-th pass in the circulator ring. The transverse emittances are observed immediately after the bunch interacts with the kicker waveform.

Figure 5 shows the turn-by-turn normalized horizontal emittance for a single bunch in the circulator ring for deflection with both the zero-gradient pulse and the flat-top pulse. For this horizontal deflection, the vertical emittance is left undisturbed.

ISBN 978-3-95450-174-8

Table 1: ELEGANT Simulation Parameters

Parameter	Unit	Value
P	MeV/c	55
$\varepsilon_{x,y}$	nm	10
σ_s	cm	3
$\sigma_{\Delta P/P}$		3e-4
n	#	25
f	MHz	476
Deflection angle	mrad	1

For the zero-gradient pulse, the simulations show a 4% growth in the normalized horizontal emittance due to the non-uniformity of the kick, and negligible emittance growth due to the residual voltages as the bunch circulates in the circulator ring. Additional growth is seen after the bunch is kicked out of the ring, but this growth occurs immediately after the final kick, and is therefore insignificant with regards to the cooling properties of the electron bunch. The effect of the flat-top pulse is more detrimental: the non-uniformity of the kick only contributes a 0.4% increase in the emittance, but the large gradients in the residual voltages on subsequent turns cause emittance growth by as much as a factor of 4 by the time the bunch has completed its circulations.

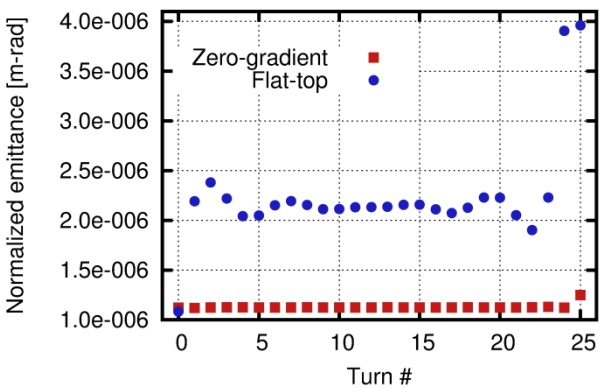

Figure 5: Turn-by-turn normalized horizontal emittance for an electron bunch kicked by the zero-gradient pulse (red squares) and flat-top pulse (blue circles).

Compensation of Phase Space Distortion

The non-uniformity of the kicking pulse is mirrored in the transverse phase space of the kicked bunch as seen in Figure 6. In the case of the flat-top pulse, this phase space distortion is amplified by the large voltage gradients felt by the bunch on subsequent turns. From a beam quality standpoint, any advantage gained from the more uniform kick is negated by the large emittance growth in the ring. The emittance growth due to the amplification of the phase space distortion suggests that a circulating bunch with little to no distortion will exhibit reduced emittance growth due to the residual voltages.

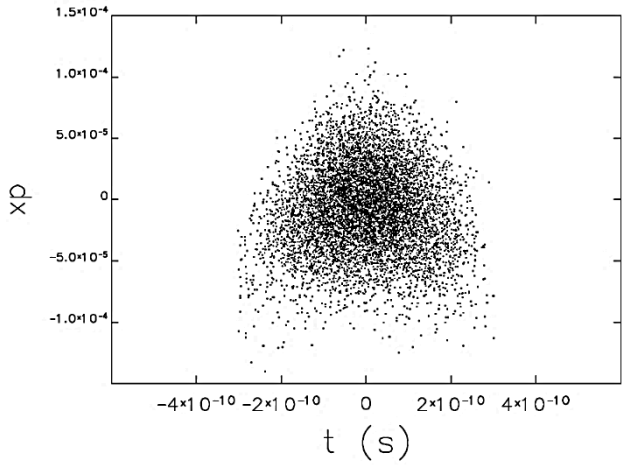

Figure 6: Distorted bunch after kick into circulator ring.

The distortion in the kicked electron bunch can be removed with an identical kicker separated from the main kicker by a phase advance of $\Delta\psi_x=\pi$. The transverse phase space behavior due to such a scheme is illustrated in Figure 7. The electron bunch is pre-distorted by the first kicking pulse. The pre-distorted electron bunch undergoes half of a betatron oscillation by the time it arrives at the main kicker, and the kick from the main kicker then cancels the pre-distortion. The cancellation of the distortion results in a matched bunch for the bunched beam electron cooling. With this phase space distortion compensation, an electron bunch kicked by the flat-top pulse experiences 5% emittance growth for the bulk of the time spent in the circulator ring, comparable to the zero-gradient case with no compensation. Figure 8 plots the turn-by-turn normalized horizontal emittance for the compensated flat-top pulse and non-compensated zero-gradient and flat-top pulses. It is noted that even with this compensation scheme, large emittance growth is still seen near the end of the bunch lifetime in the ring.

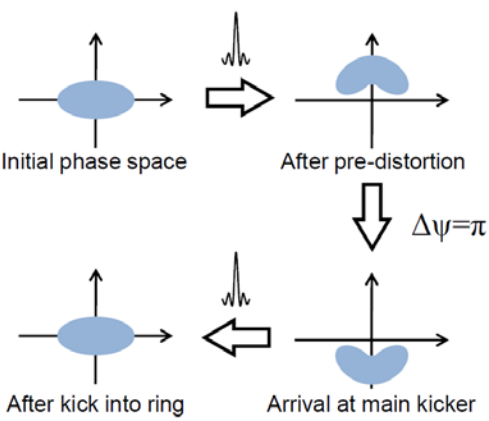

Figure 7: (Clockwise, from top left) Transverse phase space behavior for compensation scheme utilizing multiple identical kickers. Pre-distortion is induced in the electron bunch such that the main kick removes this distortion.

ISBN 978-3-95450-174-8

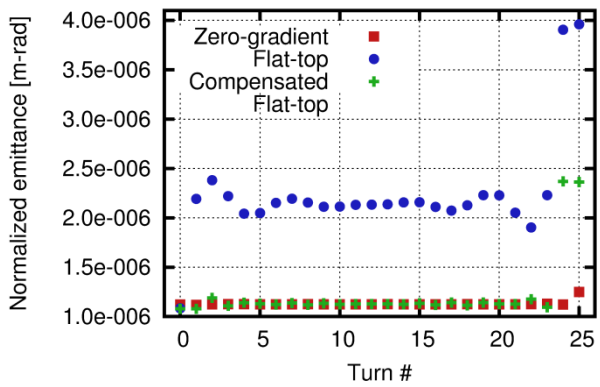

Figure 8: Turn-by-turn normalized horizontal emittance for an electron bunch kicked by the zero-gradient pulse (red squares), flat-top pulse (blue circles), and compensated flat-top pulse (green crosses).

DISCUSSION

The few percent transverse emittance growth imparted by the zero-gradient kicker waveform is a promising result for the use of such an ultra fast RF kicker based on the summation of subharmonic frequencies. Both the non-uniformity of the kicking pulse over the length of the electron bunch, as well as the residual voltages in the kicking waveform on intermediate turns in the circulator ring, contribute to the emittance growth in the plane of the deflection. Large voltage gradients on the intermediate turns in the circulator ring can amplify even very small distortions in the transverse phase space, as seen in the case of the flat-top pulse. Multiple kickers can be used to cancel this phase space distortion and prevent large emittance growth due to large voltage gradients; this compensation scheme allows for further optimization of the kicker waveform but requires further study, as the compensation is imperfect and large emittance growth can occur in the final few turns in the circulator ring. Further study of this concept for an ultra fast RF kicker is ongoing.

ACKNOWLEDGMENTS

The authors acknowledge early work regarding this concept by Edward Nissen, Balša Terzić, and Andrew Hutton. This manuscript has been authored by Jefferson Science Associates, LLC under Contract No. DE-AC05-06OR23177 with the U.S. Department of Energy. The United States Government retains and the publisher, by accepting the article for publication, acknowledges that the United States Government retains a non- exclusive, paid-up, irrevocable, world-wide license to publish or reproduce the published form of this manuscript, or allow others to do so, for United States Government purposes.

REFERENCES

[1] S. Abeyratne et al., "MEIC Design Summary," arXiv:1504.07961 [physics.acc-ph]

[2] S. Mishra et al., "Studies Pertaining to a Small Damping Ring for the International Linear Collider," FNAL Report (October 2004).

[3] Y. Huang et al., "Harmonic Resonant Kicker Design for the MEIC Electron Circular Cooler Ring," IPAC15, WEPMN025 (2015).

[4] M. Borland, "elegant: A Flexible SDDS-Compliant Code for Accelerator Simulation," Advanced Photon Source LS-287, September 2000.

ISBN 978-3-95450-174-8

SIMULATION STUDIES OF INTENSITY LIMITATIONS OF LASER COOLING AT HIGH ENERGY

L. Eidam*, TEMF, TU Darmstadt, Germany
O. Boine-Frankenheim, GSI Helmholtzzentrum für Schwerionenforschung GmbH (GSI), Germany
D. Winters, GSI Helmholtzzentrum für Schwerionenforschung GmbH (GSI), Germany

Abstract

Within the FAIR project, laser cooling of highly intense, ultra relativistic ion beams will be attempted for the first time, and in a large (circumference 1084 m) and strong (max. magnetic rigidity 100 Tm) synchrotron, called "SIS100".

Laser cooling of such ion beams should result in a further increase of the longitudinal phase space density and in non-Gaussian longitudinal beam profiles. For stable operation of such ion beams, and for optimization of the cooling process, both the laser force and the high-intensity effects have to be studied numerically in advance. The efficiency of laser cooling has been analyzed for different synchrotron frequency regimes. At high beam intensities, intra-beam scattering and space-charge effects have been found to counteract the laser cooling force. We will discuss how they influence the laser cooling efficiency and thus affect the cooling time.

INTRODUCTION

Laser cooling of stored coasting and bunched ion beams has been investigated experimentally at the TSR in Heidelberg (Germany) [1, 2], and at ASTRID in Aarhus (Denmark) [3,4]. At the ESR in Darmstadt (Germany), first laser cooling experiments with stored "bunched relativistic" ion beams were conducted [5]. In the future laser cooling will be applied to highly intense and ultra relativistic ion bunches within the FAIR project [6].

The principle of laser cooling is, especially after the Nobel Prize in 1997, very well known. Here, we consider an ion with a fast atomic transition, e.g. 2s - 2p (electric dipole), of a particular wavelength λ, and a well-defined velocity $v = \beta c$. When the ion moves towards a counter-propagating photon from a laser beam, both the energy and the momentum of the photon are absorbed in a single scattering event, see Fig. 1. This brings the ion in an excited state, which, however, de-excites almost instantaneously by fluorescence emission. The corresponding recoil then occurs in a random direction. After many scattering events, the random recoils average out to zero, but photon absorption always came from one direction, thus decelerating the ion. A pure deceleration force is highly unwanted here, but a strong reduction of the velocity spread of the ions is. Therefore, a counter-balancing force is required, which comes from bunching the ion beam: the rf-bucket force. The laser must thus address ions orbiting with relativistic velocities and performing synchrotron oscillating in the rf-bucket.

* L.Eidam@gsi.de

Since the Doppler-width of the transition is usually much smaller than the particle distribution, the laser light can only interact with a certain velocity class of ions in the beam. To address the full range of velocities, the laser must be scanned over a large range.

In this work, we analyze the dynamics of an ion beam during the laser cooling process, using a one dimensional particle-in-cell code. The transverse plain is assumed to be unaffected by the laser force. By using "macro particles" the modeling of direct coulomb interactions between single particles is not possible. The results at very low momentum spreads might therefore not be very exact, but the focus of this work lies on the cooling process and the intensity limitations of laser-cooled ion beams.

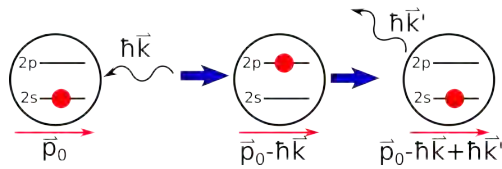

Figure 1: A single scattering event: The ion (traveling to the right) absorbs a photon from the laser beam (traveling to the left) followed by a spontaneous emission. After many scattering events, the momentum transfer of the random recoils average out to zero, but the momentum of the absorption always decelerate the ion.

The laser particle interaction is a statistical process. The probability of a spontaneous emission in a time interval Δt is given by

$$\rho_{emit} = \frac{\Delta t}{\tau} \cdot \rho_{ee} \tag{1}$$

where τ is the lifetime of the exited state and ρ_{ee} is the excitation probability. For a saturated transition the excitation probability is given by (see ref. [7])

$$\rho_{ee} = \frac{1}{2} \frac{S}{1 + S + (2\Delta\nu \cdot \tau)^2} \tag{2}$$

where S is the Saturation parameter and $\Delta\nu$ the detune between the frequency of the photon and the transition. For arbitrary excitations the optical Bloch equations have to be solved as described in [8]. The momentum kick of one spontaneous emission is given by

$$\Delta p_{lab} = \frac{\hbar\omega_{lab}}{c_0} \cdot \gamma^2(1 + \beta) \cdot 2U_j \tag{3}$$

where ω_{lab} is the frequency of the incoming photons in the laboratory frame and U_j a random number between 0 and 1, describing the projection of the randomly emitted photon.

ISBN 978-3-95450-174-8

COOLING PROCESS

The cooling process of a particles distribution requires a stable point, where the sum of all forces cancels, surrounded by a friction force. In order to achieve a stable point for laser cooling process the laser force is counteracted by the RF voltage. The narrow laser force does not interact simultaneously with all particles. Therefore the position of the laser force is scanned from the position of the particle with the highest oscillation amplitude to the synchronous particle in order to damp the oscillation in the bucket of all particles like shown in Fig. 2.

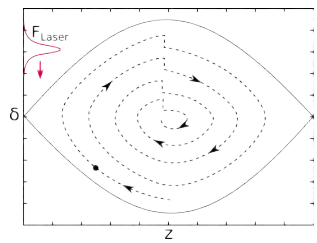

Figure 2: Sketch of the cooling process for a hot ion beam in a rf bucket. The laser force is scanned to damp continuously the synchrotron oscillation of all particles.

An example of the relative momentum rms during the cooling process is shown in Fig. 3. Up to a certain speed of the laser scan all particles are pushed in front of the laser force and the final momentum deviation reach the Doppler limit. Above this point the laser scan is too fast and particles get lost behind the narrow force. The lost particles do not interact with the laser light anymore and result in a much higher final momentum deviation as shown in Fig. 4. In the following this threshold is called 'minimal cooling time'.

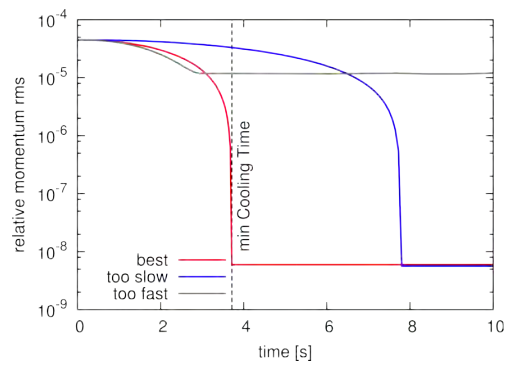

Figure 3: Relative momentum spread over time for three different speeds of the laser scan. The required time of the fastest successful cooling process is defined as minimal cooling time.

Beside the speed of the laser scan the speed of the synchrotron motion affects the efficiency of the cooling process. The synchrotron motion is characterized by the synchrotron tune, that describes the fraction of the synchrotron motion

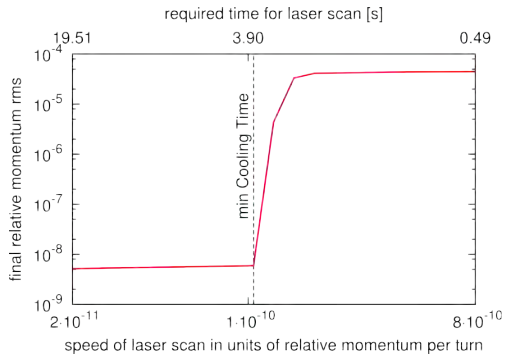

Figure 4: Minimal relative momentum deviation for different laser speeds. The required time of the fastest successful cooling process is defined as minimal cooling time.

for one turn in the synchrotron:

$$Q_s = -\frac{L\eta \cdot \hat{\delta}}{2\pi\hat{z}} \text{ with } \eta = \frac{1}{\gamma_t^2} - \frac{1}{\gamma^2} \tag{4}$$

where L is the circumference of the accelerator, γ_T the relativistic factor at transition energy and $\hat{\delta}$ and $\hat{z}$ are the amplitudes of the elliptic particle distribution in phase space. For high values of the relativistic factor ($\gamma < \gamma_T$) the speed of the synchrotron motion decreases. The synchrotron tune separates the cooling process into three different regimes. For high synchrotron tunes ($Q_s \approx 10^{-3}$) the spatial and relative momentum deviation is reduced simultaneously. Because of the high synchrotron frequency the particles are symmetrically pushed to the center of the bunch. This method was already tested in low energy storage rings as reported in ref. [9].

For medium synchrotron tunes ($Q_s \approx 10^{-4}$) the oscillation is too slow to keep the symmetry in phase space. The particles interact with the laser light for many turns and the circular motion is strongly perturbed.

For low synchrotron tunes ($Q_s \approx 10^{-5}$) the laser force becomes stronger than the kick of the RF cavities. This enables to position the laser force directly in the center of the bunch. All particles are rotated into the laser light and are captured in front of the laser force. The cooling of the bunch requires only one single synchrotron period. In contrast to the symmetric reduction in phase space the bunch length is only reduced by a factor of two. The particle motion in the bucket for these three different regimes of synchrotron tune are illustrated in detail in ref. [8].

The influence of the synchrotron tune on the required time for the cooling process is shown in Fig. 5. The spatial and relative momentum amplitudes of the initial elliptic distribution are $\hat{\delta} = 10^{-4}$ and $\hat{z} = 2.5m$. The FWHM of the laser force in units of relative momentum is $\Delta_{FWHM} = 10^{-7}$ and the interaction time of the laser light and the particle bunch is set to 40 lifetimes of the excited state. The results for three different values of relative momentum kick per scattering events are given. A detailed explanation of the analytic estimations illustrated by the dashed lines is given in ref. [8].

ISBN 978-3-95450-174-8

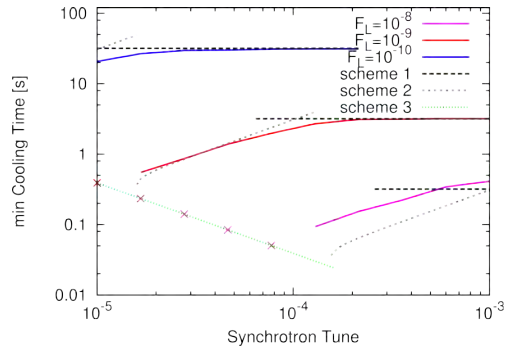

Figure 5: Required cooling time for different synchrotron tunes.

INTENSITY EFFECTS

For higher beam intensities heating processes counteract the cooling and limit the lowest attainable momentum deviation. In this section the influence of coulomb interactions of the particles is analyzed. The two effects Intra beam scattering (IBS) and space charge are discussed separately.

Intra Beam Scattering

Intra beam scattering describes the coupling of the three dimensions of motion by multiple small angle coulomb scattering events. For high energy beams the transverse oscillations are usually much stronger than the longitudinal motion and therefore heat is transfered to longitudinal oscillations. This effect can be described by the diffusion coefficient in the Vlasov-Fokker-Planck-equation. In simulations the random momentum kick for one particle is given by

$$\delta_{IBS} = Q_j \cdot \sqrt{2 D_{zz} \frac{L_{acc}}{\beta c_0}} \tag{5}$$

where Q_j is a Gaussian distributed random number and D_{zz} is the diffusion coefficient, that can be calculated for non-Gaussian distributions with the local diffusion model as described in ref. [10].

For the cooling process with a scanning laser the minimal relative momentum deviation and corresponding bunch length for different intensities is shown in Fig. 6.

The effect of IBS on the cooling process can be estimated by the rms rate equilibriums. The average of the laser force δ_L for one synchrotron motion is given by

$$\langle \Delta\delta_L \rangle_{syn} = \frac{1}{\pi} \int_0^{\pi} \cos(\phi) \cdot \Delta\delta_L(\delta_{pos} \cdot \cos(\phi)) d\phi \tag{6}$$

where δ_{pos} is the amplitude of a particle oscillation in units of relative momentum. For the final position of the laser force, close to the center of the bunch, the averaged force agrees with a linear friction force for small momentum deviations. The exponential cooling time in this region can be calculated by:

$$\tau^{-1}_{Laser} = \frac{1}{T_{rev}} \cdot \frac{\partial \langle \Delta\delta_L \rangle}{\partial \delta_{pos}} \tag{7}$$

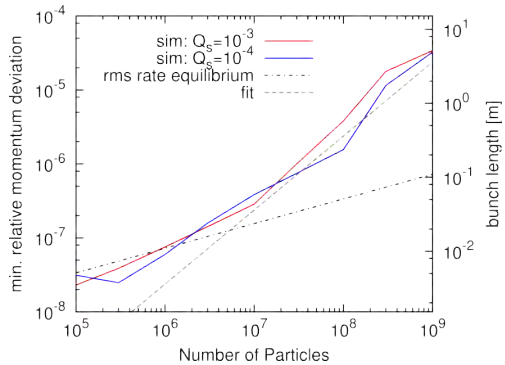

Figure 6: Influence of IBS on minimal relative momentum deviation for symmetric reduction of phase space. The rms equilibrium for low momentum deviations and the proportionality for higher momentum deviations agree with simulations.

The minimal relative momentum deviation is given by the equilibrium of the laser cooling rate and the intra beam scattering growth rate:

$$\tau^{-1}_{IBS} + \tau^{-1}_{Laser} = 0 \tag{8}$$

This equilibrium only exist for relative momentum deviations in the linear region ($\delta_{pos} < 10^{-7}$) of equ. 6. For higher momentum deviations the rms rate equilibrium is not valid anymore. Instead the minimal relative momentum deviation is limited by a critical IBS kick, that pushes the particles behind the narrow laser force.

$$\langle \delta_{IBS} \rangle_{max} = const. \Rightarrow \frac{N}{\delta_{rms}} = const. \tag{9}$$

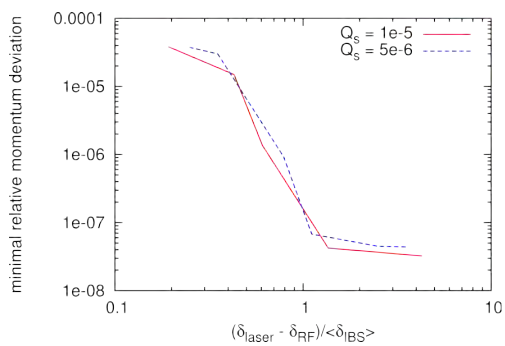

Figure 7: Influence of IBS on minimal relative momentum deviation for fixed laser scheme. The cooling is successful if the fraction of the cooling force and IBS kick is greater than one.

For the cooling process with the fixed laser position the relative momentum deviation is shown in Fig. 7. The results are plotted against the fraction of the cooling force, given by the difference of the laser force and the RF-kick, and the random IBS kick. Hence the condition for an efficient

ISBN 978-3-95450-174-8

cooling process is given by:

$$\hat{\delta}_{Laser} - \hat{\delta}_{RF} > \sqrt{2D_{zz}\frac{L_{acc}}{\beta c_0}} \qquad (10)$$

In case the beam intensity is too strong particles are kick beyond the barrier of the laser force.

Space Charge

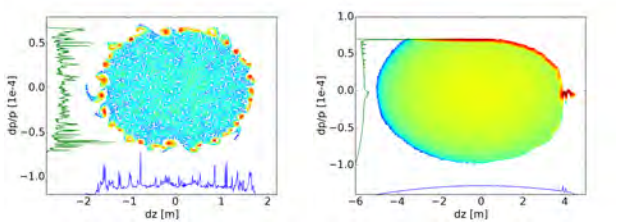

Figure 8: Longitudinal phase space of simulation with space charge. Instabilities for the two cases of high synchrotron tune left and medium synchrotron tune right.

Space charge describes the interaction of particles with the electric field of the bunch in a perfectly conducting pipe. In the longitudinal tracking code this effect is implemented by using the space charge impedance in frequency domain.

The effects of space charge on the particle bunch with scanning laser are shown in Fig. 8. For high synchrotron tune an intense, narrow ring of particles is formed in longitudinal phase space. Applying space charge this ring shows a kind of two stream instability. For high particle intensities the instability rise time is in the range of the cooling time and avoids further cooling of the particle distribution.

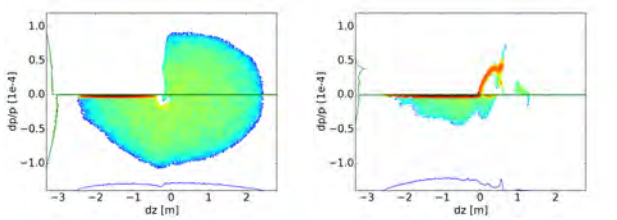

Figure 9: Longitudinal phase space of simulation with space charge of fixed laser scheme. Deformation of bunch for lower intensity (left). For higher intensities space charge kicks some particles beyond the laser force (right).

For lower synchrotron tunes the narrow peaks at the end of the bunch produce strong space charge fields (Fig. 8 right). For high particle intensities these strong space charge fields overcome the RF-kick and stop the synchrotron motion locally. Without the synchrotron motion the cooling process does not work anymore.

For the fixed laser configuration at low synchrotron tunes space charge strongly deforms the elliptic distribution. The success of the cooling process is limited by a certain intensity where the deformation is too strong and the arising space charge fields push particles beyond the laser force.

CONCLUSION AND OUTLOOK

The photon-ion interaction is successfully implemented in a longitudinal tracking code and can be analyzed for arbitrary excitation shapes. Neglecting intensity effects it was shown, that the cooling process depends strongly on the synchrotron tune. Three different regimes were separated and the required cooling times were compared. The effect of space charge and intra beam scattering were analyzed. Both effects limit the maximum intensity.

The exact limits of space charge induced instabilities have to be studied. Further intensity limiting effects like longitudinal coupling impedance has to be analyzed. Beside the effects of a current-wave laser the behavior of the particle beam interacting with a pulsed laser system has to be studied in detail.

REFERENCES

[1] S. Schröder et al. Phys. Rev. Lett. 64 (1990) 2901.

[2] I. Lauer et al. Phys. Rev. Lett. 81, 2052 (1998).

[3] J.S. Hangst et al. Phys. Rev. Lett. 67 (1991) 1238.

[4] J.S. Hangst et al. Phys. Rev. Lett. 74 (1995) 4432.

[5] U. Schramm et al. Proceedings of PAC 2005, Knoxville, USA, FOAD004 (2005) 401.

[6] D. Winters et al. Phys. Scr. (2015) - to be published

[7] H.J.Metcalf, P. van der Straten *Laser Cooling and Trapping of Atoms and Ions* Springer New York (1999)

[8] L. Eidam et al. IPAC 2015,Richmond, USA, MOPWA025 (2015) 150.

[9] M.Bussmann et al. J. Phys. Conf. Series 88 (2007) 012043(1)

[10] A.O. Sidorin et al. Nucl. Instr. Meth. Phys. Res. A 558 (2006) 325

ISBN 978-3-95450-174-8

COOLING FOR A HIGH LUMINOSITY 100 TeV PROTON ANTIPROTON COLLIDER

S. J. Oliveros*, J. G. Acosta, L. M. Cremaldi, D. J. Summers
University of Mississippi - Oxford, University, MS 38677 USA

Abstract

A 10^{34} cm^{-2} s^{-1} luminosity 100 TeV proton-antiproton collider is explored. The cross section for many high mass states is 10x higher in $p\bar{p}$ than pp collisions. Antiquarks for production can come directly from an antiproton rather than indirectly from gluon splitting. The higher cross sections reduce the synchrotron radiation in superconducting magnets and the vacuum system, because lower beam currents can produce the same rare event rates. Events are also more central, allowing a shorter detector with less space between quadrupole triplets and a smaller β^* for higher luminosity. To keep up with the antiproton burn rate, a Fermilab-like antiproton source would be adapted to disperse the beam into 12 different momentum channels, using electrostatic septa, to increase antiproton momentum capture 12x. At Fermilab, antiprotons were stochastically cooled in one debuncher and one accumulator ring. Because the stochastic cooling time scales as the number of particles, 12 independent cooling systems would be used, each one with one debuncher/momentum equalizer ring and two accumulator rings. One electron cooling ring would follow the stochastic cooling rings. Finally antiprotons in the collider ring would be recycled during runs without leaving the collider ring, by joining them to new bunches with snap bunch coalescence and longitudinal synchrotron damping.

INTRODUCTION

With the recent discovery of the Higgs boson [1] the standard model of particle physics is complete, but exploration will continue to search for beyond the standard model (BSM) physics. Colliders beyond $\sqrt{s}$ =14 TeV are necessary to fully explore new BSM physics, and this provides a great motivation for the future construction of a high energy $p\bar{p}$ collider [2, 3]. A 200 km circumference ring with 8 T NbTi magnets is chosen [4]. The tunnel is 2.5× longer than the twin 40 km tunnels proposed for the International Linear Collider. The center of mass energy considered would be 100 TeV with a luminosity of 10^{34} cm^{-2} s^{-1}. Energy frontier pp [5, 6] and $\mu^+\mu^-$ [7] colliders have also been proposed.

Synchrotron radiation of about 2 Megawatts per ring becomes a problem with circular 100 TeV pp colliders [8]. A $p\bar{p}$ collider represents a large advantage with respect to a pp collider in the point that the cross section for higher mass is around 10 times larger, which allows the collider to run with lower beam currents while still producing the same high mass event rate as pp. See Figs. 1 and 2. Synchrotron radiation in superconducting magnets and the vacuum system is reduced as well as detector radiation damage.

* solivero@go.olemiss.edu

Some important aspects to achieve high luminosity are identified in this study, such as increased momentum acceptance in a Fermilab-like antiproton source, and studies of higher antiproton cooling rates.

PROTON ANTIPROTON COLLIDERS

Proton antiproton colliders have been used at CERN [9], Fermilab [10], and GSI Darmstadt [11].

In $p\bar{p}$ collisions, antiquarks for production can come directly from an antiproton rather than indirectly from gluon splitting as is observed in Fig. 1, which shows the main process for W′ production in $q\bar{q}$ and qq collisions.

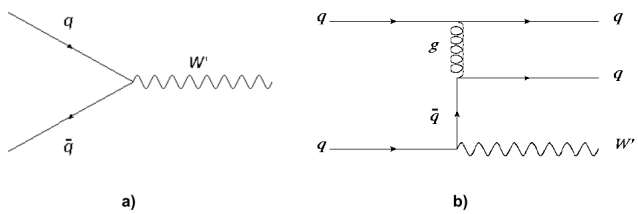

Figure 1: Feynman diagrams for W′ production in (a) $q\bar{q}$ collision, and (b) qq collision (t channel). The two final state quarks cross in the u channel, which is not shown.

In $p\bar{p}$ collisions, the cross section for most high mass states is greater than in pp collisions [2], as can observed in the Fig. 2, where the cross section is around 10x higher in $p\bar{p}$ collisions in W′ production as an example. It is important to note that the higher cross sections allow the collider to be run at lower beam currents and luminosities, which reduces synchrotron radiation in the collider's superconducting magnets and vacuum system. In addition, one beam pipe of magnets is shared by both beams, reducing costs with respect to the two beam pipes required for a pp collider, as well as simplifying the interaction region.

LUMINOSITY REQUIREMENTS

A main goal is to achieve a luminosity of 10^{34} cm^{-2} s^{-1}. As a starting point, take as reference the Tevatron collider. The luminosity can be scaled as:

$L_{scaled} = E_{increased}$ x $f_{decreased}$ x $L_{current}$ =
(50 TeV / 0.98 TeV) x (6.28 km/200 km) x (3.4 x 10^{32} cm^{-2} s^{-1}) =
5.2 x 10^{32} cm^{-2} s^{-1}
where f is collision frequency.

Thus, with 20 times more bunches a luminosity of 10^{34} cm^{-2} s^{-1} is achieved. The antiproton burn rate for a 100 TeV $p\bar{p}$ collider, with total cross section σ = 150 mbarn, is σL = 540 x 10^{10} /hr. The Fermilab Debuncher ring cooled 40

ISBN 978-3-95450-174-8

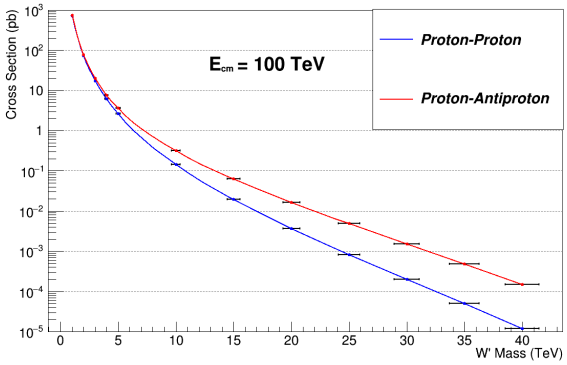

Figure 2: W′ cross section as a function of the mass using pp and $p\bar{p}$ collisions with E_{cm} = 100 TeV using MadGraph [12].

x 10^{10} $\bar{p}$/hr, thus the number of antiprotons needed is 13.5 times more. The Fermilab Accumulator ring followed the Debuncher and cooled 25 x 10^{10} $\bar{p}$/hr. Providing more time for Accumulator ring deposition orbit longitudinal and transverse cooling might improve the Accumulator ring stacking rate [13].

ANTIPROTON CAPTURE AND COOLING

For the Tevatron, antiprotons were created by hitting an Inconel (a low expansion nickel-iron alloy) target with a beam of 120 GeV protons, producing antiprotons with a momentum peak of 8.9 GeV/c. Many antiprotons were rejected because of the momentum acceptance (8.9 ±2% GeV/c). Our goal is to collect more antiprotons from a Fermilab-like target station (8.9 ± 24% GeV/c), instead of creating more antiprotons. Thus, to keep up with the high luminosity antiproton burn rate, one or more dipoles would be adapted to spread the antiprotons into 12 different momentum channels using 11 electrostatic septa. The Fermilab Fixed Target Switchyard used eight electrostatic septa strings to deliver beam to nine primary slow spill users and one fast spill user [14]. A linear Fixed Field, Alternating Gradient channel [15] might be used to transport the 8.9 ± 24% GeV/c beam until it could be split.

At Fermilab, antiprotons were stochastically precooled in the Debuncher ring during 2.2 s, with transverse emittance reduction from 300 to 30 μm, then sent them to the Accumulator ring to be stochastically cooled and stored. There, the transverse emittance was reduced from 30 to 3 μm. The stochastic cooling time scales as the number of particles [16],

$$\tau \approx N \times 10^{-8}\text{s}. \quad (1)$$

Thus, to cool 12x more antiprotons, 12 independent cooling systems [17] would be implemented as shown in Fig. 3. Each system would have a debuncher/momentum equalizer, which would use RF cavities to reduce the 2% momentum spread by decelerating fast antiprotons and accelerating slow ones. In addition the central momenta of all 12 channels would be equalized. The debuncher would alternately feed two accumulator rings. This doubles the time in the accumulator ring deposition orbit for more cooling and reduces required stack sizes. Hopefully, two accumulator rings can keep up with one 40 x 10^{10} $\bar{p}$/hr debuncher output rate. A single electron cooling ring follows the stochastic cooling. Electrons can cool large numbers of low emittance antiprotons in one ring [18].

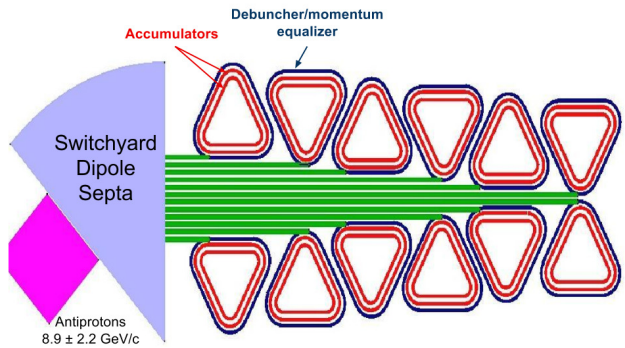

Figure 3: Independent cooling systems to cool more antiprotons. The 8.9 ± 2.2 GeV/c beam is spread by a bending magnet system and separated into 12 momentum channels using 11 electrostatic septa strings. Each debuncher ring phase rotates the beam to the lower the momentum spread and also ramps the beam central momenta up or down to 8.9 GeV/c. Each debuncher alternately outputs antiprotons to one of two associated accumulator rings.

COLLIDER PARAMETERS

For the 100 TeV $p\bar{p}$ collider, the 200 km ring could be constructed at CERN and connected to the LHC tunnel. For antiproton production, a Fermilab-like antiproton source would be adapted to the new collider with 12 debuncher and 24 accumulator rings for stochastic cooling. The 27 km LHC ring would serve as the Main Injector Ring. Table 1 lists the main parameters for the Tevatron, the LHC, a 100 TeV (pp) Future Circular Collider FCC-hh, and this100 TeV $p\bar{p}$ collider [6, 10, 19–21].

INTERACTION REGION

Events from $p\bar{p}$ collisions are more central than from pp collisions, allowing a shorter detector and quadrupole triplet focal length. Note that $\beta^*\beta_{\max}$ is proportional to f^2, where f is the focal length. The focal length is the distance from the center of the quadrupole triplet that focuses the beam to the interaction point as shown in Fig. 4. The luminosity is proportional to $1/\beta^*$ and the quadrupole bores are proportional to $\sqrt{\beta_{\max}}$. High luminosity and small quadrupole bores are desirable. The IR optics can be much improved with one rather than two rings. One beam can pass through a smaller quadrupole bore than two separated beams [24].

ISBN 978-3-95450-174-8

Table 1: Parameter List for the Tevatron, the LHC, the Future Circular Collider FCC-hh, and the 100 TeV pp^- Proposed Here

Collider Parameters	Tevatron	LHC	FCC-hh	100 TeV pp̄	Unit
Luminosity (L)	3.4 x 10^{32}	1.0 x 10^{34}	5.0 x 10^{34}	1.0 x 10^{34}	$cm^{-2}s^{-1}$
Energy Center of Mass (E_{cm})	1.96	14	100	100	TeV
Magnetic Field (B)	4.3	8.3	16	8	T
Circumference (C)	6.28	27	100	200	km
Collision Frequency (f)	0.048	40	40	1.08	MHz
Lorentz Gamma Factor (γ)	1044	7460	53304	53304	
Number of Bunches (N_B)	36	2808	10600	720	
Number of Protons/Bunch (N_p)	29 x 10^{10}	11.5 x 10^{10}	10 x 10^{10}	29 x 10^{10}	
Number of Antiprotons/Bunch (N_a)	8 x 10^{10}			8 x 10^{10}	
Normalized RMS Transverse Emittance (ε_N)	3.0 (protons)	3.75	2.2	3.0 (protons)	μm
	1.5 (antiprotons)			1.5 (antiprotons)	μm
Betatron Function at IP (β^*)	0.28	0.55	1.1	0.3	m
Beam Size at IP (σ)	33 (protons)	16.6	6.8	4.1 (protons)	μm
	29 (antiprotons)			2.9 (antiprotons)	μm
Beam-Beam Tune Shift per IP (ξ)	0.012 (protons)	0.003	0.005	0.012 (protons)	
	0.006 (antiprotons)			0.006 (antiprotons)	
Number of IPs (N_{IP})	2	4	2	2	
Hourglass Factor (H)	0.65	1	1	1	
Energy loss per turn (U_0)	0.0000095	0.0067	4.6	2.3	MeV
Longitudinal Emittance Damping Time (τ_ε)	305	13	0.5	2.0	h
Transverse Emittance Damping Time (τ_x)	610	26	1.0	4.0	h

IR parameters for a 100 TeV pp collider [23] are taken as reference to get a smaller L* (distance from the interaction point to the first quadrupole) by using the hard-edge model for quadrupoles. The beta values (β_x, β_y) are plotted as a function of the longitudinal coordinate s in Fig. 4.. The average value of β^* obtained correspond to 0.3 m. A gradient of 225 T/m could be provided by Nb_3Sn superconducting quadrupoles [25].

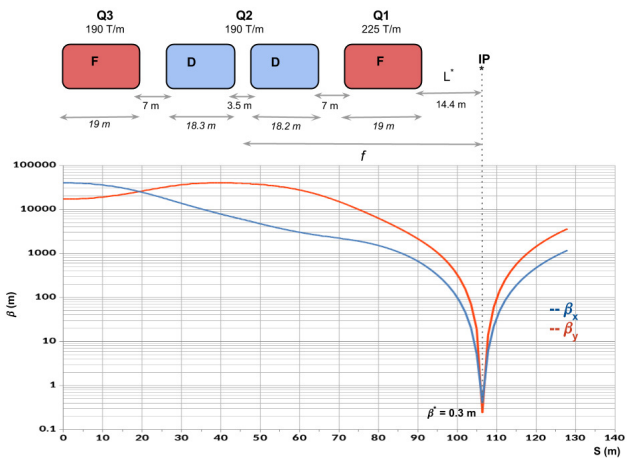

Figure 4: Betatron function distributions for the Interaction Region.

BUNCH RECYCLING

Antiprotons in the collider ring would be recycled without leaving the collider ring. This would increase the availability of antiprotons by a factor of about two. To allow this, the beam energy would have to be occasionally lowered as was done at the S$p\bar{p}$S ramping run [26]. Continuous (trickle charge) injection improved integrated luminosity at PEP-II [27]. Snap bunch coalescence [28] would be used to join new and old antiproton bunches, and then synchrotron damping would make the joined bunches smaller. Final antiproton cooling would be done by synchrotron damping in the collider ring, with longitudinal and transverse damping times of 2 and 4 hours, respectively.

CONCLUSION

A high luminosity proton-antiproton collider presents a promising future. It offers some advantages with respect to a proton-proton collider in terms of cross section for many high mass states, which are about 10x higher. This avoids high beam currents and reduces synchrotron radiation in superconducting magnets and the vacuum system. For antiproton production, Fermilab had a powerful antiproton source, which would be implemented and extended to capture and store 12 times more antiprotons, with 36 independent cooling rings. The antiproton yield increases by a factor of about 20 due to reduced accumulator ring losses.. Recycling antiprotons in the collider ring yields another factor of about two. A total of roughly 40 times more antiprotons than at the Tevatron may be enough to support two 100 TeV interaction points with a luminosity of 10^{34} cm^{-2} s^{-1} at each IP.

REFERENCES

[1] G. Aad et al. (ATLAS), Phys. Lett. **B716** (2012) 1;
S. Chatrchyan et al. (CMS), Phys.Lett. **B716** (2012) 30.

[2] Henry Frisch, private communication, 2011.

ISBN 978-3-95450-174-8

[3] G. T. Lyons III, Master's Thesis, arXiv:1112.1105;
D. J. Summers et al., AIP Conf. Proc. **1507** (2012) 860.

[4] R. B. Palmer, B. Parker, G. W. Foster, Snowmass -2001-T205;
L. Rossi, Supercond. Sci.Technol. **23** (2010) 034001.

[5] G. Ambrosio et al. (VLHC), FERMILAB-TM-2149 (2001);
J. Tang et al., arXiv:1507. 03224.

[6] Michael Benedikt, Daniel Schulte, and Frank Zimmermann, Phys. Rev. ST Accel. Beams **18** (2015) 101002.

[7] J. Gallardo et al., Snowmass 1996, BNL -52503;
D. Neuffer and R. Palmer, Conf.Proc. C940627 (1994) 52;
R. Palmer et al., Nucl. Phys. Proc. Suppl. **51A** (1996) 61;
D. Cline and D. Neuffer, AIP Conf. Proc. **68** (1980) 856;
D. Neuffer, IEEE Trans. Nucl. Sci. **28** (1981) 2034;
S. Ozaki et al., BNL-52623 (2001);
D. Neuffer, CERN-YELLOW-99-12;
C. M. Ankenbrandt et al., PRSTAB **2** (1999) 081001;
M. M. Alsharo'a et al., PRSTAB **6** (2003) 081001;
R. Palmer et al., PRSTAB **8** (2005) 061003;
D. J. Summers et al., PAC 2007, arXiv:0707.0302;
J. Gallardo and M. Zisman, AIP Conf. Proc. **122** (2010) 308;
C. Yoshikawa et al., IPAC-2014 -TUPME016;
D. Stratakis and R. Palmer, PRSTAB **18** (2015) 031003;
J. G. Acosta et al., COOL-2015-MOPF07.

[8] W. Barletta et al., Nucl. Instrum. Meth. **A764** (2014) 352.

[9] C. Rubbia, P. McIntyre, and D. Cline, eConf C760608 (1976) 683; David B. Cline, Carlo Rubbia, and Simon van der Meer, Sci. Am. **246N3** (1982) 38;
Simon van der Meer, Rev. Mod. Phys. **57** (1985) 689.

[10] J. Peoples, IEEE Trans. Nucl. Sci. **30** (1983) 1970;
Tevatron Design Report, FERMILAB-DESIGN-1984-01;
R. J. Pasquinelli et al., FERMILAB-CONF-09-126-AD;
S. Holmes et al., JINST **6** (2011) T08001;
S. Nagaitsev, arXiv:1408.0759.

[11] B. Franzke et al., Nucl. Instrum. Meth. **A532** (2004) 97;
C. Dimopoulou, IPAC-2014-MOPRI067.

[12] J. Alwall et al., JHEP **1106** (2011) 128.

[13] V. Lebedev, COOL09 -MOA1MCCO02 (2009).

[14] R. Joshel et al., Conf.Proc. C870316 (1987) 515;
L. W. Oleksiuk et al., IEEE Trans. Nucl. Sci. **20** (1973) 428;
C. H. Rode et al., IEEE Trans. Nucl. Sci. **18** (1971) 984.

[15] J.-B. Lagrange et al., Nucl. Instrum. Meth. **A691** (2012) 55.

[16] M. G. Minty and F. Zimmermann, *Measurement and Control of Charged Particle Beams* (2003) page 297;
R. B. Palmer, BNL -18395 (1973);
D. Mohl et al., Phys. Rept. **58** (1980) 73;
Simon van der Meer, AIP Conf. Proc. **153** (1987) 693;
F. Caspers and D. Mohl, Nucl. Instr. Meth. **A532** (2004) 321.

[17] Peter McIntyre, private communication, 2015.

[18] S. Nagaitsev et al., Phys. Rev. Lett. **96** (2006) 044801;
A. Shemyakin and L. R. Prost, COOL-2011-THIOA01;
S. Nagaitsev et al., JINST **10** (2015) T01001.

[19] V. Kamerdzhiev, Y. Alexahin et al., COOL2007-THM2I04;
W. Wu and D. Summers, arXiv:1505.06482;
R. Becker and W. B. Herrmannsfeldt, SLAC-PUB-11949.

[20] V. Shiltsev, EPAC08 -TUXG02 (2008).

[21] F. Su et al., arXiv:1503.01530.

[22] S. Feher and J. Strait, SNOWMASS-1996-ACC042.

[23] R. Martin et al., IPAC-2015-TUPTY001.

[24] José Luis Abelleira, CERN-THESIS-2014-072, page 119;
P. McIntyre and A. Sattarov, PAC09-WE6PFP041 (2009).

[25] P. Ferracin et al., IEEE Trans. Appl. Supercond. **24** (2014) 4002306.

[26] J. G. Rushbrooke, CERN-EP/82-6;
C. Albajar et al. (UA1), Nucl. Phys. **B309** (1988) 405.

[27] J. T. Seeman, EPAC08-TUXG01 (2008).

[28] G. W. Foster, FERMILAB -TM-1902 (1994);
I. Kourbanis et al., Conf. Proc. C930517 (1993) 3799;
S. Stahl and J. MacLachlan, FERMILAB -TM-1650 (1990).

ISBN 978-3-95450-174-8

DEVELOPMENT OF THE ELECTRON COOLING SIMULATION PROGRAM FOR MEIC*

H. Zhang#, J. Chen, R. Li, Jefferson Lab, Newport News, VA 23606, USA
H. Huang, L. Luo, Old Dominion University, Norfolk, VA 23529, USA

Abstract

In the medium energy electron ion collider project at Jefferson Lab, the traditional electron cooling technique is used to reduce the ion beam emittance at the booster ring, and to compensate the intrabeam scattering effect and maintain the ion beam emittance during collision at the collider ring. A DC cooler at the booster ring and a bunched beam cooler at the collider ring are proposed. To fulfil the requirements of and the cooler design for MEIC, we are developing a new program, which allows us to simulate the following cooling scenarios: DC cooling to coasting ion beam, DC cooling to bunched ion beam, bunched cooling to bunched ion beam, and bunched cooling to coasting ion beam. The new program has been benchmarked with existing code in aspect of accuracy and efficiency. The new program will be adaptive to the modern multicore hardware. We will present our models and some simulation results.

MEIC COOLING SCHEME

At Jefferson Lab, the medium energy electron ion collider (MEIC), to reach the frontier in Quantum Chromodynamics, will provide an electron beam with energy up to 10 GeV, a proton beam with energy up to 100 GeV, and heavy ion beams with corresponding energy per nucleon with the same magnetic rigidity. The center-of-mass energy goes up to 70 GeV. Two detectors, a primary one with full acceptance and a high-luminosity one with less demanding specification, are proposed. To achieve the ultrahigh luminosity close to 10^{34} $cm^{-2}s^{-1}$ per detector with large acceptance, the traditional electron cooling will be implemented strategically. [1]

The MEIC ion complex consists of ion sources, an SRF linac, a booster ring and a medium energy collider ring, as shown in Fig. 1. Since the electron cooling time is in proportion to the energy and the 6D emittance of the ion beam, which means it is easier to reduce the emittance at a lower energy, a multi-stage cooling scheme has been developed. A low energy DC cooler will be installed at the booster ring, which will reduce the emittance to the desired value for ion beams with the kinetic energy of 2 GeV/u. A bunched beam cooler will be installed at the collider ring, which helps to compensate the intrabeam scattering (IBS) effect and maintain the emittance of the ion beam during the injection process and during the collision.

* Work supported by the Department of Energy, Laboratory Directed Research and Development Funding, under Contract No. DE-AC05-06OR23177.
#hezhang@jlab.org

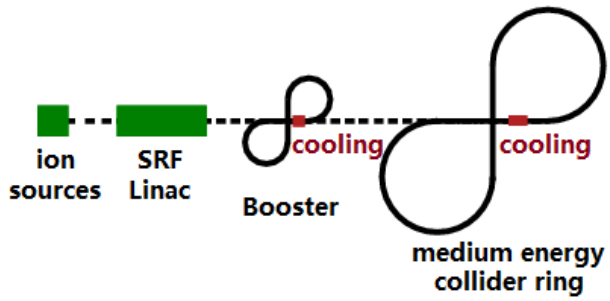

Figure 1: Components of MEIC ion complex.

CODE DEVELOPMENT GOALS

The DC cooler is within the state-of-art. [2] But the bunched beam cooler is out of the state-of-art and needs significant R&D. Numerical simulation is inevitable for the design and optimization of the MEIC electron cooling system. BETACOOL has been used in our preliminary study and it has successfully supported the MEIC design. As the study goes more in-depth, it will be beneficial to have a more efficient and more flexible tool to fulfil some specific needs of MEIC.

The goal of this new simulation program is to enhance the simulation capability for electron cooling in MEIC project. It will preferentially fulfil the needs of MEIC design. The program simulates the evolution of the macroscopic beam parameters, such as emittances, momentum spread and bunch length, in different electron cooling scenarios: DC cooling, bunched electron to bunched ion cooling, bunched electron to coasting ion cooling, etc.

Since BETACOOL has provided a collection of physical models for various electron cooling simulations [3], we decided to follow the models in BETACOOL, whenever they are applicable, and revise them when necessary. We also want to improve the efficiency by strategical arrangement of the calculation and/or by implementation of the models on modern multicore platform.

INTRABEAM SCATTERING

The intrabeam scattering (IBS) effect can cause significant increase of the emittance of the ion beam, due to the high intensity of them, in MEIC in a short time, which ruins the luminosity of the collider. The emittance change rate due to the IBS effect can be calculated using several different formulas under different assumption of the ion beam profile and lattice parameters. [4-7] Here we choose Martini model [5] for the IBS rate calculation for MEIC. Martini model assumes Gaussian distribution for the ion beam, which is reasonable at least for the first

ISBN 978-3-95450-174-8

order, and the absence of vertical dispersion of the lattice, which is true for MEIC booster ring and collider ring. In Martini model the IBS expansion rate has the following expressions:

$$\frac{1}{\tau_p} = \langle \frac{nA}{2}(1-d^2)f_1 \rangle,$$
$$\frac{1}{\tau_x} = \langle \frac{A}{2}\left[f_2 + (d^2+\tilde{d}^2)f_1\right] \rangle,$$
$$\frac{1}{\tau_z} = \langle \frac{A}{2} f_3 \rangle.$$

The brackets indicate to take average over all the elements. Function f_i is a 3D integral as follows:

$$f_i = k_i \iiint \sin\mu g_i(\mu,\nu) \exp[-D(\mu,\nu)z] \ln(1+z^2) d^3V$$

The grid (μ, ν, z) for the 3D integral is user defined. The integral in z can be replaced by the Coulomb logarithm, which is typically around 20. Function g_i is defined as

$$g_1(\mu,\nu) = 1 - 3\sin^2\mu\cos^2\nu,$$
$$g_2(\mu,\nu) = 1 - 3\sin^2\mu\sin^2\nu + 6\tilde{d}\sin\mu\sin\nu\cos\nu\,/a,$$
$$g_3(\mu,\nu) = 1 - 3\cos^2\mu.$$

All the other parameters can be derived from the TWISS parameters and/or the beam parameters.

The calculation of f_i is very expansive in time and it needs to be repeated for all the elements, the number of which easily goes up to a few hundred or more. However, most of the components of g_i only depends on the user defined grid of (μ, ν, z). The values of these components will remain the same no matter when and where they are calculated, once the grid is defined by the user. Those values only need to be calculated once and saved in the memory. They will be reused for all the elements. Avoiding the repeated computation of g_i for different elements, one can reduce the computation time significantly.

ELECTRON COOLING RATE

The electron cooling rate is defined as the emittance change in a unit time due to the electron cooling effect. We borrow two models from BETACOOL for electron cooling rate calculation: the single particle model and the Monte Carlo model. Using the single particle model, the ion beam will be sampled as a group of ions distributed evenly in the ellipsoid of the given emittance in the phase space. Using the Monte Carlo model, the ion beam will be sampled as a Gaussian bunch whose rms size is determined by the given emittance and the TWISS parameter at the cooler. The friction force on each ion will be calculated. Assuming the friction force is constant while the ion passes through the cooler, the change of momentum of each ion can be calculated. Then the new emittance and the change rate of the emittance can be calculated statistically. Although there are different formulas for friction force calculation, currently we only implement the Parkhomchuk formula in the program, because both the coolers for MEIC are magnetized.

During the injection from the booster ring to the collider ring, the bunched beam cooler will be used to compensate the IBS effect of the coasting ion beam. There are two ways in BETACOOL to model a coasting beam. One way is to put the sample particles on one crass section of the beam. Using such a model, the ion beam can only see a slice of the electron beam. So it works well for DC cooling when the electron beam is homogenous longitudinally. But for bunched electron beam, this model neglects the effect of the variance of the electron distribution. The other way is to put the sample particles all along the ring. The circumference of the MEIC collider ring is more than 2000 m, while the rms length of the electron bunch is only around 2 cm. In such a case, if the number of the ion sample is not large enough for an accurate calculation of the cooling rate. Even if the number of the ion sample is large enough, the calculation efficiency will be bad, since most of the ions do not see the electrons and the time cost on them are wasted. To avoid the above dilemma, we decide to only sample the coasting ion beam around the electron bunch, as shown in Fig. 2. A duty factor is defined as D = L_s/L_d, where L_s is the length of the sample area and L_d is the distance between two electron bunch. The cooling rate of the whole coasting ion beam is calculated as the multiplication of the cooling rate of the sample area and the duty factor. This model assumes the cooling effect is distributed evenly among the ions by diffusion. The electron bunch profile could be taken into account using this model.

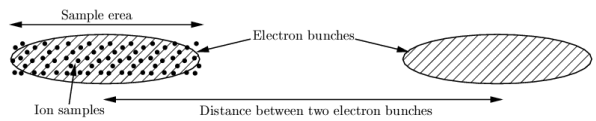

Figure 2: Model of ion beam cooled by electron bunch.

ELECTRON COOLING DYNAMICS

There are two methods in BETACOOL to simulate the evolution of the ion beam emittance during the electron cooling process: the RMS dynamics method and the model beam method. Both of them are implemented in the new program. Using the RMS dynamics method, one assumes the ion beam maintains the Gaussian distribution during the cooling process. For a given time t_i, the total emittance change rate $1/\tau$, as the summation of the IBS expansion rate and the electron cooling rate, can be calculated. Then at the next time t_{i+1} the emittance is calculated as $\varepsilon_{i+1} = \varepsilon_i \cdot e^{dt/\tau}$, where $dt = t_{i+1} - t_i$, and ε_i and ε_{i+1} are the emittances at the respective time. Using the model beam method, one creates a group of ions as the sample of the ion beam at the initial time. IBS effect is treated as a random kick to each ion, which leads to a change of the momentum. Friction force of electron cooling also changes the momentum. Besides these two effects, each ion also makes a random phase advance from time t_i to t_{i+1}. In this way, one can simulate the evolution of the ion beam distribution during the electron cooling process. For example, under a strong electron cooling effect the ion distribution often deviates from Gaussian, which has been observed in experiments, because the center of the ion beam obtains stronger cooling effect than the edge. In such a case, the model beam method is preferred. For more details about these two models, please refer to [3].

ISBN 978-3-95450-174-8

BENCHMARK

The new program has been benchmarked with BETACOOL for typical scenarios of MEIC. A few examples are given in the following. In all the figures, the results of BETACOOL are represented by lines, while the results of the new program are represented by dots.

In Fig. 3 we compare the emittance expansion due to the IBS effect during one hour for (a) the coasting proton beam in the booster ring at 800 MeV and (b) the bunched proton beam in the collider ring at 30 GeV. In Fig. 4 we compare the emittance shrink due to electron cooling in the booster ring (a, b) for coasting proton beam with DC cooler and in the collider ring (c, d) for bunched proton beam with bunched beam cooler. RMS dynamics method is used in a and c, while model beam method is used in b and d. The cooling rate is calculated by the Monte Carlo method in a, and by single particle method in c. In Fig. 5, we compare the emittance evolution under both the IBS effect and the electron cooling effect, which is simulated using RMS dynamic method. The subfigure a shows the cooling process with the DC cooler in the booster ring for the coasting proton beam at 800 MeV. The subfigure b shows the equilibrium between the IBS effect and the electron cooling effect with bunched beam cooler in the collider ring for the bunched proton beam at 100 GeV.

In all the cases, the two programs agree very well. To compare the efficiency of the two programs, we use the same step size and the same total steps to simulate the same number of particles in the last two simulations shown in Fig. 5. For the DC cooling in the booster ring, Fig. 5a, it costs 133 seconds using the new program, or 3060 seconds using BETACOOL. For the bunched beam cooling in the collider ring, Fig. 5b, it costs 31 seconds using the new program, or 422 seconds using

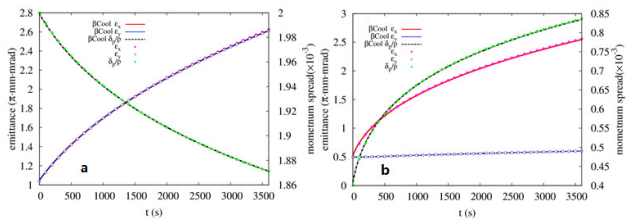

Figure 3: Emittance expansion due to IBS effect.

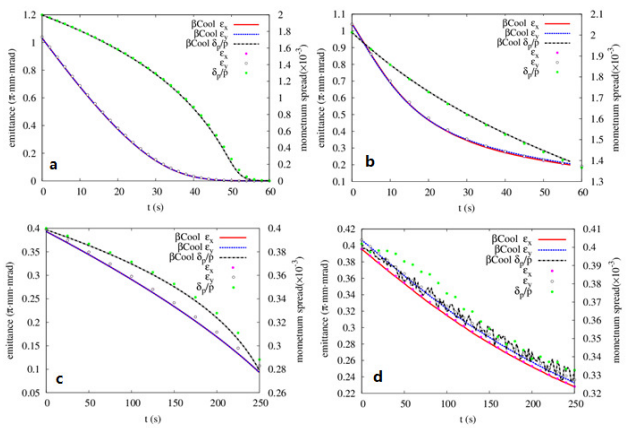

Figure 4: Emittance shrink due to electron cooling.

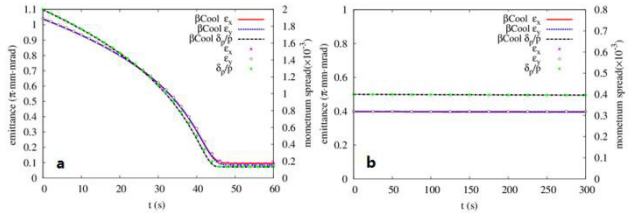

Figure 5: Emittance evolution under both the IBS effect and the electron cooling effect.

BETACOOL. The efficiency has been improved for more than ten times without any parallelization. To be fair, we want to point out that BETACOOL plots the emittance evolution curve during simulation, while the new program only dump out the data. All the plots have to be done by users.

SUMMARY

A new program has been developed to simulate the evolution of the macroscopic beam parameters under the intrabeam scattering (IBS) effect and/or electron cooling. A serial version of the program has been finished and benchmarked with BETACOOL for typical scenarios in MEIC electron cooling design. The results of the two programs agree very well. Computation efficiency has been improved significantly by avoiding redundant computation. The new program brings more flexibility to better fulfil the requirements of MEIC on electron cooling simulations. Now with moderate effort, we can integrate new models into simulations. We have actively implemented the new program in MEIC electron cooler design. At the same time we keep polishing the algorithm and the code. A multiple thread version of the program is under construction, for which one can reasonably expect a further improvements on efficiency.

REFERENCES

[1] S. Abeyratne et al., "MEIC Design Summary", arXiv:1504.07961, (2015).

[2] V. N. Bocharov, et al., "Commissioning of the 2 MeV Electron Cooler for COSY/HESR" Proc. of IPAC'12, New Orleans, Louisiana, USA (2012).

[3] I. Meshkov et al., "BETACOOL Physics Guide", (2007); http://betacool.jinr.ru

[4[A. Piwinski, "Intrabeam Scattering", Proc. of 9th Int. Conf. on High Energy Accelerators, p. 105, (1974).

[5] M. Martini, "Intrabeam Scattering in the ACOL-AA Machines", CERN PS/84-9 AA, (1984).

[6] J. D. Bjorken, S.K. Mtingwa, "Intrabeam Scattering", Particle Accelerators, Vol. 13, p. 115, (1983).

[7] J. Wei, "Evolution of Hadron Beams under Intrabeam Scattering", Proc. of PAC'93, p. 3651, (1993).

[8] V. Parkhomchuk, "New Insight in the Theory of Electron Cooling", NIM A 441.1 (2000): 9-17, p. 9, (2000).

ISBN 978-3-95450-174-8

MICE DEMONSTRATION OF IONIZATION COOLING*

Tanaz Angelina Mohayai#, Illinois Institute of Technology, Chicago, IL
on behalf of the MICE Collaboration

Abstract

The goal of the international Muon Ionization Cooling Experiment (MICE) is to demonstrate transverse emittance reduction of a muon beam through use of absorber materials, RF cavities, and focusing solenoids. Low emittance muon beams are basic to Neutrino Factory and Muon Collider studies. In summer 2014, following the P5 report, a revised project plan for MICE was approved with a cooling lattice consisting of one central (primary) and two secondary LiH absorbers for energy loss, two 201 MHz RF cavities for beam re-acceleration, two solenoidal spectrometers for emittance measurement, and two focus coils to focus the muon beam. The superconducting magnets, absorbers and detectors necessary for the final stage of the experiment are already in hand and a 201 MHz prototype RF cavity module is under test at Fermilab's MuCool Test Area. We describe the muon ionization cooling concept, the redesigned cooling lattice of the MICE Demonstration of Ionization Cooling, and the cooling performance of the redesigned lattice.

INTRODUCTION

Stored low emittance muon beams lay the foundation for intense, well-parameterized neutrino beams at the Neutrino Factory and high-luminosity Muon Colliders [1]. Typical muon beams produced at the front ends of these facilities have an emittance range of 15-20 π·mm·rad. The desired muon beam emittance range at the Neutrino Factory is 2-5 π·mm·rad [2]. The Muon Collider needs further cooling with a desired transverse emittance of 0.025 π·mm·rad and longitudinal emittance of 72 π·mm·rad [3]. In order to produce a muon beam at such facilities, a high power proton beam collides and interacts with a target to produce pions, which in turn decay to muons. Such muon beams occupy a large phase space volume and in order to optimize muon yield, fit the beam into small apertures, and achieve the required luminosity, one would need to reduce the phase space volume occupied by the beam [4]. Given the muon's large mass and short lifetime, the traditional cooling techniques—synchrotron radiation and stochastic or electron cooling—are inefficient in cooling the muon beam.

*Work supported by the (US) National Science Foundation and Department of Energy, the (Italy) Instituto Nazionale di Fisica Nucleare, and the (UK) Science and Technology Facilities Council.
#tmohayai@hawk.iit.edu

Taking advantage of the muon's long interaction length, ionization cooling is suitable (and is the only feasible technique) for reducing the muon beam emittance in a time comparable to the muon lifetime [5].

In order to accomplish sustainable ionization cooling, the muon beam transverse and longitudinal momenta must be reduced via energy loss in an absorber material, with its longitudinal momentum subsequently restored in RF cavities. The rate of change of the normalized transverse emittance is

$$\frac{d\varepsilon_{in}}{ds} \cong -\frac{\varepsilon_{in}}{\beta^2 E_\mu}\left\langle\frac{dE}{ds}\right\rangle + \frac{\beta_\perp (13.6\text{MeV})^2}{2\beta^3 E_\mu m_\mu X_0}. \qquad (1)$$

where βc, E_μ, and m_μ are the muon velocity, energy, and mass, dE/ds the energy loss rate through ionization, X_0 the absorber radiation length, and $\beta_\perp$ the transverse beta function at the absorber. The first term in Eq. 1 describes cooling via energy loss and the second term heating due to multiple Coulomb scattering. When the heating term and the cooling term are equal, the cooling channel is said to be at "equilibrium emittance". Setting $\frac{d\varepsilon_{in}}{ds}$ equal to zero yields

$$\varepsilon_{in} \cong \frac{\beta_\perp (13.6\text{MeV})^2}{X_0 2\beta m_\mu}\left\langle\frac{dE}{ds}\right\rangle^{-1}. \qquad (2)$$

A smaller equilibrium emittance leads to a more effective emittance reduction which from Eq. 2 can be achieved by minimizing $\beta_\perp$ and maximizing X_0 and dE/ds [2]. Experimentally, use of a solenoid focusing channel leads to small transverse betatron functions, and use of low-Z absorber materials such as LiH (lithium hydride) leads to large radiation length and energy loss. The muons passing through low-Z absorber material lose energy due to electromagnetic interactions with the atomic electrons of the material and in general for the cooling effect to dominate, the low-Z materials are placed in strong focusing fields [2]. The MICE cooling lattice components make use of the muon ionization cooling concept, and they are described in the following section.

ISBN 978-3-95450-174-8

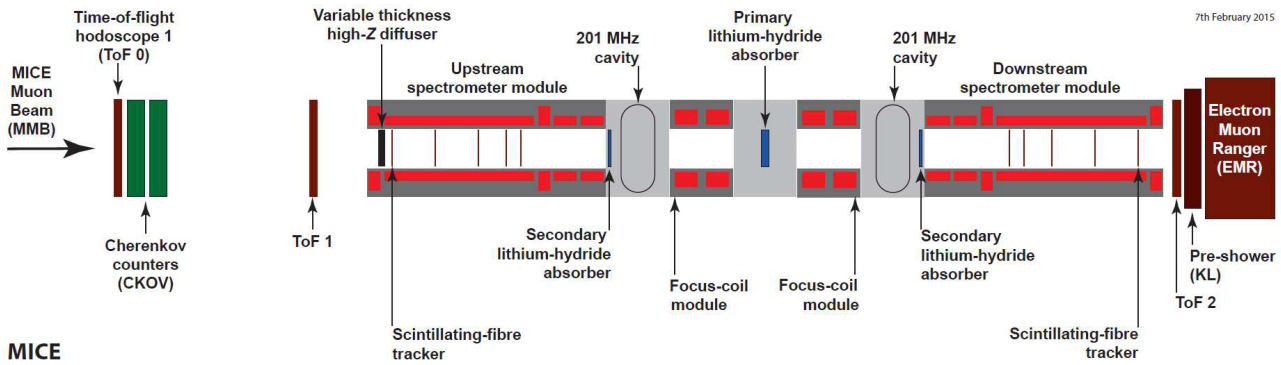

Fig 1: Schematic diagram of the final MICE cooling demonstration step.

MICE COOLING LATTICE

The revised lattice design of the Ionization Cooling Demonstration Step of MICE (shown in Fig. 1) is set to demonstrate sustainable muon cooling with reacceleration. The experiment will be operational in 2017.

The Ionization Cooling Demonstration step makes use of one central and two secondary LiH absorbers interspersed with superconducting focus coils. The two focus coils are designed to reduce multiple Coulomb scattering by providing a small beta waist at the location of the absorbers. The focus coils have two modes of operation, “solenoid” and “flip”. The purpose of the flip mode of operation is to control the accumulation of canonical angular momentum in the cooling lattice [2]. The secondary LiH absorbers are located between the RF cavities and the scintillating fiber trackers, upstream and downstream of the central absorber, and they contribute to the net reduction in transverse cooling. The secondary absorbers also screen the scintillating fiber trackers from RF cavity x-rays. The scintillating fiber trackers inside the spectrometer solenoid modules reconstruct the muon beam tracks and along with the other MICE detectors reconstruct and measure the emittance to about 0.1% accuracy [4].

The upstream and downstream spectrometer solenoids are each made of five superconducting coils. The three central coils of the spectrometer solenoids are responsible for producing a uniform 4 T magnetic field at the locations of the five scintillating fibre tracker stations. The other two superconducting coils are responsible for matching the beam entering and leaving the cooling lattice. The upstream spectrometer solenoid has a high-Z diffuser which controls the initial muon beam emittance before entry to the cooling channel [2]. The cooling lattice also has two 201 MHz RF cavities each with a peak RF gradient of around 10 MV/m for restoring the beam's lost longitudinal momentum [6]. In the section that follows, the results of the Monte Carlo simulation studies and the analysis of the cooling performance of the redesigned lattice are presented.

COOLING LATTICE PERFORMANCE

In the MICE cooling lattice design studies, a realistic input muon beam is simulated using the MICE Analysis User Software, MAUS. The role of MAUS is to model the particle trajectories and electronics response in MICE, reconstruct the particle tracks either from MC or data electronics signals, and provide the framework for accelerator physics analysis [7].

The transverse betatron function evolution along the MICE cooling lattice is shown in Fig. 2. In order to elucidate the cell performance over a range of momenta, Fig. 2 displays the transverse beta function for varying momentum values of 140 MeV/c, 200 MeV/c, and 240 MeV/c, while keeping the initial beam emittance at a constant value of 6 π·mm·rad. As expected, the transverse beta function is focused at the location of the central LiH absorber due to the focus coils, while a large beam size is observed at the locations of the RF cavities. The beta values at $z \sim \pm 4000$ mm reflect respectively the upstream and downstream uniform 4 T regions of the cooling lattice at the locations of the two scintillating fiber trackers. With smaller beta values at the location of the absorbers, one would get a more effective emittance reduction [2].

Figure 3 displays the transverse emittance evolution along the MICE cooling channel. Due to nonlinear effects in high transverse beta regions, emittance growth is observed at the RF cavity locations. However, there is an overall emittance reduction of 5.6% between the upstream and the downstream trackers [2].

Figure 4 displays the fractional change in emittance versus the input emittance. Larger input emittance leads to better overall beam emittance reduction.

Figure 5 displays the muon transmission versus initial emittance. The smaller the input emittance in Fig. 3, the higher the muon beam transmission in the cooling lattice and even at large input emittance values, we have a high transmission of muons of ~90%.

ISBN 978-3-95450-174-8

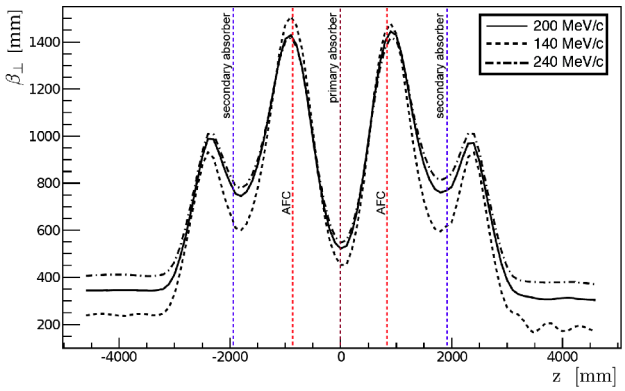

Fig 2: Evolution of the transverse betatron function along the redesigned cooling channel of MICE.

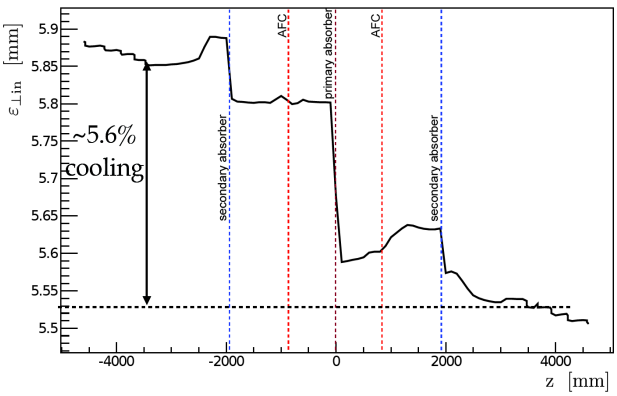

Fig 3: Evolution of 4D transverse emittance along the redesigned cooling channel of MICE for 200 MeV/c muon beam.

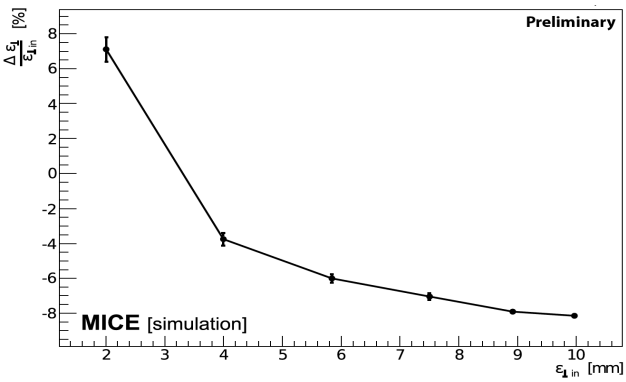

Fig 4: Fractional change in normalized 4D emittance vs. input beam emittance for 200 MeV/c muon beam; error bars represent estimated reconstructed measurement errors.

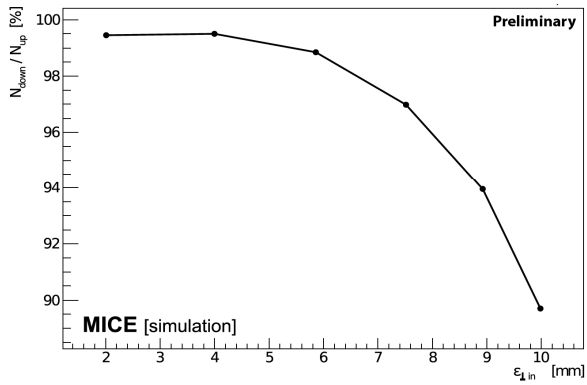

Fig 5: Muon beam transmission vs. input beam emittance for 200 MeV/c muon beam.

CONCLUSION

MICE is scheduled to demonstrate ionization cooling with reacceleration with a redesigned lattice, consisting of three lithium-hydride absorbers, two 201 MHz RF cavity modules, and two solenoidal focus coils. The required instrumentation for the MICE Demonstration of Ionization Cooling is either in hand or at an advanced stage of preparation and the redesigned cooling lattice shows excellent cooling. Demonstration of ionization cooling in MICE sets the basis for high luminosity and intense muon beams at the Neutrino Factory and the Muon Collider. As a result, a successful completion of MICE is an essential step to establishing a new technique in particle physics and accelerator physics.

ACKNOWLEDGMENT

Work described here has been made possible through generous funding from the Department of Energy, the National Science Foundation, the Instituto Nazionale di Fisica Nucleare, and the Science and Technology Facilities Council.

REFERENCES

[1] D. M. Kaplan, “From Neutrino Factory to Muon Collider”, Proc. NuFact2011, AIP Conf.Proc. 1382 (2011) 64.

[2] V. Blackmore, C. Hunt, J-B. Lagrange, J. Pasternak, C. Rogers, P. Snopok, H. Witte “The MICE Ionization Cooling Demonstration: Technical Note”, MICE Note 452 (2014).

[3] R. Palmer et al., “A Complete Scheme of Ionization Cooling for a Muon Collider”, Proc. PAC’07, Albuquerque, New Mexico, USA (2007).

[4] J. Pasternak, V. Blackmore, C. Hunt, J-B. Lagrange, K. Long, N. Collomb, V. C.

ISBN 978-3-95450-174-8

Palladino, R. Preece, C. Rogers, J. Tarrant, P. Snopok, "MICE Demonstration of Ionization Cooling", Proc. IPAC'15, IPAC-2015-THPF129, Richmond, VA, USA (2015).

[5] R. C. Fernow, J. C. Gallardo, M. Green, H. G. Kirk, D. V. Neuffer, J. Norem, R. B. Palmer, et al, "Ionization Cooling", DPF/DPB New Directions in High-energy Physics, Ch 6, BNL-52503 (1996).

[6] Y. Torun et al., "Installation and Commissioning of the MICE RF Module Prototype", Proc. WEPTY055, PAC '15, IPAC-2015-WEPTY055, Richmond, VA, USA (2015).

[7] Tunnell, C.D. et al. "MAUS: MICE Analysis User Software", Proc. IPAC'11, IPAC-2011-MOPZ013 (2011).

ISBN 978-3-95450-174-8

PROGRESS OF THE RF-SYSTEM DEVELOPMENTS FOR STOCHASTIC COOLING OF THE FAIR COLLECTOR RING

S. Wunderlich, R.M. Böhm, C. Dimopoulou, W. Maier, R. Menges, C. Peschke
GSI, Darmstadt, Germany

Abstract

An overview of the recent developments regarding the RF signal processing for the stochastic cooling system of the Collector Ring is given. In focus are the developments of RF components which can be used at different locations within the signal paths between the pickup and kicker tanks in the frequency band (1-2 GHz). Two of these components are discussed in detail, a directional power meter with high dynamic range (9 dBm to −68 dBm) , low phase distortion (±0.75 °(max)) and low attenuation (≤0.4 dB) and a variable phase shifter with exceptionally flat amplitude (±0.4 dB(max)) and linear phase response (±3.5 °(max)). Furthermore, we present the status and the newest enhancements of other components with stringent specifications, such as optical notch filters, pickup module controllers and the power amplifiers at the kickers.

INTRODUCTION

The main components of a stochastic cooling system are certainly the pickup and kicker devices. The signal processing between the pickup and kicker tanks has a great influence on the cooling performance as well. To achieve a high cooling efficiency a precise phase and amplitude control of the signals is necessary. Therefore it is crucial to monitor and affect these values according to the requirements of the integral system. The need to monitor and adjust certain values in the signal processing paths is typically not bounded to one particular point, instead there are multiple locations where phase and amplitude correction can be necessary. Standard RF components available at the market often do not fulfill crucial requirements (i.e. bandwidth, linear phase response etc.) for stochastic cooling. Therefore, the approach is to develop own RF components which meet our requirements and can be used at different locations without changing the design parameters of the respective devices. The next two sections cover the status of two in-house RF developments: a directional embedded power meter and a variable phase shifter. The subsequent sections present the development status of non-universal (i.e. fixed position, specialized purpose etc.) stochastic cooling components: notch filter, pickup module controller and power amplifies at the kickers.

EMBEDDED POWER METER

The embedded power meter consists out of two main components, a 20 dB broadband directional coupler with low insertion loss and low phase distortion and a power level detector with a high accuracy and wide dynamic range. The power level detector is a true RMS (Root Mean Square) device with a linear and temperature-compensated output voltage. It can measure any broadband signal with arbitrary waveform and crest factor changes over time [1]. The power meter should be used as a feedback to adjust the power levels and prevent gain compression. Additionally, a diagnostic I/O port was incorporated into the design, therefore the power meter can not only be used for measuring the power level of the input signal, but also to direct diagnostic signals into/out of the signal path. The diagnostic I/O port can be used to determine beam and system parameters which affect the cooling setup and performance. All components were dimensioned to work within the 1-2 GHz band of the stochastic cooling system. However, the system is also somewhat sensitive to out of band signal components in the 0.7 – 2.3 GHz range, therefore the power meter must also fulfill less stringent specifications within this extended band. Figure 1 shows a schematic of the power meter. To guarantee a reliable operation of the device several selftest circuits are embedded: a 10 MHz test signal generator which can be used to perform RF tests of the 20 dB amplifier, the Wilkinson power divider (resistive splitter), the RMS power detector and the “RF1” and “RFC” connection of the solid state relay. Three DC test points can be used to perform resistance and leakage current measurements. They can be used to check the DC characteristics of the 15 MHz low pass filter, directional coupler and “RF” connections of the solid state relay.

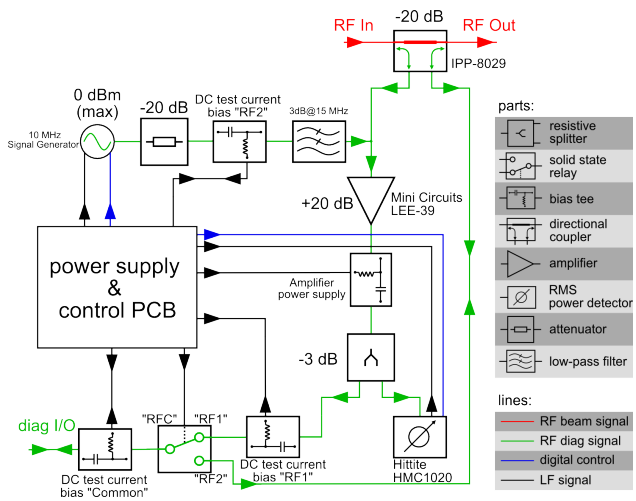

Figure 1: Block diagram of the embedded power meter.

A prototype (Fig. 2) of the power meter was build and the S-parameters were recorded. The determined electrical parameters of the prototype are given in Table 1[1].

[1] Phase distortion is defined as the deviation from the ideal linear phase response.

ISBN 978-3-95450-174-8

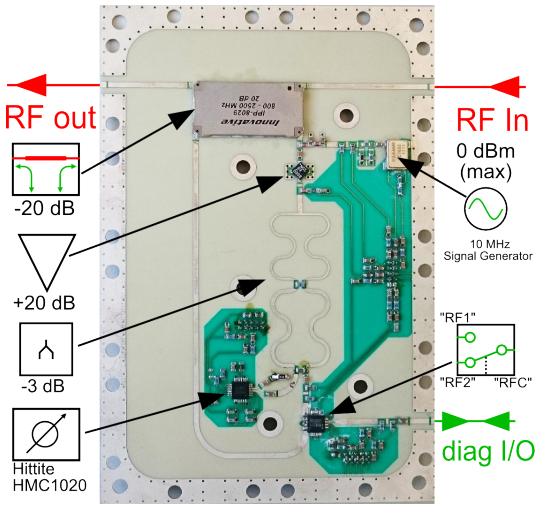

Figure 2: Prototype of the RF PCB of the power meter.

Table 1: Measured RF Values of the Power Meter

Parameter	Frequency	Values
Insertion Loss	0.7 - 2.3 GHz	0.2 dB - 0.55 dB
Insertion Loss	1 - 2 GHz	0.3 dB - 0.4 dB
Phase Distortion	0.7 - 2.3 GHz	±0.6 °
Group Delay	0.7 - 2.3 GHz	0.86 ns
Return Loss	0.7 - 2.3 GHz	≥ 14 dB
Dynamic Range	1.5 GHz	−68 dBm - 9 dBm
Detector Accuracy	1 - 2 GHz	≤ ± 1 dB

The data show that the critical values: insertion loss, amplitude response, phase distortion and group delay are within acceptable limits. Therefore, the device poses only a small imperfection to the signal path, which was a critical design aspect. At the same time, the dynamic range is quite high which provides versatile application possibilities for the power meter.

VARIABLE PHASE SHIFTER

Feeding the kicker modules with a correctly phase-shifted signal is crucial for the stochastic cooling system. A continuously variable phase shift is necessary to compensate position-dependent phase errors of the movable pickups. Therefore, the development of a variable phase shifter has begun. Simulations of the design show promising results, the prototype is underway. The basic concept of the phase shifter is a vector modulator (Fig. 3), the benefits of which are: high bandwidth (mainly dependent on the used 90 ° hybrid couplers), precise amplitude control, precise phase control and a simple structure with few active components (this guarantees a long lifetime and easy maintainability). Drawback of the design is an inherent 3 dB loss of the RF signal which increases the insertion loss of the device.

Basic principle of the vector modulator is to split the incoming RF signal into two components using a 90 ° hybrid coupler: an in-phase component (I component) and

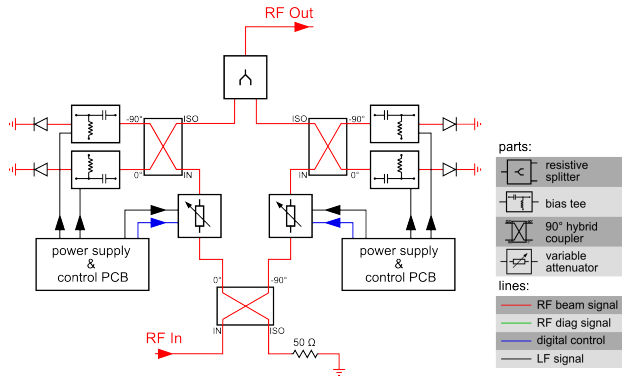

Figure 3: Block diagram of the variable phase shifter.

a 90° phase-shifted quadrature component (Q component). These two components can then be fed independently into a 0 °/180 ° phase shifter. In this case the 0°/180° phase shifter is constructed by using a 90 ° hybrid coupler with PIN diodes connected to the *coupled* and *through* ports. The impedance of the two PIN diodes can be changed from short circuit ($Z_L \approx 0\ \Omega$) to open circuit ($Z_L \approx \infty\ \Omega$). Depending on the status of the PIN diodes the signal than recombines at the *isolation* port of the respective hybrid coupler with a specific phase shift compared to the phase at the *input* port, 0 ° if Z_L is at maximum ($Z_L \gg Z_0 = 50\ \Omega$) and 180 ° if $Z_L \ll Z_0 = 50\ \Omega$). The 0 °/180 ° phase shifters can be used to determine in which quadrant of the constellation diagram the signal should be located. However, additional variable attenuators are necessary to achieve a fine phase adjustment. Any possible phase shift can be achieved by adjusting the magnitude of the I and Q components and recombining them using an in-phase (Wilkinson) combiner [2]. The actual phase resolution depends on the step size and accuracy of the used attenuators.

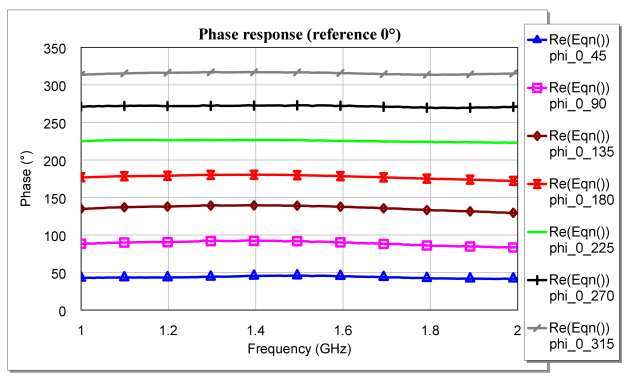

Figure 4: Phase Response (in 45 ° steps) of the phase shifter (in relation to 0 °).

The simulated S-parameters show satisfying results, especially regarding amplitude and phase response (Fig. 4). Table 2 shows the determined RF parameters.

ISBN 978-3-95450-174-8

Table 2: Simulated RF Values of the Phase Shifter

Parameter	Frequency	Values
Insertion Loss	1 - 2 GHz	7.25 dB - 8.75 dB
Amplitude Response	1 - 2 GHz	±0.4 dB
Amplitude Response	0.7 - 2.3 GHz	±1.5 dB
Phase Distortion	1 - 2 GHz	±3.5 °
Phase Distortion	0.7 - 2.3 GHz	±7.5 °
Average Group Delay	1 - 2 GHz	1.818 ns ± 7 ps
Return Loss	1 - 2 GHz	≥ 15 dB
Phase Resolution	1 - 2 GHz	≤ ± 1 °
Switching Freq.	1 - 2 GHz	25 kHz

OPTICAL NOTCH FILTER

Longitudinal stochastic cooling with the notch filter method is essential in the CR. Two notch filters (one for antiprotons at v=0.97 c, revolution frequency=1.315 MHz; one for RIBs at v=0.83 c, revolution frequency=1.124 MHz) have been developed and built.

The initial design was similar to the notch filter prototype in the ESR [3]. The first optimization was to substitute the symmetric optical splitter by an asymmetric one (Fig. 5). The asymmetric splitter makes additional attenuation on the short branch redundant. The short branch determines the propagation delay t_0 (i.e. the electrical length) of the filter, in our case t_0 = 3.45 ns. Each branch (the short and the long one) is demodulated to a RF signal (Fig. 5). The second optimization was to use a 180 ° power combiner (ZAPDJ-2-S) instead of the previously used 180 ° hybrid (ANZAC H 183-4) to substract those signals and provide the notch filter transfer function. The power combiner is linear (in amplitude and phase) in a broader frequency range that the hybrid.

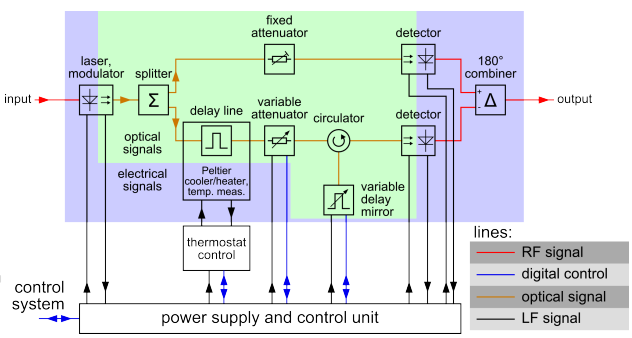

Figure 5: Block diagram of the CR optical notch filter.

In practice, within the bandwidth, a real filter has a finite (i.e. non-zero) low transmission (notch depth) at all harmonics nf_0. Because of non-linearity there is also a small deviation $f_n - nf_0$ between the frequencies f_n at which the transmission minima occur and the harmonics nf_0 (frequency periodicity error). Both effects affect the filter performance and lead to an increase of the equilibrium momentum spread of the cooled beam with respect to the ideal filter case.

We measured the transfer function of the notch filter in the pass band 1 to 2 GHz according to the CR requirements. The notch filter is mainly defined by the length of its optical delay line, for a fibre length of 160 m a time delay of 460 ps was necessary to setup a notch distance of $f_{0,set}$=1.234 966 MHz. The lower and higher harmonic number of $f_{0,set}$ in the bandwidth are n_1 = 810 and n_2 = 1619 respectively. As an example, the response at midband is shown in Fig. 6.

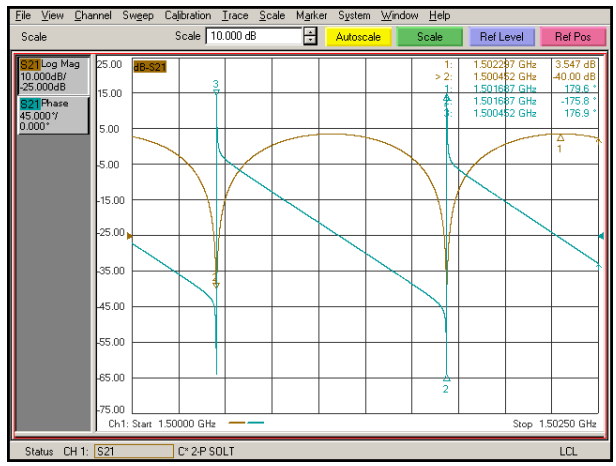

Figure 6: Measured response of the notch filter close to 2 notches at midband (1.5 GHz). The notch distance is 1.235 MHz. Because of the finite notch depth, the phase jump at each notch was less (177 °) than the 180 ° expected in the ideal case. The variable attenuator was set at 0.99 dB. (Due to temperature dependence of the setup later measurements vary in attenuation.)

In Fig. 7 the envelope (bottom line) of the measured amplitude $|S_{21}|$ at all in-band minima of the transfer function is displayed. In comparison, the envelope of $|S_{21}|$ at all in-band maxima (top line) represents the insertion loss mainly caused by the components in the long branch of the notch filter. It was found to be practically constant close to 3.5 dB within the whole band. All in-band notches have a depth $|S_{21}|_{\min} - |S_{21}|_{\max}$ lower than -30 dB. A vector network analyser and an automated test setup were used for these measurements (see [3] for details).

In order to quantify the periodicity error in the band, a linear regression fit was applied to the measured frequencies f_n (position of notches) for all harmonics n within the bandwidth: $f_n = f(n) = f_0 \times n + b$ = (1.234832 MHz) ×n-35.7 kHz. The slope f_0 represents a mean notch distance within the band. Because of the non-linearity it is slightly different than the setup notch distance $f_{0,set}$ given above. In the storage ring, the beam will be ultimately cooled by the notch filter to the revolution frequency f_0. So, optimally, f_0 has to be tuned at the beginning to the nominal revolution frequency of the beam. The ordinate intercept point b expresses the mean periodicity error. The difference between the measured notch positions f_n of the notch filter transfer function and the ascending linear regression line nf_0 , scaled to the harmonic number n of the notches in the

ISBN 978-3-95450-174-8

pass band represents an absolute periodic frequency error $\Delta f = (f_n - nf_0)/n$ (Fig. 8).

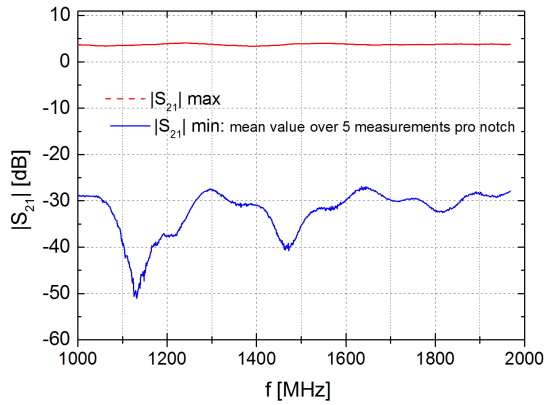

Figure 7: Envelopes of max. and min. $|S_{21}|$ for all notches in the bandwidth 1-2 GHz.

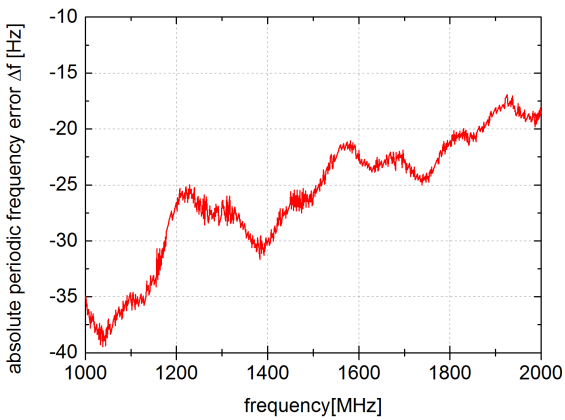

Figure 8: Absolute periodicity error for all notches in the bandwidth 1-2 GHz. The relative periodicity error $\alpha = |\Delta f|/f_0$ within the full band 1-2 GHz was always below 32 ppm.

PICKUP MODULE CONTROLLER

A pickup module controller is implemented, to control the slotline electrode arrays along the beam in the pickup tanks of the CR stochastic cooling system [4]. Four pickup module controllers are needed, 2 for the horizontal pickup tank (left/ right arrays of 64 slots in total) and 2 for the vertical pickup tank (top/ bottom arrays of 64 slots in total).

The pickup module controller consists of a power supply unit, a microcontroller unit, 8 channel controller cards, a 4-channel temperature measurement card and an RF input card. The switching power supply converts 230 V AC to 50 V/ 600 W and 18 V/100 W and in a second stage to 5 V digital and 8 V analog supply voltage. The analog supply voltage is reduced to 5 V by a linear controller at each specific analog card to reduce supply noise. The 50 V supply provides the 50 W power for each of the eight channel controller cards to heat up the module for vacuum purposes. It could be switched off to avoid distortion during beam time. The channel controller cards feed the amplifier boards or the switch boards in the pickup module with −5 V to 15 V respectively by an adjustable switching power supply. Each of these power supplies are fed with 18 V from the power supply unit. All system voltage levels and settings are controlled by the microcontroller unit. The communication between the units is transmitted by I²C Bus or SPI. The temperature of each of the 8 slotline arrays per tank side is monitored by one of the corresponding 8-channel controller cards in a four-wire measurement setup.

For test purposes a RF Signal ($f \in [0.5, 2.5\,\text{GHz}]$; $P < -10\,\text{dBm}$) from an external signal generator (e.g. of the network analyzer) is fed to the SMA plug at the RF attenuator card of the pickup module controller. The signal can be reduced by a step attenuator. Additional amplification with a driver amplifier is implemented to keep a proper level for the following signal splitter. Via the backplane the signal is split to the channel cards. From the channel cards the RF signal is fed in transmitting antennas in the slotline arrays. The loop is closed by measuring the signal with the pickup slotline arrays and sending it through the diagnostic signal processing chain to the network analyzer.

POWER AMPLIFIERS AT THE KICKERS

The procurement contract for the water cooled 1-2 GHz power amplifiers at the kickers has been awarded. Because of the very demanding antiproton cooling a total cw microwave power of 8 kW (= 32 × 250 W units) is required. This is in combination with stringent requirements on amplitude flatness and phase linearity within the 1-2 GHz band i.e. ≤ 1 dB amplitude response and ≤ 10 ° phase distortion at 10 dB below OP_{-1dB} as well as very short (≤ 4.8 m/16 ns) allowed electrical length for each unit. The preseries unit is under development.

REFERENCES

[1] Hittite, HMC1020LP4E Documentation v02.0511 (2015) https://www.hittite.com/content/documents/data_sheet/hmc1020lp4.pdf

[2] Yong-Chae Jeong, "Design of a Novel Vector Modulator", Microwavejournal, October 2001, http://www.microwavejournal.com/articles/3318-design-of-a-novel-vector-modulator

[3] W. Maier et al., JACoW Proc. COOL'13, Mürren, WEPPO19 (2013).

[4] C. Dimopoulou et al., presented at COOL'15, Newport News, VA, USA, paper MOYAUD04, *these Proceedings*, and references therein.

ISBN 978-3-95450-174-8

HIGH EFFICIENCY ELECTRON COLLECTOR FOR THE HIGH VOLTAGE ELECTRON COOLING SYSTEM OF COSY

M.I.Bryzgunov, A.V.Bubley, V.A.Chekavinskiy, I.A.Gusev, A.V.Ivanov, M.N. Kondaurov, V.M.Panasyuk, V.V.Parkhomchuk, D.N.Pureskin, A.A.Putmakov, V.B.Reva, D.V.Senkov, D.N.Skorobogatov, Budker INP, Novosibirsk, Russia

Abstract

A high efficiency electron collector for the COSY high voltage electron cooling system was developed. The main feature of the collector is usage of special insertion (Wien filter) before the main collector, which deflects secondary electron flux to special secondary collector, preventing them fly to the electrostatic tube. In first tests of the collector in COSY cooler efficiency of recuperation better then 10^{-5} was reached. Before assembling of the cooler in Juelich upgrades of the collector and electron gun were made. After the upgrade efficiency better then 10^{-6} was reached. Design and testing results of the collector are described.

INTRUDUCTION

In electron cooling method the process of heat exchange between ions and electrons occurs in the beam reference system. As a result the process almost doesn't change electron beam energy. It means that after interaction with ion beam electrons with sufficiently high energy must be utilized. Utilization of the beam on full energy is serious technical task, because stored power in the beam is very large. Moreover, such approach means that high voltage power supply (PS) must be constructed for big load current (about 1 A). To avoid this problem the method of recuperation of electron beam energy is used in electron cooling devices. An idea of the method is to decrease electron beam energy in electrostatic tube that is connected to the same high voltage PS which is used for acceleration of electrons. After that electron beam is directed to a special collector where they are absorbed by its surface. Usual energy of electrons absorbed in a collector is 1÷5 keV and it is defined by a special collector PS.

Using recuperation method one can decrease maximum load current of the high voltage power supply to the value of about several mA, or even less, because its consumption is determined only by high voltage divider, which distributes voltage along acceleration column, and by leakage current from the high voltage terminal to the ground. Load current for collector PS is equal to beam current but its operation voltage is several kV. Moreover, stability of collector PS voltage can be much worse.

Power consumption in divider is determined during system design and doesn't change during operation. The most important cause of appearance of the leakage current from high voltage terminal is losses of full energy electrons (I_{leak}). The most part of such electrons are secondary particles reflected from a collector. The ratio I_{leak}/I_{beam} (where I_{beam} – main beam current) is called efficiency of recuperation. Besides increasing of load to high voltage PS bad efficiency of recuperation in electron cooling systems can cause other problems. Full energy electrons which hit wall of vacuum chamber are source of radiation. Besides worsen of radiation safety it can cause problems in reaching good vacuum conditions and decrease electric strength of the cooler.

In coolers EC-35, EC-40 and EC-300 produced in BINP for IMP (China) and CERN the efficiency was improved with the help of special electrostatic bending plates installed in toroid parts of the coolers [1]. These method allows to increase efficiency of cooler recuperation from 10^{-3} to 10^{-6}. But in 2 MeV cooler for COSY shape of magnetic system and high energy of electrons make using of such method very complicated. In this case one should improve collector efficiency.

Efficiency limit of the axially symmetric collector with electrostatic and magnetic closing of secondary electrons, which are usually used in electron cooling devices, was estimated in [2] and its value is about 10^{-4}. For COSY high voltage electron cooler [3] such efficiency is not enough because needed value is about 10^{-5} [4]. In order to satisfy the requirement a new collector with suppression of secondary electrons by Wien filter was designed.

WORK PRINCIPLE

The main idea of the collector with Wien filter is to install a special insertion with crossed transverse electric and magnetic fields before ordinary collector (Fig. 1).

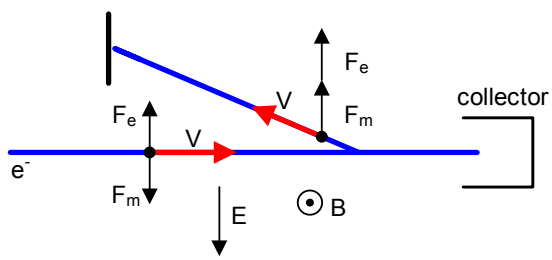

Figure 1: Principle of the collector with Wien filter work.

For main beam action of fields compensate each other but for secondary beam, which moves back, magnetic field acts in opposite direction and secondary beam is deflected to a special electrode (secondary collector). In the 2 MeV cooler the collector with Wien filter is placed in longitudinal magnetic field that is related with features of the cooler [3]. Because of the field, secondary electrons move not to electrostatic plates in but in direction parallel to them that protects the plates and their PS.

ISBN 978-3-95450-174-8

During entrance to the filter, electron is accelerated or decelerated by edge fields of the plates, that depends on coordinate of an electron. It means that in the filter, electrons, flying closer to positive plate, have higher velocity than in the center of the beam. Since Lorenz force depends on the particle velocity, resulting force for primary beam is not equal to zero for accelerated and decelerated electrons. This results in change of shape of the primary beam and can decrease perveance and efficiency of electron collector. In order to avoid this problem transverse magnetic field should have gradient n:

$$B_x = B_\perp \frac{n}{R} y, \quad B_y = B_\perp \left(1 + \frac{n}{R} x\right),$$

where $R = \frac{pc}{eB_\perp}$, $n = \frac{1}{2\gamma^2}$, x and y – coordinates in transverse direction [5]. For low energy beam $n \approx 0.5$.

CONSTRUCTION

The collector consists of two parts: main collector and Wien filter (Fig. 2). The bottom flange of the combined collector is attached to the deceleration tube of the cooler.

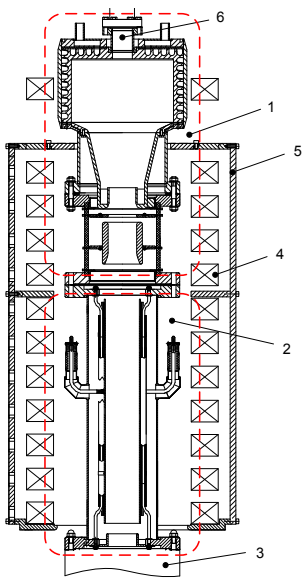

Figure 2: Sketch of the collector: 1 – main collector with the suppressor and pre-collector electrodes, 2 – vacuum chamber of the Wien filter, 3 – electrostatic tube, 4 – coil for longitudinal magnetic field, 5 – magnetic shield, 6 – flange for additional vacuum pumping

Main Collector

Main collector (Fig. 3) is intended to collect almost all electrons of main beam and need to be cooled, since power of main electron beam is up to 15 kW. Its construction is based on collectors, which were used is previous electron cooling devices produced by BINP for CSR (China) and LEIR (CERN). Efficiency of the main collector is about 10^{-3}.

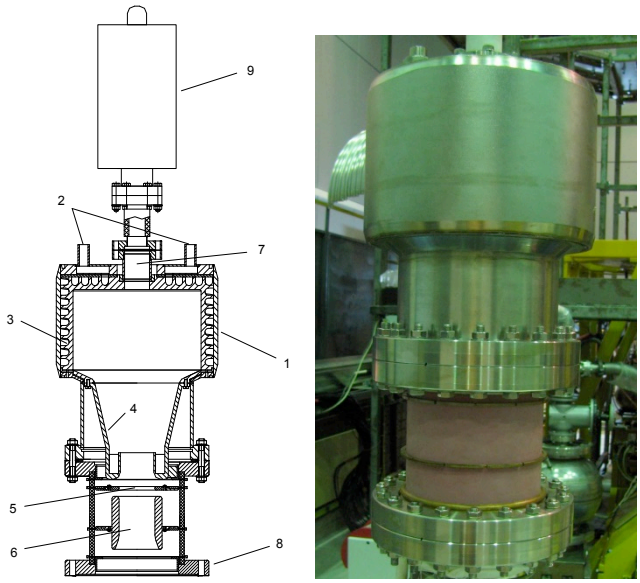

Figure 3: Left – sketch of the main collector: 1 – cooled main electrode, 2 – tubes for input and output of oil for cooling, 3 – channels for collector cooling, 4 – input part of the main electrode, 5 – suppressor electrode, 6 – pre-collector electrode, 7 – tube for additional vacuum pumping, 8 – vacuum flange, 9 – additional vacuum pump. Right – photo of the main collector.

Wien Filter

To produce magnetic field in the collector it is placed in solenoid which consists of 12 coils: 11 coils in magnetic shield and one last coil with opposite current (Fig. 2). The coil provides more uniform distribution of electron flux on the collector surface to avoid its local overheat and to increase efficiency of magnetic closing of secondary electrons. The solenoid is covered by magnetic screen. In Fig. 4 a top view of the Wien filter and part of the magnetic screen with permanent magnets are shown.

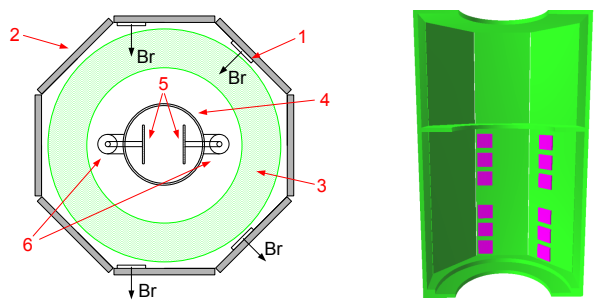

Figure 4: Left – tor view of the wien filter, right – 3D view of magnetic system of Wien filter from Mermaid program.

Permanent magnets were chosen to produce transverse magnetic field in the filter. Such solution decreases size of the system and exclude additional PS. Total number of magnets is 24 with Br=1.3 kG. Integral of transverse magnetic field along axis is 1400 G·cm. Length of electrostatic plates is 38 cm.

ISBN 978-3-95450-174-8

Permanent magnets (1) are placed on plates of magnetic screen (2) around coils of longitudinal magnetic field (3). Vacuum chamber (4) contains electrostatic plates (5) for production of transverse electric field. The plates are connected to high voltage power supplies via special connectors (6).

Vacuum chamber of the filter (see Fig. 2) includes electrostatic plates and secondary collector which absorbs electrons reflected from the collector and deflected in Wien filter. Inner diameter of the secondary collector is 5 cm. Main beam diameter in this region is about 3 cm.

UPGRADE OF THE WIEN FILTER

As it was said, electric field in the Wien filter is produced by two plates. Width of the plates is equal to distance between them. It lead to big inhomogeneity of the field. This inhomogeneity results to change of the main beam shape and to increase its characteristic size, which can worsen collector efficiency.

After tests of the collector in special test bench and in high voltage electron cooler it was decided to upgrade its construction in order to improve homogeneity of the field. For this a special shim was added in edges of electrostatic plates (Fig. 5).

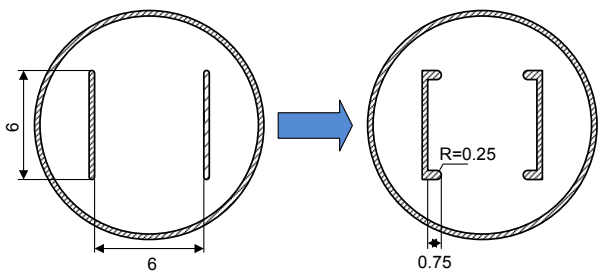

Figure 5: Shim added to plates of the Wien filter during the upgrade. Left – before upgrade, right – after upgrade.

The electric field was calculated for such construction with the Mermaid program [6]. In Fig. 6 one can see that the field was improved significantly in the region ±2 cm where main beam with radius 1.5 cm.

In Fig. 7 changes of the main beam shape for constructions before the upgrade and after it are shown. One can see that before the upgrade beam has almost triangular shape, but after the upgrade it is round i.e. effective beam size remains unchanged.

EXPERIMENTAL RESULTS

Test Bench

First experiments on recuperation with the new collector were made on a special test bench [5]. The test bench is a straight system with a gun in the bottom and collector in the top. The system was used to test the high voltage terminal of the 2 MeV cooler with all electronics.

In Fig. 8 results of collector efficiency measurements on the main beam current are shown

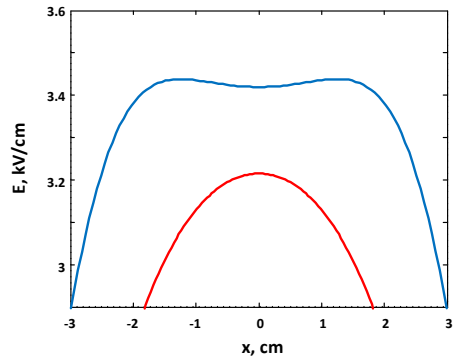

Figure 6: Transverse elecric field in Wien filter: red – before upgrade, blue – after upgrade

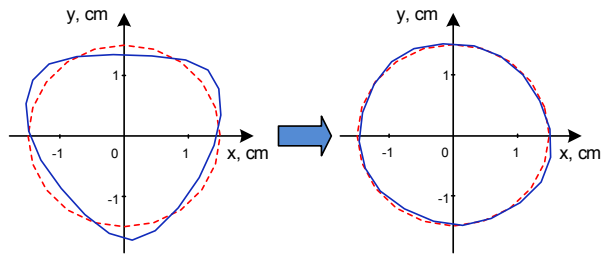

Figure 7: Main beam profule before (red) and after passing the Wien filter (blue): left – before upgrade, right – after upgrade.

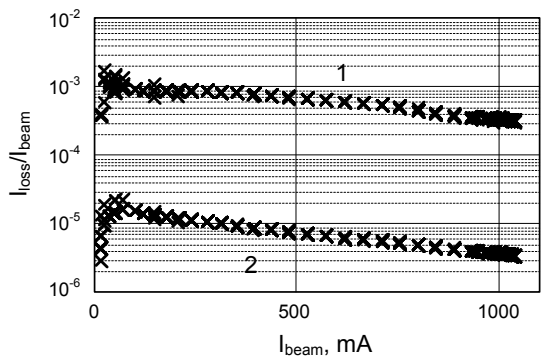

Figure 8: Dependence of efficiency of the main collector (1) and combined collector (2) on main beam current in test bench.

One can see that efficiency of the collector is about $3 \cdot 10^{-6}$ for current higher than 1 A. But the problem of measurement in such straight system is that electrons, reflected from the collector go to the gun, where they can be reflected by electrostatic potential and fly again in the collector. It means that efficiency measured in such system can be much better then real efficiency of the collector.

Commissioning in BINP

After tests in the test bench the collector was installed in the high voltage cooler during its assembling in the

ISBN 978-3-95450-174-8

Budker INP. Many tests were carried out for the different electron energy in the coiling section. Results show that efficiency of recuperation strongly depends on quality of beam transportation, because uncompensated transverse kicks can significantly increase beam size.

In Fig. 9 the best results of collector efficiency measurements on beam current are shown. The measurements were made for energy 30 keV where motion of the electrons though electron cooling system is adiabatic and beam transportation from gun to collector is much easier.

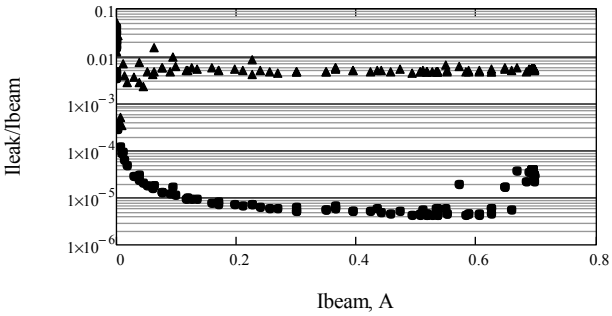

Figure 9: Dependence of efficiency of the main collector (triangulars) and combined collector (rounds) on main beam current. Experiment on HV cooler in BINP.

Generally the efficiency is slightly worse then for measurements in the test bench. It is difficult to define the reason of the difference: does it related with worse transportation of the beam or with not ideal measurements in the straight system (i.e. test bench).

Commissioning in COSY

As it was said, after the disassembling of the cooler in BINP the collector was upgraded. First tests of the upgraded collector were carried out only after assembling of the cooler in the COSY ring.

In Fig. 10 results of efficiency measurements on beam current are shown. Electron energy in the cooling section is 908 keV. One can see that efficiency of the collector is better then 10^{-6} for current 0.9 A that is much better then in tests before the upgrade.

Worse efficiency for lower current is related with features of the cooler. In the cooler beam position depends on beam current. Because of this for different currents we need to adjust transport channel optics to obtain optimal recuperation efficiency. For the measurements shown in Fig. 10 the transport channel was optimized for 0.9 A, which results in worse efficiency for lower currents.

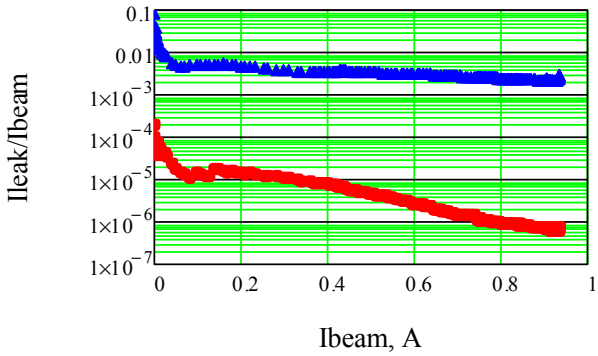

Figure 10: Figure 8: dependence of efficiency of the main collector (blue) and combined collector (red) on main beam current. Experiment on HV cooler in COSY.

CONCLUSION

Using a Wien filter together with axially symmetric electron collector allows to improve recuperation efficiency in high voltage electron cooling devices to the values 10^{-6} or better. Efficiency of such collector strongly depends on quality of electron beam transportation from gun to collector.

Inhomogeneity of transverse electric field in the Wien filter worsens collector efficiency by changing main beam shape.

REFERENCES

[1] V.N. Bocharov, A.V. Bubley, M. Vedenev, et al, “Commissioning of electron cooler EC-300”, preprint, Budker INP, Novosobirsk, 2004.

[2] A.Shemyakin, “Electron beam collector with a transverse magnetic field”, Proc. EPAC 2000, p. 1268-1270.

[3] V.Reva, N.Alinovsky, A.Batrakov et al. “The first commission results of the high voltage magnetized cooler for COSY”, Proc. COOL’11, p. 37-42.

[4] M.I.Bryzgunov, A.V.Ivanov, V.M.Panasyuk, et al. “Efficiency improvement of an electron collector intended for electron cooling systems using a Wien filter”, Technical Physics, 2013, Vol. 58, No. 6, pp. 911–918.

[5] M.I. Bryzgunov, A.V. Bubley, V.A. Chekavinskiy, et al, “Electron collector for 2 MeV electron cooler for COSY”, Proc. COOL’11, p. 103-106.

[6] Mermaid for Windows XP. User’s Guide, ed. by A.N. Dubrovin, 2005, Novosibirsk.

ISBN 978-3-95450-174-8

DECOUPLING AND MATCHING OF ELECTRON COOLING SECTION IN THE MEIC ION COLLIDER RING*

G.H. Wei[1,#], V.S. Morozov[1], Fanglei Lin[1], He Zhang[1]
[1]JLab, Newport News, VA 23606, USA

Abstract

To get a luminosity level of 10^{33} $cm^{-2}sec^{-1}$ at all design points of the MEIC, small transverse emittance is necessary in the ion collider ring, which is achieved by an electron cooling. And for the electron cooling, two solenoids are used to create a cooling environment of temperature exchange between electron beam and ion beam. However, the solenoids can also cause coupling and matching problem for the optics of the MEIC ion ring lattice. Both of them will have influences on the IP section and other areas, especially for the beam size, Twiss parameters, and nonlinear effects. A symmetric and flexible method is used to deal with these problems. With this method, the electron cooling section is merged into the ion ring lattice elegantly.

INTRODUCTION

The MEIC ion ring has cooling requirement from injection to the final collision stage. To realize ion beam cooling, a solenoid element is inserted in the ion ring to create an environment for heat extraction from the ion beam by an electron beam [1]. However, the solenoids can introduce coupling and matching problems which should be carefully dealt with.

ELECTRON COOLING SECTION IN MEIC ION RING

The MEIC ion collider ring accelerates protons from 9 to up to 100 GeV/c or ions in the equivalent momentum range and is designed to provide luminosity above 10^{33} $cm^{-2}s^{-1}$ in the momentum range from 20 to 100 GeV/c [2, 3, 4]. The overall layout of the ion collider ring is shown in Figure 1.

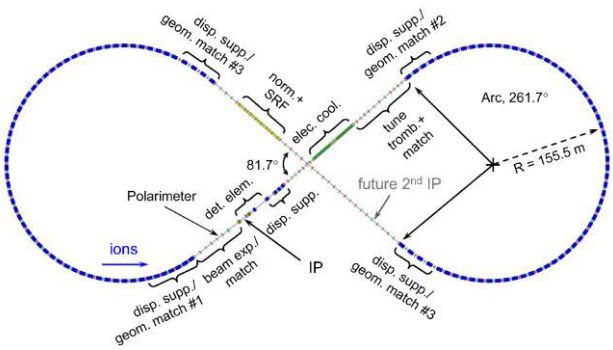

Figure 1: Layout of the MEIC ion collider ring. Main components are shown including IP and electron cooling section.

#gwei@jlab.org

The ring consists of two 261.7° arcs connected by two straight sections intersecting at an 81.7° angle. The two arc sections are composed mainly of FODO cells and a Chromaticity Compensation Block (CCB) section with larger beta and dispersion parameters. The lattice and Twiss parameters are shown in Figure 2. Including the two straight sections, the circumference of the overall ion collider ring is 2153.89 meters.

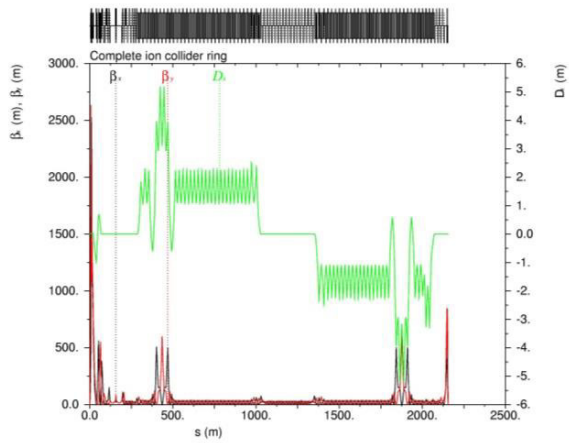

Figure 2: Lattice and twiss parameters of the MEIC ion collider ring.

As can be seen from Figure 2, between the 2 arc sections, one straight section houses an Interaction Point (IP) region, tune trombone matching section, election cooling section just 100 meters downstream of IP, and many matching sections. The maximum horizontal and vertical betas of 2574/2640 meters are located in IP region of Final Focus Quadrupoles. The second straight is mostly filled with FODO cells, while equipping with SRF system and retaining the capability of inserting a second interaction region.

Detailed lattice and Twiss parameters of the cooling section are shown in Figure 3. It has two main drifts of 30 meters which are reserved for placing a large solenoid each one and assistant equipment. Optics based on triplet focusing is used to provide such long drifts. There is a matching segment at each end of the cooling section connecting it the interaction region on one side and a straight FODO of a tune trombone on the other side.

Spin dynamics considerations require that the net solenoid field integral is compensated. Therefore, our proposed solution is to have the fields in the two solenoids opposite to each other so that one cooler solenoid serves as an anti-solenoid for the other as discussed below.

ISBN 978-3-95450-174-8

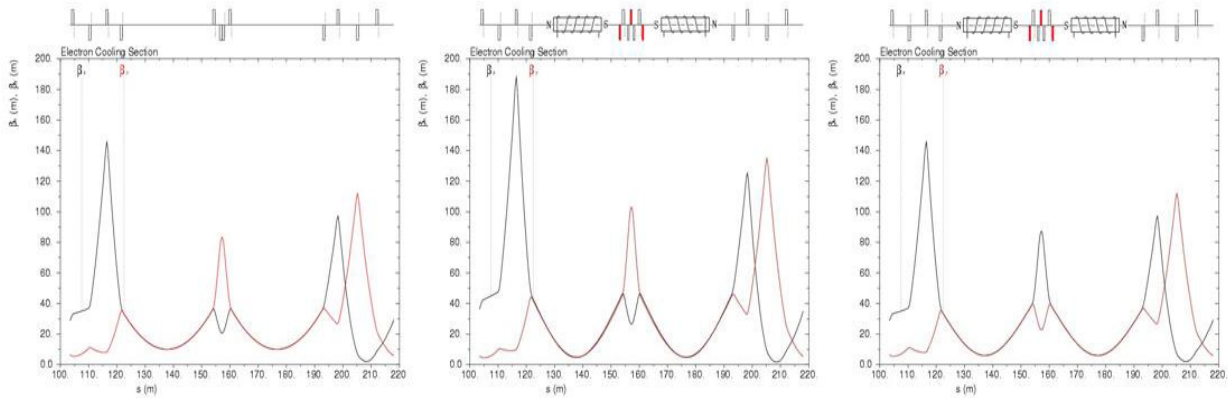

Figure 3: Lattice and twiss parameters of the electron cooling inserts in the MEIC ion collider ring. (Left: without electron cooling inserts; middle: with electron cooling inserts and without matching; right: with electron cooling inserts and with matching)

MECHANISM FOR DECOUPLING AND MATCHING OF ELECTRON COOLING SECTION IN ION RING

A solenoid is often a source of coupling in a ring, for example, a detector solenoid or solenoids used in electron cooling and spin rotators. A matrix, which can represent a solenoid in an accelerator physics calculation, can be written as [5].

$$\mathrm{M_{sol}} = \begin{bmatrix} C^2 & SC/K & SC & S^2/K \\ -KSC & C^2 & -KS^2 & SC \\ -SC & -S^2/K & C^2 & SC/K \\ KS^2 & -SC & -KSC & C^2 \end{bmatrix}$$

Where, $\mathrm{C} = \cos(KL)$, $\mathrm{S} = \sin(KL)$, $\mathrm{K} = B_{sol}/(2B\rho)$

It can be presented as a multiplication of a focusing part and a rotation part.

$$\mathrm{M_{sol}} = \begin{bmatrix} C & S/K & 0 & 0 \\ -KS & C & 0 & 0 \\ 0 & 0 & C & S/K \\ 0 & 0 & -KS & C \end{bmatrix} R[KL] = M_{sol}^{focus} R$$

where,

$$\mathrm{R}(\alpha) = \begin{bmatrix} I\cos\alpha & I\sin\alpha \\ -I\sin\alpha & I\cos\alpha \end{bmatrix}, I = \begin{bmatrix} 1 & 0 \\ 0 & 1 \end{bmatrix}$$

Although the simplest way to compensate coupling of a solenoid is to put an anti-solenoid (a solenoid with a field integral equal in magnitude and opposite in sign) next to it, sometimes focusing quadrupoles need to be inserted between the two solenoids to keep transverse focusing. Then the compensation will not work as before.

$$M_{a.sol}[-KL]M_{ins}M_{sol}[KL] = M_{a.sol}^{focus}R[-KL]M_{ins}R[KL]M_{sol}^{focus} \quad (1)$$

Eq. (1) above can still be decoupled if the quadrupole section is tilted by the solenoid rotation angle as shown in Eq. (2) and (3):

$$M_{ins}^{tilt} = R[KL]M_{ins}R[-KL] \quad (2)$$

$$M_{a.sol}[-KL]M_{ins}^{tilt}M_{sol}[KL] = M_{a.sol}^{focus}M_{ins}M_{sol}^{focus} \quad (3)$$

In MEIC case, nuclear physics studies are planned not only for collisions at a single energy and with a proton beam, but also at other energies and many other particle species. For different energies and different particle species, the tilt angle should be adjusted according to the rotation angle of the solenoid. In this case, an effect analogous to quadrupole rotation can be dynamically produced by appropriately combining a normal quadrupole component (strength: kn) and a skew component (strength: ks), which is shown in Eq. (4).

$$\alpha = \frac{1}{2} arc\tan\frac{ks}{kn} = \frac{B_{sol}L}{2B\rho}. \quad (4)$$

SIMULATION OF DECOUPLING AND MATCHING OF ELECTRON COOLING SECTION IN MEIC ION RING

For the MEIC ion collider ring, a simulation assuming at 3T solenoid strength is done for a proton case from 9 to up to 100 GeV/c. Beam coupling, beam size change at the IP and mismatch around the total ring are found in a simulation.

ISBN 978-3-95450-174-8

Mismatching around the MEIC Ion Ring

After adding electron cooling section to the MEIC ion ring lattice, shown in Figure 3, mismatching of the beam optics can be seen all over the ion collider ring.

While the solenoids add extra focusing in both horizontal and vertical directions, coupling also influences the strength of quadrupoles, which affects the proton beam. Then mismatch of the beam envelope occurs as shown in the middle of Figure 3.

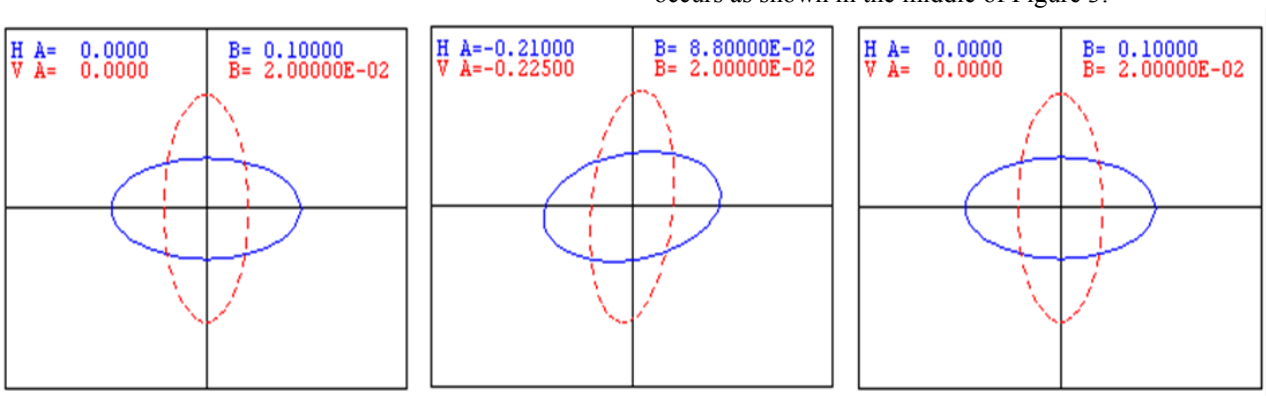

Figure 4: Beam transverse phase space at the Interaction Point of the MEIC ion collider ring (Left: without electron cooling inserts; middle: with electron cooling inserts and without matching; right: with electron cooling inserts and with matching)

By adjusting the normal and skew components of the triplet quadrupoles, the beam envelopes outside of the electron cooling section can be matched, which can be seen in the right picture of Figure 3.

Change of Beam Phase Space at the Interaction Point of the MEIC Ion Ring

Mismatching of the beam envelopes in the cooling section leads to a change in the Twiss parameters at the Interaction Point, which can be seen in the middle picture of Figure 4.

After the matching mentioned earlier, the Twiss parameters at the IP are returned to the design values, which is shown in the right picture of Figure 4. The Twiss values are listed in Table 1.

Table 1: Twiss parameters at the Interaction Point Considering Influence of the Election Cooling Section

	β_x (m)	α_x	β_y (m)	α_y
No cooling	0.100	0.000	0.020	0.000
With cooling & no matching	0.088	-0.210	0.020	-0.225
With cooling & matching	0.100	0.000	0.020	0.000

Coupling Influence and Decoupling

The solenoids can produce focusing and rotation of the ion beam. This rotation will result in coupling of the beam in the horizontal and vertical phase space. The difference in the transport matrix can be seen in the upper part of Figure 5.

In the upper part of Figure 5, the R13, R14, R23, and R24 matrix parameters are shown along the ion ring circumference.

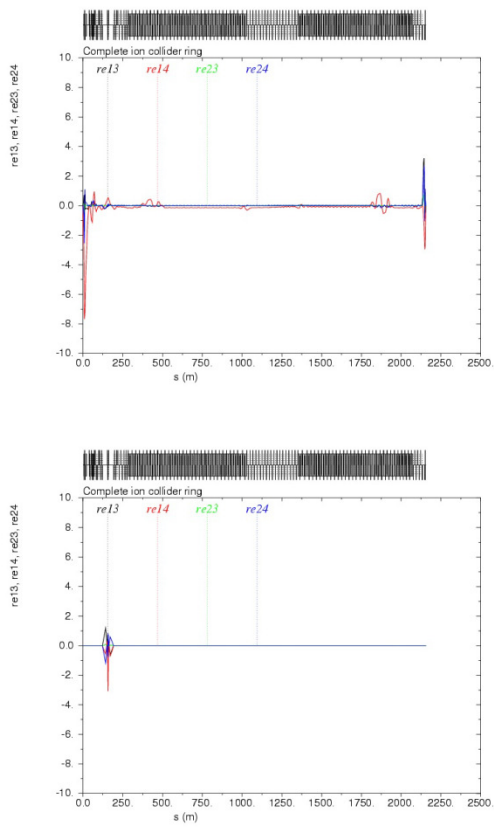

Figure 5: Coupling parameters caused by the electron cooling section in the MEIC ion collider ring (upper: with electron cooling inserts and without matching; lower: with electron cooling inserts and with matching)

ISBN 978-3-95450-174-8

An effective dynamic tilt angle produced by the normal and skew quadrupoles of the triplet cell undoes the coupling caused by the two solenoids. As shown in Eq. (3?), after creating a suitable dynamic tilt angle α, the R matrix parameters, R13, R14, R23, and R24, become 0 outside of the cooling section, which means optics has been decoupled.

CONCLUSION

A method to deal with coupling and mismatch caused by electron cooling in the MEIC ion ring is presented. The mechanism of how the method works is described. Normal and skew quadrupoles are used in a triplet to generate an effective dynamical tilt angle needed for decoupling. Independent strength values of the two kinds of quadrupoles also provide matching of the beam envelopes outside of the electron cooling section.

For managing different collider energies and ion species, changes in strengths of the two kinds of quadrupoles as functions of energy and ion species should be studied as a next step.

Alternating fields of the two solenoids can make the net longitudinal field integral zero to compensate their effect on the ion spin, which also needs to be studied.

ACKNOWLEDGMENT

This manuscript has been authored by Jefferson Science Associates, LLC under U.S. DOE Contracts No. DE-AC05-06OR23177 and DE-AC02-06CH11357. the United States Government retains a non- exclusive, paid-up, irrevocable, world-wide license to publish or reproduce the published form of this manuscript, or allow others to do so, for United States Government purposes.

REFERENCES

[1] He Zhang et al. IPAC'15 TUPWI037, p. 2326(2015).
[2] S. Abeyratne et al., arXiv:1504.07961 [physics.acc-ph].
[3] V. S. Morozov et al., IPAC'14, MOPRO005, p. 71 (2014).
[4] F. Lin et al., PAC'13, TUPAC28, p. 508 (2013).
[5] USPAS Lecture on Coupled Motion, by V. S. Morozov (2015)

ISBN 978-3-95450-174-8

HARMONIC STRIPLINE KICKER FOR MEIC BUNCHED BEAM COOLER*

J. Guo#, H. Wang, Thomas Jefferson National Accelerator Facility, Newport News, VA 23606 USA

Abstract

In the current design of JLab's Medium-energy Electron-Ion Collider (MEIC), the ion collider ring needs to be cooled by a bunched electron beam of up to 200 mA 55 MeV, with the possibility to upgrade to 1.5 A. To reduce the technical risk and cost associated with such an ERL, a scheme was proposed to recirculate the electron bunches in a ring for up to 25 turns until the bunch's beam quality is degraded, reducing the beam current in the ERL by a factor of 25. This scheme requires one or a pair of fast kickers that kick one in every 25 bunches. In this paper, we will analyze the efficiency of a harmonic stripline kicker for this circulator ring, and compare to the harmonic resonator kicker.

INTRODUCTION

In the MEIC design, bunched electron beam cooling of the ion beam is essential to achieve and maintain low emittance and small beam size in the colliding ion beam, reaching the luminosity goal [1]. In MEIC's bunched beam cooler, a 200mA 55MeV electron beam with a repetition rate of f_0=476.3MHz will be used to cool the ion beam, with the possibility to be upgraded to 1.5A and/or 952.6MHz. In the baseline design, an ERL will be used to provide such a beam, recovering 80%-90% of the electron beam energy. To reduce the technical risk and cost in such an ERL, especially the beam current and RF power in the booster and gun, a circulator ring scheme [2] has been proposed, as shown in Fig. 1. In this scheme, the electron bunches will be injected from the ERL into the ring with a fast kicker, circulate for N turns in a ring until the beam quality degrades, and then kicked out into ERL for energy recovery. The proposed scheme chose N=25 nominally, but we use the example of N=10 in part of this paper for simpler demonstration. This scheme reduces the bunch repetition rate and the beam current in the ERL by a factor of N, but requires one or two faster kickers with sub-nanosecond rise/fall time and repetition rate of f_0/N, or 19MHz, and a kicking voltage of 55kV to achieve 1mrad deflecting angle for a 55MeV beam. This set of parameters will be prohibitive for switching DC pulse kickers, but could be achieved by harmonic RF kickers, in which the kicking waveform is constructed by a series of CW RF harmonics, plus a DC bias.

There are several different approaches to implement the harmonic kicker. One is the resonant cavity kicker [3], which would be more efficient, but requires a number of bulky cavities to generate the desired waveform. Another option is the stripline kicker, which can be very compact in the system.

* Authored by Jefferson Science Associates, LLC under U.S. DOE Contract No. DE-AC05-06OR23177

#jguo@jlab.org

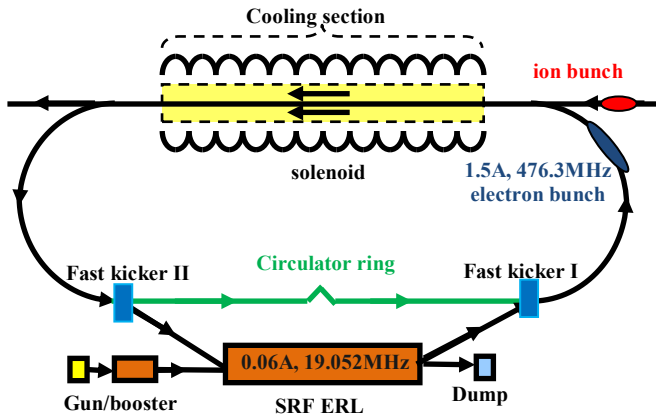

Figure 1: Layout of the MEIC bunched beam cooler, with the option of circulator upgrade.

EFFICIENCY OF STRIPLINE KICKERS

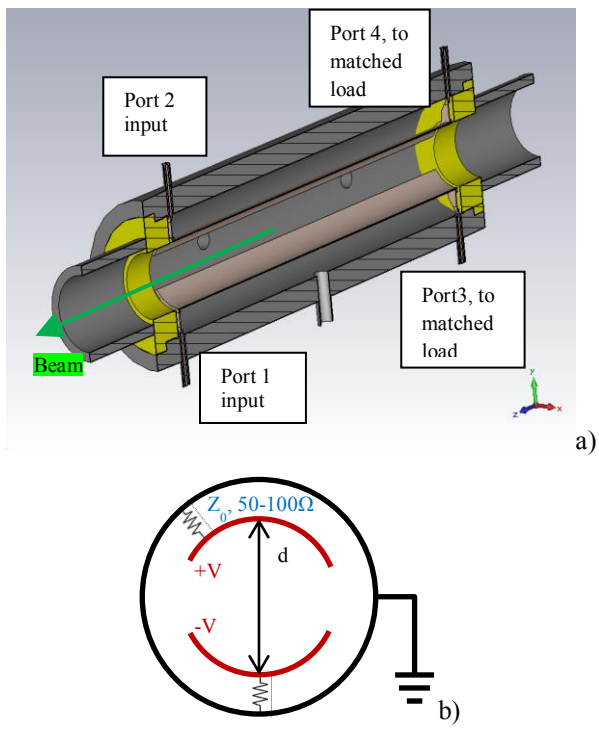

Figure 2. a) 3D model of the stripline kicker; b) cross-section model of the stripline kicker

A typical stripline RF kicker represented by the PEP-II coupled bunch feed-back kicker [5] is shown in Fig. 2. It utilizes the TEM mode travelling wave propagating from the input ports to the terminated ports, between two oppositely biased electrode plates and the grounded outer cylinder. The beam needs to travel in the direction

ISBN 978-3-95450-174-8

opposite to the RF propagation, as the electric kick and magnetic kick will add constructively. This also results in a transit time issue, and the length of the kicker needs to be optimized to maximize the efficiency. This efficiency can be quantified by transverse shunt impedance $R_\perp = V_\perp^2/P$, in which $V_\perp$ is the effective transverse kicking voltage seen by the beam.

In the kicker as shown in Fig. 2b, the transverse electric field at the center of the kicker is

$$E=2V/(g\cdot d). \quad (1)$$

g is a factor depending on the 2-D cross-section geometry, d is the distance between the two electrodes. Adding the effect of the magnetic kick, the effective kicking filed is $2E$. For the RF mode with angular frequency ω, the kicking field seen by the beam at the speed of light alternates at 2ω. The effective kicking voltage is the longitudinal integral of the transverse effective kicking field. For a kicker with length L and centered at z=0, the kicking voltage of mode ω seen by the particle with initial position z_0 is

$$V_\perp(z_0)=\int_{-L/2}^{L/2} 2E\cdot\cos\left[\frac{2\omega(z-z_0)}{c}+\varphi_0\right]dz = \frac{4cV}{\omega gd}\sin(\omega L/c)\cos(\varphi_0-\omega z_0/c) \quad (2)$$

To maximize the kicking voltage on the bunches to be kicked, we can choose $\varphi_0 - \omega z_0/c = 0$, so

$$V_\perp = \frac{4cV}{\omega gd}\sin(\omega L/c) \quad (3)$$

For the DC mode, $V_\perp = 2VL/(gd)$.

To generate the $\pm V$ RF voltage on both plates, the RF power needed from EACH input port will be $V^2/(2Z_0)$, and the total RF power needed is $P=V^2/(2Z_0)$. As a result, the transverse shunt impedance for one mode ω is

$$R_\perp = Z_0\left[\frac{4\sin(\omega L/c)}{gd\omega/c}\right]^2 \quad (4)$$

Currently, a scaled PEP-II coupled bunch feedback kicker design can be used to evaluate the technology. By solving the 2-D electrostatic problem for this cross-section with Superfish, we can find g=0.843, regardless of scaling. For single mode operation, the transverse shunt impedance of the kicker will be maximized if the kicker is quarter wavelength long, and will be 0 at half or full wavelength. The 0.63m length of the PEP-II kicker is the wavelength of 476MHz and is designed to cover the DC - 119MHz band. For multiple frequency operation, the kicker length needs to be optimized to avoid zero shunt impedance for all the modes and minimize the total power. To compare with the resonant cavity kicker in [3], the cross-section is scaled to d=70mm, while Z_0 is still 50Ω. We simulated such a kicker with L=0.409m in 3_D solver CST MWS for the first 10 harmonics of 47.63MHz. The simulation results agree very well with eq. 4, as shown in Fig. 3.

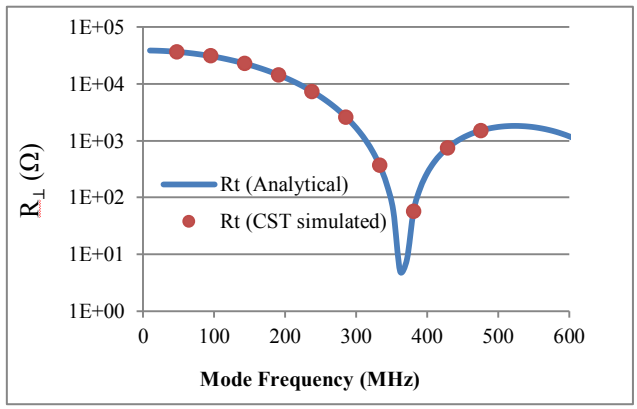

Figure 3: Transverse shunt impedance of a scaled PEP-II kicker, L=0.409m, d=0.07m.

SYNTHESIZING THE KICKER WAVEFORM

In a cooler ring with bunches recirculating for N turns, the required kicker waveform is a square wave with a flat top equals to the length of a bunch bucket and repetition rate of f_0/N, so only one in every N bunches will get a kick, while the others won't be disturbed. The waveform can be synthesized with a set of finite RF harmonics with fundamental frequency at f_0/N, delivered from a broadband amplifier to the input ports. There are several mathematical solutions to approximate the ideal waveform with finite harmonics, such as Fourier series [3] and constraint methods [4, 6]. The result from Fourier series has non-zero voltage and voltage slopes at the center of those bunches not to be kicked, as well as higher required mode voltages (and higher kicker power). The slope will provide unwanted crabbing to the beam, degrading the beam quality, especially when the circulator ring uses only one kicker for both injection and extraction [4]. The alternative is to apply both amplitude and slope constraints at the center of each bunch and solve the equation system and get the "zero gradient" waveform, as shown in the following equation system:

$$V_\perp(z_0)=\begin{cases} 55\text{kV}, & \frac{N\omega_0 z_0}{2\pi c}=0 \\ 0, & \frac{N\omega_0 z_0}{2\pi c}=1,2,\ldots,N-1 \end{cases} \quad (5)$$
$$\frac{dV_\perp(z_0)}{dz_0}=0, \quad \frac{N\omega_0 z_0}{2\pi c}=0,1,2,\ldots,N-1$$

A simple solution to eq. 5 is:

$$V_{\perp 0}=55kV/N$$
$$V_{\perp n}=\frac{55kV\cdot 2(N-n)}{N^2}, n=1,2,\ldots N. \quad (6)$$

Fig. 4 illustrates the ideal kicker waveform and synthesized "zero gradient" waveform solution in eq. 6, with N=10. The optimized kicker length for such a set of harmonic kicking voltage is 0.289m. Table 1 lists the transverse shunt impedance and RF power for each RF

ISBN 978-3-95450-174-8

mode in this solution. The total RF power in this kicker is 30.7kW. If we increase the recirculation turns to N=25, the total RF power reduces further to 13kW.

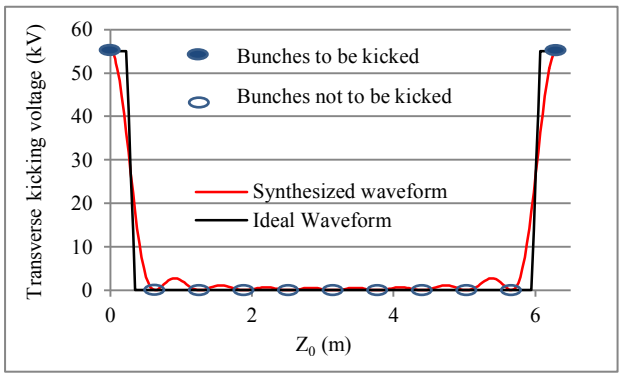

Figure 4: Ideal and synthesized zero gradient kicker waveforms for circulator ring with N=10 turns.

Table 1: Transverse Shunt Impedance and RF Power in Each Mode for the "Zero Gradient" Waveform

f (MHz)	$R_\perp$ (Ω)	$V_\perp$ (kV)	Power(kW)
DC	∞	5.5	0
47.63	18662	9.9	5.252
95.26	17151	8.8	4.515
142.89	14851	7.7	3.992
190.52	12047	6.6	3.616
238.15	9071	5.5	3.335
285.78	6241	4.4	3.102
333.41	3820	3.3	2.851
381.04	1975	2.2	2.451
428.67	765	1.1	1.581
Total/avg	98550	55	30.7

If a pair of kickers will be used in the circulator ring, the crabbing due to the voltage slope can be cancelled locally by setting the betatron phase advance between the two kickers to 180°. In this case, the slope constraints in eq. 5 can be removed; the number of modes will be reduced by half, as shown in eq. 7.

$$V_{\perp 0} = 55kV/N$$
$$V_{\perp n} = \begin{cases} \dfrac{2\cdot 55kV}{N}, n = 1,2,\ldots \dfrac{N-2}{2} \text{ or } \dfrac{N-1}{2}. \\ \dfrac{55kV}{N}, n = \dfrac{N}{2} \text{ (even } N \text{ only)} \end{cases} \quad (7)$$

For N=25 and 55kV total kicking voltage, we only need 12 RF modes with a total of 11.6kW [6].

If we can split the kicking voltage to two kickers, the RF power in each device can be reduced to 1/4, or around 3kW, and the system is still more compact than the resonant kickers. We can also try to redesign the stripline geometry and increase the characteristic impedance to 100Ω, reducing the power by another half. The PEP-II feedback kicker can only handle hundreds of watts of RF power. However, the power capacity of the kicker can also be increased with redesigned ports, making it possible to meet the required kicking voltage and RF power.

SUMMARY

We analyzed the electrodynamics of the stripline RF kicker and re-derived the analytical equation to estimate the shunt impedance; the results well agree with numeric simulation. We are able to optimize the length of such a kicker, so that the RF power needed to construct a waveform using certain set of harmonics can be minimized. To generate a 55kV "zero gradient" kick in every 25th bunches with 24 RF modes in the MEIC recirculating electron cooler, the power needed is 13kW with a kicker scaled from the PEP-II feedback kicker to 70mm electrode plate diameter. The power requirement for the stripline kicker is 2-3 orders of magnitude higher than a set of resonant kickers, but is not prohibitive. With additional measures to reduce the required RF power further, it's possible to design and build a stripline kicker to meet the specification for the MEIC recirculating electron cooler.

REFERENCES

[1] S. Abeyratne et al., "MEIC Design Summary for NSAC EIC Cost Estimate Sub-Committee", edited by G. A. Krafft, (2015).
[2] E. Nissen et al., "A Harmonic Kicker Scheme for the Circulator Cooler Ring in the Medium Energy Electron Ion Collider", MOPWO078, Proc. of IPAC'2013.
[3] Y. Huang et al., "Ultra-fast Harmonic Resonant Kicker Design for the MEIC Electron Circular Cooler Ring", WEICLH2063, Proc. of ERL'2015.
[4] A. Sy et al., "Development of an Ultra Fast RF Kicker for an ERL-based Electron Cooler", TUYAUD04, these proceedings.
[5] Barry, W. et. al. "Design of the PEP-II Transverse Coupled-Bunch Feedback System" Proceedings of the Particle Accelerator Conference 1995.
[6] J. Guo et al., JLAB-TN-15-020.

ISBN 978-3-95450-174-8

OPTICAL STOCHASTIC COOLING AT IOTA RING*

V. A. Lebedev# and A. L. Romanov, FNAL, Batavia, IL 60510, USA

Abstract

The optical stochastic cooling (OSC) represents a promising novel technology capable to achieve fast cooling rates required to support high luminosity of future hadron colliders. The OSC is based on the same principles as the normal microwave stochastic cooling but uses much smaller wave length resulting in a possibility of cooling of very dense bunches. In this paper we consider basic principles of the OSC operation and main limitations on its practical implementation. Conclusions will be illustrated by Fermilab proposal of the OSC test in the IOTA ring.

INTRODUCTION

The stochastic cooling [1 - 4] has been successfully used in a number of machines for particle cooling and accumulation. Cooling rates of few hours required for luminosity control in hadron colliders cannot be achieved in the microwave frequency range (~10^9-10^{10} Hz) usually used in stochastic cooling. Large longitudinal particle density used in such colliders requires an increase of cooling bandwidth by few orders of magnitude. To achieve such increase one needs to make a transition to much higher frequencies. A practical scheme operating in the optical frequency range was suggested in Ref. [5]. The method is named the optical stochastic cooling (OSC). It is based on the same principles as the stochastic cooling but uses much higher frequencies. Consequently, it is expected to have a bandwidth of ~10^{13}–10^{14}Hz and can create a way to attain required cooling rates.

Fermilab plans to make an experimental test of the OSC in IOTA ring [6]. Details of the project have been changing with improved understanding of the experiment. In particular, the basic wave length of the wiggler radiation was changed from 0.8 to 2.2 μm to achieve reasonably large cooling and dynamic apertures. The reasons of this transition will be discussed in the following sections.

In the OSC a particle emits e.-m. radiation in the first (pickup) wiggler. Then, the radiation amplified in an optical amplifier (OA) makes a longitudinal kick to the same particle in the second (kicker) wiggler as shown in Figure 1. A magnetic chicane is used to make space for the OA and to delay a particle so that to compensate for a delay of its radiation in the OA resulting in simultaneous arrival of the particle and its amplified radiation to the kicker wiggler. A particle passage through the chicane has a coordinate-dependent correction of particle longitudinal position which, consequently, results in a correction of relative particle momentum, $\delta p/p$, with amplitude ξ_0 so that:

$$\delta p / p = -\xi_0 \sin\left(k\,\Delta s\right) . \qquad (1)$$

Here $k = 2\pi/\lambda$ is the radiation wave-number,

$$\Delta s = M_{51}x + M_{52}\theta_x + M_{56}\left(\Delta p / p\right) \qquad (2)$$

is the particle displacement on the way from pickup to kicker relative to the reference particle which experiences zero displacement and obtains zero kick, M_{5n} are the elements of 6x6 transfer matrix from pickup to kicker, x, θ_x and $\Delta p/p$ are the particle coordinate, angle and relative momentum deviation in the pickup.

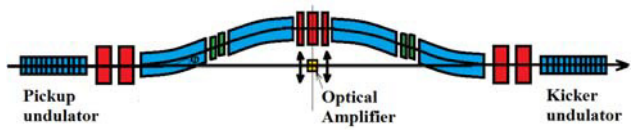

Figure 1: OSC schematic; blue – dipoles, red quadrupoles, green - sextupoles.

For small amplitude oscillations the horizontal and vertical cooling rates per turn are [7]:

$$\begin{bmatrix}\lambda_x\\ \lambda_s\end{bmatrix} = \frac{k\xi_0}{2}\begin{bmatrix}M_{56}-S_p\\ S_p\end{bmatrix}, \qquad (3)$$

where $S_p = M_{51}D_p + M_{52}D'_p + M_{56}$ is the partial slip-factor introduced so that for a particle without betatron oscillations and with momentum deviation $\Delta p/p$ the longitudinal displacement relative to the reference particle on the way from pickup to kicker is equal to $S_p\Delta p/p$, and D_p and D'_p are the dispersion and its derivative in the pickup. Eq. (3) assumes an absence of x-y coupling in the chicane. Introduction of x-y coupling outside the cooling area redistributes the horizontal cooling rate between two transverse planes but does not change the sum of cooling rates which is equal to: $\Sigma\lambda_n = k\xi_0 M_{56}/2$, $n = x, y, s$.

Although M_{56} and, consequently, the sum of cooling rates depend only on focusing inside the chicane, S_p and the ratio of cooling rates depend on the dispersion at the chicane beginning, *i.e.* on the ring dispersion. Eq. (3) yields the ratio of cooling rates:

$$\lambda_x / \lambda_s = M_{56} / S_p - 1 . \qquad (4)$$

A non-linear dependence of kick on Δs in Eq. (1) results in a dependence of cooling rates on amplitudes [7]:

$$\begin{aligned}\lambda_x(a_x,a_s) &= \left(2\,\mathrm{J}_0(a_s)\,\mathrm{J}_1(a_x)/a_x\right)\lambda_x \quad ,\\ \lambda_s(a_x,a_s) &= \left(2\,\mathrm{J}_0(a_x)\,\mathrm{J}_1(a_s)/a_s\right)\lambda_s \quad ,\end{aligned} \qquad (5)$$

where a_x and a_s are the amplitudes of longitudinal particle displacement relative to the reference particle on the way from pickup to kicker due to betatron and synchrotron oscillations expressed in the units of e.-m. wave phase:

$$\begin{aligned}a_x &= k\sqrt{\varepsilon_1\left(\beta_p M_{51}^{\,2} - 2\alpha_p M_{51}M_{52} + \left(1+\alpha_p^{\,2}\right)M_{52}^{\,2}\right)},\\ a_p &= k\left|S_p\right|\left(\Delta p / p\right) \quad ,\end{aligned} \qquad (6)$$

ε_1 is the Courant-Snyder invariant of a particle, β_p and α_p are the horizontal beta-function and its negative half derivative in the pickup, and $(\Delta p/p)$ is the amplitude of particle synchrotron motion. As one can see from Eqs. (5) each cooling rate changes its sign if any of amplitudes

*Work supported by Fermi Research Alliance, LLC, under Contract No. DE-AC02-07CH11359 with the United States Dep. of Energy
#val@fnal.gov

ISBN 978-3-95450-174-8

exceeds the first root, μ_{01}, of the Bessel function $J_0(x)$. Thus the cooling area is bounded by $a_x=\mu_{01}$ and $a_y=\mu_{01}$ where $\mu_{01}\approx 2.405$. Using Eqs. (6) one obtains from these equations the cooling area boundaries:

$$\varepsilon_{\max} = \frac{{\mu_{01}}^2}{k^2\left(\beta_p {M_{51}}^2 - 2\alpha_p M_{51}M_{52} + \left(1+{\alpha_p}^2\right){M_{52}}^2\right)}, \quad (7)$$

$$\left(\Delta p / p\right)_{\max} = \mu_{01}\Big/\left(k\left|S_p\right|\right) \ .$$

As one can see the cooling boundary for betatron motion does not depend on the ring dispersion in the OSC area but depends on the ring horizontal beta-function.

BEAM OPTICS OF OSC INSERT

The IOTA ring is a dual purpose storage ring aimed at experiments in the integrable optics [8, 9] and the OSC. Normally the machine is expected to operate with electrons up to 150 MeV kinetic energy. Operation with 2.5 MeV protons (~70 MeV/c momentum) is also anticipated in the program of integrable optics studies.

The energy for the OSC test is chosen to be 100 MeV [6]. The OSC system will take one of four ring straight sections with total length of about 4.5 m. The main parameters of the IOTA ring operating with OSC are shown in Table 1. It is implied that the rms horizontal emittance and momentum spread are determined by synchrotron radiation (SR) and *x-y* coupling is absent.

Table 1: Main Parameters of IOTA Storage Ring for OSC

Circumference	40 m
Nominal beam energy	100 MeV
Bending field	4.8 kG
Tunes, Q_x/Q_y	5.45/3.45
Rms hor. emittance, ε (no *x-y* coupling)	9.1 nm
Rms momentum spread, σ_p	$1.07\cdot10^{-4}$
SR cooling rates (ampl.), $\lambda_x=\lambda_y/\lambda_s$, s^{-1}	0.54/0.92

The cooling chicane consists of four dipoles with parallel edges (Figure 1). In the absence of additional focusing inside the chicane M_{56} and S_p are equal and horizontal OSC is absent. An introduction of quadrupole focusing in the chicane center makes M_{56} and S_p different and, consequently, creates transverse cooling. To understand interdependencies between major parameters we use a thin lens approximation. Leaving only leading terms one obtains the following estimates for elements of kicker-to-pickup transfer matrix:

$$M_{51}=M_{26}\approx -\Phi h\ ,\ M_{52}=M_{16}\approx -\Phi h L_{tot}\ ,\ M_{56}\approx 2\Delta L\ . \quad (8)$$

That results in $S_p \approx 2\Delta L - \Phi D^* h$. Here ΔL and h are the path lengthening and the trajectory offset in the chicane, $\Phi \equiv -1/F$ is the defocusing strength of the quad, and L_{tot} is the half-length of the chicane (distance from its center to the outer edge of outer dipole). Assuming $dD/ds=0$ in the chicane center and neglecting dispersion changes in the chicane one obtains from Eq. (4):

$$R_c \equiv \lambda_x/\lambda_s \approx \Phi D^* h / \left(2\Delta L - \Phi D^* h\right)\ , \quad (9)$$

where is D^* is the dispersion in the chicane center. Note that the above requirement of $dD/ds=0$ minimizes the equilibrium beam emittance set by SR. As one can see from Eq. (9) $\Phi D^* h/\Delta L$ uniquely determines the ratio of cooling rates.

Similarly, using Eqs. (7) and (9) one obtains estimates for the cooling area boundaries:

$$\left(\frac{\Delta p}{p}\right)_{\max} \approx \frac{\mu_{01}}{\left(2\Delta s - \Phi D^* h\right)k} = \frac{\mu_{01}\left(1+R_c\right)}{2k\Delta L}\ , \quad (10)$$

$$\varepsilon_{\max} \approx \frac{{\mu_{01}}^2}{k^2 h^2 \Phi^2 \beta^*} \approx \frac{{\mu_{01}}^2 {D^*}^2}{4\Delta L^2 k^2 \beta^*}\left(\frac{1+R_c}{R_c}\right)^2\ , \quad (11)$$

where $\beta^* \approx L^2/\beta$ is the beta-function in the chicane center, and we took into account that $\varepsilon_{\max}$ achieves maximum when $d\beta/ds=0$ in the chicane center. One can see that the cooling acceptance, $\varepsilon_{\max}$, is inversely proportional to β^*, which in the case of IOTA results in a collider type optics in the cooling area with minimum of horizontal beta-function in the chicane center. The value of ΔL is determined by a delay in the OA and has been chosen to be 3 mm. As one can see from Eqs. (10) and (11) an increase of R_c results in an increase of longitudinal cooling acceptance but reduces the transverse one.

Non-linear contributions to the longitudinal particle displacement omitted in Eq. (2) represent another important limitation on the cooling chicane parameters. These contributions are dominated by path lengthening due to betatron motion on the travel from pickup to kicker. In the case of small β^* in the chicane center one obtains that the non-linear path lengthening oscillates with betatron phase and at maximum the second order contribution is estimated as [7]:

$$\Delta s_2 \approx -\frac{1}{2}\int \theta(s)^2 ds \approx -\frac{\varepsilon_1}{\beta^*} L_{tot}\ . \quad (12)$$

Table 2: Optics Structure for Half of OSC Insert

	Length [cm]	B/G/S
Chicane center	-	-
D quad (half)	3	-86 G/cm
Drift	5	
F quad	6	0
Drift	7	
Dipole	8	-3060 G
Drift	10	
D sextupole	10	-830 G/cm^2
Drift	11	
F sextupole	10	1550 G/cm^2
Drift	10	
Dipole	8	3060 G

One can see that Δs_2 is proportional to the particle Courant-Snyder invariant and is inversely proportional to the beta-function in the chicane center. That yields that the 2-nd order contribution due to horizontal betatron motion will be much larger than due to vertical motion. Two pairs of sextupoles located between each couple of chicane dipoles (see Figure 1 and Table 2) are added for non-linear lengthening compensation.

The above estimates were directing the choice of chi-

ISBN 978-3-95450-174-8

cane parameters. After a few iterations we came to a reasonable compromise between contradictory requirements. Tables 2 and 3 present parameters of the OSC insert structure and the major parameters of OSC optics. Figure 2 shows the beta-functions and dispersion in the OSC straight. The cooling ranges in Table 3 are determined as ratio of cooling boundaries of Eq. (7) to the rms horizontal emittance set by SR in absence of coupling or the rms momentum spread: $n_{\sigma x}=\varepsilon_{max}/\varepsilon$, $n_{\sigma s}=(\Delta p/p)_{max}/\sigma_p$.

Table 3: Major Parameters of OSC Optics

Delay in the chicane, Δs	3 mm
Horizontal beam offset, h	43 mm
M_{56}	5.81 mm
Dispersion in the chicane center, D^*	600 mm
Beta-function in the chicane center, β^*	52 mm
Cooling rates ratio, λ_x/λ_s (no x-y coupl.)	1.7
Cooling ranges (before OSC), $n_{\sigma x}/n_{\sigma s}$	5.9 / 3.7

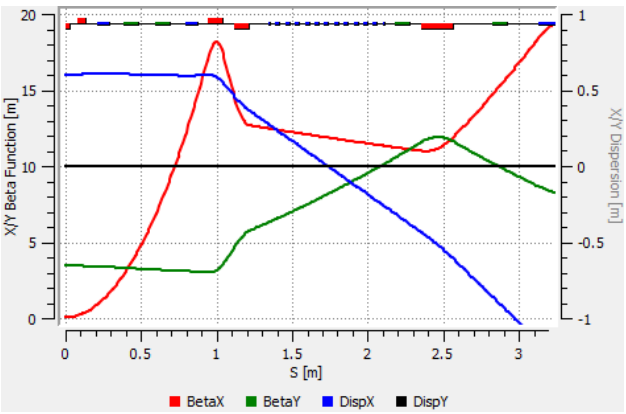

Figure 2: The beta-functions and dispersion in the half of OSC straight (from the chicane center to the first dipole).

To compute the longitudinal particle displacement on the way from pickup to kicker, Δs, we considered idealized model which has ideal rectangular dipoles with rigid edges and point-like sextupoles. Particle motion inside dipole was described by a piece of spiral to account for the vertical betatron motion. Vertical focusing of the dipole edges due to finite gap in the dipoles was accounted. As it was expected, in the absence of sextupole compensation the longitudinal particle displacement is dominated by the non-linear contribution coming from the betatron motion. As can be seen in Figure 3 that results in a significant reduction of the cooling boundaries - to about 1.5 and 5σ for the horizontal and vertical betatron motions, respectively. The sextupole compensation greatly reduces the non-linearities and increases the cooling boundaries to about 5σ and 7σ. Note that in the absence of nonlinearities the curves shown in Figure 3 would represent concentric ellipses required for OSC. Computations show that non-linearity in the longitudinal degree of freedom is negligible. Note also that Eq. (12) underestimates non-linear contribution to particle displacement by about 50%.

The sextupoles in the OSC straight introduce considerable nonlinearity to the betatron motion. Figure 4 presents distortion of constant action ellipses after passing the OSC chicane. As one can see the distortions are well visible for 4σ ellipse in the horizontal plane but hardly visible for the vertical plane even for 8σ amplitudes.

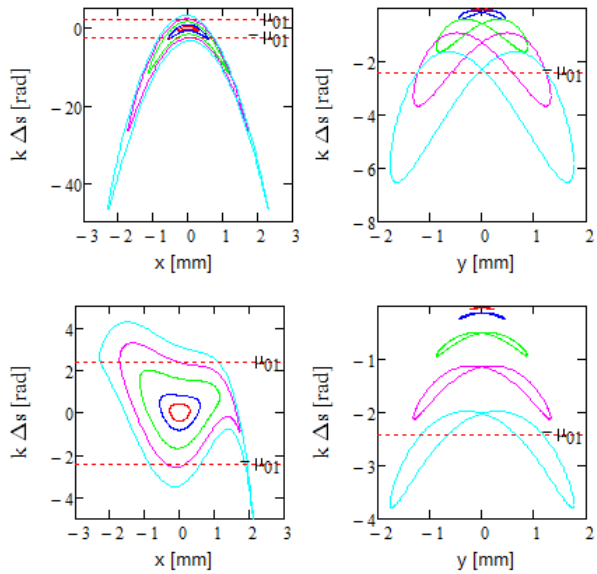

Figure 3: Dependence of the normalized longitudinal particle displacement in the kicker, $k\Delta s$, on the transverse particle position in the pickup for particles located at ellipses of 1σ, 2σ, 4σ, 6σ and 8σ; left and right - horizontal and vertical betatron motions, respectively; bottom and top - with and without sextupole correction, respectively. Amplitudes of betatron motion are referenced to the equilibrium horizontal emittance, ε, in the absence of x-y coupling. Horizontal lines mark cooling boundaries.

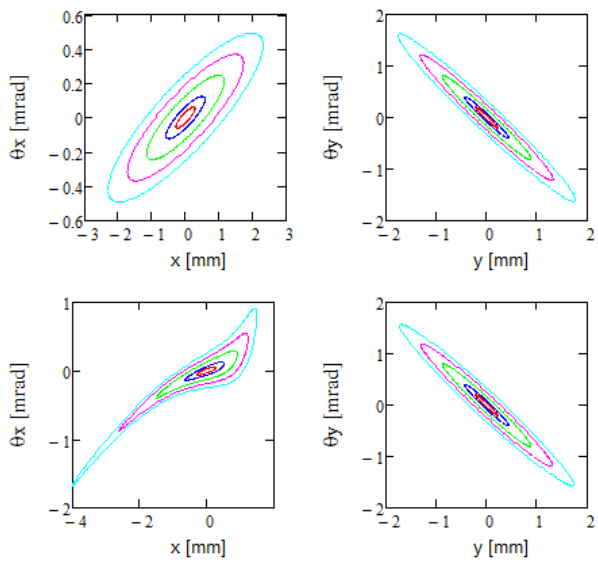

Figure 4: Horizontal (left) and vertical (right) phase spaces after coming through the chicane with (bottom) and without (top) sextupole correction. Initially particles were located at ellipses of 1σ, 2σ, 4σ, 6σ and 8σ in x or y plane.

The ring optics is symmetric relative to the chicane center. Figure 5 presents the dispersion and beta-functions for half of the ring. The optics was designed to minimize

ISBN 978-3-95450-174-8

the equilibrium emittance. It required minimization of the dispersion invariant, $A = \left(1+\alpha^2\right)D^2/\beta + 2\alpha DD' + \beta D'^2$, in the dipoles. Rewriting Eq. (11) in the following form,

$$A^* \equiv \frac{D^{*2}}{\beta^*} \approx \frac{4\varepsilon_{\max} k^2 \Delta s^2}{\mu_{01}^2}\left(\frac{R_c}{1+R_c}\right)^2, \qquad (13)$$

one can see that the dispersion invariant in the OSC chicane is determined by the ratio of cooling rates and weakly depends on other details of OSC optics. For the considered above OSC proposal the value of invariant in the OSC chicane is 6.8 m. It greatly exceeds its natural value in the IOTA ring. An adjustment of focusing for quads adjacent to the both sides of the chicane results in a reduction of the invariant after the first dipole by about two orders of magnitude. The invariant value stays at this small level for the rest of the ring. This quad adjustment has been crucial to obtain tolerable transverse emittances.

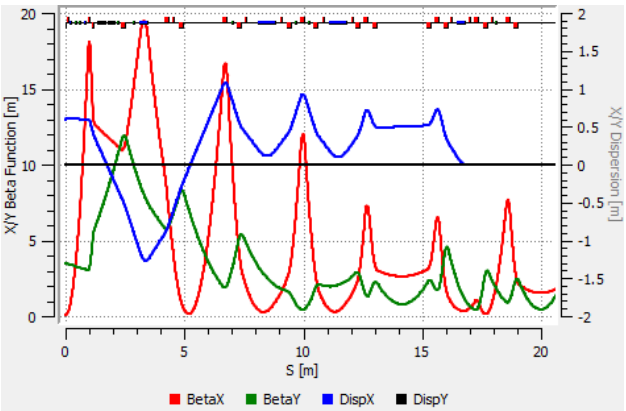

Figure 5: Optics functions for half of IOTA ring starting from the OSC section center.

Operation at the coupling resonance redistributes the SR and OSC cooling rates between horizontal and vertical planes resulting approximately equal equilibrium transverse emittances and, consequently, twice smaller horizontal emittance.

The OSC area sextupoles increase the ring chromaticity to $pd\nu_x/dp \approx 250$, $pd\nu_y/dp \approx -70$. The chromaticities were corrected by ring sextupoles split into five families. Tracking and FMA (frequency map analysis) with both chromaticities supressed to zero exhibit the dynamic apertures of about 4σ for both transverse planes. We expect that an improvement of sextupole correction and linear optics will yield further improvement of dynamic aperture. Note that the considered above cooling boundaries and dynamic apertures were referenced to the horizontal emittance of uncoupled optics. Their values need to be increased by $\sqrt{2}$ for the coupled case.

COOLING AND BEAM PARAMETERS

Presently we consider two steps in a study of the OSC. First, we will use a passive cooling where an OA is not used and the radiation of pickup undulator is focused to the kicker undulator with lens telescope. Such arrangement should be capable to increase the SR cooling rate by about an order of magnitude. The second step implies a usage of OA which should deliver further increase of OSC rates.

The OSC rates were computed using the results of Ref. [7]. Main parameters of the passive cooling scheme are shown in Table 4. In computation of cooling rates we assumed an ideal lens with optical band 2.2 - 2.9 μm. Such bandwidth is an estimate and it not supported yet by detailed design of the lens telescope. The OSC rates in Table 5 also imply operation on the coupling resonance so that the horizontal and vertical rates are equal to about half of the horizontal rate in the absence of coupling.

For operation on coupling resonance both the *x* and *y* beam emittances are about half of the equilibrium emittance, *ε*. That determines the beam sizes in the undulators to be ~250 μm for the coupled case (see Figure 6). The diffraction limited size of particle radiation in the kicker wiggler is somewhat larger, ~350 μm (radius at half height). The reduction of cooling rate for high amplitude particles was also neglected in the cooling rate estimate.

Table 4: Main Parameters for Passive OSC

Undulator parameter, K	0.8
Undulator period	12.9 cm
Peak magnetic field	664 G
Radiation wavelength at zero angle	2.2 μm
Radiation band used for OSC	2.2 - 2.9 μm
Number of periods, *m*	6
Total undulator length, L_w	77 cm
Distance between undulator centers	3.3 m
Telescope aperture, 2*a*	13 mm
Cooling rates in amplitude (*x*=*y*/*s*)	6.3/5.2 s^{-1}

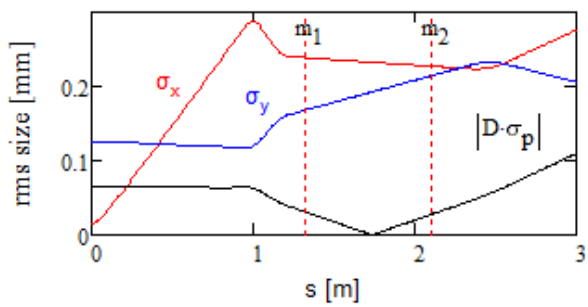

Figure 6: Rms beam sizes (vertical – σ_y, horizontal due to betatron motion – σ_x, and due to momentum spread - $|D\sigma_p|$) in the OSC region starting from the cooling chicane center. Vertical lines mark location of wiggler.

A small value of dynamic aperture greatly reduces the beam lifetime due to scattering on the residual gas. Therefore obtaining very good vacuum is a high priority task. The long term goal is $2\cdot10^{-10}$ Torr H_2 equivalent. It corresponds to 50 min. beam lifetime due to single electromagnetic scattering, and also yields that the emittance growth rate due to scattering on the residual gas is ~1% of the emittance growth rate due to quantum fluctuations of SR. The major beam and ring parameters are presented in Table 5.

ISBN 978-3-95450-174-8

The maximum number of particles per bunch is 10^6. It was chosen so that the Touschek lifetime would be longer than about 1 hour; and increases in the bunch length and horizontal emittance due to multiple IBS would not exceed 20% of their values set by the SR radiation. In computation of IBS rates we assume an operation on the coupling resonance so that $\varepsilon_x=\varepsilon_y=\varepsilon/2$ and the horizontal growth rate is equally split into x and y planes. Note also that for this small number of particles and small OSC cooling rates the cooling system operates orders of magnitude below optimal gain and the particle interaction through the OSC system can be neglected.

Table 5: Major Beam Parameters for OSC in IOTA

Geometric acceptance	5 μm
Dynamic acceptance	0.15 μm
Average vacuum (H_2 equivalent)	$2\cdot10^{-10}$ Torr
Vacuum beam lifetime	50 min.
SR losses per turn	13.3 eV
RF voltage amplitude	30 V
RF harmonic number	4
Momentum compaction	-0.0178
RF bucket height, $(\Delta p/p)_{max}$	10^{-3}
RMS bunch length (no OSC)	22 cm
Number of particles	10^6
Touschek lifetime ($\varepsilon_x=\varepsilon_y=\varepsilon/2$)	1.3 hour
Hor. emittance growth rate due to IBS	0.1 s^{-1}
Long. emittance growth time due to IBS	0.44 s^{-1}

ACTIVE AND PASSIVE OSC

In the above cooling rate estimate we assumed that the radiation emitted by a particle in the course of its motion in the pickup is focused to the location of the same particle in the kicker (when the particle arrives to it) in the course of particle entire motion in the kicker. It is automatically achieved for the lens located at the infinity (*i.e.* if the distance to the lens is much larger than the length of undulator) – the condition which is impossible to achieve in practice. A practical solution can be obtained with a lens telescope which has the transfer matrix $\mathbf{M}_T$ from the center of pickup to the center of kicker equal to $p\mathbf{I}$, where $\mathbf{I}$ is the identity matrix and $p=\pm1$. In this case the transfer matrix between emitting and receiving points is $\mathbf{O}(l)\mathbf{M}_T\,\mathbf{O}(-l)=\pm\mathbf{I}$, *i.e.* coincides with the matrix for the system where the lens is located at infinity. Here $\mathbf{O}(l)$ is the transfer matrix for a drift with length l. The simplest telescope requires 3 lenses (see Figure 7). For symmetrically located lenses there are only two possible solutions:

$$\text{(I)}\quad F_1=L_1,\quad F_2=-\frac{L_1^2}{2(L-L_1)},\quad p=-1;$$
$$\text{(II)}\quad F_1=\frac{LL_1}{L+L_1},\quad F_2=\frac{L_1^2}{2(L+L_1)},\quad p=1. \qquad (14)$$

The first solution requires weaker focusing, has smaller focusing chromaticity, and therefore is preferred. It also has defocusing lens in the center which is preferred from manufacturing point of view. The lens telescope is located inside the cooling chicane which determines its parameters: L=165 cm, $L_1=F_1=20$ cm, $F_2=-1.6$ cm. The diagonal elements of transfer matrix for the beam optics are also negative ($M_{11}=M_{22}=-1.03$, $M_{33}=M_{44}=-2.07$). It greatly mitigates the problem of cooling rate reduction for particles with large betatron amplitudes due to transverse separation of a particle and its radiation in the kicker undulator. As M_{11} and M_{22} are quite close to -1 this effect is strongly suppressed for the horizontal betatron motion.

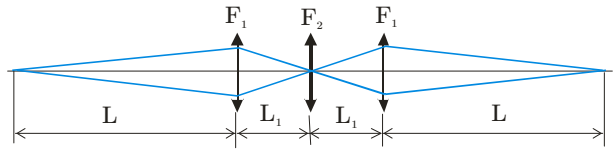

Figure 7: Light optics layout for passive cooling.

Non-linear contribution to the sample lengthening forced us to increase the base wave length for OSC test from 0.8 μm to 2.2 μm. As result we switched from the OA based on Ti: Sapphire crystal to Cr:ZnSe crystal. This crystal can support ~10% bandwidth with gain of about 10 Db. Further details can be found in Ref. [10].

CONCLUSIONS

IOTA ring construction is started. Its operation with electrons is expected in 2017. The concept of the OSC test in IOTA is getting matured. The beam optics is close to be finalized. It still has potential for further optimization. In particular, an increase of the beam dynamic aperture is desirable. Suppression of dispersion effects in the e.-m. wave focusing is our next high priority task. We expect to finish the conceptual design within one year.

Acknowledgements: The authors would like to express their gratitude to M. Andorf, P. Piot and J. Ruan.

REFERENCES

[1] S. van der Meer, Rev. Mod. Phys. 57, 689 (1985)
[2] D. Mohl, Stochastic cooling, in CERN Accelerator School, Fifth Advanced Accelerator Physics Course, ed. by S. Turner (CERN, Geneva, 1995), pp. 587–671.
[3]. J. Bisognano, C. Leemann, Stochastic cooling, in Summer School on High Energy Particle Accelerators, AIP Conference Proceedings 87, ed. by R.A. Carrigan et al. (American Institute of Physics, Melville, NY, 1982), pp. 584–655
[4] V. Lebedev, V. Shiltsev, "Beam Physics at Tevatron Collider", Springer, 2014.
[5] M. S. Zolotorev and A. A Zholents, Phys. Rev. E, **50**, 4, p. 3087 (1994).
[6] V. Lebedev, Yu. Tokpanov and M. Zolotorev, PAC'13, p. 422-424 (2013).
[7] V. Lebedev, "Optical Stochastic Cooling" in ICFA Beam Dynamics Newsletter, **No. 65**, p. 100 (2014), http://icfa-usa.jlab.org/archive/newsletter/icfa_bd_nl_65.pdf
[8] S. Nagaitsev, *et. al.*, p.16, IPAC-2012, (2012).
[9] G. Stancari, *et. al.*,, "Electron Lenses and Cooling for the Fermilab Integrable Optics Test Accelerator,", this conference.
[10] M. Andorf, *et. al.*, "Single pass amplifier for Optical Stochastic cooling proof-of-principle experiment at IOTA", this conference.

ISBN 978-3-95450-174-8

SINGLE-PASS-AMPLIFIER FOR OPTICAL STOCHASTIC COOLING PROOF-OF-PRINCIPLE EXPERIMENT AT IOTA*

M.B. Andorf[1], V.A. Lebedev[2], P. Piot[1,2], and J. Ruan[2]
[1] Department of Physics and Northern Illinois Center for Accelerator & Detector Development, Northern Illinois University DeKalb, IL, USA
[2] Fermi National Accelerator Laboratory, Batavia, IL, USA

Abstract

Test design of a single-pass mid-infrared Cr:ZnSe optical amplifier for an optical stochastic cooling (OSC) proof-of-principle experiment foreseen at the Integrable Optics Test Accelerator (IOTA) ring part of Fermilab Accelerator Science & Technology (FAST) facility. We especially present an estimate of the gain and evaluate effects of thermal lensing. A conceptual design of the amplifier and associated optics is provided.

INTRODUCTION

Optical stochastic cooling is a promising technique to mitigate luminosity degradation in hadron colliders [1]. In OSC, the beam information is obtained via electromagnetic-radiation process (pick-up) and the required correction is applied by coupling back the amplified radiation to the beam (kicker). In Ref. [1] considered the use of pick-up and kicker quadrupole-wiggler magnets. The OSC was subsequently extended to enable cooling of beams with large initial emittances [2]. In the latter case, the pick-up and kicker are conventional dipole-type undulator magnets. The electron beam and undulator radiation are physically separated between the two undulators to permit amplification of the radiation and to delay the electron beam using a four-dipole chicane beam line. Fermilab is planning a proof-of-principle experiment of OSC in IOTA located at FAST [3]. The experiment will employ a 100-MeV electron beam so that sufficient undulator-radiation flux from the pick-up undulator reaches the kicker undulator with or without an optical amplifier (OA) to yield to an observable cooling effect.

The design of OA is considerably constrained. The longitudinal and transverse cooling ranges are respectively defined as $n_s = (\frac{\Delta P}{P})_{max}/\sigma_p$ and $n_x = \sqrt{(\epsilon_{max}/\epsilon)}$. Here P is the design momentum, σ_p is the rms momentum and ϵ is the horizontal beam emittance. $(\frac{\Delta P}{P}_{max})$ and ϵ_{max} represent boundaries for which particles that fall within will be cooled.

In case of equal damping rates in both planes it can be shown [4] that the cooling ranges reduce to

$$n_s \approx \frac{\mu_{01}}{\sigma_P k \Delta S}, \qquad n_x \approx \frac{\mu_{01}}{2k\Delta S}\sqrt{\frac{D^{*2}}{\epsilon\beta^*}}, \tag{1}$$

with $\mu_{01} \approx 2.405$ being the first zero of the Bessel function, $k = 2\pi/\lambda$ the wavenumber of the radiation (determined by the wavelength λ of the OA), ΔS is the electron-beam path-length delay introduce by the chicane and sets the optical delay of the OA system, and D^* and β^* are the respectively the dispersion and beta functions at the center of the chicane. From Eq. (1) we note that a longer operating wavelength for the OA allows for a larger delay and thus a longer crystal (resulting in a higher gain). A review of the available lasing media prompted us to choose Cr:ZnSe as our gain medium (center wavelength of $\lambda \simeq 2.49\,\mu$m) resulting in a delay ΔS of a few millimeters.

Previous OA designs for OSC were based on Ti:Sp ($\lambda \simeq 0.8\,\mu$m) as the gain medium [5, 6] because of its excellent bandwidth (95 THz FWHM [7]) and ability to produce high gain. Cooling rate is inversely proportional to the amplifier bandwidth and for Cr:ZnSe it is just 50 THz [8]. However to keep the same cooling range Eq. (1) indicates a Ti:Sp crystal would need to be 0.6 the length of a Cr:ZnSe crystal [the signal delay of an amplifier with a crystal of length L and index of refraction n is given as $\Delta S = L(n-1)$]. Furthermore even if both crystals could have the same delay it was shown in Ref. [9] that Cr:ZnSe is expected to produce superior gain at lower pump intensities.

Another advance of Cr:ZnSe is the large number of pumping options in the mid-IR range. Therefore we investigated how the pumping wavelength will affect the amplifier performances. Optical parametric amplification has been ruled out as it would require pulses long enough to cover the length of a bunch in IOTA (~ 14 cm corresponding to 470-ps duration) at a repetition rate of 7.5 MHz. Instead we concentrate on the design of a single-pass amplifier with CW pumping.

GAIN EQUATIONS

In this section we demonstrate how to calculate the gain of a signal passing through a pumped medium. We start with the population rate equation for a 4-level system. Let N_0 be the population density of the ground state and N_i, $i = 1, 2, 3$ be population densities of the excited states. If we only allow for spontaneous emission to occur between nearest energy levels the rate equations are given as

$$\frac{dN_3}{dt} = -\kappa_3 N_3 - \frac{\sigma_{pa} I_p}{h\nu_p}(N_3 - N_0), \tag{2}$$

$$\frac{dN_2}{dt} = \kappa_3 N_3 - \kappa_2 N_2 - \frac{\sigma_s I_s}{h\nu_s}(N_2 - N_1) - \frac{\sigma_{pe} I_p}{h\nu_p}(N_2 - N_0), \tag{3}$$

* Work supported by the by the US Department of Energy (DOE) contract DE-SC0013761 to Northern Illinois University. Fermilab is operated by the Fermi research alliance LLC under US DOE contract DE-AC02-07CH11359.

ISBN 978-3-95450-174-8

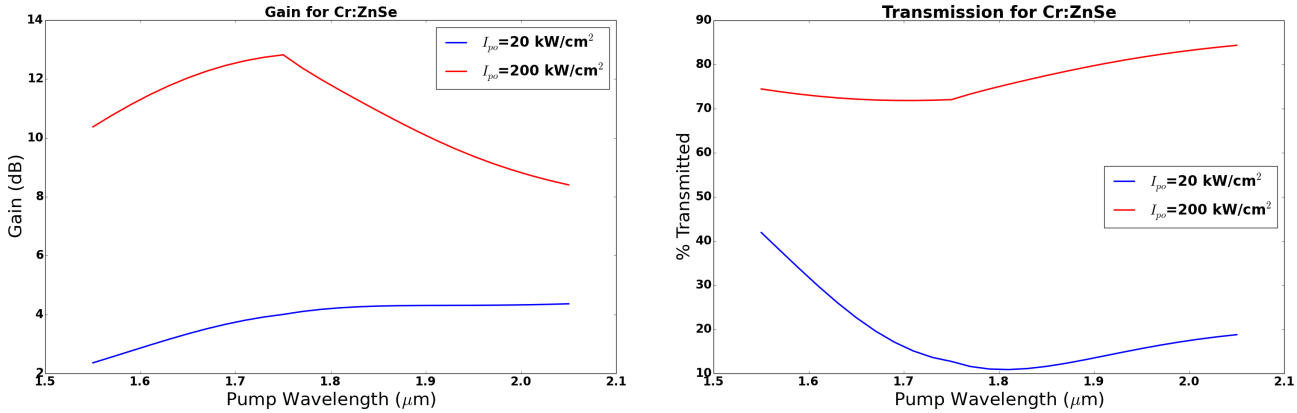

Figure 1: Left: Gain dependence on frequency for I_{po} 20 kW/cm^2 (blue) and 200 kW/cm^2 (red). Right: Corresponding transmission for both intensities as a function of wavelength.

$$\frac{dN_1}{dt} = \kappa_2 N_2 - \kappa_1 N_1 + \frac{\sigma_s I_s}{h\nu_s}(N_2 - N_1), \quad (4)$$

$$\frac{dN_0}{dt} = \kappa_1 N_1 + \frac{\sigma_{pa} I_p}{h\nu_p}(N_3 - N_0) + \frac{\sigma_{pe} I_p}{h\nu_p}(N_2 - N_0). \quad (5)$$

In the above, $\kappa_i = 1/\tau_i$ is the spontaneous decay constant (τ is the decay time), h is Planck's constant, ν is the photon frequency, σ is the frequency-dependent cross section, and I is intensity. The subscript s is for the signal (undulator radiation) to be amplified and the subscript p is for the pump laser. We further denote the cross sections of the pump with 'pa' for pump absorption and 'pe' for pump emission. This is specifically important for Cr:ZnSe because the corresponding absorption and emission cross sections overlap for wavelengths > 1.75 µm [8].

Attenuation of the pump laser intensity I_p as it propagates a distance z through the gain medium is given by

$$\frac{dI_p}{dz} = -I_p[\sigma_{pa}(N_0 - N_3) + \sigma_{pe}(N_0 - N_2)], \quad (6)$$

and growth of the signal intensity I_s is

$$\frac{dI_s}{dz} = I_s \sigma_s (N_2 - N_1). \quad (7)$$

The spontaneous decay rates of the first and third levels are prompt so that for a steady state $N_0 \gg N_3$ and $N_2 \gg N_1$ and Eq. (4) is approximated as $N_3 \simeq \frac{I_p \sigma_{pa} N_0}{h\nu_p \kappa_3}$ which in turn can be used to eliminate N_3 and κ_3 from Eq. (3).

The undulator radiation at the crystal entrance, I_{so} will be on the order of mW/cm^2. This is too small to affect the population dynamics and so stimulated emission due to undulator radiation is neglected in the rate equations. Using these simplifications with Eqs. (3), (6) and (7) yields

$$\frac{dI_s}{dz} = -\sigma_s A \frac{dI_p}{dz}, \quad (8)$$

with $A \equiv \frac{\tau_2}{h\nu_p}$. Defining the amplifier gain as $G = I_s/I_{so}$ the above equation is solved to give

$$G = e^{\sigma_s A (I_{po} - I_p)} \quad (9)$$

To calculate G the pump intensity dependence along the crystal must be known. To find this we first note that since $N_0 \gg N_3$ and $N_2 \gg N_1$ that the total doping concentration $N_t \approx N_0 + N_2$. This can be used to eliminate N_2 from Eq. (3) and (6). After substituting use Eq. (3) to solve for N_0

$$N_0 = \frac{N_t(1 + I_p \sigma_{pe} A)}{I_p A(\sigma_{pa} + 2\sigma_{pe}) + 1} \quad (10)$$

Finally we put the expression for N_0 into Eq. (6) to get

$$\frac{dI_p}{dz} = -I_p N_t \left(\frac{(1 + I_p \sigma_{pe} A)(\sigma_{pa} + 2\sigma_{pe})}{I_p A(\sigma_{pa} + 2\sigma_{pe}) + 1} - \sigma_{pe} \right) \quad (11)$$

Equation (11) can be integrated numerically. Equation (9) can then be used to study the gain dependence on various parameters such as the crystal length, doping concentration, and the frequencies of the signal and pumping laser (including both the explicit frequency dependence but also the implicit frequency dependence of the cross sections).

Figure 1 gives the dependence of the amplifier gain as a function of wavelength for two different initial pump intensities of $I_{po} = 200$ kW/cm^2 and $I_{po} = 20$ kW/cm^2 respectively refer to as "low" and "high" intensities cases. For both intensities the crystal parameters are identical and fixed to a doping concentration of $N_t = 2.0 \times 10^{19}$ ion/cm^3 and length $L = 1.4$ mm resulting in a signal optical delay of 2 mm.

σ_{pa} was approximated as a Lorentzian with a peak of 1.05×10^{-18} cm^2 at 1.78 µm and FWHM of 0.4 µm. σ_{pe} was treated as a continuous piece-wise function with $\sigma_{pe} = 0$ for wavelengths less than 1.75 µm and from 1.75 to 2.05 µm a straigh line with a slope of 2.5×10^{-18} cm^2/µm and an intercept of -4.36×10^{-18} cm^2. σ_s was kept constant at 1.2×10^{-18}cm^2 corresponding to the emission peak of Cr:ZnSe, 2.49 µm.

At high intensities the amplifier gain reaches its maximum at 1.78 µm where $\Delta I_p = I_p(z = 0) - I_p(z = L)$ is maximized. Although the absorption cross section is well approximated by a symmetric Lorentzian distribution, the gain appears asymmetric because of the overlap between absorption and emission cross sections at wavelengths below 1.75 µm, a region where the pump begins to self-stimulate. This latter

ISBN 978-3-95450-174-8

feature, along with a depleted ground state from the high intensity, renders the crystal very transparent at wavelengths above 1.75 µm.

At lower pump intensities the effect of self-stimulation is small. Rather for low intensities larger wavelengths lead to a slight increase of the gain at wavelengths past the absorption peak were ΔI is decreasing. This rise in the gain at larger wavelengths comes from the reduction in absorbed intensity that goes into heat, $I_h = \Delta I_p(1 - \frac{\lambda_p}{\lambda_s})$. The transmission as a function of wavelength is shown in the right side of Fig. 1.

For the case when $\sigma_{pe} = 0$, Eq. (11) can be solved in terms of the Lambert function $W(z)$, defined as the solution of $z = W(z)\exp[W(z)]$, and a closed-form solution for the gain can be obtained by expliciting

$$I_p = I_{sat} W\left(\frac{I_{po}}{I_{sat}} e^{-\alpha T + \frac{I_{po}}{I_{sat}}}\right) \tag{12}$$

into Eq. (9). In Eq. (12). we define $\alpha \equiv N_t \sigma_{pa}$ and $I_{sat} \equiv \frac{h\nu_p}{\sigma_{pa}\tau_2}$.

THERMAL LENSING

Cr:ZnSe is expected to have considerable thermal lensing due to the relatively high temperature dependence of the index of refraction and the high pumping intensities needed for the desired gain. The pump will have a flat top transverse distribution to help manage the lensing. For a cylindrical crystal with its surface temperature fixed and a uniform power distribution the focal length is given as [10]

$$f = \frac{\kappa A}{P_h}\left(\frac{1}{2}\frac{dn}{dT}\right)^{-1} = \frac{\kappa}{I_h}\left(\frac{1}{2}\frac{dn}{dT}\right)^{-1}, \tag{13}$$

with $\kappa = 1$ W/cm-K for cryogenically cooled Cr:ZnSe [11], and A is the transverse spot size. Figure 2 shows thermal lensing for high intensity. The increase in lensing with increased wavelength is again associated with an increase in transparency and a decrease in the fraction of absorbed intensity going to heat.

Another contribution to thermal lensing comes from the bulging of the flat faces of the crystal. The associated focal length is $f_b = \frac{\kappa}{I_h}\frac{\alpha r_o (n_o - 1)}{L}$ [10] with $n_o = 2.44$, $\alpha = 7.3 \times 10^{-6}$ K^{-1} [12] being the expansion coefficient and r_o the pump spot size. For example using the high intensity and crystal parameters from the previous section a Thulium laser at 1.93 µm with $r_o = 100$ µm would result in a $f_b = 160$ cm. Therefore bulging has a minor contribution to the overall thermal lensing.

PUMP LASER SELECTION

Now that the effects of the pump wavelength laser are well understood we can select the most appropriate one. We consider two choices an Erbium laser at 1.55 µm and a Thulium laser at 1.93 µm. Both lasers can be bought off the shelf with at least 60 W of pump power. We note that both lasers have similar gain (as inferred from Fig. 1) with Erbium and Thulium matched at high intensity and Thulium performing better at low intensities.

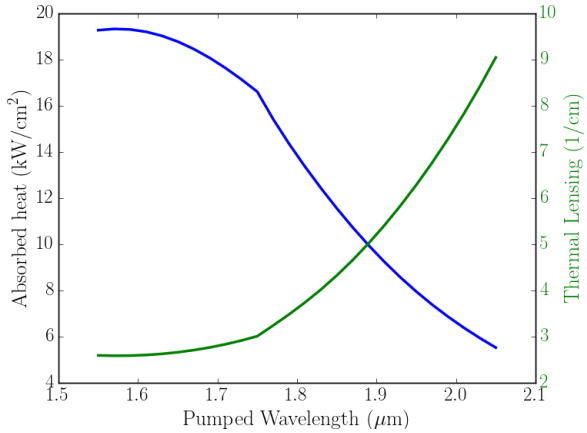

Figure 2: Thermal lensing (blue) and associated absorbed heat (green) evolution as a function of pump-laser wavelength. Both plots use the pump intensity $I_{po} = 200$ kW/cm^2.

It is clear that for optimal gain the crystal must be pumped as intensely as possible and given the high power available from these lasers this means pumping near the damage threshold is possible. Calculating the damage threshold is complicated as it depends on many factors, but generally it will decrease with decreasing wavelength [10] and from Figure 2 we see this is probably due to increasing absorbed heat at a fixed intensity. At 1.93 µm the absorbed heat drops by more than a factor of 2 thereby favoring the Thulium laser to pump at a higher intensity than the Erbium.

OPTICS

Beyond just the gain medium the OA requires some optics to accomplish three things (*i*) focus the pump laser to the required size at the crystal for desired intensity, (*ii*) focus the radiation from the pick-up undulator within the pump spot size at the crystal, and (*iii*) focus radiation originating from a certain longitudinal position in the pick-up to the corresponding point in the kicker. The latter of these requirements is accomplished by having the transfer matrix from pick-up to kicker center be $\pm\mathbf{I}$, the identity matrix [4].

In order to investigate possible optics designs we carried out a numerical simulation of the undulator radiation using the synchrotron radiation workshop SRW [13]. The radiation electric-field $\mathbf{E}(\mathbf{x})$ components are recorded on a transverse plane [$\mathbf{x} = (x, y)$] downstream of the undulator exit. In our convention the undulator radiation is polarized along the $\hat{x}$ direction so that the corresponding Wigner function is computed from the field component $E_x(\mathbf{x})$ following

$$\mathcal{W}_x(x, k_x) = \frac{1}{\lambda^2}\int_{-\infty}^{+\infty} E_x\left(x - \frac{x'}{2}\right) E_x\left(x + \frac{x'}{2}\right) \times e^{ik_x x'} dx', \tag{14}$$

where k_x the horizontal component of the wavevector and λ the radiation wavelength. Equation (14) can be rewritten for the vertical axis doing the substitution $x \leftrightarrow y$. Figure 3 shows a typical Wigner function produced by the undulator

ISBN 978-3-95450-174-8

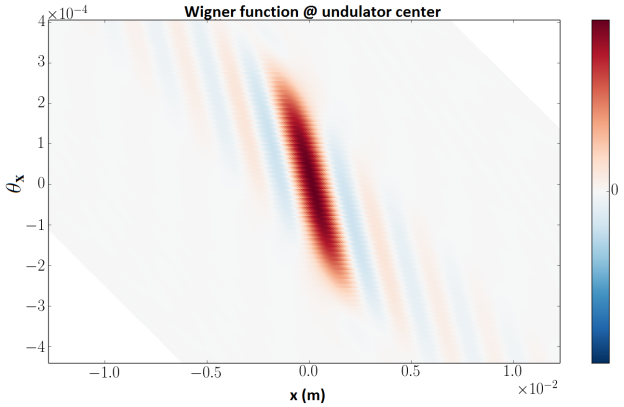

Figure 3: Example of Wigner function associated to the undulator radiation produced by a single electron; see Tab. 1 for the corresponding parameters. The Wigner function is back-propagated at the undulator center.

with parameters gathered in Table 1. A statistical analysis of the Wigner function provides the Courant-Snyder parameters of the photon beam that can be used as initial conditions for the optical design. Figure 4 shows a generic four-lens

Table 1: Undulator and Electron Parameters Used in the Optical Transport Design

Beam Energy	100 MeV
Undulator Period	12.9 cm
Number of Periods	6
Peak Magnetic Field	664 G
Zero angle wavelength	2.2 µm

setup. A simpler system incorporating two symmetric lenses only resulted in a spot radius on the crystal of $\approx 600\,\mu$m (assuming $f = 5$ cm from thermal lensing). The latter design would require a pump laser of 2300 watts for $I_{po} = 200$ kW/cm^2 which is unrealistic. Adding two more lenses reduces the radiation spot size on the crystal thereby relaxing the requirement on the pump-laser power. For the entire transfer matrix to be described by a unity matrix we require $D_1 = D_3$, $D_2 = D_4$ and $f_1 = (D_1 + D_2)/2$; see Fig. 4. The drifts D_1 and D_4 must be long enough to respectively be downstream and upstream of the first and last dipoles of the chicane. In our analysis we further consider the case $D_1 = D_4$ which results in the requirement $D_3 = D_2$. With the outer drifts chosen we find $L_1 = \sqrt{2fK}$, $F = \frac{LL_1}{K}$, $L = K/2 - L_1$ where $K \equiv (L_t - 4D_1)/2$ with $L_t = 3.3$ m being the total distance between the undulator centers. The additional lenses results in a spot size at the crystal of 100 µm thereby relaxing the laser power to $\sim$ 60 W. Considering the crystal discussed in the previous section pumped by a Thulium laser would result in 13 W of absorbed power with 3 W deposited as heat.

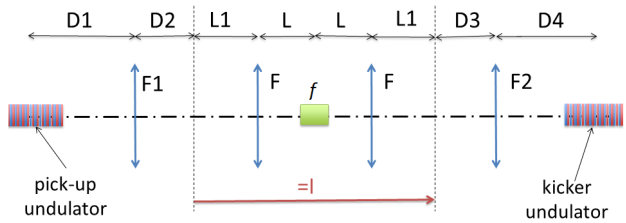

Figure 4: Optical system used to collect and transport the pick-up undulator radiation up to the kicker undulator. The double-arrowed lines represent optical lenses (Fn are the associated focal lengths).

FUTURE WORK

A potential limitation that needs to be investigated is the potential phase distortions occurring during amplification. Because the corrective kick a particle receives depends on the phase of the electromagnetic wave, this effect can impact the cooling performances. This effect will be quantify via an interferometry experiment. For a bench test an optical parametric amplifier will be built to mimic the large broadband of the undulator radiation. We must also investigate and minimize dispersion that will occur from the optics as this again impacts the phase of the electromagnetic wave. The chance for near zero dispersion exist because dispersion for Cr:ZnSe has the opposite dependence of most glass used for lenses in the mid-IR spectrum.

REFERENCES

[1] A.A. Mikhailichkenko, M.S. Zolotorev, Phys. Rev. Lett. **71** (25), p. 4146 (1993).

[2] M.S. Zolotorev, A.A. Zholents, Phys. Rev. E, **f50** (4), p. 3087 (1994).

[3] S. Nagaitsev et al., Proc. IPAC'12, New Orleans LA USA, p. 106 (2012).

[4] V.A. Lebedev, "Optical Stochastic Cooling," ICFA Beam Dyn.Newslett. **65** pp. 100-116 (2014).

[5] V.A. Lebedev et al., Proc. NAPAC'13 Pasadena, CA, USA, p. 422 (2013)

[6] A. Zholents, M. Zolotorev. Proc. PAC'97, Vancouver, B.C. Canada, p. 1805 (1998).

[7] Titan CW CW Ti:Sapphire Laser Operation Manual. Q-Peak Inc.

[8] Tm:ZnSe /S Series Data sheet available from IPG Photonics Inc. (2012).

[9] M.B. Andorf et al., Proc. IPAC'15, Richmond, VA, p. 659 (2015).

[10] W. Kochner, *Solid-State Laser Engineering*, 5th ed. Springer (1999).

[11] G. Slack, Phys. Rev. B 6, (10), p.3791, (1972).

[12] I.T. Sorokina, Opt. Mat. **26**, pp.395-412, (2004).

[13] O. Chubar, P. Elleaume, Proc. EPAC98, Stockholm Sweden, p.1177 (1998).

ISBN 978-3-95450-174-8

EMITTANCE GROWTH FROM MODULATED FOCUSING AND BUNCHED ELECTRON BEAM COOLING*

M. Blaskiewicz, J. Kewisch, C. Montag
BNL, Upton, NY 11973, USA

Abstract

The low energy RHIC electron cooling (LEReC) project at Brookhaven employs a linac to supply electrons with kinetic energies from 1.6 to 2.6 MeV. Along with cooling the stored ion beam the electron bunches create a coherent space charge field which can cause emittance growth. This process is investigated both analytically and through simulation.

INTRODUCTION AND THEORY

The low energy RHIC electron cooling project is currently under construction at BNL. We are using an electron linac with bunch lengths of a few centimeters to cool gold beams with lengths of several meters. Let γ be the Lorentz factor of the ions, α_p be the momentum compaction factor, σ_p be the rms fractional momentum spread, $\eta = 1/\gamma_t^2 - 1/\gamma^2$, and T_0 be the revolution period. The rms longitudinal slip per turn is $\sigma_{slip} = T_0|\eta|\sigma_p$. Table 1 shows this and other RHIC parameters.

Table 1: Gold Beam Parameters

parameter	$\gamma = 4.1$ value	$\gamma = 6.0$ value
σ_{tg}(ns)	11.7	9.6
σ_p	3.5×10^{-4}	3.8×10^{-4}
N_{ion}	6×10^8	1×10^9
emittance μm	2.5	2.5
f_0 (kHz)	75.8	77.2
σ_{slip}(ps)	280	127

Table 2: Electron Beam Parameters

parameter	$\gamma = 4.1$ value	$\gamma = 6.0$ value
σ_{te}(ps)	100	67
σ_p	$4 - 8 \times 10^{-4}$	$4 - 8 \times 10^{-4}$
Q_e(pC)	65 – 130	78-156
emittance μm	1-2	1-2
bunch spacing (ns)	1.42	1.42
bunches per train	31	25

The electron parameters are still under discussion but ranges are shown in Table 2. In the tables σ_{tg} and σ_{te} are the root mean square (rms) bunch durations, Q_e is the electron bunch charge, and N_{ion} is the number of ions per bunch.The emittance is the rms normalized emittance. There is a train of electron bunches of length $\sim 4\sigma_{tg}$ as illustrated in Figure 1. For all cases one has $\sigma_{te} < \sigma_{slip}$ which means that if an ion is subjected to a maximal space charge force on one turn it will not be subject to a significant force on the next turn. Unpublished work by Gang Wang and Vladimir Litvinenko has shown that it is critical that the electron bunches not slip with respect to the ion bunches. We assume this is the case but this still leaves the possibility of synchrobetatron resonances.

To study these resonances assume the cooling section is centered on β^* with $\alpha^* = 0$ and take the transverse ion coordinates to be x and $p = \beta^* x'$ so that the one turn matrix is just a rotation with phase advance $\psi_0 = 2\pi Q_x$. As a first approximation assume a single electron bunch centered on the ion bunch so that an ion interacts with it twice per synchrotron oscillation. Assuming the electron bunch has focusing strength k the map for half a synchrotron oscillation is

$$\begin{bmatrix} x_{n+1} \\ p_{n+1} \end{bmatrix} = \begin{bmatrix} \cos\frac{\pi Q_x}{Q_s} & \sin\frac{\pi Q_x}{Q_s} \\ -\sin\frac{\pi Q_x}{Q_s} & \cos\frac{\pi Q_x}{Q_s} \end{bmatrix} \begin{bmatrix} 1 & 0 \\ \beta^* k & 1 \end{bmatrix} = \begin{bmatrix} x_n \\ p_n \end{bmatrix}, \tag{1}$$

where Q_s is the synchrotron tune. When Q_x/Q_s is close to an integer the map is unstable. Taking $\sin(\pi Q_x/Q_s) = \epsilon$ and assuming an eigenvalue $\lambda = 1 + \delta$ one finds $\delta \approx \sqrt{\beta^* k \epsilon - \epsilon^2}$. The resonances for LEReC are typically very weak with $\beta^* k \sim 10^{-5}$. When coupled with the small fraction of time the ions interact with the electrons one expects a very small fraction of the beam would be harmed by these resonances. However there is another important dynamical effect. Longitudinal intrabeam scattering causes the longitudinal action to wander and with it the synchrotron tune. This causes individual particles to wander back and forth through resonances, usually increasing betatron amplitude with each passage. If we look at it in terms of statitical averages the average increase in amplitude will be proportional to the maximum growth and the fraction of time growing is proportional to the resonance width. Since both terms are linear in the charge of the electron bunch one expects the emittance growth rate to scale as the square of the electron bunch charge.

A better model can be obtained using perturbation theory. Since we only consider a matrix and a thin lens cooling region we take $|Q_x| < 1/2$. The equations of motion are generated by the hamiltonian

$$H(x, p; \theta) = \frac{Q_x}{2}\left(p^2 + x^2\right) + \delta_p(\theta) F_e(\tau) \ln\left(1 + x^2/a^2\right), \tag{2}$$

* Work supported by United States Department of Energy

ISBN 978-3-95450-174-8

where we use azimuth θ as the time-like variable, $\tau = \tau(\theta)$ is the arrival time of the ion relative to the synchronous particle, a characterizes the radius of the electron beam,

$$\delta_p(\theta) = \sum_{k=-\infty}^{\infty} \delta(\theta - 2\pi k) = \sum_{m=-\infty}^{\infty} \frac{e^{2\pi i m\theta}}{2\pi}$$

and

$$F_e(\tau) = \frac{-\beta^* Z_0 I_e(\tau)\ell}{4\pi\beta^3\gamma^3 mc^2/q}.$$

In F_e we have a cooling section of length ℓ, $\beta = v/c$, $Z_0 = 377\Omega$, $I_e(\tau)$ is the electron current, and the ion has charge q and mass m. In the simplest approximation take $\ln(1 + x^2/a^2) \approx x^2/a^2$ and $\delta_p(\theta) \approx 1/2\pi$. This leaves only the slow variation associated with $\tau(\theta)$. Assuming interaction with a single synchrotron harmonic we have

$$\frac{d^2x}{d\theta^2} = -Q_x^2 x - 2Q_x\hat{C}\cos(pQ_s\theta), \tag{3}$$

where $pQ_s = 2Q_x + \delta$ with $|\delta| \ll 1$ and

$$\hat{C} = \left| \int_0^{2\pi} \frac{d\psi_s}{2\pi} e^{ip\psi_s} \frac{F_e(\hat{\tau}\cos\psi_s)}{\pi a^2} \right|, \tag{4}$$

where $\hat{\tau}$ is the amplitude of the synchrotron oscillation. Equation (4) leads to parametric resonances [1]. The amplitude of oscillation grows as $e^{s\theta}$ with

$$s = \frac{1}{2}\sqrt{\hat{C}^2 - \delta^2}.$$

As with the previous analysis the strength and width of the resonance are both proportional to the electron bunch charge. When synchrotron tune wander is included it follows that this analysis also predicts the emittance growth rate should scale as the square of the electron bunch charge.

The previous analyses assumed a linear restoring force for the electrons. While a detailed non-linear analysis has not been obtained a few general comments are in order. First we use action angle variables with $x = \sqrt{2J}\cos\psi$ and the slow approximation on (2) yielding.

$$H(J,\psi;\theta) = Q_x J + \frac{F_e(\tau)}{2\pi}\ln\left(1 + \frac{2J\cos^2\psi}{a^2}\right) \tag{5}$$

$$= Q_x J + \frac{F_e(\tau)}{2\pi}\sum_{m=0}^{\infty} a_n(J/a^2)\cos(2m\psi). \tag{6}$$

Define $b = J/a^2$. For $m = 0$ we find [2]

$$a_0(b) = \ln\left(\frac{1 + b + \sqrt{1 + 2b}}{2}\right). \tag{7}$$

For $m > 0$

$$a_m(b) = \frac{-2}{m}\left(\frac{-b}{1 + b + \sqrt{1 + 2b}}\right)^m. \tag{8}$$

The detuning term in the Hamiltonian increases without bound as b increases but the change in tune will be quite small. The other terms $a_m(b)$ are bounded by $2/m$ even as $b \to \infty$ so the driving terms saturate with betatron amplitude. For our parameters it is likely the single resonance approximation will hold at any given $\hat{\tau}$ but the important resonance could change with $\hat{\tau}$. It is also likely that other sources of detuning will dominate a_0 but these are easily added.

SIMULATIONS

The simulation code is based on a simple one turn map for the ions and a thin lens treatment of the electron-ion interaction. The one turn map is defined by betatron tunes, coupling, chromaticities, detuning coefficients and sine wave RF. Also we include longitudinal IBS with total growth rate given by Piwinski's [3]coasting beam formula and Zenkevich's [4] viscous force. Transverse IBS is not included because the model assumes a uniform focusing lattice which yields negative growth rates. Actual rates are about 10% of the longitudinal rates [5].Transverse space charge is implemented as a phase shift that is a function of betatron amplitude and longitudinal position within the bunch.

The electron ion interaction consists of a coherent space charge kick where the electron bunch is taken to be a 3 D gaussian. Electron cooling is non-magnetized and treated with the Coloumb logarithm outside the integral. The local density is multiplied by a cooling force that has the same form as the electrostatic force [6]. The electron beam is assumed round and the cooling force is calculated at the start of the simulation and stored in a two dimensional array. A version where only one transverse variable is tracked has also been developed.

We begin by determining what parameters are relevant to the dynamics. Figure 2 shows results for $\gamma = 4.1$ but with 10 times the nominal electron bunch charge to speed things up. We can draw several conclusions. First, the two dimensional (2D) simulation in red with chromaticity $\xi = -2$ is quite similar to the one dimensional version shown in blue. We conclude the second transverse dimension is not fundamental to the emittance growth, justifying our earlier 1D analysis. The magenta and green curves in Figure2 show the nihl effect of changing chromaticity. The purple and navy lines show the effect of reducing the longitudinal IBS by factors of 10 and 100, respectively. There is clearly an effect but it is weak. For no IBS the blue line shows no growth, hence some IBS is necessary for emittance growth. Finally the yellow curve shows the effect of linear RF. Clearly the growth is much reduced when the synchrotron tune does not depend on synchrotron amplitude.

Figure 3 shows the effect of 5 different initial random seeds with 1000 and 10,000 simulation particles. The slopes of all the curves are very simular showing that the emittance growth does not depend on microscopic details. Figure 4 shows the growth rate of the emittance for 2D simulations as the betatron tunes vary for 1000 and 10,000

ISBN 978-3-95450-174-8

macroparticles. The growth rates change by factors of two in a nonuniform way with tune, verifying that emittance growth is a resonant phenomena.

Figures 5 and 6 show emittance growth rates as a function of electron bunch charge for 1D and 2D beams respectively. For each curve we used linear least squares to fit

$$\ln\left[\frac{d\ln\epsilon}{dn}\right] = a + bQ_e + \text{error}, \qquad (9)$$

with parameters a and b where Q_e is the electron bunch charge. The curves in Figures 5 and 6 are labeled by the betatron tune and the fitted value of b. For 1D we have $1.8 \le b \le 2.16$ and for 2D $1.68 \le b \le 2.14$ which agrees with the value of 2 obtained by our earlier analysis.

Figures 7 and 8 show best guess results for the situation in RHIC. For both cases the smaller emittance and lower intensity gives the best transverse cooling.

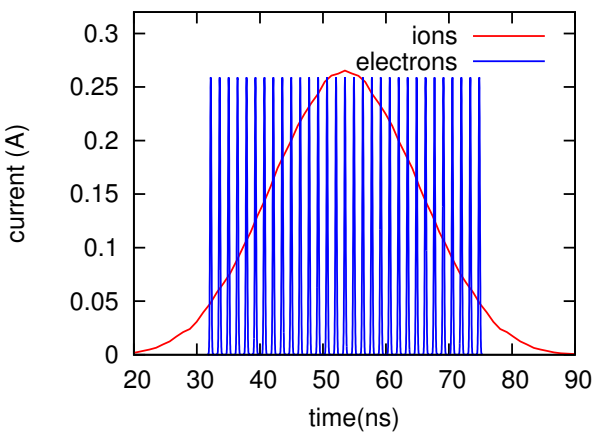

Figure 1: Ion and electron currents for $\gamma = 4.1$ with 65 pC electron bunches.

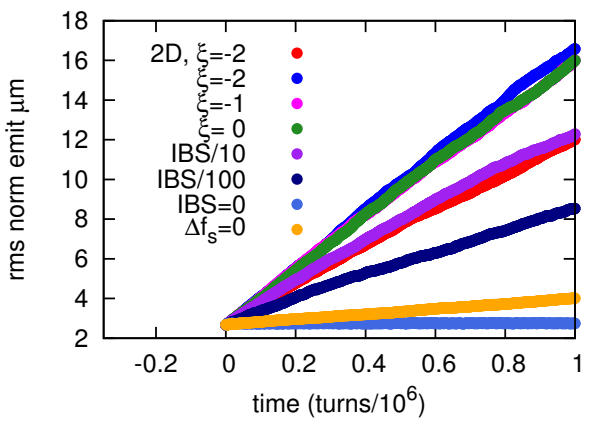

Figure 2: Simulations of emittance growth for a range of parameters, see the text for details.

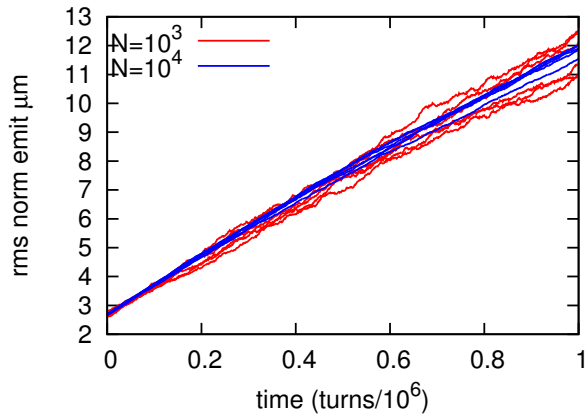

Figure 3: Emittance versus time for identical physical parameters with different random seeds and number of simulation particles.

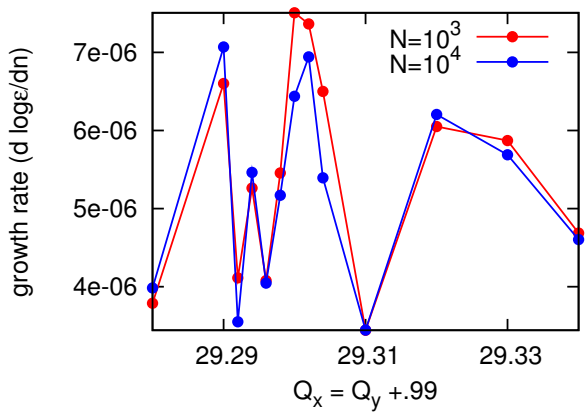

Figure 4: Growth rate as a function of betatron tune. The fine structure implies many resonances are relevant.

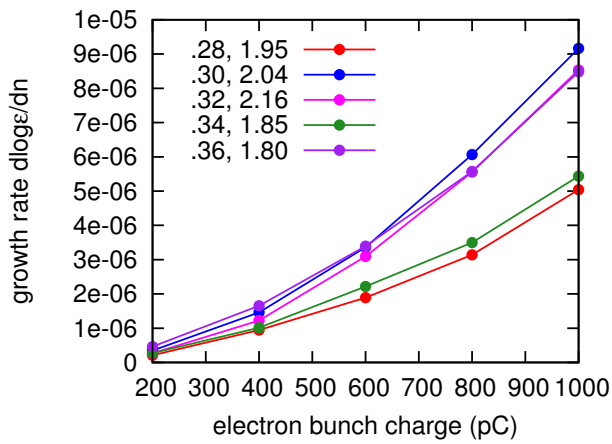

Figure 5: Growth rate versus bunch charge for 1D simulations. The curves are labeled by the non-integer part of the betatron tune and the power law for the growth rate obtained by fitting equation (9).

ISBN 978-3-95450-174-8

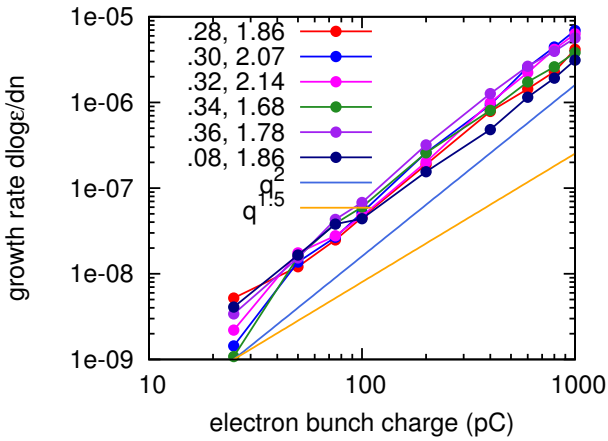

Figure 6: Growth rate versus bunch charge for 2D simulations. The curves are labeled by the non-integer part of the betatron tune and the power law for the growth rate obtained by fitting equation (9). Curves for power laws of 1.5 and 2 are shown for comparison.

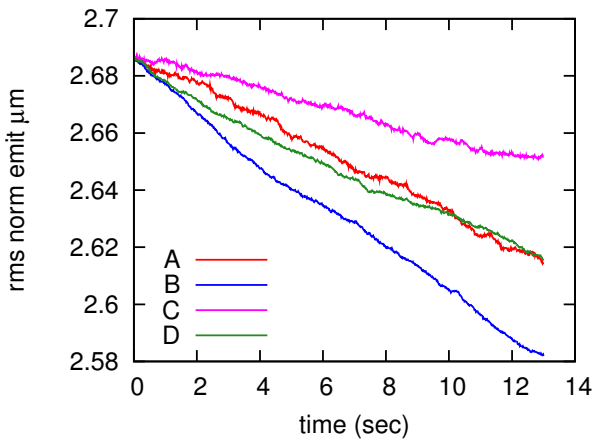

Figure 7: Ion emittance versus time for $\gamma = 4.1$ for various electron beam parameters:
A, $\sigma_p = 4 \times 10^{-4}$, $\epsilon = 2$ μm, $Q_e = 130$ pC;
B, $\sigma_p = 4 \times 10^{-4}$, $\epsilon = 1$ μm, $Q_e = 65$ pC;
C, $\sigma_p = 8 \times 10^{-4}$, $\epsilon = 2$ μm, $Q_e = 130$ pC;
D, $\sigma_p = 8 \times 10^{-4}$, $\epsilon = 1$ μm, $Q_e = 65$ pC.

CONCLUSION

Using bunched beams for electron cooling can lead to dynamically generated emittance growth. There are 3 required ingredients:

1. electron bunches that are of comparable length to the rms longitudinal slip per turn of the ions,
2. variation of the synchrotron frequency with amplitude,
3. longitudinal intrabeam scattering, although the dependence on rates is weak.

The emittance growth rate of the ions scales (approximately) like the square of the electron bunch charge. This was motivated theoretically and verified using simulations.

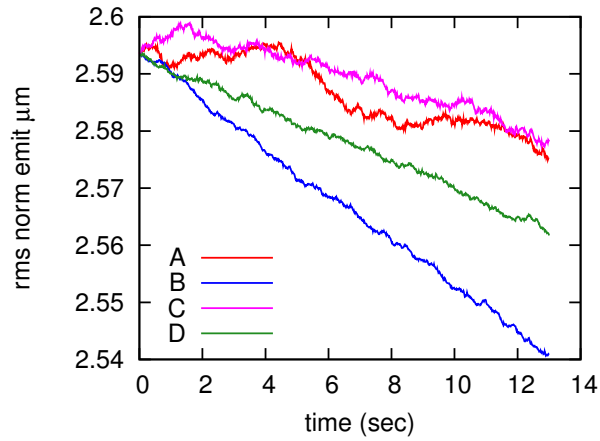

Figure 8: Ion emittance versus time for $\gamma = 6$ for various electron beam parameters:
A, $\sigma_p = 4 \times 10^{-4}$, $\epsilon = 2$ μm, $Q_e = 156$ pC;
B, $\sigma_p = 4 \times 10^{-4}$, $\epsilon = 1$ μm, $Q_e = 78$ pC;
C, $\sigma_p = 8 \times 10^{-4}$, $\epsilon = 2$ μm, $Q_e = 156$ pC;
D, $\sigma_p = 8 \times 10^{-4}$, $\epsilon = 1$ μm, $Q_e = 78$ pC.

ACKNOWLEDGMENT

This work followed from earlier unpublished work by Gang Wang and Vladimir Litvinenko. The present work has benefitted from conversations with Alexei Fedotov, Wolfram Fischer and Yun Luo.

REFERENCES

[1] See e.g. section 27 of Landau and Lifshitz, *Mechanics* 3rd edition, Pergamon (1989).

[2] See 4.224.9 and 3.613.3 in Gradshteyn and Ryzhik *Table of Integrals Series and Products* academic press, 1980.

[3] A. Piwinski in *Handbook of Accelerator Physics and Engineering*, Eds A. Chao and M. Tigner, p125, World Scientific (1999)

[4] P. Zenkevich, O. Boine-Frankenheim, A. Bolshakov, NIMA, Vol 561, Issue 2, p284 (2006).

[5] Alexei Fedotov, *private communication*.

[6] H. Poth, Physics Reports, Volume 96, No 3&4 (1990).

ISBN 978-3-95450-174-8

ELECTRON COOLING AT GSI AND FAIR - STATUS AND LATEST ACTIVITIES

J. Roßbach, C. Dimopoulou, M. Steck, GSI, Darmstadt, Germany

Abstract

The status, function and operation parameters of the existing and future electron coolers at GSI and FAIR are presented. We report on the progress of the ongoing recommissioning of the former CRYRING storage ring with its electron cooler at GSI. First systematic results on the cooling of a 400 MeV proton beam during the last ESR beamtime are discussed. Motivated by the demands of the experiments on high stability, precise monitoring and even absolute determination of the velocity of the electrons i.e. the velocity of the electron- cooled ion beams, high precision measurements on the electron cooler voltage at the ESR were carried out towards the refurbishment of the main high-voltage supply of the cooler. Similar concepts are underway for the CRYRING cooler high-voltage system.

INTRODUCTION

Following machines with electron coolers are available at GSI (Table 1) or foreseen within the FAIR project:

- SIS18 (18 Tm, electron cooling), in operation [1]: accumulation of stable ions.
- ESR (10 Tm, stochastic and electron cooling, internal target), in operation [1]: accumulation, storage, deceleration, experiments with stable ions / rare isotope beams (RIB).
- CRYRING (1.44 Tm, electron cooling), under installation and commissioning: storage, deceleration, experiments with stable ions/RIB (also antiprotons as a future option).

CRYRING AND ITS ELECTRON COOLER

Initially, CRYRING was the designated storage ring for FLAIR [2]. It was moved into a cave behind the ESR [3] to benefit from an earlier realisation of a working machine for ions. Activities concentrate around this CRYRING@ESR project as it also serves as a test bench for FAIR developments (control system, beam diagnostics, vacuum etc.).

CRYING@ESR is dedicated to low-energy experiments with highly-charged heavy ions like collision spectroscopy at the electron cooler, a transverse electron target and a laser spectroscopy setup [4]. The electron cooler is the most important device for preparation of (decelerated) stored beams and most experiments. In particular, for electron-ion recombination studies: (i) The adiabatic magnetic expansion by a factor 100 offers a transversally very cold electron beam with $k_B T_\perp = 1.5 - 3.5$ meV [5, 6] (compared to $k_B T_\perp \approx$ 200 meV in the ESR). The expected longitudinal electron beam temperature $k_B T_\parallel = 0.05 - 0.20$ meV is as usual determined by the longitudinal-longitudinal relaxation. (ii) The electron beam energy has to be ramped in a small range around the nominal electron energy which is matched to the ion velocity. Fast and precise ramping of the cooler voltage will be realised by a special HV amplifier in the range ± 2 kV installed on the HV platform [4].

Table 1: Basic Operation Parameters of the Electron Coolers at GSI. Typical values are in brackets.

Parameter	SIS18	ESR	CRYRING
main HV power supply (kV)	≤ 35	≤ 320	≤ 20
e^- energy/HV (kV)	[≤ 7]	[2-220]	[≤ 8]
e^- current (A)	[0-1.5]	[0-1]	[0-0.15]
gun perveance (µperv)	2.9	2	1.68
cathode diameter (inch)	1	2	0.16
adiab. exp. factor	1-8	1	10-100
guiding B field (T)		[0.02-0.1]	
in gun	≤ 0.4 [0.18]		≤ 4 [3]
in cool. section	≤ 0.15 [0.06]		≤ 0.3 [0.03]
cool. section length/eff. (m)	3.4/2.8	2.5/1.8	1.1/
ring circumference (m)	216	108	54
vacuum (mbar)	10^{-11}	10^{-12}-10^{-11}	10^{-12}-10^{-11}

In 2015 considerable efforts were made to rebuild the CRYRING machine and provide the associated infrastructure (Fig. 1). In parallel, the cooler had to undergo repairs because of damage to the gun toroid vacuum chamber, which occured after the transport from Sweden (complete disman-

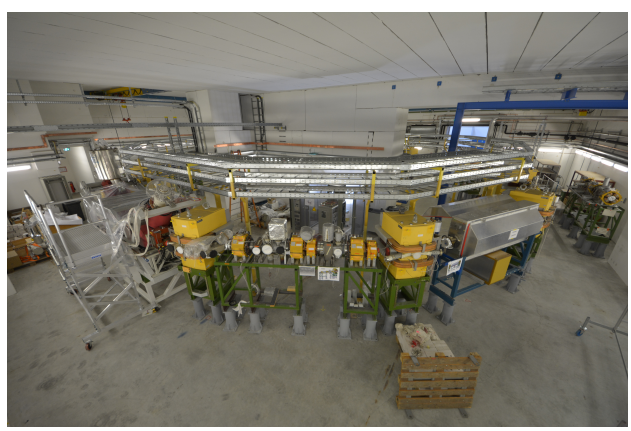

Figure 1: CRYRING in the cave behind the ESR.

ISBN 978-3-95450-174-8

tling of the cooler gun side was necessary for welding purposes). Refurbishments were also made to cabling, cooling water circuits and to the vacuum system by adding gauges and some new heating jackets. After successful leak test the cooler was moved to its final position inside the cave (Fig. 2). Many tasks still remain, like cabling of the magnets, cabling of the HV system and the isolation transformer that powers the components on the HV platform, preparation of control software and the installation of a cryogenic He transfer line for easy handling and fast refilling of the superconducting gun solenoid.

Figure 2: CRYRING cooler in the cave.

According to the current time table, vacuum pumping and commissioning of the ring without beam starts at the end of 2015. First-turn commissioning of the ring with light ions from an internal ion source [4] will take place in 2016. First standalone operation of the cooler with electron beam is scheduled for early 2016.

RECENT ESR COOLER OPERATION

During the beam time in 2014 several machine development experiments were carried out. The feasibility of a possible future use of the ESR in a chain of decelarators for antiprotons at FAIR has been investigated. Both stochastic and electron cooling systems at the ESR were used to cool a proton beam at 400 MeV. For 10^8 protons with an initial rms momentum spread of $4 \cdot 10^{-4}$ the longitudinal damping time was about 8 s for stochastic cooling with the notch filter method. As expected, for electron cooling, the damping time was much longer i.e. 600 s for protons at the edge of the initial momentum distribution with 0.25 A electron current (Fig. 3). On the other hand, the final rms momentum spread reached with electron cooling was $2 - 3 \cdot 10^{-5}$ compared to $1 - 2 \cdot 10^{-4}$ with stochastic cooling.

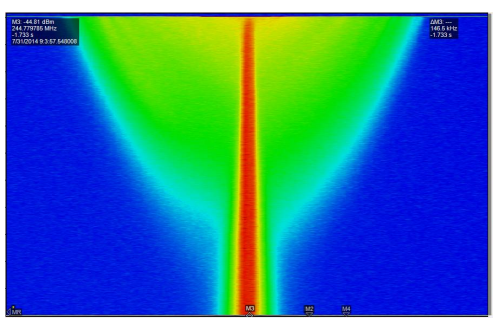

Figure 3: Longitudinal electron cooling of a 400 MeV proton beam with an electron beam current of 0.25 A in the ESR. Frequency spectrum measured with the resonant Shottky pickup [7] at 245 MHz (125th harmonic), span=200 kHz, total recording time = 650 s. The momentum spread was reduced from $4 \cdot 10^{-4}$ down to $3 \cdot 10^{-5}$ in 7 min.

At high beam phase space density, Schottky signal suppresion due to collective effects is expected [8]. This effect was demonstrated during strong electron cooling of a high-intensity proton beam at 400 MeV (Fig. 4). For stochastic cooling with the notch filter, the longitudinal damping time for 10^9 protons was about 15 s, whereas Schottky signal suppression was not observed.

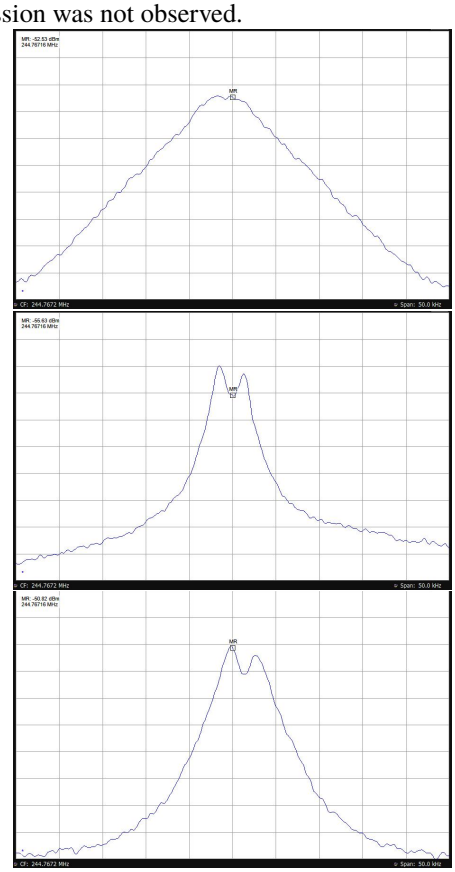

Figure 4: Schottky signal suppression (double peak structure, reduction of total integrated noise power) appearing in the momentum distribution of a beam of $1.3 \cdot 10^9$ protons with increasing electron cooler current; top: 100 mA, middle: 250 mA, bottom: 500 mA. Frequency spectra from the resonant Schottky pickup at 245 MHz, span=50 kHz.

HV MEASUREMENTS AT THE ESR COOLER

The versatile operation of the ESR cooler relies on the high stability of the velocity of the electron-cooled ion beams, realised by an adjustable, highly-stable (within ±1 V) accelerating voltage for the electron beam within an operation range of 2-220 kV. This is achieved with the main DC HV power supply of the cooler, which is a -320 kV device in a pressurized vessel filled with SF_6 gas.

ISBN 978-3-95450-174-8

Experiments, like the laser spectroscopy of Bi ions and the precise energy matching to the HITRAP decelerating linac [9] demand absolute determination and the continuous precise monitoring of the applied HV accelerating the electron beam.

Before the last beam time in 2014, the HV power supply was serviced at the manufacturer site for correction of minor voltage instability and renewal of the SF_6 system. It was then transported to the german National Metrology Institute Physikalisch-Technische Bundesanstalt (PTB) for HV calibration. Unfortunately, the device was seriously damaged during transport, had to be refurbished again at the manufacturer site and was delivered back to GSI. To avoid more damage by transport an alternative concept was applied: a portable highly-precise HV divider callibrated against the PTB standards was used for real-time monitoring of the output of the HV power supply of the cooler.

A $^{209}Bi^{82+}$ beam at 390 MeV/u was used in a laser spectroscopy experiment of the hyperfine transition of hydrogen-like bismuth [10]. This was achieved by monitoring the applied voltage to the cooler with a calibrated HV divider. To meet the demands of the experiment, the PTB provided a high precision voltage normal. This voltage divider HVDC2.1 (Fig. 5 - top) featured a relative accuracy of $1.3 \cdot 10^{-5}$ in the Bi experiment performed at 214 kV cooler voltage [10, 11]. This increased the measurement accuracy compared to former beam times when the relative accuracy was below 10^{-4} [12] . Thus, it was found that the output voltage of the HV power supply showed significant variations over time: ±20 V (or even more) at 200 kV. This was independently confirmed in the longitudinal Schottky spectra of the ion beam (Fig. 6). With the high-precision HV divider the variations could be recorded online and were taken into account in the data during offline analysis.

The large variations of the output voltage resulted from damage to HV diodes and HV resistors in the output divider inside the HV power supply. The power supply had to be repaired again by the manufacturer on the GSI site (to avoid transportation risks). Since then, it has recovered its value of relative stability and operates as specified.

OUTLOOK

In the near future, it is foreseen to have a dedicated HV divider for experiments. This divider has aleady been tested and calibrated against the national standards of the PTB (Fig.5 - bottom).

In consideration of a prolonged operation of the ESR until 2030 a replacement for the main HV power supply (manufactured in 1988) will be needed.

Similar concepts are foreseen for the low-energy range (<20 kV), both at the ESR and the CRYRING coolers: a calibrated precise (≤ 1ppm) HV divider up to 20 kV based on the established PTB/KATRIN technology [4, 13, 14] will be implemented in their high voltage systems.

Figure 5: The Faraday room of the electron cooler. Top: The -320 kV power supply is shown on the left and the HV platform on the right. The HVDC2.1 200 kV (2 GΩ) DC HV divider (property of the PTB) is installed (in orange). Bottom: The Ohmlabs HVS 250 kV (250 MΩ) DC HV divider (property of the TU Darmstadt) specified for 10^{-4} precision is installed. The isolating transformer (in grey) powering the HV platform is seen in the back.

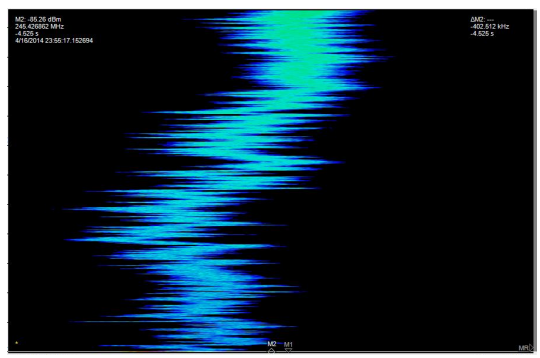

Figure 6: The instability of the electron cooler voltage observed in the longitudinal spectrum of the beam in the ESR. Frequency variation of ± 5 kHz around 245 MHz (span =20 kHz) corresponding to $\Delta V/V = \pm 10^{-4}$ i.e. ± 20 V at 200 kV for the cooler voltage. Total recording time= 90 min.

ACKNOWLEDGMENT

We thank the CRYRING@ESR group, the team of W. Nörtershäuser at the TU Darmstadt and the PTB experts for their valuable input and many fruitful discussions. We specially thank our technicians M. Bräscher and J.Krieg and acknowledge the support from the GSI transport/ installation and UHV groups.

ISBN 978-3-95450-174-8

REFERENCES

[1] M. Steck, F. Nolden, ICFA Beam Dynamics Newsletter No. 64, p.87 (2014).

[2] C. P. Welsch et al., Hypefine Interactions 172, Issue 1-3, p.71 (2007).

[3] M. Lestinsky et al., Proc. of STORI'14, to appear in Phys. Scripta (2015).

[4] M. Lestinsky et al., Technical Design Report: Experimental Instrumentation of CRYRING@ESR, internal report (2015).

[5] H. Danared et al., Nucl. Instr. and Meth. A 441, p.123 (2000).

[6] G. Gwinner et al., Phys. Rev. Lett. 84, p.4822 (2000).

[7] F. Nolden et al., Nucl. Instr. and Meth. A 659, p.69 (2011).

[8] S. Cocher, I. Hofmann, Particle Accelerators 34, p. 189 (1990).

[9] T. Beier et al., Nucl. Instr. and Meth. B 235, p.473 (2005).

[10] J. Ullmann et al., J. Phys. B 48, p.144022 (2015).

[11] J. Hallstrom et al., Conference on Precision Electromagnetic Measurements 2012, 10.1109/CPEM.2012.6250874.

[12] M. Lochmann et al., Phys. Rev. A 90, 030501(R) (2014).

[13] T. Thümmler et al., New J. Phys. 11, 103007 (2009).

[14] S. Bauer et al., J. Inst. 8, P10026 (2013).

ISBN 978-3-95450-174-8

THE SNS LASER STRIPPING EXPERIMENT AND ITS IMPLICATIONS ON BEAM ACCUMULATION

S. Cousineau, A. Aleksandrov, T. Gorlov, Y. Liu, A. Menshov,
M. Plum, A. Rakhman, ORNL, TN 37922, USA
D. Johnson, Fermilab, Batavia, IL 60510, USA

Abstract

The laser assisted H^- charge exchange concept is under development at the SNS as on option for replacing traditional carbon-based foil technology in future HEP accelerators. A laser based stripping system has the potential to alleviate limiting issues with foil technology, specifically radiation from beam scattering and foil survivability, paving the way for accumulation of higher density proton beams. This paper discusses the advantages and limitations of a laser-based stripping system compared with traditional foil-based charge exchange systems for various beam accumulation scenarios, scaling from SNS experience with high power beam injection and calculations of laser stripping parameters. In addition, preparations for an experimental demonstration of laser assisted stripping for microsecond long 1 GeV, H^- beams are described.

INTRODUCTION

The standard method for accumulating intense beams of protons is through H^- charge exchange from a linac into a synchrotron. In this scheme, an H^- beam from a linear accelerator is merged with a circulating proton beam in a ring. The merged beam is subsequently passed through a thin (~μm) carbon foil that strips the electrons from the H^- ions to yield a proton beam [1]. While in principle this non-Liousvillian technique can yield indefinitely dense proton beams, in practice the beam density is limited by the stripping mechanism.

The presence of the foil in the beamline introduces two major performance limitations. First, energy deposition in the foil leads to foil heating. Foils suffer vulnerabilities in their structural integrity when thermal effects are high causing warps, holes and tears. The primary failure mechanism for foils is sublimation above a certain temperature threshold, which translates into constraints on the achievable beam power densities. Existing high power machines such as the SNS accelerator are already estimated to operate just below this limit [2]. Second, particle scattering in the foil leads to large levels of beam loss and activation. This issue is pervasive across machines that utilize H^- charge exchange injection, and results in residual radiation levels typically an order of magnitude greater than the rest of the accelerator [3].

While schemes such as injection painting can be used to minimize beam foil trav0ersals and their subsequent effects, they are not infinitely scalable because they result in progressively larger beam emittances and machine apertures. An interesting question to consider is what a proton accumulation scenario would look like if the charge exchange process could be accomplished without the use of a foil. This paper will explore this question through a set of experiments in the SNS proton accumulator ring. Following this, the development of laser stripping method, a foil-free alternative stripping scheme, will be described.

HIGH DENSITY EXPERIMENT AT SNS

Experimental Configuration

The SNS accumulator ring accumulates up to 1.5e14, 1 GeV protons during a 1 ms, 1000 turn accumulation cycle. The injection process utilizes 400 μg/cm2 nanocrystalline diamond foils. Correlated dual plane injection painting is employed via a set of injection kickers which fall off by 52% over 1000 turns in a $\sqrt{turns}$ fashion.

The purpose of the experiment was to approximate what beam parameters could be accomplished in the absence of injection foil limitations. While the injection foil can not in reality be removed from the system, the beam can be run in a configuration with reduced repetition rate, i.e., 1 Hz instead of the 60 Hz, to avoid foil heating and allow for temporarily higher levels of beam loss. Besides the repetition rate, the remainder of the beam parameters were fixed at nominal production values, with 1.43e14 ppp accumulating over 1000 turns. This produces a "1.4 MW equivalent" beam in a per pulse sense.

The effects of three injection painting scenarios were explored: 1) No painting, 2) Nominal painting, and 3) Shallow painting with an injection kicker amplitude fall of 30% (compared with the nominal 52%). For each of these scenarios, the initial injection kicker amplitudes were varied to alter the beam emittance, up until the point where injection losses exceeded acceptable values even at 1 Hz. For each setting, the beam loss in the ring and the final beam emittance was recorded. Due to constraints on the allowable peak beam density on target, the emittances were only measured directly for the nominal production configuration. The remainder of the emittances were derived from ratios of the rms beam sizes with the production case at a common wirescanner location.

Results

Fig. 1 shows the results of the measured emittances for the various beam configurations. The upper right point, with emittance (ε_x=29 mm*mrad, ε_y=36 mm*mrad), represent the nominal configuration. By contrast, the smallest emittance achieved was (ε_x=12 mm*mrad, ε_y=17 mm*mrad), roughly a factor of two smaller in each plane.

ISBN 978-3-95450-174-8

Figure 2 shows the horizontal profiles for the nominal case compared with the smallest emittance case. No visible tails were seen on the smaller emittance case, and no space charge limitations were encountered.

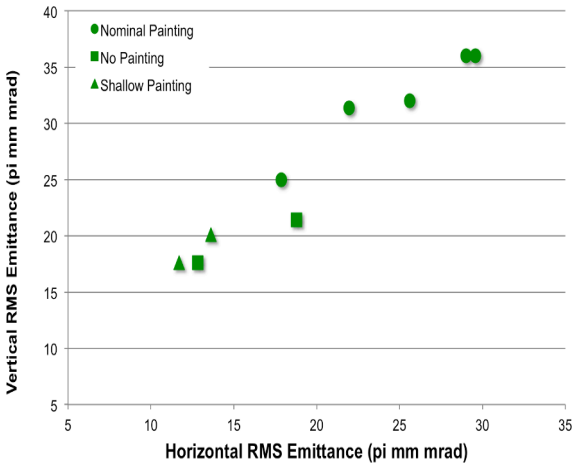

Figure 1: Measured horizontal and vertical rms emittances.

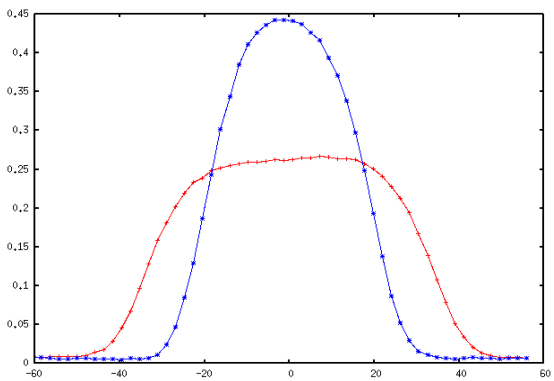

Figure 2: Horizontal beam profiles after extraction from the ring for the upper right most data point on Fig. 1 (red), and the lower leftmost data point on Fig. 1 (blue).

The lower bound on beam emittance in the experiment was set by the injected beam loss. Fig. 3 shows the beam loss monitor (BLM) signal for one of the main injection area BLMs, versus measured beam emittance for the various accumulation scenarios. As seen, a factor of two decrease in emittance resulted in a factor of ten increase in injected beam loss. Even with the reduced repetition rate, it was considered hazardous to the injection foil to decrease the emittance beyond this point.

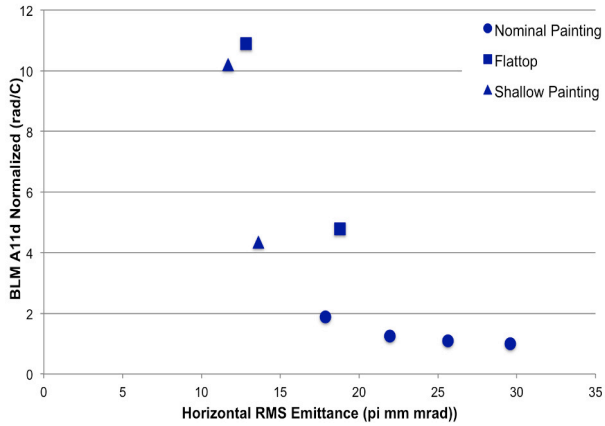

Figure 3: Injection BLM reading versus measured horizontal emittance.

Discussion of Results

It is interesting to consider the implications of the lowest emittance case, by scaling the current SNS full-power parameters with these numbers for scenarios (a) with an injection foil, and (b) without an injection foil.

Case (a): The current residual radiation values in the SNS injection region are about 0.8 – 1 rem/hr at 30 cm. The observed factor of ten increase in beam loss, corresponding to the smallest emittance beam, would result in roughly 10 rem/hr of radiation in this region. This would have severe implications on routine maintenance of the injection foil system components. In addition, from simulations, the estimated foil temperatures for the nominal 1.4 MW operation peak at about 1550 K, which is just below the predicted sublimation range of 1575 K-2270 K [2]. The thermal power radiated scales as temperature to the fourth power, and thus a factor of ten increase in radiation would result in foil temperatures in the neighbourhood of 2700 K. At these temperatures, the foils would sublimate within minutes when operating at the full repetition rate of 60 Hz.

Case (b): Without the injection foil present, neither the issue of foil sublimation nor the issue of activation from foil scattering would exist. Radiation levels in the injection region would be reduced to the nominal SNS ring levels of < 5 mrem/hr. Furthermore, operation with a factor of two smaller in beam emittance would translate in to a factor of $\sqrt{2}$ reduction beam pipe aperture. For instance, in principal the nominal SNS ring aperture could have been reduced from 100 mm to 70 mm, which would have saved in fabrication costs and vacuum requirements. Finally, the current painting scheme, which is designed to minimize circulating beam foil traversals, could be optimized for other purposes, such as mitigating space charge effects.

ISBN 978-3-95450-174-8

LASER ASSISTED STRIPPING

The Laser Stripping Concept

An alternative approach to foil based charge exchange injection is laser-assisted H^- stripping. In this concept, an H^- ion beam is passed through a dipole magnet which strips off the first electron through the process of Lorentz stripping (H^- to H^0). The second, inner electron is too tightly bound to be stripped off using a conventional magnet while in the ground state, and thus a laser is used to excite the electron to a higher quantum state with a smaller binding energy (H^0 to H^{0*}). While in the excited state, the H^{0*} is passed through a second dipole magnet of comparable strength to the first, which strips off the remaining electron to produce a proton (H^{0*} to p). Due to the absence of material in the path of the beam, this technique does not suffer from the same performance limitations as foil-based charge exchange injection, and is scalable to infinitely high beam densities.

Though the idea of laser stripping was conceptualized over three decades ago [4], the technique was limited by the Doppler broadening of the resonant excitation frequency of the laser, and available laser technology. This limitation was overcome in a 2006 proof of principle experiment which utilized a diverging laser beam to introduce a frequency sweep in the rest frame of the laser. The experiment demonstrated successful (>90%) stripping of a 6 ns, 1 GeV H^- beam using a 10 MW UV laser [5]. Unfortunately, a direct scaling of this experiment to full duty factors results in unrealistically large laser powers. To advance this concept one must find ways to reduce the laser power requirement to achievable levels.

The 10 μs Laser Stripping Experiment

The next step in the development of the laser stripping method is a demonstration of stripping for a 10 μs beam. This is a factor of one thousand improvement over the initial demonstration of the concept. The experiment will take place in the SNS High Energy Beam Transport line (HEBT) which connects the superconducting linac (SCL) to the ring, and will rely on the successful implementation of a number of laser power savings techniques [6].

Laser Power Savings Techniques The laser power savings techniques can be broken down into to categories: 1) Methods for reducing the required peak power, and 2) Methods for reducing the required average power.

To reduce the require laser peak power, one must overcome the problem of the resonant frequency spread without using a diverging laser beam, which reduces the laser light density and therefore requires more peak power. The required laser frequency for resonant excitation of an H^0 particle depends on the particle's energy and the angle between the particle and laser beam trajectory. The dispersion function, which relates a particle's energy with its trajectory, can be tailored to manipulate the individual angles such that each energy and angle pair yields the same resonant excitation frequency [7]. Once the dispersion tailoring is accomplishment, the remaining energy spread is due to transverse divergence of the beam and can be minimized by requiring that Twiss α=0. Finally, in order to maximize the interaction between the laser and ion beam, the vertical beam size should be minimized at the interaction point. The dispersion and Twiss parameters are accomplished through tuning of quadrupoles upstream of the experiment, and have been demonstrated simultaneous in a repeatable fashion. Taken together, these methods result in a factor of ten reduction in the required UV laser peak power, from 10 MW to 1 MW.

The average required laser power can be computed through the following equation:

$$P_{average} = P_{peak}(\sigma_v, \Delta f_{resonant}) \times (\sigma_l \; f_{micro} \; f_{macro}) \times \Delta t$$

The 1 ms SNS macropulse is composed of a 402.5 MHz train of ~50 ps micropulses. Thus for the majority of the time there is no ion beam present for the laser to interact with, and a significant reduction in average laser power can be realized by temporal matching the pulse structure of the laser beam with the ion beam. Fig. 2 shows the configuration of the laser pulse and the resulting 402.5 MHz, 50 ps micropulses. The laser is a master oscillator power amplification (MOPA) scheme with 402.5 MHz, ~50 ps pulses generated from a 1064 nm seed laser and passed into a pulse picker to create 10 μs macropulse bursts. The light is then amplified in three stages before a two-stage harmonic conversion to the required 355 nm wavelength. This laser has been measured to produce 1 – 3 MW peak power, for 30 – 55 ps bursts.

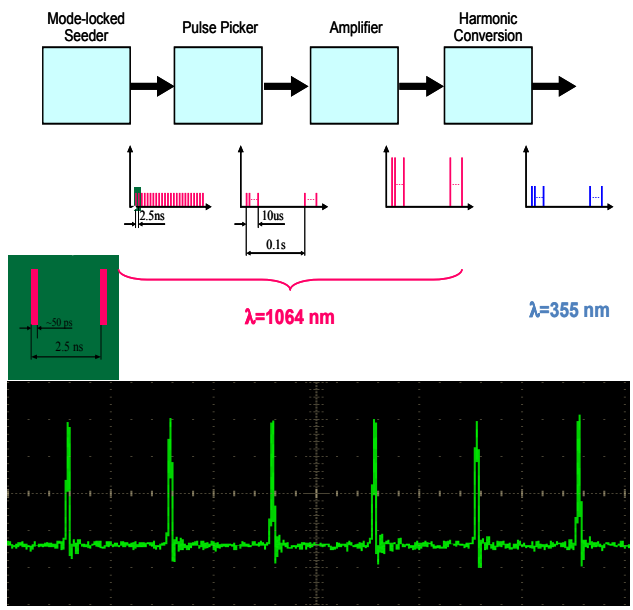

Figure 4: (Top) Schematic of the MOPA configuration for the high power UV laser beam. (Bottom) Meausred 402.5 MHz, 50 ps UV laser pulses.

ISBN 978-3-95450-174-8

The final savings on average laser power comes from a longitudinal squeeze of the ion beam to produce full overlap with the laser beam pulse. Nominally, the ion beam expands under the influence of space charge and momentum spread after exiting the last accelerating cavity. For the laser stripping experiment, however, the last ten superconducting cavities are configured to provide a longitudinal waist in the beam at the downstream interaction point for the experiment. This technique has been successfully demonstrated several times.

Putting together all of the power savings techniques, the final average laser power is ~2 W, which is sufficient for the 10 μs stripping experiment, including some margin.

Experimental Configuration The interaction point for the laser stripping experiment will be located in the SNS HEBT, in a low radiation region downstream of the ninety degree achromat. This location takes advantage of the bend for dispersion tailoring and has the upstream optics necessary to achieve all of the required Twiss parameters. The designed and as-installed experimental vessel for the interaction point is shown in Fig. 3 below. The vessel contains two ~ 1 T permanent dipole magnets mounted on a retractable actuator, a dual plane wirescanner to confirm the transverse beam parameters at the interaction point, a downstream BCM for validating the experiment, and input an exit windows for the laser as well as two viewports.

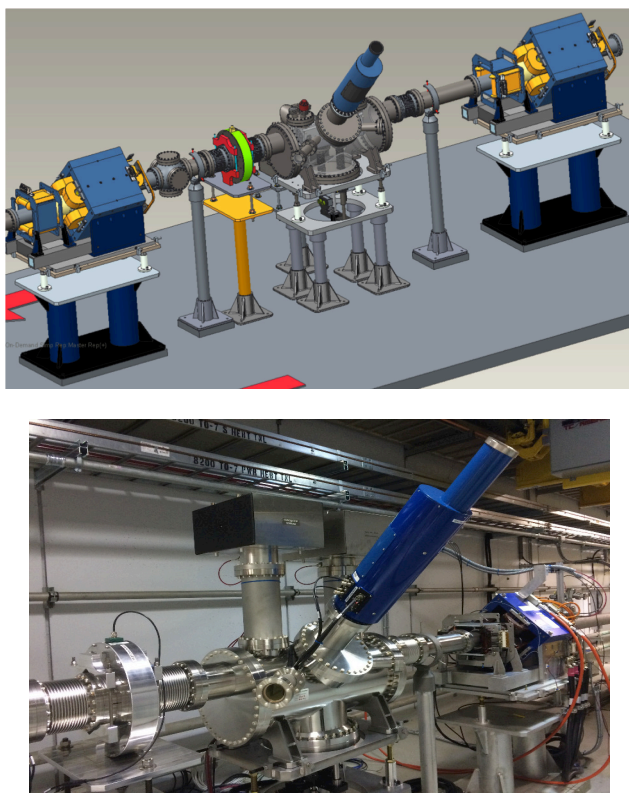

Figure 5: (Top) Engineering drawing of the laser stripping experimental vessel. (Bottom) Photo of the as-installed vessel.

In order to protect the laser and provide flexibility in the experimental schedule, the high power UV laser will be located in the ring service building and transported 70 m to a local optical table adjacent to the interaction point. Two major concerns with remote placement of the laser were power loss in transport and pointing stability.

The power losses on the mirrors and windows were independently measured, and the total path length in air was simulated by cycling the laser through six iterations of an 8 m, four-mirror loop. The results are promising: The power loss per mirror was less than 1%, and the power loss in air, extrapolated to 70 m, was less than one third. The major source of the power loss in air is believed to be Fresnel diffraction at the aperture and loss of higher order modes in transport, an effect which diminishes with distance. Furthermore, it was determined that a single piezo-electric transducer (PZT) would be sufficient to provide laser pointing stability.

Taking into account the estimated power loss in transport, and inputting the experimentally-measured ion and laser beam parameters into the pyORBIT model of the stripping system [8], the final laser stripping efficiency is estimated to be >90%. The installation for the experiment is nearly complete and the demonstration of 10 μs stripping is expected to commence in Spring 2016.

Laser Power Recycling and 1 ms Stripping

To extend the laser stripping concept beyond microsecond pulse lengths and into operational parameter regimes, one must find a way to extend the high power laser pulse without exceeding commercially available average UV laser powers in the range of 1-10 W. Since only one in 10^7 photos is "spent" during each passage of the laser beam through the ion beam, a logical option is to recycle the laser pulses. Optical power recycling cavities provide power enhancement through the process of coherent addition, allowing lasers of arbitrary burst lengths to be amplified to high peak powers. As such, for a constant input laser power, one can utilize a longer duration pulse with a lower peak power, and subsequently amplify to high peak power in the cavity.

After the 10 μs demonstration, the next step in the laser stripping development will be to employ such a power recycling cavity to demonstrate 1 ms capable laser stripping of the SNS 1 GeV H^- beam. The current experimental vessel, shown in Fig. 5, was designed to accommodate the recycling cavity with only minor modification. In addition, a doubly resonant power enhancement cavity scheme was has been under development to realize amplification of burst mode UV laser pulses. In the most current version of the concept, an auxiliary IR laser beam is used to lock the cavity and provide stable amplification of the UV laser macrobursts through a frequency tuning approach [9]. The scheme resulted in a factor of 50 enhancement of a lower power UV beam, exceeding the initial proposal goal by almost a factor of two. However, at this stage the peak in cavity power is limited to 120 kW, solely by the cavity mirror

ISBN 978-3-95450-174-8

damage threshold. Modifications to the system to overcome this limitation have been identified and will be implemented in the near future.

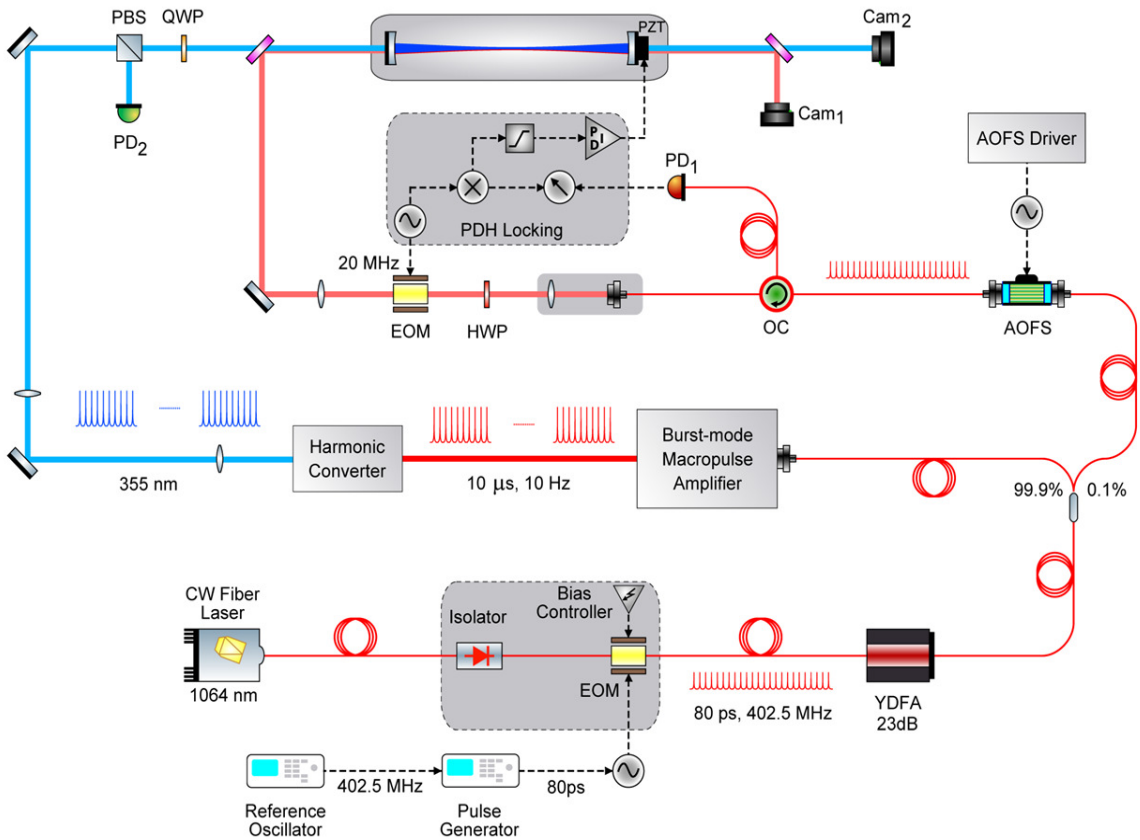

Figure 6: Schematic of the doubly resonant power recycling cavity for amplification of burst mode UV laser pulses.

ACKNOWLEDGMENT

This work has been partially supported by U.S. DOE grant DE-FG02-13ER41967. Oak Ridge National Laboratory is managed by UT-Battelle, LLC, under contract DE-AC05-00OR22725 for the U.S. Department of Energy.

REFERENCES

[1] S.Y Lee, Accelerator Physics, World Scientific, 1998.

[2] Michael Plum, Jeffrey A Holmes, R.W. Shaw, and C.S. Feigerle, "SNS Stripper foil development program," Nuclear Instruments and Methods in Physics Research A, vol. 590, pp. 43-46, 2008.

[3] Sarah Cousineau, "High Power Proton Beam Facilities: Operational Experience, Challenges, and the Future ," in International Particle Accelerator Conference 2015, Richmond, 2015, pp. 4102-4106.

[4] A. Zelensky, S.A. Kokohanovskiy, V.M. Lobashev, N.M. Sobolevskiy, and E.A. Volferts, Nuclear Instruments and Methods Phys. Res., Sect. A, vol. 227, no. 429, 1984.

[5] V. Danilov et al., "Proof-of-principle demonstration of high efficiency laser-assisted H- beam conversion to protons," PRST-AB, vol. 10, no. 053501, 2007.

[6] Sarah Cousineau, "Status of Preparations for a 10 microsend laser-assisted H0 beam stripping experiment," in International Particle Accelerator Conference 2014, Dresden, pp. 1864-1866.

[7] V. Danilov, "Future prospects for laser stripping injection in high intensity machine," in *Proceedings of the ICFA 2008 Workshop on High Brightness Hadron Beams*, Nashville, 2008, pp. 284-289.

[8] T. Gorlov, V. Danilov, and A. Shishlo, "Laser-assisted H- charge exchange injection in mangetic fields," *PRST-AB*, vol. 13, no. 050101, 2010.

[9] Abdurahim Rakhman, Yun Liu, Chunning Huang, and Mark Notcutt, "Doubly-resonant Fabry0Pero cavity for power enhancement of burst-mode picosecond ultraviolet pulses," in CLEO, San Jose, 2015.

ISBN 978-3-95450-174-8

RF TECHNOLOGIES FOR IONIZATION COOLING CHANNELS *

B. Freemire†, Y. Torun, Illinois Institute of Technology, Chicago, IL 60616, USA
D. Bowring, A. Moretti, D. Peterson, A.V. Tollestrup, K. Yonehara, FNAL, Batavia, IL 60510, USA
A. Kochemirovskiy, University of Chicago, Chicago, IL 60637, USA
D. Stratakis, BNL, Upton, NY 11973, USA

Abstract

Ionization cooling is the preferred method of cooling a muon beam for the purposes of a bright muon source. This process works by sending a muon beam through an absorbing material and replacing the lost longitudinal momentum with radio frequency (RF) cavities. To maximize the effect of cooling, a small optical beta function is required at the locations of the absorbers. Strong focusing is therefore required, and as a result normal conducting RF cavities must operate in external magnetic fields on the order of 10 Tesla. Vacuum and high pressure gas filled RF test cells have been studied at the MuCool Test Area at Fermilab. Methods for mitigating breakdown in both test cells, as well as the effect of plasma loading in the gas filled test cell have been investigated. The results of these tests, as well as the current status of the two leading muon cooling channel designs, will be presented.

INTRODUCTION

Ionization cooling appears to be the only method of significantly reducing the emittance of a muon beam within the lifetime of a muon. The Muon Ionization Cooling Experiment (MICE) will validate simulation codes and demonstrate ionization cooling with reacceleration of a muon beam, and is currently underway [1]. The change in normalized transverse emittance with path length is given by

$$\frac{d\epsilon_n}{ds} = \frac{1}{\beta^3}\frac{\beta_\perp (0.014)^2}{2E_\mu m_\mu X_0} - \frac{1}{\beta^2}\left\langle\frac{dE_\mu}{ds}\right\rangle\frac{\epsilon_n}{E_\mu} \qquad (1)$$

where $\beta = v/c$, $\beta_\perp$ is the transverse optical beta function, E_μ and m_μ are the energy and mass of the muon, respectively, and X_0 and $\left\langle\frac{dE_\mu}{ds}\right\rangle$ are the radiation length and stopping power of the absorbing material, respectively. The first term in Eq. 1 is the heating term, due to multiple scattering, and the second is the cooling term. To minimize the effect of multiple scattering, a small beta function at the location of the absorbers and a large absorber radiation length are ideal. Hydrogen and lithium hydride have been selected as absorbing materials, due to their radiation length and stopping powers.

A small beta function dictates strong focusing, and as longitudinal momentum lost in the absorbers is replaced by radio frequency (RF) cavities, these cavities are subject to external magnetic fields larger than 1 T. This immediately rules out the use of superconducting cavities, and an experimental program set out to determine how normal conducting RF cavities performed in such an environment at Lab G and currently the MuCool Test Area (MTA), both at Fermilab.

BREAKDOWN IN RF CAVITIES

High voltage breakdown in both vacuum and gas has been studied extensively. The presence of a multi-tesla external magnetic field provided a new variable, however. As ionization cooling depends on RF cavities operating in such an environment, the performance of said cavities must be understood and characterized.

Early experiments focused on 805 MHz vacuum RF cavities. Both a six cell standing wave cavity and a single cell pillbox cavity were tested. The pillbox cavity allowed for different materials (copper, beryllium, molybdenum) and endplate structures (flat, curved, electrode) to be studied. The results of each indicated that there was a strong negative correlation between maximum accelerating gradient in the cavity and applied external magnetic field [2–5]. Plots from these experiments are shown in Figures 1 and 3.

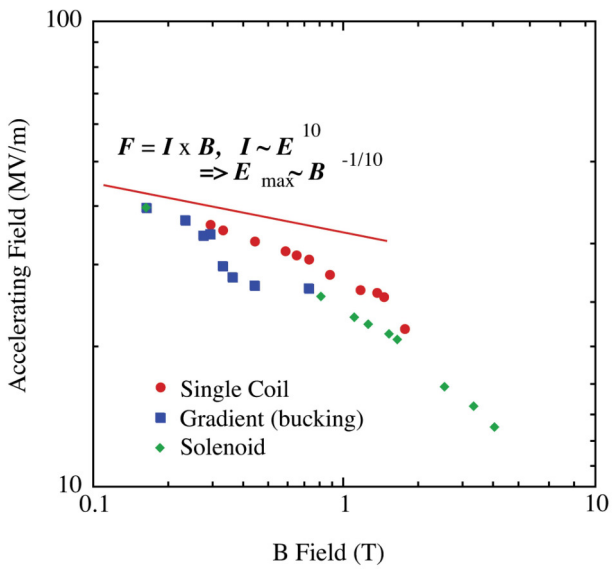

Figure 1: Maximum accelerating gradient as a function of external magnetic field from Ref. [3]. The data were collected with an 805 MHz vacuum pillbox cavity. Various coil configurations of the solenoid are shown.

A model to explain breakdown of RF cavities in external magnetic fields was proposed [6]. In this model, the mag-

* Work supported by the Fermilab Research Alliance, LLC under Contract No. DE-AC02-07CH11359.
† freeben@hawk.iit.edu

ISBN 978-3-95450-174-8

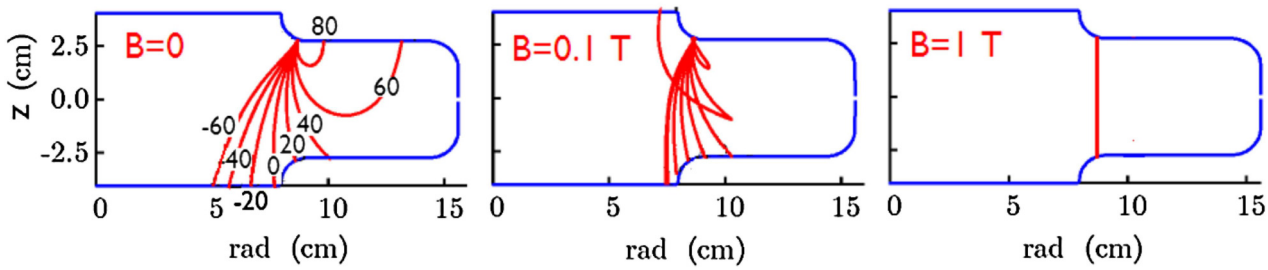

Figure 2: Simulation of the trajectories of field emission electrons as a function of magnetic field in an 805 MHz vacuum pillbox cavity from Ref. [6]. Phases of emitted electrons relative to the peak of the electric field are shown.

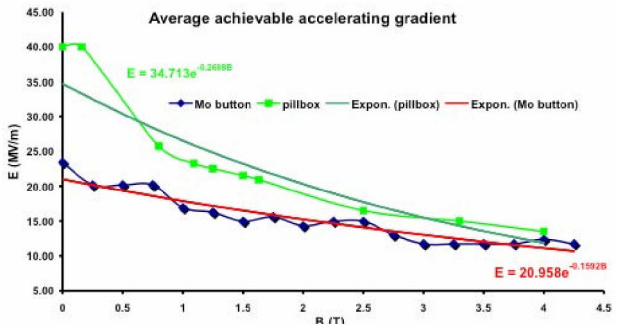

Figure 3: Maximum accelerating gradient as a function of external magnetic field from Ref. [2]. The data were collected with an 805 MHz vacuum pillbox cavity. Data for both the configuration of flat copper plates and a molybdenum electrode placed on the cavity axis are shown.

netic field focuses field emission electrons along trajectories with radii determined by the strength of the magnetic field. These "beamlets" of electrons impact the opposite surface of the cavity, depositing their energy. The surface heats after repeated bombardment, becoming damaged and creating new sources of field emission. This limits the achievable electric field. The stronger the magnetic field, the more focused the beamlets become, depositing energy in a smaller volume and more quickly leading to damage on the surface of the cavity. Figure 2 shows a simulation of how an external magnetic field affects the trajectories of electrons emitted from a location on one surface of an RF cavity.

GAS FILLED CAVITIES

It was suggested that filling an RF cavity with a high pressure gas would both prevent high voltage breakdown and provide an absorbing material [7]. Field emission electrons lose energy through collisions with gas molecules, regardless of the presence of an external magnetic field. The denser the gas, the more quickly energy is lost. The physics of gas breakdown still applies, and once electrons gain enough energy to ionize the gas, an electron cascade will take place, shorting the cavity.

In addition to pushing the breakdown limit higher, the gas can act as a cooling medium for the beam. Hydrogen provides an ideal stopping power and radiation length for ionization cooling. Experiments on both gas species and metallic material were performed. The results are shown in Figures 4 and 5.

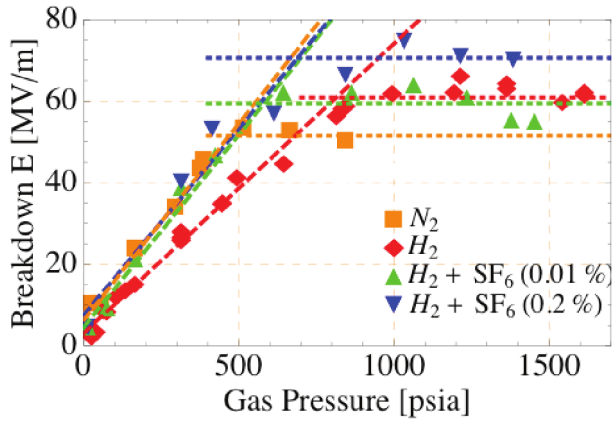

Figure 4: Maximum electric field as a function of gas pressure from Ref. [8]. Different gas species and dopants are shown for this 805 MHz pillbox cavity. A copper electrode was placed on the cavity axis to localize breakdown.

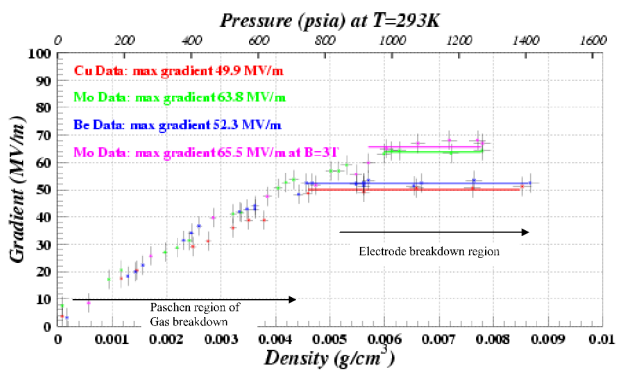

Figure 5: Maximum electric field as a function of gas pressure from Ref. [9]. Different material electrodes were placed on the cavity axis. This 805 MHz pillbox cavity was filled with hydrogen gas.

There was little difference in the breakdown gradient using molybdenum electrodes in hydrogen gas between no external magnetic field and a 3 T field. This provided the first

ISBN 978-3-95450-174-8

demonstration of a technique to mitigate RF breakdown in an external magnetic field.

To demonstrate the viability of a gas filled RF cavity in an ionization cooling channel, the effect of an intense beam passing through a gas filled cavity was studied. The beam will ionize the gas within the cavity, creating a plasma. The plasma dissipates RF power through collisions with gas molecules; this process is called plasma loading. The amount of RF power a charged particle dissipates depends on its mobility (which roughly scales with mass) and the gas density. The plasma evolves over time through a number of processes. First, electrons recombine with positively charged ions. To speed up the charge neutralization time, an electronegative dopant may be added. Electrons may become attached to an electronegative molecule, and this process is typically much faster than electron-ion recombination. Finally, the negative ions formed by electron attachment may neutralize with positive ions, with a time scale longer than either electron-ion recombination or electron attachment. The RF envelopes shown in Figure 6 demonstrate this narrative.

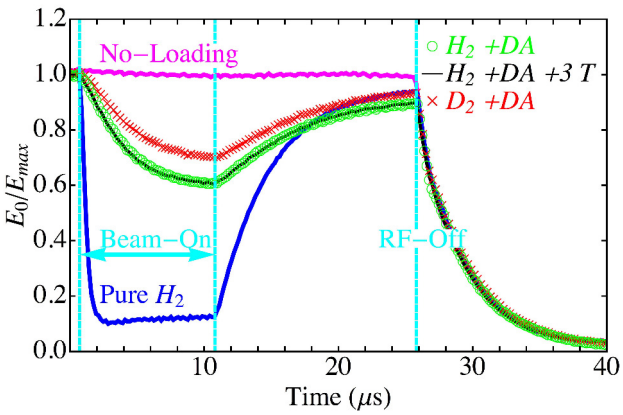

Figure 6: Normalized RF electric field envelope as a function of time from Ref. [10]. Various conditions are shown: normal RF envelope / "No Loading" (magenta), pure hydrogen with beam (blue), hydrogen doped with dry air with beam (green), hydrogen doped with dry air with beam in a 3 T external magnetic field (black), and deuterium doped with dry air with beam (red). The vertical dashed lines indicate the times at which the beam turned on and off, and the time at which the RF source shut off. The RF turn on has been omitted.

An RF envelope showing the flat top and decay once the source was turned off is shown for reference. Significant plasma loading in pure hydrogen is observed with the beam is turned on. The electric field recovers once the beam is turned off, as electrons recombine with hydrogen ions. When hydrogen or deuterium is doped with dry air, electrons may become attached to oxygen, which happens much faster than recombination. The observed plasma loading is then significantly less. The performance of the cavity is virtually identical in the presence of a 3 T external magnetic field.

Current High Pressure Program

Calculations of the plasma loading in two muon cooling channel schemes have been done, and indicate the desired beam intensity should not prohibitively load the cavities [11, 12]. Simulation studies are currently underway to more accurately investigate the effects of the plasma on the performance of the cavity, and the plasma on the evolution of the beam [13, 14].

As it appears that gas filled RF cavities are feasible for use in ionization cooling channels, an experimental effort to validate a possible engineering design is underway. In order to accommodate the small diameter bores of high field superconducting magnets, methods of shrinking the radial size of gas filled cavities are being pursued. One possibility is making the cavities reentrant. Another is increasing the dielectric constant of the material inside the cavities. This can be investigated using the existing high pressure test cell, and adding a dielectric insert. Low power measurements of a number of materials' dielectric constant and loss tangent have been made [15]. Four high purity alumina (Al_2O_3) inserts were subsequently fabricated and are currently being tested to determine their dielectric strength and the interaction in a beam-gas-plasma-dielectric system.

MITIGATING BREAKDOWN IN VACUUM CAVITIES

Recently, techniques to mitigate breakdown in vacuum cavities have been investigated. Figure 7 shows such data, with one data set from Ref. [2] plotted for reference.

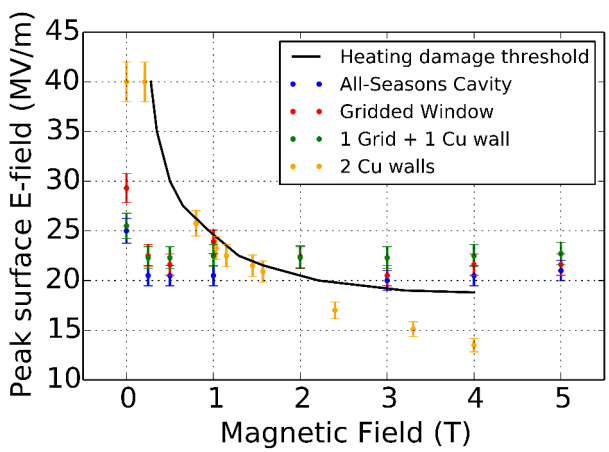

Figure 7: Peak surface electric field as a function of external magnetic field from Ref. [16]. Several experimental data sets from 805 MHz vacuum pillbox cavities are shown: two copper coated stainless steel endplates - "All-Seasons Cavity" (blue), two gridded windows (red), 1 gridded window and one copper endplate (green), and the pillbox data set from Fig. 3 (orange). The black line represents the threshold for surface fracture based on beamlet heating.

ISBN 978-3-95450-174-8

One technique tested was to select a cavity length such that the energy of electrons that traversed the cavity and impacted the oppposite side was a minimum, which minimizes energy deposition in the end plates. An 805 MHz vacuum pillbox cavity made of copper coated stainless steel was built in part for this purpose. The results from this cavity are the blue data points in Fig. 7.

If a cavity is terminated with a gridded window, field emission electrons are allowed to exit the cavity volume, without impacting the surface. A set of grids made of aluminum that was then electropolished and titanium nitride coated were fabricated. Two configurations, one with both grids and one with one grid and one copper window, were tested. These are shown in red and green, respectively, in Fig. 7.

All three data sets show better performance than the nominal shorter cavity with two copper end plates and dictate the need for further investigation

CURRENT VACUUM CAVITY EXPERIMENTAL PROGRAM

201 MHz Program

A prototype 201 MHz vacuum pillbox cavity for MICE has recently been tested at the MTA. Figure 8 shows the cavity mounted in its vacuum vessel. This cavity was electropolished in an effort to ensure the surface be as smooth as possible and assembled in a clean room.

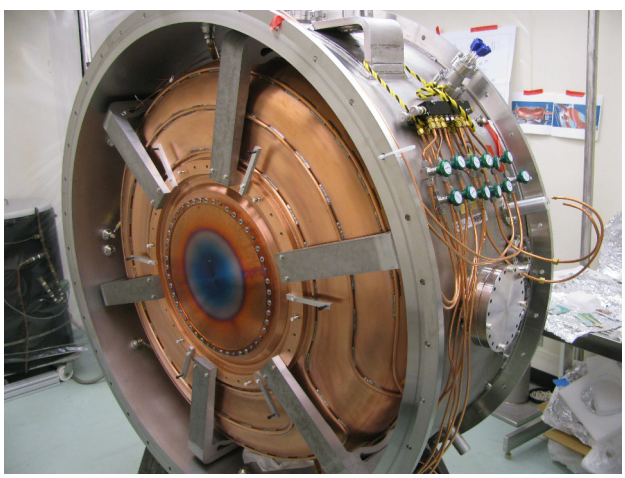

Figure 8: The MICE prototype cavity module opened to expose the 201 MHz vacuum pillbox RF cavity. The cavity is terminated with copper windows.

This cavity was commishioned with both flat copper endplates and curved beryllium windows. The cavity module was placed in the fringe field of the 5 T superconducting magnet in the MTA. With the copper endplates, the breakdown rate at 13.5 MV/m was measured to be 10^{-6} without magnetic field. With beryllium windows, the cavity achieved the MICE specification of 10.3 MV/m with and without magnetic field with no sparks observed. The cavity was then run up to 14.5 MV/m with Be windows in the fringe field and minimal sparking was observed. The gradient limit in this case was due to the RF source power, rather than breakdown.

805 MHz Program

The apparent success of specialized geometric design and superconducting RF (SRF) techniques (electropolishing, TiN coating, ...) - see Fig. 7 - prompted the design and fabrication of a new 805 MHz vacuum pillbox cavity with the goal of investigating how these techniques, as well as material type, affect vacuum cavities' performances in an external magnetic field.

The cavity, shown in Figure 9, has been named the Modular Cavity as it has replaceable components. The central body is made of copper, and may be replaced with another copper body of different length, in order to investigate the cavity body length dependence indicated by the All Seasons Cavity results. It is currently terminated with two flat copper walls, which have been electropolished and TiN coated, in order to study the effect of SRF preparation techniques. Two Be walls are in fabrication, and will undergo the same SRF preparation. Beryllium has a longer radiation length for electrons than copper, so field emission electrons should deposit their energy in a larger volume.

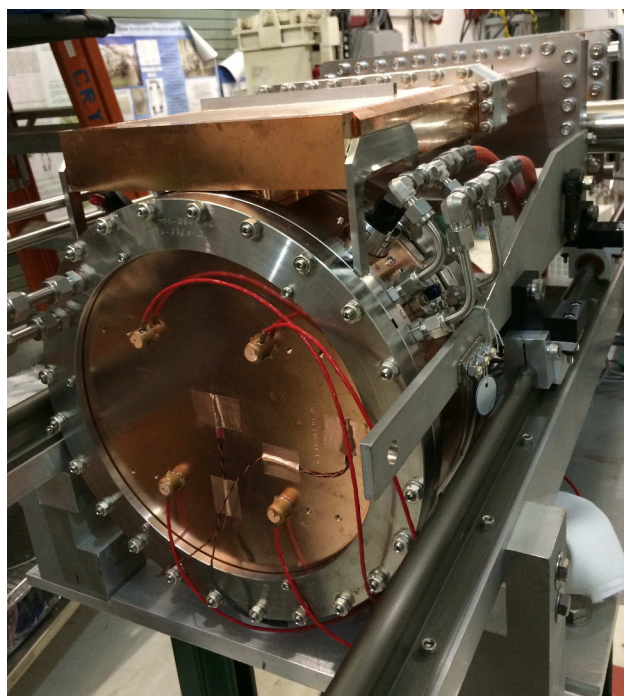

Figure 9: The 805 MHz vacuum pillbox Modular Cavity. The cavity is mounted on rails that secure it in place within the magnet bore. The cavity is side coupled. Instrumentation and water cooling lines are visible.

The Modular Cavity has been commishioned to above 40 MV/m with copper walls at a 10^{-5} sparking rate without magnetic field. A detailed inspection of the copper walls is underway to provide a baseline for the subsequent study in a magnetic field. After the copper walls have been tested,

ISBN 978-3-95450-174-8

beryllium walls will be attached and a similar program followed.

CONCLUSION

A demonstration experiment of ionization cooling is underway. A requisite of ionization cooling is the operation of high gradient radio frequency cavities in strong external magnetic fields. Initial indications were that traditional vacuum cavities experienced significant accelerating gradient degredation in strong magnetic fields. Filling an RF cavity with a high pressure gas has been demonstrated to be a solution, and furthermore initial findings are that plasma loading is managable in a realistic ionization cooling channel. Recent results based on various techniques used on vacuum cavities appear promising, and have spurred an experimental program aimed at demonstrating such techiques are a viable solution to operating vacuum RF cavities in an ionization cooling channel as well.

ACKNOWLEDGEMENT

The work presented in these proceedings encompasses an experimental program spanning more than a decade. The authors wish to acknowledge and thank everyone who contributed, particularly members of the Muon Accelerator Program and Muons, Inc., and our colleagues at Brookhaven National Laboratory and Lawrence Berkeley National Laboratory.

REFERENCES

[1] C. Rogers, "Status, Recent Results and Prospect of the International Muon Ionization Cooling Experiment (MICE)", COOL'15, Newport News, Virginia, USA, September 2015, TUWAUD01, These Proceedings.

[2] J. Norem et al., Phys. Rev. ST Accel. Beams 6, 072001 (2003).

[3] A. Moretti et al., Phys. Rev. ST Accel. Beams 8, 072001 (2005).

[4] A. Hassanein et al., Phys. Rev. ST Accel. Beams 9, 062001 (2006).

[5] J. Norem et al., "Recent RF Results from the MuCool Test Area", PAC'07, Albuquerque, New Mexico, USA, June 2007, WEPMN090 (2007).

[6] R.B. Palmer et al., Phys. Rev. ST Accel. Beams 12, 031002 (2009).

[7] R.P. Johnson and Y. Derbenev, Phys. Rev. ST Accel. Beams 8, 041002 (2005).

[8] K. Yonehara et al., "Doped H_2-Filled RF Cavities for Muon Beam Cooling", PAC'09, Vancouver, British Columbia, Canada, May 2009, TU5PFP020 (2009).

[9] P. Hanlet et al., "High Pressure RF Cavities in Magnetic Fields", EPAC 2006, Edinburgh, Scotland, June 2006, TUPCH147 (2006).

[10] M. Chung et al., PRL 111, 184802 (2013).

[11] B. Freemire et al., "High Pressure Gas-Filled RF Cavities for Use in a Muon Cooling Channel", NA-PAC 2013, Pasadena, California, USA, October 2013, TUODA1 (2013).

[12] B. Freemire, D. Stratakis and K. Yonehara, "Influence of Plasma Loading in a Hybrid Muon Cooling Channel", IPAC 2015, Richmond, Virginia, USA, May 2015, TUPWI059 (2015).

[13] K. Yu et al., "Simulation of Beam-Induced Plasma in Gas Filled Cavities", IPAC 2015, Richmond, Virginia, USA, May 2015, MOPMN013 (2015).

[14] J. Ellison and P. Snopok, "Beam-Plasma Effects in Muon Ionization Cooling Lattices", IPAC 2015, Richmond, Virginia, USA, May 2015, WEPWA063 (2015).

[15] B. Freemire et al., "Low Powered RF Measurements of Dielectric Materials for Use in High Pressure Gas Filled RF Cavities", IPAC 2015, Richmond, Virginia, USA, May 2015, WEPTY050 (2015).

[16] D. Bowring et al., "RF Breakdown of 805 MHz Cavities in Strong Magnetic Fields", IPAC 2015, Richmond, Virginia, USA, May 2015, MOAD2 (2015).

ISBN 978-3-95450-174-8

FRONT END AND HFOFO SNAKE FOR A MUON FACILITY*

D. Neuffer#, Y. Alexahin, Fermilab, Batavia, IL 60510, USA

Abstract

A neutrino factory or muon collider requires the capture and cooling of a large number of muons. Scenarios for capture, bunching, phase-energy rotation and initial cooling of μ's produced from a proton source target have been developed, for neutrino factory and muon collider scenarios. They require a drift section from the target, a bunching section and a ϕ-δE rotation section leading into the cooling channel. The currently preferred cooling channel design is an "HFOFO Snake" configuration that cools both μ^+ and μ^- transversely and longitudinally. The status of the design is presented and variations are discussed.

INTRODUCTION

Scenarios have been developed for using muons in a storage ring based neutrino source or "neutrino factory" and in a high-energy high-luminosity "muon collider". [1, 2] The scenarios are outlined in Figure 1. In both scenarios high intensity proton bunches from a proton source strike a production target producing secondary particles (mostly $\pi^{\pm}$'s). The π's decay to μ's and the μ's from the production are captured, bunched, cooled and accelerated into a storage ring for neutrinos or high energy collisions. The present paper discusses the section of the scenarios labelled the "front end" in figure 1, between the target and the accelerator for the neutrino factory and between the target and "6-D" cooling section of the muon collider.

In the Front End, pions from the production target decay into muons and are focused by magnetic fields and bunched by time-varying electric fields into an initial cooling system that forms the muons into a beam suitable for the following acceleration and/or cooling.

μ's from the target and decay are produced within a very broad energy spread and length. Initially, capture within a single bunch was considered, but that requires either very low frequency rf (<20MHz) or novel induction linacs. The scale and cost of such a system would be uncomfortably large. Instead a novel system of higher frequency rf cavities (~200—500 MHz) was developed that forms the μ's into a train of manageable bunches, using current-technology rf cavities and power sources.[3,4] The same system can be used for both neutrino factory and collider scenarios.

The rf bunching naturally forms the beam for an initial cooling section. For the IDS neutrino factory design study, this uses a simple solenoidal focusing system with LiH absorbers that provides only transverse cooling (4-D phase-space cooling). More recently a 6-D initial cooling system (the "HFOFO Snake") using tilted solenoids and LiH wedge absorbers was developed,[5] and is currently considered somewhat superior, particularly for a collider scenario. The initial cooling concepts are discussed and compared.

*Work supported by Contract No. De-AC02-07CH11359 with the U. S. Department of Energy.

#neuffer@fnal.gov

FRONT END OVERVIEW

The Front End concept presented here was generated for the Neutrino Factory design studies,[6] and subsequently extended and reoptimized for the Muon Accelerator Program (MAP) muon collider design studies. The Front End system takes the π's produced at the target, and captures and initiates cooling of the resulting decay μ's, preparing them for the μ accelerators. Figure 2 shows an overview of the system, as recently developed for the MAP studies. In this figure, the transport past the target is separated into drift, buncher, rotator and cooling regions.

Drift

The multi-GeV proton source produces short pulses of protons that are focused onto a target immersed in a high-field solenoid with an internal beam pipe radius r_{sol}. The proton bunch length is 1 to 3 ns rms (~5 to 15 ns full-width), B_{sol} =20 T, and r_{sol} = 0.075 m, at initial baseline parameters. Secondary particles are radially captured if they have a transverse momentum p_T less than $\sim ecB_{sol}r_{sol}/2$ = 0.225 GeV/c. Downstream of the target solenoid the magnetic field is adiabatically reduced from 20T to 2T over ~14.75 m, while the beam pipe radius increases to ~0.25 m. This arrangement captures a secondary pion beam with a broad energy spread (~50 MeV to 400 MeV kinetic energy).

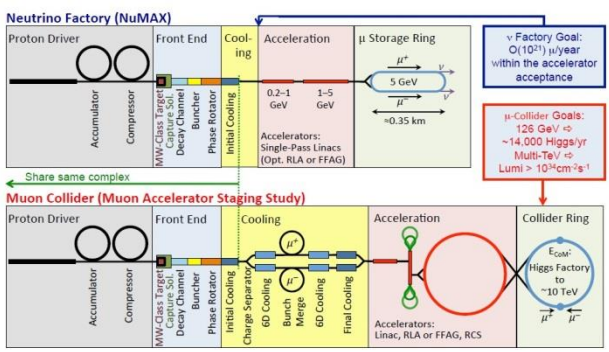

Figure 1: Block diagrams of neutrino factory and muon collider scenarios. The present paper discusses the "Front End" section from the Target to the Cooling/Acceleration, including "Initial Cooling". The same Front End can be used in both scenarios.

ISBN 978-3-95450-174-8

The initial proton bunch is relatively short, and as the secondary pions drift from the target they spread apart longitudinally, following: $c\tau(s) = s/\beta_z + c\tau_0$, where s is distance along the transport and $\beta_z = v_z/c$. Hence, downstream of the target, the pions and their daughter muons develop a position-energy correlation in the RF-free drift. In the MAP baseline, The total drift length is L_D = 64.6 m, and at the end of the decay channel there are about 0.2 muons of each sign per incident 8 GeV proton.

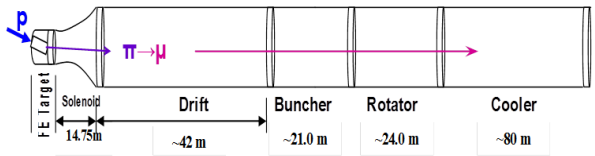

Figure 2: Overview of the MAP front end, consisting of a target solenoid (20 T), a capture solenoid (20 T to 2.0T, 14.75 m), Drift section (42 m), rf Buncher (21 m), an energy-phase Rotator (24 m), with a Cooler (80 m).

RF Buncher

The drift channel is followed by a buncher section that uses rf cavities to form the muon beam into a train of bunches, and a phase-energy rotating section that decelerates the leading high-energy bunches and accelerates the later low-energy bunches to the same mean energy.[3] To determine the buncher parameters, we consider reference particles (0, *N*) at P_0= 250 MeV/c and P_N = 154 MeV/c, with the intent of capturing muons from a large initial energy range (~50 to ~400 MeV). The rf frequency f_{rf} and phase are set to place these particles at the center of bunches while the rf voltage increases along the transport. This requires that the rf wavelength λ_{rf} increases, following:

$$N_B \lambda_{rf}(s) = N_B \frac{c}{f_{rf}(s)} = s\left(\frac{1}{\beta_N} - \frac{1}{\beta_0}\right)$$

where *s* is the total distance from the production target, β_1 and β_2 are the velocities of the reference particles, and *N* is an integer. For the baseline, *N* is chosen to be 12, and the buncher length is 21m. Therefore, the rf cavities decrease in frequency from ~490 MHz (λ_{rf} = 0.61 m) to ~365 MHz (λ_{rf}= 0.82m) over the buncher length.

The initial geometry for rf cavity placement uses 2 0.25 m long cavities placed within 0.75 m long cells. The 2T solenoid field focusing of the decay region is continued through the Buncher and the Rotator. The rf gradient is increased along the Buncher, and the beam is captured into a string of bunches, each of them centered about a test particle position with energies determined by the $\delta(1/\beta)$ spacing from the initial test particle:

$$1/\beta_n = 1/\beta_0 + n\,\delta(1/\beta),$$

where $\delta(1/\beta)=(1/\beta_N - 1/\beta_0)/N$. In the initial design, the cavity gradients follow a linear increase along the buncher: $V'_{rf}(z) \approx 15\left(\frac{z}{L_{Bf}}\right)\ MV/m$.

where *z* is distance along the buncher and L_{Bf} is the bucher section length. The gradual increase in voltage gradient enables a somewhat adiabatic capture of muons into separated bunches.

In practical implementation this linear ramp of varying-frequency cavities is approximated by a sequence of rf cavities that decrease in frequency along the 21 m length of the buncher. A total of 54 rf cavities are specified, with frequencies varying from 490 to 366 MHz, and rf gradients from 0 to 15 MV/m The number of different rf frequencies is limited to a more manageable 14 (~4 rf cavities per frequency). Table 1 lists the rf cavity requirements. At the end of the buncher, the beam is formed into a train of positive and negative bunches of different energies.

Phase-Energy Rotator

In the rotator section, the rf bunch spacing between the reference particles is shifted away from the integer N_B by an increment δN_B, and phased so that the high-energy reference particle is stationary and the low-energy one is uniformly accelerated to arrive at the high-energy at the end of the Rotator. For the MAP example, δN_B = 0.05 and the bunch spacing between the reference particles is $N_B + \delta N_B$ = 12.05. The Rotator consists of 0.75 m long cells with 2 0.25 m rf cavities at 20 MV/m. The rf frequency of cavities decreases from 365 MHz to 326 MHz down the length of the 42 m long rotator region. The rotator uses 64 rf cavites of 16 different frequencies. (see Table 1) At the end of the rotator the rf frequency matches into the rf of the ionization cooling channel (325 MHz).

The constant solenoidal focusing field of 2 T is maintained throughout the rotator and is matched into an alternating solenoidal field for the cooler. The match is obtained by perturbations on the focusing coil currents of the first four cells of the cooler lattice.

Cooler

The IDS baseline cooling channel design consists of a sequence of identical 1.5 m long cells (Fig. 2). Each cell contains two sets of two 0.25 m-long rf cavities, with 1.5cm thick LiH absorbers blocks at the ends of each cavity set (4 per cell) and a 0.25 m spacing between cavities, and alternating solenoidal focusing coils. The LiH provides the energy loss material for ionization cooling. The total length of the cooling section is ~75m (50 cells). Based on simulations, the cooling channel reduces the transverse emittances by a factor of 2.5.

The cells contain two solenoidal coils with the coils containing opposite sign currents. The coils produce an approximately sinusoidal variation of the magnetic field on axis in the channel with a peak value on-axis of ~2.8T, providing transverse focusing with $\beta_\perp \cong$ 0.8m.

At the end of the cooler, simulations indicate that there are ~0.1 μ^+ and μ^- per initial ~8 GeV proton within the projected acceptance of the downstream muon accelerator. (Particles with amplitudes $\varepsilon_{x,y}$ < ~0.03 m and londitudinal amplitudes A_L <0.2 m are considered to be within that acceptance.)

ISBN 978-3-95450-174-8

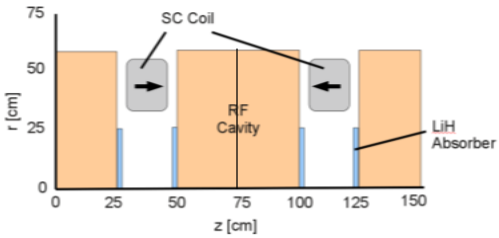

Figure 3: Layout of one period of the Alternating Solenoid cooling lattice, showing the alternating solenoid coils, the rf cavities and LiH absorbers.

Table 1: Summary of Front End rf Requirements

Region	Number of Cavities	Number of frequencies	Frequencies [MHz]	Peak Gradient {MV/m]
Buncher	54	14	490 to 366	0 to 15
Rotator	64	16	366 to 326	20
Cooler	200	1	325	25
Total	318	31	490 to 325	1700 MV

Rf Breakdown, Energy Loss

The baseline design requires the use of high-gradient rf (~325MHz, 15MV/m) in moderately high magnetic fields (~2T). Initial experiments and analysis showed that rf gradients could be limited in high magnetic fields, and it was uncertain that the baseline parameters could be achieved.[7, 8] More recent results using carefully prepared rf cavity surfaces have shown greater tolerance for magnetic fields. 800 MHz rf cavites operated at 20 MV/m within 5T magnetic fields in recent experiments.[9]

Experiments have also shown that gas-filled rf cavities suppress breakdown, even within high magnetic fields and the presence of rf accelerating beams. Variations of the Front End using gas-filled rf cavities were developed and found to obtain capture and acceptance approximately equal to vacuum cavity examples, provided the rf gradients are increased to compensate energy loss in the gas.[10] Operation of gas-filled rf has a complication in that beam loading by electrons from beam ionization can drain rf power; this can be moderated by adding a small fraction of electronegative dopant (O_2) to the H_2, to facilitate electron recombination.[11, 12]

The transport line from the target is designed to accept a maximal number of secondaries and therefore includes a large flux of particles that are not accepted into the final muon beams. These particles are mostly lost in the walls of the vacuum chamber (at up to 1 kW/m), potentially causing large activation. This includes a large flux of protons of all energies (up to the primary proton beam energy), as well as many pions and electrons. A chicane and absorber system following the target region was designed to localize losses to the target/chicane/absorber system, without greatly reducing downstream μ^+ and μ^- acceptance.[13] Fig. 4 shows the front end modified with a chicane absorber; an additional length of ~30m is required.

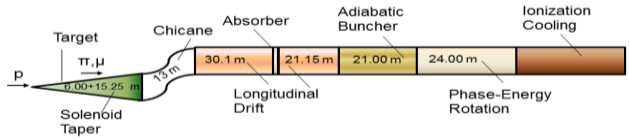

Figure 4: Layout of the Front End with a chicane and absorber.

IMPROVED COOLING: THE "HFOFO SNAKE"

The "HFOFO Snake" was designed to obtain simultaneous transverse and longitudinal cooling, for both μ^+ and μ^-. The HFOFO snake is based on two principles: alternating solenoid focusing and resonant dispersion generation by a helical perturbation[5]. In a homogeneous longitudinal magnetic field the two transverse modes are the cyclotron and drift modes.[14] Ionization losses cool only the cyclotron mode. Changing the solenoid polarity exchanges the identity of the cyclotron and drift modes, so that in an alternating solenoid lattice both modes are damped. (This principle is also used in the initial baseline 2-D cooling channel.) In the HFOFO channel the solenoids are tilted in a periodic helical pattern, generating a helical closed orbit perturbation with dispersion. This perturbation introduces a path length increase with momentum (positive momentum compaction) through the absorbers which yields a longitudinal cooling effect. Wedges matched to the dispersion can give an additional cooling effect.

After some parameter variation and optimization, an HFOFO solution for the Front End was generated.[14] One period of the channel is shown in Fig. XX. It consists of:

- 6 Alternating solenoids (coil parameters: $L = 30$ cm, $R_{in} = 42$ cm, $R_{out} = 60$ cm) placed with a period of 70 cm along the axis. With current density 94.6 A/mm^2 the solenoids provide focusing with betatron phase advance ≈74°/step at a muon momentum of 230 MeV/c. To create a transverse magnetic field component, the solenoids are periodically inclined in rotating planes at $x\cdot\cos(\phi_k)+y\cdot\sin(\phi_k) = 0$, $\phi_k = \pi(1-2/N_s)(k+1)$, $k = 1,2,\ldots,N_s$. N_s is the number of solenoids/period, $N_s = 6$ in the present case. The rotation angles ϕ_k are: $4\pi/3$, 0, $2\pi/3$, $4\pi/3$, 0, $2\pi/3$; $\phi = 0$ corresponds to a tilt in the vertical plane. The chosen pitch angle of 2.5 mrad is too small to be visible in the figure.
- 6 Paired RF cavities ($f_{RF} = 325$ MHz, $L = 2\times25$ cm, $E_{max} = 25$ MV/m) filled with H_2 gas at a density that is 20% of liquid hydrogen, with Be windows. The radius and thickness of the Be windows are reduced in 3 steps along the channel: $R_w = 30$ cm, $w = 0.12$ mm (first 10 periods), $R_w = 25$ cm, $w = 0.10$ mm (next 10 periods) and $R_w = 20$ cm, $w = 0.07$ mm (last 10 periods). (Slab LiH absorbers could be used to replace the H_2, if vacuum-filled rf is preferred.)
- LiH wedge absorbers, providing additional longitudinal cooling. Although the momentum

ISBN 978-3-95450-174-8

compaction factor of the lattice is positive, it is not sufficient for longitudinal cooling and wedges must be added. The wedge angle smoothly varies along the channel from 0.17 rad to 0.20 rad. The tip of the wedge just intercepts the channel axis so the muons on the equilibrium orbit (see Fig. 5) traverse no more than 0.3 mm of LiH.

An important feature of the design is that μ^- in solenoids 4, 5, 6 see exactly the same forces as μ^+ in solenoids 1, 2, 3 and vice versa, so that μ^- and μ^+ orbits have exactly the same form, with a longitudinal shift by a half period (three solenoids), and are not mirror-symmetric as one might expect. This allows us to find an orientation of the wedge absorbers (with periodicity = 2) such that they provide longitudinal cooling for both μ^- and μ^+. The complete cooling channel contains 30 periods for a total length of 126 m.

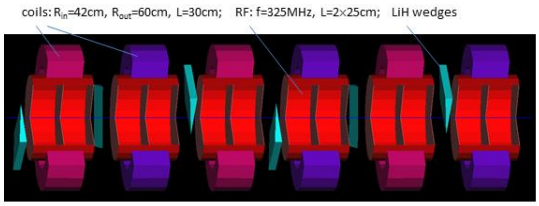

Figure 5: Layout of one period of the HFOFO lattice, showing the alternating solenoid coils (violet and blue), the rf cavities (red) and wedge LiH absorbers (cyan).

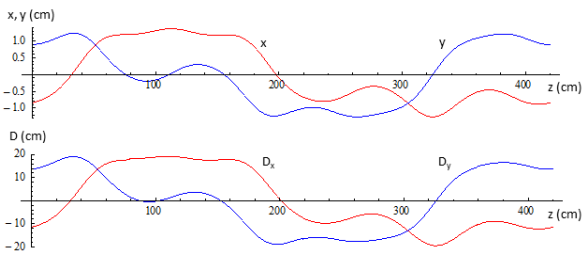

Figure 6: Closed orbit(above) and dispersion (below) in one period of the HFOFO lattice.

The closed orbit through the period plus the dispersion (for μ^+) are shown in figure 6. The closed orbit approximately follows a circle of radius ~1.2cm, and the dispersion follows a ~20cm amplitude circle through the helical orbit. The normal mode tunes of the lattice are $(\nu_1, \nu_2, \nu_3) = (1.23+0.01i, 1.238+0.0036i, 0.189+0.0049i)$, where the first two modes are transverse and the last is predominantly longitudinal; the imaginary part indicates the damping from ionization cooling.

The HFOFO channel was matched in closed orbit and betatron functions to the output of the Front End Rotator, using perturbations of the first 9 HFOFO solenoid strengths and tilts. In the HFOFO, the central momentum is gradually reduced from the ~250 MeV/c of the Rotator to ~210 MeV/c at the end of the HFOFO cooler.

Beam from the Front End Rotator was matched into the HFOFO cooler and tracked using the G4BeamLine simulation code. Results of the simulation are presented in Figure [7]. Both μ^+ and μ^- beams are cooled. The rms transverse emittance $\varepsilon_t = (\varepsilon_1 \varepsilon_2)^{1/2}$ is reduced from ~16 mm to ~2.6mm, which is a factor of ~6. Longitudinal emittance is reduced from ~24 mm to ~7.4 mm, about a factor of 3. Beam survival of the core muon beams (from decay and aperture losses) was ~70%.

The transverse cooling is greater than that of the previous 2-D cooling system. This is in part due to the stronger focussing and longer channel length. Initial losses are ~10% greater, partly from the more complicated 6-D phase space match, and partly from aperture losses in adding the helical orbit to the transverse motion. However the additional longitudinal cooling enables the use of the longer channel and provides a better match into downstream systems, which are likely to have more limited longitudinal acceptances.

Because of the superior cooling and the better match into downstream systems, The HFOFO snake is presently the preferred initial cooling system.

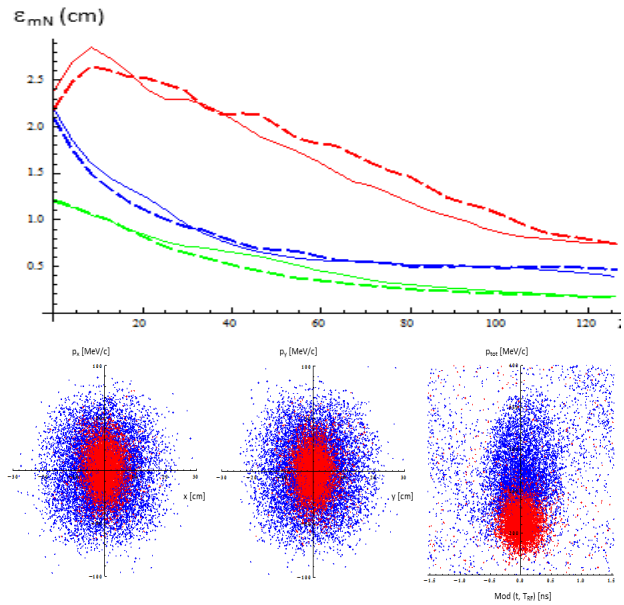

Figure 7: Results of beam simulations of cooling. (Above) Evolution of the eigenemittances (ε_1, ε_2, ε_3) through the 124m channel (solid lines are μ^+, dashed are μ^-) (Below) Phase space distributions of the initial μ+ beam (blue) and of the cooled beam in the exit solenoid (red). (x-p_x, y-p_y, p-ct) All bunches were projected onto the same RF bucket in the last plot. No cuts applied.

CONCLUSION

The results here present a baseline design for the muon Front End as developed by the MAP collaboration. It would provide a large-acceptance and capture system that could provide an intense source of bunched and cooled μ+ and μ-. The example presented is certainly not a final, optimized design and the research has suggested many possibilities for future improvement and modification.
For example, the 2T baseline focussing is not optimum; stronger focusing of ~3T should provide more capture.

The present channel was developed for muon collider/neutrino factory applications. The same methods

ISBN 978-3-95450-174-8

could also be adapted to obtain intense low-energy muon sources.

ACKNOWLEDGMENT

We thank M. Palmer, D. Stratakis, C. Rogers, P. Snopok, V. Shiltsev, and the MAP collaboration for helpful contributions and support.

REFERENCES

[1] M. Appollonio et al., "Accelerator Concept for Future Neutrino Facilities", RAL-TR-2007-23, *JINST* **4** P07001 (2009).

[2] J. P. Delahaye et al., *Enabling Intensity and Energy Frontier Science with a Muon Accelerator Facility in the U. S.*, FERMILAB-CONF-13-307-APC, (2013).

[3] D. Neuffer and A. Van Ginneken, Proc. PAC 2001, Chicago IL p.2029 (2001).

[4] J. S. Berg *et al.*, "Cost-effective Design for a Neutrino Factory", **Phys. Rev. STAB 9**, 011001(2006).

[5] Y. Alexahin, "Helical FOFO snake for 6D ionization cooling of muons", AIP Conf. Proc. 1222 (2010), pp. 318-323.

[6] C. T. Rogers et al., "Muon Front End for a Neutrino Factory", **Phys. Rev. STAB 16**, 040104(2013).

[7] A. Moretti et al., "Effects of high solenoidal magnetic fields on rf accelerating cavities", **Phys. Rev. STAB 8**, 072001 (2005).

[8] R. B. Palmer et al., "rf breakdown with external magnetic fields in 201 and 805 MHz cavities", **Phys. Rev. STAB 12**, 031002 (2009).

[9] D. Bowring et al. "rf Breakdown of 805 MHz Cavities in Strong Magnetic Fields", Proc. IPAC2015, Richmond VA, p. 53 (2015).

[10] D Stratakis and D. Neuffer, "Utilizing gas filled cavities for the generation of an intense muon source", Proc. IPAC2015, Richmond VA USA, p. 2830 (2015).

[11] B. Freemire et al., "High-Pressure rf Cavities for Use in a Muon Cooling Channel,", Proc. PAC 2013, Pasadena, CA USA, p. 419 (2013).

[12] J. Ellison et al., "Beam-plasma Effects in Muon Ionization Cooling Lattices", Proc. of IPAC2015, Richmond, VA USA, p. 2649 (2015)

[13] C. Rogers, D. Neuffer, and P. Snopok, "Control of beam losses in the Front End for the Neutrino Factory", Proc. IPAC2012, New Orleans LA, p, 223 (2012).

[14] A. Burov, Y. Derbenev, S. Nagaitsev, **Phys. Rev. E 66**, 016503 (2002).

[15] Y. Alexahin, "H2 Gas-Filled Helical FOFO Snake for Initial 6D Ionization Cooling of Muons", MAP-doc-4377, http://map-docdb.fnal.gov/cgi-bin/ShowDocument?docid=4377, May 2014.

ISBN 978-3-95450-174-8

CRYSTALLINE BEAM STUDIES WITH ANDY SESSLER*

Jie Wei[#1], Xiao-Ping Li[2], Hiromi Okamoto[3]
[1] Facility for Rare Isotope Beams, Michigan State University, East Lansing, USA
[2] Skyworks Solutions, Inc., USA
[3] Hiroshima University, Higashi-Hiroshima, Japan

Abstract

For more than two decades since 1992, Andy Sessler worked with us as a hobby on the topic of crystallization of charged ion beams and cooling methods. In this paper, we review the studies jointly performed with Andy highlighting major findings and challenges, and discuss current status and possible future topics and directions.

INTRODUCTION

Beam crystallization has been a topic of interests since first evidence of experimental anomaly was observed on an electron-cooled proton beam at the storage ring NAP-M in 1980 [1]. Starting 1985, J. Schiffer and co-workers studied the properties of one-component, non-relativistic charged particles in the external potential of a simple harmonic oscillator using the molecular dynamics method [2]. Since then, strong space-charge dominated phenomena and one-dimensional (1-D) ordering states were reported with both proton and heavier ions at storage rings TSR [3], ASTRID [4], ESR [5], CRYRING [6], and S-LSR [7] (Table 1).

In 1992, A.G. Ruggiero introduced A.M. Sessler and J. Wei (JW) to the discussion of studying crystalline beams in realistic storage ring conditions. The study immediately involved X.-P. Li (XPL) who is a condensed matter physicist by training. We realize that the most straightforward and rigorous approach is to derive the equations of motion in the so-called beam rest frame where the reference particle is at rest. In this frame, the conventional method of condensed matter physics can be readily applied.

It took JW six month to adopt the formalism of general relativity to derive the equation of motion in the beam rest frame using numerical algebra methods [8]. In another month, XPL developed the beam dynamics algorithms as well as other relevant condensed matter analysis algorithms. Together we created the codes SOLID that can be used to rigorously study beams at ultra-low temperature regime [9].

To attain an ordered state, effective beam cooling is needed to overcome beam heating caused by coherent resonance crossing and intra-beam scattering. Furthermore, the cooling force must conform to the dispersive nature of a crystalline ground state in a storage ring for 3-D structures. To reach the state of crystalline beams in numerical simulations, we used artificial cooling methods enforcing periodicity of the particle motion in the beam rest frame. H. Okamoto (HO) led the analysis of actual beam cooling methods including coupled cooling and tapered cooling [10]. Thus, the entire theoretical approach on beam crystallization was developed.

For more than two decades since 1992, Andy worked closely with us on all major topics of beam crystallization from the derivation of equations of motion to numerical simulation and then to realization with practical cooling methods. Figures 1 to 6 show various occasions associated with Andy during the past 20 years. Andy hosted our extended visits to Lawrence Berkeley National Laboratory (LBNL) in formulating the study approaches and identifying major directions of breakthrough (Fig. 1). He led the interaction with major experimental groups at Aarhus, Denmark and Heidelberg, Germany, providing insights in experimental benchmarking (Fig. 2). Starting from 1997, Andy visited Kyoto University, Japan, for extended periods of time stimulating both experimental and theoretical beam cooling and crystallization work in Japan. Later, he stayed at Hiroshima University collaborating with H. Okamoto and his students (Fig. 4).

Andy has been our mentor, role model, colleague, and friend. He was always fresh with new ideas and passionate about physics, life, and friendship. During early years of study at Berkeley, he often came up with a dozen new ideas a day as we explored the fascinating physics of beam crystallization. Even though most did not survive the subsequent trial and error, some most important findings originated from Andy's imagination.

Figure 1: A.M. Sessler in Muir Woods, California, USA, 1993 (photo taken by J. Wei). Andy hosted extended visits to LBNL at multiple stages of beam crystallization studies.

*Work supported by the U.S. Department of Energy Office of Science under Cooperative Agreement DE-SC0000661 and the National Science Foundation under Cooperative Agreement PHY-1102511.
#wei@frib.msu.edu

ISBN 978-3-95450-174-8

Table 1: A compilation of experimental parameters and observations at existing storage rings: NAP-M [1], TSR [3], ASTRID [4], ESR [5], CRYRING [6], and S-LSR [7].

	NAP-M	TSR	ASTRID	ESR	CRYRING	S-LSR
E_u [MeV/u]	65.7	1.9	0.00417	360	7.4	7
Circumference [m]	47.25	55.4	40	108.36	51.63	22.557
γ	1.07	1.002	1.00000444	1.384	1.00789	1.00746
γ_T	1.18	2.96	4.34	2.67	2.25	1.23
N_{SP}	4	2	4	6	6	6
$\frac{\nu_x}{N_{SP}} / \frac{\nu_y}{N_{SP}}$	0.338 / 0.315	1.285 / 1.105	0.345 / 0.33	0.383 / 0.383	0.383 / 0.383	0.24 / 0.24
Species	Proton	$^{7}Li^{+}$	$^{24}Mg^{+}$	$^{197}Au^{79+}$	$^{129}Xe^{36+}$	Proton
Cooling Method	EC	LC	LC	EC	EC	EC
ξ [μm]	4.6	4.15	21.8	12.7	11.2	4.82
$T_{Bx,y}$ / T_{Bz} [K]	50 / 1	-- / 3	>0.1 / 0.001	13580.6 / <10	27.2 / 18.1	9.05 / 1.54
$T_{x,y}$ / T_z	13.9 / 0.28	-- / 0.75	>0.132 / 0.00132	1.68 / <0.001	0.014 / 0.009	2.64 / 0.45
N_0 (anomaly)	2×10^{7}	--	5.5×10^{8}	4000	1000—10000	2000
N_0 (1-D to 2-D)	6.0×10^{6}	1.4×10^{7}	1.1×10^{6}	7.9×10^{6}	4.7×10^{6}	2.9×10^{6}
Observations	Schottky anomaly	Indirect transverse cooling	Schottky anomaly	1-D ordering	1-D ordering	1-D ordering

Figure 2: J. Wei, A.G. Ruggiero, A.M. Sessler, J. Hangst, and J. Schiffer (from left to right) at the *31st Workshop of the INFN Eloisatron Project on Crystalline Beams and Related Issues*, Erice, Italy, 1995 (photo taken by R. Ma).

Andy was an avid outdoor person and loved sharing physical activities, such as skiing, hiking, and jogging (Fig. 1). We routinely jog during lunchtime to the "Inspiration Point" at Berkeley, sharing jokes and solving physics challenges. Just as he loved sharing the outdoors, he loved sharing ideas, thoughts, knowledge, and life-time experiences. We went to Andy not only on physics problems but also upon life and career decisions.

Andy believed that physics is means to great friendship. He enjoyed friendship worldwide and across several generations of scientists. Andy frequently hosted students and junior physicists from Asia, Europe, and USA working on diverse subjects of accelerator physics. He loved travels not only to conferences, workshops and meetings in different continents but often on adventure trips to faraway places in the world.

Figure 3: J. Wei, X.-P. Li, K. Takayama and S. Yu (from left to right) at the *Andy Sessler Symposium*, Berkeley, USA, 2003. (From photos.lbl.gov, © Regents of UC through LBL.)

ISBN 978-3-95450-174-8

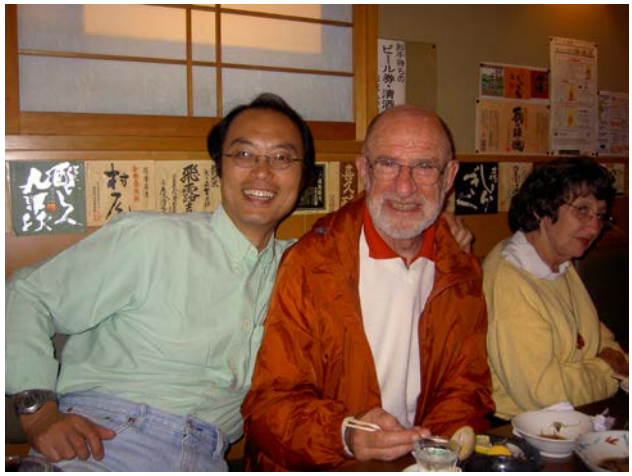

Figure 4: H. Okamoto, A.M. Sessler and S. Adams (from left to right) in Hiroshima, Japan, 2006.

Figure 5: A. Hofmann, A.M. Sessler, E. Wilson, E. Keil, B. Zotter and D. Möhl (from left to right) at CERN, Switzerland, 2009 (photo taken by H. Okamoto).

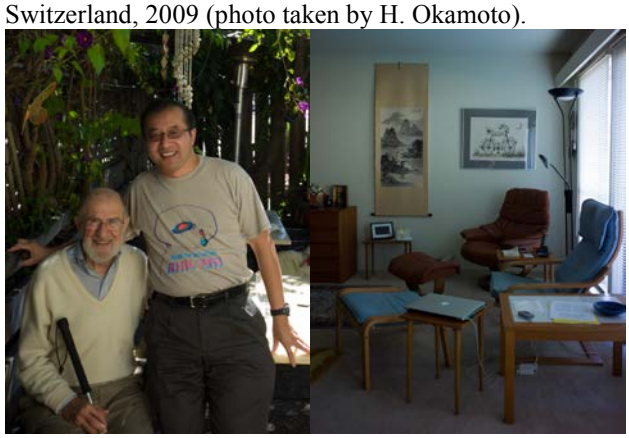

Figure 6: A.M. Sessler and J. Wei discussing work (left) near Andy's apartment (right) at Oakland, USA, October 3, 2013.

Andy has always been optimistic and realistic facing physics problems as well as life situations. Referring to his deteriorating medical situation, Andy wrote on August 16, 2013: "I have had a wonderful life: family, professionally, recreation, travel. Couldn't ask for more. I have taken it as it comes, and in the same spirit I am taking this."[11] When JW visited him in October 2013, six months before his passing (Fig. 6), Andy spent half a day discussing candidates that Michigan State University and the Facility for Rare Isotope Beams (FRIB) Project should approach and recruit. He had strong opinion on the importance of retaining free energy and on the long-range wellbeing of basic, non-programmatic beam sciences.

Upon receiving the Enrico Fermi Award in February 2014, Andy said: "Actually, it has been great fun developing all these things. I had more fun doing that—through the years—than I am enjoying even now on this happy day." "I am pleased that this award recognizes the activity of accelerator and beam scientists. I was fortunate to be in, almost at the beginning, when the power of theoretical physics was first brought to bear on accelerators." [12]

Figure 7: S. Adams, B. Obama and A.M. Sessler at the 2013 Enrico Fermi Award Ceremony in the White House, Washington D.C., USA, on February 3, 2014 [12].

CRYSTALLINE BEAM IN STORAGE RINGS

In this section, we summarize major results obtained during our study on crystalline beams.

For a system of particles with charge Ze and mass Am_0, the characteristic length ξ is given by [9]

$$\xi = \left(\frac{Z_0^2 r_0 \rho^2}{A\beta^2\gamma^2}\right)^{\frac{1}{3}}$$

where r_0 is the proton classical radius, βc and $\gamma A m_0 c^2$ are the velocity and energy of the reference particle, and ρ is the radius of curvature of the main bending region of the storage ring. In a typical accelerator (Table 1) this characteristic length corresponds to a regime where quantum effects are negligible and classical dynamics is adequate [13].

Crystalline Beam Ground State

In the classical dynamics limit, the "ground state" of a crystalline beam corresponds to "zero emittance" state where the motion of the circulating particles is periodic in time with the period of the machine lattice. As shown in

ISBN 978-3-95450-174-8

Fig. 8, particle trajectory in the transverse direction conforms to AG focusing (breathing), and in the longitudinal direction conforms to the change in bending radius (shear). In the presence of a longitudinal electric field, momentum p_z also varies periodically conforming to the energy gain at the cavity.

The goal of beam crystallization is to reach such kind of zero-emittance state where all "betatron" (transverse) and "synchrotron" (longitudinal) motions vanish and where all particles follow the periodic "closed orbit" as the external focusing force and intra-particle Coulomb force balance each other [8,14].

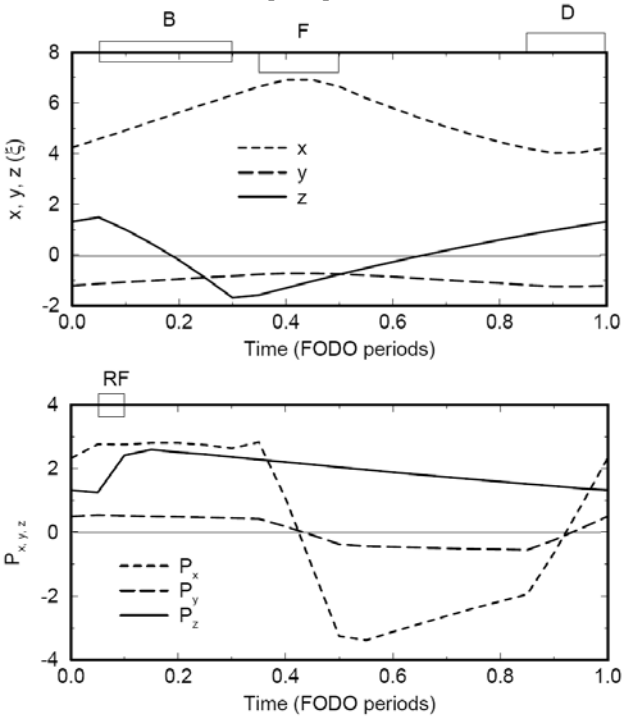

Figure 8: Particle trajectory of a bunched crystalline beam. The machine consists of 10 FODO cells with ν_x=2.8, ν_y = 2.1, and γ =1.4. Lattice components in each cell are displayed on the figure: B is a bending section, F and D are focusing and de-focusing quadrupoles, and RF is the bunching rf cavity.

General Relativity Derivation of Beam Rest Frame Hamiltonian

Although there can be more simplified method, we decided to adopt the general relativity formalism by C. Møller [15] to rigorously derive the equation of motion in the beam rest frame by tensor algebra. For a storage ring consisting of dipole magnetic of field B_0, quadrupole magnet of field gradient $\frac{\partial B_y}{\partial x}$, and accelerating electrical field (E_s), the motion can be represented by the Hamiltonian [8]

$$H_{bend} = \sum_i \frac{1}{2}\left[P_{ix}^2 + P_{iy}^2 + P_{iz}^2\right] - \gamma x_i P_{iz} + \frac{1}{2}\left[(1-n)x_i^2 + n y_i^2\right] + V_{ci}$$

for the bending region of radius ρ of the storage ring and

$$H_{non-bend} = \sum_i \frac{1}{2}\left[P_{ix}^2 + P_{iy}^2 + P_{iz}^2\right] + \frac{1}{2}\left[-n\, x_i^2 + n\, y_i^2\right] + V_{ci} + U_s$$

for the non-bending region of the ring, where

$$V_{ci} = \sum_{j\neq i} \frac{1}{\sqrt{(x_i - x_j)^2 + (y_i - y_j)^2 + (z_i - z_j)^2}}$$

is the Coulomb potential,

$$\mathrm{n} = -\frac{\rho}{B_0}\frac{\partial B_y}{\partial x},\quad \frac{\partial U_s}{\partial z} = -\frac{Z_0 e \xi E_s}{m_0 c^2}\left(\frac{\rho}{\xi\beta\gamma}\right)^2.$$

Condition for Ground State Existence

The storage ring must be alternating-gradient focusing operating below the transition energy, γ_T:

$$\gamma < \gamma_T.$$

Although some colleagues may argue that this condition is equivalent to avoiding the negative-mass instability [16], we derived it from the very first principle that the beam-frame Hamiltonian is bounded [17]. It arises from the criterion of stable kinematic motion under Coulomb interaction when particles are subject to bending in a storage ring.

Condition to Avoid Phonon Resonances

The bare transverse phase advances per lattice period need to be less than 90°, i.e.

$$\frac{\nu_{x,y}}{N_{SP}} < \frac{1}{4}$$

where ν_x and ν_y are the bare horizontal and vertical tunes, and N_{SP} is the lattice super-periodicity of the storage ring.

Although some colleagues argue that this condition is equivalent to avoiding the envelope instability [18], we again derived it from the very first principle of single-particle dynamics as the criteria that there is no linear resonance between the phonon modes of the crystalline structure and the machine lattice periodicity, and that linear resonance stopbands are not crossed during the entire cooling process as the 3-D beam density is increased.

Ground State Structure

The ground state structure is a 1-D chain when the beam line density is low [19]. The structure becomes 2-D lying in the plane of weaker transverse focusing if the line density λ in the machine is

$$\lambda > 0.62\gamma\xi^{-1}\left[\min\left(\nu_y^2, \nu_x^2 - \gamma^2\right)\right]^{\frac{1}{3}}$$

For even higher density, the particles arrange themselves into 3-D crystals, becoming helices and then helices within helices. Figure 9 shows such a multi-shell structure at a de-focusing location of the lattice. The maximum spatial density in the laboratory frame is approximately $\gamma\nu_y\sqrt{\nu_x^2 - \gamma^2}/(2\xi^3)$. If a sinusoidal electric field is present, the crystalline structure can be bunched azimuthally [18].

ISBN 978-3-95450-174-8

Beam and Lattice Heating

The minimum cooling rate needed for beam crystallization corresponds to the intra-beam scattering heating in an AG-focusing lattice. At any non-zero temperature the beam absorbs energy and heats up under time-dependent external forces caused by variations in lattice focusing and bending. In the high temperature limit, this intra-beam scattering results in a growth rate proportional to $\lambda T^{-5/2}$. The peak heating rate occurs at the temperature of about $T \approx 1$ when the ordering starts to occur, as shown in Fig. 10. Typically, strong spatial correlation appears in all directions when the temperature is below $T \approx 0.05$. Lattice shear and AG focusing have similar effects on beam heating. Heating behavior is similar for both bunched and coasting beams.

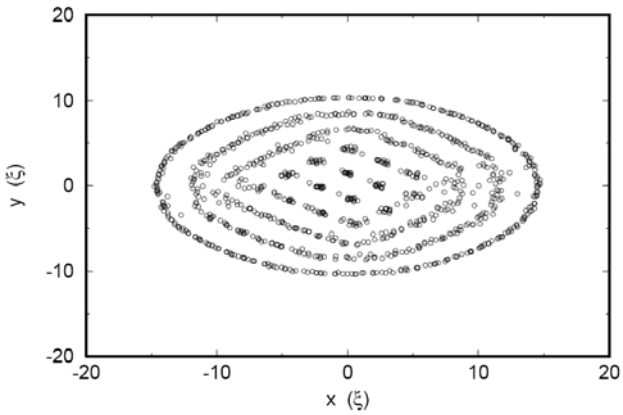

Figure 9: A multi-shell structure with particle positions projected into the x-y plane ($\lambda = 25\gamma\xi^{-1}$).

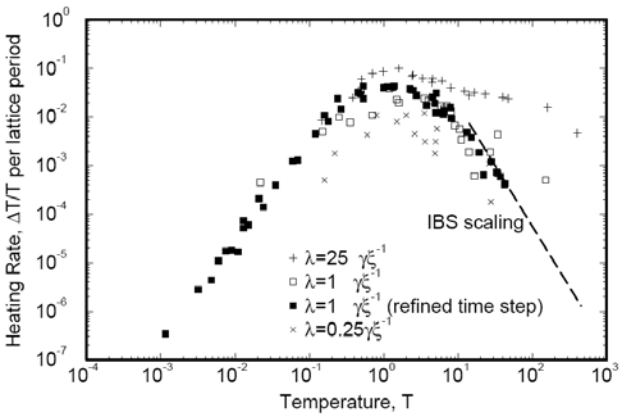

Figure 10: Typical heating rates as functions of temperature obtained by MD simulation at various line density, λ.

The normalized temperature T is related to be conventionally defined beam-frame temperature T_B and laboratory-frame parameters by

$$T_{x,y,z} = \frac{k_B \rho^2}{A m_0 c^2 \beta^2 \gamma^2 \xi^2} T_{Bx,y,z}$$

where

$$[T_{Bx}, T_{By}, T_{Bz}] = \frac{\beta^2\gamma^2 m_0 c^2}{2k_B}\left[\frac{\epsilon_x}{\langle\beta_x\rangle}, \frac{\epsilon_y}{\langle\beta_y\rangle}, \frac{1}{\gamma^2}\left(\frac{\delta p}{p}\right)^2\right].$$

Here, $\epsilon_{x,y}$ are the unnormalized emittances, $\delta p/p$ is the rms momentum spread, $\langle\beta_{x,y}\rangle$ are the average betatron amplitude function of the storage ring, and k_B is the Boltzmann constant.

CONDENSED MATTER METHODS FOR THR BEAM REST FRAME

In this section, we outline the framework to numerically solve the Hamiltonian for crystalline beams in order to study their condensed matter properties. We will conclude with speculations and open questions.

Method

The derivation of the Hamiltonian [8] makes it convenient to study the condensed matter properties of crystalline beams in storage rings. It is straight forward to write a molecular dynamics program to simulate the motion of particles, either to cool down the beam using efficient but unrealistic cooling methods to find ground states, or to employ realistic cooling methods to simulate the dynamics of a crystalline beam.

For condensed matter properties, it is desirable to separate the hopefully smaller time-dependent part in the Hamiltonian from the time-independent part, and then treat the time-dependent part as a perturbation. The time-independent part of the Hamiltonian is obtained by the Smooth Approximation [8].

Recall that with the smooth approximation, the Hamiltonian is

$$H = \sum_i \frac{1}{2}\left[P_{ix}^2 + P_{iy}^2 + (P_{iz} - \gamma X_i)^2\right] + \frac{1}{2}\left[(\nu_x^2 - \gamma^2)X_i^2 + \nu_y^2 Y_i^2\right] + V_{ci}$$

The only part that needs special attention in molecular dynamics or other numerical studies is the long-range nature of Coulomb interaction between the particles, when the beam is uniformly spread throughout the storage ring, that is, not bunched. Periodic boundary conditions in the longitudinal direction can be applied in this case.

Using the notation that L is the size of the periodic cell, $\varrho = \sqrt{X^2 + Y^2}$ is radius in the transverse direction, N is the total number of particles in a cell, λ is the linear density, then the Coulomb energy per particle is

$$\frac{V_c}{N} = \frac{1}{NL}\sum_{j<i} \Phi(\varrho_{ij}, Z_{ij})$$

where Z_{ij} is understood to be modulo L. The detailed algebra to efficiently calculate $\Phi(\varrho, z)$ had been worked out by Avilov [20] and Hasse [21]. Avilov [20] gives

$$\Phi(\varrho, Z) = \frac{4}{L}\sum_{m=1}^{\infty} K_0\left(\frac{2\pi m\varrho}{L}\right)\cos\left(\frac{2\pi m Z}{L}\right) - \frac{2}{L}\left[\ln\left(\frac{\varrho}{2L}\right) + \gamma\right]$$

Where $K_0(r)$ is the zeroth order McDonald function, and γ is the Euler constant. This expansion converges rapidly as long as ρ is not near 0.

ISBN 978-3-95450-174-8

Based on Avilov, Hasse [21] gives another elegant formula:

$$\Phi(\varrho,Z)=\frac{1}{(\varrho^2+Z^2)^{1/2}}-\sum_{\mu=0}^{\infty}\frac{\left(-\frac{\varrho^2}{4}\right)^{\mu}}{(\mu!)^2}\frac{d^{(2\mu)}}{dz^{(2\mu)}}[\psi(Z)+\psi(-Z)+2\gamma]$$

Where

$$\psi(Z)+\psi(-Z)+2\gamma=-2\sum_{n=0}^{\infty}[\zeta(2n+1)-1]Z^{2n}$$

And $\zeta(n)$ is the Rieman zeta function of integer argument. This series converges fast when ϱ is small.
In practice, we can use Hasse's formula for small ϱ and Avilov's formula for larger ϱ.

Ground States

With Smooth Approximation and employing a downhill-type algorithm like conjugate gradient, we can calculate the time-independent ground state structures and energies. A typical ground state energy versus linear density curve is shown in Fig. 11.

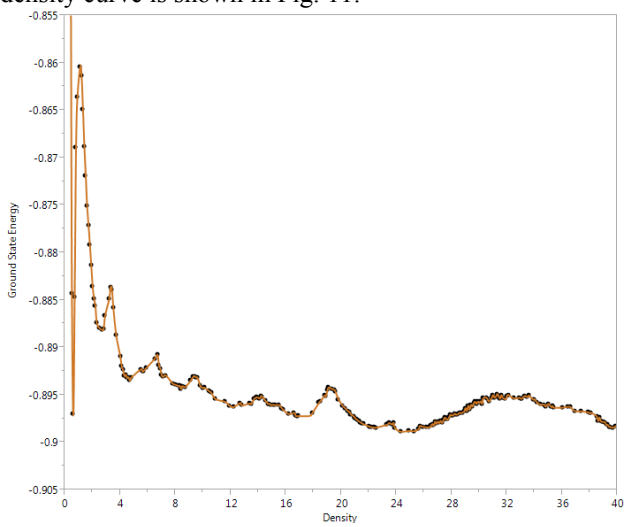

Figure 11: Typical ground state energy versus linear density of crystalline beams in storage rings.

Figure 12 shows some example ground state structures when linear density increases.

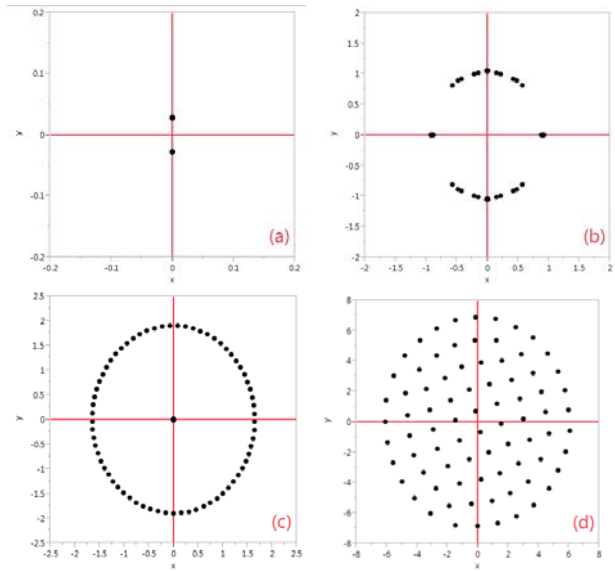

Figure 12: Examples of ground state structures. (a) Zig zag chain; (b) One shell; (c) A second shell starts to emerge in the center; (d) Multiple shells which resembles a lattice near the center.

Phonon Spectrum

Once the time-independent ground state structure is found, we need to find the excited states in order to study the effects of the time-dependent part of the Hamiltonian, as well as finite temperature properties. The low-lying excited states can be approximated by small vibrations of the particles, or phonons. Another important reason to study the phonon spectrum is that, as established earlier, a stabilization criterion is related to the highest phonon frequency [22].

The Coulomb interaction term is the only non-linear term that needs a small vibration expansion. Using capital letters (X,Y,Z) to denote the coordinates of equilibrium positions and $(\tilde{x},\tilde{y},\tilde{z})$ the magnitude of the small deviations from the equilibrium position, applying periodic boundary conditions, the linearized equations of motion are [23]

$$\begin{aligned}&\omega^2\tilde{x}_i\\&=-i\gamma\omega\tilde{z}_i+(\nu_x^2-\gamma^2)\tilde{x}_i\\&+\sum_{n=-\infty}^{\infty}\sum_{j=1}^{N}\{\left[\frac{1}{R_{nij}^3}-\frac{3(X_i-X_j)^2}{R_{nij}^5}\right]\left[e^{ik(Z_i-Z_j-nL)}\tilde{x}_j-\tilde{x}_i\right]\\&-\frac{3(X_i-X_j)(Y_i-Y_j)}{R_{nij}^5}[e^{ik(Z_i-Z_j-nL)}\tilde{y}_j-\tilde{y}_i]\\&-\frac{3(X_i-X_j)(Z_i-Z_j-nL)}{R_{nij}^5}[e^{ik(Z_i-Z_j-nL)}\tilde{z}_j-\tilde{z}_i]\}\end{aligned}$$

ISBN 978-3-95450-174-8

$$\omega^2\tilde{y}_i = \nu_y^2\tilde{y}_i + \sum_{n=-\infty}^{\infty}\sum_{j=1}^{N}\{-\frac{3(X_i-X_j)(Y_i-Y_j)}{R_{nij}^5}\left[e^{ik(Z_i-Z_j-nL)}\tilde{x}_j-\tilde{x}_i\right] + \left[\frac{1}{R_{nij}^3}-\frac{3(Y_i-Y_j)^2}{R_{nij}^5}\right][e^{ik(Z_i-Z_j-nL)}\tilde{y}_j-\tilde{y}_i] - \frac{3(Y_i-Y_j)(Z_i-Z_j-nL)}{R_{nij}^5}[e^{ik(Z_i-Z_j-nL)}\tilde{z}_j-\tilde{z}_i]\}$$

$$\omega^2\tilde{z}_i = i\gamma\omega\tilde{x}_i + \sum_{n=-\infty}^{\infty}\sum_{j=1}^{N}\{-\frac{3(X_i-X_j)(Z_i-Z_j-nL)}{R_{nij}^5}\left[e^{ik(Z_i-Z_j-nL)}\tilde{x}_j-\tilde{x}_i\right] - \frac{3(Y_i-Y_j)(Z_i-Z_j-nL)}{R_{nij}^5}\left[e^{ik(Z_i-Z_j-nL)}\tilde{y}_j-\tilde{y}_i\right] + \left[\frac{1}{R_{nij}^3}-\frac{3(Z_i-Z_j-nL)^2}{R_{nij}^5}\right][e^{ik(Z_i-Z_j-nL)}\tilde{z}_j-\tilde{z}_i]\}$$

Where $R_{nij}=\sqrt{(X_i-X_j)^2+(Y_i-Y_j)^2+(Z_i-Z_j-nL)^2}$ and $i=1,2,\ldots,N$. It is understood that the $R_{nij}=0$ term is excluded from the double sum.

The double sum again has infinite number of terms, which seems to call for some algorithm, like the Ewald Summation, to perform it efficiently. However, considering that all the terms are in the order of $\frac{1}{R_{nij}^3}$ which is short ranged, and that modern computers are fast, it is probably easier to perform the sum by brute force to whatever accuracy required.

Due to the long-range nature of the Coulomb interaction and the fact that this system is quasi one dimensional, the phonon spectrum has a singularity at $k=0$. The singularity is very week, only logarithmic in nature, in the order of $k(\log(k))^{1/2}$, and does not seem to cause anything interesting.

There is another somewhat significant difference between this phonon problem and traditional phonon problems – the frequency ω appears in the off-diagonal of the matrix. This is caused by the cross term between x and p_z in the Hamiltonian. Fortunately when ω is real, the matrix is still Hermitian as expected. Because of this difference, a little extra work is needed to solve this matrix numerically compared to typical eigenvalue problems. We found that it is reasonably easy to solve this whole phonon problem by finding one ω at a time, iteratively until self-consistency.

An example of phonon dispersion curves is shown in Fig. 13, and typical phonon densities of states are shown in Fig. 14.

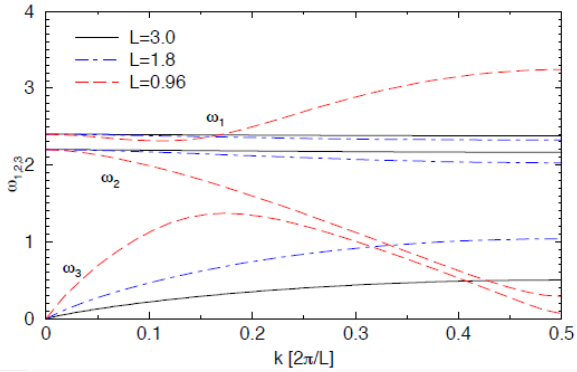

Figure 13: Example phonon dispersion curves.

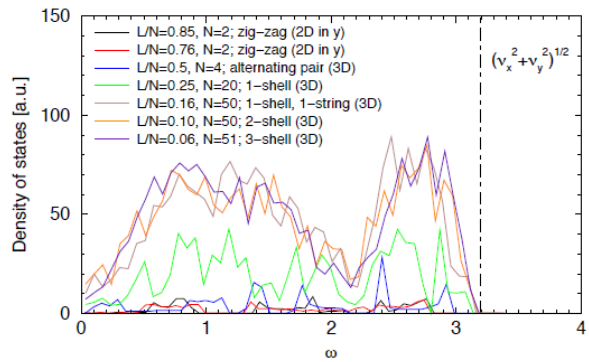

Figure 14: Example phonon densities of states.

Other Considerations

Is there a phase transition? We have established earlier that in order for a crystalline beam to possibly exist, the storage ring has to satisfy $\gamma < \nu_x$. What happens near $\gamma = \nu_x$?

The partition function $Z = Tr(e^{-\beta H})$ for the Hamiltonian under smooth approximation can be written as

$$Z = \left(\frac{2\pi}{\beta}\right)^{\frac{3}{2}N}\left(\frac{2}{\beta}\right)^{\frac{3}{2}N}\left(\frac{1}{(\nu_x^2-\gamma^2)\nu_y^2}\right)^{\frac{N}{2}}\mathbb{Z}(\beta,\nu_x^2-\gamma^2,\nu_y^2)$$

Where $\mathbb{Z}(\beta,\nu_x^2-\gamma^2,\nu_y^2)$ is a massive integration too hard to calculate.

The mean square displacement in the x direction is

$$\langle X^2\rangle = -\frac{2}{\beta N}\frac{\partial \ln(Z)}{\partial \nu_x^2} = \frac{1}{\beta(\nu_x+\gamma)(\nu_x-\gamma)} - \frac{2}{\beta N}\frac{\partial \ln\left(\mathbb{Z}(\beta,\nu_x^2-\gamma^2,\nu_y^2)\right)}{\partial \nu_x^2}$$

Here is a leap of faith – assuming that the last term is analytic near $\gamma = \nu_x$ at $T=0$. The first term shows that there is a second order phase transition at $\gamma = \nu_x$ with a critical exponent 1. However, this is pure speculation. What the last term does is anyone's guess, and temperature effects are also unknown. We do know that $\mathbb{Z}$ arises from the Coulomb interaction. If Coulomb interaction can be neglected, like at very high temperature

ISBN 978-3-95450-174-8

and low density, then $\mathbb{Z}$ is a constant, and the last term in $\langle X^2 \rangle$ is 0, and the phase transition we see here is exact.

Reconcile with von Hove's Theorem. von Hove's theorem [24] is understood to mean the general non-existence of phase transitions in 1D systems with short-range interaction. A beam in a storage ring is a quasi 1D system (it only goes to infinity in the longitudinal direction, yet not zero in the other two dimensions) with long-range Coulomb interaction, thus does not fall to the category of von Hove's theorem. However, it is helpful to understand the possible phase transition if we exam the argument underlining von Hove's theorem.

One of the arguments is given by Landau and Lifshitz [25]. The energy cost of a domain wall is finite, and the entropy caused by the number and locations of the domain walls is $\propto \ln(L)$ where L is the size of the system, therefore the total free energy decreases when the number of domain walls increases at any finite temperature, until no macroscopic domains exist.

In our quasi 1D system, the effect of the long-range Coulomb interaction on the energy cost of a domain wall is beside the point. We observe that in the possible phase transition, the "domain wall" is parallel to the longitudinal direction, thus the energy cost of such a "domain wall" is $\propto L$. So the formation of such a "domain wall" is unfavorable, at least at low temperatures.

"Magic Densities". In private communications with Andy, we raised the question, are there magic densities where crystalline beams are more likely to be observed?

The question arises from the observation that the ground state energy versus density curve has peaks and valleys. Near the peaks, it is less favorable for the density to stay constant throughout the storage ring, as depicted in a (unrealistic) example in Fig. 15. It is therefore more likely to find crystalline beams at densities near the minima of the curve.

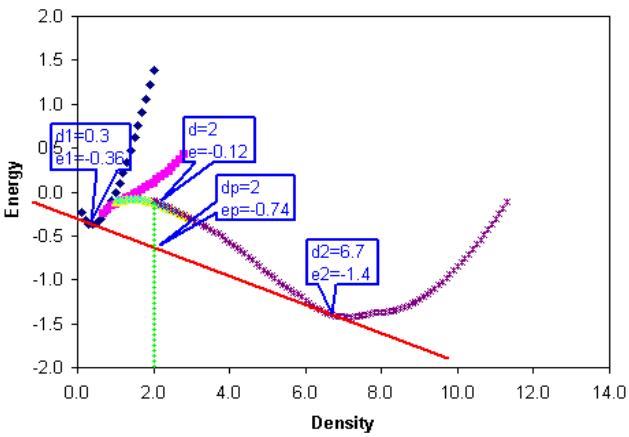

Figure 15: Possible "magic densities" if the ground state energy versus density curve has peaks and valleys. In this illustrative picture, two minima are assumed to be at densities d1 and d2. For a density d between d1 and d2, it is favorable to have a mixture of densities d1 and d2 rather than a uniform density d.

TOWARDS ULTRA LOW TEMPERATURE

Needless to say, it is important to ask whether any realistic cooling method is available to reach a crystalline ground state in practice. The Coulomb coupling constant Γ, defined as the ratio of the average Coulomb energy to the average thermal energy of a beam, is well above 100 in an ideal crystalline state (while $\Gamma \sim 1$ in any regular beams). This typically corresponds to a temperature of a mK range, very close to the absolute zero! In the early 1990's, we only had few cooling methods technically well-established and applicable to hadron beams, i.e., "electron cooling" [26] and "stochastic cooling" [27]. These cooling techniques were, however, insufficient for our ultimate goal because of the achievable temperature much higher than mK. Andy thus paid attention to "Doppler laser cooling" [28,29]. Laser cooling was relatively new to the accelerator community and, as a matter of fact, only two European teams had just begun to apply this sophisticated technique to fast circulating ions in storage rings. The TSR group of Max Planck Institute [3] and the ASTRID group of Aarhus University [4] soon succeeded in demonstrating the promising potential of laser cooling experimentally. Theoretically, the Doppler cooling limit reaches the mK range or even lower, so we naturally concluded that this technique should be the only means for us to approach a crystalline state.

Resonance Cooling

We, however, immediately encountered a serious problem. We learned that laser cooling is effective only in the direction of beam propagation when ions are running at high speed along a particular orbit; no direct cooling force is obtainable in the directions perpendicular to the beam orbit because it is very difficult to ensure a sufficient spatial overlap between a tiny laser spot and fast traveling ions. Dieter Möhl joined us in 1993 to solve this difficulty and, a few months later, we wrote up the idea of using synchro-betatron coupling resonance to indirectly enhance the transverse cooling efficiency [10]. This simple idea was eventually employed at the storage ring S-LSR where a Japanese team successfully confirmed the expected transverse indirect laser-cooling effect under a coupling resonance condition [30,31]

Tapered Cooling

In an early stage of systematic MD simulations, we noticed that too strong a longitudinal linear frictional force could worsen the stability of a large (shell) crystalline configuration [14]. This effect is peculiar to a storage ring that has the momentum dispersion induced by bending magnets. In March 1997, we got together in Kyoto for a couple of weeks, made lots of discussion, and later published a couple of papers summarizing our thoughts at that moment [14,32]. It is well known that multi-shell Coulomb crystals can readily be produced in a compact ion trap with a Doppler cooling system. By contrast, we found it almost hopeless to stabilize such a

ISBN 978-3-95450-174-8

large 3D crystalline beam without the so-called tapered cooling force. Our MD results so far have strongly supported this conclusion [33]. We currently believe that the existence of momentum dispersion in a regular storage ring is one of the most serious obstacles to beam crystallization. In order to overcome the dispersive heating effect, an optimized tapered force must be developed. The effect of cooling is described by a reduction in P_z in the cooling region by

$$\Delta P_z = -f_z(P_z - C_{xz}x)$$

where the coefficient describing the strength of cooling is f_z, and the coefficient describing the extent of tapering C_{xz} is proportional to the lattice dispersion. Alternatively, attempts have been made to design storage rings with dispersion eliminated all around the ring [34]. For this purpose, a unique bending element has been proposed and theoretically studied [35]. Shear-free ring lattices consisting of both magnets and electrodes were designed at S-LSR so that 3-D crystalline structures may be formed without using tapered cooling forces.

Machine Lattice Periodicity Consideration

The condition to avoid phonon resonance discussed in Section 2 is equivalent to avoiding the transverse collective instability driven by the periodic nature of the external alternating-gradient potential for beam focusing. No such instability occurs in a uniform focusing channel. We have repeatedly emphasized the importance of this effect from the very beginning of our fruitful collaboration because it imposes severe restrictions on the lattice design of a dedicated cooler ring. The betatron phase advance per lattice period has to be sufficiently small (most preferably, less than 90 degrees) to avoid crossing a strong linear resonance stop band during a cooling process toward beam crystallization [14,18,33,36,37]. This requirement is very difficult to meet in practice. As any machine involves finite mechanical errors in reality, the original lattice symmetry is always weakly broken. Even if all lattice elements were constructed perfectly and placed precisely at ideal positions, additional coupling sources introduced to enhance transverse laser-cooling efficiency inevitably disturbs the lattice in an asymmetric way. We have confirmed that such weak symmetry breaking can destroy or, at least, affect a large crystalline structure [33,35]. Even the dissipative interactions with laser photons every turn can deteriorate the crystal stability unless the cooling lasers are applied to the beam in all straight sections to strictly hold the symmetry of external forces. These facts suggest that the stabilization of a multi-shell crystalline beam in a storage ring is still quite challenging, although it seems possible to form and maintain the ordered configuration in a carefully designed cooler ring by keeping the cooling lasers on [38]. On the other hand, many past MD results have also shown that the production of the 1D string or 2D zigzag configuration is probably possible even in an existing storage ring. Most recent MD simulations have actually indicated the feasibility of stable string formation of ions in S-LSR with optimized lattice and laser parameters, despite that the ring is equipped with only a single, relatively low-power laser [39].

DISCUSSIONS AND SUMMARY

The crystalline beam corresponds to the ultimate state of zero temperature and zero emittance of charged particle beams. Andy was fascinated by the rich and challenging physics and worked with us as his hobby for more than twenty years. Our contributions range from the fundamental analytical formulation leading to guiding conditions of crystalline beam formation, to numerical methods and confirmation, and then to advising experimentalists in practical realization.

Among practical purposes of beam crystallization, ordered multidimensional beams were proposed for ion-ion colliders for increased luminosity [40]. Machine lattices of high or imaginary transition energy were proposed so that high-energy or colliding crystals may be realized in storage rings of moderate circumference. High-density 1-D strings were proposed for high-luminosity ion-electron collisions with rare radioactive ions [41, 42].

Despite for the efforts made during the past three decades, only 1-D ordering was realized experimentally in storage rings using electron cooling or laser cooling. Higher density, 3-D crystalline structures were only realized in ion traps; efforts to form 3-D crystalline beams in storage rings have not been successful.

Major challenges in beam crystallization are to design and construct storage rings with high lattice periodicity and low transverse phase advance to avoid linear resonances, and to implement effective beam cooling that conforms to the dispersive nature of the beam.

Ion traps have been used to experimentally simulate features of an AG-focusing storage ring [43]. However, it is difficult to study with such a set up the shear effects of the bending magnets in storage rings [44,45]. Combination of a storage ring and an ion trap may simulate the environment of colliding crystals.

Some fundamental questions remain to be answered. Crystalline beam corresponds to a new state of matter of one-component plasma where particles are confined by a periodic, time-dependent external potential with finite transverse boundary. Basic condensed-matter physics of such a system including phase-transition properties remains to be studied.

Since a 3-D crystalline beam has not been observed, the most fundamental question is, does a crystalline beam at a higher density (other than a 1-D string) really exist? If not, why? If yes, under what conditions? There are many variables in the equation, a thorough theoretical understanding and then a comprehensive numerical study of the phase diagram would be most helpful. This is apparently not an easy task. We envision that the first realistic step is to fully understand the already observed phase transition at very low density. It seems to be first order in nature, and progress has been made for its understanding. But why does the transition happen at that

ISBN 978-3-95450-174-8

density? Is it related to the phase transition near $\gamma = \nu_x$ that we speculated? Hopefully an understanding of this transition will have some predicting power and shed lights on higher density conditions.

REFERENCES

[1] E.E. Dement'ev et al, Zh. Tekh. Fiz. **50** (1980) 1717; N.S. Dikanskii, D. V. Pestrikov, Proc. Workshop on Electron Cooling and Related Applications, KfK 3846 (1984); V.V. Parkhomchuk, A. H. Skrinsky, Reports on Progress in Physics, **54** (1991) 919.

[2] J. P. Schiffer and P. Kienle, Z. Phys. A **321**, 181 (1985); A. Rahman and J. P. Schiffer, Phys. Rev. Lett. **57**, 1133 (1986); J. P. Schiffer and A. Rahman, Z. Phys. A **331**, 71 (1988).

[3] S. Schröder et al. Phys. Rev. Lett. **64**, 2901 (1990); H.-J. Miesner et al, Phys. Rev. Lett. **77**, 623 (1996).

[4] J. S. Hangst et al, Phys. Rev. Lett. **67** (1991) 1238, Phys. Rev. Lett. **76**, 1238 (1991); N. Madsen, et al, Phys. Rev. Lett. **83**, 4301 (1999); J. S. Hangst, et al, Phys. Rev. Lett. **74,** 86 (1995).

[5] M. Steck et al, Phys. Rev. Lett. 77, 3803 (1996).

[6] H. Danared et al, Phys. Rev. Lett. 88, 174801 (2002).

[7] T. Shirai et al, Phys. Rev. Lett. 98, 204801 (2007).

[8] J. Wei, X.-P. Li, A.M. Sessler, BNL Report 52381 (Brookhaven National Laboratory, 1993); J. Wei, PAC2001 (Chicago, 2001), p. 1678.

[9] J. Wei, X-P Li, A.M. Sessler, Phys. Rev. Lett. 73, 3089 (1994).

[10] H. Okamoto, A. M. Sessler, and D. Möhl, Phys. Rev. Lett., **72**, 3977 (1994); H. Okamoto, Phys. Rev. E, **50**, 4982 (1994).

[11] Private communications with J. Wei (Oct. 2013).

[12] Web site: https://www.whitehouse.gov/blog/2014/02/03/ president-obama-welcomes-2013-fermi-award-winners-white-house

[13] J. Wei, X.-P. Li, A.M. Sessler, PAC1995 (Dallas, 1995) p. 2948.

[14] J. Wei, H. Okamoto, and A. M. Sessler, Phys. Rev. Lett., **80**, 2606 (1998).

[15] C. Møller, *The Theory of Relativity*, Oxford, 1952

[16] X. Nielsen, A.M. Sessler, Proc. Int. Conf. High Energy Acc. (1959) p. 239.

[17] I. Hofmann, J. Struckmeier, Proc. Workshop on Crystalline Ion Beams (1988) p.140.

[18] J. Wei, A. Draeseke, A. M. Sessler, and X.-P. Li, Proc. of the 31st INFN Eloisatron Workshop on Crystalline Beams and Related Topics (Erice, Italy, 1995) p. 229.

[19] R.W. Hasse, J.P. Schiffer, Ann. Phys. **203** (1990) 419.

[20] V.V. Avilov, Solid State Commun. 44, 555 (1982).

[21] R.W. Hasse, Phys. Rev. Lett. 67, 600 (1991).

[22] X-P Li, A.M. Sessler and J. Wei, EPAC '94, 1379 (1994).

[23] X-P Li, H. Enokizono, H. Okamoto, Y. Yuri, A.M. Sessler and J. Wei, Proc. 2005 Particle Acc. Conf, 4111, (2005).

[24] L. von Hove, Phisica **16**, 137 (1950).

[25] L.D. Landau and E.M. Lifshitz, Statistical Physics I, Pergamon Press, New York (1980).

[26] G.I. Budker, Atomnaya Energiya **22**, 346 (1967).

[27] S. van der Meer, CERN Internal Report CERN/ISR-PO/72-31 (1972).

[28] D.J. Wineland and H. Dehmelt, Bull. Am. Phys. Soc., **20**, 637 (1975).

[29] T. Hänsch and A. Shawlow, Opt. Commun., **13**, 68 (1975).

[30] M. Nakao et al., Phys. Rev. ST Accel. Beams **15**, 110102 (2012).

[31] H. Souda et al., Jpn. J. Appl. Phys. **52**, 030202 (2013).

[32] H. Okamoto and J. Wei, Phys. Rev. E **58**, 3817 (1998).

[33] Y. Yuri and H. Okamoto, Phys. Rev. ST Accel. Beams **8**, 114201 (2005).

[34] R. E. Pollock, Z. Phys. A 341, 95 (1991).

[35] M. Ikegami et al., Phys. Rev. ST Accel. Beams **7**, 120101 (2004); M. Ikegami, H. Okamoto, and Y. Yuri, Phys. Rev. ST Accel. Beams **9**, 124201 (2006).

[36] K. Okabe and H. Okamoto, Jpn. J. Appl. Phys. **42**, 4584 (2003).

[37] X.-P. Li *et al.*, Phys. Rev. ST Accel. Beams **9**, 034201 (2006).

[38] H. Okamoto, Proc. COOL2013 (Mürren, Switzerland, 2013), p. 152.

[39] K. Osaki and H. Okamoto, Prog. Theor. Exp. Phys. **2014**, 053G01 (2014).

[40] J. Wei, A.M. Sessler, EPAC 98, p.862; J. Wei et al, COOL 07, p.91.

[41] I. Meshkov et al, RIKEN Report: RIKENAF-AC-34 (2002).

[42] T. Katayama, D. Möhl, RIKEN Report RIKEN-AF-AC-39 (2002).

[43] H. Okamoto and H. Tanaka, Nucl. Instrum. Meth. **437** (1999) 178; H. Okamoto et al., Nucl. Instrum. Meth. **733** (2014) 119; E. Gilson et al., Phys. Rev. Lett. **92** (2004) 155002.

[44] F. Diedrich et al, Phys. Rev. Lett. **59** (1987) 2931; D.J. Wineland et al, Phys. Rev. Lett. **59** (1987) 2935; S.L. Gilbert et al, Phys. Rev. Lett. **60** (1988) 2022; I. Waki et al., Phys. Rev. Lett. **68** (1992) 2007; N. Kjægaard and M. Drewsen, Phys. Rev. Lett. **91** (2003) 095002; N. Kjægaard, K. Mølhave, and M. Drewsen; M. Drewsen et al., Phys. Rev. Lett. **81** (1998) 2878.

[45] T. Schätz, U. Schramm, D. Habs, Nature (London) **412**, 717 (2001); U. Schramm, M. Bussmann, D. Habs, NIM A **532**, 348 (2004); U. Schramm, T. Schätz, and D. Habs, Phys. Rev. E **66** (2002) 036501.

ISBN 978-3-95450-174-8

STOCHASTIC COOLING EXPERIMENTS AT NUCLOTRON AND APPLICATION TO NICA COLLIDER*

N. Shurkhno#, I. Gorelyshev, A. Sidorin[1], G. Trubnikov[1], JINR, Dubna, Russia
R. Stassen, FZ Jülich, Jülich, Germany
T. Katayama, GSI, Darmstadt, Germany
[1] - St Peterburg State University, Russia

Abstract

Stochastic cooling is the key element for the NICA accelerator facility that is presently under development at JINR, Russia. Beam cooling will work with the high-intensity bunched beams in the 3-4.5 GeV energy range; all three degrees of freedom will be treated simultaneously. The preparatory experimental work on stochastic cooling is carried out at accelerator Nuclotron (JINR, Dubna) since 2010. During this work hardware solutions and automation techniques for system adjustment have been worked out and tested. Based on the gained experience the overall design of the NICA stochastic cooling system was also developed. The report presents the conceptual design of the NICA stochastic cooling system and overviews the results of cooling experiments at Nuclotron and the developed adjustment automation techniques.

INTRODUCTION

Nuclotron-based Ion Collider Facility (NICA) is an intensively developing flagship project of Joint Institute for Nuclear Research (JINR) [1]. Stochastic cooling will be used in the collider ring during experiments with heavy ions for beam accumulation and intra-beam scattering (IBS) suppression to avoid luminosity reduction, which implies full 3D cooling of intense bunched beams. Beam accumulation process requires only longitudinal cooling and implies almost coasting beam with reduced intensities, therefore primary requirements for stochastic cooling systems arise from the IBS counteraction.

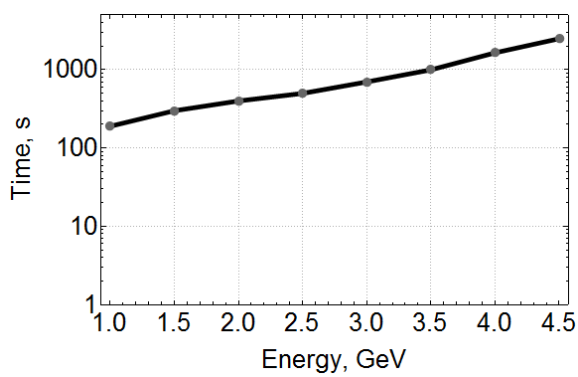

Figure 1: IBS heating times for Au^{79+}.

Stochastic cooling must provide cooling times lower than corresponding IBS heating times to prevent beam emittance growth and keep the luminosity, Figure 1 shows expected IBS heating times in the energy range of the collider operation.

At lower energies IBS process becomes much faster and accompanied with significant phase slip factor growth, which makes stochastic cooling hardly feasible at this region and therefore here electron cooling is foreseen. Nevertheless, it's highly advantageous to cover as wide as possible energy range with stochastic cooling, because it doesn't have additional beam losses unlike electron cooling (due to ion recombination).

The parameters of NICA collider are listed in Table 1:

Table 1: Parameters of the NICA Collider

Circumference, *m*	503		
Ions	Au^{79+}		
Number of bunches	22		
RMS bunch length, *m*	0.6		
γ_{cr}	7.088		
Energy, *GeV/u*	1	3	4.5
Bunch intensity × 10^9	0.2	2.4	2.3
$\Delta p/p \times 10^{-3}$	0.55	1.15	1.5
$\varepsilon_x, \pi \cdot mm \cdot mrad$	1.1	1.1	1.1
$\varepsilon_y, \pi \cdot mm \cdot mrad$	0.95	0.85	0.75
Phase slip factor η	0.215	0.037	0.009
IBS heating time, *s*	160	460	1800

LONGITUDINAL COOLING

There are three experimentally tested techniques to achieve longitudinal stochastic cooling – time-of-flight, Palmer and notch-filter methods. Further we shortly review the possibilities of implementation of these methods in the NICA collider.

Time-of-flight method provides the largest momentum spread acceptance for cooling system compared to the other methods. Time-of-flight method uses longitudinal pick-up and 90° phase shifter (which acts like differentiator) to make the signal to be proportional to the beam's momentum deviation. This method was recently experimentally tested at Forschungszentrum Jülich (FZJ) [2]. Unfortunately, time-of-flight method provides best

*Work supported by FAIR-Russia Research Center grant
#n.shurkhno@fz-juelich.de

ISBN 978-3-95450-174-8

performance for beams with large momentum spread, and according to simulations with Fokker-Planck equation it will not provide enough efficiency in case of NICA collider parameters.

The Palmer method for longitudinal cooling also provides quite large momentum spread acceptance. In this method the horizontal pick-up is placed in the region with high dispersion and small beta-function values, so that the resulting signal would be proportional only to the momentum deviation. Thus to have effectively operating Palmer cooling one has to have

$$\sqrt{\epsilon_x \beta_x} \ll D_x \frac{\Delta p}{p_0},$$

where ϵ_x, β_x, D_x – horizontal emittance, beta-function and dispersion correspondingly, $\Delta p/p_0$ – momentum spread.

The implementation of Palmer method in the NICA collider encounters two difficulties. First, dispersion in the whole ring is quite small and has a maximum value of only ~2.5 m. Second, the maximal values of dispersion function are always accompanied by the betatron motion of the same order (Fig. 2):

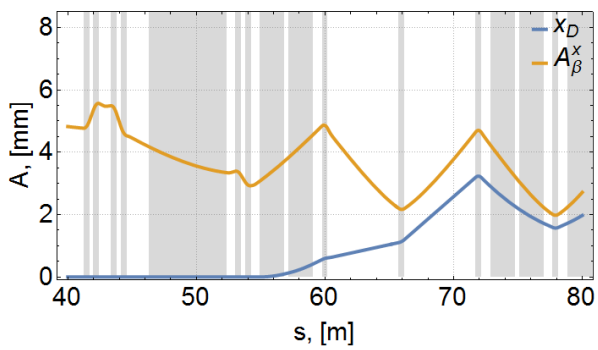

Figure 2: Deviation due to dispersion $D_x \Delta p/p_0$ (blue) and amplitude of betatron motion $\sqrt{\epsilon_x \beta_x}$ (orange).

Presence of transverse signal will cause cross-heating between two degrees of freedom unless the kicker is placed with a proper distance from the pick-up, so simultaneous longitudinal and horizontal coolings would be possible. This modification of Palmer method is known as *Palmer-Hereward* method [3]. The theoretical and particle tracking simulations show that Palmer-Hereward method wouldn't provide the required cooling times for both degrees of freedom.

The Palmer method alone (simulation without additional transverse signal) provides sufficient cooling rates for wide energy range 3-4.5 GeV. So it is advantageous still to consider it. Non-integer parts of betatron tunes in the NICA collider are close to 0.5, and in the frequency domain corresponding betatron sidebands would be located in between of the longitudinal Schottky bands (no overlap occurs), so it is also possible to discuss a special comb-filter to filter out the transverse signal. This approach requires further experimental investigation.

Lastly the **notch-filter method** is a well-known and dispersion-independent method for longitudinal stochastic cooling. In this method the signal from the longitudinal pick-up is being filtered out by a notch-filter (comb filter to be more exact) with notches and phase inversions at the harmonics of revolution frequency. The main disadvantage of this method in the frame of NICA is that is has considerably narrower momentum spread acceptance due to additional one-turn delay line in the filter. Consequently, this limits the energy range for stochastic cooling only to 4-4.5 GeV/u, so it's advantageous to look for other solutions.

MÖHL'S METHOD FOR LONGITUDINAL COOLING

Another method, in which two longitudinal pick-ups are used, could be proposed for longitudinal cooling at NICA. This method was firstly proposed by D. Möhl [4], and respecting this further we will refer to this method as Möhl's method. The basic idea of this method is very similar to the Filter method, which uses the difference of two longitudinal signals, separated by revolution period. In Möhl's method, instead of dividing the original signal, longitudinal signals are obtained from two separated longitudinal pick-ups (Fig. 3):

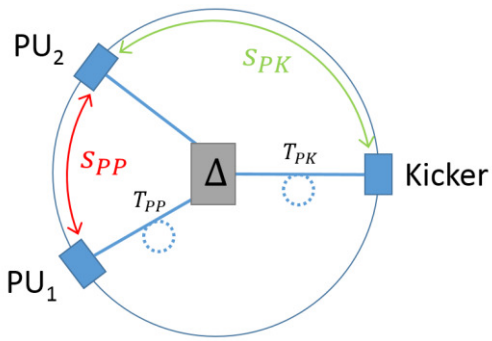

Figure 3: Möhl's method layout.

Eventually the difference of these signals with additional 90° phase shift will also produce a correctional signal proportional to the particles' momentum deviation.

The theoretical investigation of the Möhl's method could be thoroughly performed by solving the corresponding Fokker-Planck equation. The latter includes coherent and incoherent terms, which could be expressed via transfer functions of the elements of cooling system [5]. To figure out the transfer function for Möhl's method let us write the correction signal of a test-particle at the kicker:

$$S_n \propto j[delay_n(T_{PK}) i_n(T'_{PK}) - delay_n(T_{PK} + T_{PP}) i_n(T'_{PK} + T'_{PP})]$$

where $delay_n(t) = \exp(-j\omega_n t)$ – system signal delay of t sec at harmonic n, $i_n(f,t) \propto \exp(j\omega'_n t)$ – test-particle's current at harmonic n, $\omega_n = 2\pi f_0 n$, $\omega'_n = 2\pi f'_0 n$, where

ISBN 978-3-95450-174-8

f_0, f_0' - nominal and particle's own revolution frequencies, T_{PK}, T_{PK}' – pick-up to kicker travelling times for nominal and off-momentum particles, T_{PP}, T_{PP}' – 1st pick-up to 2nd pick-up travelling times for nominal and off-momentum particles.

After mathematical transformations the correctional signal could be expressed as

$$S_n \propto e^{j\omega_n \Delta T_{PK}} \cdot j(1 - e^{-i\omega_n \Delta T_{PP}}),$$

where $\Delta T_{PK} = T_{PK}\eta_{PK}\,\Delta p/p_0$, $\Delta T_{PP} = T_{PP}\eta_{PP}\,\Delta p/p_0$, η_{PK}, η_{PP} – local slip-factors between pick-up and kicker or two pick-ups correspondingly.

The first factor $e^{j\omega_n \Delta T_{PK}}$ represents a regular mixing between the second pick-up (that is closer to the kicker) and the kicker, accordingly the expression

$$M_n = j(1 - e^{-i\omega_n \Delta T_{PP}}) = j\left(1 - Exp[-i\omega_n \frac{s_{PP}}{\beta c}\eta_{pp}\frac{\Delta p}{p}]\right),$$

where s_{PP} – distance between two pickups, could be regarded as the transfer function for Möhl's method. As can be seen for Möhl's method slip-factor η_{PP} between two pick-ups should have a non-zero value. The new parameter – distance between the pick-ups s_{PP} – directly controls the momentum acceptance range of the system. The provided range could vary between two extremities – first, if the pick-ups are very close to each other the Möhl's method would have the same acceptance as Palmer method, and second, if the pick-ups are separated by the whole ring, then the acceptance will be similar to the notch-filter method (Fig. 4). Eventually it would be advantageous for NICA to have both pick-ups possibly closer to each other in order to widen the momentum acceptance range.

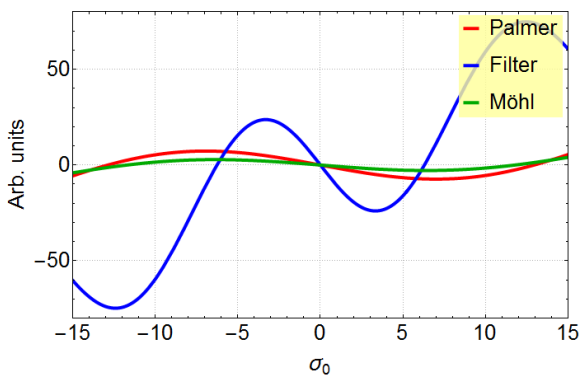

Figure 4: Coherent term of Fokker-Planck equation for Palmer (red), notch-filter (blue) and Möhl (green) methods for NICA at 4.0 GeV/u.

This method has three main advantages: it's dispersion-independent, utilizes strong sum signals from pick-ups and could provide wide momentum acceptance. Möhl's method can also help to reduce the strong coherent signal of bunched beam due to subtraction of longitudinal signals.

To provide best performance the pick-ups should be as identical as possible as well as all electronics before the subtractor.

At the NICA collider the Möhl's method theoretically is capable to cover whole IBS-dominated regime 3-4.5 GeV/u. But this method has not yet been tested experimentally, so additional theoretical and experimental studies are required, dedicated experiments are foreseen at the Nuclotron.

TRANSVERSE COOLING

It's planned to use slot-ring couplers for pick-ups and kickers of the NICA stochastic cooling systems [6]. These devices are capable to work simultaneously with all degrees of freedom, hence it is desirable to find solutions, when same pick-ups and/or kickers are used in several systems. The most beneficial scheme for NICA would be using same pick-up and kicker for transverse systems, this is favorable from the lattice point of view (beta-function and dispersion values), this will also reduce the dissipated power at the electrodes of the kicker, because transverse systems have separated feeding electrodes.

The main restriction for the transverse systems (betatron cooling) is the proper phase advance between the pick-up and the kicker ($\Delta\psi_{PK} = \pi/2 + \pi n$). For this reason the pick-up and the kicker, which are used simultaneously for horizontal and vertical systems, should be located in the ring so that both horizontal and vertical phase advances would have optimum values. To determine optimum pick-up and kicker locations it is convenient to draw the dependence of an optimum phases from its' positions, which is governed by the solutions of the equation $\Delta\psi(s_P, s_K) = \pi/2 + \pi n$, where s_P, s_K – positions of pick-up and kicker (Fig. 5).

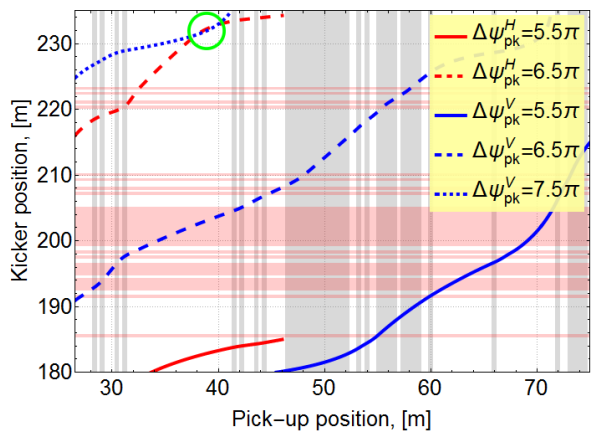

Figure 5: Optimum phase curves for horizontal (red) and vertical (blue) systems, semi-transparent red and grey – lattice elements, distances are counted from IP1.

To have optimum phases for transverse systems with merged pick-up and kicker the corresponding optimum phase curves should intersect. There exists only one region with such intersection (see Fig. 5), which implies

ISBN 978-3-95450-174-8

feasibility of having "merged" pick-up and kicker for transverse systems at the NICA collider.

STOCHASTIC COOLING SYSTEM FOR THE COLLIDER

Finally, each ring of the collider will have three stochastic cooling systems (6 in total), transverse systems will use same pick-ups and kickers (Fig. 6):

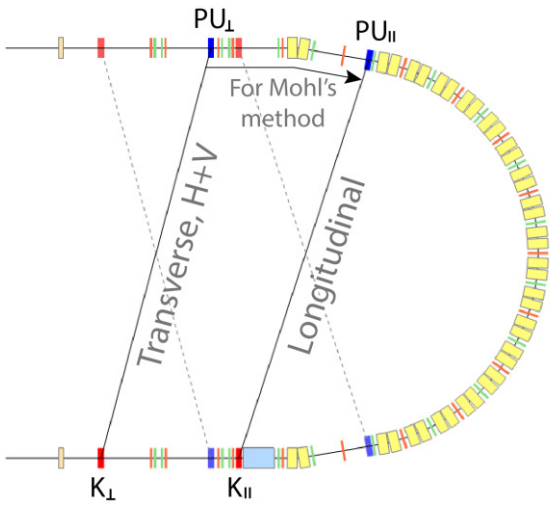

Figure 6: Stochastic cooling systems for NICA collider.

The longitudinal system will have enough spare system delay to install the cable from first pick-up to the second simply along the beam-pipe for Möhl's method (thick arrow at Fig. 6). The pick-ups and the kickers will be the slot-ring couplers of the same type, that will be used at the HESR facility of FAIR [7]. It's strongly desirable for Möhl's method to have the pick-ups as identical as possible, so the length of the pick-ups will be determined by the transverse sensitivity of the devices (in our case 64 rings, ~1 m).

The bandwidth of all systems is 2-4 GHz. The estimated CW power depends on the energy, its maximum is ~ 1 kW, including safety factor 10. The power will be provided by a series of amplitude- and phase-optimized 80 W solid-state amplifiers.

The staging is foreseen for the NICA collider – it will start operation with so-called start-up configuration, which involves significantly reduced intensities, momentum spreads, IBS rates; consequently, the requirements for the cooling times will be much less severe [8]. Such start-up scenario requires only longitudinal cooling and system with a notch-filter would be capable to provide the necessary cooling times. Thus start-up configuration will include only one pick-up and kicker per ring for longitudinal cooling with the notch-filter method. A prototype of such channel was developed and tested at the Nuclotron facility in collaboration with FZJ. Later on during start-up period it is planned to install second pick-up for experimental study of the Möhl's method. Also for start version it's planned to use 200 W TWT power amplifiers, that was kindly loaned to JINR by FNAL from the decommissioned cooling systems of Tevatron, which should significantly reduce the initial commissioning costs.

STOCHASTIC COOLING AT NUCLOTRON

As a preparatory work for the NICA collider dedicated experiments at Nuclotron facility were carried out. The developed Nuclotron stochastic cooling system is longitudinal 2-4 GHz system with optical notch-filter and fiber system delay [9]. During experiments the prototype slot-ring couplers were tested for different operational regimes and powers. In 2014 a new 60W power amplifier was installed. This amplifier was not optimized for phase and group delay, but the performance was sufficient for first tests and significantly improved the performance of the system compared to previous 16W power amplifier (Fig. 7):

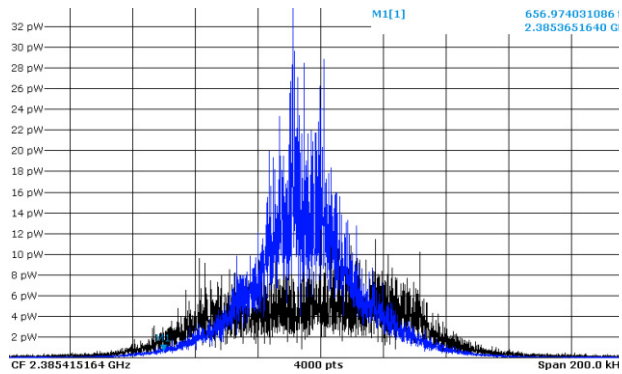

Figure 7: Cooling of 2×10^8 C^{6+} ions within 20s. Screenshot from spectrum analyser taken at 2078th harmonic.

The software for control and adjustment automation of the stochastic cooling systems is also developing. This software could be seamless integrated into NICA control system, based on the TANGO.

A number of automation techniques and algorithms were developed for fast system adjustment, like automatic notch-filter adjustment, automation of open-loop measurements and system delay adjustment, etc. The algorithm for the notch-filter allows fully automatic adjustment of filter's frequency and amplitude within a very short time. The basic idea is to downsample the filter frequency response signal from VNA to get the maximum number of notches within a single sweep, which is then analyzed locally with a simple PC. All developed software is universal and could be seamlessly integrated into NICA or FAIR control systems.

CONCLUSION

Stochastic cooling of 3D intense bunched beams at the NICA collider represents a challenging task, which

ISBN 978-3-95450-174-8

requires deep theoretical and experimental researches. A dedicated experimental stochastic cooling system was developed at the Nuclotron facility in collaboration with Forschungszentrum Jülich. The experiments at Nuclotron proved the developed theoretical approaches and provided the basis for developing a stochastic cooling system of NICA collider – both for hardware and software. The hardware developments include tests of prototype pick-up and kicker, switching and amplification schemes, precise notch-filter and optical system delays. The software developments engage control, diagnostic and different automation techniques for fast system adjustments. The developed software is universal and also is planned to use at the HESR facility of FAIR.

The investigation of possible implementations of the stochastic cooling at NICA revealed the advantage of the different approach for longitudinal cooling, Möhl's method, which was theoretically studied and proposed for the collider.

Based on detailed theoretical research and experience with stochastic cooling at Nuclotron the CDR for the NICA stochastic cooling system had been worked out.

ACKNOWLEDGMENT

Authors are very grateful for invaluable help, advise and support to a large international collaboration: I. Meshkov, H. Stockhorst, L. Thorndahl, F. Caspers, V. Lebedev, S. Nagaitsev, V. Parkhomchuk and R. Maier

REFERENCES

[1] G. Trubnikov et al., "Status of the NICA project at JINR", IPAC'14, Dresden, Germany, June 2014, pp. 1003-1005.

[2] H. Stockhorst et al., "Compensation of mean energy loss due to an internal target by application of a barrier bucket and stochastic momentum cooling at COSY", COOL'09, Lanzhou, China, Aug. 31 – Sept. 4 2009.

[3] D. Mohl, G. Petrucci, L. Thorndahl, and S. van der Meer, Phys. Rept. 58, p. 73, 1980.

[4] D. Möhl, "Stochastic Cooling", Proc. CERN Acc. School 1993, CERN 95-03 (part II), p. 647.

[5] T. Katayama, N. Tokuda, "Fokker-Planck Approach for the Stochastic Momentum Cooling with a notch filter", Part. Accel., Vol. 21. p. 99, 1987.

[6] R. Stassen et al., "Recent developments for the HESR stochastic cooling system", COOL'07, Bad Kreuznach, Germany, p.191, 2007.

[7] R. Stassen et al., "The stochastic cooling system of HESR", COOL'11, Alushta, Ukraine, September 2011, p.191.

[8] G. Trubnikov et al., "NICA cooling program", Cybernetics and physics, Vol. 3, No. 3, p. 137, 2014.

[9] N. Shurkhno et al., "Study for stochastic cooling system at Nuclotron, JINR", COOL'13, Mürren, Switzerland, May 2013, p. 73.

ISBN 978-3-95450-174-8

FOKKER-PLANCK APPROACH TO THE DESCRIPTION OF TRANSVERSE STOCHASTIC COOLING

F. Nolden, GSI, Darmstadt, Germany

Abstract

A Fokker-Planck equation for transverse stochastic cooling is presented, based on some simplifying assumptions. The calculation of the drift and diffusion coefficients is derived from the signal theory of the pick-up response and the dynamics of the kicker response. The equilibrium transverse action (emittance) distribution turns out to be exponential. Furthermore there is a special solution of the time-dependent equation for the case that the initial action distribution is exponential, as well. The distribution remains exponential, and the average action decreases exponentially towards equilibrium. The cooling rate is equal to the standard textbook rate.

THEORETICAL PRELIMINARIES

Fokker-Planck Equation

Let $2J$ be the usual one-particle emittance. J is an action variable in Hamiltonian theory. ϕ is the betatron angle, conjugate to J. The betatron phase advance between pick-up and kicker is denoted $\mu_k - \mu_p$. The beta functions are β_p and β_k.

The Fokker-Planck equation describes the evolution of the distribution function $\Psi(J_x, J_y, \delta p/p)$. It is a continuity equation with a flux Φ in action space

$$\frac{\partial \Psi}{\partial t} + \mathrm{div}\Phi = 0 \tag{1}$$

The flux is

$$\Phi = F\Psi - \frac{1}{2} D \ \mathrm{grad}\Psi \tag{2}$$

The drift coefficient F describes the average cooling. It generally has three components, e.g.

$$F_x = \lim_{\tau \to 0} \left\langle \frac{\delta J_x}{\tau} \right\rangle \tag{3}$$

The limit $\tau \to 0$ always leads to physical interpretation problems, as a rule of thumb one might say that no essential change of the distribution function should happen during τ. The diffusion tensor D describes the diffusion, its components are

$$D_{mn} = \lim_{\tau \to 0} \left\langle \frac{\delta J_m \delta J_n}{\tau} \right\rangle \tag{4}$$

The Fokker-Planck equation is frequently used for the calculation of the longitudinal momentum distribution (see [1] and references therein). In this work the transverse case is presented. All details of the calculations of the drift and diffusion coefficients are not given, they can be derived along the lines presented in [1].

Simplifying Assumptions

In the following we make the assumption that longitudinal cooling works independently of transverse cooling, and that the longitudinal momentum distribution is given somehow. Then the transverse cooling is decoupled and both cooling pcrocesses can be described by one-dimensional Fokker-Planck equations.

1. All kickers and pick-ups are placed at locations of zero dispersion.
2. All electrodes can be described by a simple linear response model.
3. There is no overlap between different Schottky bands.
4. Chromaticity is neglected.

Because of the decoupling between phase spaces, we derive here a separate Fokker-Planck equation for horizontal cooling, where the horizontal distribution is simply called $\Psi(J)$. We normalize it to 1. We also need the longitunal distribution $\psi(\delta p/p$ which we define to be normalized to the number of particles N.

SIGNALS AND BEAM RESPONSE

Sensitivity and Single Particle Signals

The sensitivity $S(\Omega)$ is used for the description of the quality of delivering accelerating voltages to a beam paricle in a kicker electrode.

It is the ratio between the effective accelerating voltage $U(\Omega)$ and the voltage $V_k(\Omega)$ at the input port of the kicker:

$$U(x, y, \Omega) = S(x, y, \Omega) V_k(\Omega) \tag{5}$$

S depends on the beam velocity and on the position of the particle with respect to the electrode.

In the following it will be assumed that S is linear in x over the full range of betatron amplitudes.

$$S(x, y, \Omega) = xS'(\Omega) \tag{6}$$

The formalism becomes much more complicated if this simplification is abandoned [2].

If such an electrode is used as a pick-up electrode and if it is reciprocal, a particle with revolution frequency ω produces a signal at the betatron sidebands

$$\omega_{m,\pm} = \omega(m \pm Q_x) \tag{7}$$

where ω is the revolution frequency (which depends on the longitudinal momentum via the well-known relationship

ISBN 978-3-95450-174-8

$\delta\omega/\omega = \eta\delta p/p$), and Q_x is number of horizontal betatron oscillations per turn. The signal is

$$U_p(\Omega) = \frac{QeZ_l\sqrt{2J_x\beta_x}S'_p(\Omega)}{4}\sum_{m=-\infty}^{+\infty}\exp(i\Omega t_0) \quad (8)$$
$$\times \left[e^{i\mu_x}\delta(\Omega-\omega_{m,+}) - e^{-i\mu_x}\delta(\Omega-\omega_{m,-})\right]$$

where Z_l is the line impedance at the output port.

The horizontal deflection after one pass through the kicker follows from the Panofsky-Wenzel theorem

$$\delta p_x = \frac{Qe}{i\Omega}S'_k(\Omega)V_k(\Omega) \quad (9)$$

p is the particle momentum. For a single kick, the emittance changes by

$$\delta J_x = \frac{Qe}{i\Omega p}S'(\Omega)V_k(\Omega)\sqrt{2J_x\beta_x}\sin\mu_x \quad (10)$$

Voltage Power Density

The spectral voltage density $C(\Omega)$ is the Fourier transform of the voltage autocorrelation function $R(\tau) =< V(t)V(t+\tau) >$. The brackets <> denote the expectation value. For coasting beams the autocorrelation R is independent of t, because V is a 'stationary process'.

With the mean emittance

$$< J >= \frac{\int_0^\infty J\Psi\, dJ}{\int_0^\infty \Psi\, dJ} \quad (11)$$

the Schottky density at each pick up at the transverse harmonics is

$$C_p(\Omega_\perp) = \frac{(QeZ_l)^2\,\omega\beta_p}{16\pi\,|m\eta|}\left|S'_p\right|^2 < J > \psi(\delta p/p) \quad (12)$$

It is proportional to the mean emittance and to the momentum density.

Another statistical signal is due to thermal noise. It is often expressed by an effective temperature:

$$C_n = \frac{1}{2}Z_l k_B T_{\text{eff}} \quad (13)$$

Signal Combination and Amplification

The amplification chain (Fig, 1) consists of the signal combination networks at the pick-ups and kickers and an overall voltage gain.

We assume n_p pick-ups, connected such that they are matched to the beam velocity. The voltage gain after power combination is

$$g_p = \sqrt{n_p} \quad (14)$$

The electronic voltage gain is modeled as

$$G = G_0\exp i\Omega T_{pk} \quad (15)$$

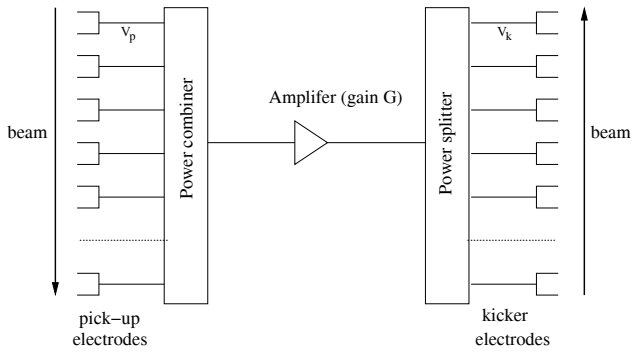

Figure 1: Model of amplification chain.

where G_0 is constant inside the cooling band. T_{pk} is adjusted to the time of flight between pick-up and kicker for design particle. For off-momentum particles

$$\frac{\delta T_{pk}}{T_{pk}} = -\eta_{pk}\frac{\delta p}{p} \quad (16)$$

Here, $\eta_{pk} = \gamma^{-2} - \alpha_{pk}$ must be calculated as a local value from the local momentum compaction between pick-up (at s_p and kicker (at s_k):

$$\alpha_{pk} = \frac{1}{s_k - s_p}\int_{s_p}^{s_k} ds\frac{D(s)}{\rho(s)} \quad (17)$$

where D is the dispersion function and ρ is the radius of the closed orbit.

Then the effective overall accelerating voltage is

$$U_k = xS'_k\, g_k\, G\, g_p\, V_p \quad (18)$$

The effective overall accelerating voltage density becomes

$$C_k = \left|xS'_k\right|^2|g_k|^2|G|^2\left[\left|g_p\right|^2 C_p + C_n\right] \quad (19)$$

TRANSVERSE COOLING

Equations for Transverse Cooling

In the following we use a notation

$$\sum_{m,\pm} = \sum_{m=-\infty}^{+\infty}\sum_{\pm} \quad (20)$$

as we always sum over both sidebands at all harmonics.

The transverse drift then is

$$F_\perp = -\frac{J(Qe\omega)^2 Z_l}{16\pi^2 p}\sqrt{\beta_p\beta_k} \quad (21)$$
$$\times \sum_{m,\pm}\frac{\pm 1}{\Omega}S'_k g_k\, G\, g_p\, S'_p$$
$$\times \exp\left[\pm i\left(\mu_k - \mu_p\right) - i\eta_{pk}\left(m \pm Q\right)\omega T_{pk}\delta p/p\right]$$

In order to get a cooling effect, the amplification G must be imaginary, i.e. there must be a 90^0 phase shift in the

ISBN 978-3-95450-174-8

amplification chain. Also, as is well known, the betatron phase shift $\mu_k - \mu_p$ must be an odd integer multiple of $\pi/2$. We define the dimensionless system gain

$$g_\perp = \frac{(Qe)^2\,\omega Z_l}{8\pi p\,\Omega}\sqrt{\beta_p\beta_k}\;S'_k\;g_k\;G\;g_p\;S'_p \qquad (22)$$

Note that it is independent of J, but depends on frequency. The definition Eq. (22) differs from the usual textbook definition [1] by a missing factor N as we shall discuss later.

With Eq. (22) the transverse drift becomes

$$\begin{aligned} F_\perp &= \frac{J\omega}{2\pi}\sum_{m,\pm}\pm g_\perp \exp\left[\pm i\left(\mu_k-\mu_p\right)\right. \qquad (23)\\ &\times \left. -i\eta_{pk}\,(m\pm Q)\,\omega T_{pk}\delta p/p\right] \end{aligned}$$

We split the transverse diffusion into two terms: one is due to Schottky noise, the second is caused by thermal noise:

$$D_\perp = D_S + D_H \qquad (24)$$

With Eq. (12) and Eq. (19) we get for the Schottky term

$$D_S = J\,<J>\,\psi(\delta p/p)\frac{\omega}{2\pi}\sum_{m,\pm}\frac{|g_\perp|^2}{|m\eta|} \qquad (25)$$

In order get diffusion due to thermal noise, one has to replace the term $\left|g_p\right|^2 C_p$ by C_n.

$$D_n = J\frac{4k_BT_{\rm eff}}{(Qe)^2\,Z_l\beta_p\left|g_p\right|^2}\sum_{m,\pm}\left|\frac{g_\perp}{S'_p}\right|^2 \qquad (26)$$

Altogether the drift and diffusion coefficients can be written in the form

$$\begin{aligned} F_\perp &= -CJ \qquad (27)\\ D_\perp &= J\,(S\,<J>\,+H) \qquad (28) \end{aligned}$$

where the cooling term C, the Schottky diffusion term S and the thermal noise heating term H do not depend on J.

It is worth noting that both coefficients Eq. (27) and Eq. (28) are proportional to J. Therefore, the flux Φ (see Eq. (2)) vanishes at zero emittance. This satisfies the physical boundary condition that there can be no flux toward negative emittances (see Fig. 2).

Transverse Equilibrium Emittance

The condition for equilibrium is

$$-F_\perp\Psi_\infty(J) + \frac{1}{2}D_\perp\frac{\partial\Psi_\infty}{\partial J} = 0 \qquad (29)$$

With the coefficients Eq. (27) and Eq. (28) we get

$$\frac{\partial}{\partial J}\left(\ln\Psi_\infty(J)\right) = \frac{\partial\Psi_\infty/\partial J}{\Psi_\infty} = \frac{2F_\perp}{D_\perp} = \frac{-2C}{S\,<J>\,+H} \qquad (30)$$

This equation is solved by

$$\Psi_\infty(J) = \Psi_0\,\exp\left(-\frac{2C}{S\,<J>_\infty+H}\;J\right) \qquad (31)$$

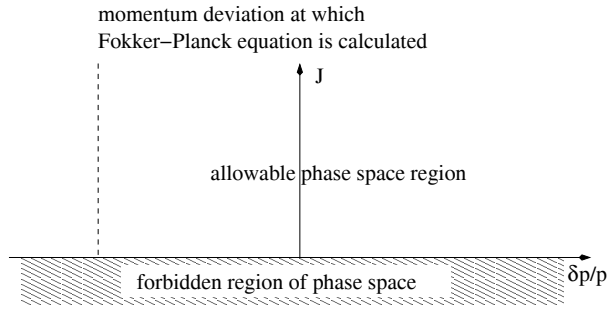

Figure 2: Notation for momentum distribution.

i.e. it is an exponential distribution with average emittance

$$<J>_\infty = \frac{\int_0^\infty J\Psi_\infty\,dJ}{\int_0^\infty \Psi_\infty\,dJ} = \frac{S\,<J>_\infty+H}{2C} \qquad (32)$$

Ψ_0 is a normalizing constant. Solving Eq. (32) for $<J>_\infty$ yields

$$<J>_\infty = \frac{H}{2C-S} \qquad (33)$$

The minimum equilibrium emittance is limited by the heating due to thermal noise (if no other heating mechanisms such as intra-beam scattering are taken into acoount). To maintain a normalized solution the condition $2C > S$ is required. Under this condition Eq. (31) is equivalent to

$$\Psi_\infty(J) = \Psi_0\,\exp\left(-\frac{2C-S}{H}\;J\right) \qquad (34)$$

with the normalization $\Psi_0 = <J>_\infty$.

Time Dependent Exponential Solution

As the equilibrium transverse distribution is exponential in case of the drift and diffusion coefficients Eq. (27) and Eq. (28), it is reasonable to investigate the following problem: if the initial distribution is exponential, will it remain to be so forever? Hence we try the ansatz

$$\Psi(J,t) = \alpha(t)Ne^{-\alpha(t)J} \qquad (35)$$

with the mean emittance

$$<J> = \frac{1}{\alpha} \qquad (36)$$

The partial derivatives of the distribution function are

$$\begin{aligned} \frac{\partial\Psi}{\partial t} &= \dot\alpha\left(\frac{1}{\alpha}-J\right)\Psi \qquad (37)\\ \frac{\partial\Psi}{\partial J} &= -\alpha\Psi \qquad (38) \end{aligned}$$

The Fokker-Planck flux becomes

$$\Phi = F_\perp\Psi - \frac{1}{2}D_\perp\frac{\partial\Psi}{\partial J} = \left(-C+\frac{S+\alpha H}{2}\right)J\Psi \qquad (39)$$

Because of

$$\frac{\partial}{\partial J}J\Psi = \alpha\left(\frac{1}{\alpha}-J\right)\Psi \qquad (40)$$

ISBN 978-3-95450-174-8

the Fokker-Planck equation $\partial\Psi/\partial t + \partial\Phi/\partial J = 0$ is equivalent to the ordinary differential equation

$$\frac{\dot{\alpha}}{\alpha} + \left(-C + \frac{S + \alpha H}{2}\right) = 0 \tag{41}$$

confirming that Eq. (35) solves the Fokker-Planck equation indeed. In terms of $< J >$ (see Eq. (36)) we get the equivalent equation

$$\frac{d}{dt} < J > + \left(C - \frac{S}{2}\right) < J > - \frac{H}{2} = 0 \tag{42}$$

Because the time derivative in the Fokker-Planck equation is applied only to Ψ, but not to Φ, Eq. (41) remains valid even if the coefficients C, S, and H are *explicitly time-dependent*, as they are if

- the system amplification $g_\perp$ is changed during the cooling process,
- the transverse sensitivities $\partial S/\partial x$ are changed by moving (plunging) the electrodes,
- simultaneous longitudinal cooling is applied, changing the distribution $\psi(\delta p/p)$ (see Eq. (25)).

Equation (42) can be solved analytically with the solution (holding only for constant coefficients)

$$< J > (t) = (J_0 - J_\infty)\, e^{-t/\tau} + J_\infty \tag{43}$$

with the exponential decay time (*not* the instantaneous cooling time)

$$\frac{1}{\tau} = C - \frac{S}{2} \tag{44}$$

and the equilibrium emittance $J_\infty = H/(2C - S)$ which is already known from Eq. (33). Note, however, that Eq. (31) is more general, because the equilibrium distribution always becomes exponential regardless of the initial distribution.

The instantaneous cooling rate is given by the quantity $\dot{\alpha}/\alpha$ of Eq. (41), i.e.

$$\frac{1}{\tau_\perp} = C - \frac{1}{2}S - \frac{H}{2 < J >} \tag{45}$$

This relationship is the base of the following estimates.

COOLING RATE ESTIMATES

General Expression

From Eq. (23), Eq. (25) and Eq. (26) we get

$$\begin{aligned} C &= \frac{\omega}{2\pi} \sum_{m,\pm} \pm g_\perp \exp\left[\pm i \left(\mu_k - \mu_p\right)\right] \\ &\times \exp\left[-i\eta_{pk}\,(m \pm Q)\,\omega T_{pk}\delta p/p\right] \end{aligned} \tag{46}$$

$$\frac{1}{2}S = \frac{\omega\psi(\delta p/p)}{4\pi} \sum_{m,\pm} \frac{|g_\perp|^2}{|m\eta|} \tag{47}$$

$$\frac{H}{2 < J >} = \frac{1}{< J >} \frac{2k_B T_{\text{eff}}}{(Qe)^2\, Z_l \beta_p \left|g_p\right|^2} \sum_{m,\pm} \left|\frac{g_\perp}{S'_p}\right|^2 \tag{48}$$

The first term in this expression is due to the cooling effect in the presence of undesired mixing. The second term is due to Schottky noise heating including the effect of good mixing. The last term is due to thermal noise heating. Equation (46) is still rather general as the amplification term $g_\perp$ is treated as frequency dependent.

Approximations

In order to get a rough estimate of the expected cooling rate, we make the following assumptions:

1. The system gain $g_\perp$ is constant over the system bandwidth W and zero outside. Denote by m_1 and m_2 the harmonic numbers at the lower and upper limits of the cooling band W. The harmonic number at midband is denoted by $m_c = (m_1 + m_2)/2$, the number of harmonics inside the cooling band is $\Delta m = m_2 - m_1$.
2. The betatron phase advance between pick-up and kicker is exactly 90^0.
3. The real part of $g_\perp$ vanishes.
4. The momentum distribution can be approximately written $\psi = N/(\Delta p/p)$. The quantity $\delta p/p$ denotes the momentum deviation where the transverse rate equations are calculated (Fig. 2), whereas $\Delta p/p$ is the total width of the momentum distribution. This quantity is only needed in the Schottky heating term of the rate Eq. (46). It will reappear in the mixing number Eq. (53).

Undesired Mixing

In order to treat the effect of undesired mixing we introduce the angle $\phi_u = \omega T_{pk}\eta_{pk}\delta p/p$ such that the sum in the cooling term of Eq. (46) becomes

$$\begin{aligned} &\sum_{m,\pm} \pm \exp\left[\pm i\frac{\pi}{2} - im\phi_u\right] \\ &= 4i\text{Re}\left(\frac{e^{im_2\phi_u} - e^{im_1\phi_u}}{e^{i\phi_u} - 1}\right) \\ &= 4i\frac{\cos\left[\left(m_c - \frac{1}{2}\right)\phi_u\right]\sin\left[\Delta m\frac{\phi_u}{2}\right]}{\sin\left[\frac{\phi_u}{2}\right]} \\ &\approx 4i\Delta m\cos\left[m_c\phi_u\right] \end{aligned} \tag{49}$$

We have used the approximation $m \pm Q \approx m$. The last approximation is valid if the undesired mixing is tolerable, i.e. if $\phi_u \ll \pi/(m_2 + m_1)$. To be rigourous we define the undesired mixing number

$$B := \cos\left[m_c\phi_u\right] B_1 \tag{50}$$

where the correction

$$B_1 = \frac{\sin\left[\Delta m\frac{\phi_u}{2}\right]}{\Delta m \sin\left[\frac{\phi_u}{2}\right]} \tag{51}$$

is of the order of unity.

ISBN 978-3-95450-174-8

Optimum Gain and Cooling Rate Estimate

The sum in the Schottky heating expression can be approximately written

$$\sum_{m=m_1}^{m_2} \frac{1}{m} \approx \ln\left(m_2/m_1\right) \tag{52}$$

This gives rise to the mixing number

$$M = \frac{1}{|\eta|\Delta p/p} \frac{\ln\left(m_2/m_1\right)}{m_2 - m_1} \approx \frac{1}{m_c|\eta|\Delta p/p} \tag{53}$$

One gets the last approximation (F. Pedersen, D. McGinnis, priv. comm.) by linearizing the logarithm according to $\ln m_{12} \approx \ln m_c \pm (m_2 - m_1)/2m_c$.

The noise heating term is

$$h = \frac{8k_B T_{\text{eff}}}{Z_l\,(Qe)^2\,\omega\left|g_p\right|^2 \beta_p \left|S_p'\right|^2 < J >} \tag{54}$$

Then we can write instead of Eq. (46)

$$\frac{1}{\tau_\perp} \approx 2W\left[2B\,|g_\perp| - (MN + h)\,|g_\perp|^2\right] \tag{55}$$

Equation (55) looks much like the standard textbook cooling rate, except for the particle number N, which does not appear in front, but only in the desired mixing term M. This is due to a different definition of system gain Eq. (22), which should reasonably not depend on N, because neither the coherent cooling (see Eq. (23)) nor the thermal diffusion (see Eq. (26)) depend physically on the particle number.

The optimum system gain is

$$|g_\perp|_{\text{opt}} = \frac{B}{MN + h} \tag{56}$$

and the optimum cooling rate is

$$\left(\frac{1}{\tau_\perp}\right)_{\text{opt}} = \frac{2WB^2}{MN + h} \tag{57}$$

The quantities C, H and S from Eq. (27) and Eq. (28) are related to B, M and U via the relationships

$$C = 4Wg_\perp B \tag{58}$$

$$\frac{S}{2} = 2W\,|g_\perp|^2\,MN \tag{59}$$

$$\frac{H}{2 < J >} = 2W\,|g_\perp|^2\,h \tag{60}$$

Remarks

- The noise to signal ratio h/N is the noise power at the effective temperature T_{eff} divided by the Schottky power of a beam of N particles with average emittance $< J >$ at one betatron sideband. If the emittance decreases during the cooling process, h can be inhibited from increasing too fast by using plunging electrodes. They have the effect of increasing the electrode responses S_p' and S_k'.
- One should note the $1/\Omega$ dependence in the system gain Eq. (22). If the sensitivity slope S' is constant over the bandwidth, then one has to increase the electronic amplification G by 6 dB per octave in order to get a constant system gain. This is a consequence of the $1/\Omega$-scaling of the transverse kicks strength due to the Panofsky-Wenzel theorem Eq. (9).

CONCLUSIONS

1. We have given explicit expressions for the drift and diffusion coefficients of transverse stochastic cooling.
2. We have expressed the system gain in terms of electronic parameters.
3. We have proved from very general assumptions that the equilibrium emittance distribution is exponential.
4. We have proved that an initial exponential emittance distribution remains exponential during the cooling process.
5. We have presented a general, frequency-dependent cooling rate equation.
6. We have shown that in the case of constant system gain over a given bandwidth, we can reproduce the results of standard stochastic cooling theory.
7. In this case, we have given explicit expressions for the mixing number M and the noise heating term h.

REFERENCES

[1] D. Möhl, Stochastic Cooling of Particle Beams, Lecture Notes in Physics 866, Springer 2013

[2] F. Nolden, J.X. Wu, presented at COOL'15, Newport News, VA, USA, paper MOPF09, *these proceedings*.

ISBN 978-3-95450-174-8

DESIGN OF THE PALMER PICKUP FOR STOCHASTIC PRE-COOLING OF HOT RARE ISOTOPES AT THE CR

D. J. Barker, C. Dimopoulou and C. Peschke, GSI, Darmstadt, Germany.
L. Thorndahl, CERN, Geneva, Switzerland.

Abstract

We report on the design of a Faltin type pickup for the stochastic pre-cooling of rare isotope beams at 740 MeV/u, using a bandwidth of 1-2 GHz, for the Collector Ring (CR) in the FAIR project at GSI. The design difficulties inherent in Faltin rails at these frequencies are described. Measurements of prototypes and HFSS simulations are compared, to check the simulations, and show good agreement. The pickup impedance and signal output phase with respect to ions traveling at 0.83c are simulated and presented for the final design both with and without the use of damping material, showing the need to damp unwanted modes present in the beam chamber.

INTRODUCTION

The CR is designed for 6D stochastic cooling of antiprotons at 3 GeV or rare isotopes beams (RIBs) at 740 MeV/u [1]. The CR stochastic cooling system will operate in a frequency band of 1-2 GHz. For the noise-limited antiproton cooling, slotline pickups and kickers are foreseen [2]. RIB cooling in the CR is limited by the undesired mixing for which the Schottky bands overlap, so that only the Palmer method [3] can initially be applied. After the momentum spread is decreased so as to fit into the acceptance of the notch filter, cooling will proceed with the slotline pickups down to the final beam quality. The RIBs must be cooled from ε_{xy} = 35 mm – mrad and δp/p = 0.2% to ε_{xy} = 0.125 mm – mrad and δp/p = 0.025% (all values are 1 σ values) within 1.5 s.

6D Cooling at the Palmer Pickup

The Palmer pickup is placed at a point of high dispersion in the ring so as to fulfill momentum cooling as envisioned by R. Palmer in 1975, private communication. The signals at the pickup are combined so as to extract vertical error signals and combined horizontal and longitudinal error signals as shown in Fig. 1. Figure 1 also shows an added time of flight (TOF) option for longitudinal cooling.

The Palmer pickup tank will be equipped with Faltin type pickups which are favorable due to their low number of feedthroughs, robustness and ease of manufacture.

Faltin Electrode

The Faltin electrode [4] is a rectangular coaxial waveguide with slots which couple to the beam. Figure 2 shows a diagram of a section of the Palmer pickup tank containing four Faltin rails intended for horizontal and vertical difference measurements. Figure 2 also shows the horizontal and vertical beam apertures of 400mm and 132mm respectively,

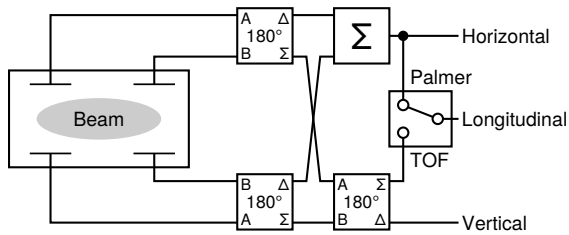

Figure 1: Diagram of the Palmer cooling method (including an optional TOF method) as foreseen in the CR showing the combination of signals in sum and difference modes.

and the position ferrite absorbing material needed to damp unwanted modes in the beam chamber.

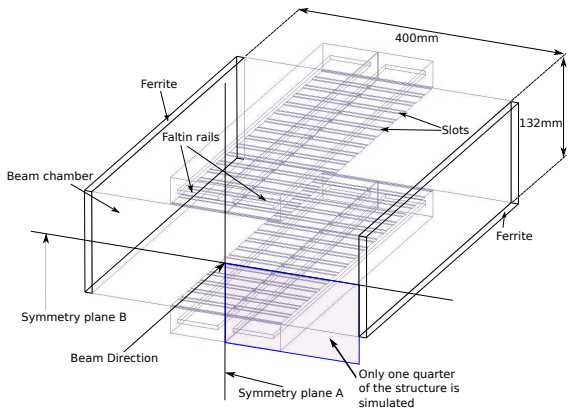

Figure 2: Diagram of a section of length of the Palmer pickup showing Faltin rails, beam chamber, ferrite absorbing material and symmetry planes used during simulations.

The wave in the pickup induced by the beam travels parallel to the beam and at the same velocity such that induction from beam to waveguide through each slot adds constructively. Therefore, in a Faltin type pickup (or any traveling wave pickup), it is crucial that the phase velocity in the waveguide approximately equals the particle velocity across the desired frequency band of operation.

Previous work on these type of pickups has included analytical approaches to calculating the coupling and the characteristics of induced waves [5, 6]. Experimental results were later published for a slot to TEM type pickup [7]. In addition, simulations using HFSS have been performed on similar structures for use in the SPS at CERN [8].

Pickups for stochastic cooling require an output signal with a large but flat amplitude over the band, and a linear phase with respect to the particle. The larger the amplitude

ISBN 978-3-95450-174-8

of a pickup output signal the faster the cooling can be. The more linear the pickup output signal is with respect to the particle the easier it is to correct allowing a kick to the particle to be made with the correct phase, again leading to faster cooling. In order to design and optimize pickups, a coupling impedance can be defined, which is proportional to output signal amplitude and can be defined as

$$Z_{pu} = \frac{P_{pu}}{I_b^2} \tag{1}$$

where P_{pu} is the power from the pickup and I_b is the current in the beam. The amplitude and phase of the relevant signal is contained within P_{pu}. Both the coupling of the waveguide to the beam (through the slots), and the phase velocity of the wave in the waveguide as a function of frequency determine the output signal amplitude. Therefore Z_{pu} and phase are the primary parameters to be optimized.

In general, the Faltin rail suffers from the fact that as Z_{pu} is increased the phase of the associated signal becomes more non linear with respect to the particle. In our case, we are limited by electrical length between pickup and kicker, meaning there is limited space allowed for phase correctors. Therefore we limited ourselves to a maximum non linear phase deviation of approximately 40° at the pickup output. Within this limit, our task was then to maximize Z_{pu}.

An advantageous modification was to split each rail into two sections and combine the signals outside the vacuum, such that approximately the same Z_{pu} would be attained but with half the non linear phase deviation. Although this modification would increase the number of vacuum feedthroughs from 8 to 16, it is necessary to gain acceptable values of Z_{pu} and phase.

The large size of the aperture in the Palmer tank (see Fig. 2) supports strong TM modes within 1-2 GHz which interfere with the horizontal and vertical difference signals and must be damped. To damp these unwanted modes, lossy ferrite TT2-111 from Trans-Tech will be used. Ferrite is placed far from the rails (see Fig. 2) so as not to damp wanted signals.

PICKUP SIMULATION METHOD

The pickup is designed as a kicker (which is possible due to reciprocity between kicker and pickup) using High Frequency Structural Simulator, HFSS [9]. A power of 1 W is input into the waveguide and the accelerating voltage is found by integrating the electric field along a particle trajectory above the slots. The input power and voltage then yield the kicker impedance, Z_k, which is then converted to Z_{pu}. Only one quarter of the pickup is simulated as indicated in Fig. 2. Although the pickup is a horizontal and vertical difference pickup, when simulating as a kicker it is necessary to determine the longitudinal kick. Choosing planes A and B (see Fig. 2) as electric and magnetic field symmetry planes respectively, forces a particle on symmetry plane B to feel a longitudinal kick, and also corresponds to a pickup in horizontal difference mode.

While simulating as a kicker, to extract phase one measures the phase of the integrated accelerating electric field, experienced by a particle, with respect to a plane wave traveling at the velocity of the particle. To find the nonlinear components of the phase data with respect to the particle a straight line is fitted between 1 and 2 GHz only, and then subtracted.

RESULTS

Figure 3 shows pickup impedance and phase with respect to the particle per unit length for two different Faltin rail structures. The relevant dimensions of the structures are detailed in Table 1.

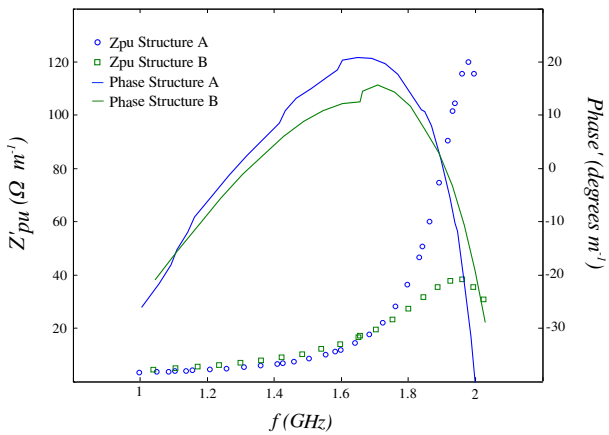

Figure 3: Pickup impedance and nonlinear phase deviation per unit length for two different designs of Faltin rails, structures A and B.

Table 1: Faltin Rail Dimensions for Structures A and B

Structure	A	B
Slot length	30.1 mm	10 mm
Slot width	65.7 mm	50 mm
Cell length	43.9 mm	15 mm
Inner Conductor width	59.7 mm	36 mm
Inner Conductor thickness	5 mm	5 mm
Outer Conductor width	65.7 mm	60 mm
Outer Conductor height	34 mm	35 mm

The maximum pickup impedance per unit length, shown in Fig. 3, is $Z'_{\mathrm{pu}} = 120\,\Omega/\mathrm{m}$ and $Z'_{\mathrm{pu}} = 40\,\Omega/\mathrm{m}$ for structures A and B respectively, which both occur at approximately 1.97 GHz. If these structures were used to fill the available tank space (1.47m), structures A and B would result in total pickup impedances of $Z_{\mathrm{pu}} = 177\ \Omega$ and $Z_{\mathrm{pu}} = 59\ \Omega$ respectively.

Between the frequencies of 1.64 GHz and 1.99 GHz, Fig. 3 shows a maximum nonlinear phase deviation of $63.4°/\mathrm{m}$ and $32.6°/\mathrm{m}$ for structures A and B respectively. If these structures were used to fill the available tank space, the total

ISBN 978-3-95450-174-8

non linear phase deviation would be 93.45° and 48.05° for structures A and B respectively.

Figure 3 therefore shows that structure A has a larger pickup impedance but a worse phase, while structure B has smaller pickup impedance but better phase. The reasons for this can be seen in the structures dimensions shown in Table 1 which shows that structure A has a much larger slot size relative to structure B which increases the coupling to the beam, increasing the pickup impedance. The larger slot size also has the effect of decreasing the phase velocity in the waveguide. To compensate this, the size of the inner conductor of structure A was increased resulting in a small gap between inner and outer conductor of approximately 3mm. This small gap alters the TEM mode of the waveguide more towards a quasi-TEM mode, which results in a rapidly varying phase when operating near cutoff.

In order to test initial designs and the accuracy of HFSS, prototypes of the pickup were made and tested. Figure 4 shows a photograph of one such prototype.

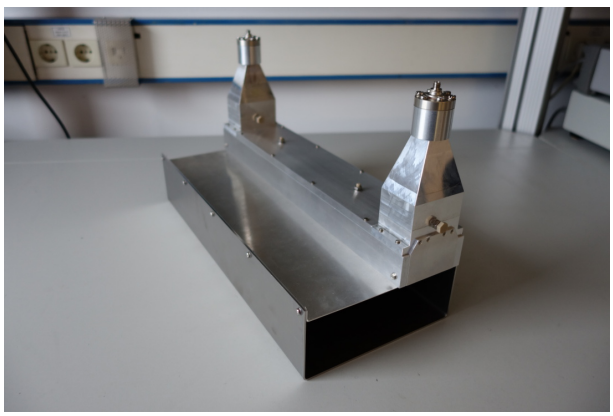

Figure 4: Photograph of a prototype made to test the design and the accuracy of HFSS. The prototype is only one quarter of the full pickup.

Figure 5 compares measurements of transmission coefficient made using a network analyzer on the prototype shown in Fig. 4 and lossless simulations made using HFSS. Figure 5 shows that there is general agreement between HFSS and measurements of the prototype apart from a difference in magnitude which is due to the fact that the simulation was lossless. Figure 5 also shows a divergence in agreement between the two traces at higher frequencies which can be attributed to small physical differences (bad connectors for instance) between the prototypes and the HFSS model which have larger effects at smaller wavelengths.

Due to the fact that we are limited by electrical length (which is a physical limit) rather than cooling time (which is a requirement), the structure with the smallest nonlinear phase deviation, structure B, was chosen. Allowing additional length for impedance matching pieces, a maximum number of 98 slots of structure B can be fit in to the available tank space. Therefore the final design of the Palmer pickup tank consists of two Faltin rails (in each quadrant) comprising

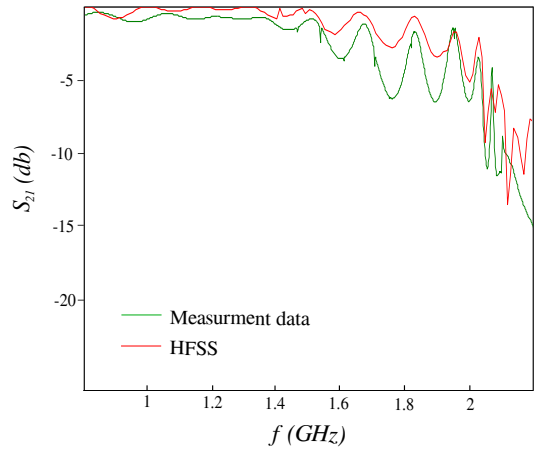

Figure 5: Comparision of transmission coefficient, S_{21}, from prototype measurments and HFSS simulations.

49 slots each, of dimensions of structure B, whose pickup signals will be combined.

Figure 6 shows the total combined pickup impedance and phase, from simulations, for the final design both with and without the presence of lossy ferrite.

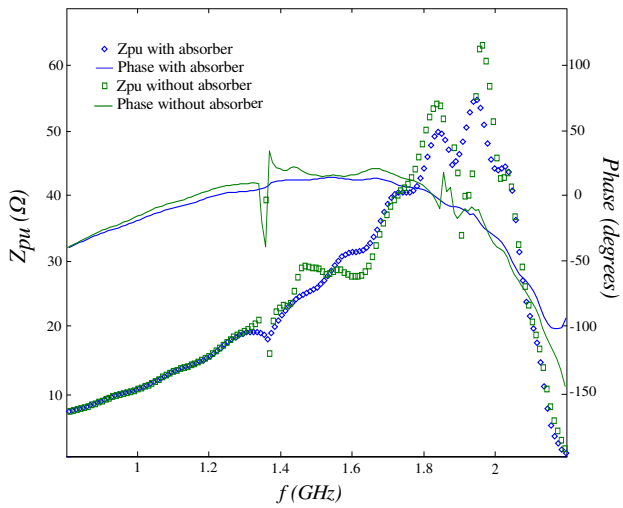

Figure 6: Pickup impedance and nonlinear phase deviation for Faltin rail structure B consisting of two rails of 49 slots each whose signals have been combined. The performance both with and without the presence of ferrite damping material is shown. Simulations are done with a beam centred vertically and with horizontal offset of 40 mm.

When lossy ferrite is added Fig. 6 shows maximum and minimum pickup impedances of Z_{pu} = 54 Ω at 1.94 GHz and Z_{pu} = 10.24 Ω at 1 GHz respectively. Figure 6 also shows that when lossy ferrite is used to damp unwanted modes the pickup produces a maximum nonlinear phase deviation of 44.2° between 1.57 GHz and 2 GHz.

Figure 6 shows that the Z_{pu} with and without a ferrite absorber are comparable. However, the case without the

ISBN 978-3-95450-174-8

ferrite shows increased interference with unwanted modes at 1.38 GHz and 1.9 GHz which can also be seen in the phase data. The nonlinear phase component shown in Fig. 6 without the ferrite shows rapidly changing values at 1.38 GHz and 1.9 GHz which is undesirable for the stochastic cooling system. In addition the ferrite also damps other unwanted modes not included in the simulation results shown in Fig. 6 such as in the vertical difference mode case or travelling waves from adjacent tanks.

The output signal phase of the pickup would benefit by further splitting the rail into rails of less slots and adding the signals. However, this would require more feedthroughs, extra design, and is not necessary.

CONCLUSION

The problem of increasing nonlinear phase deviation with respect to particle when increasing the pickup impedance of Faltin rails has been shown. Transmission coefficient measurements of prototypes were shown to give good agreement to HFSS simulations indicating the simulation results to be reliable. Due to limitations of nonlinear phase deviation of output signals, pickup impedance was sacrificed, and an acceptable final design was chosen consisting of two separate rails whose signals will be combined outside the tank. The simulation results for the final design were shown with and without the presence of damping material indicating interference between wanted and unwanted modes in the beam chamber. The design including ferrite comprises an acceptable nonlinear phase deviation and pickup impedance for the stochastic pre-cooling of heavy ions in the CR. The design stage of the pickup is finished and is now entering the fabrication and testing stage.

REFERENCES

[1] C. Dimopoulou et al., COOL'15, Newport News, MOYAUD04 (2015)

[2] C. Peschke et al., COOL'09, Lanzhou, THPMCP003 (2009)

[3] H. G. Hereward, in Proc. Course of Internatinal School of Particle Accelerators, Geneva, CERN/77-13, p.281 (1977)

[4] L. Faltin, Nucl. Instr. and Meth. **148**, pp. 449-455, (1977)

[5] H. H. Lai, IEEE Trans. Nucl. Sci. **3**, NS-28, (1981)

[6] F. E. Mills, "Faltin Pick-up and Kicker System", FNAL T24, (1981)

[7] J. D. Simpson, S. L. Kramer, D. Suddeth, and R. Konecny, IEEE Trans. Nucl. Sci. NS-30, 4, (1983)

[8] J. Cesaratto et al., IPAC14, Dresden, TUPRI087 (2014)

[9] HFSS, http://www.ansys.com, 2013

ISBN 978-3-95450-174-8

LEPTA - THE FACILITY FOR FUNDAMENTAL AND APPLIED RESEARCH

E. Ahmanova, P.Horodek, I. Meshkov, O. Orlov, A.A. Sidorin, JINR, Dubna, Russia
A. Kobets# JINR, Dubna and Institute of Electrophysics
and Radiation Technologies, NAS of Ukraine
M. Eseev JINR, Dubna and M.V. Lomonosov Pomor State University, Russia

Abstract

The project of the Low Energy Positron Toroidal Accumulator (LEPTA) is under development at JINR. The LEPTA facility is a small positron storage ring equipped with the electron coolin system. The project positron energy is of 2 – 10 keV. The main goal of the facility is to generate an intense flux of positronium atoms – the bound state of electron and positron.

Storage ring of LEPTA facility was commissioned in September 2004 and is under development up to now. The positron injector has been constructed in 2005 ÷ 2010, and beam transfer channel – in 2011. By the end of August 2011 experiments on injection into the ring of electrons and positrons stored in the trap have been started. The recent results are presented here.

LEPTA POSITRON INJECTOR

Positron injector consist of cryogenic slow positron source, positron trap and positron transfer channel (Figure 1).

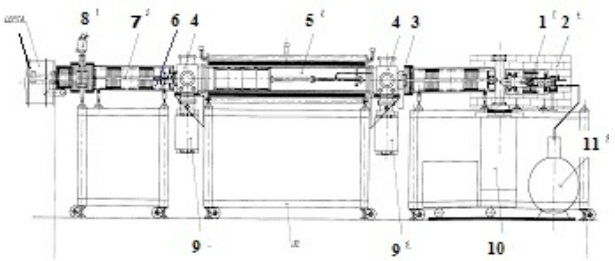

Figure 1: The positron injector. 1 – positron source 22Na, 2 – radioactive shield, 3 – vacuum valve, 4 – vacuum chamber for pumping out and diagnostic tools, 5 – positron trap, 6 – vacuum isolator, 7 – positron vacuum channel, 8 – vacuum "shatter", 9 – ion pump, 10 – turbo pump, 11 – liquid He vessel.

The solid neon is uses as a moderator in the positron source. The positrons lose energy passing thought neon layer and wide energy spectrum of 22Na the thin line of slow positrons is formed.

From the source slow positrons move to the positron trap. We use so called Penning-Malnberg-Surko (PMS) trap. The trap consists of the solenoids, of the vacuum chamber and of the electrodes which form static electric field (Figure 2).

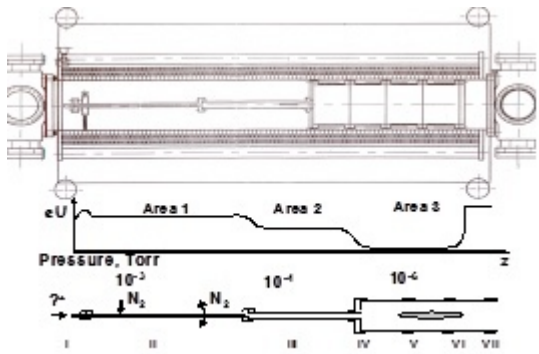

Figure 2: Assembly drawing of the positron trap (upper picture), potential and pressure distributions along the electrode system.

The trap of the LEPTA facility has the traditional geometry of the PMS trap [2]. In 2014, the trap pumping speed was significantly enhanced by implementation of turbo-molecular and cryogenic pumps. The choice of the potentials distribution on the electrodes 1-8 and pressure of the buffer gas (high-purity molecular nitrogen) is critical. At optimal allocation of potentials and pressure positrons, "jumping" on the atomic and molecular levels, very quickly overcome the energy region where the probability of annihilation is maximal (the so-called Ore gap [1]).

Rotating electrical field (RW) is generated in the electrode 4, cut into 4 sectors, which have permanent and (in pairs) alternative potentials. This method allows us to compress bunch and to increase number of particles in the bunch. The accumulation process is well described by the dependence of the number of accumulated particles N_{trap} on accumulation time at fixed values of the efficiency of the particle capture ε, the flux of the injected positrons $\dot{N}$ and the lifetime of the trapped particles τ:

$$N_{trap}(t) = \varepsilon \dot{N} \tau \left(1 - e^{\frac{t}{\tau}}\right) \Rightarrow \begin{cases} \varepsilon \dot{N} \tau, t << \tau \\ \varepsilon \dot{N} \tau, t >> \tau \end{cases} \quad (1)$$

At known flux $\dot{N}$ the, first of the asymptotics in formula (1) allows us to determine the value of the efficiency ε, and the second asymptotics - the value of the τ. Both these values are dependent of buffer gas pressure: ε is increases, τ is decreases but their product increases up to some optimal value of gas pressure. Experimental results are presented in the Table 1.

#kobets@jinr.ru

ISBN 978-3-95450-174-8

Table 1: Dependence of Storage Process Parameters on Buffer Gas Pressure

P, 10^{-6} Torr	τ, sec RW off/RW	ε, % RW off/RW	ε × τ, % × sec
1.5	4,1/10,5	2,3/2,1	9,43/22,05
2	4/9,5	3/2,9	12/27,55
2.5	3,7/9	4,3/3,6	15,91/32,4
4	3,9/8	6,7/6,4	26,13/51,2

Basically new results were obtained in measurements of the "RW spectra", i.e. dependencies of N_{trap} , ε and τ on the frequency of the RW field. For the first time in a unified approach the different modes of the low and high intensities of the injected particle flux and accumulated bunch has been investigated, new low frequency resonances of the RW field causing significant increase in the number of accumulated particles has been found (Fig. 3). The "anti-resonance" at low (of the order of tens of Hz) frequency of the RW field when the rotation of the field leads to the complete destruction of accumulated bunch have been discovered.

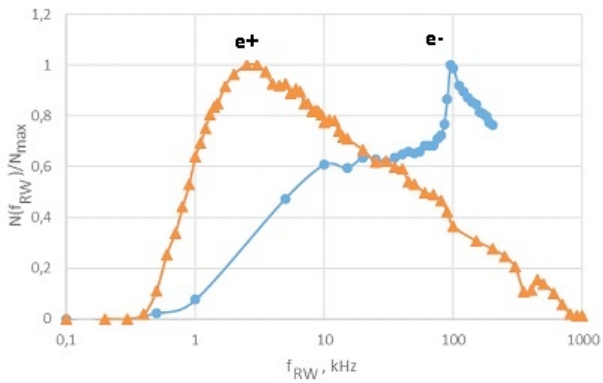

Figure 3: The resonant dependence of the stored particles' number (normalized) – positrons and electrons – on the RW-field frequency (kHz).

We think that RW-field mechanism is rather simple [3]. Charged particle rotates in the RW-field along the circular orbit of the radius

$$R_{RW} = cE_{RW}/B\omega_{RW} >> \rho_L. \quad (2)$$

Here E_{RW} and ω_{RW} are the amplitude and frequency of the RW-field, B is the trap magnetic field, c – the speed of light, ρ_L – the particle Larmor radius. After reflection from potential barrier the particle escapes from RW-field and travel along the trap magnetic field until it reaches the exit potential barrier. Reflected on it the particle returns into RW field at certain phase of the field rotation.

When traveling in the trap the particle rotates around the trap axis in the crossed fields B and Er – radial component of the electric fields of the trap electrodes and the bunch space charge ("magnetron rotation"). In the RW-field the particle has time to move along a short arc of the circular orbit. If after traveling in the trap it returns into RW-field at optimal phase of RW-field and "magnetron rotation" it will continue its way in the same direction as in the previous "round". When traveling ("bouncing") in the trap the particle loses its energy in the collisions with the buffer gas atoms (the "frictional cooling" again!). As result, the length of the arcs is decreasing and finally the particle does not penetrate into RW-field that is overlapped with the potential barrier of the sectioned electrode. And the particle looks as a small Larmor circle.

With the increase of the intensity, the azimuthal drift in crossed fields of the bunch space charge and longitudinal magnetic field plays the decisive role and increases the resonant frequency (Figure 4).

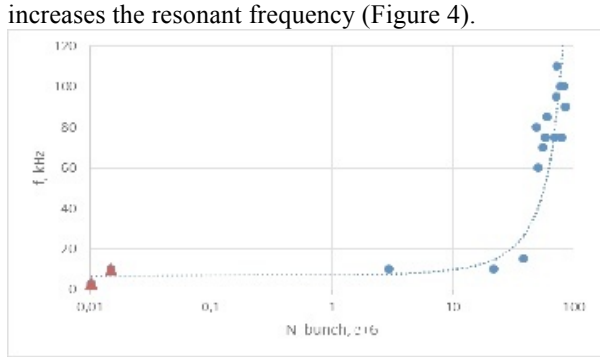

Figure 4: Dependence resonant frequency of RW-field vs number of particles in the stored bunch.

THE POSITRON ANNIHILATION SPECTROSCOPY

Another application of LEPTA positron injector is Positron Annihilation Spectroscopy (PAS). The method of the doppler broadening of the annihilation gamma line have been developed. This method allow us to study defects concentration in the matter depending of depth. The laboratory for the samples preparation has been equipped with the different tools (sendblast apparatus, vacuum oven and press).

Positron Injector Development

Now positron injector is under development. The main problems we have: deficit of liquid helium, low vacuum conditions and low intensity of slow positron flux.

We have bought cryocooler and designed and constructed the new cryogenic source (Figure 5).

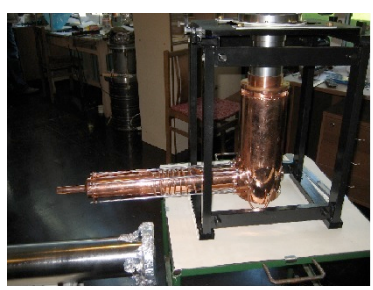

Figure 5: The new cryogenic source.

ISBN 978-3-95450-174-8

It allow us to have closed loop of the positron source cooling. Also we designed new channel for PAS (Figure 6).

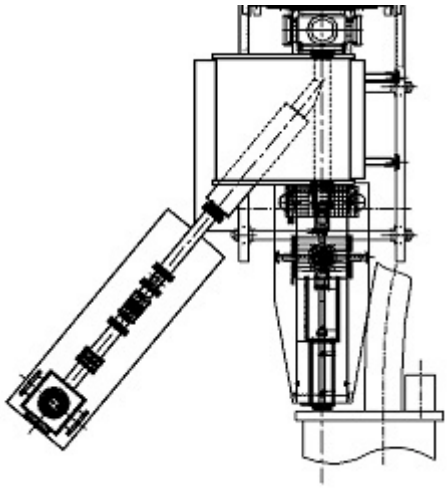

Figure 6: The new PAS channel drawing.

Now all elements of vacuum system and some elements of magnetic system are fabricated.

CONCLUDING REMARKS

The development of the LEPTA project is approaching the stage of experiments with circulating positron beam. The development of positron injector will allow us to study materials separately from investigations of storage process in the trap.

REFERENCES

[1] C. M. Surko, M. Leventhal, and A. Passner, Phys. Rev. Lett. 62, 901 (1989).
[2] M. K. Eseev, A. G. Kobets, I. N. Meshkov, A. Yu. Rudakov, and S. L. Yakovenko, Plasma Phys. Rep. 39(10), 787 (2013).
[3] M.Eseev, A.Kobets, I.Meshkov. A.Sidorin, O.Orlov, JETP Lett., v. 192 (2015) 291.

ISBN 978-3-95450-174-8

COMMISSIONING OF THE RARE-RI RING AT RIKEN RI BEAM FACTORY

Y. Yamaguchi*, Y. Abe, F. Suzaki, M. Wakasugi, and Rare-RI Ring collaborators
RIKEN Nishina Center, Wako, Japan

Abstract

The Rare-RI Ring is an isochronous storage ring to measure masses of short-lived rare nuclei by using relative TOF measurement method. The expected precision of the measured mass is of the order of ppm.

We examined the basic performance of the devices, i.e. injection line, septum magnets, dipole magnets with trim-coils, and fast-kicker system by using α-source in 2014. We demonstrated that trim-coils, which are fixed on the dipole magnets of the ring, can adjust the isochronous condition of the ring. An α-particle was injected into the ring individually by using self-trigger mechanism and was extracted from the ring several turns after the injection.

In June 2015, a commissioning run using a ^{78}Kr beam was performed and basic performances of the Rare-RI Ring were verified. We succeeded in injecting a particle, which was randomly produced from a DC beam using cyclotrons, into the ring individually with the fast-kicker system, and in extracting the particle from the ring less than 1 ms after the injection with same kicker system. We measured time-of-flight (TOF) of the ^{78}Kr particles between the entrance and the exit of the ring to check the isochronism. Through the first-order adjustment with trim-coils, the isochronism on the 10-ppm order was achieved for the momentum spread of ±0.2%. Higher-order adjustment employed in future will lead us to the isochronism on the order of ppm. In addition, we confirmed that a resonant Schottky pick-up successfully acquired the frequency information of one particle in storage mode.

In this paper, the technical aspects of the Rare-RI Ring and the preliminary results of the beam commissioning will be described.

INTRODUCTION

Systematic mass measurements, especially for neutron-rich exotic nuclei very far from the stability, are essential for solving the r-process path. However, nuclei in such regions have very short half-lives and have a very low production rate even with the powerful accelerator complex in RI Beam Factory, therefore, very fast and sensitive apparatus is needed. To this end, we have proposed a unique apparatus, the so called "Rare-RI Ring" about 10 years ago [1], to precisely measure masses of such rare-RIs.

Figure 1 shows the conceptual design of mass measurement by using the Rare-RI Ring. When a produced secondary particle passes through the timing detector at F3 of the BigRIPS separator [2], a trigger signal is generated. The trigger signal is transmitted to a fast-kicker system via a high speed coaxial tube. Kicker magnets are then immediately excited by thyratrons. In the meanwhile, the particle goes through the BigRIPS separator, the SHARAQ spectrometer [3], and an injection line. The particle that arrives at the entrance of the ring is injected into an equilibrium orbit of the ring using septum and kicker magnets. After the particle revolves in the ring about 700 μs, it is extracted using another septum and the same kicker magnets to measure TOF. In the end, it is identified by ΔE-E detectors. In addition to the short measurement time, this method enables us to measure the mass of even one particle which is suited to measure masses in the r-process region.

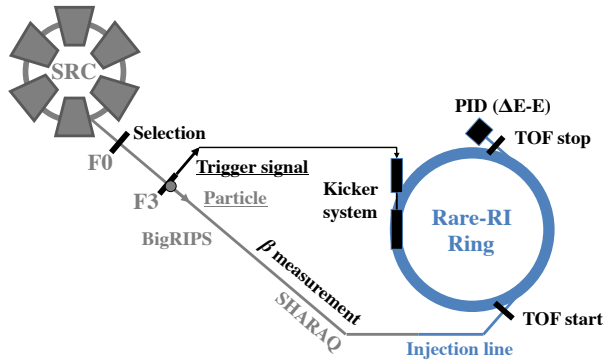

Figure 1: Conceptual design of mass measurement with the Rare-RI Ring.

PRINCIPLE OF MASS MEASUREMENTS

We adopted the relative mass measurements with references in Isochronous Mass Spectrometry (IMS). In IMS, orbital of the particle is determined by its rigidity. If the rigidity of the particles to be obtained the mass (m_1/q) is the same as that of the reference particle (m_0/q), the flight-pass lengths are identical and the following equations are fulfilled:

$$\frac{m_0}{q}\gamma_0\beta_0 = \frac{m_1}{q}\gamma_1\beta_1, \tag{1}$$

$$\beta_0 T_0 = \beta_1 T_1, \tag{2}$$

where $m_{0,1}/q$ are mass-to-charge ratio, $T_{0,1}$ and $\beta_{0,1}$ are the revolution time and the velocity of the particles with $m_{0,1}/q$ and $\gamma_{0,1} = 1/\sqrt{1-\beta_{0,1}^2}$. By using Eq. (1) and (2), the m_1/q can be expressed as

$$\frac{m_1}{q} = \frac{m_0}{q}\frac{T_1}{T_0}\frac{\gamma_0}{\gamma_1} = \frac{m_0}{q}\frac{T_1}{T_0}\sqrt{\frac{1-\beta_1^2}{1-(\frac{T_1}{T_0}\beta_1)^2}}. \tag{3}$$

* yamaguch@ribf.riken.jp

ISBN 978-3-95450-174-8

The relative uncertainty of m_1/q is given by

$$\frac{\delta(m_1/q)}{m_1/q} = \frac{\delta(m_0/q)}{m_0/q} + \gamma_0^2 \frac{\delta(T_1/T_0)}{T_1/T_0} + k\frac{\delta\beta_1}{\beta_1}, \quad (4)$$

where

$$k = -\frac{\beta_1^2}{1-\beta_1^2} + (\frac{T_1}{T_0})^2 \frac{\beta_1^2}{1-(T_1/T_0)^2\beta_1^2}. \quad (5)$$

Because the isochronism is basically adjusted to the reference particle, the isochronism for the particle of m_1/q is slightly different. Then the velocity measurement is essential. The coefficient k is on the order of 10^{-2} for $\delta(m/q) \sim \delta T \sim 1\%$. Therefore, mass of the particle within a m/q difference of 1% can be determined with an order of 10^{-6} precision by measuring $T_{0,1}$ with an accuracy of better than 10^{-6} and β_1 with an accuracy of better than 10^{-4} independently, under the condition that the isochronism for a reference particle is optimized with an order of 10^{-6} precision.

THE RARE-RI RING

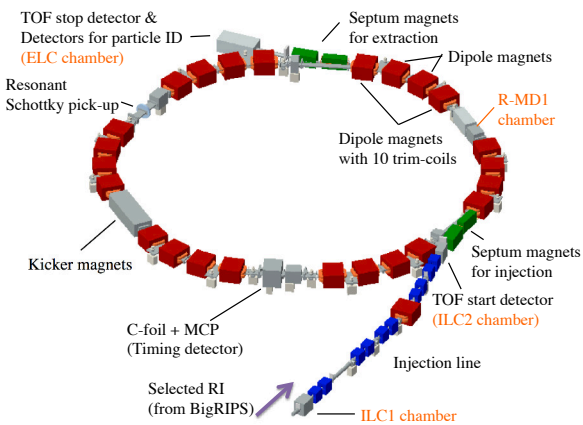

Figure 2: Components of Rare-RI Ring.

Figure 2 shows the components of the Rare-RI Ring. Injection line consists of five quadrupole doublets and one dipole. TOF start detector is located in the ILC2 chamber (see Fig. 2), in addition to two septa for injecting the particles. The ring consists of six magnetic sectors, each consisting of four dipoles. There is no quadrupole for the ring. This dipole is a rectangular magnet with a radially homogeneous magnetic field. The circumference of the ring is about 60.35 m, and the length of a straight section is about 4.02 m. Kicker magnets are located in the position of the phase advance $3\pi/2$ from the injection septa, and the extraction septa are located in the position of the phase advance $3\pi/2$ from the kicker magnets. In order to ensure an isochronism of the ring by making a gradient magnetic field, the two outer dipoles of each magnetic sector were equipped each by ten trim-coils. The ring has beam diagnostic devices in each straight section. Plastic scintillation counters located in all straight sections to check the injection trajectory. Resonant Schottky pick-up [4] and MCP [5] devices are used to measure the frequency of the revolving particle. Figure 3 shows the bird's-eye view photograph of the Rare-RI Ring.

Figure 3: Bird's-eye view photograph of Rare-RI Ring.

Technical Challenges

The individual injection method, which has been proposed in Ref. [6], is a crucial technique for injecting a rare particle into the ring. In order to realize the individual injection, kicker magnets must be excited before the particle arrives at the kicker magnets. For this purpose we constructed a high speed coaxial tube to transmit the trigger signal from F3 of the BigRIPS separator to the kicker system as fast as possible and a fast-response mechanism with thyratron switch to excite the kicker magnets as soon as possible. In addition, fast recharge is necessary to extract a particle from the ring in 700 μs by using same kicker magnets. Therefore, we developed a fast-recharging mechanism, the so called "hybrid charging system", which has main and sub part. Figure 4 shows an example of one set of the Pulse Forming Network (PFN) charging waveform for injection/extraction by using the hybrid charging system. Main part provides

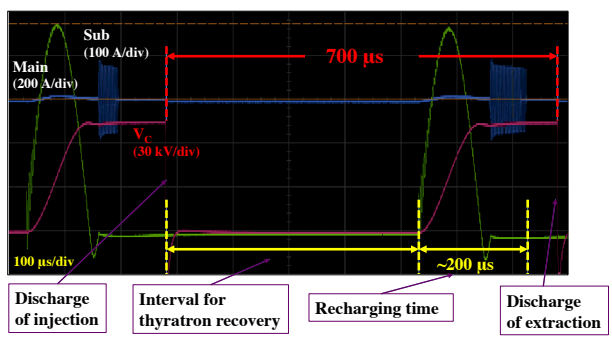

Figure 4: One set of PFN charging waveform for injection/extraction by using the hybrid charging system. Green, blue and red lines indicate the current of main charger, current of sub charger, and PFN charging voltage Vc, respectively.

90% of the charging voltage, and the remaining 10% is supplied by sub part of the system. Sub part works to maintain

ISBN 978-3-95450-174-8

a constant charging voltage level within the range of fluctuation of less than ±1%. The time of recharge by this system is achieved in 200 μs. The details of the fast-kicker system can be found in Ref. [7].

Second challenge concerns the isochronous adjustment using trim-coils. We recently performed the isochronous adjustment of the ring with α-particles by using trim-coils. The α-source (^{241}Am) was installed on the central orbit of the ring in the R-MD1 chamber (see Fig. 2). Two detectors were installed just before/after the α-source to measure the TOF of one turn. Then, we checked the condition of the isochronism based on the TOF width. Figure 5 shows

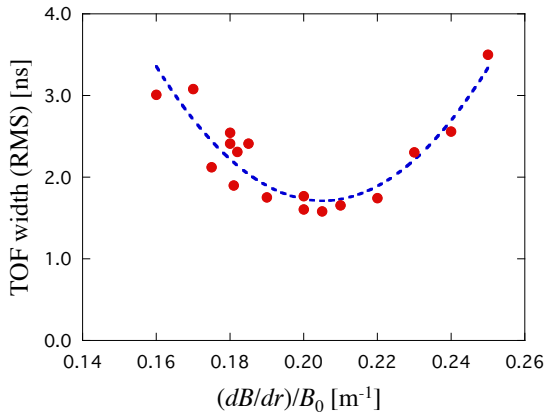

Figure 5: TOF width of one turn of α-particles as a function of the first-order trim field $(dB/dr)/B_0$.

the results of the TOF width as a function of the first-order trim field ($(dB/dr)/B_0$). The minimum value of the TOF width is obtained with $(dB/dr)/B_0 = 0.205$ m^{-1}. This is consistent with the results calculated by using the α-source energies, which confirmes that the trim-coils play the role of adjusting the isochronism. The details of the study by using the α-source can be found in Ref. [8].

BEAM COMMISSIONING

In June 2015, we performed a beam commissioning using ^{78}Kr with 168 MeV/u, the energy of which matches to the individual injection. Specifications of the ring for this commissioning are given in Table 1.

Table 1: Specifications of the Ring for this Commissioning

Transition γ_{tr}	1.18
Betatron tune	$\nu_x = 1.18$, $\nu_y = 0.93$
Beta function	$\beta_x = 8.4$ m, $\beta_y = 11.9$ m
Dispersion	7.0 m
Kick angle	11 mrad

First, we transported the beam to the ring with a dispersion matching at the center of kicker magnets in accordance with the optical calculations. After that, we injected ^{78}Kr particles individually on the equilibrium orbit of the ring using the fast-kicker system. We confirmed the periodic signals of the circulating particles with the MCP, which is located on the closed orbit of the ring. Figure 6 shows the TDC (Aquiris TC890) spectrum for circulating particles. The particle cannot be stored for long time and it's lost after 25 μs due to the penetration efficiency at the MCP material. After removing the MCP from the closed orbit, we succeeded in extracting the circulating particles from the ring after 700 μs.

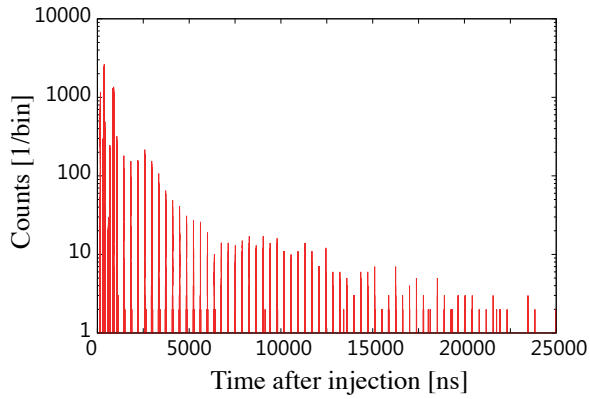

Figure 6: TDC (Aquiris TC890) spectrum for circulating particles.

Isochronism

Figure 7 shows the TOF of ^{78}Kr particles as a function of the momentum spread with different values of the $(dB/dr)/B_0$. We understand from this figure that the ex-

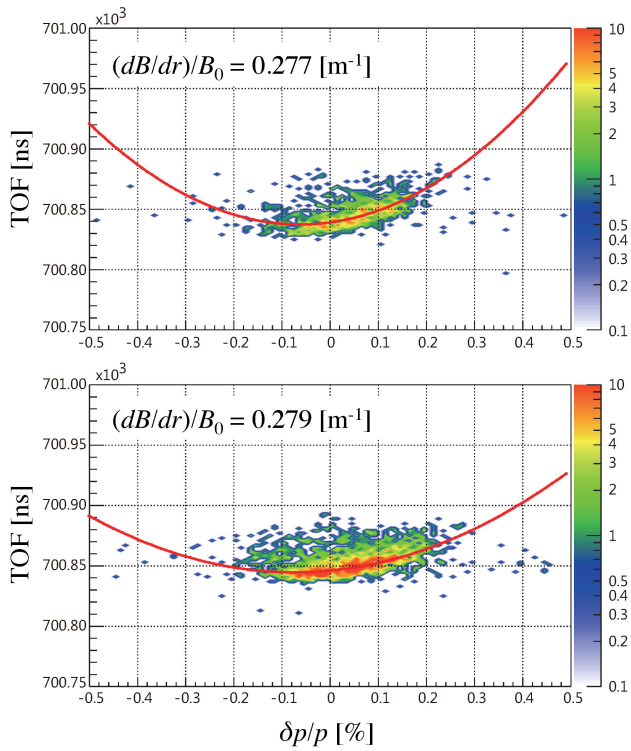

Figure 7: TOF spectra as a function of the momentum spread with different value of $(dB/dr)/B_0$. Red lines shows the quadratic fitting curve of TOF spectra.

ISBN 978-3-95450-174-8

tractable momentum spread is about ±0.2 %. The TOF width of $(dB/dr)/B_0 = 0.279\ \mathrm{m}^{-1}$ is about 25 ns in FWHM as a result of fitting in the projection on the vertical axis. Therefore, the degree of isochronism is about 3.5×10^{-5} for the momentum spread of ±0.2 %.

The value of $(dB/dr)/B_0 = 0.279\ \mathrm{m}^{-1}$ is an optimum value by using a numerical analysis. However, the experimental optimum value of it may be a little bigger since the quadratic curve is still not symmetry. We haven't enough time to tune the first-order trim field any further, but we were able to achieve a 10-ppm isochronism by adjusting the first-order trim field.

Resonant Schottky Pick-up

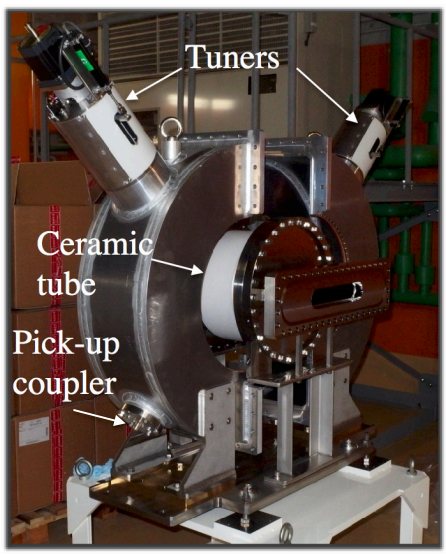

Figure 8: Photograph of resonant Schottky pick-up.

Resonant Schottky pick-up consists of a pillbox-type resonant cavity and ceramic gap, as shown in Fig. 8. Outer diameter, length, and inner diameter of the cavity are 750 mm, 200 mm, and 320 mm, respectively. When a particle pass through the resonant Schottky pick-up, an electromagnetic field is induced in the cavity. The change of magnetic flux in the induced electromagnetic field is detected by a pick-up loop. The coupling factor of the pick-up loop was optimized to be one. By adjusting the position of two tuners, the resonance frequency can change in the range of 173±1.5 MHz. In addition, the shunt impedance Rsh is 161 kΩ and the unloaded quality factor Q_0 is 1880, respectively.

In this beam commissioning, we verified that a resonant Schottky pick-up successfully acquired the frequency information of one ^{78}Kr particle in a storage mode. The frequency resolution is about 1.3×10^{-6} in FWHM, which is sufficient resolution as a monitor for the isochronous adjustment.

A particle was stored in the ring about 4 seconds while changing its frequency, as shown in Fig. 9. The change in frequency is due to the poor degree of vacuum in the ring, and the shape of curve is influenced by the isochronism for

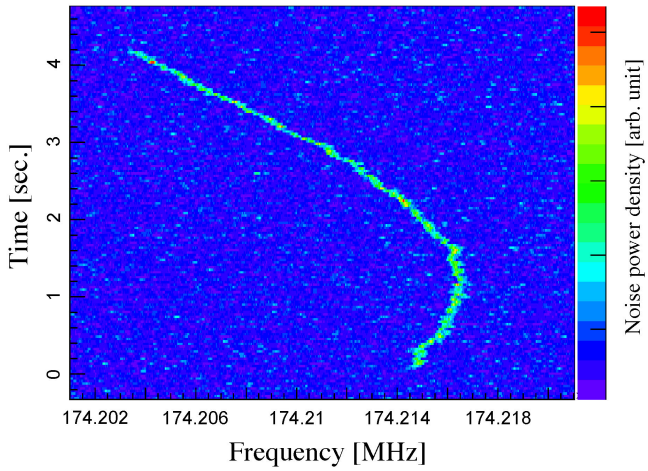

Figure 9: Frequency information of one ^{78}Kr particle from resonant Schottky pick-up.

each momentum. Black line in Fig. 10 shows the Schottky data obtained by converting Fig. 9 to understand this phenomena. The revolution time was calculated from the resonance frequency using the number of harmonics. The degree of vacuum was about 4×10^{-5} at the worst point in the ring, and we assumed H_2O as a residual gas to calculate the momentum. The tendency of the black line is consistent with that of the quadratic fitting curve of TOF spectrum.

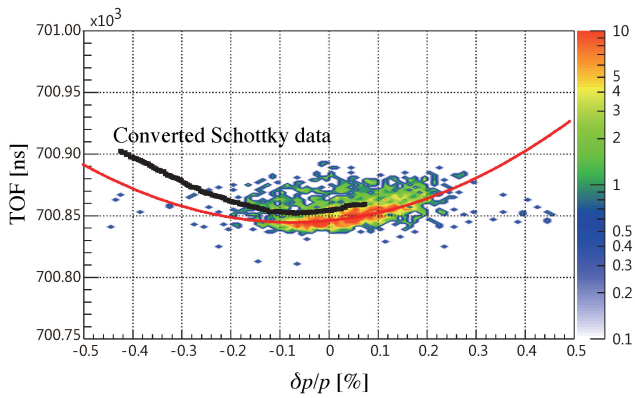

Figure 10: Black line shows converted Schottky data coupled with the result of TOF spectrum of $(dB/dr)/B_0 = 0.279\ \mathrm{m}^{-1}$.

SUMMARY AND PROSPECTS

^{78}Kr beam commissioning run was conducted successfully and the off-line analysis is in progress. First-oder trim field can adjust the isochronism in an order of 10-ppm. To achieve more higher isochronism, we will perform second-order adjustment with trim-coils. Then, the resonant Schottky pick-up can be used for checking the isochronism.

We are planning the next commissioning using the secondary particles to verify the principle of mass measurements in December 2015. The mass measurement experiments will start from 2016. On the other hand, the life-

ISBN 978-3-95450-174-8

time measurement of rare-RIs using the resonant Schottky pick-up is also planned. We need to improve the degree of vacuum in the ring by baking to do it. In the future, we will also be carried out the nuclear reaction experiments, such as proton elastic scattering and so on, using an internal target with a RF cavity.

ACKNOWLEDGMENT

Beam commissioning was performed at RI Beam Factory operated by RIKEN Nishina Center and CNS, University of Tokyo. This work was partially supported by JSPS KAKENHI no. 26287036.

REFERENCES

[1] Y. Yamaguchi, et al., "Rare-RI ring project at RIKEN RI beam factory", Nucl. Instrum. and Methods, B266, 4575 (2008).

[2] T. Kubo, "In-flight RI beam separator BigRIPS at RIKEN and elsewhere in Japan", Nucl. Instrum. and Methods, B204, 97 (2003).

[3] T. Uesaka, et al., "The SHARAQ spectrometer", Prog. Theor. Exp. Phys, 03C007 (2012).

[4] F. Suzaki, et al., "Performance of a resonant Schottky pick- up for Rare-RI Ring project", JPS Conf. Proc. 6, 030119 (2015).

[5] Y. Abe, et al.,"Developments of time-of-flight detectors for Rare-RI Ring", JPS Conf. Proc. 1, 013059 (2014).

[6] I. Meshkov, et al., "Individual rare radioactive ion injection, cooling and storage in a ring", Nucl. Instrum. and Methods, A523, 262 (2004).

[7] Y. Yamaguchi, et al., "Fast-kicker system for rare-RI ring", Proc. of STORI'14, Sankt Goar, Germany (2014).

[8] Y. Abe, et al., "Isochronous field study of the Rare-RI Ring", Proc. of STORI'14, Sankt Goar, Germany (2014).

ISBN 978-3-95450-174-8

List of Authors

Bold papercodes indicate primary authors

ISBN 978-3-95450-174-8

ISBN 978-3-95450-174-8

ISBN 978-3-95450-174-8

ISBN 978-3-95450-174-8

Institutes List

Aarhus University
Aarhus, Denmark
- Drewsen, M.
- Hansen, A.K.

Albert Einstein, Leibniz Universität
Hannover, Germany
- Schmidt, P.O.

Allrussian Electrotechnical Institute
Moskow, Russia
- Kokurkin, M.N.
- Lysov, N.Yu.

ANL
Argonne, USA
- Erdelyi, B.
- Sun, Y.

BINP SB RAS
Novosibirsk, Russia
- Bryzgunov, M.I.
- Bubley, A.V.
- Chekavinskiy, V.A.
- Gusev, I.A.
- Ivanov, A.V.
- Kondaurov, M.N.
- Morozov, I.A.
- Panasyuk, V.M.
- Parkhomchuk, V.V.
- Pureskin, D.N.
- Putmakov, A.A.
- Reva, V.B.
- Senkov, D.V.
- Skorobogatov, D.N.
- Skrinsky, A.N.

BNL
Upton, Long Island, New York, USA
- Ben-Zvi, I.
- Blaskiewicz, M.
- Brennan, J.M.
- Fedotov, A.V.
- Kayran, D.
- Kewisch, J.
- Litvinenko, V.
- Mernick, K.
- Montag, C.
- Palmer, R.B.
- Pinayev, I.
- Ptitsyn, V.
- Sheehy, B.
- Stratakis, D.
- Wang, E.
- Wang, G.
- Xu, W.

CERN
Geneva, Switzerland
- Belochitskii, P.
- Eriksson, T.
- Jørgensen, L.V.
- Nissen, E.W.
- Thorndahl, L.
- Tranquille, G.

CPPM
Marseille, France
- Pedregosa, J.

Fermilab
Batavia, Illinois, USA
- Alexahin, Y.I.
- Bowring, D.L.
- Burov, A.V.
- Lebedev, V.A.
- Moretti, A.
- Nagaitsev, S.
- Neuffer, D.V.
- Palmer, M.A.
- Piot, P.
- Prebys, E.
- Romanov, A.L.
- Ruan, J.
- Stancari, G.
- Tollestrup, A.V.
- Valishev, A.
- Yonehara, K.
- Zolkin, T.

FRIB
East Lansing, Michigan, USA
- Wei, J.

FZJ
Jülich, Germany
- Breitkreutz, B.
- Halama, A.J.
- Kamerdzhiev, V.
- Katayama, T.
- Lorentz, B.
- Maier, R.
- Prasuhn, D.
- Schug, G.
- Stassen, R.
- Stockhorst, H.

GSI
Darmstadt, Germany
- Barker, D.
- Boine-Frankenheim, O.

ISBN 978-3-95450-174-8

- Böhm, R.M.
- Dimopoulou, C.
- Eidam, L.
- Hettrich, R.
- Katayama, T.
- Maier, W.
- Menges, R.
- Nolden, F.
- Peschke, C.
- Roßbach, J.
- Steck, M.
- Stuhl, A.
- Winters, D.F.A.
- Wunderlich, S.

GWU
Washington, USA
- Afanasev, A.

Heidelberg University, Physics Institute
Heidelberg, Germany
- Klawitter, R.

Helmholtz-Zentrum Dresden-Rossendorf (HZDR), Institute of Radiation Physics
Dresden, Germany
- Schramm, U.
- Siebold, M.

HIM
Mainz, Germany
- Aulenbacher, K.
- Bruker, M.W.
- Dietrich, J.
- Hofmann, A.
- Weilbach, T.

Hiroshima University
Higashi-Hiroshima, Japan
- Higaki, H.

HU/AdSM
Higashi-Hiroshima, Japan
- Okamoto, H.

HZDR
Dresden, Germany
- Bussmann, M.H.
- Löser, M.

IIT
Chicago, Illinois, USA
- Freemire, B.T.
- Mohayai, T.A.
- Torun, Y.

IKP
Mainz, Germany
- Aulenbacher, K.

Illinois Institute of Technology
Chicago, Illinois, USA
- Kaplan, D.M.

IMP/CAS
Lanzhou, People's Republic of China
- Chai, W.P.
- Chuai, X.
- Hai, B.
- He, Y.
- Hu, X.J.
- Huang, Y.L.
- Huang, Z.
- Li, J.
- Li, P.
- Li, X.N.
- Ma, X.M.
- Ma, X.
- Mao, L.J.
- Mao, R.S.
- Shen, G.D.
- Sheng, L.N.
- Sun, L.T.
- Tang, M.T.
- Wang, H.
- Wen, W.Q.
- Wu, J.X.
- Xia, J.W.
- Xiao, G.Q.
- Xu, H.S.
- Yan, T.L.
- Yang, J.C.
- Yang, J.
- Yang, W.Q.
- Yang, X.D.
- Yin, D.Y.
- Yuan, Y.J.
- Zhan, W.-L.
- Zhang, D.
- Zhao, D.
- Zhao, H.W.
- Zhao, H.
- Zhou, X.H.
- Zhu, X.

INFN-Napoli
Napoli, Italy
- Palladino, V.C.

Institut für Kernphysik, Westfälische Wilhelms-Universität Münster
Münster, Germany
- Frekers, D.

ISBN 978-3-95450-174-8

JINR
Dubna, Moscow Region, Russia
- Ahmanova, E.V.
- Butenko, A.V.
- Horodek, P.
- Khodzhibagiyan, H.G.
- Kobets, A.G.
- Meshkov, I.N.
- Orlov, O.
- Shokin, V.I.
- Shurkhno, N.
- Sidorin, A.A.
- Sidorin, A.O.
- Trubnikov, G.V.
- Yakovenko, S.

JLab
Newport News, Virginia, USA
- Benson, S.V.
- Bogacz, S.A.
- Chen, J.
- Derbenev, Y.S.
- Douglas, D.
- Guo, J.
- Hannon, F.E.
- Hutton, A.
- Kimber, A.J.
- Li, R.
- Lin, F.
- Marhauser, F.
- Morozov, V.S.
- Musson, J.
- Poelker, M.
- Rimmer, R.A.
- Sy, A.V.
- Tennant, C.
- Tsai, C.-Y.
- Wang, H.
- Wang, S.
- Wei, G.H.
- Zhang, H.
- Zhang, Y.

LBNL
Berkeley, California, USA
- Wurtele, J.S.

MPI-K
Heidelberg, Germany
- Crespo López-Urrutia, J.R.
- Feuchtenbeiner, S.
- Micke, P.
- Piest, B.
- Schmöger, L.
- Schwarz, M.
- Versolato, O.O.
- Windberger, A.
- Wolf, A.

MPI
Muenchen, Germany
- Schupp, R.

Muons, Inc
Illinois, USA
- Johnson, R.P.

NAFU
Arkhangelsk, Russia
- Eseev, M.K.

Nihon University
Narashino, Chiba, Japan
- Katayama, T.

Northern Illinois University
DeKalb, Illinois, USA
- Abeyratne, S.
- Andorf, M.B.
- Erdelyi, B.
- Maloney, J.A.
- Piot, P.

NSU
Novosibirsk, Russia
- Reva, V.B.

ODU
Norfolk, Virginia, USA
- Huang, H.
- Luo, L.

ORNL
Oak Ridge, Tennessee, USA
- Cousineau, S.M.
- Gorlov, T.V.
- Liu, Y.
- Menshov, A.A.
- Plum, M.A.
- Rakhman, A.

PSI
Villigen PSI, Switzerland
- Knecht, A.

PTB
Braunschweig, Germany
- Kohnen, M.
- Leopold, T.
- Micke, P.
- Schmidt, P.O.
- Schmöger, L.
- Schwarz, M.
- Ullrich, J.

ISBN 978-3-95450-174-8

RadiaSoft LLC
Boulder, Colorado, USA
- Bruhwiler, D.L.

RIKEN Nishina Center
Wako, Japan
- Suzaki, F.
- Wakasugi, M.

RIKEN
Saitama, Japan
- Abe, Y.
- Ohnishi, T.
- Wakasugi, M.
- Watanabe, M.
- Yamaguchi, Y.

Rikkyo University
Tokyo, Japan
- Enokizono, A.
- Kurita, K.

SFU
Burnaby, BC, Canada
- Andreoiu, C.

Skyworks Solutions, Inc.
Newbury Park. California, USA
- Li, X.-P.

STFC/RAL/ASTeC
Chilton, Didcot, Oxon, United Kingdom
- Rogers, C.T.

Stony Brook University
Stony Brook, USA
- Ben-Zvi, I.
- Deshpande, A.
- Kayran, D.
- Litvinenko, V.
- Ptitsyn, V.

Tech-X
Boulder, Colorado, USA
- Bell, G.I.
- Pogorelov, I.V.

Texas A&M University
College Station, USA
- Gerity, J.
- McIntyre, P.M.

Tohoku University, Research Center for Electron Photon Science
Sendai, Japan
- Suda, T.
- Tamae, T.
- Tsukada, K.

TRIUMF, Canada's National Laboratory for Particle and Nuclear Physics
Vancouver, Canada
- Barquest, B.
- Chowdhury, U.
- Even, J.
- Good, M.
- Kootte, B.A.
- Kwiatkowski, A.A.
- Lascar, D.
- Leach, K.G.
- Lennarz, A.
- Maloney, J.A.
- Short, D.A.

TU Darmstadt
Darmstadt, Germany
- Birkl, G.
- Rein, B.
- Walther, T.

TU Dresden
Dresden, Germany
- Schramm, U.

UBC & TRIUMF
Vancouver, British Columbia, Canada
- Bale, J.
- Dilling, J.
- Finlay, A.
- Gallant, A.A.
- Leistenschneider, E.

UMiss
University, Mississippi, USA
- Acosta, J.G.
- Cremaldi, L.M.
- Hart, T.L.
- Oliveros, S.J.
- Summers, D.J.

Universität Muenster, Physikalisches Institut
Muenster, Germany
- Alanssari, M.

University of Calgary
NW Calgary, Alberta, Canada
- Mayer, A.J.

ISBN 978-3-95450-174-8

University of Chicago
Chicago, Illinois, USA
- Kochemirovskiy, A.V.

University of Manitoba
Manitoba, Canada
- Gwinner, G.

UW/Physics
Waterloo, Ontario, Canada
- Li, T.T.

Virginia Polytechnic Institute and State University
Blacksburg, Virginia, USA
- Tsai, C.-Y.

ISBN 978-3-95450-174-8

Participants List

ISBN 978-3-95450-174-8